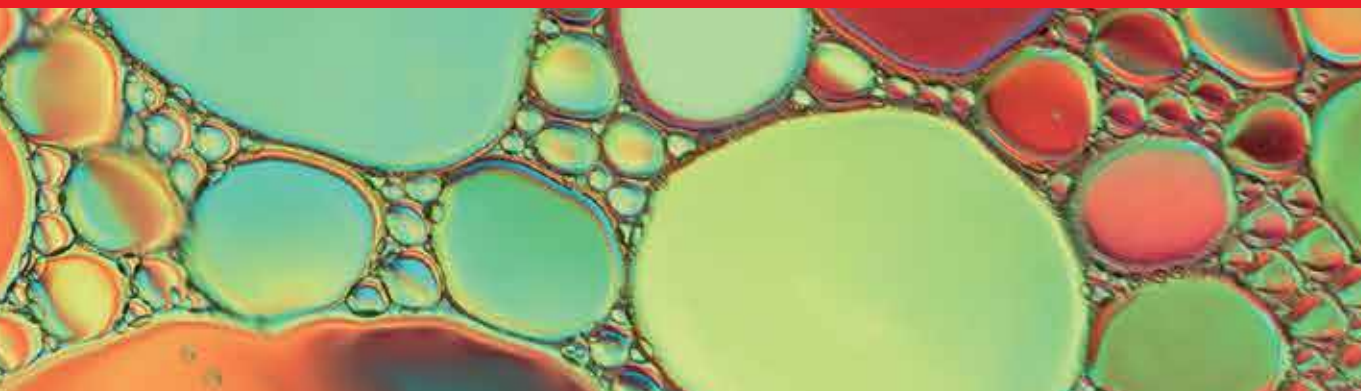


**IntechOpen**

# Computational Fluid Dynamics Technologies and Applications

*Edited by Igor V. Minin and Oleg V. Minin*







---

# **COMPUTATIONAL FLUID DYNAMICS TECHNOLOGIES AND APPLICATIONS**

---

Edited by **Igor V. Minin** and **Oleg V. Minin**

## Computational Fluid Dynamics Technologies and Applications

<http://dx.doi.org/10.5772/686>

Edited by Igor V. Minin and Oleg V. Minin

### Contributors

Lei Xie, Longjiang Shen, Bingyan Jiang, Pradip Majumdar, Muhamad Husaini Abu Bakar, Zahurin Samad, Mohd Rizal Arshad, Behshad Jodeiri Shokri, Faramarz Doulati Ardejani, Kumars Seifpanah Shabani, Raghu Singh, Ernest Baafi, Rodrigo Lopes, Rosa Quinta-Ferreira, Donna Guillen, Piyush Sabharwall, Suzelle Barrington, Mohammad Hossein Mirbagheri, sadegh firoozi, Hossein Bayani, Mojtaba Barzegari, C Bhasker, Oleg Minin, Marek Warzecha, Stephan C. Kaiser, Sören Werner, Christian Löffelholz, Dieter Eibl, Adam Cwudziński

### © The Editor(s) and the Author(s) 2011

The moral rights of the and the author(s) have been asserted.

All rights to the book as a whole are reserved by INTECH. The book as a whole (compilation) cannot be reproduced, distributed or used for commercial or non-commercial purposes without INTECH's written permission.

Enquiries concerning the use of the book should be directed to INTECH rights and permissions department ([permissions@intechopen.com](mailto:permissions@intechopen.com)).

Violations are liable to prosecution under the governing Copyright Law.



Individual chapters of this publication are distributed under the terms of the Creative Commons Attribution 3.0 Unported License which permits commercial use, distribution and reproduction of the individual chapters, provided the original author(s) and source publication are appropriately acknowledged. If so indicated, certain images may not be included under the Creative Commons license. In such cases users will need to obtain permission from the license holder to reproduce the material. More details and guidelines concerning content reuse and adaptation can be found at <http://www.intechopen.com/copyright-policy.html>.

### Notice

Statements and opinions expressed in the chapters are those of the individual contributors and not necessarily those of the editors or publisher. No responsibility is accepted for the accuracy of information contained in the published chapters. The publisher assumes no responsibility for any damage or injury to persons or property arising out of the use of any materials, instructions, methods or ideas contained in the book.

First published in Croatia, 2011 by INTECH d.o.o.

eBook (PDF) Published by IN TECH d.o.o.

Place and year of publication of eBook (PDF): Rijeka, 2019.

IntechOpen is the global imprint of IN TECH d.o.o.

Printed in Croatia

Legal deposit, Croatia: National and University Library in Zagreb

Additional hard and PDF copies can be obtained from [orders@intechopen.com](mailto:orders@intechopen.com)

Computational Fluid Dynamics Technologies and Applications

Edited by Igor V. Minin and Oleg V. Minin

p. cm.

ISBN 978-953-307-169-5

eBook (PDF) ISBN 978-953-51-6020-5

# We are IntechOpen, the world's leading publisher of Open Access books Built by scientists, for scientists

4,000+

Open access books available

116,000+

International authors and editors

120M+

Downloads

151

Countries delivered to

Our authors are among the  
Top 1%

most cited scientists

12.2%

Contributors from top 500 universities



WEB OF SCIENCE™

Selection of our books indexed in the Book Citation Index  
in Web of Science™ Core Collection (BKCI)

Interested in publishing with us?  
Contact [book.department@intechopen.com](mailto:book.department@intechopen.com)

Numbers displayed above are based on latest data collected.  
For more information visit [www.intechopen.com](http://www.intechopen.com)





# Meet the editors



Igor V. Minin is a full Professor in the Department of Information Protection at Novosibirsk State Technical University (NSTU), Russia. Dr. Minin received a B.A. in Physics from the Novosibirsk State University, a PhD in Physics from Leningrad Electro-Technical University in 1986, and a Doctor of science from NSTU in 2002. Dr. Minin has over twenty years of international industrial and academic experience and has played key roles in a number of projects including 3D millimeter wave real-time imaging and antiterrorism applications. He is the author or coauthor of approximately 350 research articles, seven monographs (including *Diffractive optics of millimeter waves* (IOP Publisher, Boston-London, 2004), *Basic Principles of Fresnel Antenna Arrays* (Springer, 2008)), and has been awarded 24 patents and inventions. He is the author of several books and book chapters in technical publications and has been the Editor of several books including *Microwave and Millimeter Wave Technologies Modern UWB antennas and equipment* (InTech, Austria 2010) and *Microwave and Millimeter Wave Technologies from Photonic Bandgap Devices to Antenna and Applications* (InTech, Austria 2010).



Oleg V. Minin received a B.A. in Physics from the Novosibirsk State University, a PhD in Physics from Tomsk State University in 1987 and a Doctor of science from NSTU in 2002. Currently he is a full Professor in the Department of Information Protection at Novosibirsk State Technical University (NSTU), Russia. From 1982 to 2001 he was Chief Research Scientist at the Institute of Applied Physics, Novosibirsk, Russia. Dr. Minin's research interests are in the areas of diffractive optics and antenna experiment (including explosive plasma antenna), millimeter wave and THz photonics and nanophotonics, information security, detection of hidden weapons as well as development of antiterrorism devices, experiment technologies, explosive physics. He is a member of SPIE, COST-284 and COST-ic0603 and he is the author of several books and book chapters in technical publications. For his work Dr. Minin was awarded the Commendation for Excellence in Technical Communications (*LaserFocusWorld*, 2003) and commendation by the Minister of Defense of Russia, 2000.



---

# Contents

---

**Preface XI**

**Part 1 Modern Principles of CFD 1**

Chapter 1 **Calculation Experiment Technology 3**  
Vladilen F. Minin, Igor V. Minin and Oleg V. Minin

Chapter 2 **Application of Lattice Boltzmann Method  
in Fluid Flow and Heat Transfer 29**  
Quan Liao and Tien-Chien Jen

**Part 2 CFD in Physics 69**

Chapter 3 **CFD Applications for Predicting Flow Behavior  
in Advanced Gas Cooled Reactors 71**  
Donna Post Guillen and Piyush Sabharwall

Chapter 4 **CFD for Characterizing Standard and Single-use  
Stirred Cell Culture Bioreactors 97**  
Stephan C. Kaiser, Christian Löffelholz,  
Sören Werner and Dieter Eibl

Chapter 5 **Application of Computational Fluid Dynamics (CFD)  
for Simulation of Acid Mine Drainage Generation  
and Subsequent Pollutants Transportation  
through Groundwater Flow Systems and Rivers 123**  
Faramarz Doulati Ardejani, Ernest Baafi, Kumars Seif Panahi,  
Raghu Nath Singh and Behshad Jodeiri Shokri

Chapter 6 **Computational Flow Modelling of Multiphase Reacting  
Flow in Trickle-bed Reactors with Applications  
to the Catalytic Abatement of Liquid Pollutants 161**  
Rodrigo J.G. Lopes and Rosa M. Quinta-Ferreira



- Chapter 7 **Simulating Odour Dispersion about Natural Windbreaks 181**  
Barrington Suzelle, Lin Xing Jun and Choiniere Denis

**Part 3 CFD in Industrial 217**

- Chapter 8 **Simulation of Three Dimensional Flows in Industrial Components using CFD Techniques 219**  
C. Bhasker

- Chapter 9 **Computational Fluid Dynamics Analysis of Turbulent Flow 255**  
Pradip Majumdar

- Chapter 10 **Autonomous Underwater Vehicle Propeller Simulation using Computational Fluid Dynamic 293**  
Muhamad Husaini, Zahurin Samad and Mohd Rizal Arshad

**Part 4 CFD in Castle 315**

- Chapter 11 **Modelling and Simulation for Micro Injection Molding Process 317**  
Lei Xie, Longjiang Shen and Bingyan Jiang

- Chapter 12 **Simulation of Liquid Flow Permeability for Dendritic Structures during Solidification Process 333**  
S. M. H. Mirbagheri, H. Baiani, M. Barzegari and S. Firoozi

- Chapter 13 **Numerical Modelling of Non-metallic Inclusion Separation in a Continuous Casting Tundish 359**  
Marek Warzecha

- Chapter 14 **Numerical Simulation of Influence of Changing a Dam Height on Liquid Steel Flow and Behaviour of Non-metallic Inclusions in the Tundish 375**  
Adam Cwudziński

---

# Preface

---

One key figure in fluid dynamics was Archimedes (Greece, 287-212 BC). He initiated the fields of static mechanics, hydrostatics, and pycnometry (how to measure densities and volumes of objects). One of Archimedes' inventions is the water screw, which can be used to lift and transport water and granular materials.

Leonardo da Vinci's (Italy, 1452-1519) contributions to fluid mechanics are presented in a nine part treatise (*Del moto e misura dell'acqua*) that covers the water surface, movement of water, water waves, eddies, falling water, free jets, interference of waves, and many other newly observed phenomena.

During 18<sup>th</sup> and 19<sup>th</sup> century period, significant work was done trying to mathematically describe the motion of fluids:

- Daniel Bernoulli (1700-1782) derived Bernoulli's equation.
- Leonhard Euler (1707-1783) proposed the Euler equations, which describe conservation of momentum for an inviscid fluid, and conservation of mass. He also proposed the velocity potential theory.
- Claude Louis Marie Henry Navier (1785-1836) and George Gabriel Stokes (1819-1903) introduced viscous transport into the Euler equations, which resulted in the Navier-Stokes equation. This forms the basis of modern day CFD.
- Osborne Reynolds (1842-1912) introduces Reynolds number, which is the ratio between inertial and viscous forces in a fluid. This governs the transition from laminar to turbulent flow.

Much work was done on refining theories of boundary layers and turbulence in the 20<sup>th</sup> century:

- Ludwig Prandtl (1875-1953): boundary layer theory, the mixing length concept, compressible flows, the Prandtl number, and more.
- Theodore von Karman (1881-1963) analyzed what is now known as the von Karman vortex street.

- Geoffrey Taylor (1886-1975): statistical theory of turbulence and the Taylor microscale.
- Andrey Kolmogorov (1903-1987): the Kolmogorov scales and the universal energy spectrum.
- George Keith Batchelor (1920-2000): contributions to the theory of homogeneous turbulence.

In 1922, Lewis Fry Richardson developed the first numerical weather prediction system:

- Division of space into grid cells and the finite difference approximations of Bjerknæs's "primitive differential equations."
- His own attempt to calculate weather for a single eight-hour period took six weeks and ended in failure.

During the 1960s the theoretical division at Los Alamos contributed many numerical methods that are still in use today, such as the following methods:

- Particle-In-Cell (PIC).
- Marker-and-Cell (MAC).
- Vorticity-Streamfunction Methods.
- Arbitrary Lagrangian-Eulerian (ALE).

Hence these methods were taken up as a basis for developing a new method – the method of individual particles (1979, developed under the scientific leaderships of Prof. Vladilen F. Minin, Russia) to extend the areas of applicability of the particle methods.

The development of modern computational fluid dynamics (CFD) began with the advent of the digital computer in the early 1950s. CFD is the science of determining a numerical solution to the governing equations of fluid flow whilst advancing the solution through space and time to obtain a numerical description of the complete flow field of interest. CFD is becoming a critical part of the design process for more and more companies. CFD makes it possible to evaluate velocity, pressure, temperature, and species concentration of fluid flow throughout a solution domain, allowing the design to be optimized prior to the prototype phase. So CFD is developing rapidly in its technology and applications. Its use can cut design times, increase productivity and give significant insight to fluid flows. On the other hand Computational Fluid Dynamics has traditionally been one of the most demanding computational applications. It has therefore been the driver for the development of the most powerful computers.

This book is planned to publish with an objective to provide a state-of-art reference book in the area of computational fluid dynamics for CFD engineers, scientists, applied physicists and post-graduate students. Also the aim of the book is the continuous and timely dissemination of new and innovative CFD research and developments.

This reference book is a collection of 14 chapters characterized in 4 parts: modern principles of CFD, CFD in physics, industrial and in castle.

This book provides a comprehensive overview of the computational experiment technology, numerical simulation of the hydrodynamics and heat transfer processes in a two dimensional gas, application of lattice Boltzmann method in heat transfer and fluid flow, etc.

Several interesting applications area are also discusses in the book like underwater vehicle propeller, the flow behavior in gas-cooled nuclear reactors, simulation odour dispersion around windbreaks and so on.

Editors:

**Prof. Dr. Igor V. Minin**

**Prof. Dr. Oleg V. Minin**

Department of Information Protection  
at Novosibirsk State Technical University (NSTU)  
Russia



# **Part 1**

## **Modern Principles of CFD**





# Calculation Experiment Technology

Vladilen F. Minin, Igor V. Minin and Oleg V. Minin  
*Novosibirsk State Technical University*  
*Russia*

## 1. Introduction

There are two common approaches for numerical solution of continuum equations in mechanics: Lagrangian and Eulerian. The choice usually depends on exploiting specific features of these approaches that are suitable for the problem at hand. In the Lagrangian approach the computational grid that discretizes the domain deforms with the material. However Lagrangian method is not suitable for applications involving large distortion and large rotation, or for cases where boundary itself is modified as the solution proceeds. On the other hand, in the Eulerian approach the computational grid is fixed in space. The material moves through this grid as it flows and deforms. Even though large distortions are handled easily in this method, interface tracking and contact surface algorithms pose considerable difficulty.

Novel methods have been developed that discretize the continuum domain by discrete Lagrangian particles. Harlow's Particle In Cell (PIC) method [1] may be considered to be one of the precursors. This method eliminates the shortcomings of the traditional Lagrangian and Eulerian methods while retaining the good aspects of them. This method allows one to solve a broader class of problems by allowing large distortions and efficient calculation at interfaces. The PIC method also allows precise distinction of material boundaries. In spite of these advantages the PIC method shows certain limitations for problems where variables are history dependent, for example in elasto-plasticity, viscoelasticity, various relaxation processes, and for problems dealing with low pressures. Another shortcoming of this approach is that the solution fluctuates due to the method of discretization of mass, energy and momentum, and the way by which density is calculated. A more serious limitation arises out of the complexity of pressure calculation in a mixed cell.

From the above mentioned of existing computational methods for non-stationary continua it is clear that none of them satisfy the requirements for large-scale computation. The grid and particle methods such as PIC and GAP [2] seem to possess the best characteristics in this regard. Hence these methods were taken up as a basis for developing a new method – the method of individual particles (1979, developed under the scientific leaderships of Prof. V.F.Minin) to extend the areas of applicability of the particle methods. Some particle methods in Astrophysical Fluid Dynamics are discussed and available at [3].

---

On the calculation experiment technology Prof. V.F.Minin is the winner of the State premium of the USSR.

## 2. The general scheme of “Individual Particles” (IP) method

In the IP (Individual Particles) method, which is described below, a continuum is discretized into small volumes each of which is represented by a particle. All the physical quantities such as mass, velocity, and thermodynamic variables like density, energy etc. of the entire flow field are represented by those of the particles whose coordinates are known at all times. The particles can have changing shapes (as opposed to being point masses) depending on local flow parameters. The particles can also unite or divide into new particles depending on the flow parameters.

The main goal of developing the new method is to eliminate the limitations of both PIC and GAP methods, e.g. oscillation of solutions, complexity of “mixed cell” calculations, non-physical discontinuities in otherwise continuous solutions etc. However, it is important to preserve basic advantages of the earlier methods such as the natural way of computations for multi-component media experiencing large strain, and transport of materials across interfaces.

Let's write out the set of equations for a two-dimensional plane symmetry or axisymmetric compressible medium in Eulerian coordinates:

$$\frac{\partial p}{\partial t} + p \operatorname{div} \vec{V} = 0, \quad (2.1)$$

$$\rho \frac{du}{dt} = \frac{\partial P^{zz}}{\partial z} + \frac{\partial P^{zr}}{\partial r} + \left( \frac{P^{zr}}{r} \right)^*, \quad (2.2)$$

$$\rho \frac{dV}{dt} = \frac{\partial P^{rz}}{\partial z} + \frac{\partial P^{rr}}{\partial r} + \left( \frac{P^{rr} - P^{\varphi\varphi}}{r} \right)^*, \quad (2.3)$$

$$\rho \frac{de}{dt} = P^{zz} \frac{\partial U}{\partial z} + P^{zr} \left( \frac{\partial V}{\partial z} + \frac{\partial U}{\partial r} \right) + P^{rr} \frac{\partial V}{\partial r} + \left( P^{\varphi\varphi} \frac{V}{r} \right), \quad (2.4)$$

$$P^{zz} = -p + S^{zz}, \quad (2.5)$$

$$P^{rr} = -p + S^{rr}, \quad (2.6)$$

$$P^{\varphi\varphi} = -p - (S^{zz} + S^{rr}), \quad (2.7)$$

$$P^{zr} = S^{zr}, \quad (2.8)$$

$$p = p(\rho, e), \quad (2.9)$$

$$\frac{dS^{zz}}{dt} = 2\mu \left[ \frac{\partial U}{\partial z} - \frac{1}{3} \operatorname{div} \vec{V} \right] + \delta^{zz}, \quad (2.10)$$

$$\frac{dS^{rr}}{dt} = 2\mu \left[ \frac{\partial V}{\partial r} - \frac{1}{3} \operatorname{div} \vec{V} \right] + \delta^{rr}, \quad (2.11)$$

$$\frac{dS^{zr}}{dt} = \mu \left[ \frac{\partial U}{\partial r} + \frac{\partial V}{\partial z} \right] + \delta^{zr}, \quad (2.12)$$

$$\operatorname{div} \vec{V} = \frac{\partial U}{\partial z} + \frac{\partial V}{\partial r} + \left( \frac{V}{r} \right)^*, \quad (2.13)$$

$$\delta^{zz} = S^{zr} \left( \frac{\partial V}{\partial z} - \frac{\partial U}{\partial r} \right), \quad (2.14)$$

$$\delta^{rr} = S^{zr} \left( \frac{\partial U}{\partial r} - \frac{\partial V}{\partial z} \right), \quad (2.15)$$

$$\delta^{zr} = \frac{S^{rr} - S^{zz}}{2} \left( \frac{\partial V}{\partial z} - \frac{\partial U}{\partial r} \right), \quad (2.16)$$

$$(S^{zz})^2 + (S^{rr})^2 + (S^{zr})^2 + S^{zz}S^{rr} \leq \frac{1}{3}\sigma_0^2. \quad (2.17)$$

Here the variables are:  $t$  - time,  $r, z$  - spatial coordinates ( $z$  - axes of a symmetry in cylindrical coordinates),  $\rho$  - density,  $U$  - velocity in  $z$ -direction,  $V$  - velocity in  $r$ -direction,  $P^{ij}$  - components of the stress tensor,  $S^{ij}$  - deviatoric stress components,  $p$  - hydrostatic pressure,  $\mu$  - shear modulus. For the two-dimensional plane symmetry case, the terms marked with an asterisk are set equal to zero.

The equations (2.10-2.12) are obtained from the generalized Hooke's law for an isotropic elastic medium in terms of strain increments and the ensuing stress increments. The magnitudes  $\delta^{ij}$  in the equations (2.14-2.16) represent Yaumann stress corrections due to rotation.

The inequality (2.17) represents von Mises yield condition with yield stress of  $\sigma_0$ . In the plastic range the inequality in (2.17) is enforced by multiplying

$$\frac{\sqrt{\frac{1}{3}\sigma_0}}{(S^{zz})^2 + (S^{rr})^2 + (S^{zr})^2 + S^{zz}S^{rr}} \quad (2.18)$$

to the deviatoric stress components. In case of inviscid and adiabatic flow of fluids the set of equations (2.1-2.17) become the equations of gas dynamics:

$$\frac{dp}{dt} + \rho \left[ \frac{\partial U}{\partial z} + \frac{\partial V}{\partial r} + \left( \frac{V}{r} \right)^* \right] = 0, \quad (2.18)$$

$$\rho \frac{dU}{dt} + \frac{\partial p}{\partial z} = 0, \quad (2.19)$$

$$\rho \frac{dV}{dt} + \frac{\partial p}{\partial r} = 0, \quad (2.20)$$

$$\frac{de}{dt} - p \frac{1}{\rho^2} \frac{d\rho}{dt} = 0, \quad (2.21)$$

and the equation of state,

$$p = p(\rho, e), \quad (2.22)$$

For the two-dimensional plane symmetry case, the terms marked with an asterisk in equations (2.1-2.22) are set equal to zero. The set of equations (2.1-2.17) and (2.18-2.22) containing spatial partial derivatives of stress tensor, pressure and velocity components apply to discrete Lagrangian volumes. As a result, the only additional condition that need to be enforced for cases where more than one material are involved, is the continuity of the normal stress and normal component of velocity at the boundaries.

The basic idea of this method is the following. The set of equations (2.1-2.17) or (2.18-2.22), describing the motion is numerically integrated for each particle. Two grids are considered for the calculation purpose. A Lagrangian grid on which all flow parameters are defined, and a Eulerian grid, which is arbitrarily defined at each time step. The nodes in the Lagrangian grid coincide with the particles. Pressure is calculated from the internal energy and density. Then pressure, stress tensor and the velocity fields are mapped to the Eulerian

grid on which all necessary derivatives are carried out. Then the values of these derivatives are mapped back on to the Lagrangian grid by interpolation. The application of conservation laws (energy, mass and momentum) in finite difference form results in the new values of density, velocity and internal energy at the nodes (centers of particles) of the Lagrangian grid. New positions of the particles are then determined from the new velocity field. If required, uniformity of particle distribution can be achieved by merging smaller particles, and dividing larger particles into smaller ones. This completes the calculation for the given time step. The mapping schemes that map data to and from the Eulerian grid and the Lagrangian grid are similar.

Some of the distinct features of this method are as follows.

1. The problem associated with calculation of pressure in "mixed cells" is removed, since the calculations are performed on the Lagrangian grid comprising of homogeneous material.
2. The density calculation is done on the particles based on the continuity equation. It completely eliminates the fluctuations of solutions that is normally seen in Eulerian calculations.
3. Since the density and other flow parameters change continuously, the condition that limits the minimum number of particle in a cell is the continuity condition itself. It means, that the calculation can be carried out with only one particle in a mesh. This reduces memory size requirement and the computational time by an order of magnitude compared to other particle methods.
4. The information about the particles is necessary only for calculation of the next time step, since after an interpolation of values of derivatives from the Eulerian grid to the particles, the Eulerian grid information is not necessary. This property of the algorithm allows us to reduce computer memory required to store grid information. Calculation is carried out on a minimum necessary "quantum" Eulerian grid, and then moved to the field of particles.
5. One virtue of representing a medium by Lagrangian particles (individual volumes that carry full state information of the flow field at a given point) is the ease of tracking history dependent variables. Any number of history variables can be tracked for a particle. Therefore different bodies can be described by different equations of state. This does not complicate the computational algorithm. For example, to describe an elastic-plastic process the additional parameters are the components of stress deviator. Similarly, for calculation of detonation of explosives (HE) (taking into account the kinetics of its decomposition in shock waves) the additional parameters are the values of relative specific volume of solid and gaseous phases and the degree of transformation of HE in the detonation products. The simulation of damage processes, calculation of polymorphic phase changes can be effected similarly. In all such cases only the subroutines that calculate appropriate equation of state, kinetics and rheological conditions are changed. The main program is not affected.

Also, it is easy in IP method to calculate rigid body interaction with deforming medium by not allowing particles to move into the rigid body but allowing them to transfer momentum at the same time.

6. The algorithm of IP method is simple and is homogeneous, that allows one to effectively implement it in parallel and multiprocessor computers.

The various implementations of the IP method differ from each other on the type of Eulerian grid used (regular, irregular, adapted to singularities of flow etc.), mode of division and

merger of particles, interpolation schemes used to map values from Lagrangian grid to Eulerian grid and back etc. The specific implementation also depends on the computer architecture. In the following pages we describe the implementation in a single processor type computer.

### 3. Implementation of the IP method

In the following, we describe the computational method for non-stationary, inviscid and adiabatic flow in an axi-symmetric or planar symmetric continuum. A computational grid containing discrete particles is overlaid on the physical domain as shown in fig-3.1.

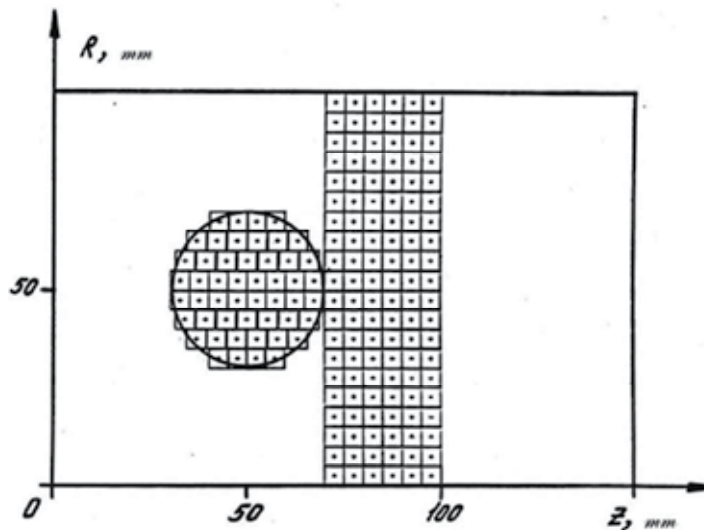


Fig. 3.1. Representation of a domain as particles and individual volumes

Each particle represents a discrete homogeneous volume (that is, the volume occupied by one material) and is characterized by the following parameters: mass,  $M$ ; coordinates of the center,  $z$  and  $r$ ; components of velocity,  $U$  and  $V$ , in  $z$  and  $r$  directions respectively; density,  $\rho$ ; specific internal energy,  $e$ ; artificial viscosity,  $q$ ; and a number,  $N_B$  describing its material properties. For solids (media with strength effects), the list of parameters for each particle also includes the components of stress deviator  $S^{zz}, S^{rr}, S^{rz}$ . Let's assume that in the  $z - r$  plane the form of cell is quadrilateral, at the center of which all its parameters are defined. The particles in each cell in the planar case have identical mass, whereas in the axi-symmetrical case the mass is proportional to the radial distance of the particles from the axis of symmetry. The boundaries can be rigid, reflective, or boundaries through which substances can enter or leave. In case of axi-symmetric flow, the boundary  $r = 0$  is the axis of symmetry. We may also include a rigid body, stationary or moving, inside the computational grid. For each particle, the set of equations of gas dynamics (2.18-2.22) is integrated. Unknown values of space derivatives,  $\frac{\partial p}{\partial z}, \frac{\partial p}{\partial r}, \frac{\partial U}{\partial z}, \frac{\partial V}{\partial r}$  for each particle are determined in the fixed Eulerian grid. The mesh density is chosen so that there is no discontinuity. In most cases this condition is fulfilled by arranging the grid in such a way that each cell contains at least one particle. Further, we shall use a uniform Eulerian grid with square cells.

**Stage-I** - interpolation from "particle to grid": The pressure is calculated for each particle using the formula  $\bar{p} = p + q$ . Here  $p$  is the hydrostatic pressure obtained from equation (2.22),  $q$  is the linear artificial viscosity calculated on the previous time step. At the centers of particles, pressure  $\bar{p}$  and velocity components  $U, V$  are known. These are then interpolated to the nodes of Eulerian grid. The interpolation can be done by various methods, for example, "weighing" on squares denoted by  $S_N^{ij}$  (defined in Fig.3.2):

$$A = \frac{\sum_N A_N S_N^{ij}}{\sum_N S_N^{ij}}, \quad (3.1)$$

where the indices  $I, j$  refer to the node  $(I, j)$  of the Eulerian grid, index  $N$  refers to the  $N^{\text{th}}$  particle,  $A = (\bar{p}, U, V)$ . Each particle contributes to the four adjacent nodes. In fig. (3.2) crosses and circles represent centers of two types of particles. The dotted line shows the partition of a cell into squares in inverse proportion to the contribution of each particle to the respective nodes. Accurate interpolation can be produced in many other ways as well.

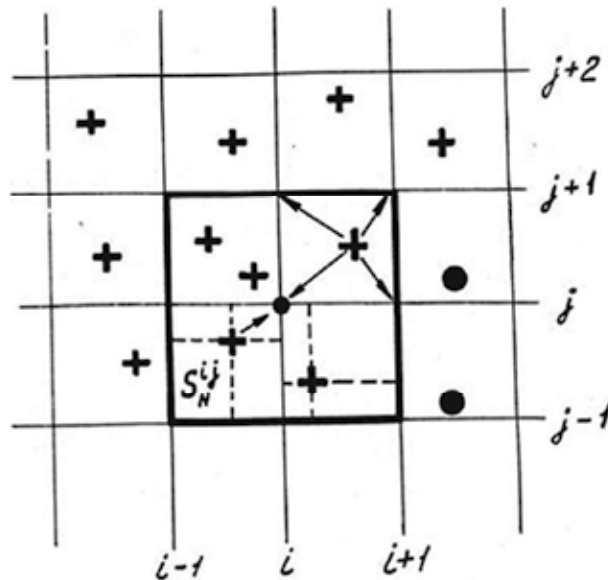


Fig. 3.2. An interpolation of "particle - grid"

In addition to the interpolated values from "particle to grid", each particle also contributes to the information about its membership of the material category to the node. Thus each node can be categorized into the following four classes (fig.3.3):

1. A "Vacuum" node - there are no particles in the adjacent cells.
2. An interior node - the particles in the adjacent cells are on same material type.
3. A node on the contact boundary - the adjacent cells contain particles of two and more material types.
4. Node on the free boundary - one from adjacent nodes is a "vacuum" node.

The dotted line on fig.3.3 designates the contact boundary between two substances their common free surface. Let's note that such classification of nodes resolves the boundary to within one cell size.

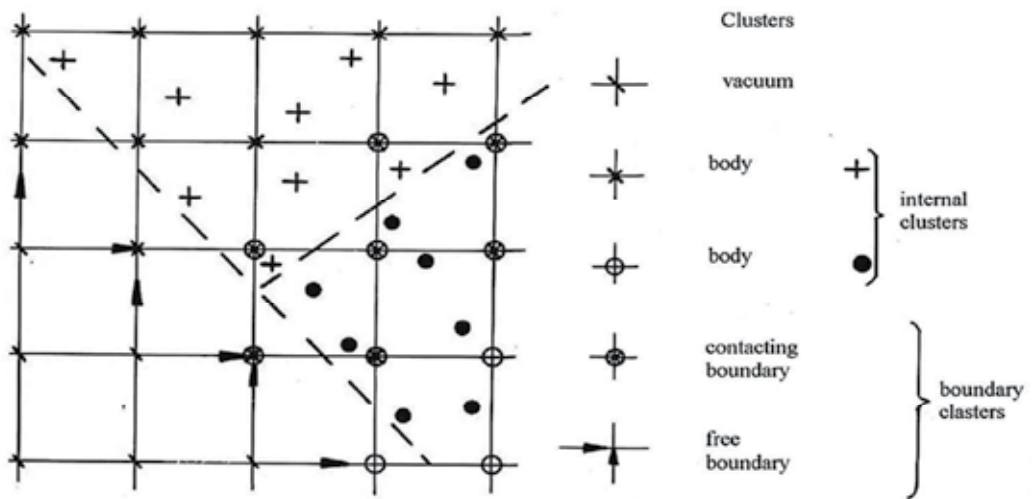


Fig. 3.3. Classification of nodes in Eulerian grid (the dotted line designates the boundaries of mixed fields)

**Stage-II** - statement of boundary conditions on the Eulerian grid (see below).

**Stage-III** - "grid to particle" interpolation and calculation of new values of particle parameters. The spatial derivatives are calculated at the nodes of the Eulerian grid (fig.2.4). In the interior nodes, all the derivatives are approximated by central differences, for example, in z-coordinate (two-sided derivative on fig.3.4):

$$\left(\frac{\partial A}{\partial z}\right)_{ij} = \frac{A_{i+1,j} - A_{i-1,j}}{2h} \tag{3.2}$$

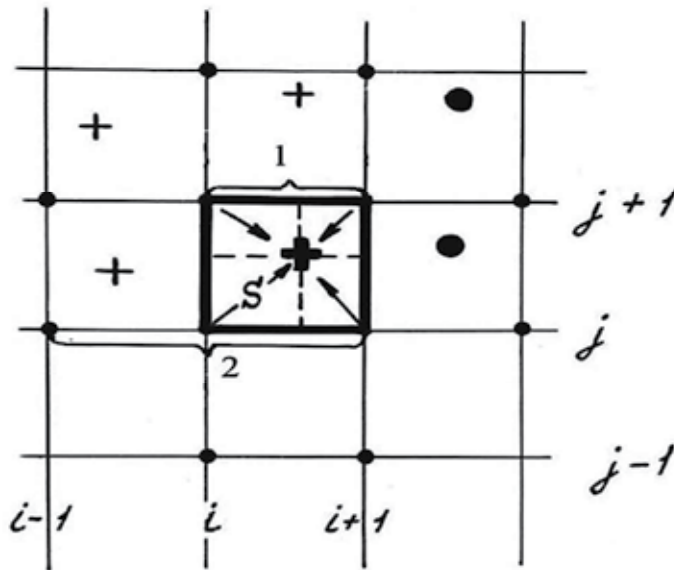


Fig. 3.4.



In boundary nodes the calculation of derivatives of velocity components are carried out using one-sided difference formula, for example, the derivative of component  $U$  in  $z$  coordinate is given by:

$$\left(\frac{\partial U}{\partial z}\right)_{i,j+1} = \frac{U_{i+1,j+1} - U_{i,j+1}}{h}. \quad (3.3)$$

Central difference scheme is used for the derivative of pressure. The values of derivatives at a particle are determined by linear interpolation of appropriate grid values as follows.

$$\left(\frac{\partial A}{\partial z}\right)_N = \frac{\sum_{ij} \left(\frac{\partial A}{\partial z}\right)_{ij} S_N^{ij}}{\sum_{ij} S_N^{ij}}, \quad \sum_{ij} S_N^{ij} = h^2. \quad (3.4)$$

The summation is carried over the nodes. Here  $\left(\frac{\partial A}{\partial z}\right)_N$  is the value of derivatives at particles,  $\left(\frac{\partial A}{\partial z}\right)_{ij}$  is the value of derivatives at nodes,  $h$  is the mesh size.

Thus obtained values of spatial derivatives at the particles are used for calculation at the next time step using the following difference scheme:

$$\begin{aligned} U_N^{k+1} &= \tilde{U}_N^k - \frac{\Delta t}{\rho_N^k} \left(\frac{\partial \tilde{p}}{\partial z}\right)_N^k, \quad V_N^{k+1} = \tilde{V}_N^k - \frac{\Delta t}{\rho_N^k} \left(\frac{\partial \tilde{p}}{\partial r}\right)_N^k, \\ z_N^{k+1} &= z_N^k + U_N^{k+1} \Delta t, \quad r_N^{k+1} = r_N^k + V_N^{k+1} \Delta t, \\ \rho_N^{k+1} &= \rho_N^k / [1 + (\text{div} \vec{V})_N^k \Delta t], \quad e_N^{k+1} = e_N^k - \frac{p_N^k}{\rho_N^k} (\text{div} \vec{V})_N^k \Delta t \\ q_N^{k+1} &= \begin{cases} -Bc_N^k h (\text{div} \vec{V})_N^k, & \text{if } \rho_N^{k+1} \geq \rho_N^k \\ 0, & \text{if } \rho_N^{k+1} \leq \rho_N^k \end{cases} \end{aligned} \quad (3.5)$$

where divergence is defined as follows:

$$(\text{div} \vec{V})_N^k = \left(\frac{\partial U}{\partial z}\right)_N^k + \left(\frac{\partial V}{\partial r}\right)_N^k + \left(\frac{V}{r}\right)_N^k,$$

The index  $N$  refers to a particle with number  $N$ ,  $k$  refers to the time step number,  $\Delta t$  is the time step size,  $C$  is the velocity of a sound,  $B$  is the constant for the given substance. The value of  $B$  ( $\sim 1$ ) used, depends on stability conditions requiring artificial viscosity. Let's note that in evaluation of velocity components  $U_N^{k+1}$ ,  $V_N^{k+1}$  at a particle, the right hand side of the appropriate formulas does not use the old values of velocity, rather the intermediate magnitudes  $\tilde{U}_N^k$ ,  $\tilde{V}_N^k$ , obtained by interpolating the nodal velocities. From conservation of total energy at a particle, the value of its specific internal energy in this case is modified by:

$$\tilde{e}_N^k = e_N^k + \frac{(U_N^k)^2 + (V_N^k)^2 - (\tilde{U}_N^k)^2 - (\tilde{V}_N^k)^2}{2}. \quad (3.6)$$

Thus the total energy and the momentum of the particle system do not vary. A "smoothing" procedure (by which, the average value of particles velocity is calculated) for particle velocity is required for every 5-10 time steps to ensure monotonicity of the solution. The smoothing at each time step reduces the spreading of shock wave to 2 to 3 cells. For the time

step without smoothing the values  $U_N^{k+1}, V_N^{k+1}$  and  $e_N^k$  are used in (3.5) instead of the intermediate values of  $\tilde{U}_N^{k+1}, \tilde{V}_N^{k+1}$  and  $\tilde{e}_N^k$ . The scheme (3.5) is conservative and is first order accurate in time and space.

In presence of elastic-plastic effects the system (2.1-2.17) is evaluated on some time step  $k$  as follows.

The values of momentum at particles are interpolated at nodes, and then subsequently nodal values of velocities are calculated using boundary conditions. Nodal values of derivatives of velocities are carried out. Then these derivatives are mapped onto the particles.

New density:

$$\rho_N^{k+1} = \rho_N^k / [1 + (\text{div} \vec{V})_N^k \Delta t],$$

a. New specific internal energy:

$$e_N^{k+1} = e_N^k + \frac{\Delta t}{\rho_N^k} \left\{ P_N^{zz} \left[ \left( \frac{\partial U}{\partial r} \right)_N + \left( \frac{\partial V}{\partial z} \right)_N \right] + P_N^{rr} \left( \frac{\partial V}{\partial r} \right)_N + P_N^{\varphi\varphi} \left( \frac{V}{r} \right)_N \right\},$$

Here

$$P_N^{ij} = -(p_N^k + q_N^k) + (S_N^{ij})^k, \text{ if } i = j, P_N^{zr} = (S_N^{ij})^k,$$

b. Linear artificial viscosity:

$$q_N^{k+1} = \begin{cases} -B\rho_N^k c_N^k h (\text{div} \vec{V})_N^k, & \text{if } \rho_N^{k+1} > \rho_N^k, \\ 0, & \text{if } \rho_N^{k+1} \leq \rho_N^k. \end{cases}$$

c. New components of stress deviator:

$$(S_N^{zz})^{k+1} = (S_N^{zz})^k + \left\{ 2\mu \left[ \left( \frac{\partial U}{\partial z} \right)_N - \frac{1}{3} (\text{div} \vec{V})_N \right] + \delta_N^{zz} \right\} \Delta t,$$

$$(S_N^{rr})^{k+1} = (S_N^{rr})^k + \left\{ 2\mu \left[ \left( \frac{\partial V}{\partial r} \right)_N - \frac{1}{3} (\text{div} \vec{V})_N \right] + \delta_N^{rr} \right\} \Delta t,$$

$$(S_N^{zr})^{k+1} = (S_N^{zr})^k + \left\{ 2\mu \left[ \left( \frac{\partial U}{\partial r} \right)_N - \left( \frac{\partial V}{\partial z} \right)_N \right] + \delta_N^{zr} \right\} \Delta t,$$

Magnitudes of  $\delta_N^{ij}$ - single-error correction due to rotation

$$\delta_N^{zz} = (S_N^{zr})^k \left[ \left( \frac{\partial V}{\partial z} \right)_N - \left( \frac{\partial U}{\partial r} \right)_N \right], \delta_N^{rr} = -\delta_N^{zz}, \delta_N^{zz} = \frac{(S_N^{rr})^k - (S_N^{zz})^k}{2} \left[ \left( \frac{\partial V}{\partial z} \right)_N - \left( \frac{\partial U}{\partial r} \right)_N \right],$$

d. The Von Mises yield criterion is satisfied as follows.

$$J = [(S_N^{zz})^{k+1}]^2 + [(S_N^{rr})^{k+1}]^2 + [(S_N^{zr})^{k+1}]^2 + (S_N^{zz})^{k+1} (S_N^{rr})^{k+1}.$$

To satisfy the inequality  $J \leq \frac{1}{3} \sigma_0^2$  all terms of the stress deviator  $(S_N^{ij})^{k+1}$  are multiplied by on a factor  $\sqrt{\frac{1}{3J}} \sigma_0$ .

e. "Smoothing" of velocity and adjustment of specific internal energy is produced

$$\bar{U}_N^k = \sum_{ij} U_{ij} \Delta_N^{ij}, \bar{V}_N^k = \sum_{ij} V_{ij} \Delta_N^{ij},$$

$$\bar{e}_N^{k+1} = e_N^{k+1} + \frac{(U_N^k)^2 + (V_N^k)^2 - (\bar{U}_N^k)^2 - (\bar{V}_N^k)^2}{2}, \text{ where } \Delta_N^{ij} \text{ - square of } S_N^{ij} \text{ (see Fig.2.2).}$$

Here  $\bar{U}_N^k, \bar{V}_N^k$  are the smoothed values of velocity components,  $\bar{e}_N^{k+1}$  is the corrected value of a specific internal energy. For each particles with known values of density and specific internal energy with a given equation of state the hydrostatic pressure  $p_N^{k+1} = p(N_B, \rho_N^{k+1}, \bar{e}_N^{k+1})$  is calculated. Then the components of stress tensor  $P_N^{ij} = -(p_N^{k+1} + q_N^{k+1}) + (S_N^{ij})^{k+1}$  are calculated and are interpolated at the nodes. Then after taking into account of boundary conditions, the grid values of derivatives of stress tensor components are determined. For each particle, the new values of velocities and coordinates are calculated as follows.

$$U_N^{k+1} = \bar{U}_N^k + \frac{\Delta t}{\rho_N^{k+1}} \left[ \left( \frac{\partial P^{zz}}{\partial z} \right)_N + \left( \frac{\partial P^{zr}}{\partial r} \right)_N + \frac{P_N^{zr}}{r_N} \right], V_N^{k+1} = \bar{V}_N^k + \frac{\Delta t}{\rho_N^{k+1}} \left[ \left( \frac{\partial P^{zr}}{\partial z} \right)_N + \left( \frac{\partial P^{rr}}{\partial r} \right)_N + \frac{P_N^{rr} - P_N^{\varphi\varphi}}{r_N} \right],$$

$$z_N^{k+1} = z_N^k + U_N^{k+1} \Delta t, r_N^{k+1} = r_N^k + V_N^{k+1} \Delta t.$$

With this the calculation for the next time step is completed. After the first stage of calculation in the IP method the values of pressure and velocity components are known at the nodes. The type of each node - "vacuum", boundary or interior is also known. It is possible to divide boundary conditions on the Eulerian grid into two groups (implementation of which is carried out at the second stage of calculation): 1) Boundary conditions of a designated field (e.g. a rigid inclusion) and 2) conditions on free and contact surfaces.

Let's consider boundary conditions on a designated boundary. In that case, when the boundary is a rigid wall or line of symmetry, the boundary conditions for a continuous medium require that the flow should be parallel to the boundary, that is, the normal component of velocity should be equal to zero. We use a method of reflection for such cases. Exterior to the boundary additional sets of fictitious nodes are introduced, which contain anti-symmetric reflection of normal velocity components, and symmetric reflection of remaining variables. So the following values of parameters are set in fictitious meshes for non-reflecting rigid boundary or for the lines of symmetry.

$$V_{j-1} = -V_{j+1}, U_{j-1} = U_{j+1}, \tilde{P}_{j-1} = \tilde{P}_{j+1}.$$

Condition  $V_j = 0$ , here index  $j$  refers to the set of nodes on the boundary,  $j-1$  refers to fictitious nodes,  $j+1$  refers to nodes adjacent to the boundary in the interior. The linear extrapolation of parameters in the fictitious nodes is carried out using the condition of outflow of substance from the interior area as follows.

$$A_{j-1} = 2A_j - A_{j+1}, A = (\tilde{p}, U, V).$$

In both cases (rigid wall and axis of symmetry), the type of node (interior, contact etc.) is also transmitted to the fictitious nodes.

#### 4. Special algorithms to treat boundary nodes and particle shapes

Before implementing boundary conditions along contact and free surfaces, we must know the spatial orientation of boundary surfaces. To achieve this, we use a single normal vector  $\bar{N}$  that assigns orientation of the boundary surface at each node on the (pre-marked) free surfaces and contact boundaries. For contact boundaries, the normal vector is a normalized sum of vectors directed from the node under consideration to eight nearest nodes after taking into account their material contents. For contact surfaces, the normal vector is the normalized sum of vectors directed from the node under consideration to the nearest vacuum nodes. For example, in figure 4.1 the vector normal to free boundary at node  $(i,j)$  is the average of vectors from  $N_{ij}$  to  $N_{i-1,j+1}$ ,  $N_{i-1,j}$ ,  $N_{i-1,j-1}$ ,  $N_{i,j-1}$ .

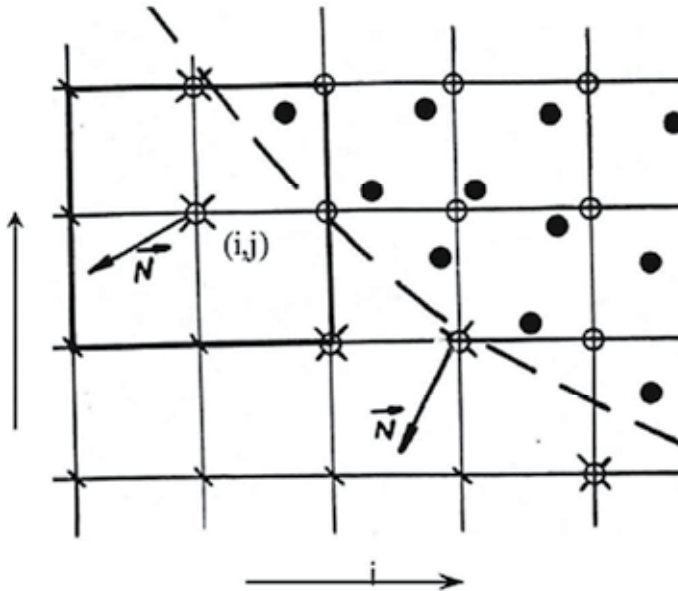


Fig. 4.1. Orientation of a normal vector  $\bar{N}$  on free surface (dotted line)

This procedure permits the determination of normal direction at boundaries within an accuracy of  $\pi/8$ . In most cases, the accuracy can be enhanced by using normal directions at adjacent boundary nodes. In fig.4.2 an example of the application of this algorithm is shown for the particle configuration discussed in figure 3.1. At each particle on the boundary, a line is drawn through the particle center and normal to the normal vector. The thicker lines pertain to the contact boundary.

On the free surfaces, the normal component of stress vector is set equal to zero. For gas-dynamics calculations, the pressure is set equal to zero at the nodes on free surfaces. The sliding contact condition is enforced by recalculating the velocity components at particles such that the normal velocity component remains unchanged.

$$\bar{U} = U_{ij}N_z^2 + U_N N_r^2 + (V_{ij} - V_N)N_z N_r, \tag{4.1}$$

$$\bar{V} = V_{ij}N_z^2 + V_N N_r^2 + (U_{ij} - U_N)N_z N_r, \tag{4.2}$$

Where  $U_{ij}, V_{ij}$  - velocity components on contact boundary,  $\bar{U}_{ij}, \bar{V}_{ij}$  - appropriate recalculating value,  $N_z, N_r$  - component of normal vector at  $ij^{\text{th}}$  node,  $U_N, V_N$  - velocity components at  $N^{\text{th}}$  particle.

When the tensile stress at a node on contact boundary exceeds some critical value  $p^*$ , a free boundary is introduced through the node, and the particle's normal stress component is set equal to zero. Thus a possible separation of materials along contact boundary is facilitated. The choice  $p^*$  is arbitrary. Good results are obtained by using a value that is small (by two orders of magnitude) compared to the characteristic stress in the flow field.

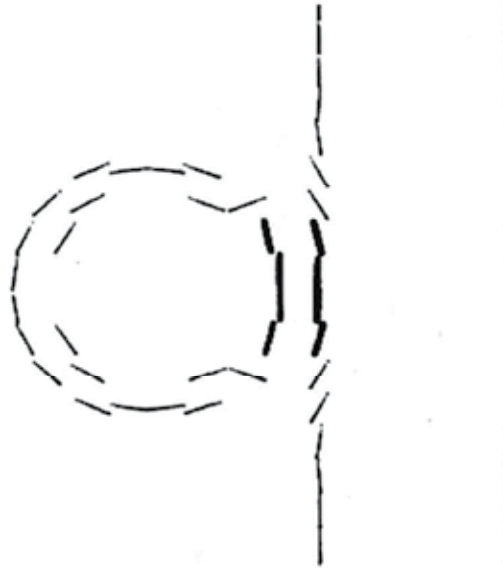


Fig. 4.2. An example of application of algorithm to determine boundaries for the configuration of particles represented on fig.3.1. (Thick lines show contact boundary)

During the calculation, some particles may cross over rigid boundaries. For such cases, a distance  $l_{\min}$  is calculated based on the mass and density of the particles. When a particle reaches within this distance to the rigid boundary, its normal velocity component  $V_{\bar{n}}$  is set equal to zero, and the internal energy is raised by  $\Delta e = V_{\bar{n}}^2/2$  which equals the loss of kinetic energy due to velocity adjustment. The velocity component along the rigid boundary does not change. In case of outflow of substance through the open boundary (prescribed as calculation limit) the particle does not participate in further calculations. As the calculation proceeds in the IP method, there may arise a situation where empty (Eulerian) cells occupy the space between cells containing particles. (i.e. some cells do not contain any particles). Such cases arise in zones of large expansion and in zones experiencing large strains. In such cases, some particles cease "to feel" each other as the area of influence of each particle is limited to the cell where it resides. This is a typical characteristic of particle in cell methods. One elementary way to eliminate this problem is to use large number of particles initially in the areas where such problem may potentially occur. But this is a cumbersome and inefficient way as it is not always possible to foresee where such problems may occur. A more rational means to eliminate such problems arising out of discontinuity is presented here.

For monitoring local violations of continuous presence of particles in each cell, new parameters are included to describe a particle in vector form (fig. 4.3). In planar symmetry case, the particle represents a rectangular parallelepiped of unit length, while for axisymmetric case it is a torus. The projection of a parallelepiped or a torus on  $(z,r)$  plane is a rectangle. Stretch and rotation of the rectangle are defined by components of a vector, which determines the orientation of the particle. The two sides of the rectangle,  $a$  and  $b$  are related to the vector components  $L_z$  and  $L_r$  as follows.

$$a = \sqrt{L_z + L_r}, b = \frac{M}{da\phi'} \tag{4.3}$$

Where the parameter  $d$ , having dimension of length, is equal to 1 for planar symmetry, and is equal to  $2\pi r_N$  for rotational symmetry ( $r_N$  -  $r$  coordinate of particle center). The orientation of the triangle with respect to the  $z$ -axis is given by,

$$\varphi = \arctg\left(\frac{L_z}{L_r}\right). \tag{4.4}$$

The vector components  $L_r$  and  $L_z$  evolve with time as follows:

$$\frac{dL_z}{dt} = \frac{\partial U}{\partial r} L_r + \frac{\partial U}{\partial z} L_z, \frac{dL_r}{dt} = \frac{\partial V}{\partial r} L_r + \frac{\partial V}{\partial z} L_z. \tag{4.5}$$

The interpolation of velocity and pressure to Eulerian grid is carried out from the center of individual particles, irrespective of their form or orientation.

During transition of a particle in a flow field it can (not changing the form of a rectangle):

1. Stretch and rotate,
2. Increase in size without changing shape, for example, during dilatational wave.

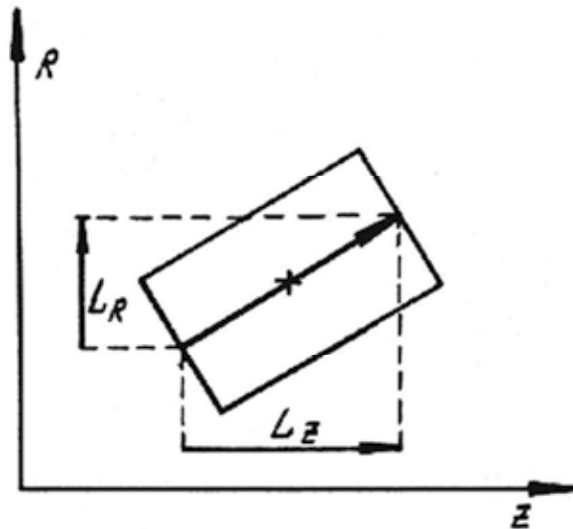


Fig. 4.3. The vector-form of a particle

In both cases continuous distribution of particles (at least one particle per cell) may be disrupted. Empty cells may arise in the direction of stretching for the first case above, or in the orientation directions of its sides as in the second case. It is natural to entertain virtual

particles ("virtual" - because the parameters of these particles are not stored in the computer memory), i.e., to assume that the base particle consists of two (for case-1) or four (for case-2) particles. The virtual particles have equal mass whose sum is equal to the mass of the base particle. The remaining parameters, other than the coordinates, at the virtual particles are identical. Thus, the interpolation at the nodes is carried out from one base particle, two (for case-1) virtual particles or four (for case-2) virtual particles. The virtual particles are introduced based on the value of a dimensionless number  $\eta$ . The base particle is substituted by two virtual particles when  $a/b > \eta$ , and by four particles when  $a/h > \eta$ , where  $a$  and  $b$  are the larger and smaller sides of the rectangle respectively, and  $h$  is the node spacing. The location of virtual particles inside a base particle is determined from their rectangular distribution in the domain. For most practical calculations the value of  $\eta$  starts at 1.2. For larger values the quality of observance of continuous distribution of particles in cells worsens, while for smaller values the computational time increases due to emergence of large number of virtual particles.

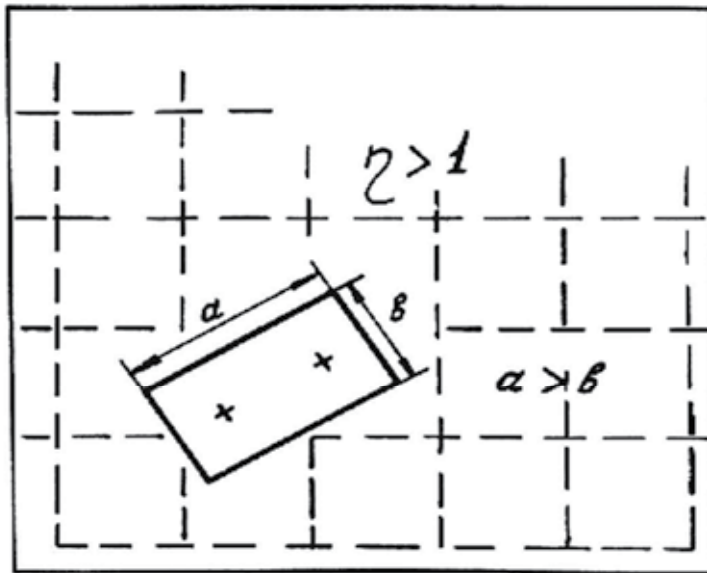


Fig. 4.4. Formation of virtual particles

In the event that the particle is stretched to twice its original size (or the size of virtual particle equals the original size of the base particle), it is better to divide the base particle into two particles. As a result, the virtual particles become real particles, and the computer memory is accordingly adjusted.

An example illustrating how virtual particles form is shown in fig.4.5. A bar of aluminum impacts a rigid wall at  $1 \text{ mm}/\mu\text{s}$ . Planar symmetry is used. Cells of  $1 \text{ mm} \times 1 \text{ mm}$  size are used in the Eulerian grid. The bar is  $5 \text{ mm}$  along  $z$ -axis and  $10 \text{ mm}$  along  $r$ -axis. The left boundary is the axis of symmetry. Distribution of horizontal component of velocity is shown at  $10 \text{ ms}$ . The dotted lines show discontinuity in solution when no account is taken of the form of the particles. The solution in such case does not describe actual physical situation. On the other hand, when the form of the particles is taken into account and the particles are allowed to subdivide, the discontinuity in the solution disappears. In the figure 4.5b, zones



of various levels of strain are depicted by degree of stretch, rotation, and subdivision of particles. This provides additional information about singularities in solution. Near free surface, where strain is insignificant, particle subdivision does not take place. Thus by introducing virtual particles algorithm in the IP method, automatic adaptivity is achieved that enables capture of singularity in the solution.

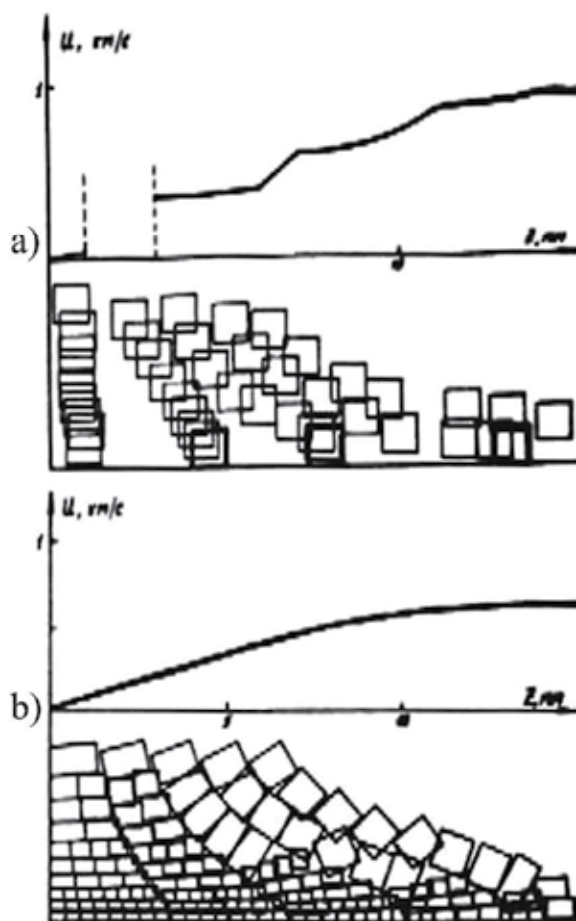


Fig. 4.5. An aluminum bar impacting a rigid wall. a) Without accounting for the form of particles, b) Accounting for the form of particles and their subdivision. The dotted line indicates disruption of continuity of the velocity profile along the wall

## 5. Examples

The basic aspects of the technology of the computational experiment (CE), principles of program-technical systems (PTS) construction, developed under the scientific leadership of Professor Vladilen F. Minin (Novosibirsk, USSR) on the basis of experience of development and usage of similar systems for 35 years and designed for realization of mass computational experiment are formulated in the given work. The main parameters of PTS

are yielded, some most interesting trends of CE conduction are shown, each of them is illustrated with the relevant solved problems.

The development of the mathematical physics, computational mathematics and means of computer technology gives the possibility to analyze the processes of pulse action upon a substance by conducting the computational experiment. It should be noted that in a general case the notion of CE is wider than the notion of simple modulation. The main difference is in the fact that CE makes possible to answer the question: "*What will be if ...?*"

On the basis of experience of development and usage of PTS the following main principles of PTS construction were formulated [4-5]:

- the problem solution can be carried out by a researcher who is not a specialist in the region of numerical methods and programming;
- PTS operate in a dialogue regime in terms of a researcher;
- all the initial and resulting information is represented in a convenient form analysis and displayed, that is the principle of "no dumps" is realized;

The PTS satisfying the requirements given above was realized using two 64-processor computers on the basis of the multiprocessor PS-2000 and a serial graphic display station. For complete realization of multiprocessor possibilities a special code allowing to carry out its paralleling was developed to solve the equation of continuum mechanics. For the solution of a wide class of problems besides generally used mathematical models of description of material and substance properties the wide-range equations of state of metals and description models of nonstationary detonation of heterogeneous explosives taking into account the kinetics of their decomposition in shock waves were included in PTS.

The main parameters of PTS are as follows: the RAM capacity is 2000000 24-digit words, the calculation field size is to 200000 units per one step in time, the calculation time of one step is 6-8 s, the average calculation time of one variant of the problem using the method of individual particles [6] was 2-3 hours.

A computation experiment on the computer complex was conducted in the following sequence [6]:

- the required and achievable space resolution, the time step, the regime of the algorithm operation, the boundaries of the calculation configuration variation and so on were defined in the first phase;
- the calculation of the subsequent variants was carried out in the regime of recording of a display-film, that is, the information about the process run was recorded on the magnetic disks with a sufficiently short time step which practically excluded the possibility of the data loss about the details of the process. But at the same time numeric data were not stored only the packed graphic information about the dynamics of the process occupying not much disk space was recorded. The character of the flow configuration change and the parameter change was shown by means of the colour palette and different grades of brightness for each colour. The velocity of look of the display-film with the frame size about 50000 pixels was about one frame per second.
- for obtaining the total numeric information about the run of the process the most typical and important (from view point of the investigator) variants are rerun once more in the regime of the full recording. The processing of the obtained frames in this case is carried out with displaying of the graphic information about the behavior of an arbitrary parameter ( $P$ ,  $\rho$ ,  $e$ ,  $U$  or  $V$ ) in an arbitrary point of the calculation field.

The wave configurations of the SW were discriminated and analyzed in the frames of the our computer complex by three techniques [7]: using a differential analyzer, by the maximum of the artificial viscosity - the values proportional to the pressure gradient and by pressure maximums in this cross-section of the calculation region. The first two techniques are essentially equivalent.

We should note that the technique of the differential analyzer allows to discriminate zone of fast change of calculated values which are associated with the SW fronts. The width of such zones in calculations is not more than 3-5 cells. Localization of the SW front (about 1 cell) is made by the line selection on which the velocity of change of the relevant calculated parameter is maximum.

Maximum pressure discrimination of wave fronts is made on the basis of the assumption that the transition from the incident wave to the reflected wave is accompanied by the normal deflection of the maximum locations to the axis Z to the side inverse to the front of the incident SW. Such an analysis allows to discriminate the location of contact points of two SW with the precision to one cell. The calculated value of the reflection (incidence) angle of the SW is defined by the average slope of the front of the reflected (incident) wave almost over 5 cell.

The development of the basis of the technology of CE conduction and long-term usage of the created PTS allowed carrying out a series of CE and obtaining new knowledge in the following main directions [8]:

- Simulation of cosmogeneous bombardment of the Earth and the project of the "space protection" of the planet, problems of the shock-explosive tectonics [9]. The system of equations describing the dynamics of the volume increase of microcracks (microvoids) was used in simulation of impact. It could be noted that the problems connected with formation of a crater and with movement of the ground in the explosion of a meteorite near the surface or upon collision with the ground are of constant interest. The basic mechanical properties characterizing this process are the parameters of the shock wave formed in the ground and the pattern of permanent displacements produced (in particular, the dimensions of the crater formed). The possibility of estimating shock-wave parameters for an explosion near the surface using known relationships for underground explosions has been discussed several times. The question of defining parameters for pulse application to some point of the surface of a semispace remains quite complex. As has been noted previously [10], cavity growth in electrical explosion on the surface of water proceeds according to a law close to the law of self similar motion at constant energy. It seems it was pioneer work because this fact allow to introduce the energy transferred to the ground and estimate its value (perhaps somewhat arbitrarily) by comparing the mechanical action parameters of contact and slightly submerged charges.
- dynamics simulation of high-speed collapses of dust particles of the Galley comet with protective screens of space vehicles in the project "Vega" [11-12], Fig.5.1; The wide-diapason equation of state was used. Also the computer simulation of the cumulative effect due to high - velocity (1-20 km/s) impact interaction of projectiles with different thin screens and massive targets, arranged behind the screens, as well as of the destruction processes in these systems taking into account thermo-physical and reological properties of real constructive materials were investigated. The results of the computer simulation were in a good agreement with both the available experimental

data and the analytical estimations in terms of a hydrodynamical theory of cumulation.

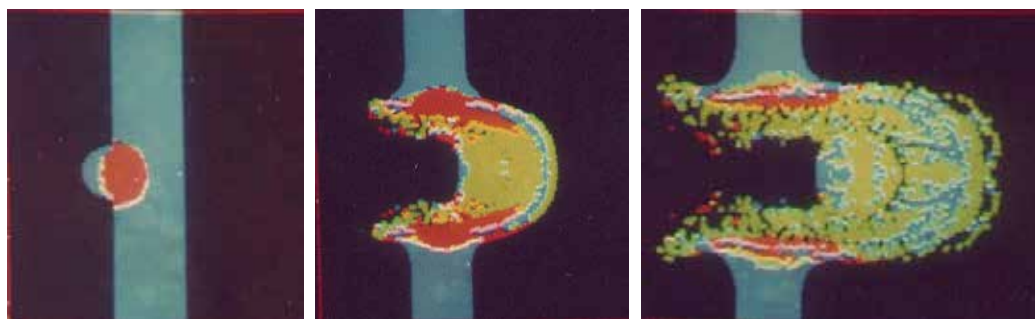


Fig. 5.1. Simulation of the macroparticle impact ( $V \sim 30$  km/s) with aluminum screen: blue – solid, red – liquid, green – plasma states of matter

- work optimization of conical thermonuclear targets in the section of simulation of interaction of flat plates with a conical cavity [13];
- investigation of functioning of different constructions of generators of powerful Mach shock waves [14,15] – Fig. 5.2.; These devices utilize the effect of geometric cumulation under conditions of irregular (Mach) reflection of conically convergent shock waves and are characterized by an additional concentration of energy during the shock wave convergence to the axis of symmetry and, at the same time, by an increased stability of flow as compared to the spherical convergence of shock waves.

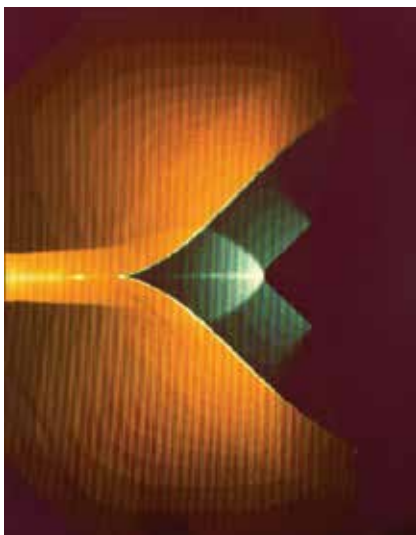


Fig. 5.2. Shock wave configuration on loaded conical target

- The peculiarities of the processes occurring on the shock-wave front and its stability were studied, and a new way to synthesize diamond in a shock- and detonation wave was developed as well as the way to synthesize wurtzite-like boron nitride widely used in industry (Fig.5.3).

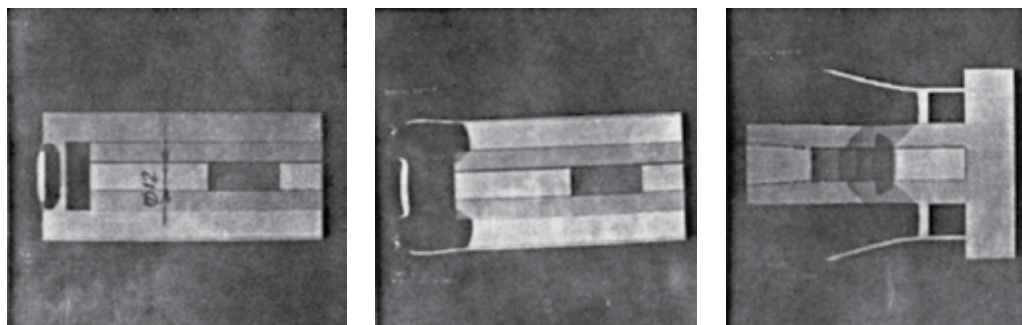


Fig. 5.3. Dynamic loading and Mach shock wave formation to synthesize diamond and wurtzite-like boron nitride

- development and simulation of the generation principle of powerful shock in a target while exposing it to space-modulated high-energy radiation [16];
- development and simulation of a new regime of a forced jet formation of high-speed plasma cumulative plasma jets (PJ) for thermonuclear projects while exposing profiled targets to radiation [17], fig. 5.4.;

It can be shown [17] that for the suggested regime of Jet formation in the first approximation

$$V_{\max} \sim \operatorname{ctg}(\alpha) \sqrt{1 + 2C_f \frac{x}{r_0}},$$

$$x = (1 - \cos(\alpha + \beta)) / ((2 + \cos(\alpha) - \cos(\alpha + \beta)) \sin(\alpha)),$$

where  $\alpha$  - is a semiangle of the cone,  $\beta$  - is an angle between the plate and the symmetry axis,  $C_f$  - a coefficient of friction at the PJ propagation in a dense medium.

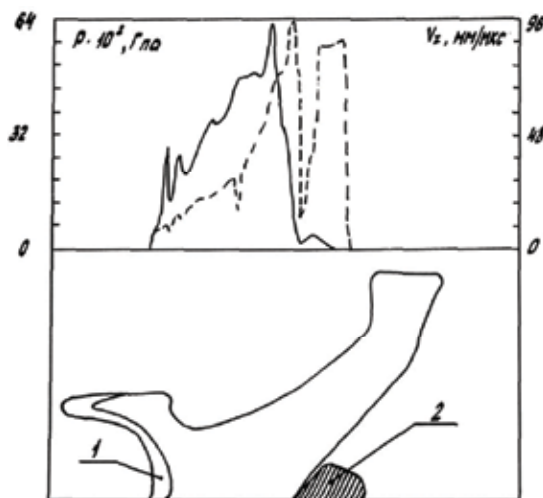


Fig. 5.4. Plasma forced jet formation in a conical target: 1 - pushed plate, 2 - plasma jet

It has been shown the realization of the forced Jet formation principle allows to increase both the speed and the pulse of the formed plasma jet essentially. More detailed analysis of the analytical model of non-stationary formation of the PJ shows that at the propagation of

PJ not in vacuum but in the medium with a low coefficient of resistance, as mentioned above, there is the effect of some increase of the PJ speed. And this medium as preliminary numerical experiments show makes a stabilizing action on the radial expansion of the PJ. It could be noted that as it is well known that the necessary requirements for the lack of a cumulative jet are established via the non-stationary collapsing of a liner of a cumulative hole. It has been also shown [18], that in a rotationally symmetric case the criterion by Wolsh is inapplicable. It was demonstrated that a rotationally symmetrical case that is produced by a current associated with a symmetrical axis produced by a shock wave can never be realized.

- a series of CE on studying of shock wave focusing possibilities into the space area of an arbitrary form in nonlinear regime by means of diffraction optics "taken" from the optical region into the continuum mechanics [19-20], fig.5.5.

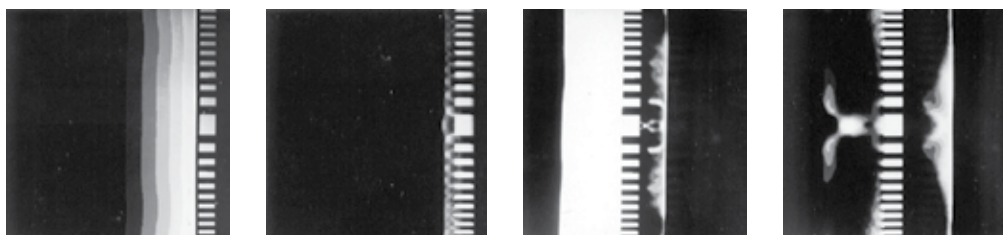


Fig. 5.5. The dynamics of shock wave focusing into the ring by means of diffractive element

- Numerical simulation of explosive plasma antenna [21]. For example, pulsed power generators as a sources are made on the magnetic cumulative generator or flux compression generator (FCG) bases the task of decreasing of dimensions and weight of them keeps being relevant. FCGs use the chemical energy from high explosives to accelerate a metallic conductor that traps and compresses a magnetic field initially created by a seed energy source such as a capacitor bank, battery, or another pulsed generator (figure 5.6).

The numerical experiments were also based on the following program complex, developments under the scientific leadership of Prof. Vladilen Minin:

- 3D supersonic aerodynamics [22],
- new methods of a modified large particles [23] allows to calculate explosive physics problems,
- The mathematical modeling of joint and magnetic-pulse welding processes [24],
- The mathematical modeling of castle. For example, in [25] the process of solidification and melting of the rod are described in the approximation of quasi-phase zone. Thermophysical parameters of the rod, casting and forms are different and equal to their average values in the range of temperatures.

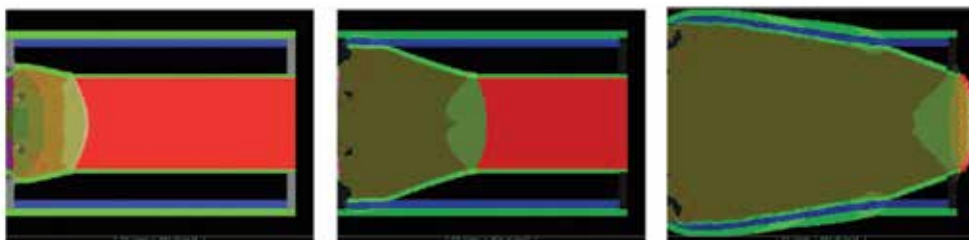


Fig. 5.6. Simulation of the FCG operation in dynamic [21]

A direct experimental analysis of the dynamics of the form of pulsating gaseous cavities prof.V.F.Minin [26] discovered that under the action of shock wave a bubble collapses asymmetrically with the formation of a cumulative jet, which forms in the process of collapse and causes fragmentation of the bubble. It could be noted that in the paper [27] the cumulative jet or jet at all was not mentioned. There is no jet and on the experimental photographs presented in the paper. Moreover, when the dimension of gas bubble diameter of 0.7 ... 2 cm, it was placed in a thin rubber membrane. Therefore, direct observation of the jet formation during compression of a gas bubble under the shock wave in the said article was not fulfilled. Experiments on the analysis of the attenuation of waves in bubble screens with different acoustic properties also were begun by V.F.Minin (1958), who examined also the first convenient model of a screen - a sequence of alternating flat one-dimensional liquid and gas layers.

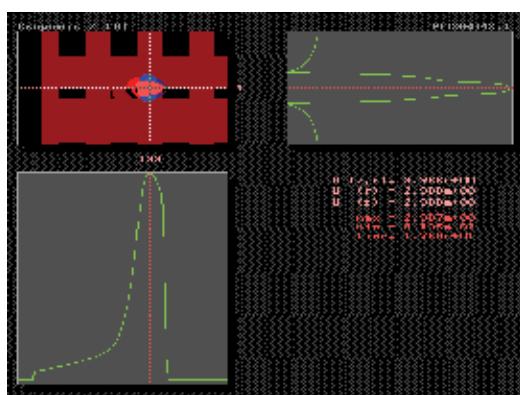


Fig. 5.7. Cumulative jet formations on air bobble collapsing under the shock wave: upper - screenshot of jet formation (the axial velocity is shown), right - distribution of axial velocity along horizontal axis, bottom - distribution of axial velocity along vertical axis

The accumulated potential energy and energy of external field is converted as a result into the energy of cumulative jet. A jet pierces the cavity and this leads to the destruction of the cavity.

The maximum speed of cumulative jet exceeds the maximum speed of compression and it is more than the maximum speed of forward motion of cavity without taking into account deformation. The conversion of kinetic energy of compression into the kinetic translational energy does occur and later on, after the deformation, it converts to the kinetic energy of stream.

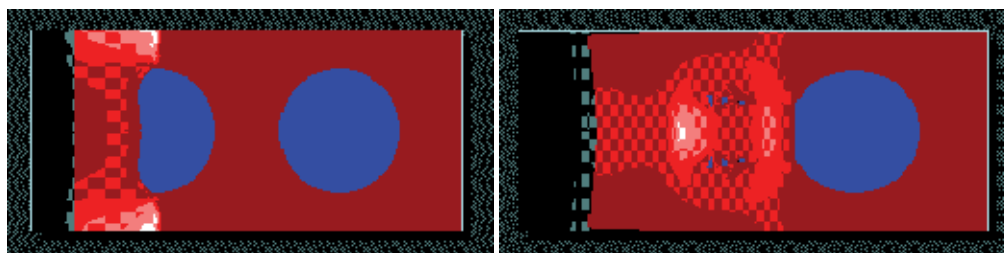


Fig. 5.8. Bubble collapsing and pulsation

The process to form a jet for a bubble in cavitation field was also investigated. The sound field radiated by a vibrating bubble near a rigid (or a soft) boundary can be regarded as a superposition of the field of two bubbles which carried out in- (or out-) phase vibration when the boundary disappears. A numerical computation shows that in the neighborhood of its compressed phase, a compressed quasi-shock wave forms in it, which will be reflected at its center and becomes an expanding quasi-shock wave, then a large negative curvature or a very strong negative surface tensile will be produced suddenly in the part of the deformed bubble's surface where the reflected shock arrives there first, so that a jet will be formed, the top of which will point the rigid boundary (or back from the soft boundary). A calculation shows also the jet could generate new shock and may cause bubbles nearby to form new jets or to produce a chain-like reaction. The forces of surface tension are not considered in simulation.

### **5.1 Hypercumulation - cumulative charges for efficient perforation of boreholes [28]**

The effect of cumulation at collision of liner with angles larger than 90 degrees from the axis of symmetry and corresponding compressing jets we called 'Hypercumulation' due to the fact that this process significantly increases energy content of a 'cumulative jet' and practically all of the liner material turns into high speed body - a 'jet' which can perform the required work. In experiments with liners at larger opening angles first occurs the process of classic cumulation with the production of a slug and a jet complying with normal cumulative flow and only after the liner passes the angle of 90 degrees a hypercumulation flow starts and the flow of cover metal is mostly transported into a cumulative jet, whose mass starts growing. This effect increases as increases collision angle and by a certain moment metal flow into the slug practically stops. Thus in this case we have two processes - classic at the beginning and hypercumulative - some time later. It is necessary to note that both these processes are well detectable in X-rays pictures by many authors.

We managed to realise a hypercumulative process both in its pure form (Fig. 5.9) and in combination with a classic process and, what is the most important, we managed to regulate the maximal speed of the forefront part of the jet voluntarily.

This allows creating necessary speed gradients in order to stretch the jet and thus increase its efficiency, as well as to diminish the mass and slug diameter, at which it can enter the hole and increase explosion yield, especially in cases of oil rocks.

The process realising hypercumulation can be carried out in a number of ways, which can be employed in the various constructions depending on requirements. These include situations when required inorganic or organic substances, their compositions with metal, pure metals and alloys not decomposing under the impact of high pressure and vice versa - turning under such pressures into a gas medium or other components - can be placed into a hole perforated in a well, cement and rock.

To ensure hypercumulative process and improving the characteristics of cumulation, special - more suitable - bodies with various systems for control of the detonation wave have been created which reduce the dimensions of perforating devices and amount of debris materials in order to minimally pollute the borehole and effectively carry out hypercumulation, both in its pure form and in combination with the elements of classic cumulation with a slug not exceeding the jet's maximal diameter.

Increasing the thickness of the cumulative jet requires increasing metal plasticity in order to achieve stretching of jet produced under the velocity gradient, as well as increasing the limit of jet's strength.


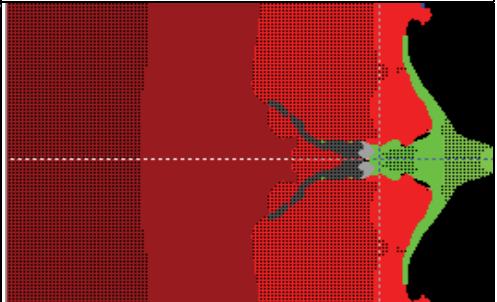


Fig. 5.9 shows certain results of calculation experiments made in regime of pure hypercumulation using liners made of different materials – copper, iron, aluminium.

We managed to find the solution for increasing plasticity and strength limit of certain materials at cumulative flow due to creating anisotropic cumulative liners. There are very strict requirements set forth to liner’s material in respect of its anisotropic properties and its homogeneity, and, in particular, to the grain size in the structure of the material, to structural homogeneity which appears when the material is rolled.

In its appearance and structure the material is already anisotropic. But the properties of thread like crystals inside the jet prevent the material from being homogeneous, since the properties of these threads produced from microcrystals of different crystallographic direction are different within a very broad scope. And, as we know, all this notwithstanding the jet consisting even of such thread-like crystals of different quality is capable of anomalous stretching which is also a reason of its expanding capacity to punch the barrier.

We managed to create a special medium for cumulative covers, which is anisotropic from the point of view of normal approach to material and ideal for being used in cumulative process. In such a material all the crystals locate in set direction – that of efficient deformation at cumulative explosion. Material with such a structure beyond the blast front attains a state close to thermodynamic balance. All the crystals stretch similarly turning into long threads. In such a medium there practically does not exist limitations for the size of grain crystals. Cumulative jet consists of long homogeneous thread-like crystals. Perforation does not depend on the size of crystals inside the liner and increases due to ever greater enlargement of a flying jet. In the experiment, even in the absence of optimal testing conditions, the effect of the charge increases. The abatement of the second viscosity of the medium characteristic for unbalanced processes at its flowing in the process of exploding can increase the mass of material turning into cumulative jet related both with the process of its formation and with decreasing energy intake for heating the material. For the first time cumulative process in the experiment was done with the liner having anomalously large crystals which in certain experiments attained the length of 1 cm and which do not affect the action of the product.

|                |   |   |
|----------------|---|---|
| No<br>fig<br>. | Initial configuration of shaped charge  | Cumulative jets for different liners design.<br>The mass of jet is more than mass of a slug.  |
| 1              |  |  <p data-bbox="714 1603 1214 1699">Red color - products of a detonation, gray color – metal (Pb), green color – Cu, cumulative jet.</p> |

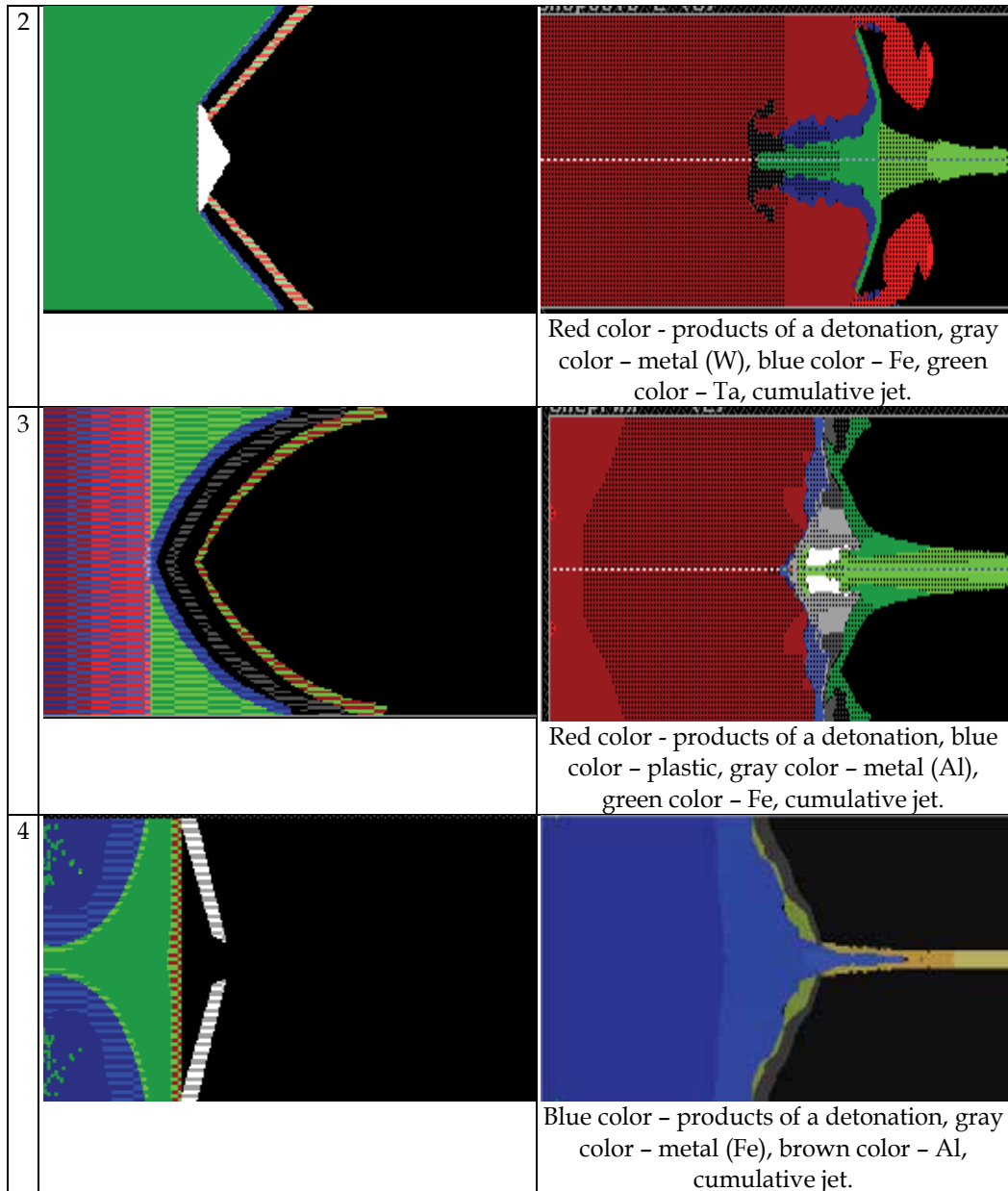


Fig. 5.9.

## 6. References

- [1] Harlow, Francis H. (1964). The particle-in-cell computing method for fluid dynamics. *Methods Comput. Phys.* 3: 319–343.
- [2] Marder B.H. (1975). GAP - a PIC-type fluid code // *Math. Of comput.*, v.29, N130.

- [3] Frederic A. Rasio. Particle Methods in Astrophysical Fluid Dynamics. Retrieved from <http://ciera.northwestern.edu/rasio/Papers/58.pdf>
- [4] Minin V.F. (1984) Complex of resources of express simulation on the computer of processes of physics of explosion and flow. The paper was presented at the 3 All-Union schools - seminars on physics of explosion and application of explosion in experiment, June 25-29, Krasnoyarsk. (in Russian)
- [5] Minin V.F. (1986) Computer science and computing experiment. The paper was presented at All-Union conference "Computer science and automation of handle", Kiev, April 1-3. (in Russian)
- [6] Minin V.F. et al (1989). Development and realization of the methods of numerical modeling of nonstationary flow of multicomponent compressible media by means of multiprocessor PS-2000. Preprint of the Institute of control problems. Moscow.- P.1-54. (in Russian). See also: Minin V.F., Minin I.V., Minin O.V. The calculation experiment technology. - Proc. of the Int. Symp. on Intense Dynamic Loading and its Effects.- Chengdu, China, June 9-12, 1992, p.431-433.
- [7] Minin V.F. et al (1989). Numerical modeling of nonregular interaction of the shock wave in condense matter. Preprint of the Institute of chemical physics. Moscow.-P.1-72. (in Russian)
- [8] Minin V.F. et al (1989). Numerical simulation of nonstationary high energy processes using real equation of metals state. / Collection of works: *Investigations of substance properties in extreme conditions* (IHT, USSR Academy of Sciences)-P. 89-96. (in Russian)
- [9] Minin V.F., Alekseev A.S., Kryukov B.P. (1989) The cosmogenios factors of effect on an earth's surface. - *Scientific seminar on mathematical modelling and prediction natural and technogenios catastrophes*, September 15-16, Computer centre SB AS USSR.
- [10] V. F. Minin (1964), *Zh. Prikl. Mekh. Tekh. Fiz.*, No. 3, see also: High-velocity impact phenomena, ed by R.Kinslow, Academic Press N.Y. and London, 1970. - 579 p.
- [11] V.F.Minin et al (1984). Thermophysical and Gasodynamical Problems of Meteorite Defense of Cosmic Apparatus "VEGA". - *Teplofiz. Vys.Temp.*, 22, v.5, P.964-983.
- [12] Minin V.F., Anisimov A.I., Sagdeev R.Z., Fortov V.E. (1986) Shock wave and extreme state of conditions in the Vega project of comet Galley investigation // 8 *Symp. on explosion*, Tashkent, 1986.
- [13] Minin V.F. et al (1987). Hydrodynamic cumulative effects in conic thermonuclear targets. *Book of abstracts 18-th ECLIM*, Prague, May 4-8, p.187.
- [14] Minin V.F. et al (1989). The numerical modeling of non-regular shock wave reflection in condensing matter. /Preprint of the Inst.of chemical physics. Moskow, p.1-71. (The paper was presented in the all-union conf. "Equation of state", February 1988).
- [15] Minin V.F, Pyalling A.A., Kryukov B. P., Landin A.A., Ternovoi V.Ya., Fortov V.E. (1996) Influence of conditions of initiation on flow regimes at creation of the Mach configuration, *Book of abstracts of the International conference "Mathematical models and numerical methods of a continuum mechanics "*, Novosibirsk, May 27 - June 2.
- [16] Minin I.V., Minin O.V. (1992) The strong shoek-wave generation by means of space modulation of laser beams interaction with target./The paper was presented in

- International Conf. "Physics and gasodynamics of shock waves", May 27-June 2, Minsk, Belarus.*
- [17] Minin I.V. and Minin O.V. (1990) The methods of the plasma jets control in the cone ablations. The paper was presented in: *All Union Conf. "Zababachin's scientific readings", January 16-19, Chelyabinsk-70*; See also: I.V.Minin, O.V.Minin. Analytical and computation experiments on forced plasma jet formation. - Proc. of the Int. Symp. on Intense Dynamic Loading and Its Effects.- Chengdu, China, June 9-12, 1992, P. 588-591.
- [18] V.F. Minin, I.V. Minin, O.V.Minin (2006). Criterion of jet formation on axisymmetrical shaped charge // *Izv. VUZov*, №6 (27), pp. 380-389. (In Russian)
- [19] Minin V.F., Minin I.V., Minin O.V. (1991) The dynamics of shock wave focussing with the elements of diffraction quasioptics./ Book of Abstracts the 18 Int. Symp. on Shock Waves. Sendai, July 21-26.-P.39-40.
- [20] Minin I.V., Minin O.V. (1992) Diffractive quasioptics. - Moskow: InformTei, - 180 p. (in Russian). See also: Minin O.V. and Minin I.V. Diffractive optics of millimeter waves. IOP Publisher, Boston-London, 2003.
- [21] I.V. Minin, O.V.Minin (2010). Explosive pulsed plasma antennas for information protection. Chapter in: *"Microwave and Millimeter Wave Technologies: Semiconductor Devices, Circuits and Systems"*, ISBN 978-953-307-031-5, IN-TECH, Austria 2010
- [22] Dushin V.R., Minin I.V., Minin O.V. et al. (1989) Investigation of the space supersonic flows of the axisymmetrical body by the real gas.- *Vestnik MGU*, v1, #4, 41-49. (in Russian)
- [23] Minin V.F., Musatov V.V., et al. (1986) Modification of the "large particles" method for 2D non-stationary problems of continuous mechanics// *Mechanics of high-speed process*, Novosibirsk, N73, pp. 78-85. (in Russian)
- [24] V.F. Minin, I.V. Minin, O.V.Minin. (2000) The mathematical modelling of joint and magnetic-pulse welding processes// *Vestnik SF Moskow State University of press*, vol 1. M., P.9-20. (in Russian)
- [25] V.F. Minin, et al. (1998) Application of computational experiments in the study of the formation of the casting. *Proc. of the conference "Problems of industrial crystallization and computer modeling of metallurgical technologies"*, June 1-3, Izhevsk, pp.88- 89. (in Russian)
- [26] V.F. Minin. The interaction of underwater shock wave with a bubble curtain. PhD dissertation, Novosibirsk, 1959, Institute of hydrodynamics of SB of Russia, 117 p.
- [27] Kedrinskii V.K., Soloukhin R.I. (1961) Compression of a spherical gas cavity in water shock wave. *PMTF*, № 1.
- [28] Minin V.F., Minin I.V., Minin O.V. (2010) Method and devices of high-speed cumulative jet formation for perforation of boreholes with big diameter and without slug. - Patent RU № 2009145359/20(064634)

# Application of Lattice Boltzmann Method in Fluid Flow and Heat Transfer

Quan Liao<sup>1</sup> and Tien-Chien Jen<sup>2</sup>

<sup>1</sup>College of Power Engineering, Chongqing University, Chongqing,

<sup>2</sup>Department of Mechanical Engineering, University of Wisconsin-Milwaukee, Milwaukee

<sup>1</sup>P.R. China

<sup>2</sup>USA

## 1. Introduction

### 1.1 Computational Fluid Dynamics (CFD) methods

In fluid dynamics, there are three levels to describe the motion of a fluid: microscopic level, mesoscopic level and macroscopic level [1]. On different levels, there exist the corresponding models to represent the fluid flow. No matter what kind of model used, eventually each of these models should satisfy the general conservation laws, i.e., conservation of mass, conservation of momentum and conservation of energy in the macroscopic world, in which the corresponding macroscopic variables (velocity, pressure and temperature) could be measured by using various kinds of sensor.

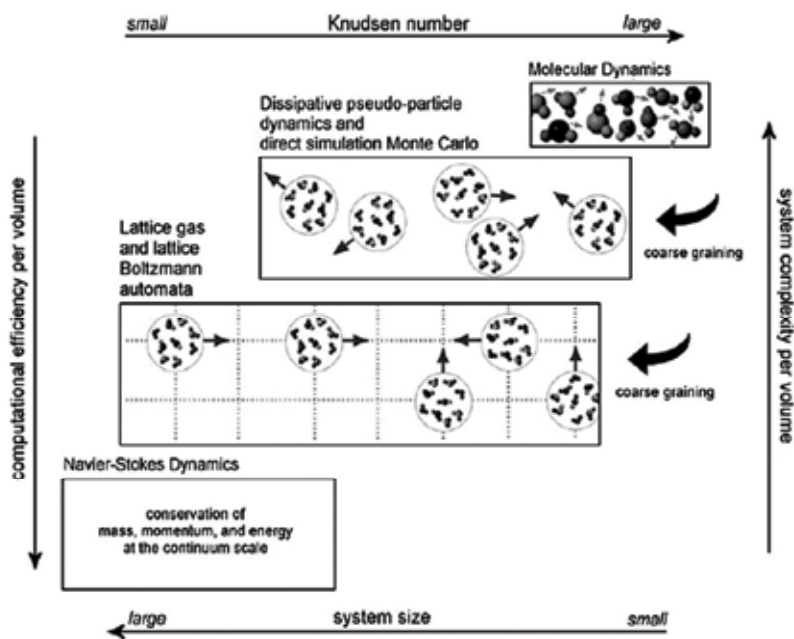


Fig. 1. Various approaches to describe fluid flow at different level

As shown in Figure 1 [2], the molecular dynamics (MD) method could be adopted to describe the fluid flow at the microscopic level. At this level, all the fluids are treated as the cluster of simple particles, such as molecule, atom and so on. All these particles are assumed to comply with the classical Newton's law of motion. Therefore, integrating the Newton's equations of motion for a set of molecules on the basis of an intermolecular potential, all the basic information (e.g., microscopic velocities) for each particle at the microscopic level could be obtained; After that if the coarse-grained procedure is introduced, all the macroscopic variables (e.g., macroscopic velocities, pressure and etc.) could be evaluated. For other models (such as dissipative particle dynamics and direct simulation Monte Carlo) at this level, they are all off-lattice pseudo-particle methods [3-8] in conjunction with Newtonian dynamics at microscopic level. In a word, at microscopic level, all the fluids are regarded as cluster of simple particles and this assumption is consistent with the reality.

At the second higher level (i.e., mesoscopic level), lattice gas and lattice Boltzmann methods treat flows in terms of coarse-grained fictitious particles which reside on a mesh and conduct translation as well as collision steps entailing overall fluid-like behavior. Therefore, it is safe to say that the fluid is still treated as a bunch of simple particles at mesoscopic level; and there is not any more particle motion equations, such as Newton's law of motion, involved except the special treatment has to be adopted for the collision procedure. At the meantime, the coarse-grained or statistical averaging process is introduced, and then the connections between microscopic and macroscopic variables (e.g., velocity, pressure and temperature) are developed.

The highest level as shown in Figure 1 is the macroscopic level. At this level, the fluid is treated as continuous medium, which means there is no space between the fluid particles and the entire domain are fully filled. Based on the continuous assumption and Newton's law of motion, the Navier-Stokes equations, which are the second order nonlinear partial differential equations (PDEs), are derived according to the general conservation laws (i.e., conservation of mass, momentum and energy).

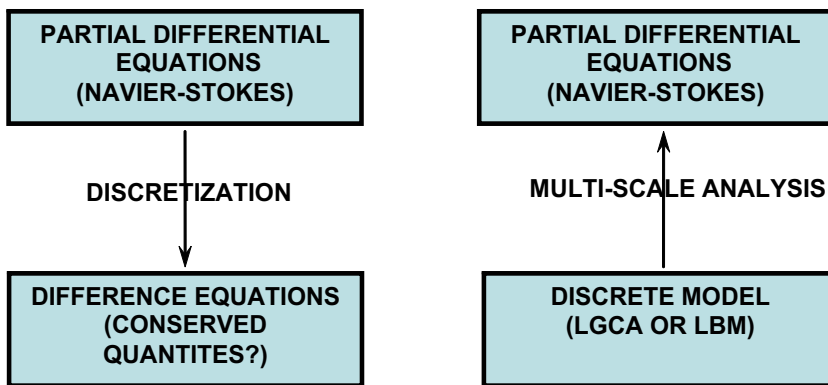


Fig. 2. Top-down versus bottom-up model

According to the methods mentioned above, it is easy to say that all of these approaches, which are at different levels, belong to two different categories: bottom-up and top-down models [1], as shown in Figure 2. At macroscopic level, the Navier-Stokes equations associated with continuity equation are adopted to describe the fluid flow. For the specific flow problem, all the boundary conditions and the corresponding initial conditions if it

needs are usually given, after solving these nonlinear PDEs, all the macroscopic variables on the specific interesting regions are obtained. Since the general procedure to solve such complicated PDEs is to discretize these governing equations in the computational domain by different methods such as finite difference, finite element or spectral method, and then the corresponding algebraic equations are solved by iteration method for the macroscopic variables at each mesh point in the interested region. This approach, which is based on the macroscopic governing equations to obtain the specific discrete macroscopic variables, is called as top-down method. Although this top-down approach seems to be straightforward, it is not without any difficulties. In many books of the numerical solution of PDEs, the author put much emphasis on the truncation error which is due to the truncation of Taylor series when going from differential equations to finite difference equations. However, engineers are usually more concerned about whether certain quantities are conserved by the discretized form of the equations. The latter property is most important for integrations over long time scales in a closed domain like in the simulation of the world oceans. A small leakage would transform the ocean into an empty basin after a long time integration. In addition, numerical instability to solve the discretized algebraic equations is another problem of this type of numerical methods.

As compared to the top-down approach, the bottom-up method that includes all those models mentioned above (i.e., Molecular Dynamics (MD) method, Lattice Gas Cellular Automata (LGCA) and Lattice Boltzmann Equation (LBE) methods), are based on the fact that all the fluids are not perfectly continuous medium, but consist of simple particles, such as molecular, atom and so on. In MD approach, one tries to simulate macroscopic behavior of real fluids by setting up a model which describes the microscopic interactions for each particle as well as possible by using classical Newton's law of motion. This usually requires large amount of particles to describe a macroscopic behavior of the fluid flow. Unfortunately, the complexity of the interactions in MD restricts the number of particles and the time of integration that could be consumed in a simulation. As compared to MD, LGCA and LBE models are quite different variants of the bottom-up approach where the starting point is a discrete microscopic model which was developed by conserving the desired quantities (conservation of mass and momentum). These models are unconditionally stable (for LGCA) or exhibit good stability properties (for LBE). However, the derivation of the corresponding macroscopic equations (Navier-Stokes equation) requires lengthy calculations by multi-scale analysis. A major problem with the bottom-up approach is to detect and avoid spurious invariant which is also a problem for the models derived by the top-down approach.

## **2. Lattice Boltzmann Equation (LBE) model**

### **2.1 Background of LBE model**

The LBE model historically is originated from a Boolean fluid model known as the Lattice Gas Cellular Automata (LGCA), which simulates the motion of fluids by particles moving and colliding on a regular lattice. The averaged fluid variables, such as mass density and velocity, are shown to satisfy the Navier-Stokes equations. It has been proved that the LBE could be derived from the continuous Boltzmann equation directly as a discrete equation, in which velocity space is discretized with the minimum set of values. The latter derivation implies a compatibility of the LBE with the Boltzmann equation. In other words, the simulation of fluid flows by using the LBE method is based on kinetic equations and statistical physics, unlike those of conventional methods which are based on continuum mechanics.

The theoretical premises of the LBE method are as follows: (1) hydrodynamics are insensitive to the details of microscopic physics, and (2) hydrodynamics could be preserved as long as the conservation laws and associated symmetries of lattice are respected locally at the microscopic or mesoscopic level. Therefore, the computational advantage of the LBE method is attained by drastically reducing the particle velocity space to only a few discrete directions without seriously degrading hydrodynamics. At the same time, the interactions between particles are restricted locally (which means the LBE model has authentically parallelism characteristic). This is possible because the LBE method rigorously preserves the hydrodynamic moments of the distribution function, such as mass density, momentum fluxes, and the necessary lattice symmetries [9-11].

The LBE method eliminates the time consuming statistical averaging step in the original LGCA due to its kinetic nature. Therefore, the LBE method is able to simulate the complicated fluid flows such as multiphase flows, chemically reacting flows, visco-elastic non-Newtonian flows. In addition, simplified collision models are developed and used to replace the collision operator derived from the LGCA to improve both the computational efficiency and accuracy. It is worth noting that the simple collision model of Bhatnagar., Gross., and Krook (BGK) was applied to the lattice Boltzmann equation and yielded the so-called lattice BGK model. Since the extra flexibility in this approach is to allow the removal of the artifacts of the LGCA (i.e., the lack of Galilean invariance and the dependence between velocity and pressure in LGCA), eventually this method was numerically found to be at least as stable, accurate, and computationally efficient as traditional CFD methods for simulation of simple single-phase incompressible fluid flows. More importantly, the microscopic physics of the fluid particles could be incorporated as easily as in other particle collision methods since fluid motion is simulated at the level of distribution functions. Due to interparticle interactions such as capillary phenomena, multiphase flows and nonlinear diffusion, many complex fluid phenomena could be simulated naturally by LBE model.

In conclusion, from a computational point of view, the notable advantages of LBE method are parallelism of algorithm (local collision), simplicity of programming (only collision and streaming steps), ease of incorporating microscopic interactions and the simplicity of modeling complex geometry flow problems.

## 2.2 From Boltzmann equation to LBE model

The Boltzmann equation, devised by Ludwig Boltzmann, describes the statistical distribution of particles in a fluid. It is one of the most important equations for non-equilibrium statistical mechanics that deals with systems far from thermodynamic equilibrium. For example, if a temperature gradient or electric field is applied on a system, the Boltzmann equation is used to study how a fluid transports physical quantities such as heat or charge, and to derive the transport properties such as thermal conductivity and electrical conductivity.

It is well known that the Boltzmann equation is an integro-differential equation for the single particle distribution function  $f(x, v, t)$  :

$$\partial_t f + v \cdot \partial_x f + \frac{K}{m} \cdot \partial_v f = Q(f, f) \quad (1)$$

where,  $v$  is the particle velocity,  $K$  is the external body force,  $f(x, v, t) d^3 x d^3 v$  is the probability to find a particle in the volume  $d^3 x$  around  $x$  and with velocity between  $v$  and



$v + dv$ , and the collision integral with  $\sigma(\Omega)$  the differential collision cross section for the two-particle collision which transforms the velocities from  $\{v, v_1\}$  (incoming) into  $\{v', v'_1\}$  (outgoing) is as follows.

$$Q(f, f) = \int d^3v_1 \int d\Omega \sigma(\Omega) |v - v_1| \left[ f(v') f(v'_1) - f(v) f(v_1) \right] \quad (2)$$

In order to solve Eq.1, one can start with arbitrary velocity distribution and make this distribution evolve according to the Boltzmann equation; eventually it will relax to equilibrium Maxwell distribution or Maxwell-Boltzmann distribution

$$f^{(M)} = f(x, v) = \rho_0 \left( \frac{m}{2\pi k_B T} \right)^{D/2} \exp \left[ -\frac{m}{2k_B T} (v - u)^2 \right] \quad (3)$$

where,  $\rho_0$  is the particle density,  $m$  particle mass,  $D$  dimension (for example,  $D=2$  for 2D case and  $D=3$  for 3D case),  $v$  microscopic particle speed,  $u$  macroscopic fluid velocity,  $k_B$  Boltzmann constant,  $T$  temperature. This equilibrium distribution is guaranteed by the famous Boltzmann H-theorem.

One of the major problems of dealing with Boltzmann equation is the complicated nature of the collision integral. It is therefore not surprising that alternative, simpler expressions have been developed. The idea behind this replacement is that the large amount of detail of two-body interactions is not likely to significantly influence the values of many experimentally measured quantities. However, the simpler operator  $J(f)$  which replaces the collision operator  $Q(f, f)$  should satisfy two constraints [1]:

1.  $J(f)$  conserves the five collision invariants  $\psi_k$  of  $Q(f, f)$ , that is

$$\int \psi_k J(f) d^3x d^3v = 0 \quad (k=0, 1, 2, 3, 4) \quad (4)$$

where,  $\psi_0 = 1$  for conservation of mass,  $\psi_{1,2,3} = v$  for conservation of momentum and  $\psi_4 = v^2$  for conservation of energy.

2. The collision term has the capability to lead the velocity distribution toward a Maxwellian distribution (H-theorem)

Both constraints are fulfilled by the most widely known model usually called the BGK approximation. The simplest way to take the second constraint into account is to imagine that each collision changes the distribution function  $f(x, v, t)$  by an amount proportional to the departure of  $f(x, v, t)$  from a Maxwellian  $f^M(x, v)$ :

$$J(f) = \omega \left[ f^M(x, v) - f(x, v, t) \right] = -\frac{1}{\tau} (f(x, v, t) - f^M(x, v)) \quad (5)$$

The coefficient  $\omega$  is called the collision frequency and  $\tau$  is called the collision time or relaxation time. From the first constraint it follows that

$$\int \psi_k J(f) d^3x d^3v = \omega \left( \int \psi_k f^M(x, v) d^3x d^3v - \int \psi_k f(x, v, t) d^3x d^3v \right) = 0 \quad (6)$$

At any space point and time instant, the Maxwellian  $f^M(x, v)$  must have exactly the same density, velocity and temperature of the fluid as given by the distribution  $f(x, v, t)$ . Since

these values will, in general, vary with space and time,  $f^M(x, v)$  is called the local Maxwellian distribution function.

Therefore, if the external body force is neglected and the BGK model is used to replace the collision integral, the following Boltzmann equation with BGK approximation can be obtained:

$$\frac{\partial f}{\partial t} + \mathbf{v} \cdot \nabla f = -\frac{1}{\tau} (f - f^M)$$

or

$$\frac{\partial f}{\partial t} + \mathbf{v} \cdot \nabla f = -\frac{1}{\tau} (f - f^{(eq)}) \quad (7)$$

where,  $f^{(eq)}$  is the local equilibrium distribution or local Maxwellian distribution.

Based on the above equation, it could be seen that the mass density distribution function,  $f(x, v, t)$ , depends on the space, velocity and time. At the same time, the  $v$ -space could be discretized by introducing a finite set of velocities,  $v_i$ , and associated distribution functions,  $f_i(x, t)$ , which are governed by the discrete Boltzmann equation:

$$\frac{\partial f_i}{\partial t} + \mathbf{v}_i \cdot \nabla f_i = -\frac{1}{\tau} (f_i - f_i^{(eq)}) \quad (8)$$

Introducing the reference parameters such as characteristic length scale,  $L$ , the reference speed,  $U$ , the reference density,  $n_r$ , and the time interval between particle collisions,  $t_c$ , the following discrete dimensionless Boltzmann equation could be obtained:

$$\frac{\partial F_i}{\partial \hat{t}} + \mathbf{c}_i \cdot \hat{\nabla} F_i = -\frac{1}{\hat{\tau} \cdot \varepsilon} (F_i - F_i^{(eq)}) \quad (9)$$

where,  $c_i = \frac{v_i}{U}$ ,  $\hat{\nabla} = L \nabla$ ,  $\hat{t} = \frac{t \cdot U}{L}$ ,  $\hat{\tau} = \frac{\tau}{t_c}$ ,  $F_i = \frac{f_i}{n_r}$  and  $\varepsilon = t_c \frac{U}{L}$ .

The parameter  $\varepsilon$  could be interpreted as either the ratio of collision time to flow time or as the ratio of mean free path to the characteristic length (i.e., Knudsen number).

A discretization of the above equation is given by:

$$\begin{aligned} & \frac{F_i(\hat{x}, \hat{y}, \hat{z}, \hat{t} + \Delta \hat{t}) - F_i(\hat{x}, \hat{y}, \hat{z}, \hat{t})}{\Delta \hat{t}} \\ & + c_{i_x} \frac{F_i(\hat{x} + \Delta \hat{x}, \hat{y}, \hat{z}, \hat{t} + \Delta \hat{t}) - F_i(\hat{x}, \hat{y}, \hat{z}, \hat{t} + \Delta \hat{t})}{\Delta \hat{x}} \\ & + c_{i_y} \frac{F_i(\hat{x}, \hat{y} + \Delta \hat{y}, \hat{z}, \hat{t} + \Delta \hat{t}) - F_i(\hat{x}, \hat{y}, \hat{z}, \hat{t} + \Delta \hat{t})}{\Delta \hat{y}} \\ & + c_{i_z} \frac{F_i(\hat{x}, \hat{y}, \hat{z} + \Delta \hat{z}, \hat{t} + \Delta \hat{t}) - F_i(\hat{x}, \hat{y}, \hat{z}, \hat{t} + \Delta \hat{t})}{\Delta \hat{z}} = -\frac{1}{\hat{\tau} \cdot \varepsilon} (F_i - F_i^{(eq)}) \end{aligned} \quad (10)$$

where,  $\Delta \hat{t} = \frac{\Delta t \cdot U}{L}$ . And then, Lagrangian behavior could be obtained by the selection of the

corresponding lattice spacing ( $\Delta\hat{x}$ ,  $\Delta\hat{y}$  and  $\Delta\hat{z}$ ) divided by the time step to equal the lattice velocity ( $c_{i_x} = \frac{\Delta\hat{x}}{\Delta\hat{t}}$ ,  $c_{i_y} = \frac{\Delta\hat{y}}{\Delta\hat{t}}$  and  $c_{i_z} = \frac{\Delta\hat{z}}{\Delta\hat{t}}$  or  $c_i = \frac{\Delta\hat{x}}{\Delta\hat{t}}$ ).

Therefore,

$$\begin{aligned} & \frac{F_i(\hat{x}, \hat{y}, \hat{z}, \hat{t} + \Delta\hat{t}) - F_i(\hat{x}, \hat{y}, \hat{z}, \hat{t})}{\Delta\hat{t}} \\ & + \frac{F_i(\hat{x} + c_{i_x} \cdot \Delta\hat{t}, \hat{y}, \hat{z}, \hat{t} + \Delta\hat{t}) - F_i(\hat{x}, \hat{y}, \hat{z}, \hat{t} + \Delta\hat{t})}{\Delta\hat{t}} \\ & + \frac{F_i(\hat{x}, \hat{y} + c_{i_y} \cdot \Delta\hat{t}, \hat{z}, \hat{t} + \Delta\hat{t}) - F_i(\hat{x}, \hat{y}, \hat{z}, \hat{t} + \Delta\hat{t})}{\Delta\hat{t}} \\ & + \frac{F_i(\hat{x}, \hat{y}, \hat{z} + c_{i_z} \cdot \Delta\hat{t}, \hat{t} + \Delta\hat{t}) - F_i(\hat{x}, \hat{y}, \hat{z}, \hat{t} + \Delta\hat{t})}{\Delta\hat{t}} = -\frac{1}{\hat{\tau} \cdot \mathcal{E}} (F_i - F_i^{(eq)}) \end{aligned} \quad (11)$$

Since,

$$\begin{aligned} & \frac{F_i(\hat{x} + c_{i_x} \cdot \Delta\hat{t}, \hat{y}, \hat{z}, \hat{t} + \Delta\hat{t}) - F_i(\hat{x}, \hat{y}, \hat{z}, \hat{t} + \Delta\hat{t})}{\Delta\hat{t}} \\ & + \frac{F_i(\hat{x}, \hat{y} + c_{i_y} \cdot \Delta\hat{t}, \hat{z}, \hat{t} + \Delta\hat{t}) - F_i(\hat{x}, \hat{y}, \hat{z}, \hat{t} + \Delta\hat{t})}{\Delta\hat{t}} \\ & + \frac{F_i(\hat{x}, \hat{y}, \hat{z} + c_{i_z} \cdot \Delta\hat{t}, \hat{t} + \Delta\hat{t}) - F_i(\hat{x}, \hat{y}, \hat{z}, \hat{t} + \Delta\hat{t})}{\Delta\hat{t}} \\ & = \frac{F_i(\hat{x} + c_{i_x} \cdot \Delta\hat{t}, \hat{y} + c_{i_y} \cdot \Delta\hat{t}, \hat{z} + c_{i_z} \cdot \Delta\hat{t}, \hat{t} + \Delta\hat{t}) - F_i(\hat{x}, \hat{y}, \hat{z}, \hat{t} + \Delta\hat{t})}{\Delta\hat{t}} \end{aligned} \quad (12)$$

Then,

$$\begin{aligned} & \frac{F_i(\hat{x}, \hat{y}, \hat{z}, \hat{t} + \Delta\hat{t}) - F_i(\hat{x}, \hat{y}, \hat{z}, \hat{t})}{\Delta\hat{t}} \\ & + \frac{F_i(\hat{x} + c_{i_x} \cdot \Delta\hat{t}, \hat{y} + c_{i_y} \cdot \Delta\hat{t}, \hat{z} + c_{i_z} \cdot \Delta\hat{t}, \hat{t} + \Delta\hat{t}) - F_i(\hat{x}, \hat{y}, \hat{z}, \hat{t} + \Delta\hat{t})}{\Delta\hat{t}} \\ & = \frac{F_i(\hat{x} + c_{i_x} \cdot \Delta\hat{t}, \hat{y} + c_{i_y} \cdot \Delta\hat{t}, \hat{z} + c_{i_z} \cdot \Delta\hat{t}, \hat{t} + \Delta\hat{t}) - F_i(\hat{x}, \hat{y}, \hat{z}, \hat{t})}{\Delta\hat{t}} \\ & = \frac{F_i(\hat{x} + c_i \cdot \Delta\hat{t}, \hat{t} + \Delta\hat{t}) - F_i(\hat{x}, \hat{t})}{\Delta\hat{t}} = -\frac{1}{\hat{\tau} \cdot \mathcal{E}} (F_i - F_i^{(eq)}) \end{aligned} \quad (13)$$

Therefore, the two terms on the left hand side could be canceled out and thereby the method becomes explicit. Choosing  $\Delta t = t_c$ , multiplying the above equation by  $\Delta\hat{t}$  and dropping all carets, one obtains the dimensionless lattice Boltzmann BGK equation:

$$F_i(\mathbf{x} + \mathbf{c}_i \cdot \Delta t, t + \Delta t) - F_i(\mathbf{x}, t) = -\frac{1}{\tau} (F_i - F_i^{(eq)}) \quad (14)$$

As we can see, this equation has a particularly simple physical interpretation in which the collision term is evaluated locally and there is only one streaming step or 'shift' operation per lattice velocity. This stream-and-collide particle interpretation is a result of the fully Lagrangian character of the equation for which the lattice spacing is the distance traveled by the particle during a time step. Higher order discretization of the discrete Boltzmann equation typically requires several 'shift' operations to evaluate each derivative and a particle interpretation is less obvious than the above one.

When a specific lattice scheme is introduced, the corresponding equilibrium distribution function and the related coefficients could be derived. In what follows, a D2Q9 lattice will be adopted as an example to show this derivation procedure.

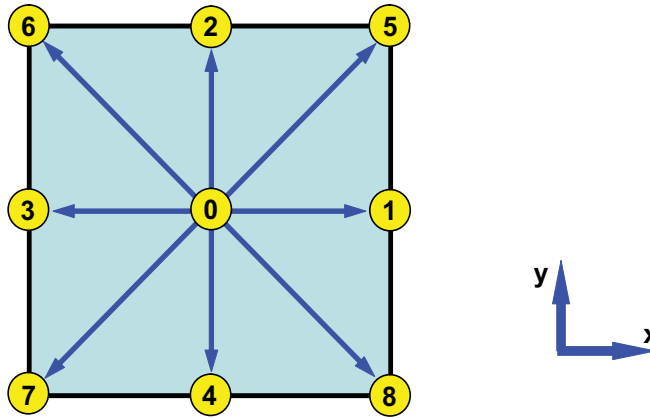


Fig. 3. D2Q9 lattice scheme

As shown in Figure 3, the corresponding lattice velocities for D2Q9 lattice are as follows:

$$\begin{aligned} c_0 &= (0,0) \\ c_{1,3,2,4} &= (\pm c, 0), (0, \pm c) \\ c_{5,6,7,8} &= (\pm c, \pm c) \end{aligned} \quad (15)$$

The mass density,  $\rho$ , and the momentum density,  $j$ , are defined by the sums over the distribution function  $F_i(x, t)$

$$\rho(x, t) = \sum_i F_i(x, t) \quad (16)$$

$$j(x, t) = \rho(x, t) \cdot u(x, t) = \sum_i c_i \cdot F_i(x, t) \quad (17)$$

For vanishing velocities, a global equilibrium distribution  $W_i$  ("fluid at rest") is defined. In the vicinity (small Mach numbers) of this equilibrium, distribution functions could be written as sums of the  $W_i$  and small perturbations  $f_i(x, t)$

$$F_i(x, t) = W_i + f_i(x, t) \quad (18)$$

With  $|f_i(x, t)| \ll W_i$ .

The  $W_i$  should be positive to guarantee the positive mass density, as shown in Eq.16. They are chosen of Maxwell type in the following sense. The lattice velocity moments up to fourth order over the  $W_i$  shall be identical to the respective velocity moments over the Maxwell distribution as shown in Eq.3.

Thus, the odd moments vanish:

$$\sum_{i=0}^8 W_i c_{i\alpha} = 0 \quad (19)$$

$$\sum_{i=0}^8 W_i c_{i\alpha} c_{i\beta} c_{i\gamma} = 0 \quad (20)$$

And the even moments read:

$$\sum_{i=0}^8 W_i = \int d\mathbf{v} \cdot f^{(M)}(\mathbf{x}, \mathbf{v}) = \rho \quad (21)$$

$$\sum_{i=0}^8 W_i c_{i\alpha} c_{i\beta} = \int d\mathbf{v} \cdot f^{(M)}(\mathbf{x}, \mathbf{v}) \cdot v_\alpha \cdot v_\beta = \rho \frac{k_B T}{m} \delta_{\alpha\beta} \quad (22)$$

$$\sum_{i=0}^8 W_i c_{i\alpha} c_{i\beta} c_{i\gamma} c_{i\delta} = \int d\mathbf{v} \cdot f^{(M)}(\mathbf{x}, \mathbf{v}) v_\alpha v_\beta v_\gamma v_\delta = \rho \left( \frac{k_B T}{m} \right)^2 (\delta_{\alpha\beta} \delta_{\gamma\delta} + \delta_{\alpha\gamma} \delta_{\beta\delta} + \delta_{\alpha\delta} \delta_{\beta\gamma}) \quad (23)$$

Note that the last constraint (i.e., Eq.23) is more rigorous than the requirement of pure lattice isotropy [1].

Nonnegative solutions of the above three equations, Eq. 21-23, for  $W_i$  could be obtained whenever the number of lattice velocities  $c_i$  is large enough [1]. For the D2Q9 lattice, after going through the calculations, one obtains

$$\frac{W_i}{\rho} = \frac{4}{9} \quad i = 0 \quad (24)$$

$$\frac{W_i}{\rho} = \frac{1}{9} \quad i = 1, 2, 3, 4 \quad (25)$$

$$\frac{W_i}{\rho} = \frac{1}{36} \quad i = 5, 6, 7, 8 \quad (26)$$

$$\frac{k_B T}{m} = \frac{c^2}{3} \quad (27)$$

The evolution of the LBE model consists of the recurring alternation between translation to the local equilibrium and propagation of the distributions to neighboring sites according to the lattice velocities. From Eq.12 the dimensionless BGK kinetic equation reads

$$F_i(\mathbf{x} + \mathbf{c}_i \cdot \Delta t, t + \Delta t) = (1 - \omega) F_i(\mathbf{x}, t) + \omega \cdot F_i^{(eq)}(\mathbf{x}, t) \quad (28)$$

Where,  $\omega = \frac{1}{\tau}$  is the dimensionless collision frequency. The local equilibrium distributions  $F_i^{(eq)}$  depend only on the local values of mass and momentum density

$$F_i^{(eq)}(\mathbf{x}, t) = F_i^{(eq)}(\rho(\mathbf{x}, t), \mathbf{j}(\mathbf{x}, t)) \quad (29)$$

They could be derived by applying the maximum entropy principle [1] under the constraints of mass and momentum conservations. Up to second order in momentum density, one obtains

$$F_i^{(eq)}(\rho, \mathbf{j}) = \frac{W_i}{\rho} \left\{ \rho + \frac{m}{k_B T} c_i \cdot \mathbf{j} + \frac{m}{2\rho \cdot k_B T} \left[ \frac{m}{k_B T} (c_i \cdot \mathbf{j})^2 - j^2 \right] \right\} \quad (30)$$

or more explicitly

$$F_i = \frac{4}{9} \rho \cdot \left[ 1 - \frac{3}{2} \cdot \frac{u^2}{c^2} \right] \quad i = 0 \quad (31)$$

$$F_i = \frac{1}{9} \rho \cdot \left[ 1 + 3 \frac{c_i \cdot \mathbf{u}}{c^2} + \frac{9}{2} \frac{(c_i \cdot \mathbf{u})^2}{c^4} - \frac{3}{2} \cdot \frac{u^2}{c^2} \right] \quad i = 1, 2, 3, 4 \quad (32)$$

$$F_i = \frac{1}{36} \rho \cdot \left[ 1 + 3 \frac{c_i \cdot \mathbf{u}}{c^2} + \frac{9}{2} \frac{(c_i \cdot \mathbf{u})^2}{c^4} - \frac{3}{2} \cdot \frac{u^2}{c^2} \right] \quad i = 5, 6, 7, 8 \quad (33)$$

Based on the equilibrium distributions and lattice velocities, the lengthy and complicated multi-scale technique (Chapman-Enskog expansion [1]) yields the Navier-Stokes equation with pressure  $p = \rho \cdot k_B T / m$ , and the corresponding kinetic shear viscosity is

$$\nu = \frac{k_B T}{m} \left( \frac{1}{\omega} - \frac{1}{2} \right) \Delta t = \frac{c^2}{3} \left( \frac{1}{\omega} - \frac{1}{2} \right) \Delta t = \frac{2 - \omega}{6\omega} c^2 \Delta t = \frac{c^2}{3} \left( \tau - \frac{1}{2} \right) \Delta t \quad (34)$$

The above given presentation of the LBE model contains all information necessary to set up the computer code. The algorithm proceeds as follows:

1. For given initial values of mass  $\rho(\mathbf{x}, t)$  and momentum density  $\mathbf{j}(\mathbf{x}, t)$ , evaluate the equilibrium distributions  $F_i^{(eq)}(\rho(\mathbf{x}, t), \mathbf{j}(\mathbf{x}, t))$  from Eq.30 or Eq.31-33, and set  $F_i = F_i^{(eq)}$ .
2. Apply the kinetic equation (Eq.28), i.e., add the the (non-equilibrium) distribution function  $F_i(\mathbf{x}, t)$  and the equilibrium distribution function  $F_i^{(eq)}(\mathbf{x}, t)$  with the appropriate weights  $(1 - \omega)$  and  $\omega$ , and then propagate it to the next neighbor (except for the distribution of 'rest particles' with  $c_0 = 0$ ).
3. Evaluate the new values of  $\rho(\mathbf{x}, t)$  and  $\mathbf{j}(\mathbf{x}, t)$  from the propagated distributions according to the corresponding definitions, Eq.16 and Eq.17.
4. Check the convergence criterion and calculate the new equilibrium distributions with the latest values of  $\rho(\mathbf{x}, t)$  and  $\mathbf{j}(\mathbf{x}, t)$ , and then go back to the second step of the algorithm until the convergence criterion is satisfied.

As shown in BGK-LBE model, the collisions are not explicitly defined like that in LGCA, but are accomplished by the transition to local equilibrium (the term  $\omega \cdot (F_i^{(eq)}(x,t))$  in the kinetic equation).

### 2.3 Incompressible D3Q27 LBE model

For the 3D fluid flow problem, the lattice D3Q15, D3Q19 and D3Q27 are commonly adopted for the different situations. However, since the lattice D3Q27 has more isotropy than other 3D lattice schemes, it is more stable and more accurate than other 3D schemes for the same fluid flow problem. Therefore, in what follows, the D3Q27 lattice model will be used as an example to show how to develop the incompressible LBE model.

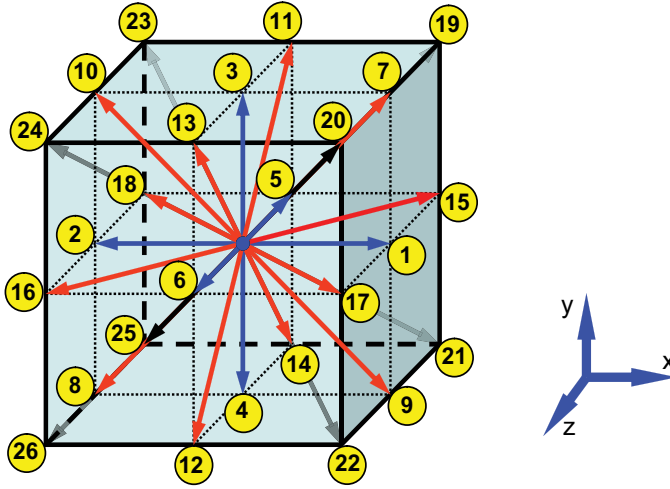


Fig. 4. D3Q27 lattice model

For the D3Q27 LBE model as shown in Figure 4, the corresponding discretized Boltzmann equation and equilibrium distribution functions are as follows:

$$f_\alpha(\mathbf{x} + \mathbf{e}_\alpha \cdot \Delta t, t + \Delta t) - f_\alpha(\mathbf{x}, t) = -\frac{1}{\tau} [f_\alpha(\mathbf{x}, t) - f_\alpha^{(eq)}(\mathbf{x}, t)] \quad (35)$$

$$f_\alpha^{(eq)} = \omega_\alpha \rho \left[ 1 + \frac{3}{c^2} \mathbf{e}_\alpha \cdot \mathbf{u} + \frac{9}{2c^4} (\mathbf{e}_\alpha \cdot \mathbf{u})^2 - \frac{3}{2c^2} (\mathbf{u} \cdot \mathbf{u}) \right] \quad (36)$$

Where,  $\mathbf{e}_\alpha$  is the discrete velocity,  $c = \Delta x / \Delta t$  the lattice speed,  $\mathbf{u}$  the macroscopic velocity,  $\omega_\alpha$  the weighting factors, and  $\Delta x$  and  $\Delta t$  are the lattice constant and time step, respectively. The lattice velocities and corresponding weighting factors for equilibrium distribution functions are as follows:

$$\mathbf{e}_\alpha = \begin{cases} (0,0,0), & \alpha = 0 \\ (\pm 1, 0, 0)c, (0, \pm 1, 0)c, (0, 0, \pm 1)c, & \alpha = 1, 2, \dots, 6 \\ (\pm 1, \pm 1, 0)c, (0, \pm 1, \pm 1)c, (\pm 1, 0, \pm 1)c, & \alpha = 7, 8, \dots, 18 \\ (\pm 1, \pm 1, \pm 1)c & \alpha = 19, 20, \dots, 26 \end{cases} \quad (37)$$

$$\omega_\alpha = \begin{cases} 8/27, & \alpha = 0 \\ 2/27, & \alpha = 1, 2, \dots, 6, \\ 1/54, & \alpha = 7, 8, \dots, 18 \\ 1/216, & \alpha = 19, 20, \dots, 26 \end{cases} \quad (38)$$

Using the Chapman-Enskog expansion, the viscosity in the corresponding Navier-Stokes equation could be derived based on the Eq.35-38.

$$\nu = \frac{c^2}{3} \left( \tau - \frac{1}{2} \right) \Delta t \quad (39)$$

This choice for the viscosity makes the BGK-LBE scheme formally a second order method for solving compressible fluid flow and the fluid flow problem could be solved by the following two steps:

Collision step:

$$\bar{f}_\alpha(\mathbf{x}, t) = f_\alpha(\mathbf{x}, t) - \frac{1}{\tau} [f_\alpha(\mathbf{x}, t) - f_\alpha^{(eq)}(\mathbf{x}, t)] \quad (40)$$

Streaming step:

$$f_\alpha(\mathbf{x} + \mathbf{e}_\alpha \cdot \Delta t, t + \Delta t) = \bar{f}_\alpha(\mathbf{x}, t) \quad (41)$$

Where,  $\bar{f}_\alpha$  denotes the post-collision state of the distribution function. Note that the collision step is completely local, and the streaming step is uniform and requires little computational effort.

It is worth mentioning that the above equations are based on the compressible fluid flow assumptions, i.e., the density is one of the independent variables. Since the incompressible fluid assumption is widely used in the real industrial applications and the corresponding error is small enough and acceptable, the incompressible LBE model is necessary to derive for the industrial applications. Because the pressure could be treated as an independent variable instead of density, the incompressible D3Q27 LBE model [12] could be obtained through the following procedures.

It is well understood that in an incompressible fluid the density is approximately a constant,  $\rho_0$ , and the density fluctuation,  $\delta\rho$ , should be of the order  $O(M^2)$  in the limit of Mach number  $M \rightarrow 0$  [13]. If we explicitly substitute  $\rho = \rho_0 + \delta\rho$  into the equilibrium distribution function,  $f_\alpha^{(eq)}$ , and neglect the terms proportional to  $\delta\rho(u/c)$ , and  $\delta\rho(u/c)^2$ , which are of the order  $O(M^3)$  or higher, then the equilibrium density distribution function becomes:

$$f_\alpha^{(eq)} = \omega_\alpha \left\{ \rho + \rho_0 \left[ \frac{3}{c^2} \mathbf{e}_\alpha \cdot \mathbf{u} + \frac{9}{2c^4} (\mathbf{e}_\alpha \cdot \mathbf{u})^2 - \frac{3}{2c^2} (\mathbf{u} \cdot \mathbf{u}) \right] \right\} \quad (42)$$

If a local pressure distribution function,  $p_\alpha \equiv c_s^2 f_\alpha$ , is introduced into the above equilibrium equation, the pressure representative equilibrium equation for an incompressible fluid could be evaluated as follows:



$$p_{\alpha}^{(eq)} = c_s^2 f_{\alpha}^{(eq)} = \omega_{\alpha} \left\{ p + p_0 \left[ 3 \frac{(\mathbf{e}_{\alpha} \cdot \mathbf{u})}{c^2} + \frac{9}{2} \frac{(\mathbf{e}_{\alpha} \cdot \mathbf{u})^2}{c^4} - \frac{3}{2} \frac{u^2}{c^2} \right] \right\} \quad (43)$$

Where,  $c_s$  is the speed sound, and  $c_s = \frac{c}{\sqrt{3}}$  for D3Q27 model,  $p_0$  is the average pressure and the equation of state for this incompressible fluid is  $p = c_s^2 \rho$ . Accordingly, the evolution equation of the LBE system for the incompressible fluid becomes,

$$p_{\alpha}(\mathbf{x} + \mathbf{e}_{\alpha} \cdot \Delta t, t + \Delta t) - p_{\alpha}(\mathbf{x}, t) = -\frac{1}{\tau} [p_{\alpha}(\mathbf{x}, t) - p_{\alpha}^{(eq)}(\mathbf{x}, t)] \quad (44)$$

The macroscopic parameters of pressure,  $p$ , and velocity,  $\mathbf{u}$ , are given by

$$p = \sum_{\alpha} p_{\alpha} \quad (45)$$

$$p_0 \mathbf{u} = \sum_{\alpha} \mathbf{e}_{\alpha} p_{\alpha} \quad (46)$$

Since the equilibrium equation and evolution equation (i.e., Eq.43 and Eq.44) for incompressible fluid have been obtained, the pressure representative incompressible LBE system could be solved by following the same procedure (i.e., collision and streaming steps as mentioned before) as the density representative compressible LBM in Eq.40 and Eq.41.

### 3. Thermal Lattice Boltzmann model

In the past 15 years, there has been rapid progress in developing the method of the lattice Boltzmann equation (LBE) for solving a variety of fluid flow problems. However, the effort for construction of stable thermal lattice Boltzmann equation (TLBE) models in order to simulate heat transfer has been initiated more recently. McNamera and Alder first succeeded in simulating heat transfer phenomena by adopting multispeed thermal fluid lattice Boltzmann models [14]. In general, the thermal lattice Boltzmann models could be classified into two categories: the multispeed or double-population model [15] and the passive-scalar approach [16].

#### 3.1 Multispeed approach for thermal lattice Boltzmann model

The multispeed approach or internal energy density distribution function (IEDDF) model is also called double-population method. In this approach, an independent internal energy density distribution function was introduced to obtain the temperature field. Therefore, two independent density distribution functions, i.e., mass density distribution function and internal energy density distribution function, are adopted to describe the fluid flow and heat transfer, respectively. As compared to the passive-scalar method, this model can exactly recover the energy conservation equation for compressible fluid flow at the macroscopic level, i.e., the viscous dissipation and compression work done by the pressure could be taken into account in this method.

Since the different independent density distribution functions are adopted to describe the fluid flow and heat transfer, these two density distribution functions may not share the same lattice model (or lattice velocity) and corresponding equilibrium distribution

functions. For example, in the 3D case the fluid flow might use D3Q27 lattice model, however, the internal energy could use D3Q19 or higher lattice model and associated equilibrium distribution function.

For the incompressible thermal problem, He *et al.* [17] proposed two distribution functions: mass density distribution function and internal energy density distribution function. The governing equations for these two functions are:

$$f_\alpha(x + e_\alpha \Delta t, t + \Delta t) - f_\alpha(x, t) = -\frac{1}{\tau_v} [f_\alpha(x, t) - f_\alpha^{(eq)}(x, t)] + \delta F \quad (47)$$

$$g_\alpha(x + e_\alpha \Delta t, t + \Delta t) - g_\alpha(x, t) = -\frac{1}{\tau_T} [g_\alpha(x, t) - g_\alpha^{(eq)}(x, t)] \quad (48)$$

Where,  $F$  is an external body force term,  $\tau_v$  and  $\tau_T$  are the fluid flow and heat transfer relaxation times, respectively.

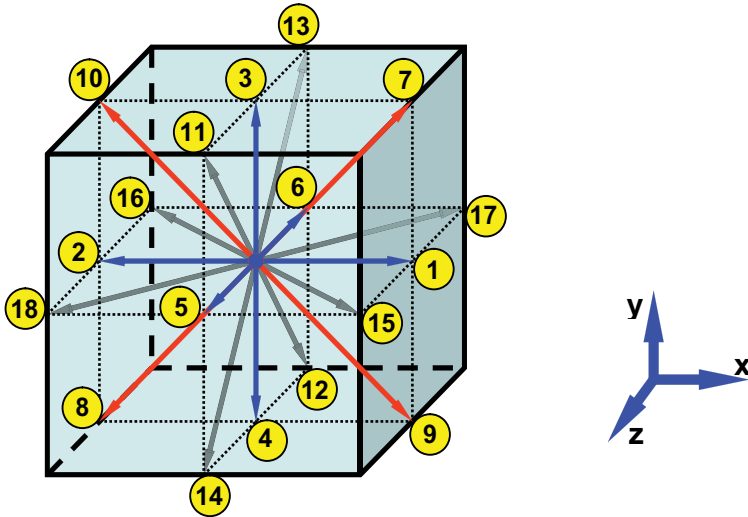


Fig. 5. D3Q19 Lattice Model

As shown in Figure 5, the D3Q19 lattice model is presented. The corresponding lattice velocities [18] of D3Q19 lattice model are defined as:

$$e_\alpha = \begin{cases} (0,0,0), & \alpha = 0 \\ (\pm 1, 0, 0)c, (0, \pm 1, 0)c, (0, 0, \pm 1)c, & \alpha = 1, 2, \dots, 6 \\ (\pm 1, \pm 1, 0)c, (0, \pm 1, \pm 1)c, (\pm 1, 0, \pm 1)c, & \alpha = 7, 8, \dots, 18 \end{cases} \quad (49)$$

And the associated mass density equilibrium distribution functions are given as:

$$f_\alpha^{(eq)} = \omega_\alpha \rho \left[ 1 + \frac{3}{c^2} e_\alpha \cdot u + \frac{9}{2c^4} (e_\alpha \cdot u)^2 - \frac{3}{2c^2} (u \cdot u) \right] \quad (50)$$

The weighting factors for each lattice direction are:

$$\omega_\alpha = \begin{cases} 1/3, & \alpha = 0 \\ 1/18, & \alpha = 1, 2, \dots, 6, \\ 1/36, & \alpha = 7, 8, \dots, 18 \end{cases} \quad (51)$$

In this model, the fluid pressure is determined by the equation of state  $p = c_s^2 \rho$  and the sound speed is  $c_s^2 = \frac{c^2}{3}$ , the viscosity in this model is calculated from the equation  $\nu = \frac{c^2}{3} \left( \tau_v - \frac{1}{2} \right) \Delta t$ , in which  $\tau_v$  is the fluid flow relaxation time. The corresponding mass density and macroscopic velocities could be evaluated by the following equations:

$$\rho = \sum_\alpha f_\alpha \quad (52)$$

$$\rho \cdot \mathbf{u} = \sum_\alpha f_\alpha \mathbf{e}_\alpha \quad (53)$$

Usually, the higher order quadrature for velocity is required for the thermal LBE model as compared to the fluid flow LBE model. Following the similar procedure of fluid flow LBE model, the LBE thermal models could be derived by properly discretizing the continuous evolution equation (Boltzmann equation) for the internal energy density distribution in temporal, spatial and velocity spaces. Therefore, the continuous equilibrium distribution function for the internal energy density distribution function can be represented by [19]

$$g^{(eq)} = \frac{\rho \mathcal{E}}{(2\pi RT)^{D/2}} \exp\left(-\frac{e^2}{2RT}\right) \left[ \frac{e^2}{DRT} + \left(\frac{e^2}{DRT} - \frac{2}{D}\right) \frac{(\mathbf{e} \cdot \mathbf{u})}{RT} + \frac{(\mathbf{e} \cdot \mathbf{u})^2}{2(RT)^2} - \frac{u^2}{2RT} \right] \\ + \frac{\rho \mathcal{E}}{(2\pi RT)^{D/2}} \exp\left(-\frac{e^2}{2RT}\right) \left[ \left(\frac{e^2}{DRT} - \frac{D+4}{D}\right) \frac{(\mathbf{e} \cdot \mathbf{u})^2}{2(RT)^2} - \left(\frac{e^2}{DRT} - \frac{D+2}{D}\right) \frac{u^2}{2RT} \right] \quad (54)$$

The zeroth- through second-order [17] moment of the second term in the above equation vanishes. Consequently, this term can be eliminated without affecting the recovery of the macroscopic energy equation from the energy evolution equation. The zeroth- through second-order moment of remaining part of the energy equilibrium distribution involves only zeroth- through fifth-order moment of  $\int \xi^m \exp(-\xi^2) d\xi = \sum w_\alpha \xi_\alpha^m$ . Therefore, the third-order Gauss-Hermite quadrature is still valid. Thus, the same lattice models for the internal energy density distribution function as those used for the mass density distribution function can be adopted (e.g., D3Q19 lattice model). At the same time, it can be seen from the thermal equilibrium distribution function that after omitting the second term, the equilibrium internal energy density distribution function has the similar form as the equilibrium mass density distribution function. Following the same derivation procedure, the equilibrium internal energy density distribution functions for D3Q19 can be obtained.

$$g_0^{(eq)} = -\frac{\rho \mathcal{E}}{2} \frac{u^2}{c^2} \quad (55)$$

$$g_{1-6}^{(eq)} = \frac{\rho \varepsilon}{18} \left[ 1 + \frac{\mathbf{e}_\alpha \cdot \mathbf{u}}{c^2} + \frac{9 (\mathbf{e}_\alpha \cdot \mathbf{u}^2)}{c^4} - \frac{3 \mathbf{u}^2}{2 c^2} \right] \quad (56)$$

$$g_{7-18}^{(eq)} = \frac{\rho \varepsilon}{36} \left[ 2 + 4 \frac{\mathbf{e}_\alpha \cdot \mathbf{u}}{c^2} + \frac{9 (\mathbf{e}_\alpha \cdot \mathbf{u}^2)}{c^4} - \frac{3 \mathbf{u}^2}{2 c^2} \right] \quad (57)$$

The internal energy is related to the temperature by  $\varepsilon = 3RT/2$ , where  $R$  is the gas constant. Then the macroscopic density, velocity and temperature could be evaluated by

$$\rho = \sum_{\alpha} f_{\alpha} \quad (58)$$

$$\rho \cdot \mathbf{u} = \sum_{\alpha} \mathbf{e}_{\alpha} \cdot f_{\alpha} \quad (59)$$

$$\rho (3RT/2) = \sum_{\alpha} g_{\alpha} \quad (60)$$

The corresponding thermal diffusivity  $\alpha$  for D3Q19 model is determined by

$$\alpha = \frac{5}{9} \left( \tau_r - \frac{1}{2} \right) \Delta t \quad (61)$$

### 3.2 Passive-scalar approach for thermal lattice Boltzmann model

The passive-scalar approach [16] utilizes the fact that the macroscopic temperature satisfies the same evolution equation as a passive scalar if the viscous dissipation and compression work done by the pressure are negligible. Therefore, in the passive-scalar thermal LBE model, the temperature is simulated by using a separate distribution function which is independent of the mass density distribution, however, this independent distribution function shares the same lattice model and equilibrium distribution functions with the mass density distribution function, this is different than the double-population method or multispeed LBE thermal model.

The main advantage of this method is the enhancement of numerical stability as compared to the previous multispeed thermal lattice Boltzmann model. It has been shown that this passive-scalar method has the same stability with the fluid flow LBE model. However, since the temperature distribution function shares the same lattice model and equilibrium distribution functions with fluid flow LBE model, the viscous dissipation and compression work done by the pressure can not be taken into account in this model.

The passive-scalar thermal LBE model is originated from the multiple component LBE model with interparticle interaction [20], which was developed for the simulation of multiphase flow and phase transitions. In the multiple components LBE model, the components can be miscible or partially immiscible depending on the strength of the interaction. When the interaction is weak or in a single phase region of a multiphase system, this model can be used to simulate diffusion due to various driving mechanisms [21]. In this passive-scalar approach, the distribution function of each component evolves according to the discretized Lattice Boltzmann equation. The same form of the equilibrium distribution

function is used for all the components except that density and velocity are calculated separately for each component. In the absence of any interaction and external forces, the distribution functions of all the components were assumed to have a common velocity  $\mathbf{u}'$ , and the conservation of the total momentum at each collision requires that

$$\mathbf{u}' = \frac{\sum_{\sigma=1}^S m_{\sigma} n_{\sigma} \mathbf{u}_{\sigma}}{\sum_{\sigma=1}^S m_{\sigma} n_{\sigma}} \quad (62)$$

Where  $S$  is the number of components in the system,  $m_{\sigma}$ ,  $\tau_{\sigma}$  and  $n_{\sigma} = \sum_{\alpha} n_{\alpha}^{\sigma}$  are the molecular mass, the relaxation time, the number density of the component  $\sigma$ , respectively. And  $m_{\sigma} n_{\sigma} \mathbf{u}_{\sigma} = m_{\sigma} \sum_{\alpha} n_{\alpha}^{\sigma} \mathbf{e}_{\alpha}$  is the momentum of component  $\sigma$  calculated from its distribution function  $n_{\alpha}^{\sigma}$ . When the force term,  $F_{\sigma}$ , applied to component  $\sigma$ , the momentum has to be correspondingly increased, and this was done by replacing velocity in the equilibrium distribution functions with the summation of old velocity and related velocity increment.

The force  $F_{\sigma}$  in general includes both interparticle forces and external forces.

In the most general multiple components LBE model with interparticle interaction and external forces, there are three types of diffusions due to different driving mechanisms [21]. They are ordinary diffusion, pressure diffusion and forced diffusion. With the equilibrium distribution functions, the pressure diffusion does not appear. If a common acceleration is applied to all the components, namely  $F_{\sigma} = \rho_{\sigma} \mathbf{g}$ , forced diffusion is also absent. The only type of diffusion left is the ordinary diffusion due to concentration gradients which obeys Fick's Law. In addition, a component (e.g., component S) can be made to behave as a passive scalar by setting its molecular mass to zero together with its interaction with all the other components. Therefore, this component will not contribute to the total momentum of the mixture. It is simply advected "passively" and diffuses into the main flow, having no effect on the flow. Similar to the kinetic viscosity in fluid flow LBE model, the corresponding thermal diffusivity in the passive scalar model is defined as:

$$\alpha = \frac{c^2}{3} \left( \tau_T - \frac{1}{2} \right) \Delta t \quad (63)$$

Where,  $\tau_T$  is the corresponding heat transfer relaxation time.

Since the viscosity in the LBE model is defined as

$$\nu = \frac{c^2}{3} \left( \tau_v - \frac{1}{2} \right) \Delta t \quad (64)$$

Therefore, the corresponding Prandtl number of the fluid is

$$\text{Pr} = \frac{\nu}{\alpha} = \frac{2\tau_v - 1}{2\tau_T - 1} \quad (65)$$

In a word, to compare these two thermal LBE models, it is easy to make the conclusion that the passive scalar method is much easier and better than multispeed approach if the viscous dissipation and compression work done by the pressure can be negligible.

#### 4. Boundary treatments for LBE model

In the previous sections, the fluid flow lattice Boltzmann equation model, the thermal lattice Boltzmann model and corresponding algorithm to solve for the macroscopic variables (i.e., velocity, pressure and temperature) are demonstrated. In order to properly proceed the algorithm and eventually get the meaningful results, special attentions must be paid at the boundary treatments, which is as important as it usually does for solving the Navier-Stokes equations by finite difference, finite elements or any other top-down models.

For the top-down model, since it starts with macroscopic variables, such as velocity, temperature, pressure, and ends up with the same macroscopic variable distributions. It is straightforward to specify the macroscopic variables on the boundary to the corresponding algebraic equations. However, for the bottom-up models (such as LBE model, MD model), all the calculations are proceeded at the microscopic or mesoscopic level and we do not have the corresponding microscopic or mesoscopic information to specify, but only the macroscopic boundary information in the computational domain. Therefore, how to develop the connections between the microscopic or mesoscopic and macroscopic levels on the specific physical boundaries is one of the necessary steps before these bottom-up methods can be used to do some real case simulations.

Specifically, for the LBE model, since the calculation process is very simple, i.e., streaming and collision, the boundary treatment schemes focus on how to find out the directional density distribution functions on the boundary nodes pointing from outside of domain (or solid) to inside of computational domain (or fluid). However, the difficulties arise from that there is no essential information provided by streaming process at the previous time level on the boundary nodes, and how to transfer the macroscopic information (e.g., velocity and pressure) to the mesoscopic information, i.e., density distributions functions for the boundary nodes.

##### 4.1 Periodic boundary scheme

The simplest boundary condition is “periodic” in that the system becomes closed by the edges being treated as if they are attached to opposite sides, as shown in Fig. 6. The highlight dashed edges at circumference of cylinder are attached seamlessly.

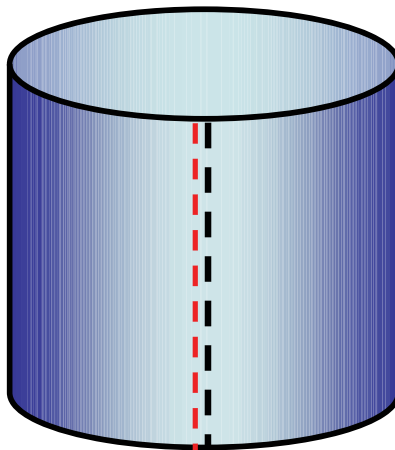


Fig. 6. Periodic boundary illustration

In the literatures, most early papers used these periodic conditions at inlet/outlet boundary along with bounce back boundaries at wall. In simulating flow in a duct for example, bounce back boundaries would be applied at the duct walls and periodic boundaries would be applied to the “open” ends of the inlet and outlet cross sections.

Fully periodic boundaries are also useful in some cases (for example, simulation of an infinite domain of multiphase fluids). In this case, the computational domain topology is like a torus, i.e., there are no specific edges or all the edges are connected together in the specific direction.

The implementation of periodic boundary treatment is very easy. On the streaming step, once the computational boundary nodes are detected, the boundary neighboring nodes, which lie outside of computational domain, will be pointed to the appropriate nodes on the opposite boundary in the same orientation.

#### 4.2 Bounce back boundary scheme

As shown in Figure 7, the so-called bounce back scheme is when a particle reaches a wall node, the particle will scatter back to the fluid nodes along its incoming direction. The collision process does not occur at the boundary, but only at the internal fluid region.

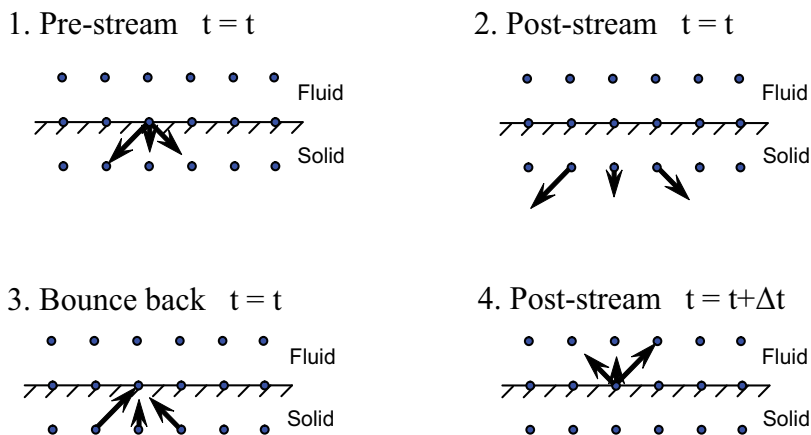


Fig. 7. Illustration of bounce back boundary treatment

In order to apply the bounce back boundary, the entire solids will be separated into two categories: boundary solids that lie at the solid-fluid interface and isolated solids that do not contact with the fluid. With this division, it is possible to eliminate unnecessary computations at inactive nodes, i.e., isolated nodes. For example, this treatment could be particularly important for the simulation of fluid flow in fractured media, where the fraction of the total domain occupied by the open space accessible to fluids might be very small.

Since bounce back boundary treatment is particularly simple, it has played a major role in making LBE model popular among modelers interested in simulating fluids in domains characterized by complex geometries such as those found in porous media. The beauty of this boundary scheme lies in that one simply needs to designate a particular node as a solid obstacle and no other special programming treatment is required. Therefore, it is trivial to incorporate images of porous media for example and immediately conduct the fluid flow simulation in them.

It has been found that the slip velocity between boundary surface and fluid is zero at the boundary as long as the momentum dissipated by boundaries is equal to the stress provided by the fluid, no matter what combination of distributions is chosen. Therefore, the bounce back boundary scheme would inevitably generate a nonzero slip velocity between the boundary surface and the fluid at the boundary because the collision step just happens only in interior fluid region. In addition, it has been already confirmed that the bounce back scheme is only of first order in numerical accuracy at the boundaries, which degrades the LBE, because the numerical accuracy of the LBE is of second order in the interior points.

Even though there are different versions of bounce back boundary scheme (e.g., modified bounce back scheme, in which the collision process is introduced at the boundary nodes, and bounce back scheme with the wall located halfway [22] between a fluid node and a bounce back node) and the accuracy of these schemes was improved a lot as compared to the original bounce back boundary scheme, the no-slip velocity still exists except the case in which the relaxation time is 1.

### 4.3 Von Neumann (Flux) boundary

Von Neumann boundary conditions specify the flux at the boundaries. For example, in 2D case, a velocity vector consisting of  $x$  and  $y$  components is specified from which density/pressure is computed on the basis of conditions inside the computational domain.

Only the macroscopic density/pressure and the unknown directional density distributions need to be computed. After the streaming step, there are three unknown directional densities at each lattice node pointing from the boundary into the computational domain, i.e., the highlighted density distributions  $f_4$ ,  $f_7$  and  $f_8$  as shown in Figure 8. These unknowns can be solved in a way that maintains the specified macroscopic velocities at their lattice nodes.

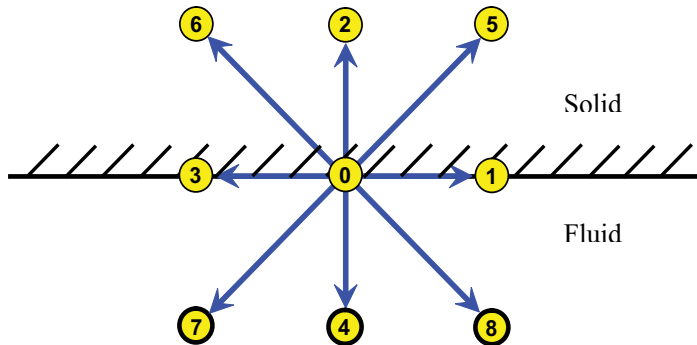


Fig. 8. Von Neumann Boundary for D2Q9 lattice

As shown in Figure 8, assuming the boundary conditions are vertical velocity  $u_y = u_{y0}$  and horizontal velocity  $u_x = 0$ . After streaming at solid-fluid boundary, there are three unknown directional density distributions, i.e.,  $f_4$ ,  $f_7$  and  $f_8$ . The other distributions are already known because they arrived from other nodes inside the computational domain. Four equations are needed to solve for  $\rho$ ,  $f_4$ ,  $f_7$  and  $f_8$ .

The macroscopic density formula can be written as:

$$\rho = \sum_{\alpha} f_{\alpha} \quad (66)$$



By considering the individual  $f_s$  that can contribute to  $x$  and  $y$  velocities, the equation for macroscopic velocity is:

$$\mathbf{u} = \frac{1}{\rho} \sum_{\alpha} f_{\alpha} \mathbf{e}_{\alpha} \quad (67)$$

This gives two equations, one for each direction:

X-direction:

$$0 = f_1 - f_3 + f_5 - f_6 - f_7 + f_8 \quad (68)$$

and

Y-direction:

$$\rho \cdot u_{y0} = f_2 - f_4 + f_5 + f_6 - f_7 - f_8 \quad (69)$$

A fourth equation can be written by assuming that the bounce back condition holds in the direction normal to the boundary

$$f_2 - f_2^{(eq)} = f_4 - f_4^{(eq)} \quad (70)$$

as proposed by Zou and He (1997) [23].

Based on Eq.66, Eq.68, Eq.69 and Eq.70, the four unknowns ( $\rho$ ,  $f_4$ ,  $f_7$  and  $f_8$ ) can be solved as follows:

$$\rho = \frac{f_0 + f_1 + f_3 + 2(f_2 + f_5 + f_6)}{1 + u_{y0}} \quad (71)$$

$$f_4 = f_2 - f_2^{(eq)} + f_4^{(eq)} = f_2 - \frac{2}{3} \rho \cdot u_{y0} \quad (72)$$

$$f_7 = f_5 + \frac{1}{2}(f_1 - f_3) - \frac{1}{6} \rho \cdot u_{y0} \quad (73)$$

$$f_8 = f_5 - \frac{1}{2}(f_1 - f_3) - \frac{1}{6} \rho \cdot u_{y0} \quad (74)$$

To briefly summarize the procedure, a velocity is specified at the boundary and solve for the macroscopic density and three unknown directional density distributions by Eq.66, Eq.68, Eq.69 and Eq.70. The equations come from the usual macroscopic variable formula and the assumption that bounce back is still satisfied in the direction normal to the boundary.

#### 4.4 Dirichlet (pressure) boundary

Dirichlet boundary conditions specify the pressure/density at the boundaries. The solution for these boundaries is closely related to that discussed above for the velocity boundaries. A density  $\rho_0$  is specified from which velocity is computed. Since the relationship between mass density and pressure can be corrected by equation of state, specifying density is equivalent to specifying pressure.

Assuming velocity tangent to the boundary is zero and solve for the component of velocity normal to the boundary. In 2D case, the velocity and a proper distribution function at the boundary nodes need to be determined (as shown in Figure 8). After the streaming step, there are still three unknown directional density distributions at each lattice node pointing from the boundary into the computational domain. These unknowns can be solved in a way that maintains the specified pressure/density  $\rho_0$  at their lattice nodes.

Given the boundary condition  $\rho = \rho_0$  and the known directional densities ( $f_0, f_1, f_2, f_3, f_5, f_6$ ), four unknowns ( $u_y, f_4, f_7$  and  $f_8$ ) need to be solved. Similarly, this can be done by:

Macroscopic density equation:

$$\rho_0 = \sum_{\alpha} f_{\alpha} \quad (75)$$

Macroscopic velocity:

$$0 = f_1 - f_3 + f_5 - f_6 - f_7 + f_8 \quad (76)$$

$$\rho_0 u_y = f_2 - f_4 + f_5 + f_6 - f_7 - f_8 \quad (77)$$

And the assumption that bounce back [23] still holds in the direction normal to the boundary:

$$f_2 - f_2^{(eq)} = f_4 - f_4^{(eq)} \quad (78)$$

Based on the above four equations (i.e., Eq.75-78) to solve the four unknowns ( $u_y, f_4, f_7$  and  $f_8$ ), it yields:

$$u_y = -1 + \frac{f_0 + f_1 + f_3 + 2(f_2 + f_5 + f_6)}{\rho_0} \quad (79)$$

$$f_4 = f_2 - f_2^{(eq)} + f_4^{(eq)} = f_2 - \frac{2}{3} \rho_0 u_y \quad (80)$$

$$f_7 = f_5 + \frac{1}{2}(f_1 - f_3) - \frac{1}{6} \rho_0 u_y \quad (81)$$

$$f_8 = f_5 - \frac{1}{2}(f_1 - f_3) - \frac{1}{6} \rho_0 u_y \quad (82)$$

It can be seen that the calculation procedure is similar to the Von Neumann boundary case.

#### 4.5 Extrapolation boundary scheme

Since the lattice Boltzmann scheme can be regarded as a special finite difference of the kinetic equation, this scheme allows us to use the extrapolation scheme for the boundary [24], which is similar to the approach for boundary conditions used in traditional finite difference schemes. The idea of this procedure is as follows: for any given fluid flow, it is assumed that there is one additional layer of sites, beyond the boundary, inside the wall (such as layer F-G-H as shown in Figure 9).

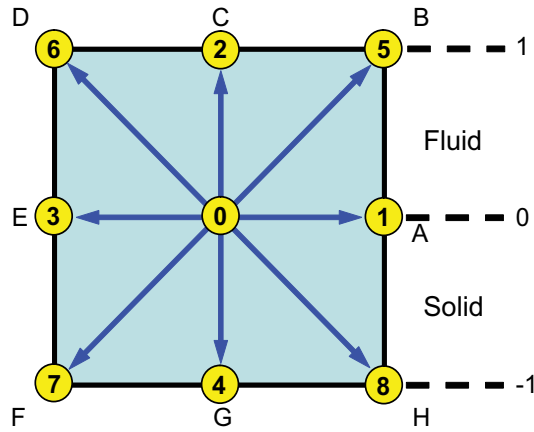


Fig. 9. Extrapolation boundary scheme for D2Q9 lattice

At each time step after the collision for the nodes on the lattice (which include inner lattice and the lattice on the boundary), all the distribution functions are known for these nodes, including the nodes at the boundary. Since the density distributions are continuous functions for each direction, the second order extrapolation method is applied to obtain the distribution functions at the extra lattice by using the value of the distribution function on the wall layer (E-O-A) and the layer of one lattice inside of the fluid (D-C-B). This implies that the following condition can be enforced at each time step and direction for the outside nodes only after the collision:

$$f_i^{-1} = 2f_i^0 - f_i^1 \quad (83)$$

where,  $f_i^{-1}$ ,  $f_i^0$  and  $f_i^1$  are the distribution functions on the outside layer, the wall layer and the first layer inside the fluid, respectively.

Once all the distribution functions at the extra nodes are obtained, it seems as if the real boundaries are the inner nodes, which are like the fluid nodes inside the computational domain. Then the streaming step in the newly expanded domain can be performed. It can be seen that there are NO unknown distribution functions for the real boundary nodes. Once the streaming step is done and the collision process will be conducted for all the nodes except the one on additional layers (because there are some unknown distribution functions on those nodes). For the real boundary nodes, the given macroscopic boundary variables (such as velocity and pressure) are enforced on the corresponding equilibrium distribution functions. However, for the inner nodes of computational domain, such macroscopic variables can be evaluated by using the known distribution functions and these values will be used to compute the corresponding equilibrium distribution functions. The different source of macroscopic variables is the only one difference between the inner nodes and the nodes on the real boundary. Therefore, the constant density (or constant pressure condition due to the equation of state in LBE model) and constant velocity can be easily implemented through the corresponding equilibrium distribution functions.

It should be noted that the extrapolation scheme does not require any specific assumptions about the incoming particle distribution. In addition, it can be seen from extrapolation scheme (Eq.83) that this scheme guarantees a second order numerical accuracy for the unknown distribution functions at the wall boundary. Since all other macroscopic

quantities, such as density, momentum flux and the strain field, are simply weighted summations of the distribution functions over particle velocity directions, it can be concluded that the corresponding macroscopic quantities have the same numerical accuracy as the distribution functions. Since the collision process occur not only on the nodes in the internal fluid region, but also on the nodes at the boundary, and the macroscopic boundary conditions are directly applied to the corresponding equilibrium distribution function for the boundary nodes, the extrapolation boundary scheme is also a no-slip boundary scheme.

#### 4.6 Thermal boundary treatment

Considering the thermal boundary conditions, the fluid flow boundary treatments (such as bounce back boundary, extrapolation boundary) can also be used by the temperature variable. However, it has been confirmed that [25-27], to date, the model of assuming a counter slip thermal energy density boundary is of the highest accurate boundary treatments because it can guarantee the fixed velocity and temperature or heat flux at the wall exactly.

For the isothermal wall boundary case, the temperature is fixed as  $T_0$  at the solid surface pointing to the fluid region. After streaming,  $g_2$ ,  $g_5$  and  $g_6$  are unknowns, as shown in Figure 10.

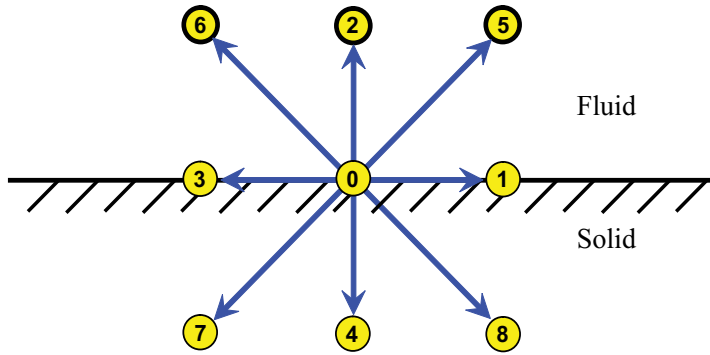


Fig. 10. Counter slip thermal boundary for D2Q9 lattice

Assume these unknown temperature density distributions are equal to their temperature density equilibrium distributions with unknown temperature  $T^*$ . Adding these three unknown temperature density distributions together (e.g., for the passive scalar thermal LBE model), it yields:

$$g_2 + g_5 + g_6 = \frac{1}{6} T^* (1 + 3u_y + 3u_y^2) \quad (84)$$

where  $u_y$  is the velocity normal to the wall and the  $x$  velocity ( $u_x$ ) is assumed to be zero. If the value of  $T^*$  is known, the unknown temperature density distributions ( $g_2$ ,  $g_5$  and  $g_6$ ) can be solved by using the corresponding temperature equilibrium distribution functions. Meanwhile, note that for the isothermal wall, it reads:

$$\sum_{\alpha} g_{\alpha} = T_0 \quad (85)$$

Substitute Eq.84 into Eq.85 and solve for  $T^*$ , it shows:

$$T^* = \frac{6}{1 + 3u_y + 3u_y^2} (T_0 - g_0 - g_1 - g_3 - g_4 - g_7 - g_8) \quad (86)$$

Eventually, the three unknown temperature density distributions ( $g_2$ ,  $g_5$  and  $g_6$ ) can be obtained by substituting  $T^*$  into the temperature density equilibrium distributions. Obviously, this method can be easily extended to the 3D case without any difficulties. For the heat flux boundary condition, a second order finite difference scheme is used to evaluate the temperature on the wall,

$$q = \left. \frac{\partial T}{\partial y} \right|_{y=0} = \frac{-3T_{i,1} + 4T_{i,2} - T_{i,3}}{2\Delta y} \quad (87)$$

After finding the wall temperature, the same procedure as described in the isothermal wall case is used to calculate the unknown temperature density distributions.

#### 4.7 Body force treatment

Since there exist all kinds of body forces (e.g., gravity, centrifugal force) in the real case simulations, how to deal with the body force in the LBE model is another important issue needed to be done before this method can be widely used in the real applications.

Consider the Newton's second law of motion, we have

$$\mathbf{F} = m\mathbf{a} = m \frac{d\mathbf{u}}{dt} \quad (88)$$

Recognizing that the density is proportional to the mass, the lattice length is the unit length in the LBE model (which means the volume for each basic lattice is also unit) and that the relaxation time  $\tau$  is the elementary time of collisions, then rearrange Eq.88, it yields:

$$\Delta\mathbf{u} = \frac{\tau \cdot \mathbf{F}}{\rho} \quad (89)$$

where  $\Delta\mathbf{u}$  is a increment in velocity due to the external body force. Finally, it can be written down like:

$$\mathbf{u}^{(eq)} = \mathbf{u} + \Delta\mathbf{u} = \mathbf{u} + \frac{\tau \cdot \mathbf{F}}{\rho} \quad (90)$$

where  $\mathbf{u}^{(eq)}$  is used to compute the equilibrium distribution functions,  $f^{(eq)}$ , and  $\mathbf{u}$  comes from the summation over the local distribution functions,  $f_\alpha$ , like Eq.17.

## 5. Application of Lattice Boltzmann model

In the previous sections, the LBE fluid flow, heat transfer models and the corresponding boundary treatments have been discussed in details. In this section, these models will be used to solve the fully developed fluid flow and heat transfer problem in a curved square duct to validate this new approach. The D3Q27 incompressible fluid flow and passive scalar

thermal LBE models are adopted to simulate the fully developed fluid flow and heat transfer in the curved square duct, and the flow driven force, i.e., pressure difference, and centrifugal force, will be taken into account in the models like body force acting on each lattice.

### 5.1 Fluid flow and heat transfer in curved square duct

The study of viscous flow in the curved ducts is of fundamental interest in fluid mechanics because of the numerous applications such as flows through turbo machinery blade passages, aircraft intakes, diffusers, heat exchangers etc. [28]. The major effect of curved duct on the fluid flow involves the strong secondary flow due to the longitudinal curvature in the geometry. The presence of longitudinal curvature generates the centrifugal force perpendicular to the main flow along the axis and produces the so-called secondary flow on the cross section of ducts. As a consequence of this centrifugal force, the axial velocity profile will be distorted (from the typical-parabolic velocity profile in straight ducts) with an outward shift of the peak axial velocity, and at the same time, the total flow rate will be reduced due to the decrease of average axial velocity.

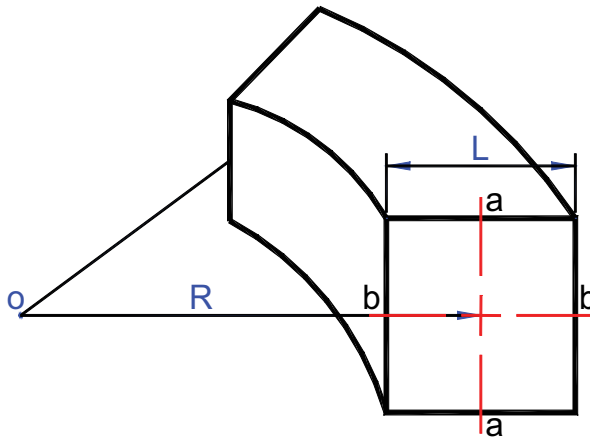


Fig. 11. The geometry configuration of curved square duct

As shown in Figure 11, a curved square duct with side length  $L$  is placed on the horizontal plane and the radius of the curved duct is  $R$ , measured from the center of duct to the center of the curve. The fluid flows in the square duct about the center of curvature toward the inside of the plane of the paper.

The curvature ratio of this curved duct is defined as:

$$C = \frac{D_h}{R} \quad (91)$$

Where,  $D_h$  is the equivalent hydrodynamic diameter of square duct, which is defined as

$$D_h = \frac{4A}{P} = \frac{4L^2}{4L} = L \quad (92)$$

The non-dimensional characteristic Dean number is defined as the function of Reynolds number and curvature ratio.

$$D_n = R_e \cdot (C)^{0.5} \quad (93)$$

$$R_e = \frac{U \cdot D_h}{\nu} \quad (94)$$

where,  $R_e$  is the Reynolds number of the duct flow. A uniform grid is used in this article, and the corresponding relaxation factors for fluid flow and heat transfer are in the range of 0.6 ~1.0.

On each cross section of curved duct, a constant pressure gradient is introduced to drive fluid flow along the duct's axial direction. Due to the longitudinal curvature and axial velocity, the centrifugal force is involved and drives the fluid flow far away from the center of curved duct (i.e., point  $O$  as shown in Figure 11), and then the so-called secondary flow is formed on the cross section. In this article, both pressure gradient and centrifugal force are treated like body forces acting on each interior lattice with different directions on the cross section of duct (which is the projection of the computational domain), and the macroscopic momentum conservation method [23, 24] is used to apply these body forces to the LBE fluid flow and heat transfer models.

As shown in Figure 11, the fluid flows in the square duct pointing toward the inside of the plane of the paper. Since the fully developed fluid flow and heat transfer will be studied numerically in this section, the axial velocity profile and dimensionless temperature distribution on the cross section will not be changed along the main flow direction. Therefore, the original computation domain, which consists of the square cross section and curved duct, can be simplified to a domain including the square cross section and a few lattice lengths perpendicular to this section plane. As a result of this simplification, the basic LBM with uniform lattice can be used to solve this problem without any special treatment for the curved boundary. It is worth noting that although the original computation domain has been simplified, the fluid flow and heat transfer simulations are still in three dimensions, i.e., two dimensions on the cross section and one dimension in the axial flow direction.

For fluid flow in pipes, the Fanning friction factor is defined as [25]:

$$C_f = \frac{2 \cdot \tau_w}{\rho \cdot V_{avg}^2} \quad (95)$$

where  $\tau_w$  is the average wall shear stress and is defined as:

$$\tau_w = \mu \cdot \frac{dU_z}{dn} \quad (96)$$

Plugging Eq.96 and Eq.94 into Eq.95 and rearranging, one obtains the following friction factor for the curved duct.

$$C_f \cdot R_e = \frac{2 \cdot D_h}{V_{avg}} \cdot \frac{dU_z}{dn} \quad (97)$$

As far as fluid flow in straight square duct is concerned, the analytical friction factor is available in literature and equals 14.25 [26].

For heat transfer in curved duct, the corresponding dimensionless temperature and Nusselt number are defined as follows:

$$T^* = \frac{T_w - T}{T_w - T_m} \quad (98)$$

$$Nu = \frac{\bar{h} \cdot D_h}{k} \quad (99)$$

where  $T_w$  and  $T_m$  are the wall temperature and mean temperature across the duct, respectively.  $\bar{h}$  is the average heat transfer coefficient around the four wall sides and is defined as:

$$\bar{h} = \frac{-k \cdot \frac{\partial T}{\partial n}}{T_w - T_m} \quad (100)$$

Plugging Eq.98 and Eq.100 into Eq.99 and rearranging, one obtains:

$$Nu = D_h \cdot \frac{\partial T^*}{\partial n} \quad (101)$$

For the fluid flow and heat transfer in a straight square duct, the analytical Nusselt number with constant wall temperature is 2.98 [26].

In order to obtain more accurate results, the two-dimensional Simpson integration method is used to calculate the average axial velocity based on the uniform lattice on the cross section.

## 5.2 Boundary conditions

In the simplified computation domain, the boundary conditions have to be specified in two parts with three directions, i.e., axial flow direction and two directions on the cross section plane.

**Axial flow direction:** Since both the fluid flow and heat transfer are fully developed, the velocity and dimensionless temperature profiles will not change along the axial flow direction (which is perpendicular to the plane of the paper and toward inside). Therefore, the simple periodic boundary can be naturally applied for both fluid flow and heat transfer in this direction, without any special treatment for the curved boundary.

**Cross section plane:** On the duct cross section, four sides of wall are needed to specify the boundary conditions. In this mathematic model, the no-slip boundary and constant wall temperature conditions are applied on the four duct walls for fluid flow and heat transfer, respectively. The second-order extrapolation boundary treatment [27] and counter-slip thermal boundary treatment [28] are employed for the fluid flow and heat transfer to determine the unknown distributions (i.e., pressure and dimensionless temperature distributions) coming from outside the computation domain.

Once all these boundary conditions are established, the fully developed fluid flow and heat transfer in the straight square duct are simulated using the current LBM model by letting curvature ratio approach to zero (i.e., the radius of curved duct,  $R$ , is big enough, for example,  $10^9$ ), and the converging criterion in this test simulation is that the relative error of



total velocity (including three components) on each uniform lattice is less than  $1.0 \times 10^{-4}$  for every 400 consecutive time steps. After the converging criterion is reached, the simulation results show that both friction coefficient and Nusselt number are very in good agreement with analytical results (i.e., the relative errors versus analytical results are less than 0.1%). This validates that this LBM model is correct and the simplification of computation domain is feasible and applicable. In addition to this bench mark validation of the straight duct, a grid convergence test was implemented before any data were adopted. For a given fluid flow problem, different number of uniform lattices (i.e.,  $50 \times 50 \times 3$ ,  $100 \times 100 \times 3$  and  $160 \times 160 \times 3$ , where three lattices are used for the periodic direction) for the same computation domain were used to compare the differences in terms of friction coefficient and flow pattern on the cross section. After a couple of comparisons, it was found that the uniform lattice  $100 \times 100 \times 3$  has both good accuracy and less computing cost. Therefore,  $100 \times 100 \times 3$  uniform lattice mesh is used in this article to simulate the fluid flow and heat transfer problems.

## 5.3 Simulation results and discussion

### 5.3.1 Fluid flow

As shown in Figure 12, the non-dimensional axial velocity distribution of cross section b-b is presented at different Dean number with a constant curvature ratio,  $C = 0.05$ . From this Figure, it is evident that, as the Dean number increases, the maximum axial velocity first shifts toward the outside of the duct from near the center position until it reaches a most outside point on the cross section; and then once the Dean number reaches a certain value (which is a function of the curvature ratio), the velocity profile on cross section b-b suddenly changes to a new pattern (as shown in Figure 12), and the location of maximum axial velocity is much closer to the center of duct than before. Moreover, as Dean number increases further, the maximum axial velocity moves toward the center of duct, which is the opposite moving direction compared to the case with smaller Dean number before the new velocity profile was observed.

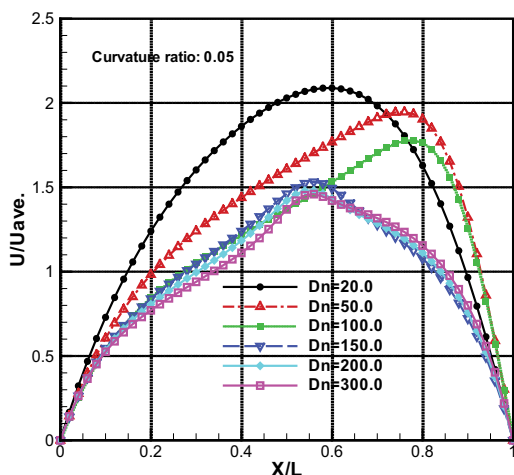


Fig. 12. Velocity distributions along b-b cross section

With the same conditions, the dimensionless axial velocity profile along cross section a-a is shown in Figure 13. In this Figure, it is apparent that as the Dean number increases, the peak of velocity profile on cross section a-a changes from one point at the beginning to two symmetrical points, and eventually up to three points (one is at the center and the other two

are symmetrical about the center one). Meanwhile, the axial velocity on this cross section a-a is becoming more uniform as Dean number increases. The switchback movement of maximum axial velocity on cross section b-b in Figure 12 and the change of number of peak velocities on plane a-a in Figure 13 can be explained as follows. On the duct cross section, the centrifugal force (which is induced by axial velocity and duct curvature) drives the fluid flow from inner side wall to the outer side wall and this fluid flow causes a symmetrical flow pattern on the cross section for the horizontal curved duct. Compared to the main axial fluid flow (which is perpendicular to cross section), the flow on the cross section is called secondary flow. When the Dean number is small, there is just one peak point on the axial velocity profile, and the secondary flow is one pair of weak symmetrical eddies due to the small centrifugal force. As Dean number keeps increasing, the axial maximum velocity moves toward the outside of wall and, at the same time, the two symmetrical eddies become stronger and stronger, eventually distorting the axial velocity from a single peak to two symmetrical peaks on cross section a-a. On the other hand, once Dean number exceeds a certain value, the secondary flow suddenly changes from one pair symmetrical eddies to two pairs of symmetrical eddies (having opposite rotating directions) due to the imbalance between centrifugal force and pressure gradient on the cross section. This is the so-called Dean instability [29, 30]. Therefore, the velocity distribution on section b-b suddenly changes and another peak velocity appears at cross section a-a, that is, there are now three peak velocities.

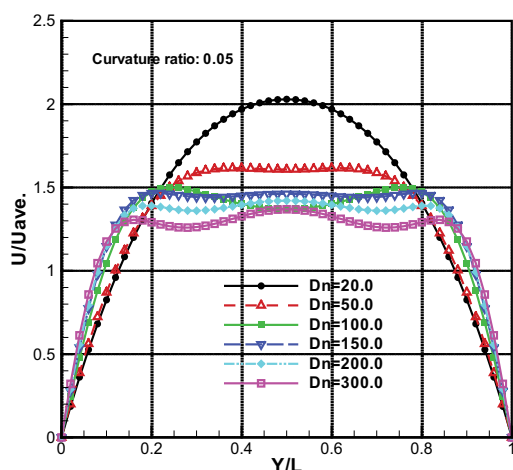


Fig. 13. Velocity distributions along a-a cross section

In Figures 14 to 17 or 18 to 21, the detailed dimensionless axial velocity distributions are presented and the transition process from one velocity peak to two peaks and eventually to three peaks are all clearly shown (i.e., Figures 14- 16 or 18- 20 in 3-D view). Based on these axial velocity contours, it is obvious that the higher Dean number, the greater velocity gradient that will be observed around the duct walls, especially for the two vertical sides, and this is consistent with the previous results in Figure 13. Moreover, since the axial velocity with the same number of uniform contour lines is provided at different Dean numbers, the distribution of uniform contour lines shows how well the axial velocity distribute uniformly on the cross section. From Figures 15-17 or 19-21, one can conclude that the axial velocity trends to be more uniform on the cross section area as Dean number increases, which is also consistent with Figures 22 and 23.

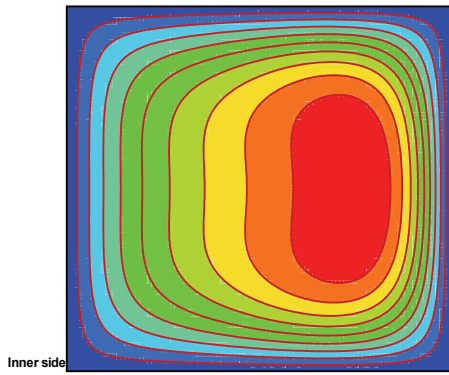


Fig. 14. Velocity contour of cross section (Dn=50.0 C=0.05)

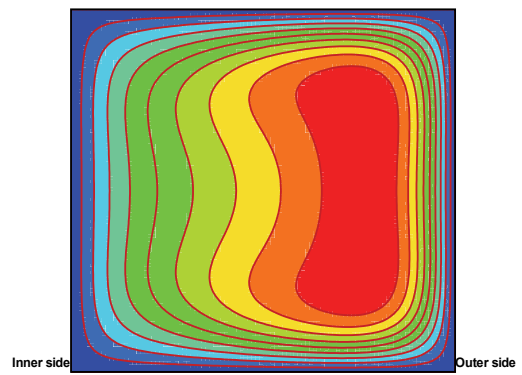


Fig. 15. Velocity contour of cross section (Dn=100.0 C=0.05)

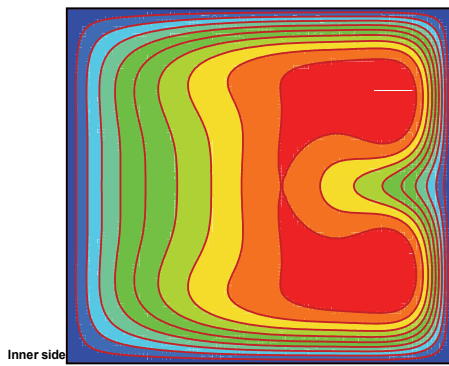


Fig. 16. Velocity contour of cross section (Dn=150.0 C=0.05)

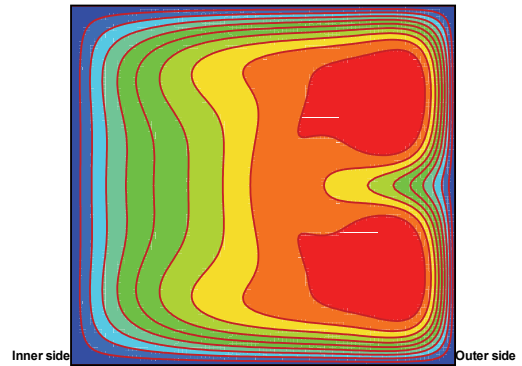


Fig. 17. Velocity contour of cross section (Dn=200.0 C=0.05)

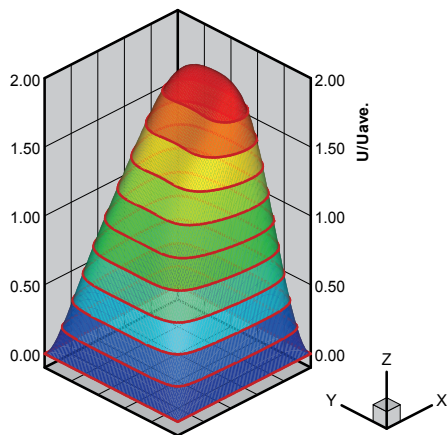


Fig. 18. Axial velocity profile in 3D view (Dn=50.0 C=0.05)

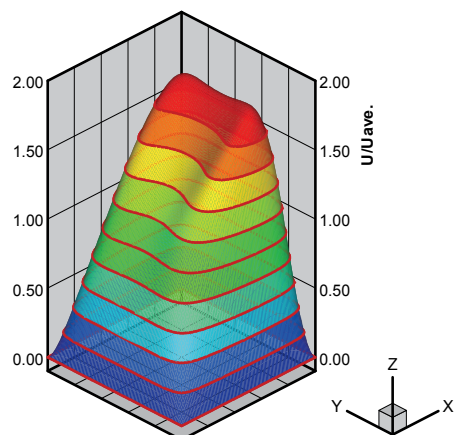


Fig. 19. Axial velocity profile in 3D view (Dn=100.0 C=0.05)

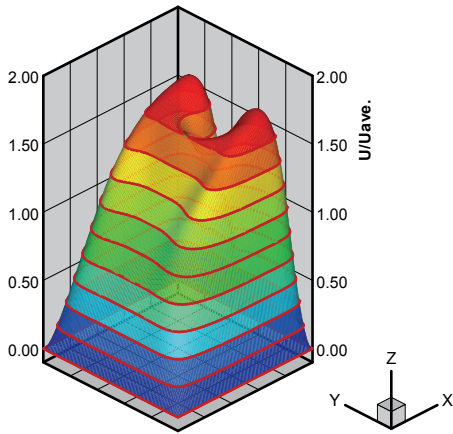


Fig. 20. Axial velocity profile in 3D view  
( $D_n=150.0$   $C=0.05$ )

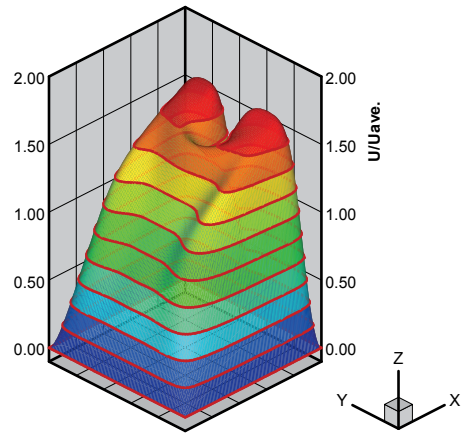


Fig. 21. Axial velocity profile in 3D view  
( $D_n=200.0$   $C=0.05$ )

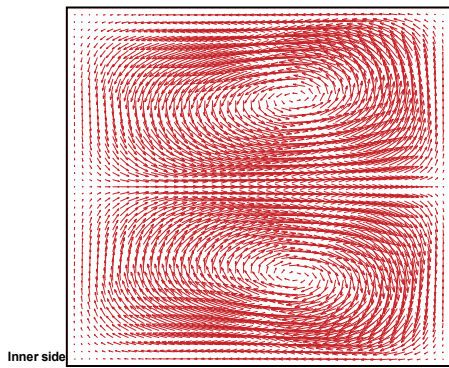


Fig. 22. Velocity vector of cross section  
( $D_n=50.0$   $C=0.05$ )

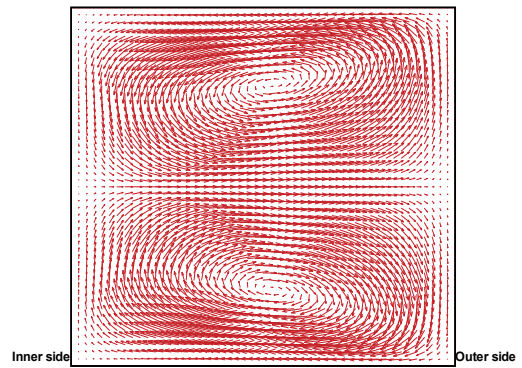


Fig. 23. Velocity vector of cross section  
( $D_n=100.0$   $C=0.05$ )

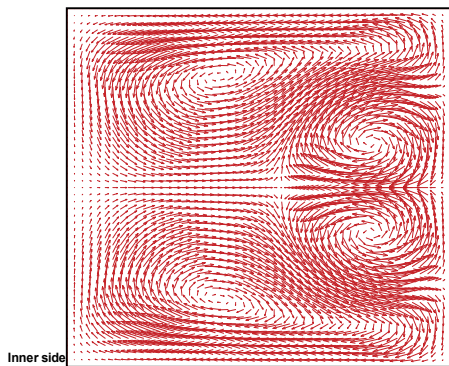


Fig. 24. Velocity vector of cross section  
( $D_n=150.0$   $C=0.05$ )

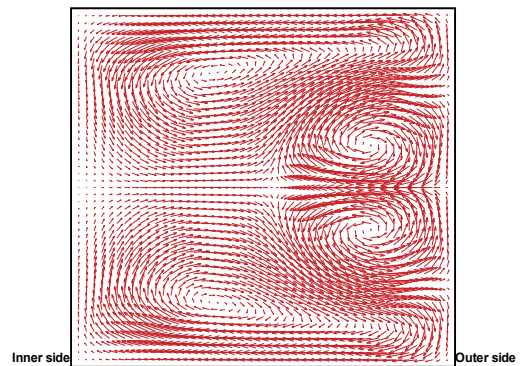


Fig. 25. Velocity vector of cross section  
( $D_n=200.0$   $C=0.05$ )

In Figures 22-25, the detailed secondary flows on the cross section are presented at different Dean numbers. These figures also clearly show the flow transition from one pair of eddies (in Figures 22 and 23) to two pairs of symmetrical eddies (in Figures 24 and 25) when the Dean number increasing up to certain values. Compared to the single-pair symmetrical eddies, in the double-pair eddies case, the additional pair eddies rotate in the opposite direction on the main vortices (as shown in Figures 24 and 25). The imbalance between the pressure gradient and centrifugal force on the cross section causes the transition from a single-vortex-pair to the double-vortex-pair structure; therefore, the location of maximum axial velocity moves closer to the outer wall in symmetrical positions above and below the radial centerline in Figures 16 and 17 or 20 and 21.

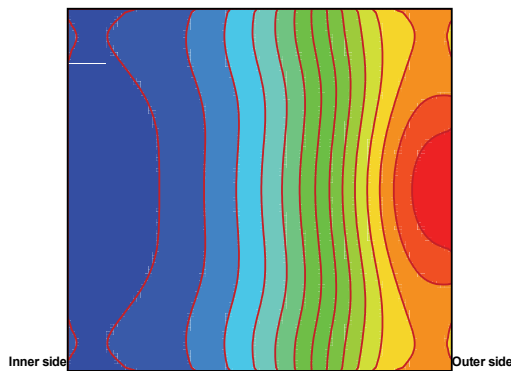


Fig. 26. Pressure contour on cross section (Dn=50.0 C=0.05)

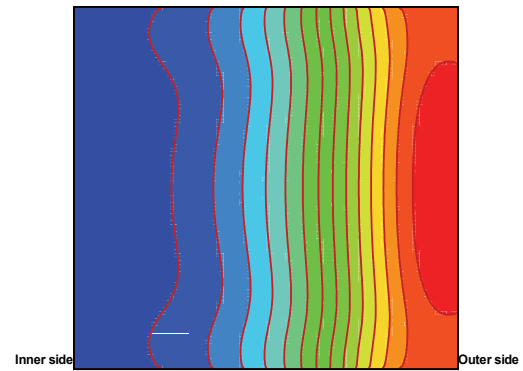


Fig. 27. Pressure contour on cross section (Dn=100.0 C=0.05)

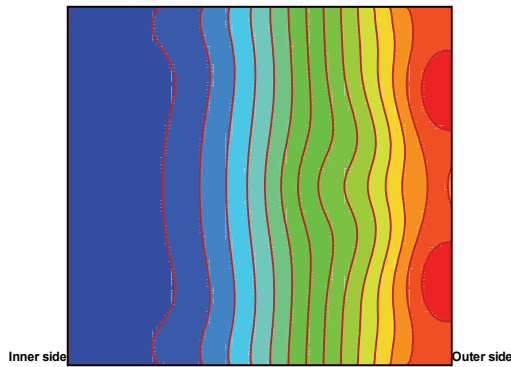


Fig. 28. Pressure contour on cross section (Dn=150.0 C=0.05)

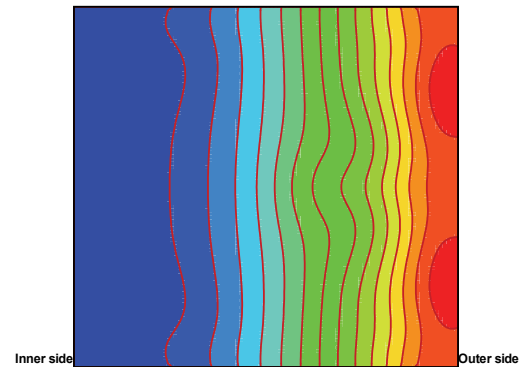


Fig. 29. Pressure contour on cross section (Dn=200.0 C=0.05)

In Figures 26-29 and Figures 30-33, the detailed pressure distributions are presented at different Dean numbers. It is apparent that the pressure contour patterns are considerably different for the double-pair eddies case (in Figures 28 and 29 or Figures 32 and 33) than the single-pair eddies' (in Figures 26 and 27 or 30 and 31). Furthermore, the pressure gradient on the cross section becomes more uniform as the Dean number continues increasing, as shown in Figures 26-28 or Figures 30-32. Since pressure is always a passive variable in fluid flow problems, the pressure profiles shown in Figures 26-29 or Figures 30-33 are a consequence of balance between centrifugal force and fluid viscous force.



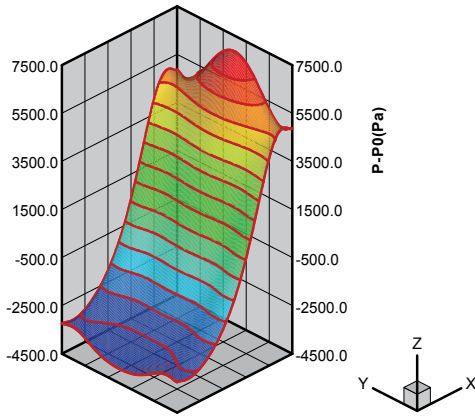


Fig. 30. Pressure profile in 3D view  
(Dn=50.0 C=0.05)

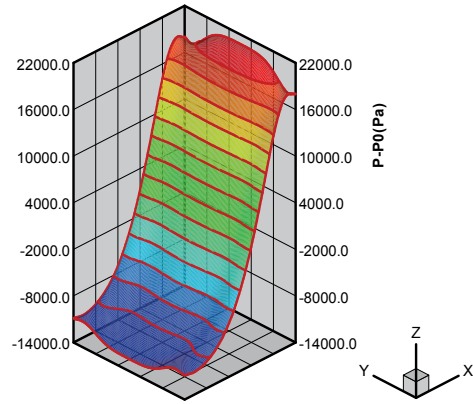


Fig. 31. Pressure profile in 3D view  
(Dn=100.0 C=0.05)

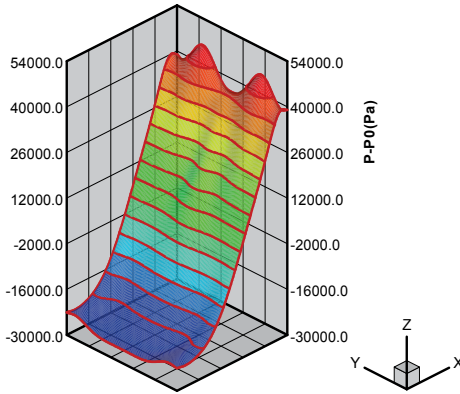


Fig. 32. Pressure profile in 3D view  
(Dn=150.0 C=0.05)

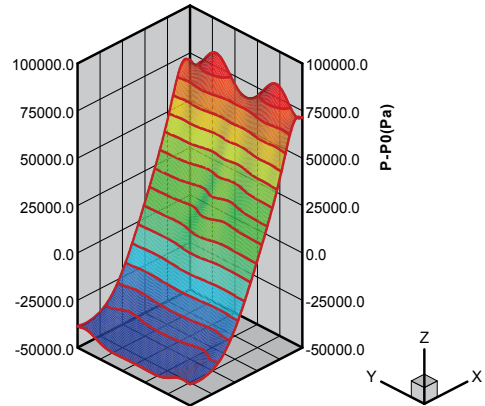


Fig. 33. Pressure profile in 3D view  
(Dn=200.0 C=0.05)

In real engineering applications, one of the most important results of fully developed flow in curved square duct is estimation of the friction factor (or flow-rate reduction). The available well-known friction factor correlation in the literature [31] is:

$$f_c / f_s = 0.225 Dn^{0.39} \quad \text{for square duct with } 100 < Dn < 1500 \quad (102)$$

In Figure 34, the computed friction factor ratios for a straight square duct at different curvature ratio are presented. It is evident that the presented LBM simulation results are in good agreement with the experimental correlation. On the other hand, it is clearly shown in this Figure that the friction coefficient for each specific curvature ratio (from 0.05 to 1.00) changes suddenly when the Dean number is between 115 and 130. This is because when Dean number increases from 115 to 130, the flow pattern on cross section changes from one pair of eddies to two pairs of eddies. This Dean number which identifies the flow pattern is called critical Dean number. As a consequence of flow pattern change, the corresponding friction coefficient is increased.

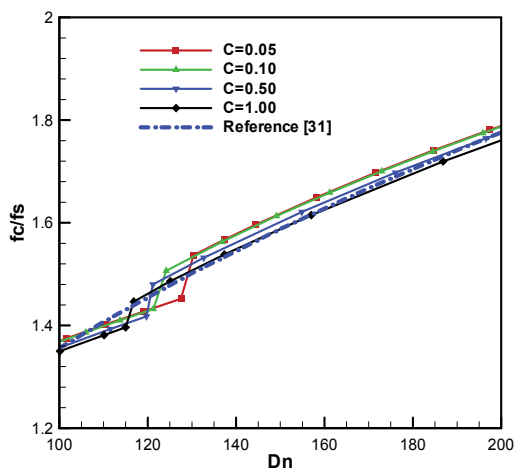


Fig. 34. Friction coefficients vs Dean number at different curvature ratio

With regard to the transition from single-pair eddies to double-pair eddies, it was proposed in [32] that, for a curved square duct, the transition is a result of a complex structure of multiple, symmetric, and asymmetric solutions. The singular value of Dean number for the transition of the two- and four- vortex flow patterns is between 113 and 191, which is consistent with the current results obtained from the LBE model, i.e., the critical Dean number is between 115 and 130.

### 5.3.2 Heat transfer

In Figures 35-42 and Figures 43-50, the dimensionless temperature contours are presented at different Dean numbers and Prandtl numbers (two kinds of typical fluid, i.e., air and water, were chosen). From all these Figures, it is obvious that the Prandtl number plays a considerable role to the temperature field at a given Dean number and curvature ratio in a curved duct flow. For example, in Figures 35 and 36 or Figures 43 and 44, the fluid flow conditions are exactly same (i.e., same Dean number and curvature ratio) but the fluid physical properties (i.e., Prandtl number) are different. As a result, the dimensionless temperature contours are significantly different for these two cases with different Prandtl number. Similar results with different Dean numbers are presented in Figures 37-42 or Figures 45-50.

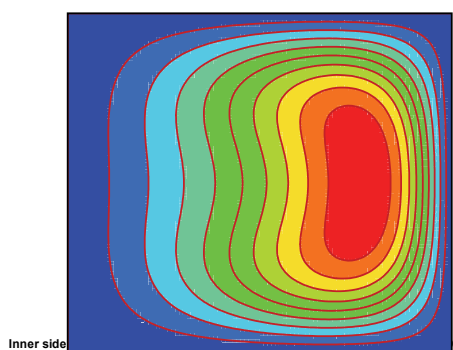


Fig. 35. Temperature contour of cross section (Dn=50.0 Pr=0.716 C=0.05)

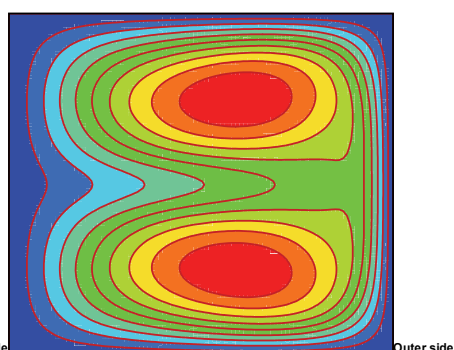


Fig. 36. Temperature contour of cross section (Dn=50.0 Pr=6.587 C=0.05)

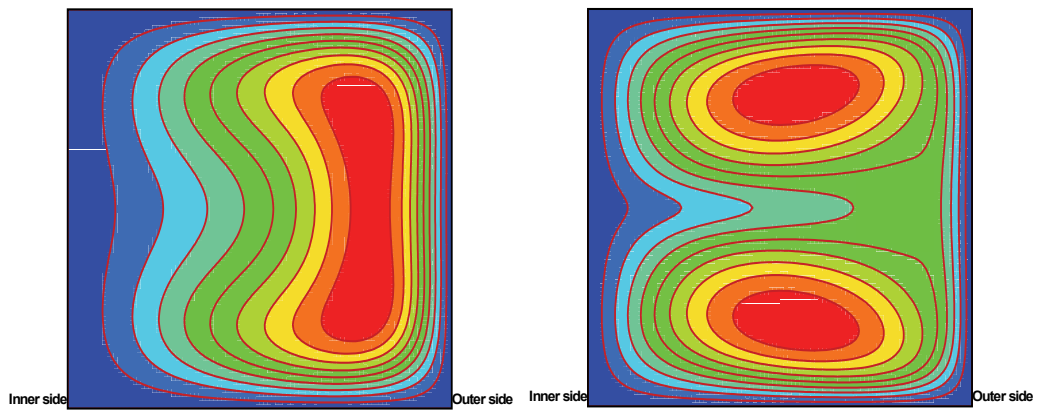


Fig. 37. Temperature contour of cross section ( $D_n=100.0$   $Pr=0.716$   $C=0.05$ )

Fig. 38. Temperature contour of cross section ( $D_n=100.0$   $Pr=6.587$   $C=0.05$ )

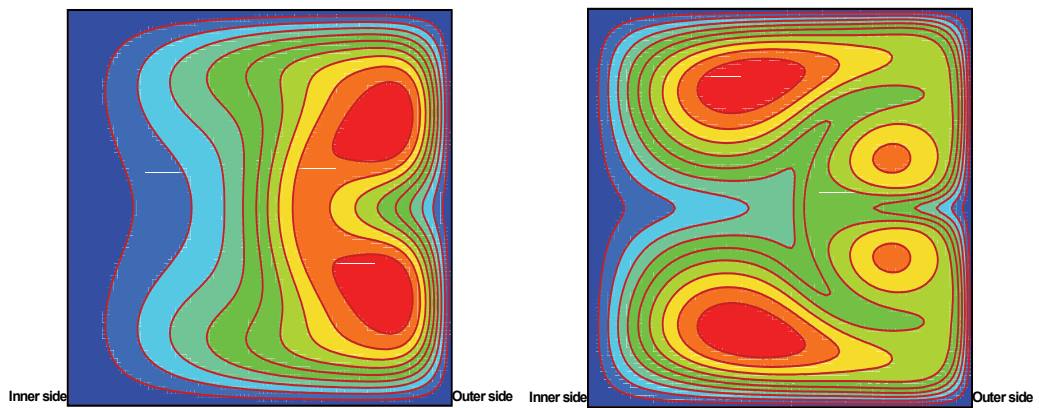


Fig. 39. Temperature contour of cross section ( $D_n=150.0$   $Pr=0.716$   $C=0.05$ )

Fig. 40. Temperature contour of cross section ( $D_n=150.0$   $Pr=6.587$   $C=0.05$ )

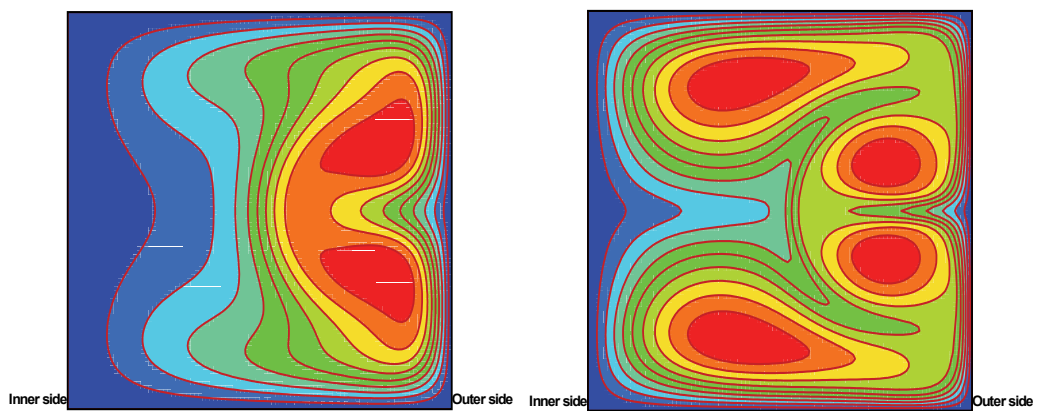


Fig. 41. Temperature contour of cross section ( $D_n=200.0$   $Pr=0.716$   $C=0.05$ )

Fig. 42. Temperature contour of cross section ( $D_n=200.0$   $Pr=6.587$   $C=0.05$ )



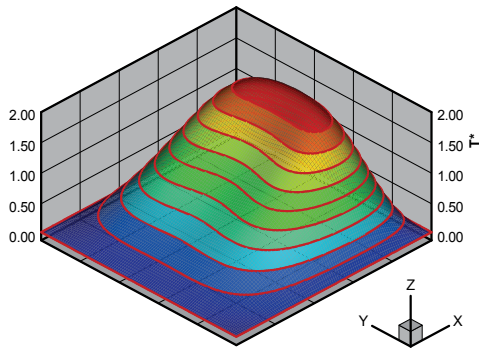


Fig. 43. Temperature profile in 3D view  
( $Dn=50.0$   $Pr=0.716$   $C=0.05$ )

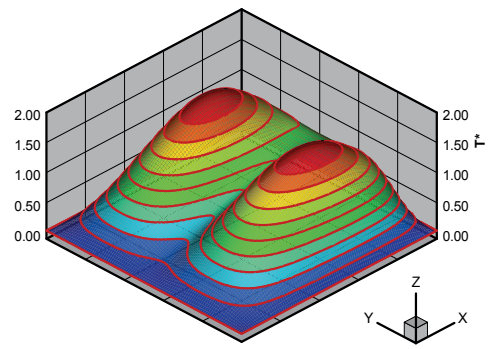


Fig. 44. Temperature profile in 3D view  
( $Dn=50.0$   $Pr=6.587$   $C=0.05$ )

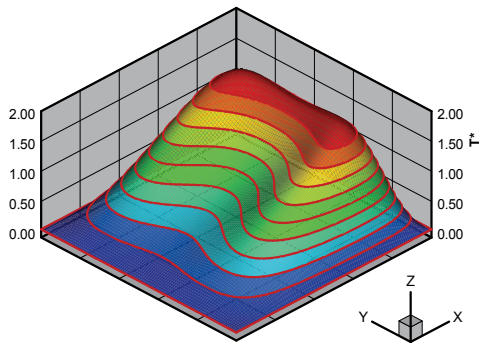


Fig. 45. Temperature profile in 3D view  
( $Dn=100.0$   $Pr=0.716$   $C=0.05$ )

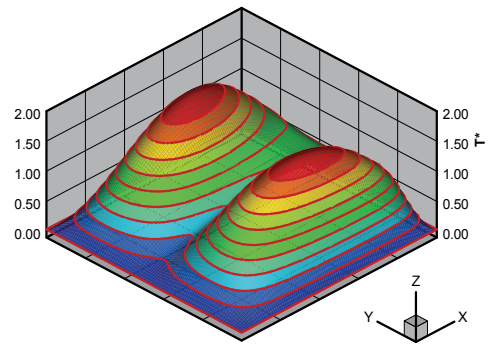


Fig. 46. Temperature profile in 3D view  
( $Dn=100.0$   $Pr=6.587$   $C=0.05$ )

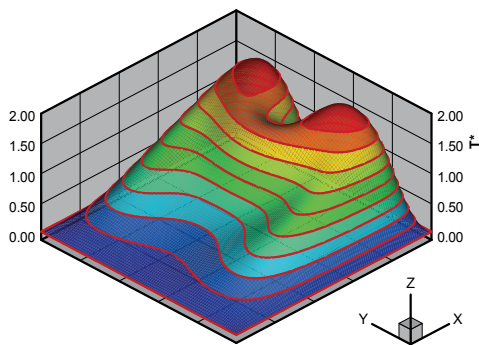


Fig. 47. Temperature profile in 3D view  
( $Dn=150.0$   $Pr=0.716$   $C=0.05$ )

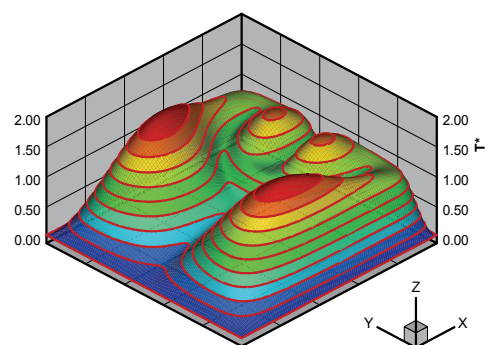


Fig. 48. Temperature profile in 3D view  
( $Dn=150.0$   $Pr=6.587$   $C=0.05$ )

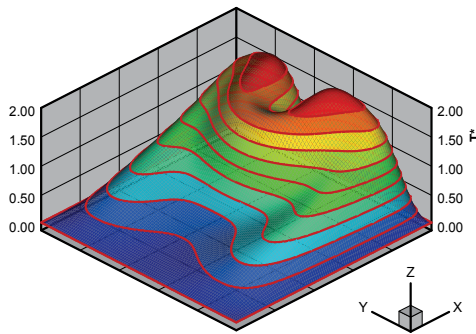


Fig. 49. Temperature profile in 3D view  
( $Dn=200.0$   $Pr=0.716$   $C=0.05$ )

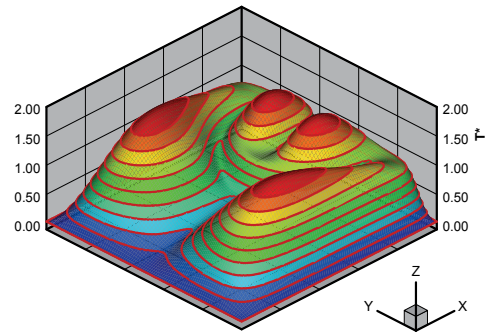


Fig. 50. Temperature profile in 3D view  
( $Dn=200.0$   $Pr=6.587$   $C=0.05$ )

Figure 51 shows a comparison of Nusselt numbers between passive-scalar thermal LBE and Fluent software results with the same fluid flow and heat transfer parameters, including boundary conditions and geometry configurations. Before the thermal results by Fluent software were adopted in Figure 51, the grid convergence test was implemented for fluid flow and heat transfer. It is also apparent from this figure that the results of LBE are very consistent with those of Fluent software (i.e., the conventional CFD method).

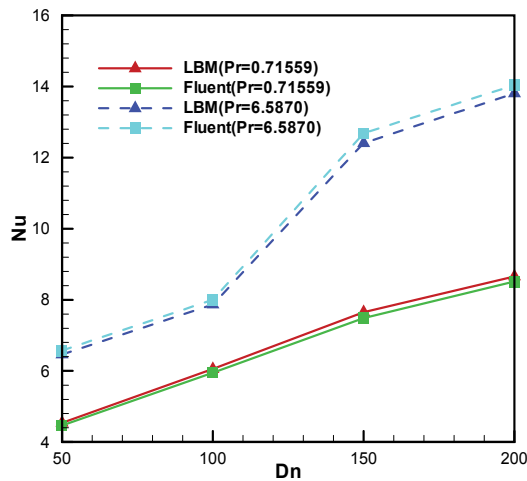


Fig. 51. Nusselt number comparisons between LBM and Fluent results ( $C=0.05$ )

In this section, the fully developed fluid flow and heat transfer in a square duct with curvature ratio (0.05--1.0) and Dean number (0--200) have been thoroughly investigated using D3Q27 incompressible LBGK model and passive-scalar thermal model, respectively. Based on the simulation results, the following conclusions can be drawn:

1. The fluid flow simulation results of D3Q27 LBE model are in good agreement with experimental correlation at the given conditions;
2. The fully Dean stability range is obtained in this article and is consistent with results in the literature.
3. LBE is a new useful successive method to solve the hydrodynamic problems; compared to the conventional CFD approach, this method is very easy to understand and

implement. The unique parallelism characteristics can save a lot of calculation time if a special programming technique is applied.

## 6. Reference

- [1] Dieter A. Wolf-Gladrow, *Lattice-Gas Cellular Automata and Lattice Boltzmann Models: An Introduction (Lecture Notes in Mathematics)*, 2000, Springer
- [2] D Raabe, Overview of the lattice Boltzmann method for nano- and microscale fluid dynamics in materials science and engineering, *Modelling and Simulation in Materials Science and Engineering*, vol. 12, pp. R13-R46, 2004
- [3] Wijmans. C. M., Smit. B., and Groot R. D., Phase behavior of monomeric mixtures and polymer solutions with soft interaction potentials, *Journal of Chemical Physics*, vol. 114, pp.7644-7654, May 1, 2001
- [4] Bird G. A. *Molecular Gas Dynamics and the Direct Simulation of Gas Flows*, Oxford Engineering Science Series, 1994
- [5] Oh C. K., Oran E. S. and Sinkovits R. S., *Journal of Thermophysics and Heat Transfer*, vol. 11, pp.497-505, 1997
- [6] Alexander F. Garcia A. and Alder B., Direct Simulation Monte Carlo for Thin Film Bearings, *Physics Fluids* 6, pp. 3854, 1994
- [7] Alexander F. and Garcia A., Direct Simulation Monte Carlo ,*Computers in Physics*, vol. 11, pp. 588, 1997
- [8] Muntz E. P., Rarefied gas dynamics, *Annual Review of Fluid Mechanics*, 21 387, 1989
- [9] X. He and L. Luo, A priori derivation of the lattice Boltzmann equation, *Physics Review E* 55, pp. R6333-R6336, 1997
- [10] X. He and L. Luo, Theory of the lattice Boltzmann method: From the Boltzmann equation to the lattice Boltzmann equation, *Physics Review E* 56, pp.6811-6817, 1997
- [11] T. Abe, Derivation of the lattice Boltzmann method by means of the discrete ordinate method for the Boltzmann equation, *Journal of Computation Physics*, vol.131, pp. 241-246, 1997
- [12] X. He and L. Luo, Lattice Boltzmann Model for the Incompressible Navier-Stokes Equation, *Physics of Fluid*, vol. 88, pp.927-944, 1997
- [13] Li-Shi Luo, Ph.D. thesis, Georgia Institute of Technology, 1993
- [14] Peng Yuan and Laura Schaefer, A Thermal Lattice Boltzmann Two-Phase Flow Model and its Application to Heat Transfer Problems—Part 1. Theoretical Foundation, *Journal of Fluids Engineering*, vol. 128-142, January 2006
- [15] Alexander F. J., Chen S. and Sterling, J. D., Lattice Boltzmann Thermohydro dynamics, *Physics Review E*. 47, pp. R2249-R2252, 1993
- [16] Shan, X., Simulation of Rayleigh–Benard Convection Using Lattice Boltzmann Model, *Physics Review E* 55, pp. 2780-2788, 1997
- [17] X. He, S. Chen, G. D. Doolen, A novel thermal model for the lattice Boltzmann method in incompressible limit, *Journal of Computational Physics*, vol. 146, pp.282-300, 1998
- [18] Renwei Mei, Wei Shyy et al., Lattice Boltzmann method for 3D flows with curved boundary, *Journal of Computational Physics*, vol. 161, pp.680-699, July 2000
- [19] Y. Peng, C. Shu and Y.T. Chew, A 3D incompressible thermal lattice Boltzmann model and its application to simulate natural convection in a cubic cavity, *Journal of Computational Physics*, vol.193, pp.260-274, 2003
- [20] X. Shan and H. Chen, Lattice Boltzmann model for simulating flows with multiple phases and components, *Physics Review E* 47. pp.1815-1819, 1993

- [21] X. Shan and G. Doolen, Diffusion in a multicomponent lattice Boltzmann equation model, *Physics Review E* 54, pp.3614-3620, 1996
- [22] He. X., Zou Q., Luo L., and Dembo. M., Analytic Solution and analysis on No-slip boundary condition for the Lattice Boltzmann BGK Model, *Journal of Statistical Physics*, vol. 87, pp. 115-136, 1997
- [23] Q. Zou and X. He, On pressure and velocity flow boundary conditions for the lattice Boltzmann BGK model, *Physics of Fluids*, vol. 9, pp.1591-1598, June1997
- [24] S. Chen, Daniel Martinez and Renwei Wei, On boundary conditions in lattice Boltzmann methods, *Physics Fluids*, vol. 8, pp.2527-2536, 1996
- [25] A. D' Orazio, S. Succi, and C. Arrighetti, Lattice Boltzmann simulation of open flows with heat transfer, *Physics of Fluids*, vol. 15 pp.2778-2781, 2003
- [26] A. D' Orazio, M. Corcione, and G. P. Celata, Application to natural convection enclosed flows of a lattice Boltzmann BGK model coupled with a general purpose thermal boundary condition, *International Journal of Thermal Sciences*, vol. 43, pp.575-586, 2004
- [27] A. D' Orazio and S. Succi, Simulating two-dimensional thermal channel flows by means of a lattice Boltzmann method with new boundary conditions, *Future Generation Computation System*, vol. 20, pp.935-944, 2004
- [28] Thangam, N. Hur, Laminar secondary flows in curved rectangular ducts, *Journal of Fluid Mechanics*, vol. 217, pp.421-440, 1990
- [29] Cheng, K. C., & Akiyama M., Laminar forced convection heat transfer in curved rectangular channels, *International Journal of Heat and Mass Transfer*, vol. 13, pp.471-490, 1970
- [30] Winter, K.H., A Bifurcation Study of Laminar Flow in a Curved Tube of Rectangular Cross-Section, *Journal of Fluid Mechanics*, vol. 180, pp.343-369, 1987
- [31] G. J. Hwang, Chung-Hsing Chao, Forced Laminar Convection in a Curved Isothermal Square Duct, *Journal of Heat Transfer*, vol.113/48, February 1991
- [32] Yong Shi, T. S. Zhao and Z. L. Guo, Finite difference-based lattice Boltzmann simulation of natural convection heat transfer in a horizontal concentric annulus, *Computers and Fluids*, vol. 35 pp.1-15, 2006
- [33] C. Shu, X. D. Niu and Y. T. Chew, Taylor-series expansion and least-squares-based lattice Boltzmann method: Two-dimensional formulation and its applications, *Physical Review E*, vol. 65, pp.036708.1-036708.13, 2002
- [34] C. Shu, X. D. Niu, Y. Peng and Y. T. Chew, Taylor series expansion-and least square-based Lattice Boltzmann method: an efficient approach for simulation of incompressible viscous flows, *Progress in Computational Fluid Dynamics*, vol. 5, pp.25-36, 2005
- [35] X. He, L. Luo and Micah Dembo, Some progress in Lattice Boltzmann Method: Part I Nonuniform Mesh Grids, *Journal of computational Physics*, vol. 129, pp.357-363, 1996

## **Part 2**

### **CFD in Physics**



# CFD Applications for Predicting Flow Behavior in Advanced Gas Cooled Reactors

Donna Post Guillen and Piyush Sabharwall

*Idaho National Laboratory, Idaho Falls, ID*

*USA*

## 1. Introduction

Nuclear energy plays an important role as a key instrument of sustainable energy supply. The 2011 U.S. EIA Annual Energy Outlook 2011 predicts a 21% growth in total energy consumption with electricity consumption growth returning to historic levels. Nuclear power can play a vital role in significantly reducing carbon emissions in the energy sector. According to the Nuclear Energy Institute (2008), nuclear energy is the nation's largest emissions-free source of power, providing more than 20 percent of the country's electricity and accounting for nearly 70 percent of U.S. emission-free power generation in 2009. Nuclear power generation emits virtually no greenhouse gases, making it a reliable power source that can provide the necessary energy to supply our growing economy while protecting the environment and ensuring the availability of energy.

Advanced nuclear reactor concepts offer potential benefits over existing reactor designs. In this work, Computational Fluid Dynamics (CFD) is applied to improve the understanding of the complex flow behavior in proposed nuclear reactor designs, such as the Very High Temperature Reactor (VHTR) and Gas Cooled Fast Reactor (GFR). The prismatic VHTR reference design, based on the General Atomics Gas Turbine Modular Helium Reactor (GT-MHR), is illustrated in Figure 1. The power conversion system (PCS) is shown to the left of the reactor. Helium coolant flows through the annulus of the hot duct as it returns from the PCS and through the annulus of the reactor vessel wall to the upper plenum. The coolant then travels downward through the fueled portion of the reactor core and into the lower plenum. The heated coolant flows out of the lower plenum and through the center of the hot duct back to the PCS to complete the cycle. The core has an annular layout with an inner and an outer reflector as well as upper and lower reflectors (graphite blocks are shown in white in Figure 1).

The GFR system features a fast neutron spectrum, helium-cooled reactor and closed fuel cycle. It can be operated at high temperatures, has a high thermal efficiency due to the high temperature reached by the coolant, and being chemically inert by nature, the coolant does not react with the structural materials in the core. The hot gases can be coupled to a direct-cycle helium turbine for electricity generation and/or to a heat exchanger where the process heat is used to produce hydrogen via high temperature steam electrolysis (O'Brien et al. 2007). Through the combination of a fast spectrum and full recycle of actinides, the GFR minimizes the production of long-lived radioactive waste. The GFR's fast spectrum also

makes it possible to use available fissile and fertile materials (including depleted uranium) much more efficiently than thermal spectrum gas reactors with once-through fuel cycles. The direction of the coolant is opposite to that of the VHTR, i.e., coolant flows upwards as can be seen from Figure 2.

The following subsections describe the CFD analyses performed for the lower plenum flow in the VHTR and upper plenum plume interaction for the GFR.

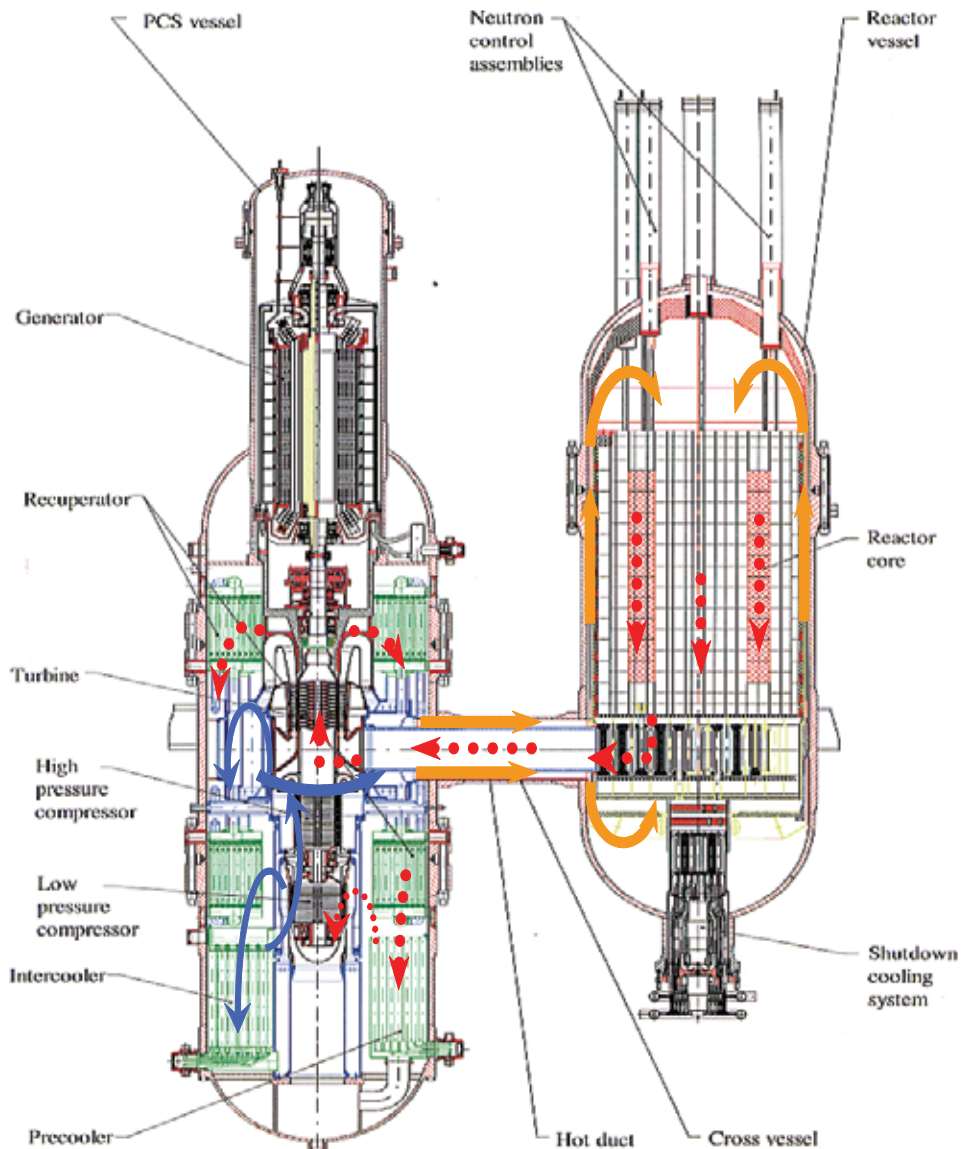


Fig. 1. Layout of the power conversion system (PCS) and reactor vessel for the gas-cooled prismatic VHTR reference design (courtesy of General Atomics)



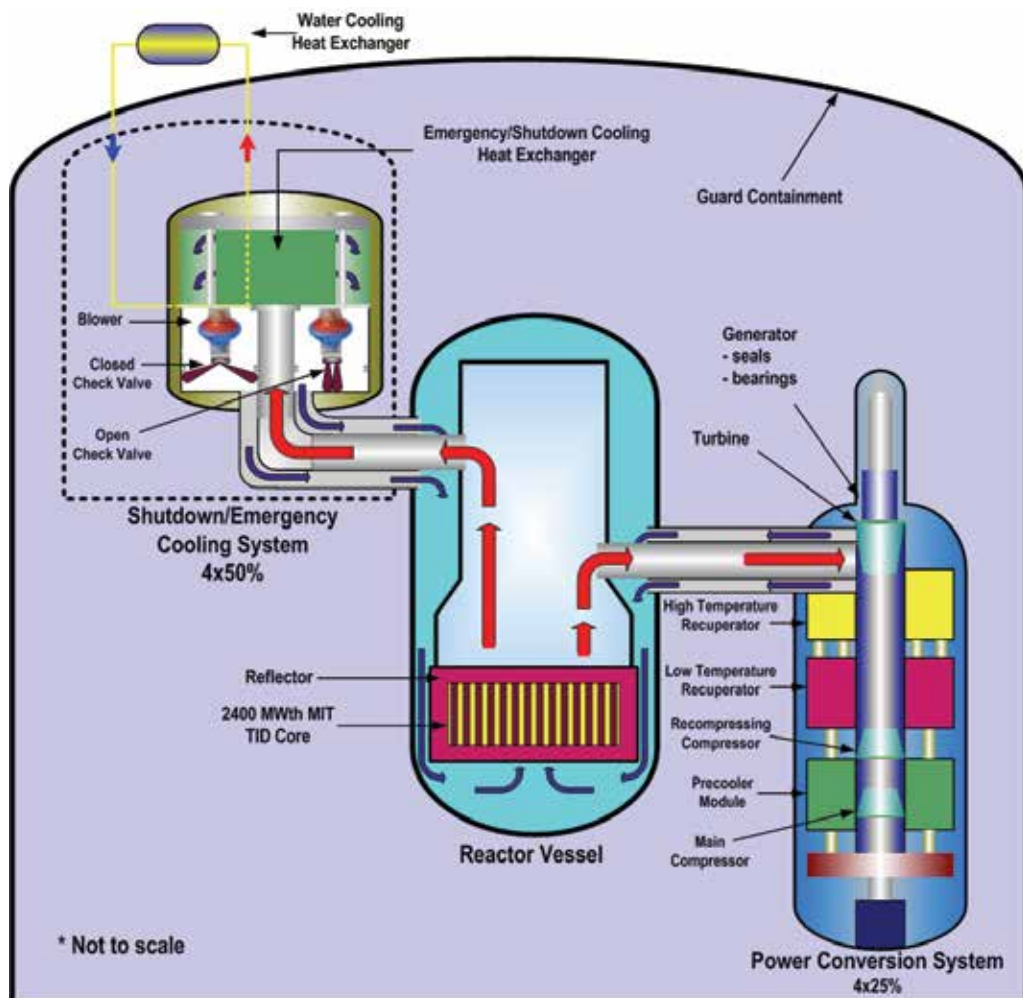


Fig. 2. Layout of the PCS and reactor vessel for the GFR (Weaver et al. 2005)

## 2. Very High Temperature Reactor

In the VHTR concept investigated herein, helium coolant flows vertically downward through the core and enters the lower plenum through a series of jets into a cross flow. The radial variation of the core power density creates jets of differing temperatures. Jets of hot gas discharge into the plenum, turn and flow horizontally past arrays of vertical cylindrical support posts towards the outlet duct, where the gases are fed to either a turbine or an intermediate heat exchanger for the production of electricity and/or hydrogen. Adequate mixing of the coolant flow is necessary to ensure that material structural temperature limits are not exceeded in the lower plenum or power conversion machinery.

The objective of this study is to model a section of the lower plenum of an advanced reactor concept using a commercial CFD code and compare the results to experimental data (Schultz et al. 2006).

### 2.1 Flow phenomena in the lower plenum of VHTR

The hundreds of coolant channels in the VHTR core combine into several dozen larger ducts just before entering the lower plenum. The lower plenum consists of a duct with structural support columns to support the graphite blocks in the core. These columns perturb the flow through the plenum. As the coolant enters the lower plenum, it turns ninety degrees to flow towards the exit duct; hence, there will be a cross-flow of coolant in the lower plenum. The cross-flow will have to negotiate the support columns and will also experience an expanding flow area on the side away from the exit duct and a converging area as it approaches the exit duct. Figure 3a illustrates a preliminary calculation of path lines of the coolant in the lower plenum colored by temperature, showing the entering jets. Figure 3b shows contours of turbulence intensity for a plan view of flow near the exit duct. The turbulence intensity is highest in the converging flow region close to the exit duct.

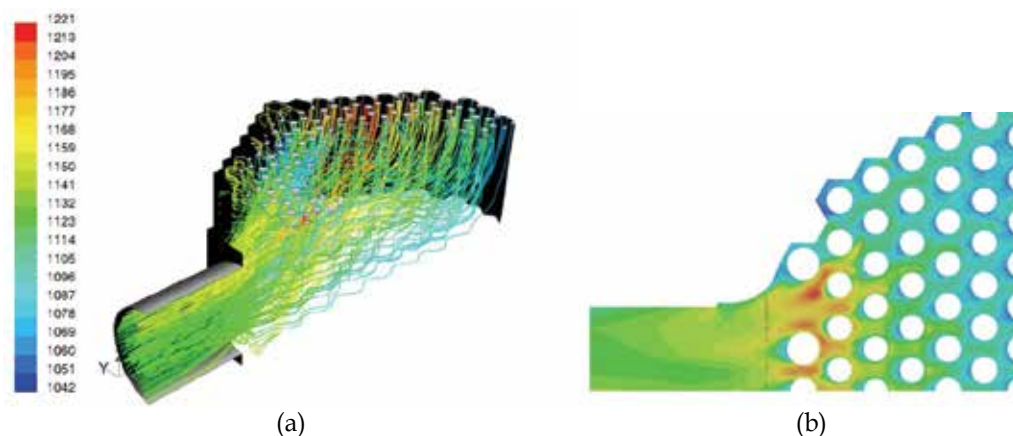


Fig. 3. Flow phenomena of lower plenum showing (a) path lines of coolant in the lower plenum and (b) contours of turbulence intensity in the lower plenum in a plan view of the flow near the exit duct (Johnson 2006)

The preliminary flow calculations illustrated in Figure 3 provide insight into the flow phenomena in the lower plenum. As the flow enters the lower plenum proper, the jets will not only have some interaction with each other but also with the support columns, which are located fairly close together as shown in Figure 3b. The location of a jet will have a significant effect on its interaction with the cross-flow. Farther away from the exit duct, the cross-flow will be weaker. Hence, these jets will penetrate deeper into the lower plenum than those closer to the exit duct.

The cross-flow will have similarities to flow in tube banks. However, the flow coming straight across from the exit duct resembles flow in staggered tube banks, while flow coming from wider angles resembles flow through in-line tube banks. The flow in the lower plenum will apparently be turbulent as may be deduced from the fact that the predicted turbulence intensity is relatively large for the preliminary calculations above. The flow is expected to be unsteady due to vortex shedding behind the support columns.

### 2.2 Methodology

In this work, an idealized model was created to reproduce a region of the lower plenum for a simplified set of conditions that permit the flow to be treated as an isothermal,

incompressible fluid with constant properties. A scaled model of a sub-region in the lower plenum was constructed and velocity field measurements were obtained using three-dimensional Particle Image Velocimetry (PIV). Analysis of the flow by (Condie et al. 2005) was performed for the simplified case of an unheated, constant property fluid. This analysis neglects buoyancy-driven flow effects and is considered representative of normal low-power operation. These unheated flow experiments provide data for the baseline case of negligible buoyancy and constant fluid properties, which are a first step to assess the fidelity of the CFD simulations.

### 2.3 Experiments

Three-dimensional PIV data was obtained in the Matched-Index-of-Refractive (MIR) Facility at the Idaho National Laboratory (INL). PIV is an optical technique employed to obtain non-intrusive flow measurements. The experiments were conducted to study the turbulent flow behavior and generate data for comparison to CFD predictions. The PIV system provides both instantaneous and ensemble-averaged velocities at discrete points in the flow.

The model shown in Figure 4 models a section of vertical cylindrical support posts arranged on an equilateral triangular pitch. A symmetrical arrangement of five cylindrical columns along the model centerline and ten half-cylinders along the two parallel side walls extend the full height of the model. The model dimensions are 0.05398 m (width)  $\times$  0.558 m (length)  $\times$  0.21750 m (height). The model measures 0.05398 m in width, 0.558 m in length, and 0.21750 m in height. The ratio of the spacing between the post centerlines,  $L$ , and the post diameter,  $D$ , is  $L/D=2.94$ . The relative scale of the model to the full-scale lower plenum section is 1:6.55 (Johnson 2006).

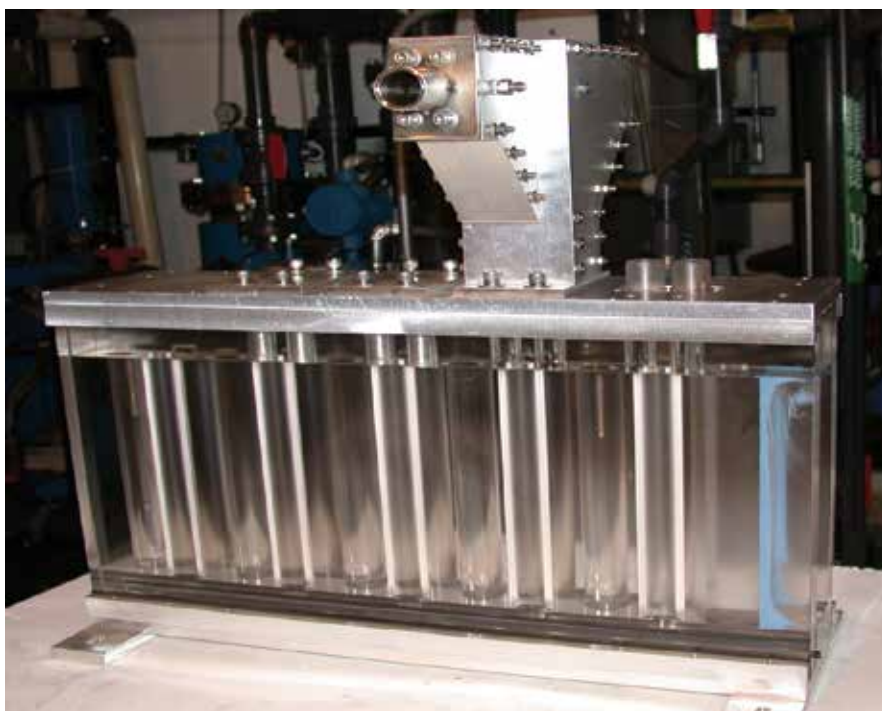


Fig. 4. MIR flow test model

The experiments, although conducted at room temperature, can be directly scaled to the prototypical system since at operational conditions the flow is momentum-dominated with negligible buoyancy and nearly constant fluid properties. Scaling studies have been performed to ensure that the flow test model with mineral oil flow under isothermal conditions duplicates the pertinent non-dimensional parameters in the lower plenum (Condie et al. 2005). The model was constructed of quartz, an optically transparent material with the same index of refraction as the mineral oil used as the working fluid of the MIR system. Seeded mineral oil with a precisely controlled temperature of 23.3 °C enters through four inlet ports above the model. The Reynolds number, based upon jet diameter and bulk flow velocity, is approximately 4300. Mineral oil from the main tunnel flows around the outside of the model at a velocity of 0.2 m/s, and mixes with the plenum flow at the model outlet.

The experiment simulates the flow in the central portion of the lower plenum, away from the outlet duct. The source of flow entering this region originates from jets exiting short coolant ducts at the corners of the hexagonal blocks, represented in the flow test model as a series of inlet jets located above the plenum. A solid wedge-shaped element at the upstream end simulates the hexagonal support block for the outer reflector and blocks cross flow from the main tunnel flow. The wedge partially blocks the inlet jet at the upstream end.

## 2.4 Computations

A three-dimensional computational mesh was created to replicate the geometry and dimensions of the test model. The experimental conditions were modeled using the commercial CFD code FLUENT version 6.3. In this study, the segregated solver uses a point Gauss-Seidel technique and algebraic multigrid V-cycle acceleration. The control volume technique consists of integrating the governing equations for each control volume, yielding discrete equations that conserve each quantity on a control volume basis. FLUENT stores discrete values of the conserved quantity at the cell centers and uses an upwind technique for determining face values of the conserved quantity for the convective terms. A Pressure Staggering Option (PRESTO) scheme was used as the interpolation scheme for calculating cell-face pressures. The Pressure-Implicit with Splitting of Operators (PISO) scheme, which uses a combination of continuity and momentum equations to derive an equation for pressure, was used for pressure-velocity coupling. The PISO algorithm performs both neighbor and skewness correction to decrease the number of iterations required for convergence of transient problems. The Monotone Upstream-Centered Schemes for Conservation Laws (MUSCL) scheme was used to interpolate the field variables (stored at cell centers) to the faces of the control volumes. This scheme produces a locally third-order convective discretization for unstructured meshes. The adaptive time-stepping feature invoked a time-step for the computations that varied between 0.01 and 0.02 seconds as the solution approached convergence.

FLUENT was used to solve the unsteady, Reynolds-averaged Navier-Stokes (RANS) equations for the turbulent flow present in the scaled model. RANS simulations treat the flow variables as having a time-averaged (mean) part and a turbulent part. The realizable  $k$ - $\epsilon$  (where  $k$  is turbulent kinetic energy [TKE] and  $\epsilon$  is the TKE dissipation rate) turbulence modeling option with enhanced wall treatment was used. This turbulence model is known for its robustness, economy and reasonable accuracy over a wide range of turbulent flows common in industry. The entire range of turbulence scales is modeled, and only mean flow features are resolved. The enhanced wall treatment, a near-wall modeling method, combines a two-layer model with enhanced wall functions that are valid even in the wall buffer region ( $3 < y^+ < 10$ ). The wall

functions were developed by smoothly blending the laminar (linear) and the turbulent (logarithmic) laws-of-the-wall. The realizable  $k-\epsilon$  model is recommended over the standard  $k-\epsilon$  model for problems where the flow features include strong streamline curvature and vortices (Fluent 2007). The  $k-\epsilon$  turbulence model solves for total TKE assuming turbulent viscosity is isotropic. However, the generation of TKE due to mean flow gradients may be different depending on which mean flow velocity gradients are being considered.

It is a challenge to create and execute a CFD model with a fine enough mesh to fully simulate the physical conditions in the experimental model, including the boundary layers on the walls. A grid refinement study was performed using three grids of successively varying mesh refinement. The “medium,” “fine,” and “super-fine” meshes shown in Figures 5a-c were generated using the Gridgen software package. The “medium” mesh was comprised of 225,243 cells, the “fine” mesh was comprised of 839,759 cells, and the “super-fine” grid was comprised of 1,265,292 cells. The unstructured grids were adapted to a polyhedral grid, which improved the speed of the calculations and yielded similar results. The “medium” polyhedral mesh was comprised of 328,816 cells, the “fine” polyhedral mesh was comprised of 689,857 cells, and the “super-fine” polyhedral mesh was comprised of 1,050,320 cells. Figure 5 shows the manner in which the adaptation procedure clustered the grid nodes in regions adjacent to solid walls (i.e., boundary layers). The goal of this study was to determine whether a  $k-\epsilon$  turbulence model and “super-fine” grid resolution can adequately resolve the flow phenomena.

The average global cell size,  $h$ , is defined as (Celik, 2006)

$$h = \left[ \frac{1}{N} \sum_{i=1}^N (\Delta V_i) \right]^{\frac{1}{3}} \quad (1)$$

Table 1 lists the average global cell size calculated using Equation 1 for the nine grids generated for this study. The volume of the fluid domain is 0.0075 m<sup>3</sup>. The refinement factor (i.e.,  $h_{\text{original}}/h_{\text{refined}}$ ) ranges from 1.2 to 1.6.

| Level of refinement | Average global cell size, $h$ (m) |            |
|---------------------|-----------------------------------|------------|
|                     | FLUENT grids                      |            |
|                     | unstructured                      | polyhedral |
| medium              | 0.0032                            | 0.0028     |
| fine                | 0.0021                            | 0.0022     |
| super-fine          | 0.0018                            | 0.0019     |

Table 1. Average global cell size for the computational meshes generated for this study

Wall boundary conditions were specified for the surfaces of the circular cylinders and half cylinders; the channel sides, top, and bottom; the hexagonal wedge; and the sides of the inlet jets. A no-slip condition was enforced at the walls. To enable specification of the flow outlet as a constant pressure outlet, the model was extended 0.3062 m beyond the physical model outlet (located at  $x=0.5588$  m). The frictional pressure drop caused by this artificial extension is less than 8 Pa. The backflow TKE was set to 0.04 m<sup>2</sup>/s<sup>2</sup>, and the turbulent dissipation rate,  $\epsilon$ , was set to 1.0 m<sup>2</sup>/s<sup>3</sup>. The initial conditions specified were the  $x$ -,  $y$ -, and  $z$ - components of

velocity and the static gage pressure set to zero (i.e.,  $V_x = V_y = V_z = P = 0$ ). The working fluid in the MIR facility is mineral oil with a density of  $831 \text{ kg/m}^3$  and a dynamic viscosity of  $0.0118 \text{ kg/m}\cdot\text{s}$ .

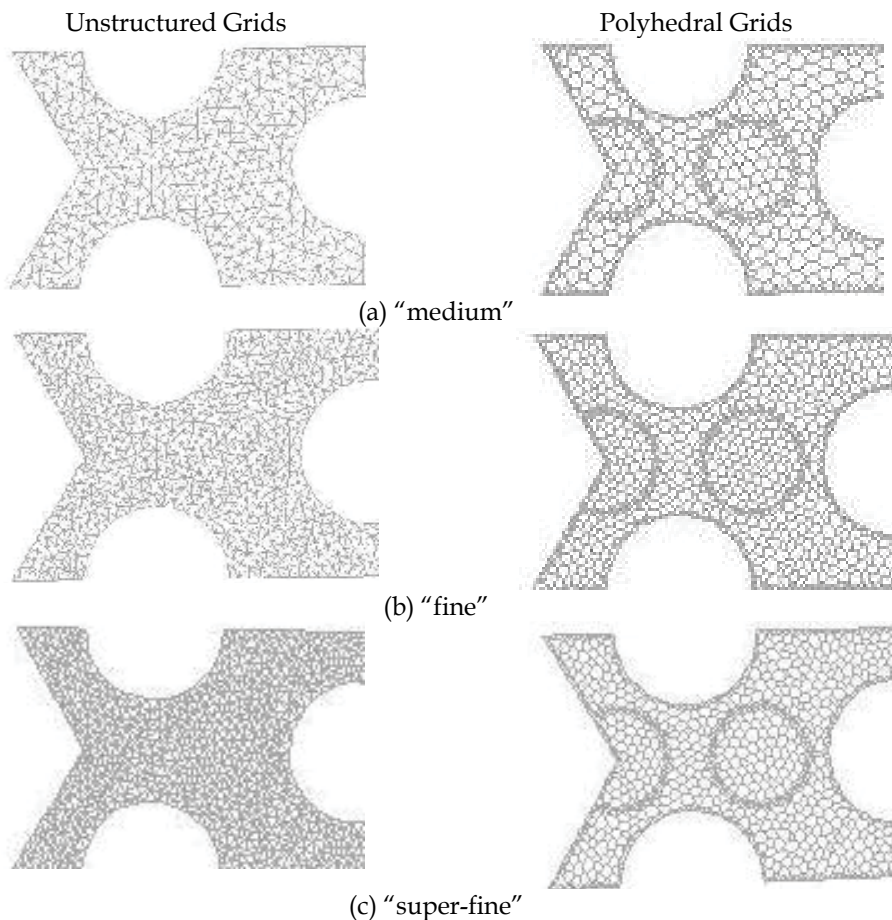


Fig. 5. Detail sections of meshes created for grid independence study using FLUENT

Due to height restrictions in the laboratory, an elbow attached to the inlet flow conditioning block is located less than 6 inlet diameters upstream of the jet outlet into the plenum. The inlet manifold incorporates a  $0.02057 \text{ m}$  long honeycomb flow straightener, as well as two mesh screens for turbulence generation. Velocity data obtained within the jets at a location approximately  $0.010 \text{ m}$  above the plenum indicate that the flow is not fully developed, as would be expected since there is insufficient pipe length to produce fully developed flow. Also, inlet jet #1 is partially blocked by the hexagonal wedge and this flow obstruction disturbs the flow as it exits the inlet pipe.

Unfortunately, the interface between the jet outlet and the plenum was obscured due to the model construction and data could not be acquired at that location. Computations were initially run using the experimentally obtained inlet velocity profiles at a location approximately  $0.01 \text{ m}$  above the interface. Unfortunately, the PIV data point density was too



coarse to adequately resolve the inlet velocity profiles. As a result, integration of the measured velocity profiles under predicts the mass flow rate in the jets by 20 to 30%. This necessitated the application of a mass flow rate boundary condition for the CFD model, rather than the use of velocity profiles at the inlet, to ensure conservation of mass. The mass flow rate boundary condition applied at the 4 inlet jets produced a uniform velocity across the inlet jet. For jet #1, the mass flow rate was set to 0.5898 kg/s and for jets #2, #3, and #4 the mass flow rate was set to 0.8782 kg/s. A similar dilemma was encountered when examining the measured turbulent kinetic energy profiles. They were found to be too coarse and irregular. An average TKE value of  $0.04 \text{ m}^2/\text{s}^2$  based upon the measurements was used at the inlets. In reality, the distribution of turbulence will be complex and vary across the inlet jets. The rate of turbulence dissipation is estimated at  $1.0 \text{ m}^2/\text{s}^3$  based upon the following equation (Celik (i), 2006)

$$\varepsilon = c_{\mu} \frac{k^2}{\nu_t} \quad (2)$$

where  $c_{\mu}$  is equal to 0.09 and  $\nu_t$  is the turbulent viscosity. These parameters were applied at a location approximately 0.01 m above the jet/plenum interface to avoid having to modify the existing grid.

Residuals of mass, momentum, TKE, and  $\varepsilon$  were monitored to determine iterative convergence. In FLUENT, these residuals are normalized values. The Unsteady RANS (URANS) solution was allowed to iterate until the residuals reached  $1 \times 10^{-6}$  for mass and momentum and  $1 \times 10^{-5}$  for TKE and  $\varepsilon$ . These convergence tolerances were based on previous research (Johnson 2006). The solution converged at each time step with a net difference in computed mass flux of  $1 \times 10^{-7}$  through the inlets and outlet.

## 2.5 Results and discussion

Experiments conducted at Utah State University (USU) (Smith et al. 2006) were conducted to aid in characterizing the flow regimes in an array of staggered vertical cylinders in a confined channel. A cylindrical array was designed to represent the VHTR lower plenum design and match the primary geometric dimensionless parameters of the MIR flow test model. The dimensionless cylinder pitch,  $P/D$ , equals 1.7, where  $P$  is the distance between adjacent cylinders and  $D$  is the cylinder diameter. The spanwise height to cylinder diameter ratio,  $H/D$ , equals 6.9. The USU model does not have a hexagonal wedge blocking the flow at the upstream end because the inlet is located there. Air enters through the inlet at a uniform  $x$ -velocity and flows across vertically-oriented cylinders and half-cylinders in a confined channel. The instantaneous velocity field across a centerline cylinder was measured using PIV and the resulting observations used to categorize the flow behavior into identifiable regimes (Smith et al. 2006).

For the INL MIR configuration, the maximum computed time-averaged  $x$ -velocity ( $V_x=1.61 \text{ m/s}$ ) is located at the bottom of the plenum, just upstream of the hexagonal wedge. The post Reynolds number at this location is 3600. The measurements obtained by the INL MIR system (for a jet Reynolds number of 4300) indicate a maximum post Reynolds number of 4450. Based upon the USU flow regime classification, the flow is expected to be turbulent outside and laminar inside the boundary layer on the posts (Smith et al. 2006).

The inlet for the USU flow configuration differs from that of the INL MIR model, where the flow enters the plenum through inlets located at the top of the model. The inlet configuration causes the flow to be highly three-dimensional for the INL MIR experiments. The downward flow from the inlets mixes with the fluid in the plenum causing the velocity to vary significantly in the y-direction, an effect that is pronounced near the inlet jets and diminishes as the flow travels downstream until it is homogeneous at the computational outlet boundary. A wake forms on the downstream side of each cylindrical support post with separation angles dependent upon flow speed (i.e., vertical location along the post). Figure 6 shows the variation in computed and measured x-velocity as a function of y-coordinate at spanwise centerline ( $z=0.0$  m) for four x-locations (0.12022 m, 0.16850 m, 0.19807 m, and 0.26729 m). Figure 7 shows the locations of these planes relative to the model origin. The four inlet jets are depicted by the red open circles, with the jets numbered from 1 to 4 from right to left. Qualitative agreement between the experimental data is good, except for the data plane that bisects inlet jet #2. This can be attributed to the application of a mass flow rate boundary condition at the inlet jets, rather than using the actual turbulent velocity profile.

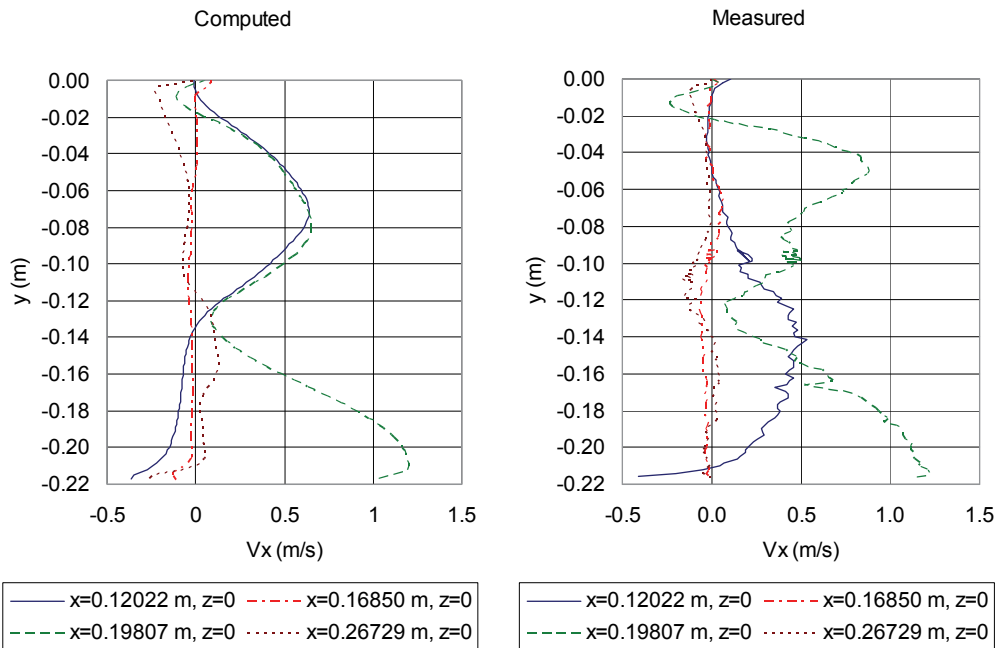


Fig. 6. Variation of x-velocity as a function of y-location in plenum

The frequency of the vortices shed from the cylindrical support posts is approximated by:

$$w_v = \frac{V_x St}{d} \quad (3)$$

Vortex shedding occurs for  $10^2 < Re_d < 10^7$ , where  $Re_d$  is the post Reynolds number and the Strouhal number,  $St$ , remains approximately constant ( $\approx 0.2$ ) over this range of Reynolds numbers (White, 2003). Using the maximum computed x-direction flow velocity,  $V_x$ , the



maximum vortex shedding frequency,  $w_v$ , is around 10 Hz. To capture the time progression of vortices shed from the cylinder, at least 20 data points per period should be acquired. This dictates a system response of at least 200 Hz for the data acquisition system.

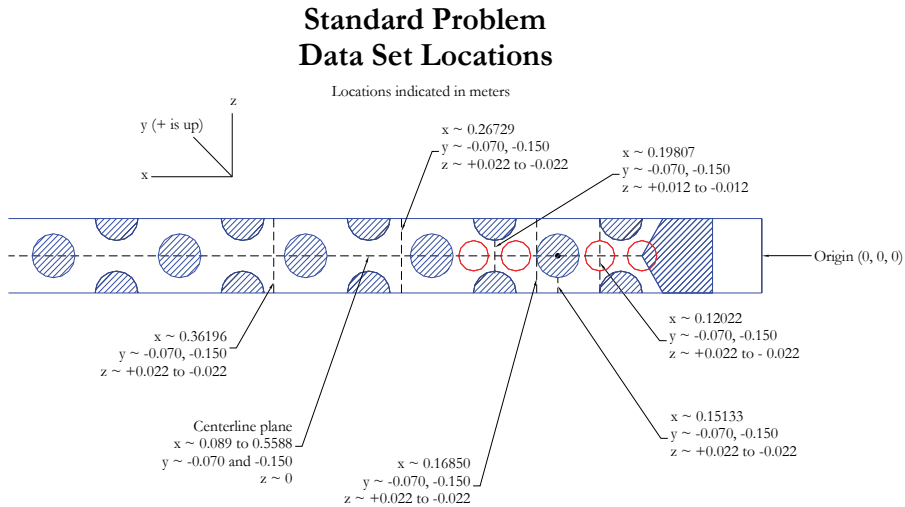


Fig. 7. Data planes relative to model axis origin for data analysis

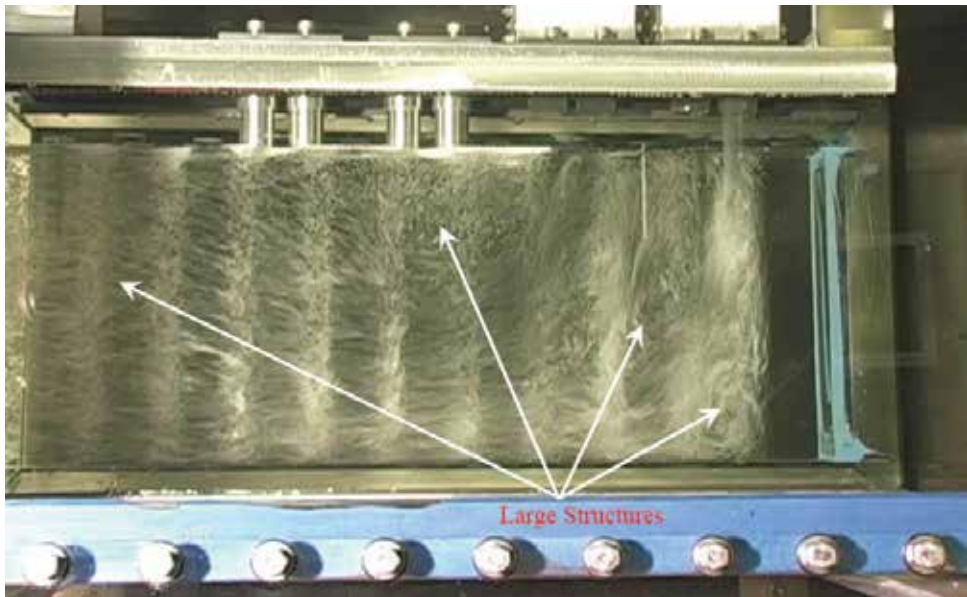


Fig. 8. Flow visualization of four jets operating at a jet Reynolds number of 4300 (McIlroy et al. 2006)

Figure 8 shows a snapshot of flow in the lower plenum model with all four jets operating (McIlroy et al. 2006). To facilitate visualization, air is injected into the flow of the rightmost jet. Air was not injected into all four jets because the resulting mass of air bubbles would

make visualization of the flow structure impossible. The bubble-laden mineral oil flows downward into the plenum and exits through the outlet on the left. Areas of flow stagnation/recirculation, as well as those with enhanced mixing, are identified. The figure shows a complicated three-dimensional flow, with four large structures. The first structure is the vortex in the bottom right corner of the model where the bottom surface of lower plenum meets the outer reflector wall. The second structure is a mixing region in the vicinity of the first centerline support post in the lower portion of the model. The third structure is a second large vertical vortex downstream of the leftmost jet in the upper third of the model, and the fourth structure is the contour of the outlet flow as it passes beneath the third structure (large vortex) and expands vertically upward to cover the entire exit area. These same structures are also observed in the computational results by examining the time-averaged x-velocity shown in Figure 9.

Since the PIV post-processing operation calculates ensemble-averaged flow quantities from the number of valid vectors identified in the instantaneous flow-field images, the CFD predictions were similarly averaged to enable a meaningful comparison with the data. Streamwise and spanwise slices located at approximately one-third and two-thirds of the depth of the model ( $y = -0.07$  m and  $y = -0.15$  m) were selected to compare the computed and experimentally measured mean velocity and turbulence quantities.

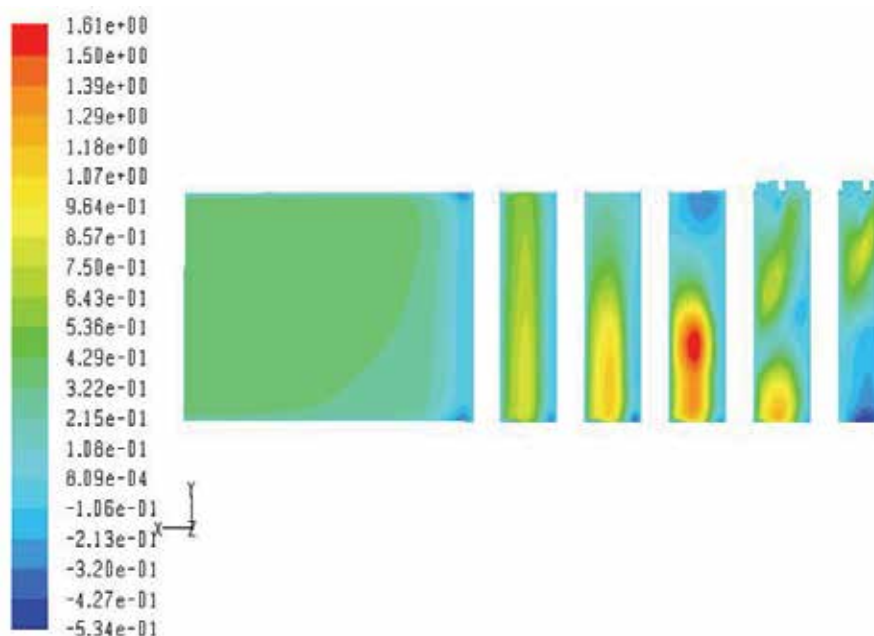


Fig. 9. Computationally-predicted recirculation zones

In FLUENT, mean statistics are collected only in interior cells and not on wall surfaces. Therefore, the plots show velocities in cells adjacent to the wall. Additionally, the velocity field measurements in this PIV data set do not adequately resolve the near-wall velocity gradients because the spatial resolution used to interrogate the raw images was designed to investigate major flow phenomena and to characterize turbulence. Consequently, the relatively large interrogation windows that were used could not accurately resolve velocity

gradients inside the boundary layers. Due to this phenomenon, the measured velocity profiles at the inlet jets could not be used as a boundary condition.

Figure 10 compares computed and measured velocities along the model centerline ( $z=0$  m) at  $y$ -locations:  $-0.07$  m and  $-0.15$  m. The locations of the support posts are indicated by shaded gray bars. Experimental data is not available beyond the  $x=0.46$  m location, because the test section supports blocked the camera views.



Legend for Figures 10 to 15.

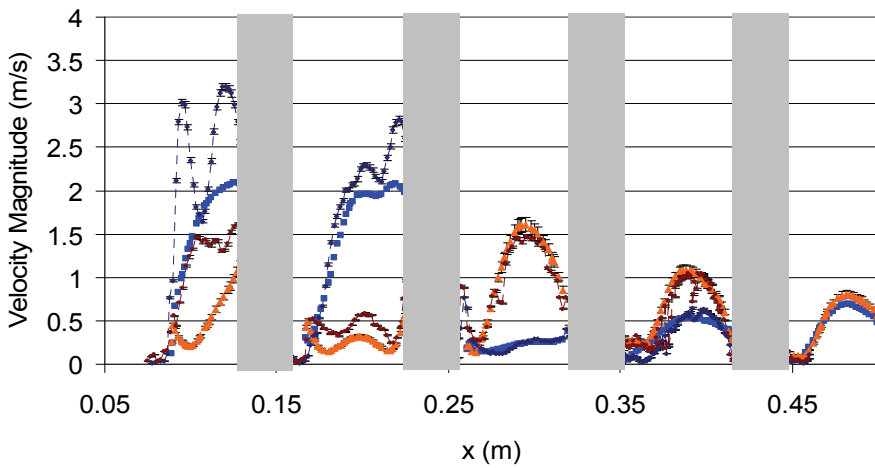


Fig. 10. Velocity along the model centerline ( $z=0$  m)

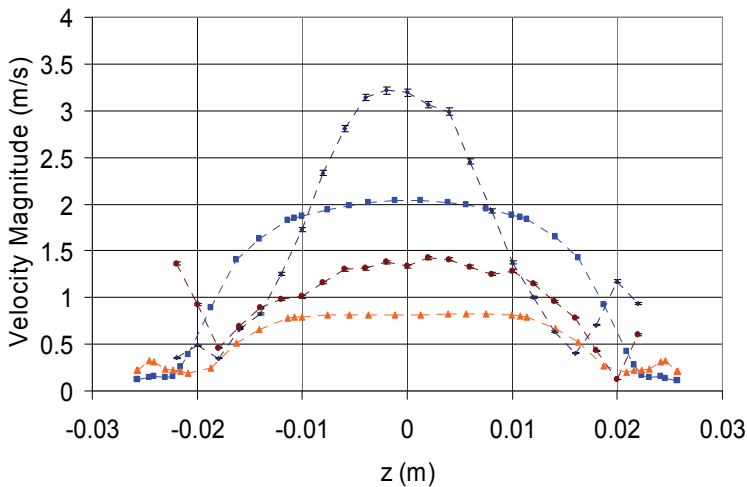


Fig. 11. Velocity on a spanwise slice ( $x=0.12022$  m)

Figures 11 through 14 compare the computationally predicted velocities to experimental data at the following x-locations: 0.12022 m, 0.16850 m, 0.19807 m, and 0.26729 m, and y-locations: -0.07 m and -0.15 m. The largest values of velocity magnitude occur in the region below inlet jet #2. The computed long time-averaged velocity magnitudes in the region near the inlet jets differ from the measured values due to the boundary condition applied at the inlet jets. Downstream from the inlet jets, better agreement between the computed and measured values is seen.

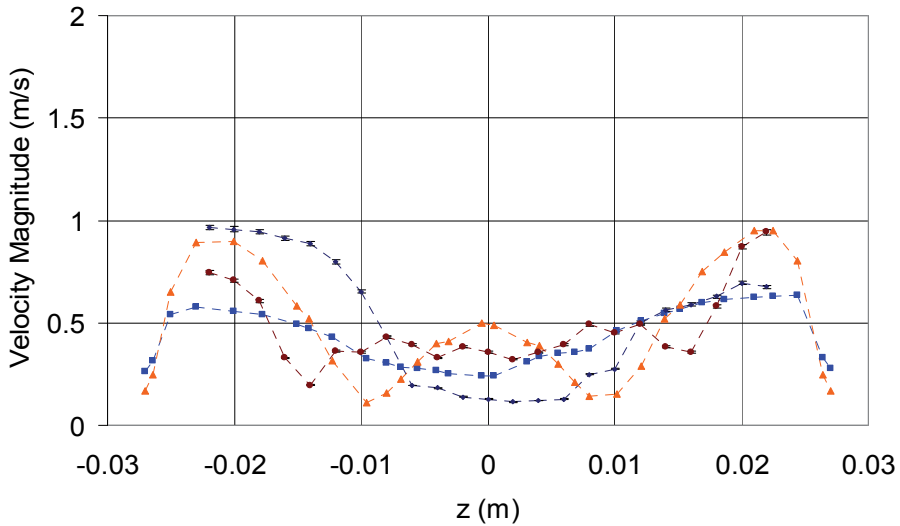


Fig. 12. Velocity on a spanwise slice ( $x=0.16850$  m)

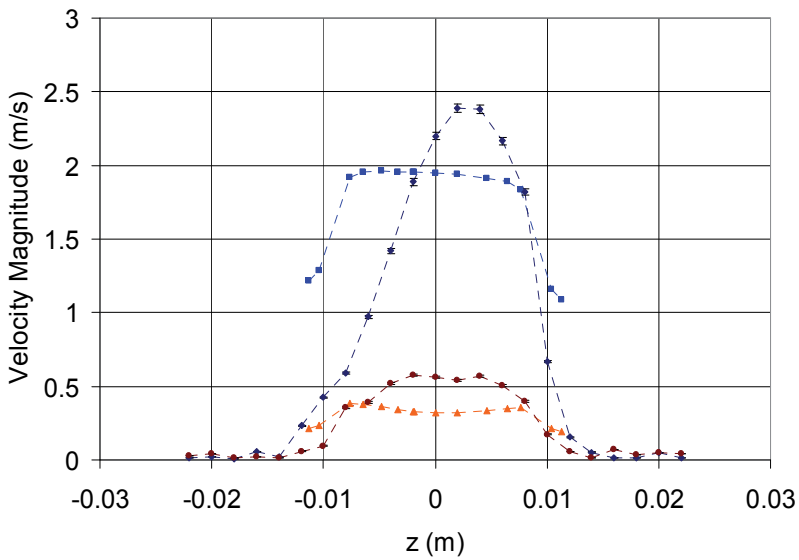


Fig. 13. Velocity on a spanwise slice ( $x=0.19807$  m)

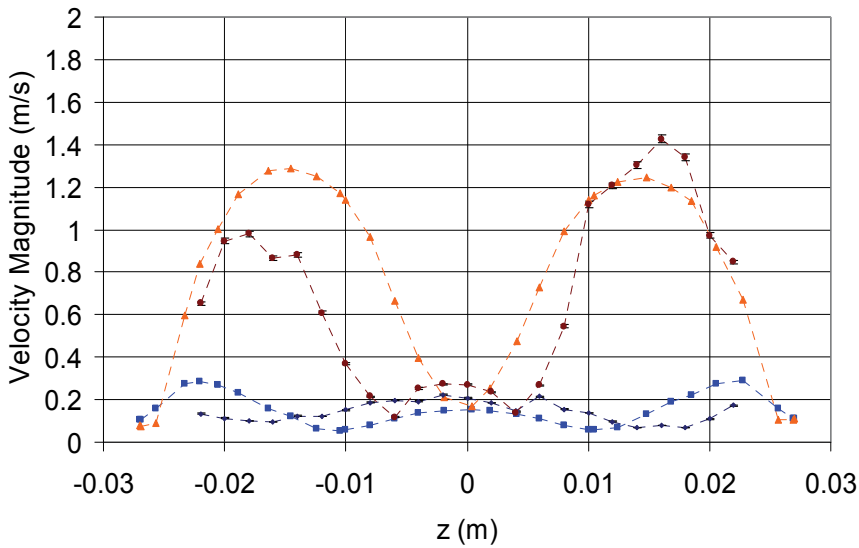


Fig. 14. Velocity on a spanwise slice ( $x=0.26729$  m)

Figure 15 compares the computed and measured turbulence intensity at  $x=0.19807$  m and  $y=-0.07$  m and  $y=-0.15$  m. The values for turbulence intensity are normalized by the maximum velocity magnitude in each data slice. Agreement between computational results and the experimental data is better for the data slice located at the top  $\frac{1}{3}$  of the plenum, than that at the lower  $\frac{2}{3}$  of the plenum. The computed turbulence intensity reaches 68% in the lower region of the plenum, approximately 56% higher than the experimentally measured results indicate. This is attributed to the lack of suitable data available to define the turbulence at the inlet.

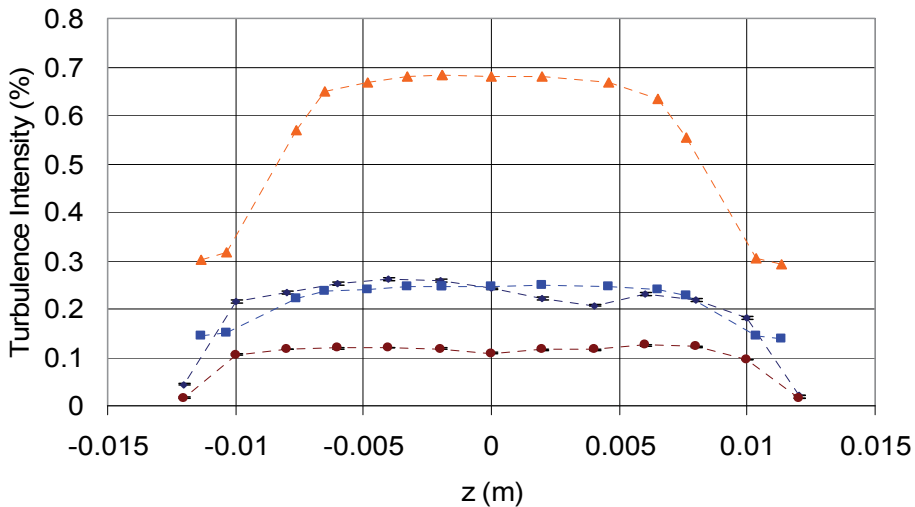


Fig. 15. Turbulence intensity ( $x=0.19807$  m)

### 3. Gas Cooled Fast Reactor (GFR)

The GFR can be operated at high temperatures, has a high thermal efficiency due to the high temperature of the coolant and, being chemically inert by nature, does not react with the structural materials in the core. Helium is used as the primary coolant. Although water is a much better coolant than helium, it is not appropriate for use in fast breeder reactors due to the neutron thermalization by the light atom hydrogen. Helium has considerable advantages over sodium as a coolant for a fast breeder reactor, especially due to its low interaction with the neutrons and its extremely low chemical activity.

Since GFR cores exhibit high power density and low thermal inertia, the decay heat removal (DHR) in depressurization accidents is a major challenge to be overcome. This is due to the facts that: (1) gases exhibit inherently inferior heat transport properties compared to liquids, and (2) the high surface heat flux of GFR, relative to the high temperature gas-cooled thermal reactor (HTGR), strongly affects the gas flow under natural circulation and places the flow into the mixed convection regime, which is not yet fully understood (Weaver et al.). One of the thermal hydraulic characteristics of GFR is that it is designed for a higher power density than the HTGR by an order of magnitude to achieve good economy. Another characteristic of GFR is its low thermal inertia due to the absence of moderator, such as graphite.

Forced convection refers to flow that is driven by an externally imposed pressure difference. The heat transfer coefficient and friction for such flows strongly depend on the Reynolds number and the Prandtl number. Even in a closed loop where there is a heat source and a heat sink, but no pump or blower to drive the flow, forced convection flow can be achieved by having a large buoyancy head due to a density gradient induced by a temperature difference between the heat source and sink. Natural or free convection, on the other hand, can be defined as the flow that is driven by the local buoyancy force induced by the wall to bulk temperature difference, and the characteristic governing non-dimensional parameters are the Grashof number and Prandtl number (Sabharwall et al. 2009).

Gas coolants at low pressures exhibit poor heat transfer characteristics. This is an area of concern for the passive response targeted by the Generation IV GFR design. For the first 24-hour period, the decay heat removal for the GFR design is dependent on an actively powered blower, which also would reduce the temperature in the fuel during transients, before depending on the passive operation. Natural circulation cooling initiates when the blower is stopped for the final phase of the decay heat removal, as under forced convection the core decay heat is adequately cooled by the running blower. The work done here focuses primarily on the period after the blower has been turned off, as the core is adequately cooled when the blowers are running, thus there was no need to carry out the analysis for the first 24 hours.

#### 3.1 Flow behavior characteristics in the upper plenum of GFR

For natural circulation, the mass flow rate and the corresponding heat removal rate both increase with system pressure. A guard containment structure surrounding the primary system is designed to support an elevated back pressure condition during a depressurization accident. In the GFR, heat is removed by a combination of active and passive systems, and the maximum fuel and core outlet temperatures are maintained within acceptable limits. For the first 24 hours after shutdown when natural circulation alone is not

sufficient to cool the core, the emergency core cooling system (ECCS) operates powered by battery powered blowers. Since the active system provides a relatively large mass flow rate, flow recirculation is unlikely and plume behavior is not considered.

For passive cooling, assessment of the ability of the coolant to flow in the reverse direction or recirculate when the blowers are off requires an understanding of the flow behavior characteristics in the upper plenum. The natural circulation mass flow rate is two orders of magnitude smaller than that for forced circulation allowing significant plume interaction during passive cooling.

### 3.2 Analysis and modeling procedure

At reduced power and reduced pressure, the mass flow rate of the coolant under natural circulation is much lower than forced circulation (blower flow). This gives rise to the dilemma of decay heat removal of GFR based only on the passive safety system, and makes the understanding of the plume behavior interaction important. In order to understand the interactions between hot plumes in the upper plenum above the core during low flow/low pressure transients, a GFR upper plenum model was generated in GAMBIT and the CFD analysis was carried out in FLUENT (version 6.3.21). The dimensions were provided by the BNL RELAP5 (version 2.4.1.1A) input deck.

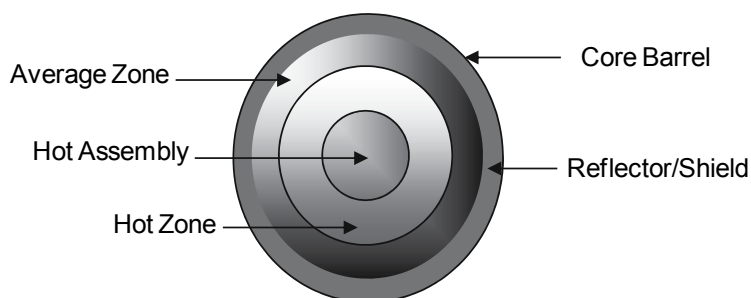


Fig. 16. Horizontal cross-section of GFR core (not to scale)

|                             | Hot Assembly | Hot Zone | Average Zone |
|-----------------------------|--------------|----------|--------------|
| Regular Assembly            | 6            | 48       | 303          |
| Control Assembly            | 0            | 7        | 54           |
| Power Fraction (%)          | 1.7          | 14.1     | 84.2         |
| Relative Radial Power Shape | 1.31         | 1.21     | 0.967        |

Table 2. Power Distribution in Fuel Zones (Lap et al. 2006)

The RELAP5 model of the fuel in the core is grouped into three radial zones by power (refer Table 2). These radial zones are the hot assembly, the hot zone, and the average zone, as can be seen in the Figure 16. 1.7 % of the power is produced by the hot assembly, 14.1% of the power is produced by the hot zone and the remaining 84.2% is produced by the average zone, here the percentage corresponds to the number of fuel assemblies in that respective radial zone. The 2400 MWt GFR is designed for a system pressure of 7.0 MPa and a core pressure drop of  $5.2 \times 10^4$  Pa. The primary coolant flow rate is 1249 kg/sec and the core inlet and outlet temperatures are 480 °C and 850 °C, respectively (Lap et al. 2006).

The upper plenum geometry, consisting of a hot assembly, hot zone and average zone, was meshed with GAMBIT. These radial zones acted as the inlet channels to the upper plenum. The gap between the core barrel and the shield along with the gap between the reflector and the shield acted as outlets from the upper plenum. Also included in the model are the power conversion unit (PCU) inlet, which acts as an outlet from the upper plenum and also the lumped PCU (combining the remaining three PCUs together, as four PCUs are required for the 2400 MWt GFR). Piping to the ECCS also acted as an outlet vent from the upper plenum. The inlet mass flow rate and the respective temperature were specified for their corresponding radial zone as inlet boundary conditions, whereas for the outlets, temperatures and pressures were used as the boundary conditions. These values were obtained with the BNL RELAP5 deck. Figure 17 shows the dimensions of the GFR upper plenum, and a 3-D rendering is shown in Figure 18. In GAMBIT, a symmetry boundary condition was applied to reduce the number of mesh nodes and corresponding computational time required to achieve a solution.

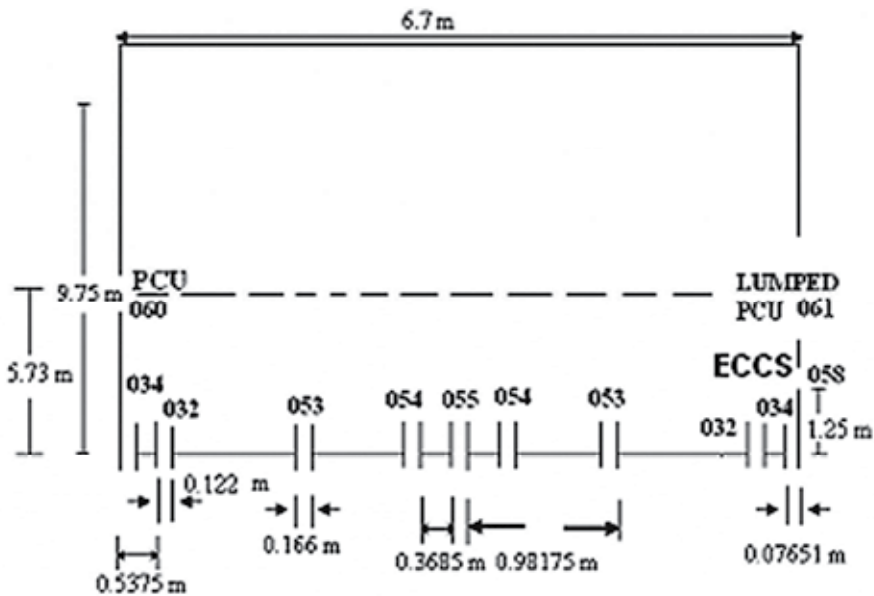


Fig. 17. GFR upper plenum geometry

Label numbers given in Figure 17 are described in greater detail in Table 3.

| Volume Number | Component Name  | Flow Area (m <sup>2</sup> ) | Radius (m) | Temperature (K) | Pressure (Pa) | Inlet/Outlet |
|---------------|-----------------|-----------------------------|------------|-----------------|---------------|--------------|
| 032           | Gap II          | 0.0154                      | 0.061      | 762.394         | 8.00522E+05   | Outlet       |
| 034           | Gap I           | 0.0103                      | 0.038255   | 579.794         | 8.00520E+05   | Outlet       |
| 053           | Average Channel | 6.2487                      | 0.083      | 994.957         | 8.00524E+05   | Inlet        |
| 054           | Hot Zone        | 0.9626                      | 0.083      | 1035.916        | 8.00524E+05   | Inlet        |
| 055           | Hot Assembly    | 0.105                       | 0.083      | 1092.152        | 8.00524E+05   | Inlet        |
| 058           | ECCS            | 2.262                       | 0.84834    | 374.456         | 8.00473E+05   | Outlet       |
| 060           | PCU             | 1.606                       | 0.7144     | 380.697         | 8.00473E+05   | Outlet       |
| 061           | Lumped PCU      | 4.818                       | 1.236      | 376.934         | 8.00475E+05   | Outlet       |

Table 3. Upper plenum parameters



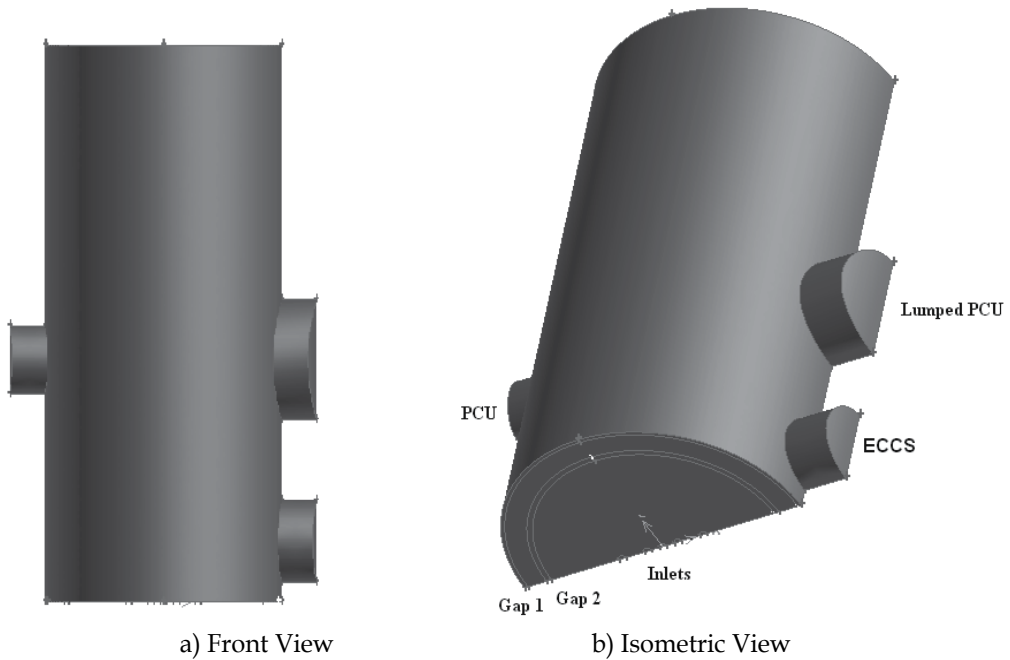


Fig. 18. Different views of the upper plenum

#### Inlets

- AZ I - First inlet channel in the average zone
- AZ II - Second inlet channel in the average zone
- HZ I - First inlet channel in the hot zone
- HZ II - Second inlet channel in the hot zone
- HA - Inlet channel in the hot assembly

#### Outlets

- ECCS - Emergency Core Cooling System
- Gap I - Gap between the core barrel and the shield
- Gap II - Gap between the reflector and the shield
- PCU - Power Conversion Unit

The different views of the upper plenum as shown in Figure 18 were created in the GAMBIT integrated preprocessor for CFD analysis, and then the meshed file was exported to FLUENT for further analyses. In order to understand the plume behavior for the GFR upper plenum, several cases were run, which will be described in detail in the next section. For each case, FLUENT was used to characterize the steady state velocity vectors and corresponding temperature in the upper plenum under passive decay heat removal conditions.

### 3.3 Modeling results

As described above, several cases were run until the convergence criterion was met. In this case, convergence criteria based upon conservation of energy was set at  $1 \times 10^{-6}$ . In our analyses, the boundary conditions for the inlet and outlet were held constant, as these

numbers were obtained from the BNL RELAP5 deck. These conditions correspond to values of mass flow rate, temperature and pressure 24 hours after the shutdown.

| Case | PCU | PCU_Lumped | ECCS | Gap I | Gap II | AZ I | HZ I | HA | AZ II | HZ II |
|------|-----|------------|------|-------|--------|------|------|----|-------|-------|
| 1    | X   | X          | X    | 0     | 0      | X    | X    | X  | X     | X     |
| 2    | X   | X          | X    | X     | X      | X    | 0    | X  | X     | 0     |
| 3    | X   | X          | X    | X     | X      | 0    | X    | X  | 0     | X     |
| 4    | X   | X          | X    | X     | X      | X    | X    | 0  | X     | X     |

Table 4. Different cases for the analyses

In Table 4, the X corresponds to “on” (coolant is flowing) and 0 corresponds to “off” (no flow). For all the cases, convergence criteria were met, both for steady and unsteady state. Conservation of mass was verified for all cases, as can be seen in Table 5.

| Case | PCU    | PCU_Lumped | ECCS   | Gap I  | Gap II | AZ I  | HZ I | HA   | AZ II | HZ II | $\delta m_{in} - \delta m_{out}$ |
|------|--------|------------|--------|--------|--------|-------|------|------|-------|-------|----------------------------------|
| 1    | -0.754 | -4.573     | -2.184 | 0      | 0      | 1.525 | 1.5  | 1.47 | 1.525 | 1.5   | 0.00935891                       |
| 2    | -0.411 | -6.884     | -1.927 | 1.975  | 2.721  | 1.525 | 0    | 1.47 | 1.525 | 0     | -0.0049226                       |
| 3    | -0.138 | -0.606     | -3.26  | -0.327 | -0.054 | 0     | 1.5  | 1.47 | 0     | 1.5   | 0.08266951                       |
| 4    | -0.026 | -3.12      | -3.022 | 0.019  | 0.19   | 1.525 | 1.5  | 0    | 1.525 | 1.5   | 0.09210049                       |

Table 5. Mass flow rate (kg/sec) for all the cases<sup>1</sup>

### Case 1

In case 1, the gap between the core barrel and the shield along with the gap between the shield and the reflector were closed. The convergence criteria were met as can be seen from Figure 19. The largest flow rate was through the lumped PCU opening, as expected.

All the velocity vectors are at nearly the same temperature, since no flow is allowed through the gaps, which makes all the plumes rise. Thus, colder plumes come into contact with the hotter plumes and attain the same temperature before leaving through other outlets.

### Case 2

In this case, two inlets (hot zones) are closed. Gaps located close to the average zone inlet have a net positive mass flow rate because the flow rate of the average zone is so high that it entrains the plumes entering the gaps with it and thus makes the gaps behave like an inlet. In this case, the maximum flow is out through the lumped PCU, as expected.

### Case 3

In this case, the average zone inlets are closed and the gaps act as an outlet unlike in case 2, thus proving the validity of the reasoning for case 2. The maximum amount of flow in this case is into the ECCS. Most of the flow exits the ECCS because the average zone inlet channels are closed. Thus, plumes near that location are comparatively cold, and do not have enough momentum to flow upwards towards the lumped PCU.

<sup>1</sup> Positive values indicate flow into the plenum, whereas negative values indicate flow out of the plenum.

### Case 4

In this case, the hot assembly inlet is closed. Since the average zone inlet is open, the gaps act as an inlet, similar to case 2. Both the ECCS and lumped PCU have almost the same amount of flow leaving from the upper plenum.

Plumes near the hot assembly exhibit colder temperatures and thus move towards the ECCS, whereas the plumes near the hot zone and average zone travel towards the lumped PCU.

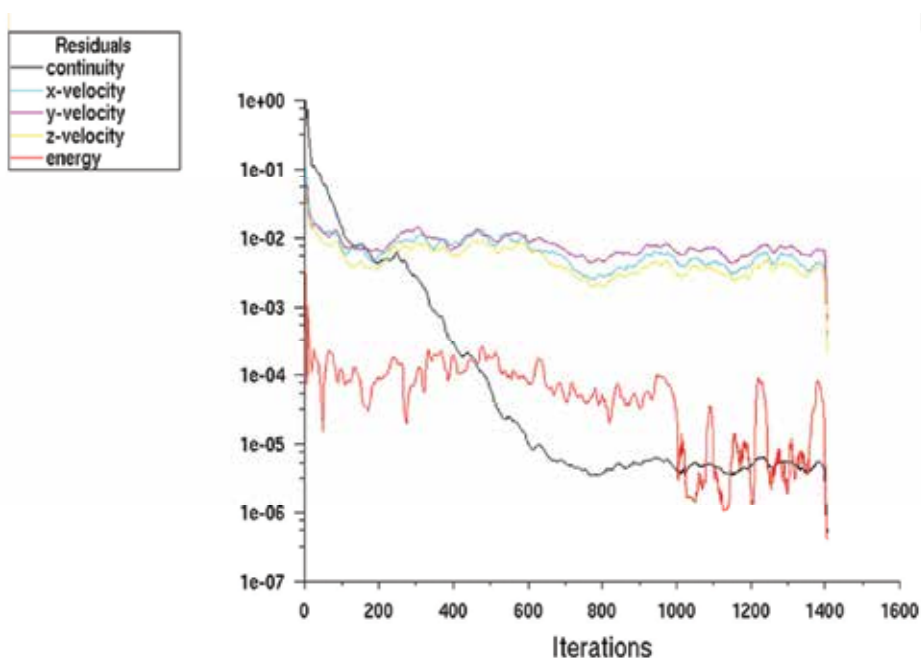


Fig. 19. Residual plot for convergence (Case 1)

### 3.4 Discussion

In all the cases investigated, as can be seen from Table 5, the net mass flow in the upper plenum is not equal to zero, because in an unsteady problem some amount of mass gets accumulated in the plenum, but the magnitude of the net mass flow was small enough to let us believe that mass was being conserved (or the problem was in steady state). The positive magnitude of the mass flow rate refers to the incoming flow whereas the negative magnitude of the mass flow rate refers to the outgoing flow. In all the cases the recirculation patterns of plumes were observed in the top of the upper plenum.

If the mesh is refined, then the net mass flow rate through the upper plenum could be further reduced and thus more precise values for the outlet mass flow rate could be obtained. The analysis done here indicates that the recirculation pattern and the outlet flow depend upon which inlet channels are open, such as in case 2 when the average channel was off. Both gaps behave as outlets and aid in the decay heat removal, whereas in the other cases there is no flow in those gaps, which in an actual system is similar to a flow stagnation, which can cause cracks to develop, and also lead to generation of hot spots in the core. To

more fully capture the plume interaction behavior, this analysis should be performed with a finer mesh and with other coolants and mixtures. This phenomenon may be important if blower power is lost. The analyses should also be carried out with CO<sub>2</sub> for comparison with helium. CO<sub>2</sub> is denser than helium and is thus a better natural convection coolant.

In an accident scenario, if air ingresses inside the vessel, air and helium can mix, which can have a detrimental effect on the helium plume rising in the upper plenum. The initial vertical velocity of the plume is soon greatly reduced, upon encountering the air. If at the same time forced flow is not available, flow reversal in some of the inlet channels could result.

### 3.5 Comparative study

In order to understand the plume behavior for the GFR upper plenum, a few different cases were run, with air, helium (Table 6) and helium-air mixture (Table 7). For each case, FLUENT was used to characterize the steady-state velocity vectors and corresponding temperature in the upper plenum under passive decay heat removal conditions. In the previous sections explanations have been provided for air as the coolant. In this section, the behavior air is compared to other coolants. In the case of helium-air mixture, maximum flow was through the lumped PCU, similar to that of the air, but with helium, maximum flow was through the ECCS, for case 1. For case 2, the maximum flow was through the gap I for the helium-air mixture, whereas maximum flow was observed through the lumped PCU for air and helium. For case 3 maximum flow was observed through the lumped PCU for both helium-air mixture and helium, whereas for air, the maximum flow was through ECCS. For case 4, maximum flow was observed through the lumped PCU for air and helium, whereas in the case of the mixture of helium and air, maximum flow was observed through gap1. The analysis done here indicates that the recirculation pattern and the outlet flow is dependent on which inlet channels are open and also indicate dependence of the mass flow on the type of the coolant, i.e., for the same conditions the behavior of plumes was observed to be different, which should be significant for the study of flow characteristics in the upper plenum during low flow/low pressure transients.

| Case | PCU   | PCU_Lumped | ECCS | Gap I | Gap II | AZ I  | HZ I | HA   | AZ II | HZ II | $\delta m_{in}-\delta m_{out}$ |
|------|-------|------------|------|-------|--------|-------|------|------|-------|-------|--------------------------------|
| 1    | 38.88 | -5.676     | -47  | 0     | 0      | 1.526 | 1.5  | 1.47 | 1.525 | 1.5   | -5.96159                       |
| 2    | 0.045 | -5.8       | -4.6 | 2.027 | 2.888  | 1.526 | 0    | 1.47 | 1.525 | 0     | -0.95866                       |
| 3    | -0.46 | -5.848     | -4   | 2.187 | 3.693  | 0     | 1.5  | 1.47 | 0     | 1.5   | -0.0062                        |
| 4    | -0.9  | -5.981     | -1.5 | 0.729 | 1.586  | 1.526 | 1.5  | 0    | 1.525 | 1.5   | -0.00664                       |

Table 6. Mass flow rate (kg/sec) for all the cases (helium)

| Case | PCU    | PCU_Lumped | ECCS   | Gap I  | Gap II | AZ I  | HZ I | HA  | AZ II | HZ II | $\delta m_{in}-\delta m_{out}$ |
|------|--------|------------|--------|--------|--------|-------|------|-----|-------|-------|--------------------------------|
| 1    | -0.754 | -4.573     | -2.185 | 0      | 0      | 1.526 | 1.5  | 1.5 | 1.53  | 1.5   | 0.009359                       |
| 2    | -0.254 | -1.178     | 0.062  | -1.859 | -1.517 | 1.526 | 0    | 1.5 | 1.53  | 0     | -0.225347                      |
| 3    | -0.113 | -2.203     | -0.077 | -1.254 | -0.515 | 0     | 1.5  | 1.5 | 0     | 1.5   | 0.307385                       |
| 4    | -0.122 | -0.63      | -0.209 | -2.811 | -2.583 | 1.526 | 1.5  | 0   | 1.53  | 1.5   | -0.303515                      |

Table 7. Mass flow rate (kg/sec) for all the cases (helium and air)

## 4. Summary and recommendations

This section summarizes the major results of the VHTR and GFR CFD studies and provides recommendations for further work.

### 4.1 Recommendations from VHTR study

FLUENT converged more readily with the polyhedral grid than with the unstructured grid. The VHTR results presented in this paper were obtained using the “super-fine” polyhedral grid. Results obtained using the polyhedral grid more closely matched the experimental data than the results obtained using the unstructured grid, although the agreement was still far from optimal. Since the inlet boundary condition was not matched exactly, differences between the computed and measured results are expected. However, the large percentage difference in the computed mean velocity between the grids used in this study indicates that additional grid studies are needed. For future studies, computations should be performed on an even more refined grid until the results do not change between subsequent grids. In this study, the computational grids became unwieldy and the solutions required long execution times when the number of grid points was increased beyond that of the “super-fine” grid.

Three-dimensional CFD predictions of flow through a complex geometry representing the lower plenum of an advanced reactor have been performed and compared with laboratory measurements obtained for a scaled model. The major trends seen in the experimental data are captured by the CFD results. The computed versus experimental results are in general agreement, but the quantitative agreement could be improved. Again, it is stressed that the purpose of this work is to better define improvements that can be made to the next set of computations and experiments. Better agreement between the computed and measured results could be achieved by modifying both the computational model and the laboratory setup. Discrepancies can be attributed to features of the current experimental setup and computational model.

#### Wall and thermal effects

Wall effects on mixing in a confined channel are likely to cause significant differences between the actual lower plenum flow and that of the flow test model. The incorporation of thermal effects will also have a significant impact on the flow in this region. These effects must be accurately described in order to produce the necessary data for licensing and safety analysis of these advanced concept reactors.

#### Data acquisition – time resolution

The time-averaging procedure used by the computational code averages the results obtained at every time-step (approximately 0.01 sec), whereas the experimental setup averages the data measured at much larger time intervals (0.1 sec). To obtain sufficient data points to capture the flow unsteadiness, the data acquisition system should have the ability to capture data with sufficient resolution (i.e., >200 Hz). A high-speed PIV system could provide this data.

#### Data acquisition – spatial resolution

Due to the fact that the PIV method employed is not accurate near the jet walls, the data in near-wall region was missing. The profiles were also very coarse – in some locations there

were only eight data points representing the velocity profile at a given location across the jet. Thus, when integrated the velocity profiles under-predicted the mass flow rate. To conserve mass in the plenum, a mass flow rate boundary condition was used, which employed a constant velocity across the inlet jet. Future studies should provide for the acquisition of adequate velocity and turbulent kinetic energy inlet profiles for use as boundary conditions to the computations. A different approach to obtain data at the inlet jets should be considered. Perhaps complementing PIV with laser Doppler velocimetry (LDV) could provide velocity data that, when integrated, yields the correct mass flow rates. LDV can resolve velocities in the proximity of the wall to about  $y^+ < 1$ , which is more precise than PIV but much more time-intensive. The uncertainty in PIV is about 0.3 pixels. LDV uses much smaller control volumes.

### **Turbulence modeling**

To accurately capture and represent turbulent mixing is a considerable experimental, theoretical and computational challenge (Dimotakis, 2005). Research by von Lavante and Laurien (Lavante and Laurien, 2007) shows that the  $k$ - $\epsilon$  turbulence model performs poorly for flows with strong streamline curvature, since the generation and dissipation of turbulence is anisotropic for these flows. For their application, two-equation turbulence models were found to be too dissipative and as a consequence rapidly dissipate the vorticity present in mixing regions. It is anticipated that the Reynolds Stress Model (RSM) would perform significantly better than the  $k$ - $\epsilon$  model when strong recirculation zones and eddies are present. For the lower plenum flow, the use of the RSM should be explored and the results compared with those obtained using the  $k$ - $\epsilon$  turbulence model.

### **4.2 Recommendations from GFR study**

The GFR flow within the upper plenum was characterized during natural circulation 24 hours after a loss of coolant accident. In future work, the same analyses should be carried out for mixtures of different gases such as helium and carbon dioxide ( $\text{CO}_2$ ), and also  $\text{CO}_2$  and air. In all the cases, investigated here, the net mass flow in the upper plenum is not equal to zero, because in an unsteady problem some amount of mass is accumulated, but the magnitude of the net mass flow was small enough to assume that problem was in steady state. The positive magnitude of the mass flow rate refers to the incoming flow whereas the negative magnitude of the mass flow rate refers to the outgoing flow. In all the cases a recirculation pattern of plumes was observed at the top of the upper plenum. Performing the analyses with different coolants and using a finer mesh will lead to an improved understanding of the plume behavior in the upper plenum at low flow and low pressure conditions.

### **4.3 Acknowledgements**

This research was supported by the U.S. Department of Energy (DOE) under DOE Idaho Operations Office Contract DE-AC07-05ID14517. References and findings herein to any specific commercial product, process, or service by trade name, trademark, manufacturer, or otherwise, does not necessarily constitute or imply its endorsement, recommendation, or

favoring by the U.S. Government, any agency thereof, or any company affiliated with Idaho National Laboratory.

## 5. References

- Celik, I. B. (2006). Procedure for Estimation and Reporting of Discretization Error in CFD Applications, Mechanical and Aerospace Engineering Department, West Virginia University.
- Celik, I.B. (i) (2006). Overview of Turbulence Modeling for Industrial Applications, Mechanical and Aerospace Engineering Department, West Virginia University.
- Cheng, L.Y., Ludewig, H., and Jo, J. (2006). Emergency Decay Heat Removal in a Gen-IV Gas-Cooled Fast Reactor, *14<sup>th</sup> International Conference on Nuclear Engineering, ICONE14-89681*, Florida.
- Condie, K.G., G. E. McCreery, H. M. McIlroy Jr., and D. M. McEligot (2005). Development of an Experiment for Measuring Flow Phenomena Occurring in a Lower Plenum for VHTR CFD Assessment, INL/EXT-05-00603, Idaho National Laboratory, September 2005.
- Dimotakis, P. E. (2005). Turbulent Mixing, *Annual Review of Fluid Mechanics*, Vol. 37, pp. 329–356.
- FLUENT (2007). FLUENT Inc.: Lebanon, NH, 03766.
- General Atomics (1996). *Gas Turbine – Modular Helium Reactor (GT-MHR) Conceptual Design Description Report*, General Atomics 910720, Rev. 1, July 1996.
- Johnson, R. W., Guillen, D.P., and Gallaway, T. (2006). *Investigations of the Application of CFD to Flow Expected in the Lower Plenum of the Prismatic VHTR*, INL/EXT-06-11756, September 2006.
- Johnson, R.W. (2006). Modeling Strategies for Unsteady Turbulent Flows in the Lower Plenum of the VHTR, *CFD4NRS Workshop on Benchmarking of CFD Codes for Application to Nuclear Reactor Safety*, Garching, Munich, Germany.
- McIlroy, H. M., McEligot, D.M., Schultz, R.R., Christensen, D., Pink, R.J., and Johnson R.C. (2006). *PIV Experiments to Measure Flow Phenomena in a Scaled Model of a VHTR Lower Plenum*, INL/EXT-08-15161, September 2006.
- Nuclear Energy Institute (2008). *Nuclear Energy: Just the Facts*, 1776 I St., NW, Washington, DC, 20006, [www.nei.org](http://www.nei.org).
- O'Brien, J.E., Stoots, C.M., Herring, J.S., and Harvigsen, J.J. (2007). Performance of Planar High-Temperature Electrolysis Stacks for Hydrogen Production from Nuclear Energy, *Nuclear Technology*, Vol. 158, p. 118-131.
- Sabharwall, P., Utgikar, V., and Gunnerson, F. (2009). Dimensionless Numbers in Boiling Fluid Flow for Thermosyphon and Heat Pipe Heat Exchangers, *Journal of Nuclear Technology*, Vol. 167, August 2009.
- Schultz, R.R., et al. (2006). Specifying Standard Problems for Validating Advanced Reactor Computational Fluid Dynamics Analysis Tools, *American Nuclear Society Transactions*, Vol. 95, p. 836-837.

Smith, B.L., Stepan, J.J., and McEligot, D.M. (2006). Velocity and Pressure Measurements Along a Row of Confined Cylinders, *2006 ASME Fluids Engineering Summer Conference*, Miami, FL: Proceedings of ASME-FED.

U.S. Energy Information Administration, *Annual Energy Outlook*, 2011.

Weaver, K., et al., Gas-Cooled Fast Reactor (GFR) *FY05 Annual Report*, Idaho National Laboratory Report INL/EXT-05-00799, September 2005.



# CFD for Characterizing Standard and Single-use Stirred Cell Culture Bioreactors

Stephan C. Kaiser, Christian Löffelholz, Sören Werner and Dieter Eibl  
*Zurich University of Applied Sciences, School of Life Sciences and Facility Management  
Switzerland*

## 1. Introduction

Driven by global competition and rising cost pressure in the pharmaceutical industry, over the last ten years single-use bioreactors have been increasingly used for animal cell cultivations in screening experiments, seed inoculum and seed train productions as well as in small and medium scale production processes of proteins (in particular, antibodies and vaccines). In contrast to re-usable bioreactors made of glass or stainless steel, single-use bioreactors consist of a flexible or rigid cultivation vessel which has been gamma-sterilized and made ready for the purchaser to use. After harvest, the cultivation vessel is discarded, which results in a lower risk of cross-contamination, and eliminates the need for steam sterilization and cleaning [Eibl et al. (2010)].

Nowadays a multitude of single-use bioreactors are commercially available, which can be categorized according to the type of power input into static and dynamic systems. The latter can be further subdivided into hydraulically, pneumatically and mechanically driven bioreactors and their combinations, the so-called hybrid systems [Eibl et al. (2011)]. Mechanically driven single-use bioreactors represent the largest group and are mixed by either orbital-shaken, wave-induced or stirrer motion.

While wave-mixed bioreactors (e.g. from GE Healthcare, Sartorius Stedim Biotech, Applikon Biotechnology) were initially dominant, nowadays stirred bag systems (such as Hyclone® Single Use Bioreactor S.U.B., BIOSTAT® CultiBag STR, XDR™-DSTB animal) are more frequently used, mainly due to the broad experience already obtained with conventional stirred cell culture bioreactors [Eibl et al. (2011)]. The flexible cultivation bags are fixed and shaped by a temperature-controlled stainless steel container. This design is also used in the BIOSTAT® CultiBag STR from Sartorius Stedim Biotech, which is available at different scales from 50 to 1,000 L. The bag geometry, the impellers and the aeration system are designed in a similar way to Sartorius Stedim's re-usable stirred cell culture bioreactors to ensure comparability of single-use and classical processes, and thus facilitate integration of single-use bioreactor technologies into modern cultivation processes [De Wilde et al. (2009); Noack et al. (2011)].

Until summer 2009, stirred bag bioreactors were available only at working volumes exceeding 50 L for manufacturing and cost reasons. The introduction of the first single-use stirred bioreactors with a rigid cultivation vessel (Mobius® CellReady 3L bioreactor and CelliGen® BLU SUB) bridged the gap for stirred systems between laboratory and pilot scale

[Kaiser et al. (2010)]. With the recent development of the UniVessel® single-use, Sartorius Stedim Biotech have extended their portfolio of the BIOSTAT® product family at bench scale. This novel cell culture bioreactor comes as close as possible to the conventional UniVessel®, but differs slightly in geometry due to the manufacturing process. Furthermore, the positioning of installations, such as harvest tubes or probes, are customized in the reusable bioreactor, but fixed in the single-use alternative.

Comparability of single-use and conventional cell culture bioreactors is essential for process development, especially when both systems have to be used side by side in hybrid solutions. A need for single-use bioreactors with design and set-up comparable to the reusable alternative is therefore evident. Hence, the aim of this case study is a comparison of the UniVessel® 2L single-use bioreactor with its conventional counterpart made out of glass (in the following, also referred to as 'small scale'). For this purpose, fluid flow investigations using computational fluid dynamics (CFD) are carried out for the single-use and conventional bioreactor to show that the small changes in the geometry of the single-use UniVessel® have no significant effect on its fluid flow. The commercial CFD software package ANSYS Fluent (version 12.1.3) is applied and engineering parameters, such as power input, mixing time and oxygen mass transfer, are determined for the first time. With regard to scale-up, the results are compared with those of the disposable BIOSTAT® CultiBag STR at 50 L scale (in the following, also referred to as 'large scale').

## 2. Issues related to scale-up in stirred cell cultures

For biomanufacturing processes requiring larger volumes, scalability of the bioreactor system is a crucial factor, because similar process characteristics have to be guaranteed over the different scales [Storhas (2003)]. The conventional scale-up of bioprocesses is based on physicochemical and geometrical similarity [Zlokarnik (2006)]. However, keeping one process parameter constant will change several others. Hence, the key parameters with the strongest influence on cell growth and productivity have to be identified. In aerobic cultivations, these are primarily oxygen mass transfer and carbon dioxide removal, mechanical stress and mixing intensity. According to Storhas (2006), all these parameters are influenced by the specific power input (power input per volume of culture broth), even though in different proportions (see Fig. 1). For example, mixing time in fully turbulent flows is proportional to the third radical of the specific power input (Eq. 1), resulting in longer mixing times at larger scales.

$$\theta_m \propto (P/V)^{-1/3} \quad (1)$$

In contrast, the highest local energy input  $\varepsilon_{\max}$ , which is often related to mechanical stress, is proportional to the specific power input:

$$\varepsilon_{\max} \propto \frac{u_{\text{tip}}^3}{d} \propto P/V \quad (2)$$

Besides the specific power input, impeller tip speed  $u_{\text{tip}}$ , impeller Reynolds number  $Re$ , mixing time  $\theta_m$ , oxygen mass transfer coefficient  $k_{La}$  and the Kolmogorov eddy length  $l_e$  are applied as scale-up/down criteria in biotechnology. However, the difficulty in the scale-up of cell culture processes results from a lack of preservation of local flow structures as the

reactor vessels are scaled-up [Venkat & Chalmers (1996)]. It is well-known that highly localized regions of high energy dissipation exist and that local flow structures greatly depend on the geometry and operation conditions of the vessels, and cannot be described adequately by global scale-up parameters. Therefore, spatial resolved data obtained by experimental [Venkat & Chalmers (1996)] and numerical techniques are increasingly being introduced in scale-up studies [Letellier et al. (2002)].

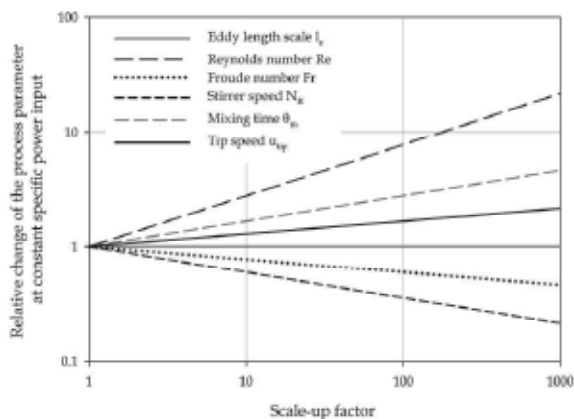


Fig. 1. Influence of scale on different process parameters at constant  $P/V$

As previously mentioned, oxygen mass transfer is another important parameter for scale-up. Due to its low solubility in aqueous media, oxygen has to be continuously supplied to the culture. Animal cells have lower metabolic rates and oxygen demands compared with yeast and bacteria, but in high cell density processes or in cases where aeration is limited by mechanical stress tolerance, oxygen mass transfer can become a limiting factor [Ozturk (1996)]. Although some other options for oxygen supply are available, the use of sparging systems (e.g. ring sparger or microsparger) remains the most practicable method, especially at large scale [Arathoon & Birch (1986); Chisti (1993); Chalmers (1994)]. However, various reports of bubble-associated cell damage can be found in the literature [Handa et al. (1987); Oh et al. (1992); Kioukia et al. (1996)]. Because most agitated bioreactors used in cell culture operate at relatively low mechanical power input, mechanical stress caused by bubbles can exceed that of agitation. Bubble rupture at the liquid surface was found to have the highest effect due to the high local energy density occurring when bubbles burst [Jöbses et al. (1991); Chisti (2000)].

Cell cultures respond to external stresses by changes in morphology, proliferation, differentiation, metabolism or even cell death [Weyand et al. (2009)]. Nevertheless, the biological effects of mechanical stress also depend on culture broth properties (viscosity, oxygen saturation, metabolite concentration, additives, etc.) and can significantly differ between the cell types, cell lines and their characteristics (such as origin, age, subcultivation number etc.) [Meneses-Acosta et al. (2001); Krampe & Al-Rubeai (2010)]. Due to the complexity of the cell damage mechanisms and the variety of factors described in literature, it is still difficult to draw any general conclusions. However, it is accepted that minimum levels of energy dissipation are desirable for scale-up in order to provide sufficient mixing and avoid sedimentation, oxygen depletion and inhomogeneities [Venkat & Chalmers (1996)].

### 3. Numerical methodology

#### 3.1 Description of bioreactors

In this study, the fluid flow patterns in stirred cell culture bioreactors at two different scales (2 L and 50 L) were investigated. The small scale bioreactors from the Sartorius Stedim Biotech's product family BIOSTAT® with the vessels UniVessel® 2L (made of glass) and its single-use counterpart, (UniVessel® 2L SU), have nearly identical geometries (see Tab. 1). Both systems have a cylindrical vessel with a dished bottom and are agitated by a combination of a Rushton turbine (RT) and a three-blade segment impeller (SBI), which are 53 mm and 55 mm in diameter respectively. Due to the manufacturing process, the diameter of the plastic vessel broadens towards the top (from 118 to 126 mm), its bottom has a different shape, and the diameter of the stirrer shaft is larger (at 15.2 mm). Furthermore, the positioning of installations, such as harvest tubes or probes, are fixed in the single-use alternative but customized in the re-usable bioreactor. For the CFD simulation of the glass vessel, the probes were designed based on the bioreactors which are used in our laboratory (see Fig. 2d).

|  | Symbol         | BIOSTAT®<br>CultiBag STR 50 L | UniVessel® 2L<br>single-use | UniVessel® 2L<br>re-usable |
|--|----------------|-------------------------------|-----------------------------|----------------------------|
| Filling height   | H              | 490                           | 180                         | 165                        |
| Vessel diameter  | D              | 370                           | 118 – 126 <sup>1)</sup>     | 130                        |
| Stirrer diameter   |                |                               |                             |                            |
| RT   | d <sub>1</sub> | 143                           | 53                          | 53                         |
| SBI  | d <sub>2</sub> | 143                           | 55                          | 55                         |
| Stirrer height   |                |                               |                             |                            |
| RT   | w <sub>1</sub> | 27                            | 10.5                        | 10.5                       |
| SBI  | w <sub>2</sub> | 68.6                          | 30.4                        | 30.4                       |
| Off-bottom clearance<br>(distance from the bottom to the<br>mid-plane of the lower impeller) | h              | 89.5                          | 48.5                        | 48.5                       |
| Clearance between<br>stirrers<br>(distance between the mid-planes<br>of the impellers)       | c              | 186                           | 70                          | 70                         |
| Shaft diameter   | s              | 20                            | 15.2                        | 10                         |

Table 1. Geometrical dimensions of the bioreactors investigated. All values are given in millimetres and the symbols are indicated in Fig. 2a. <sup>1)</sup> The single-use UniVessel® features a slight inclination of 1° due to the manufacturing process as compared to the re-usable vessel. Hence, the range of the vessel diameters is given. The mean value of 122 mm was used in calculations

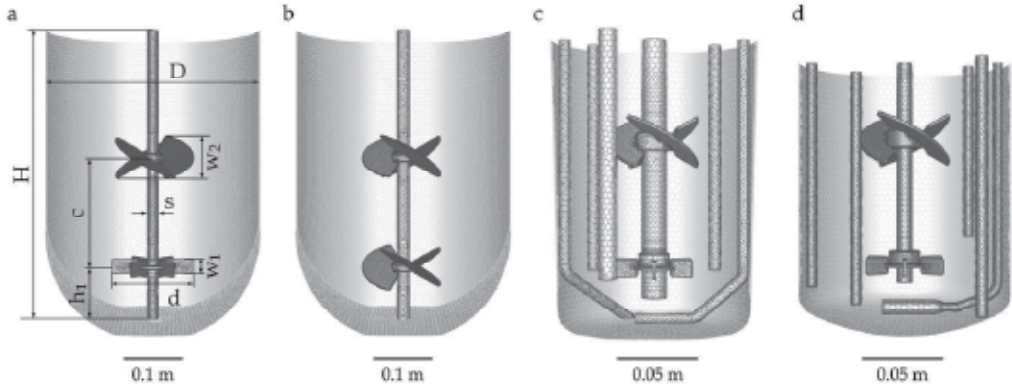


Fig. 2. CAD-models of the four bioreactors used in this study: BIOSTAT® CultiBag STR 50 L with two stirrer configurations (a) and (b), and the UniVessel® 2L single-use (c) with its conventional counterpart (d)

The geometry of the BIOSTAT CultiBag STR 50 L differs from the smaller scales primarily in its differently-shaped bottom (see Figs. 2a and 2b). Other parameters (e.g.  $d/D$ ,  $H/D$ ,  $c/D$  etc.) are geometrically similar. Inside the bag, no baffles are integrated and inside the vessel no additional elements, such as probes, are present because measurements of the pH value and oxygen concentration are realized by small optical sensors installed at the bottom of the bag near the wall. Their influence on the fluid flow is negligible.

### 3.2 Model equations and numerical details

The CFD investigations were realized using a RANS approach with the commercial software package Fluent (ANSYS, Inc. (version 12.1.3)). Using the pre-processor GAMBIT (version 2.4) the accurate bioreactor geometries, shown in Fig. 2, were discretized by body-fitted unstructured meshes. The tetrahedral control volumes were subsequently transformed to polyhedral cells as they have advantages of both tetrahedral and hexahedral cells [Paschedag et al. (2007)]. Prior to the investigations, the grid sensitivity of the CFD results was tested, indicating that meshes with about 130,000 cells for the UniVessel® and 180,000 cells for the BIOSTAT® CultiBag 50L are good compromises between acceptable calculation time and accuracy for further studies.

The governing equation for mass and momentum for single-phase flows can be written as:

$$\frac{\partial \rho}{\partial t} + \nabla \cdot (\rho \cdot \bar{\mathbf{u}}) = 0 \quad (3)$$

$$\frac{\partial (\rho \cdot \bar{\mathbf{u}})}{\partial t} + \nabla \cdot (\rho \cdot \bar{\mathbf{u}} \cdot \bar{\mathbf{u}}) = -\nabla p + \nabla \cdot \bar{\bar{\boldsymbol{\tau}}} + \rho \cdot \bar{\mathbf{g}} + \bar{\mathbf{F}} \quad (4)$$

where  $\rho$  is the fluid viscosity,  $\bar{\mathbf{u}}$  is the velocity vector,  $p$  is the static pressure, and the terms  $\rho \cdot \bar{\mathbf{g}}$  and  $\bar{\mathbf{F}}$  denote the gravitational and external body forces respectively. The Reynolds stress tensor  $\bar{\bar{\boldsymbol{\tau}}}$  was described by the standard k- $\epsilon$  turbulence model [Fluent (2006)].

For multi-phase simulations, an Euler-Euler approach was applied, which considers water as continuous and air as the dispersed phase. The mass and momentum conservation equations for the  $k^{\text{th}}$  phase are given as:

$$\frac{\partial(\alpha_k \cdot \rho_k)}{\partial t} + \nabla \cdot (\alpha_k \cdot \rho_k \cdot \bar{u}_k) = 0 \quad (5)$$

$$\frac{\partial(\alpha_k \cdot \rho_k \cdot \bar{u}_k)}{\partial t} + \nabla \cdot (\alpha_k \cdot \rho_k \cdot \bar{u}_k \cdot \bar{u}_k) = \nabla \cdot \tau_{\text{eff},k} - \alpha_k \cdot \nabla p + \alpha_k \cdot \rho_k \cdot \bar{g} + \bar{F}_k + \bar{R}_k \quad (6)$$

where  $\bar{u}_k$  is the phase velocity vector ( $k = L$  the liquid phase and  $k = G$  the gas phase),  $\rho_k$  the phase density and  $\alpha_k$  the phase volume fraction. A multi-phase  $k$ - $\epsilon$  turbulence model provided by Fluent was used with default settings [Fluent (2006)]. The drag force was modelled by a standard drag model with a correlation for the drag coefficient given by Ishii & Zuber (1979).

In both single- and multi-phase simulations, the vessel walls, the impeller and the probes were treated as non-slip boundaries with standard wall functions. Stirrer rotation was implemented using the Multiple Reference Frame model (MRF) in steady state simulations, which is a good compromise between physical accuracy and reasonable computational time. All equations were discretized using the First Order Upwind scheme, and the (phase-coupled) SIMPLE algorithm was chosen for pressure-velocity coupling. Convergence was assumed when the residuals decreased below  $10^{-5}$ .

For the simulation of mixing process, the flow field obtained was used for a transient calculation of the concentration distribution of an inert tracer superimposed on the flow field. Assuming tracer distribution by convection and diffusion, the species transport equation is given by:

$$\frac{\partial(\rho \cdot \beta)}{\partial t} + \nabla \cdot (\rho \cdot \bar{u} \cdot \beta) = -\nabla \cdot (\rho \cdot D_{\text{eff}} \cdot \nabla \beta) \quad (7)$$

where  $\beta$  is the mass fraction of the tracer and  $D_{\text{eff}}$  is the effective diffusion coefficient, which is calculated using the following equation [Fluent (2006)]:

$$D_{\text{eff}} = D_m + \frac{\eta_t}{Sc_t} \quad (8)$$

where  $D_m$ ,  $\eta_t$  and  $Sc_t$  represent the molecular diffusion coefficient, the turbulent viscosity and the turbulent Schmidt number (which is 0.7 by default) respectively. The tracer was injected at the liquid surface (at  $r/R = 0.5$ ) and the concentration was monitored at eight different points inside the bioreactor. The mixing time was defined as the time required to achieve 95% homogeneity defined by Eq. 9, where  $\beta_\infty$  is the mass fraction in its equilibrium value.

$$H(t) = \frac{|\beta(t) - \beta_\infty|}{\beta_\infty} \quad (9)$$

## 4. Results and discussion

### 4.1 Single-phase flow pattern

As described above, animal cell cultures are sensitive to shear stress, which is often related to the impeller tip speed. Although there are some doubts from the fluid dynamic perspective, maximum tolerable tip speeds are described in the literature [Fenge, et al. (1993); Varley & Birch (1999)]. Maximum tolerable tip speeds differ between cell lines: hybridoma cells were found to tolerate the highest values of up to  $1.8 \text{ m}\cdot\text{s}^{-1}$  [Chisti (2001)]. Hence, the flow fields in this study were simulated for various rotational speeds up to 625 rpm (corresponding to  $u_{\text{tip}} = 1.8 \text{ m}\cdot\text{s}^{-1}$ ) in the UniVessel® system. The tip speeds were subsequently adopted for the simulations of the 50 L scale BIOSTAT® CultiBag STR.

In the following sections, the predicted single-phase fluid flow patterns are described and compared in respect of the two small scale bioreactors. Important engineering characteristics, such as power input and mixing time, are subsequently described. Furthermore, attempts to predict mechanical stress on the cells are presented.

The CFD-predicted fluid flow pattern for the two small scale cell culture bioreactors under unaerated conditions are given in Fig. 3. In both vessels, the upper segment blade impeller (SBI) shows a clear axial flow profile in down-pumping mode while the lower Rushton turbine (RT) discharges the fluid radially towards the vessel wall. The fluid impinges on the outer wall, splits and moves upwards and downwards forming two recirculation loops per half-vessel. In the lower loop, the highest velocities in the order of  $0.5 \cdot u_{\text{tip}}$  are observed in the vicinity of the RT, dropping to  $0.1 \cdot u_{\text{tip}}$  near the vessel bottom. In the vicinity of the upper impeller, fluid velocities reach about  $0.4 \cdot u_{\text{tip}}$ , but are significantly lower near the liquid surface.

As described by Alcamo et al. (2005), the jet of the RT has a slight downward inclination, which can be explained by the absence of baffles. In contrast, slight upwardly inclined radial jets have been found in experimental [Yianneskis et al. (1987)] and numerical [Montante et al. (2001)] studies on fully baffled vessels with Rushton turbines. An interaction of the two impellers can be neglected due to the distance between their mid-planes of  $c/d \approx 1.25$  [Liepe et al. (1998); Vrabel et al. (2000)], which is also confirmed by the estimated power input (see Section 4.2.1).

A more quantitative analysis of the velocity field is presented in Figs. 4 and 5, which show normalised radial, tangential and axial fluid velocities at different positions inside the vessel. In each case, nearly identical fluid velocities are obtained in the UniVessel® single-use and its glass counterpart. The small remaining differences can be ascribed to numerical errors and the fact that the meshes are almost, but not completely, identical.

The maximum radial velocity in the RT's discharge is located below the mid-impeller plain, resulting in an asymmetric profile (see Fig. 4a). Compared with data given by Alcamo et al. (2005) for a single Rushton turbine in an unbaffled vessel, qualitative agreement is achieved, although higher values of radial velocity of up to  $0.4 \cdot u_{\text{tip}}$  are obtained in this study. This might be an effect of the indirect baffling caused by the probes used in this study since the radial velocities obtained for the completely unbaffled BIOSTAT® CultiBag 50L are more similar to data given in the literature [Alcamo et al (2005)]. In contrast, Delafosse et al. (2008) and Kresta & Wood (1991) give maximum radial velocities in the stirrer discharge of up to  $0.8 \cdot u_{\text{tip}}$ .

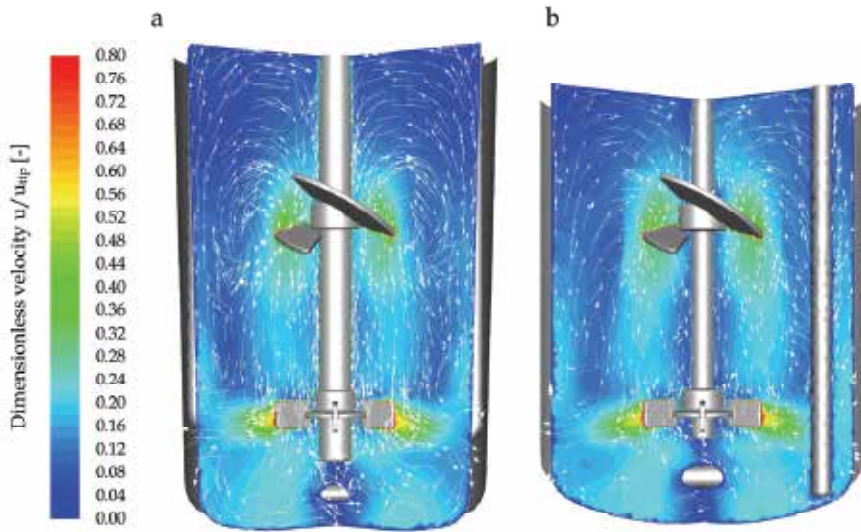


Fig. 3. Velocity distribution in the two small scale vessels UniVessel® single-use (a) and UniVessel® re-usable (b) represented by dimensionless velocity  $u/u_{tip}$ . The velocity magnitude is indicated by contour plots. The velocity vectors are projected to the given plains with fixed length

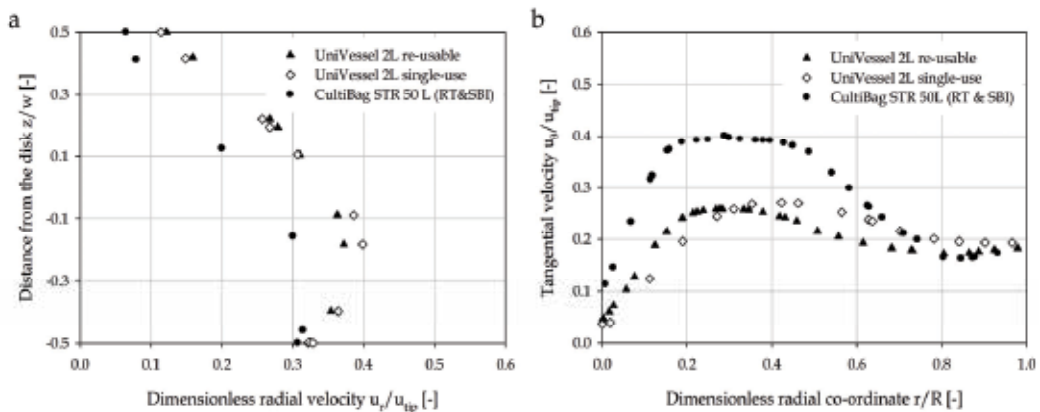


Fig. 4. Comparison of dimensionless radial (a) and tangential velocities (b) between the bioreactors investigated. The radial velocities are given at a distance of  $2r/d = 0.57$  from the impeller tip and the tangential velocities are shown for  $z/D = 0.2$

Similar results are found for tangential velocity, where good agreements between the two small scale vessels are again found. The maximum tangential velocity of  $0.3 \cdot u_{tip}$  is predicted near  $r/R = 0.4$ , which is qualitatively comparable to the findings of Alcamo et al. (2005). Due to the higher radial component found in this study, the tangential velocity is lower than those reported, whereas the values for the 50 L scale vessel are more comparable to those described in literature [Alcamo et al (2005)].



In Fig. 5, radial profiles of the axial velocities directly above and below the upper impeller are shown. The maximum axial velocities in the impeller's discharge are located at  $r/R = 0.4$  in both cases and have values of  $u_z \approx 0.2 \cdot u_{tip}$ . Zhu et al. (2009) give PIV data of an axial pumping "elephant ear" impeller (Applikon Biotechnology) in an unbaffled vessel with similar geometries to that of the SBI. Good qualitative agreement is obtained between PIV measurements and our CFD results. The recirculation points, where up- and down-flow meet and axial velocities become zero, are nearly identical between the two impellers. However, the maximum velocities determined in the impeller's discharge and near the vessel wall have lower values for the segment impeller with  $u_z = 0.2 \cdot u_{tip}$  and  $u_z = 0.05 \cdot u_{tip}$  respectively (see Fig. 5a). If the axial velocities of the small scale vessels are compared with the 50 L scale, good quantitative agreement is evident below the impeller, but some differences occur above the SBI. Thus, maximum velocity in the discharge of the larger impeller is shifted to the left (to  $r/R = 0.1$ ) and lower values of  $u_z \approx 0.02 \cdot u_{tip}$  are found near the wall (see Fig. 5b).

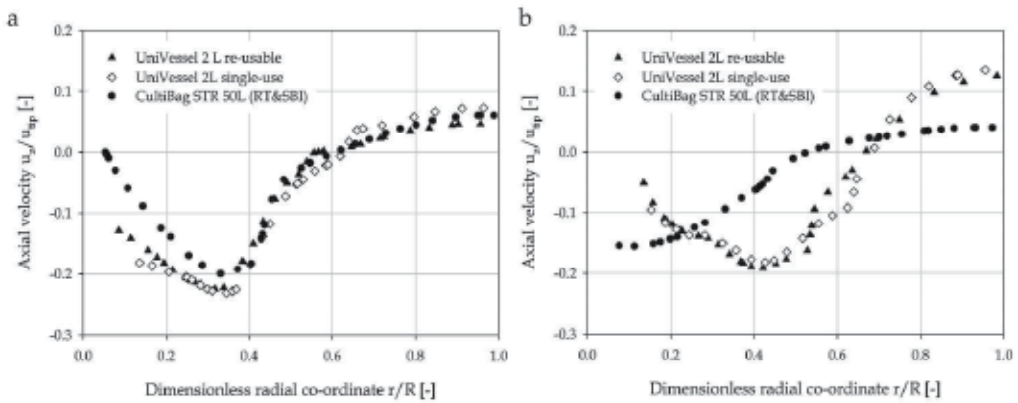


Fig. 5. Dimensionless axial velocities  $u_z/u_{tip}$  as a function of the radial co-ordinate below (a) and above (b) the upper impeller (with  $\Delta z/d = 0.27$ )

For further comparison, the dimensionless axial and radial circulation or pumping numbers  $Fl_z$  and  $Fl_r$  of the two impellers were calculated using the predicted flow field. Primary and secondary pumping numbers  $Fl_{z,p}$  and  $Fl_{z,s}$  as defined by Patwardhan et al. (1999) were calculated for the axial impeller using Eqs. 10 and 11. Both integrals were evaluated closest to the impeller in the pumping direction, whereas the axial flow was integrated over the impeller radius and to the point of reversal of the flow ( $r = R_r$ ).

$$Fl_{z,p} = \frac{2\pi}{N \cdot d^3} \int_{r=0}^{r=d/2} r \cdot v_z(r) dr \quad (10)$$

$$Fl_{z,p} = \frac{2\pi}{N \cdot d^3} \int_{r=0}^{r=R_r} r \cdot v_z(r) dr \quad (11)$$

$$Fl_r = \frac{2\pi}{N \cdot d^3} \int_{z_1}^{z_2} r \cdot v_r(z) dz \quad (12)$$

In doing so, radial flow numbers for the Rushton turbine of 0.56 and 0.36 are determined in the small and large scale vessels respectively. Again no differences are found between the

plastic and the glass bioreactor. However, as a result of the downward inclined stirrer jet investigated in this study, both values are lower than 0.71, as the value reported for fully baffled tanks by Revstedt et al. (1998). The primary and secondary axial flow numbers for the small scale vessel are found to be 0.4 and 0.77. Zhu et al. (2009) obtained a primary flow number of 0.7 for the “elephant ear” impeller and Liepe et al. (1998) reported values for the secondary flow number between 0.7 and 2.2 for different axial pumping stirrers. The latter indicate that the pumping capacity could be increased by about 30 % when baffling is used.

## 4.2 Engineering characteristics and scale-up issues

### 4.2.1 Power input

Using the predicted flow, the impellers’ power inputs were obtained from the torque acting on the stirrer and the shaft. The dimensionless power number (also called Newton number) was calculated as:

$$Ne = \frac{P}{\rho \cdot N^3 \cdot d^5} = \frac{2\pi \cdot M_R}{\rho \cdot N^2 \cdot d^5} \quad (13)$$

In Fig. 6a, the determined power numbers are given as a function of the impeller Reynolds number. Decreasing values for Ne are obtained in all investigated cases up to critical Reynolds numbers of  $Re_{crit} \approx 10^4$ , which is most often found in typical agitated systems [Zlokarnik (1999)]. Above the critical Reynolds number, the stirrer torque is not fully compensated by wall shear stresses and the power number becomes constant [Liepe et al. (1998)]. The CFD simulations resulted in values for the power number of 3.33 and 3.14 in the bioreactors agitated by RT and SBI at small and large scale respectively. As already indicated by the flow field, the probes seem to have a small effect on the power input. For the configuration with two SBIs the Newton number is lower at a value of 1.13. It is well-known that impellers in unbaffled vessels show a continuous decrease in the Newton number over a range of  $0 < Re < \approx 5 \cdot 10^5$  due to vortex formation [Liepe et al. (1998)]. However, this effect was not taken into account in this study and the predicted values are in good agreement with experimental data provided by Sartorius Stedim Biotech. These were obtained by torque measurements and revealed power numbers of 3.4 with RT and SBI, and 1.2 with two SBIs [Personal communication, Ute Noack, Sartorius Stedim Biotech, 2010].

In Fig. 6b, the specific power input is shown as a function of the tip speed. For the maximum tip speed investigated in this study ( $1.8 \text{ m}\cdot\text{s}^{-1}$ ), the highest specific power input at 50 L scale is  $240 \text{ W}\cdot\text{m}^{-3}$ . The configuration with the two SBIs reaches only  $86 \text{ W}\cdot\text{m}^{-3}$  due to the lower power number. Typical values of specific power input are about  $100 \text{ W}\cdot\text{m}^{-3}$  [Henzler & Kauling (1993)], although Nienow (2006) gives a range of 10 to  $250 \text{ W}\cdot\text{m}^{-3}$ . However, if the impeller tip speed is used as a scale-up/down criterion, the power input at small scale increases significantly, as the relationship in Eq. 14 confirms:

$$P/V \propto \frac{u_{tip}}{d} \quad (14)$$

Thus, at a tip speed of  $1.8 \text{ m}\cdot\text{s}^{-1}$  the specific power input increases up to  $960 \text{ W}\cdot\text{m}^{-3}$  in the small scale bioreactors investigated, which is unreasonably high for cell culture applications. On the other hand, if the tip speed for moderate power input in small scale systems (e.g.  $0.37 \text{ m}\cdot\text{s}^{-1}$  for about  $10 \text{ W}\cdot\text{m}^{-3}$ ) is adopted in the larger scale CultuBag STR 50L, the P/V drops significantly (to about  $1 \text{ W}\cdot\text{m}^{-3}$ ). Thus, maintaining tip speed at such low values is a major

constraint with severe implications for mass transfer as well as homogeneity (see Section 4.2.2). Although impeller tip speed is often used for scaling-up in the pharmaceutical industry, these results emphasize that the tip speed does not appear to be an important parameter for scale-up, which aligns with the findings of Nienow (2006).

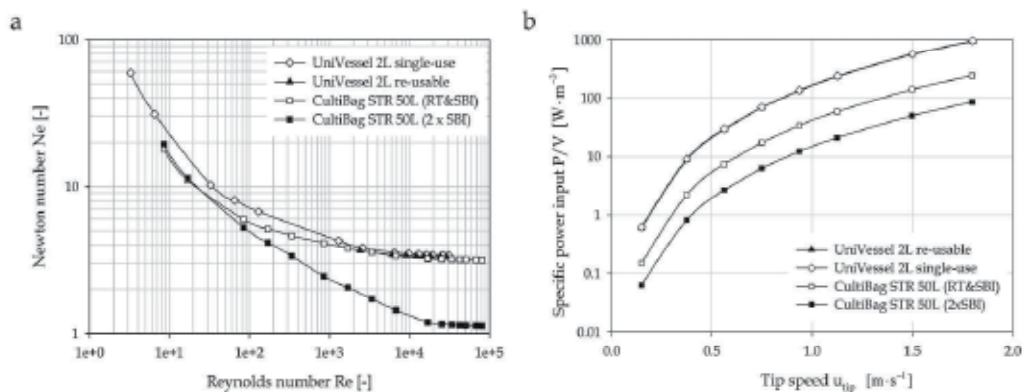


Fig. 6. Power characteristics of the four bioreactor configurations investigated (a). Specific power input as a function of tip speed (b). Note that the symbols for the UniVessel® 2L single-use are partly hidden by those of the UniVessel® re-usable

#### 4.2.2 Mixing time

Mixing time was determined by addition of an inert tracer based on predicted flow field. The volume of the added tracer was equal to 0.1 % of the vessel content in all cases investigated. Typical tracer response curves for different tip speeds at a point near the upper impeller in the UniVessel® 2L single-use are given in Fig. 7. As reported by Min & Gao (2006) and Jahoda et al. (2007), the RANS approach with standard  $k-\epsilon$  turbulence model fails to predict reasonable tracer response curves due to the under-prediction of turbulent fluctuations. However, good agreement of the mixing time with experimental results is usually obtained, as previously found in several studies in our laboratory on different glass and single-use bioreactors [Kaiser (2009); Löffelholz et al. (2011)].

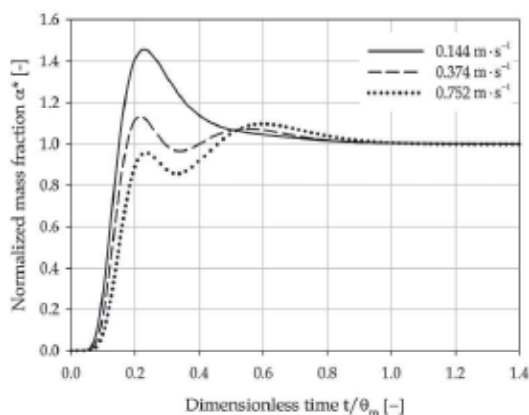


Fig. 7. Tracer response curve for different tip speeds at a point near the upper stirrer in the UniVessel 2L single-use. For better comparison, time is given as dimensionless

In Fig. 8, mixing times for all cases investigated are shown as a function of the specific power input ( $P/V$ ). For the small scale systems, mixing times between 2.3 and 7.4 s are predicted, depending on the stirrer speed. As expected, only minor variations are again observed between the single-use and re-usable vessel types, which can be attributed to the different liquid heights present for equal volumes. In the BIOSTAT® CultiBag STR 50L, mixing times between 10 and 59.8 s are required to achieve the homogeneity desired, whereas the two segment impellers show significantly lower mixing times compared with the configuration of the RT and the SBI at a certain specific power input. The reason for this is the lower power number of the SBI, which results in higher stirrer speeds being required to achieve a certain power input. The stirrer speed is directly related to turbulence intensity, which improves mixing [Liepe et al. (1998); Kraume (2003)]. The slopes of the regression functions (see Fig. 8a) are between  $-0.36$  and  $-0.3$ , and are close to the theoretical value of  $-0.33$  (see Eq. 1), which is valid for turbulent conditions where

$$c_H = \theta_m \cdot N_R = \text{const.} \quad (15)$$

The mixing numbers calculated, which represent the stirrer rotations required to achieve the homogeneity desired, are 18 and 35 for the small and large scale bioreactors respectively. These values indicate that the agitation of the Sartorius Stedim's bioreactors is in the performance range of conventional impellers, as reported by Liepe et al. (1998). Based on turbulence theory, it was suggested that mixing time is independent of impeller type and inversely proportional to turbulent diffusion so that:

$$\theta_m \propto \left( \frac{\varepsilon_T}{L_c^2} \right)^{-1/3} \quad (16)$$

where  $\varepsilon_T$  is the local energy dissipation rate and  $L_c$  is the integral scale of turbulence. Assuming that the integral scale is proportional to the vessel diameter, Nienow (1997) gives a correlation for mixing time with the third radical of the specific power input and geometrical parameters:

$$\theta_m = A \cdot \left( \frac{P}{V} \right)^{-1/3} \cdot \left( \frac{d}{D} \right)^{-1/3} \cdot \left( \frac{H}{d} \right)^{2.43} \cdot D^{2/3} \quad (17)$$

in which the term  $(H/d)^{2.43}$  was originally developed for multiple impellers but also indicates the influence of the fill height observed in large-scale animal cell culture bioreactors at an aspect ratio of 1.3 with a single impeller working in draw and fill mode [Nienow (2006)].

If this approach is adapted to the CFD-predicted mixing times, two distinct functions are obtained for the reactor mixed by the RT/SBI combination and for the two axial pumping stirrers. Thus, the proportionality factor  $A$  in Eq. 17 is found to be 6.5 and 8.7 in the two functions respectively. They are in the same order of magnitude to the value of 5.9 found by Nienow (1997). Although mixing time is not an appropriate parameter for scale-up (see Section 2), homogeneity becomes increasingly important with respect to pH and nutrients at larger scales, and thus mixing capacity should be taken into account.

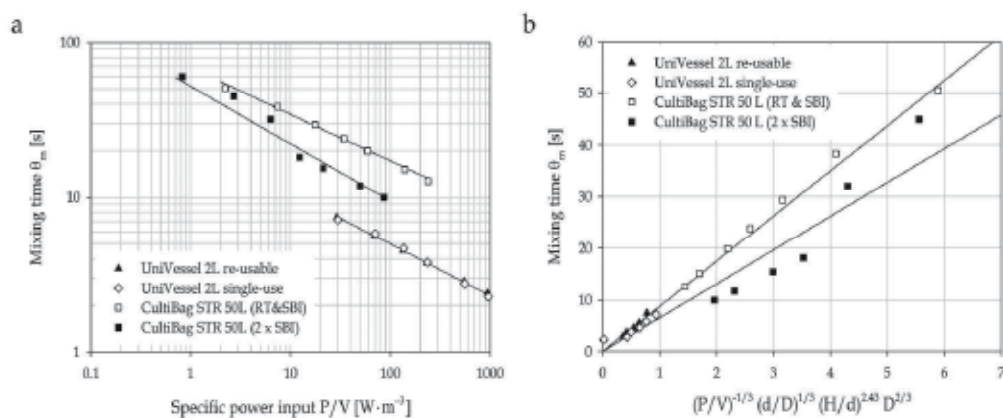


Fig. 8. Mixing time as a function of specific power input for all bioreactor configurations investigated (a). Comparison of the CFD-predicted mixing times with the correlation by Eq. 17 for all bioreactor configurations investigated (b)

#### 4.2.3 Gas distribution and oxygen mass transfer

The gas phase distribution was modelled using an Euler-Euler approach, assuming a uniform bubble size with a diameter of 1 mm. This value was found to be the mean bubble size, determined by photography in the re-usable UniVessel® filled with pure water (2 L filling volume). Spatial gas phase distribution and oxygen mass transfer were investigated for different stirrer tip speeds in the range of 0.15 to 1.8  $\text{m} \cdot \text{s}^{-1}$  for two aeration rates of 0.1 and 0.2 vvm (volume gas per volume liquid and minute), which were defined via gas inlet velocity with gas volume fractions at the inlet surface equal to one.

Due to the low gassing rate, as often used in cell culture applications, no profound effect on the shape of the flow pattern is found, which is in qualitative agreement with the findings of Zhu et al. (2009). Small effects on the liquid velocity are predicted in the jet of the radial impeller, which becomes less intensive, as well as near the stirrer shaft, where the rising gas partly compensates for the downwards directed fluid flow (data not shown).

In Fig. 9, the spatial gas phase distribution is given for impeller tip speeds of 0.37  $\text{m} \cdot \text{s}^{-1}$  and 0.94  $\text{m} \cdot \text{s}^{-1}$  at an aeration rate of 0.1 vvm and compared with experimental observations of the re-usable UniVessel®. Good qualitative agreement is achieved for all operation conditions investigated. At low agitation, the greater part of the gas rises with low dispersion as the disruptive forces induced by the RT are insufficient to overcome buoyancy, although the RT is designed and commonly used to achieve homogeneous gas-liquid dispersions. However, at such low agitation, the stirrer is considered to be “flooded” [Liepe et al. (1998); Zlokarnik (1999)]. The gas dispersion is clearly enhanced by the higher stirrer speed, as shown in Figs. 9c and 9d. Under such conditions, the air introduced is dispersed radially by the lower stirrer and reaches the vessel wall, but almost no gas is found near the bottom. This is again in qualitative agreement with experimental observations (see Fig. 9c) and is also found in experimental [Zhu et al. (2009)] and numerical investigations [Kerdouss et al. (2008)] at comparable operation conditions in other gas-liquid agitated vessels.

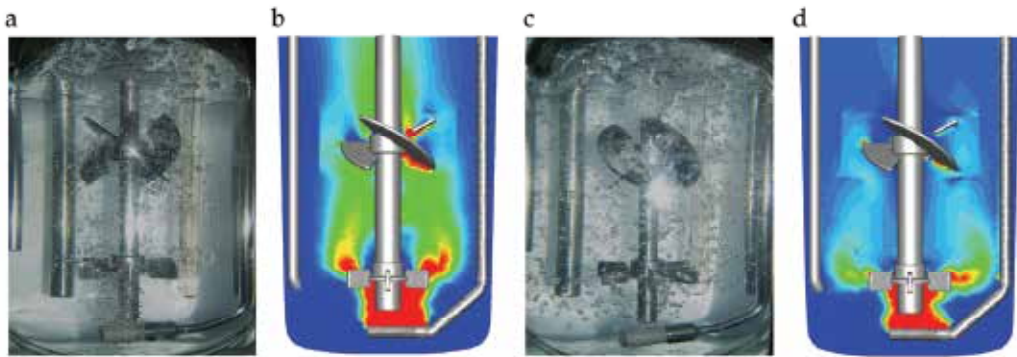


Fig. 9. Comparison of experimental observed gas distribution in the re-usable UniVessel® and CFD-predicted results for the single-use vessel at impeller tip speeds  $0.37 \text{ m}\cdot\text{s}^{-1}$  (a) and  $0.94 \text{ m}\cdot\text{s}^{-1}$  (b)

Based on the predicted flow field, specific oxygen mass transfer coefficients  $k_L a$  were calculated as the product of the liquid mass transfer coefficient  $k_L$  and the specific surface area  $a$ , as suggested by Dhanasekharan et al. (2005) and Kerdouss et al. (2008). Assuming spherical bubble shape, which is guaranteed up to a bubble diameter of 3 mm [Gimbin et al. (2009)], the specific surface area is calculated by:

$$a = \frac{6 \cdot \alpha_G}{d_b} \quad (18)$$

The liquid transfer coefficient is obtained based on Higbie's penetration theory as shown in Eq. 19, where  $D_{O_2}$  represents the diffusion coefficient ( $2.01 \cdot 10^{-9} \text{ m}^2\cdot\text{s}^{-1}$  at  $20^\circ\text{C}$ ).

$$k_L = \frac{2}{\sqrt{\pi}} \cdot \sqrt{D_{O_2}} \cdot \left( \frac{\varepsilon_L \cdot \rho_L}{\eta_L} \right)^{1/4} \quad (19)$$

The results of these calculations are summarized in Tab. 2. It is evident that oxygen mass transfer is enhanced by high agitation and aeration rates, as has been shown on numerous occasions for various stirrer systems. Higher stirrer speed (i.e. higher specific power input) results in lower oxygen transfer resistance due to the higher surface renewal rate of the bubbles [Gimbin et al. (2009)], which is represented by higher  $k_L$  values. Here, values between  $3.15$  and  $5.95 \cdot 10^{-4} \text{ m}\cdot\text{s}^{-1}$  are predicted, which are almost independent of the aeration rate. In contrast, significantly higher air volume fractions are obtained for the higher aeration rate, as expected. Interestingly, a maximum overall gas hold-up of about  $0.37\%$  and  $0.66\%$  is reached at  $30 \text{ W}\cdot\text{m}^{-3}$  for each aeration rate respectively, which is not enhanced by more rigorous agitation.

The highest  $k_L a$  value,  $96.3 \text{ h}^{-1}$ , is obtained at  $0.2 \text{ vvm}$  and  $625 \text{ rpm}$  (see also Fig. 10a). This value is more typical of microbial fermentations, where higher oxygen demands have to be met. However, these high values are not entirely unexpected since the specific power input is also very high (see discussion in Section 4.2.1). Typical values for cell culture applications are in the range of  $1$  to  $15 \text{ h}^{-1}$  [Henzler & Kauling (1993); Langheinrich et al. (2002); Nienow (2006)].

| Q [vvm] | P/V [W·m <sup>-3</sup> ] | k <sub>L</sub> [10 <sup>-4</sup> m·s <sup>-1</sup> ] | a [m <sup>2</sup> ·m <sup>-3</sup> ] | α [%] | k <sub>La</sub> [h <sup>-1</sup> ] |
|---------|--------------------------|--|--------------------------------------|-------|------------------------------------|
| 0.1     | 0.6                      | 3.15   | 14.0                                 | 0.23  | 18.7                               |
| 0.1     | 9.1                      | 3.06   | 18.8                                 | 0.31  | 25.7                               |
| 0.1     | 30.0                     | 3.25   | 21.9                                 | 0.37  | 31.5                               |
| 0.1     | 136.6                    | 4.07   | 19.1                                 | 0.32  | 34.2                               |
| 0.1     | 558.6                    | 5.32   | 18.9                                 | 0.32  | 44.4                               |
| 0.1     | 962.6                    | 5.95   | 19.3                                 | 0.32  | 51.0                               |
| 0.2     | 0.6                      | 3.16   | 22.5                                 | 0.38  | 32.5                               |
| 0.2     | 9.1                      | 3.09   | 32.5                                 | 0.54  | 45.0                               |
| 0.2     | 30.0                     | 3.23   | 39.6                                 | 0.66  | 56.4                               |
| 0.2     | 136.6                    | 4.02   | 37.5                                 | 0.63  | 64.9                               |
| 0.2     | 558.6                    | 5.26   | 37.1                                 | 0.62  | 84.1                               |
| 0.2     | 962.6                    | 5.90   | 38.0                                 | 0.63  | 96.3                               |

Table 2. Summary of the results of the multi-phase simulations in the UniVessel® single-use. The symbols Q, P/V, k<sub>L</sub>, a, α and k<sub>La</sub> represent the aeration rate, the specific power input, the liquid oxygen mass transfer coefficient, the specific surface area, and the overall oxygen mass transfer coefficient

To meet the oxygen demand of cells under steady-state conditions, the oxygen uptake rate OUR needs to be equal to the oxygen transfer rate OTR. The latter depends on mass transfer and the driving force on the gas-liquid surface, given as:

$$\underbrace{q_{O_2} \cdot X}_{\text{OUR}} = \underbrace{k_L a \cdot (c_{O_2}^s - c_{O_2})}_{\text{OTR}} \quad (20)$$

where  $q_{O_2}$ ,  $X$ ,  $c_{O_2}$  and  $c_{O_2}^s$  represent the specific oxygen uptake rate, cell concentration, oxygen concentration and oxygen saturation concentration respectively. Typical specific oxygen demands reported for mammalian and insect cells range from about  $1 \cdot 10^{-9}$  to  $1 \cdot 10^{-8}$  mmol·cell<sup>-1</sup>·day<sup>-1</sup> (see also Tab. 3 for more details). Assuming oxygen solubility in cell culture media of 5 mg·L<sup>-1</sup> and working at 30 % saturation, which are typical values in cell culture applications, the required k<sub>La</sub> values for a cell density of  $5 \cdot 10^6$  cells·mL<sup>-1</sup> are between 1.1 and 36.8 h<sup>-1</sup>, depending on the cell line. These values are already reached at an aeration rate of 0.1 vvm with a specific power input of about 140 W·m<sup>-3</sup>, and with an even lower power input of about 10 W·m<sup>-3</sup> at 0.2 vvm. In the CultiBag STR 50L a maximum k<sub>La</sub> value of 35 h<sup>-1</sup> was determined experimentally by Sartorius Stedim at an aeration rate of 0.1 vvm [Personal communication, Ute Noack, Sartorius Stedim Biotech, 2010], giving comparable results for the large scale bioreactor.

| Cell line                  | $q_{O_2}$ [ $10^{-13}$ mol·cell $^{-1}$ ·h $^{-1}$ ] | $k_{L,a_{req}}$ [h $^{-1}$ ] |
|----------------------------|--|------------------------------|
| C1a (hybridoma)            | 2.34   | 10.7                         |
| FS-4 (human diploid cells) | 0.5  | 2.3                          |
| AB2-143.2(hybridoma)       | 1.9 – 4.0  | 8.7 – 18.3                   |
| 167.4G5.3 (hybridoma)      | 0.23 – 0.87  | 1.1 – 4.0                    |
| NSO (myeloma)              | 2.19 – 4.06  | 10.0 – 18.6                  |
| MAK (hybridoma)            | 4.6  | 21.0                         |
| X-D (hybridoma)            | 2.3 – 4.2  | 10.5 – 19.2                  |
| DG44 (CHO)                 | 2.0  | 9.1                          |
| CHO                        | 5.0 – 8.04   | 22.9 – 36.8                  |
| HFN7.1 (hybridoma)         | 2.0  | 9.1                          |

Table 3. Specific oxygen uptake rates of various cell lines adopted from Ruffieux et al. (1998) and Xiu et al. (1999) and required oxygen mass transfer coefficients at defined cell densities of  $5 \cdot 10^6$  cells·mL $^{-1}$  and oxygen concentrations of 5 mg·L $^{-1}$  (see Eq. 20)

In spite of the numerous literature data in respect of oxygen mass transfer, no correlation was found for the particular stirrer configuration and operation conditions used in this study. Thus, a correlation was developed following an approach suggested by van't Riet (1979), where the  $k_{L,a}$  value is related to the specific power input and the superficial gas velocity (introduced gas per cross sectional area of the bioreactor):

$$k_{L,a} = C \cdot (P/V)^a \cdot \bar{u}_g^b \quad (21)$$

As shown in Fig. 10, very good agreements between the model and CFD-predicted  $k_{L,a}$  values are achieved for the two aeration rates investigated (with  $R^2 = 0.98$ ). The coefficients  $C$ ,  $a$  and  $b$  are found to be 6.51, 0.14 and 0.87 respectively (see Eq. 20). Hence, a rather high dependency of the  $k_{L,a}$  value on the superficial gas velocity (aeration rate) is evident and the specific power input is only of minor importance. This is in contrast to most correlations found in the literature, where the values for  $a$  and  $b$  are  $0.5 \pm 0.1$  [Nienow (2006)]. Nevertheless, Van't Riet (1979) gives a wider range of reported values in the ranges of  $0.4 < a < 1$  and  $0 < b < 0.7$ .

$$k_{L,a} = 6.51 \cdot (P/V)^{0.14} \cdot \bar{u}_g^{0.87} \quad (22)$$

The strong effect of the superficial gas velocity obtained in this study can be explained by the fact that the stirrer does not completely disperse the introduced gas at low agitation rates, and thus the aeration is comparable to a bubble column (see Fig. 9a). Similar results were recently found in our laboratory with other single-use stirred bioreactors (e.g. the Mobius® CellReady 3L bioreactor) [Kaiser et al. (2011)]. However, we would like to point



out that only twelve data points were used for the correlation in this first attempt and the results were only obtained by CFD simulations, which have to be validated by experimental data in further studies.

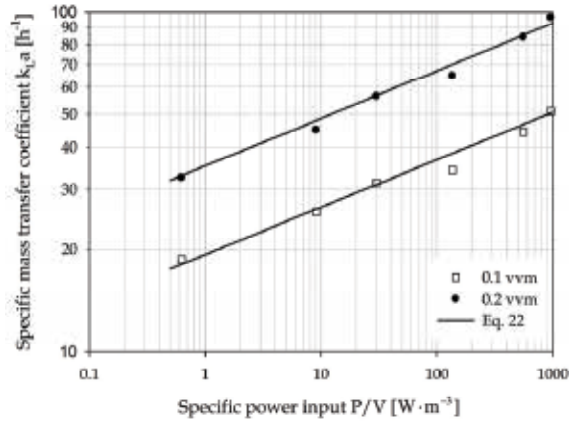


Fig. 10. CFD-predicted volume-averaged specific oxygen mass transfer coefficient  $k_{L,a}$  as a function of specific power input for the two aeration rates investigated. In addition to CFD-predicted data points, the function obtained by Eq. 22 is given

#### 4.3 Mechanical stress

##### 4.3.1 Mechanical stress caused by turbulence

Mechanical stress on cells is related to both turbulence and time-independent velocity-gradients (shear and normal gradients) [Jöbses et al. (1991); Oh et al. (1992); Chisti (2000); Fenge et al. (2003)]. A popular, but yet unproven, theory of cell damage due to turbulence suggests that the biological entity is damaged by eddies of a comparable size. Significantly smaller eddies have too little energy and larger eddies merely carry the cells convectively. Assuming local isotropic turbulence, the size of the smallest eddies is defined by the Kolmogorov length  $l_e$  (Eq. 23). Although Ranade & Joshi (1989) and Jaworski et al. (1991) state that turbulence in the impeller jet is anisotropic, theoretical considerations and experimental evidence have shown that the fine-scale structure of most anisotropic turbulent flows is actually almost isotropic locally [Hinze (1959)]. Thus, Kolmogorov's definition of eddy size would appear suitable for the complete fluid domain.

$$l_e = \left( \frac{\eta^3}{\rho^3 \cdot \varepsilon} \right)^{1/4} \quad (23)$$

In Fig. 11a, the dimensionless turbulent kinetic energy  $k/u_{tip}^2$  is shown. As expected, and in agreement with Hockey & Nouri (1996), convection of turbulence by the mean flow in the impeller jet, where the highest turbulent energies are found, is evident. The axial profiles of the turbulence kinetic energy in impeller jets are found to qualitatively agree with data given by Kresta & Wood (1991), although the predicted values are, by a factor of 5, lower in our study (data not shown). Rather high turbulence is also located near the installations, but significantly lower values are found in the bulk between the impellers and near the liquid surface. Thus, it can be argued that the turbulence distribution is very heterogeneous. For

standard Rushton turbines, Höfken et al. (1996) found differences between maximum and mean turbulent dissipation rates by two orders of magnitude ( $\varepsilon_{\max} / \bar{\varepsilon} = 40 \dots 200$ ).

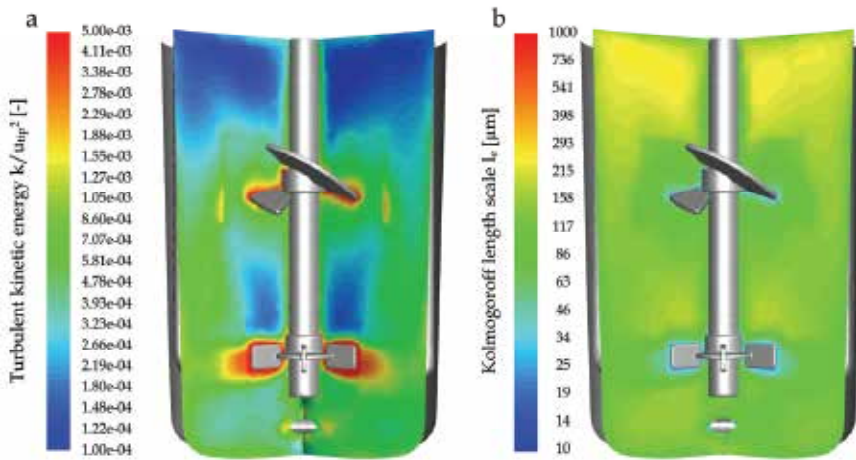


Fig. 11. Spatial distributions of the dimensionless turbulent kinetic energy  $k/u_{\text{tip}}^2$  (a) and the Kolmogorov eddy size  $l_e$  (b) at  $P/V = 230 \text{ W}\cdot\text{m}^{-3}$  in the UniVessel® 2L single-use

As mentioned in Section 4.2.1, typical values for the specific power input are in the range of 10 to  $250 \text{ W}\cdot\text{m}^{-3}$  [Nienow (2006)]. Calculating the Kolmogorov eddy size gives  $l_e = 45 \mu\text{m}$  for  $\varepsilon = (P/V)$  (see Eq. 23). If, as found by Höfken et al (1996) near the impeller of a Rushton turbine,  $\varepsilon_{\max} = 200 \cdot (P/V)$  is assumed,  $l_e$  decreases to about  $12 \mu\text{m}$ . Since animal cells are of the order of  $15\text{--}20 \mu\text{m}$ , the first cell damage would be expected at the maximum power input. In this study, the estimated Kolmogorov eddy size is lower than typical cell sizes above a specific power input of  $230 \text{ W}\cdot\text{m}^{-3}$  (see Fig. 11b) in close proximity to the impellers and installations, which is in agreement with the literature data.

Zhang et al. (1993) investigated animal cell disruption in turbulent capillary flows and developed a model of cell-hydrodynamic interactions using cell mechanical properties determined by micromanipulation. Assuming that eddies with similar or smaller sizes than the cells cause local surface deformation, they proposed that cell disruption occurs when the cells' bursting membrane tension and bursting surface energy are exceeded. Good agreement between experiments and model predictions (with an underestimation of cell disruption by about 15%) were achieved [Zhang et al. (1993)].

Garcia-Briones et al. (1994) compared CFD-predicted energy dissipation rates with those in unaerated flow devices (capillaries and viscometers). They concluded that energy dissipation rates in the order of  $5.81 \cdot 10^2 \text{ W}\cdot\text{m}^{-3}$  did not damage cells significantly, but values of  $\approx 2.25 \cdot 10^4 \text{ W}\cdot\text{m}^{-3}$  caused considerable damage. Using Eq. 22, the latter value gives an eddy length scale of  $14.5 \mu\text{m}$  for water-like media, which is comparable to the size of animal cells ( $\approx 15 \dots 20 \mu\text{m}$ ).

The turbulence theory of cell damage is also supported by the observation that viscosifying additives reduce cell damage. Croughan et al. (1989) have associated cell death protection by serum with the turbulence-dampening effect of the additive. In contrast, observing an insect cell suspension with ten times higher viscosity to water (with  $\eta \approx 10 \text{ mPa}\cdot\text{s}$  and  $\rho \approx 1000 \text{ kg}\cdot\text{m}^{-3}$ ), Tramper et al. (1996) found that cell death rapidly occurred from a specific power

input of  $2.3 \cdot 10^{-3} \text{ W}\cdot\text{kg}^{-1}$ . Even if  $\varepsilon_{\max} / \bar{\varepsilon} \approx 200$  is assumed, this gives a minimum Kolmogorov length scale of  $l_e = 240 \text{ }\mu\text{m}$ , which is considerably larger than an insect cell. Hence, it has been concluded that maximum shear stress is the more appropriate parameter for scale-up than the minimum eddy length scale [Tramper et al. (1996)].

However, bearing in mind the heterogeneous distribution of turbulence, it is important to take residence time distribution into account for the evaluation of cell damage (see Section 4.3.2 for further discussion). However, to the knowledge of the authors, such attempts have not yet been described for animal cells, unlike corresponding studies for blood cells in hemolysis experiments. Thus, the hemolysis level is often correlated with shear stress and residence time, as suggested, for example, by Giersiepen et al. (1990).

#### 4.3.2 Mechanical stress caused by velocity gradients (shear stress)

In most CFD studies, the mechanical stress on cells is only related to the strain rate magnitude  $D$ , which is an invariant velocity gradient consisting of both shear and normal gradients. However, based on model experiments, various authors have shown that cells are differently affected by shear or normal gradients [e.g. Langer & Deppe (2000)]. It is therefore advantageous if each of them is quantified separately for the evaluation of cell damage. Recently, Wollny (2010) found that local shear and normal gradients ( $\gamma_{nt}$  and  $\gamma_{nn}$ ) can be obtained from shear strain tensor using a coordinate system transformation, which results in Eqs. 24 and 25. Here,  $\tilde{w}$  are velocities in the local co-ordinate systems defined by the coordinates  $\tilde{x}, \tilde{y}$  and  $\tilde{z}$ , which are orientated along the fluid flow direction. Detailed descriptions of the mathematical derivation can be found elsewhere [Wollny (2010)].

$$\gamma_{nn} = \sqrt{2 \cdot \left( \frac{\partial \tilde{w}_x}{\partial \tilde{x}} \right)^2} \quad (24)$$

$$\gamma_{nt} = \sqrt{\left( \frac{\partial \tilde{w}_x}{\partial \tilde{y}} + \frac{\partial \tilde{w}_y}{\partial \tilde{x}} \right)^2 + \left( \frac{\partial \tilde{w}_x}{\partial \tilde{z}} + \frac{\partial \tilde{w}_z}{\partial \tilde{x}} \right)^2} \quad (25)$$

From the CFD-predicted flow fields, the local shear and normal gradients as well as the corresponding volume fractions were determined. Subsequently, the distribution was discretized into 250 bins (see Fig. 12a). It was found that the distribution follows a logarithmically normal function, which was confirmed by a chi-quadrant-test at a confidence level of 0.05 (data not shown).

From Fig. 12a it is evident that the highest volume fractions (of about 4.5 %) are found at very low velocity gradients. Depending on the impeller speed, the median value (velocity gradient with the highest volume fraction) is in the order of 1 – 30  $\text{s}^{-1}$ . Interestingly, the median differs from the volume-averaged velocity gradient and the highest volume fraction is nearly independent of the stirrers' power input. This is in qualitative agreement with our previous findings for different single-use and conventional stirred bioreactors [Löffelholz et al. (2011)].

Furthermore, high velocity gradients ( $> 100 \text{ s}^{-1}$ ) have very small volume fractions below 0.5 % of the total liquid volume. Wollny (2010) found quantitatively comparable values for a baffled bioreactor equipped with a  $3 \times 24^\circ$  pitched blade impeller or a standard Rushton

turbine operating at  $100 \text{ W}\cdot\text{m}^{-3}$ . In this study, the impeller swept volume as described by Wollny (2010) is about 2 % of the total liquid volume for the stirrer configuration investigated. Thus, it can be argued that the regions of high ‘shear’ stress are positioned close to the impeller and that the cells are, if at all, mechanically stressed in only a small region of the bioreactor.

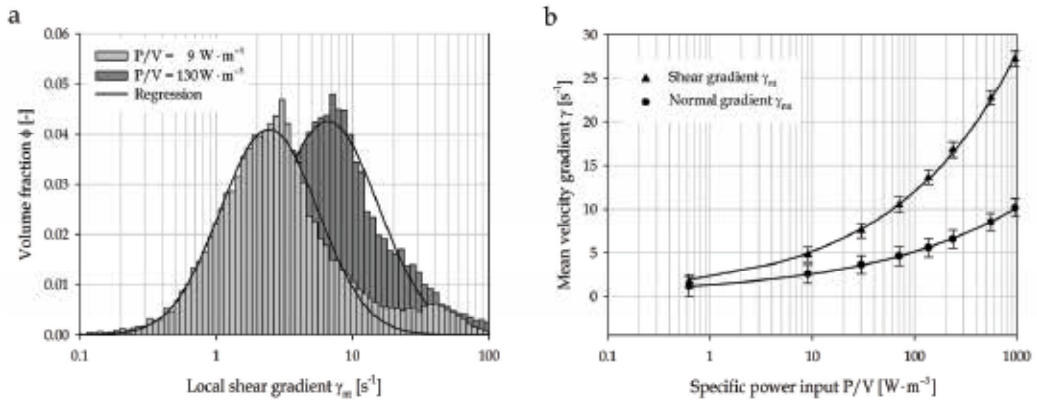


Fig. 12. Evaluation of mechanical damage to cells caused by local shear and normal gradients. Log-normal frequency distribution of local shear gradients (expressed by the volume fraction) for two agitation rates (a), and mean shear and normal velocity gradients as a function of the specific power input (b). Error bars represent simple standard deviation of the logarithmically normal distribution

In Fig. 12b, the mean velocity gradients obtained from the frequency distributions are given as a function of the specific power input. It is evident that the local shear gradients predominate compared with the normal gradients, which are suspected to cause higher cell damage [Langer & Deppe (2000)]. However, the magnitude of both mean and maximum velocity gradients is found to be significantly lower than the critical values ( $1 - 3 \cdot 10^5 \text{ s}^{-1}$ ) causing substantial cell damage, as reported by Chisti (2001). Nevertheless, physiological effects, which do not necessarily require a physical breakage of the cells, were also observed at moderate levels of stress in the range of  $0.5 - 5 \text{ N}\cdot\text{m}^{-2}$  (corresponding to  $500 - 5000 \text{ s}^{-1}$  in water-like culture broths) [Yim & Shamlou (2000)]. The maximum normal and shear gradients for the highest investigated power input ( $\approx 960 \text{ W}\cdot\text{m}^{-3}$ ) reached values of up to 4800 and 6000  $\text{s}^{-1}$  respectively. Consequently, based on the CFD results, no cell damage is expected in the small scale UniVessel® bioreactors at moderate agitation. A comparison of these results with the larger scale BIOSTAT® CultiBag STR will form part of further studies.

## 5. Conclusions

The first objective of this study was a comparison of the novel single-use UniVessel® cell culture bioreactor with its re-usable counterpart, developed by Sartorius Stedim Biotech. For this purpose, the fluid flow under non-aerated conditions was simulated using a RANS approach and the standard  $k-\epsilon$  turbulence model. Almost identical flow patterns are achieved with only minor differences in fluid velocities and turbulence distributions, which can be attributed to small variations in the meshes and the positions of the installations such

as probes and harvest tubes. The CFD simulations reveal a rather complex flow pattern, in which the radial pumping Rushton turbine induced two flow loops per half-vessel and the segment blade impeller shows a typical axial flow in down-pumping mode.

Predicted fluid velocities as well as flow numbers show good qualitative and quantitative agreement with literature data. Based on these results, it can be argued that the differences in geometry between the two small scale bioreactors have no influence on the overall fluid flow. From the fluid flow perspective, the UniVessel® 2L single-use is identical to its counterpart made of glass and thus no differences in cell cultivations are expected. This hypothesis clearly needs to be verified in cultivation experiments, which will be carried out in our laboratory in the near future.

In a second part, key engineering parameters, such as power input, mixing capacity and oxygen mass transfer, for the UniVessel® 2L single-use are presented for the first time and compared with data on its conventional counterpart as well as with those on the BIOSTAT® CultiBag STR 50L. The power numbers  $Ne$  of the two small scale systems are identical (with a value of 3.33) and somewhat lower in the CultiBag STR 50L ( $Ne = 3.14$ ) at the same stirrer configuration (RT and SBI). It is shown that unreasonably high specific power inputs for cell culture applications are obtained in the UniVessel® bioreactors, if the maximum tip speed of  $1.8 \text{ m}\cdot\text{s}^{-1}$  is used as a scale-up/down parameter for the CultiBag STR 50L. Thus, it can be concluded that (maximum) specific power input  $P/V$  is a more appropriate constraint for scale-up than tip speed when viewed from the perspective of adequate mixing and shear sensitivity of the cells, which is in agreement with the literature data. Furthermore, correlations for the mixing time are provided which are independent of the bioreactor scale, as suggested by Nienow (1997), and can thus be used in scale-up/down studies.

From multi-phase simulations using an Euler-Euler approach, gas phase distribution and oxygen mass transfer were modelled for various agitation and aeration rates. In this first attempt, a constant bubble size of 1 mm, as obtained using photography at the BIOSTAT® B plus is assumed. It is well-known that bubble size depends on media properties, such as viscosity, salt content etc., and is usually non-uniform. In addition, bubble size distribution depends on aeration (e.g. the sparger design) and the agitation system (e.g. impeller type), and is further influenced by bubble break-up and coalescence. In the last two decades, bubble size distributions have been increasingly modelled using population balance models (PBM) [e.g. Kerdouss et al. (2008); Dhanasekharan et al. (2005)]. Nevertheless, computation using PBMs becomes more complex and time-consuming due to the additional transport equations for bubble size distribution. Hence, this approach is not adopted for the first engineering characterization of the UniVessel®, but will be used in further studies in the near future. Based on the results obtained so far, it can be concluded that the oxygen transfer capacity of the UniVessel® 2L single-use has no limitations for medium cell densities achieved at gentle agitation and aeration. In addition to the results presented, the fluid flow in the small scale UniVessel® equipped with two segment blade impellers will be investigated in further studies, because Sartorius Stedim decided to provide the UniVessel® single-use with this stirrer configuration mainly due to the broad acceptance by the costumers.

In a third part, two approaches for the evaluation of mechanical stress on cells are presented. The first, which is based on the Kolmogorov turbulence theory, indicates that cell damage could occur above specific power inputs of  $230 \text{ W}\cdot\text{m}^{-3}$ . This value is also given as the upper limit of typical power inputs by Nienow (2006). However, it is shown that the

turbulence distribution inside the bioreactor is very heterogeneous. Hence, volume-weighted distributions of velocity gradients are predicted in the second approach. These velocity gradients are additionally subdivided into local shear and normal gradients, as suggested by Wollny (2010), which may allow a more detailed evaluation of cell damage mechanisms. Compared with turbulence, velocity gradients indicate lower cell stress potential. Although no cell damage is expected under typical operation conditions, it is difficult to draw general conclusions since biological effects depend on various factors, such as the cell line used, cell characteristics, culture media, additives and so on. Nevertheless, the results obtained indicate that Sartorius Stedim's novel UniVessel® 2L single-use is a viable alternative to conventional stirred cell culture bioreactors at bench scale.

## 6. Acknowledgment

The results presented are part of PhD theses. The authors are grateful to Dipl.-Ing. Ute Noack, Dr. Alexander Tappe, Dr. Gerhard Greller, Dr. Bhaskar Bandarapu, Dr. Thorsten Peuker, Dipl.-Ing. Lars Böttcher, Martin Saballus and Alexander Halt from Sartorius Stedim Biotech for providing details about the geometries of the bioreactors investigated and the experimental results of the BIOSTAT® CultiBag STR 50L as well as for their participation in helpful discussions.

## 7. References

- Alcamo, R.; Micale, G.; Grisafi, F.; Brucato, A. & Ciofalo, M. (2005). Large-eddy simulation of turbulent flow in an unbaffled stirred tank driven by a Rushton turbine. *Chemical Engineering Science*, Vol. 60, pp. 2303-2316
- Arathoon, W. & Birch, J. (1986). Large scale cell culture in biotechnology. *Science*, Vol. 232, pp. 1390-1395
- Chalmers, J. J. (1994). Cells and bubbles in sparged bioreactors. *Cytotechnology*, Vol. 15, pp. 311-320
- Chisti, Y. (1993). Animal cell culture in stirred bioreactors: Observations on scale-up. *Bioprocess Engineering*, Vol. 9, pp. 191-196
- Chisti, Y. (2000). Animal-cell damage in sparged bioreactors. *Trends in Biotechnology*, Vol. 18, pp. 420-432
- Chisti, Y. (2001). Hydrodynamic damage to animal cells. *Critical Reviews in Biotechnology*, Vol. 21, pp. 67-110
- Croughan, M. S.; Sayre, E. S. & Wang, D. I. (1989). Viscous reduction of turbulent damage in animal cell culture. *Biotechnology and Bioengineering*, Vol. 33, pp. 862-872
- De Wilde, D.; Noack, U.; Kahlert, W.; Barbaroux, M. & Greller, G. (2009). Bridging the gap from reusable to single-use manufacturing with stirred, single-use bioreactors. *BioProcess International*, Vol. 7, pp. 36-41
- Delafosse, A.; Line, A.; Morchain, J. & Guiraud, P. (2008). LES and URANS simulations of hydrodynamics in mixing tank: comparison to PIV experiments. *Chemical Engineering Research and Design*, Vol. 86, pp. 1322-1330
- Dhanasekharan, K. M.; Sanyal, J.; Jain, A. & Haidari, A. (2005). A generalized approach to model oxygen transfer in bioreactors using population balances and computational fluid dynamics. *Chemical Engineering Science*, Vol. 60, pp. 213-218

- Eibl, R.; Kaiser, S.; Lombriser, R. & Eibl, D. (2010). Disposable bioreactors: the current state-of-the-art and recommended applications in biotechnology. *Applied Microbiology Biotechnology*, Vol. 86, pp. 41-49
- Eibl, R.; Löffelholz, C. & Eibl, D. (2011). Single-use bioreactors - an overview, In: *Single-use Technology in Biopharmaceutical Manufacture*, R. Eibl & D. Eibl, (Eds.), 34-51, John Wiley & Sons, New Jersey, USA
- Fenge, C.; Klein, C.; Heuer, C.; Siegel, U. & Fraune, E. (1993). Agitation, aeration and perfusion modules for cell culture bioreactors. *Cytotechnology*, Vol. 11, pp. 233-244
- Fluent 6.3 user's guide (2006), Centerra Resource Park, 10 Cavendish Court, Lebanon, USA: Fluent Inc., Available from <http://my.fit.edu/itresources/manuals/fluent6.3/help/pdf/ug/flug.pdf>
- Garcia-Briones, M. & Chalmers, J. J. (1994). Flow parameters associated with hydrodynamic cell injury. *Biotechnology and Bioengineering*, Vol. 44, pp. 1089-1098
- Giersiepen, M.; Wurzinger, L.; Optz, R. & Reul, H. (1990). Estimation of shear stress-related blood damage in heart valve prostheses - in vitro comparison of 25 aortic valves. *International Journal of Artificial Organs*, Vol. 13, pp. 300-306
- Gimbun, J.; Rielly, C. & Nagy, Z. (2009). Modelling of mass transfer in gas-liquid stirred tanks agitated by rushton turbine and CD-6 impeller: A scale-up study. *Chemical Engineering Research and Design*, Vol. 87, pp. 437-451
- Handa, A.; Emery, A. & Spier, R. (1987). On the evaluation of gas-liquid interfacial effects on hybridoma viability in bubble column bioreactors. *Developments in Biological Standardization*, Vol. 66, pp. 241-253
- Henzler, H.-J. & Kauling, D. J. (1993). Oxygenation of cell cultures. *Bioprocess and Biosystems Engineering*, Vol. 9, pp. 61-75
- Hinze, J.O. (1959). *Turbulence*. McGraw-Hill, New York.
- Hockey, R. M. & Nouri, J. (1996). Turbulent flow in a baffled vessel stirred by a 60° pitched blade impeller. *Chemical Engineering Science*, Vol. 51, pp. 4405-4421
- Höfken, M.; Schäfer, M. & Durst, F. (1996). Detaillierte Untersuchung des Strömungsfeldes innerhalb eines Sechs-Blatt-Scheibenrührers. *Chemie Ingenieur Technik*, Vol. 68, pp. 803-809
- Ishii, M. & Zuber, N. (1979). Drag coefficient and relative velocity in bubbly, droplet or particulate flows. *AIChE Journal*, Vol. 25, pp. 843-855
- Jahoda, M.; Mostek, M.; Kukuková, A. & Machon, V. (2007). CFD modelling of liquid homogenization in stirred tanks with one and two impellers using large eddy simulation. *Chemical Engineering Research and Design*, Vol. 85, pp. 616-625
- Jaworski, Z.; Nienow, A. W.; Koutsakos, E.; Dyster, K. & Bujalski, W. (1991). An LDA study of turbulent flow in a baffled vessel agitated by a pitched blade turbine. *Chemical Engineering Research and Design*, Vol. 69, pp. 313-320
- Jöbses, I.; Martens, D. & Tramper, J. (1991). Lethal events during gas sparging in animal cell culture. *Biotechnology and Bioengineering*, Vol. 37, pp. 484-490
- Kaiser, S.C. (2009). Theoretische und experimentelle Untersuchungen zur Bestimmung der Mischzeit und des Sauerstoffeintrages in Bioreaktoren. Master Thesis. Hochschule Anhalt (FH), Köthen..
- Kaiser, S. C.; Eibl, R. & Eibl, D. (2011). Engineering characteristics of a single-use stirred bioreactor at bench-scale: The Mobius CellReady 3L bioreactor as a case study, *Engineering Life Sciences*, in submission.

- Kerdouss, F.; Bannari, A.; Proulx, P.; Bannari, R.; Skrga, M. & Labrecque, Y. (2008). Two-phase mass transfer coefficient prediction in stirred vessel with a CFD model. *Computers and Chemical Engineering*, Vol. 32, pp. 1943-1955
- Kioukia, N.; Nienow, A. W.; Al-Rubeai, M. & Emery, A. N. (1996). Influence of agitation and sparging on the growth rate and infection of insect cells in bioreactors and a comparison with hybridoma culture. *Biotechnol. Prog.*, Vol. 12, pp. 779-785
- Krampe, B. & Al-Rubeai, M. (2010). Cell death in mammalian cell culture: molecular mechanisms and cell line engineering strategies. *Cytotechnology*, Vol. 62, pp. 175-188
- Kraume, M. (2003). *Mischen und Rühren. Grundlagen und moderne Verfahren*. Wiley-VCH
- Kresta, S. & Wood, P. (1991). Prediction of the three-dimensional turbulent flow in stirred tanks. *AIChE Journal*, Vol. 37, pp. 448-460
- Langer, G. & Deppe, A. (2000). Zum Verständnis der hydrodynamischen Beanspruchung von Partikeln in turbulenten Rührerströmungen. *Chemie Ingenieur Technik*, Vol. 72, pp. 31-41
- Langheinrich, C.; Nienow, A. W.; Eddleston, T.; Stevenson, N. C.; Emery, A. N.; Clayton, T. M. & Slater, N. K. H. (2002). Oxygen transfer in stirred bioreactors under animal cell culture conditions. *Food and Bioprocess Processing*, Vol. 80, pp. 39-44
- Letellier, B.; Xuereb, C.; Swaels, P.; Hobbes, P. & Bertrand, J. (2002). Scale-up in laminar and transient regimes of a multi-stage stirrer, a CFD approach. *Chemical Engineering Science*, Vol. 57, pp. 4617 - 4632
- Liepe, F.; Sperling, R. & Jembere, S. (1998). *Rührwerke - Theoretische Grundlagen, Auslegung und Bewertung*. Eigenverlag FH Anhalt, Köthen
- Löffelholz, C.; Kaiser, S.; Werner, S. & Eibl, D. (2011). CFD as a tool to characterize single-use bioreactors, In: *Single-use Technology in Biopharmaceutical Manufacture*, R. Eibl & D. Eibl, (Eds.), 34-51, John Wiley & Sons, New Jersey, USA
- Meneses-Acosta, A.; Mendonca, R. Z.; Merchant, H.; Covarrubias, L. & Ramírez, O. T. (2001). Comparative characterization of cell death between Sf9 insect cells and hybridoma cultures. *Biotechnology and Bioengineering*, Vol. 72, pp. 441-457
- Min, J. & Gao, Z. (2006). Large eddy simulation of mixing time in a stirred tank. *Chinese Journal Chemical Engineering*, Vol. 14, pp. 1-7
- Montante, G.; Lee, K.; Brucato, A. & Yianneskis, M. (2001). Numerical simulations of the dependency of flow pattern on impeller clearance in stirred vessels. *Chemical Engineering Science*, Vol. 56, pp. 3751-3770
- Nienow, A. W. (1997). On impeller circulation and mixing effectiveness in the turbulent flow regime. *Chemical Engineering Science*, Vol. 52, pp. 2557-2565
- Nienow, A. W. (2006). Reactor engineering in large scale animal cell culture. *Cytotechnology*, Vol. 50, pp. 9-33
- Noack, U.; De Wilde, D.; Verhoeve, F.; Balbirnie, E.; Kahlert, W.; Adams, T.; Greller, G. & Reif, O. (2011). Single-use stirred tank reactor BIOSTAT CultiBag STR: Characterization and applications, In: *Single-use Technology in Biopharmaceutical Manufacture*, R. Eibl & D. Eibl, (Eds.), 34-51, John Wiley & Sons, New Jersey, USA
- Oh, S.; Nienow, A.; Al-Rubeai, M. & Emery, A. (1992). Further studies of the culture of mouse hybridomas in an agitated bioreactor with and without continuous sparging. *Journal of Biotechnology*, Vol. 22, pp. 245-270
- Ozturk, S. S. (1996). Engineering challenges in high density cell culture systems. *Cytotechnology*, Vol. 22, pp. 3-16



- Paschedag, A. R.; Kassera, V. & Sperling, R. (2007). Aktuelle Entwicklungen in der CFD für gerührte Systeme. *Chemie Ingenieur Technik*, Vol. 79, pp. 983-999
- Patwardhan, A. W. & Joshi, J. B. (1999). Relation between flow pattern and blending in stirred tanks. *Industrial & Engineering Chemistry Research*, Vol. 38, pp. 3131-3143
- Ranade, V. V. & Joshi, J. B. (1989). Flow generated by pitched blade turbines I: measurements using laser Doppler anemometer. *Chemical Engineering Communications*, Vol. 81, pp. 197-224
- Revstedt, J.; Fuchs, L. & Trägårdh, C. (1998). Large eddy simulations of the turbulent flow in a stirred reactor. *Chemical Engineering Science*, Vol. 53, pp. 4041-4053
- Ruffieux, P.-A.; von Stockar, U. & Marison, I. W. (1998). Measurement of volumetric (OUR) and determination of specific (qO<sub>2</sub>) oxygen uptake rates in animal cell cultures. *Journal of Biotechnology*, Vol. 63, pp. 85-95
- Tramper, J.; Vlask, J. & de Gooijer, C. (1996). Scale up aspects of sparged insect-cell bioreactors. *Cytotechnology*, Vol. 20, pp. 221-229
- Storhas, W. (2003). *Bioverfahrensentwicklung*. Wiley-VCH, Weinheim.
- Van't Riet, K. (1979). Review of measuring methods and results in nonviscous gas-liquid mass transfer in stirred vessels. *Industrial & Engineering Chemistry Process Design and Development*, Vol. 18, pp. 1979-357
- Varley, J. & Birch, J. (1999). Reactor design for large scale suspension animal cell culture. *Cytotechnology*, Vol. 29, pp. 177-205
- Venkat, R. V. & Chalmers, J. J. (1996). Characterization of agitation environments in 250 ml spinner vessel, 3 L, and 20 L reactor vessels used for animal cell microcarrier culture. *Cytotechnology*, Vol. 22, pp. 95-102
- Vrabel, P.; van der Lans, R. G. J. M.; Luyben, K. C. A. M.; Boon, L. & Nienow, A. W. (2000). Mixing in large-scale vessels stirred with multiple radial or radial and axial up-pumping impellers: modelling and measurements. *Chemical Engineering Science*, Vol. 55, pp. 5881-5896
- Weyand, B.; Israelowitz, M.; von Schroeder, H. & Vogt, P. (2009). Fluid dynamics in bioreactor design: considerations for the theoretical and practical approach, In: *Bioreactor Systems for Tissue Engineering*, C. Kasper, M. van Griensven & R. Pörtner (Eds.), 251-268
- Wollny, S. (2010). Experimentelle und numerische Untersuchungen zur Partikelbeanspruchung in gerührten (Bio-)Reaktoren. PhD thesis. Technische Universität Berlin, Deutschland
- Xiu, Z.-L.; Deckwer, W.-D. & Zeng, A.-P. (1999). Estimation of rates of oxygen uptake and carbon dioxide evolution of animal cell culture using material and energy balances. *Cytotechnology*, Vol. 29, pp. 159-166
- Yianneskis, M.; Popiolek, Z. & Whitelaw, J. (1987). An experimental study of the steady and unsteady flow characteristics of stirred reactors. *Journal of Fluid Mechanics*, Vol. 175, pp. 537-555
- Yim, S. S. & Shamlou, P. A. (2000). The engineering effects of fluids flow on freely suspended biological macro-materials and macromolecules, In: *Influence of Stress on Cell Growth and Product Formation*, K. Schügerl & G. Kretzmer, (Eds.), 83-122, Springer
- Zhang, Z.; Al-Rubeai, M. & Thomas, C. R. (1993). Estimation of disruption of animal cells by turbulent capillary flow. *Biotechnology and Bioengineering*, Vol. 42, pp. 987-993

- Zhu, H.; Nienow, A. W.; Bujalski, W. & Simmons, M. J. (2009). Mixing studies in a model aerated bioreactor equipped with an up- or a down-pumping 'Elephant Ear' agitator: Power, hold-up and aerated flow field measurements. *Chemical Engineering Research and Design*, Vol. 87, pp. 307-317
- Zlokarnik, M.(1999). *Rührtechnik - Theorie und Praxis*. Springer, Berlin, Heidelberg, New York
- Zlokarnik, M. (2006). *Scale-Up in Chemical Engineering (second, completely revised and extended edition)*. Wiley-VCH, Weinheim

# Application of Computational Fluid Dynamics (CFD) for Simulation of Acid Mine Drainage Generation and Subsequent Pollutants Transportation through Groundwater Flow Systems and Rivers

Faramarz Doulati Ardejani<sup>1</sup>, Ernest Baafi<sup>2</sup>, Kumars Seif Panahi<sup>3</sup>,  
Raghu Nath Singh<sup>4</sup> and Behshad Jodeiri Shokri<sup>5</sup>

<sup>1</sup>*Faculty of Mining, Petroleum and Geophysics,  
Shahrood University of Technology, Shahrood,*

<sup>2</sup>*School of Civil, Mining and Environmental Engineering, University of Wollongong,*

<sup>3</sup>*Shahrood University of Technology*

<sup>4</sup>*Nottingham Centre for Geomechanics, School of Civil Engineering,  
University of Nottingham,*

<sup>5</sup>*Faculty of Mining and Metallurgical Engineering, Amirkabir University of Technology  
(Tehran Polytechnic), Tehran*

<sup>1,3,5</sup>*Iran*

<sup>2</sup>*Australia*

<sup>4</sup>*UK*

## 1. Introduction

Many environmental problems associated with the mining industry involve the understanding and analysis of fluid or gas flow. Typical examples include groundwater flow, transport of contaminants, heat transfer, explosions, fire development and dust movements. Both experimental work and numerical models can provide the necessary information for solution of any particular problem. The long-term pyrite oxidation, acid mine drainage generation and transportation of the oxidation products are noted to be the most important problems that can be modelled in order to predict the transport of the contaminants through groundwater and rivers flow systems, to interpret the geochemistry and achieve a better understanding of the processes involved.

The use of computational fluid dynamics (CFD) to simulate flow problems has risen dramatically in the past three decades and become a fairly well established discipline shared by a number of engineering and science branches. Associated with the widespread availability of high performance and advanced computers and computational methods, CFD is rapidly becoming accepted as a cost-effective design and predictive tool. Numerical solution methods may be used for CFD analysis for the simulation of fluid flow, heat and mass transport problems when it is expressed in terms of partial differential equations

(PDEs). Recent improvement of CFD codes enables researchers to visualise easily the local velocity, temperature, concentrations of solutes and pressure fields in a domain by means of graphic facilities (Edwards et al., 1995).

CFD is a very powerful tool and applicable to a wide range of industrial and non-industrial areas, including aerodynamics of aircraft, automotive, pollution control, power plant, turbo machinery, electrical and electronic engineering, civil engineering, hydrology and oceanography, meteorology and medical science (Versteeg & Malalasekera, 1995).

CFD has been recently used in many applications relating to environmental studies as a way of estimating impacts and developing control strategies for the long-term impacts of mining on the environment and many other activities. The low response time and cost associated with the simulations compared to experiments are the main benefits provided that adequate accuracy may be obtained by the computer erally used in CFD can be classified as finite difference method (FDM), finite element method (FEM), finite volume method (FVM), or spectral methods. The choices of a numerical method and a gridding strategy are strongly interdependent to solving the CFD problems. For example, the use of finite difference method is typically restricted to structured grids (Harvard et al., 1999).

Some researchers used the finite element method to solve the PDEs for modelling of solute transport through groundwater flow systems (Pickens & Lennox, 1976; Pinder, 1973; Rabbani & Warner, 1994; Wunderly et al., 1996). Furthermore, some researchers used the finite volume method to solve the PDEs for modelling of pollutant transport through rivers flow systems (Ani et al., 2009; Kachiashvili et al., 2007; Zhi-Qiang & Hoon-Shin, 2009). Green and Clothier (1994) used the PHOENICS-code (Spalding, 1981) incorporating the finite volume method to simulate water and solutes transport into unsaturated soils. Edwards et al. (1995) have noted the applicability of the CFD analysis in mine safety and health problems such as methane control, gas or coal outbursts, dust suppression and explosions. Balusu (1993) developed a numerical model using a CFD code, FIDAP, to simulate airflow patterns and the respirable dust concentration at a longwall face in underground coal mines. The analysis of contaminant transport in groundwater systems using finite volume techniques have been carried out by Putti et al., (1990) and Binning & Celia (1996). Singh & Doulati Ardejani (2004) developed an one-dimensional numerical finite model using PHOENICS code to simulate long term pyrite oxidation, acid mine drainage generation and transportation of the oxidation products through the backfills of an open cut mine.

This chapter presents the application of computational fluid dynamics (CFD) using PHOENICS code to simulate pyrite oxidation, acid mine drainage generation and subsequent pollutants transportation through groundwater flow systems and Rivers. The simulations have been conducted by developing one- and two-dimensional models.

## 2. Computational fluid dynamics

Computational fluid dynamics (CFD) is defined as the analysis of systems involving fluid flow, heat transfer and mass transport and associated phenomena such as chemical reactions using computer-based simulation. To predict the way in which a fluid will flow for a given situation, a mathematical analysis of the fluid flow has to be made to formulate the governing equations of flow, and the CFD code enables users to calculate numerical solutions to these equations. To produce a solution, these equations have to be transformed into numerical analogues using discretisation techniques such as finite difference method (FDM), finite element method (FEM) and finite volume method (FVM).

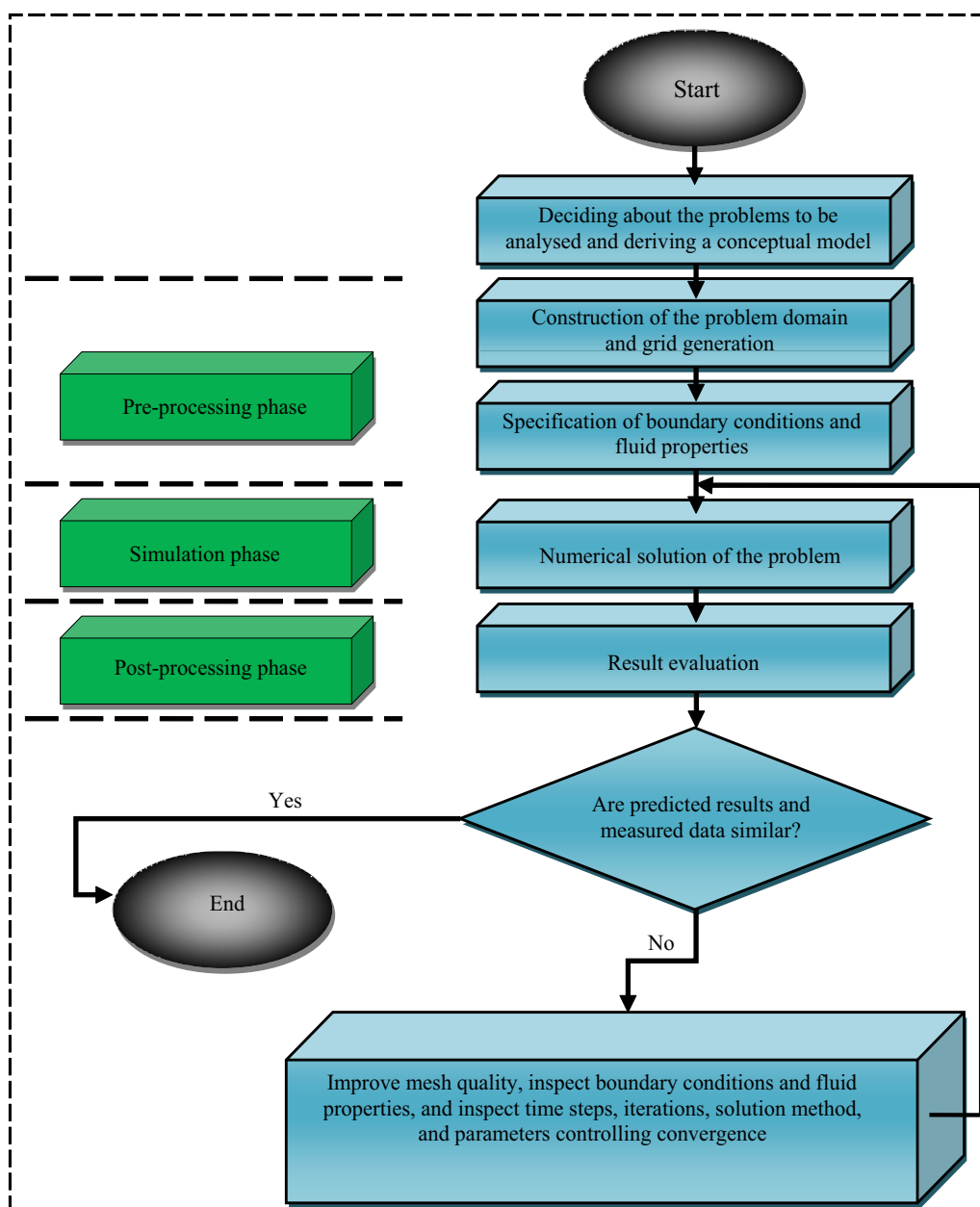


Fig. 1. Main stages in a CFD simulation

CFD codes such as FLUENT, PHOENICS, FLOW3D and FIDAP are now widely available commercially, each with its own particular set of features to deal with fluid flow problems. Edwards et al., (1995) and Doulati Ardejani (2003) has given a comparison of some commercial CFD codes. In general, a flow analysis with CFD codes can be divided into three main phases:

- Pre-processing phase includes the input of a flow problem to a CFD package using an operator-friendly interface and the subsequent transformation of this input data into an appropriate form for use by the solver. This phase mainly consists of the definition of the geometry of the problem of interest, mesh generation, specification of physical properties of the fluid and appropriate boundary conditions. An unknown flow variable such as velocity, pressure and temperature is solved at nodes inside each cell. The accuracy of a CFD solution is governed by the number of cells in the grid. The accuracy is improved by increasing the number of cells. Optimal meshes are often non-uniform. A finer mesh is constructed in areas where large variations occur from point to point and a coarser grid is used in regions with relatively small change (Versteeg & Malalasekera, 1995).
- Simulation phase including solution of the governing equation for the unknown flow variable.

Post-processing phase including domain geometry and grid display, vector plots, surface plots, x-y graphs, line and shaded contour plots and animation for dynamic result display.

### 2.1 General stages of a CFD analysis

To produce a CFD simulation, a number of key steps should be followed in order to generate an exact picture of a particular problem. Figure 1 shows the main steps for a CFD analysis.

### 2.2 PHOENICS as a CFD software

The PHOENICS program has a few different modules to perform all these three phases of flow analysis, namely SATELLITE, EARTH, and post-processing facilities including VR VIEWER, PHOTON, AUTO PLOT and RESULT (Spalding, 1981). Figure 2 shows the solution performance in the PHOENICS package.

## 3. Finite volume method (FVM)

FVM (sometimes called the control volume method) is a numerical technique for solving governing equations of fluid flow and mass transport that calculates the values of the conserved variables averaged across the control volume. The calculation domain is broken down into a finite number of non-overlapping cells or control volumes such that there is one control volume surrounding each grid point. The partial differential equation is integrated over each control volume. The resulting discretisation equation containing the values of a variable  $\phi$  for grid points involves the substitution of a variety of finite-difference-type approximations for the different terms in the integrated equation representing flow and transport processes such as convection, diffusion and source terms. The integral equations are therefore, converted into a system of algebraic equations. The algebraic equations obtained in this manner are then solved iteratively.

It is possible to start the discretisation process with a direct statement of conservation on the control volume. Alternatively we may start with the differential equation and integrate it over the control volume. The numerical solution aims to provide us with values of  $\phi$  at a discrete number of points in the flow domain. These points are called grid points, although we may also see them referred to as nodes or cell centroids, depending on the method (Murthy, 2002).

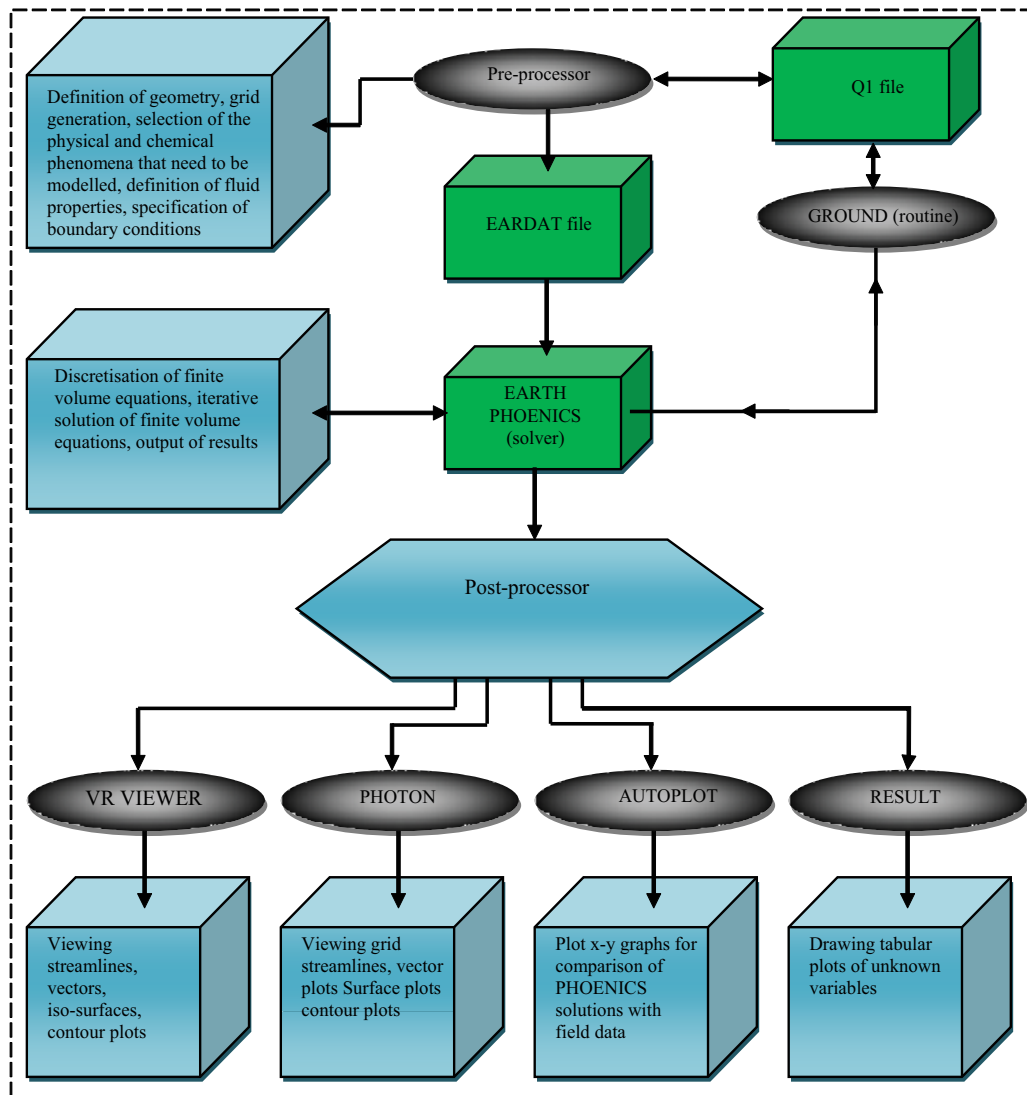


Fig. 2. The procedure of solution in PHOENICS (CHAM, 2008)

FVM has become popular in CFD as a result, primarily, of two advantages. First, they ensure that the discretisation is conservative, i.e., mass, momentum, and energy are conserved in a discrete sense. While this property can usually be obtained using a finite difference formulation, it is obtained naturally from a finite volume formulation. Second, FVM does not require a coordinate transformation in order to be applied on irregular meshes. As a result, they can be applied on unstructured meshes consisting of arbitrary polyhedral in three dimensions or arbitrary polygons in two dimensions. This increased flexibility can be used to great advantage in generating grids about arbitrary geometries (Harvard et al., 1999).

Although the finite element method is mainly used for the simulation of the contaminant transport problems through groundwater flow systems (see Barovic & Boochs, 1981; Bignoli

and Sabbioni, 1981; Fried, 1981; Kerdijk, 1981; Nawalany, 1981; Putti et al., 1990), finite volume techniques have also been used by many researchers for the solution of groundwater flow and solute transport governing equations in saturated and unsaturated flow systems (see Binning and Celia, 1996; Green and Clothier, 1994; Putti et al., 1990; Svensson, 1997).

The basic principles and concepts of the finite volume formulation are very simple and easier to understand by engineers than other numerical techniques. One advantage of the FVM over finite difference methods is that a structured grid is not required although a structured mesh can also be utilised. Furthermore, the FVM is noted to be superior to other numerical methods due to the fact that boundary conditions can be applied non-invasively because the values of the conserved variables are located within the control volumes, and not at nodes or surfaces. FVM is particularly useful in dealing with coarse non-uniform grids. The conservation of any flow variable  $\phi$  within a control volume is expressed as a balance equation between the various processes causing an increased or decreased value of  $\phi$  (Versteeg & Malalasekera, 1995).

$$\left( \begin{array}{l} \text{Net flux of } \phi \text{ due to} \\ \text{convection and diffusion} \\ \text{into the control volume} \end{array} \right) \pm \left( \begin{array}{l} \text{Rate of production or} \\ \text{consumption of } \phi \\ \text{inside the control volume} \end{array} \right) = \left( \begin{array}{l} \text{Rate of change of } \phi \\ \text{in the control volume} \\ \text{with respect to time} \end{array} \right) \quad (1)$$

The quantities being balanced are the dependent variables such as the mass of chemical species, energy, momentum and turbulence quantities.

CFD packages such as PHOENICS, FLUENT, FLOW3D and STAR-CD contain discretisation techniques appropriate for dealing with the main transport processes such as convection (i.e. transport due to fluid flow), diffusion (i.e. random motion of molecules) as well as for the source terms (i.e. chemical reaction for energy or chemical species) and the rate of change of  $\phi$  with time (i.e. accumulation within a cell).

### 3.1 The finite volume discretisation

Fundamental to the development of a numerical method (such as FDM, FEM and FVM) is the idea of discretisation. When the number of grid points is small, the departure of the discrete solution from the exact solution is expected to be large. A well-behaved numerical scheme will tend to the exact solution as the number of grid points is increased. The rate at which it tends to the exact solution depends on the type of profile assumptions made in obtaining the discretisation. No matter what discretisation method is employed, all well-behaved discretisation methods should tend to the exact solution when a large enough number of grid points is employed (Murthy, 2002).

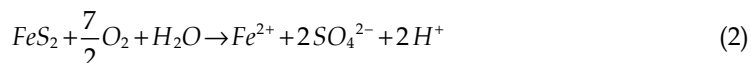
## 4. Model verification

Two problems are described to show the applications of CFD analysis in the modelling of the environmental problems. The first problem considers oxygen transport, pyrite oxidation, acid mine drainage generation and long-term leaching of the oxidation products from the backfills of an open cut mine. The second problem deals with the modelling of metal pollutants transportation associated with acid mine drainage in Shour River at Sarcheshmeh copper mine, Iran. A multi-purpose computational fluid dynamics (CFD) package called PHOENICS has been modified to model these problems.

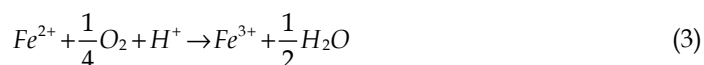


#### 4.1 Problem 1- oxygen transport, pyrite oxidation, acid mine drainage generation and long-term leaching of the oxidation products from the backfills of an open cut mine

Acid mine drainage in the backfills of an open cut mine is initially generated by the direct oxidation of pyrite by oxygen and water producing  $Fe^{2+}$ ,  $SO_4^{2-}$  and  $H^+$  (Singer & Stumm, 1970). The stoichiometric oxidation reaction is as follows:



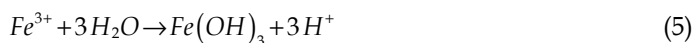
The ferrous iron formed by Reaction 2 oxidises to produce ferric iron according to Reaction 3 (Rogowski et al., 1977):



According to Singer & Stumm (1970), Reaction 3 is slow under low pH conditions. It is catalysed by the bacteria *Thiobacillus ferrooxidans* under suitable environmental conditions (Singer & Stumm, 1970). The environmental conditions must be favourable, for example bacterial action is most important in solutions having a pH between 2.0 and 3.5 (Malouf & Prater, 1961). If conditions are not favourable, the bacterial influence on pyrite oxidation and acid generation will be minimal; for example, the bacteria become inactive at temperatures above 50 °C (Cathles, 1979; Malouf & Prater, 1961). It has also been reported that the rate of ferrous iron oxidation may be accelerated in the presence of bacteria when oxygen is readily available (Jaynes et al., 1984a). The ferric iron produced by Reaction 3 can choose two path ways: It may react with pyrite and produce more ferrous iron, sulphate and hydrogen concentrations (Singer & Stumm, 1970). The stoichiometry of this process reduces to:



Alternatively  $Fe^{3+}$  may be precipitated as amorphous ferric hydroxide (Jaynes et al., 1984a; Walter et al., 1994a, 1994b) according to Reaction 5 as given below:



A number of numerical models of pyrite oxidation have been reported in the literature. They are mainly associated with mine tailings (Bridwell & Travis, 1995; Elberling et al., 1994; Walter et al., 1994a, 1994b; Wunderly et al., 1996), waste rock dumps (Cathles, 1979; Cathles and Apps, 1975; Davis 1983; Davis et al., 1986b; Lefebvre & Gelinias, 1995), open cut mines (Jaynes et al. 1984a, 1984b, Singh & Doulati Ardejani, 2004) and coal refuse piles (Doulati Ardejani et al., 2008b, 2010).

In this section a numerical finite volume model is presented for prediction of the long-term pyrite oxidation and subsequent pollutant transportation from backfilled open cut mines. This work is a further development of the model proposed by Jaynes et al., (1984a, 1984b) and is presented in both one- and two-dimensional forms with different numerical techniques. The results of a two-dimensional simulation are necessary for better understanding the mechanisms involved in pyrite oxidation and pollutant leaching related to open cut mines. The results of a two-dimensional simulation show how contaminants spread into groundwater systems and how the physical and chemical processes influence the transport of the pyrite oxidation products. Such results can be used for designing

effective site remediation programs in order to minimise environmental effects arising from abandoned backfilled open cut coalmines.

The model incorporates oxygen transport, pyrite oxidation, enthalpy balance, groundwater flow and transport of the oxidation products. The model has been implemented in the general-purpose PHOENICS computational fluid dynamic package. By creating a Q1-file (PHOENICS input file) in PHOENICS input language, the necessary settings such as domain geometry, finite volume grid, boundary and initial conditions and fluid properties were specified and for all non-standard equations and specific source terms, the required coding in FORTRAN 99 language was supplied by developing a subroutine called GROUND. This subroutine was used by the PHOENICS solver module during the course of the solution. The conceptual model proposed in developing the model is given in Doulati Ardejani et al., (2002). Figure 3 shows a schematic diagram showing pollutant leaching in backfills of an open cut mine.

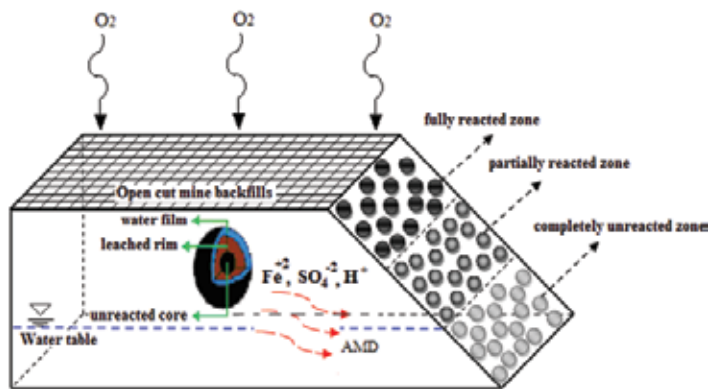


Fig. 3. A conceptual model of pyrite oxidation in the backfills of an idealized open cut mine

Figure 4 shows the physical and chemical processes affecting the fate and transport of pyrite oxidation products through the backfills of an idealized open cut mine.

#### 4.1.1 Modelling governing equations

##### Groundwater flow

The governing equation for two-dimensional steady state groundwater flow is based on the well recognised Laplace equation. This equation is obtained by coupling the continuity equation and Darcy's law. It is expressed as follows (Freeze & Cherry, 1979):

$$\frac{\partial}{\partial x} \left( K_x \frac{\partial h}{\partial x} \right) + \frac{\partial}{\partial y} \left( K_y \frac{\partial h}{\partial y} \right) + W = 0 \quad (6)$$

where,

$x$  and  $y$  = Cartesian coordinates;

$K_x$  and  $K_y$  = hydraulic conductivities in  $x$  and  $y$  directions;

$h$  = hydraulic head;

$W$  = recharge or discharge rate per unit volume.

The components of the groundwater velocity are obtained by solving Equation 6 and are then used in the mass transport equation for each product of pyrite oxidation.

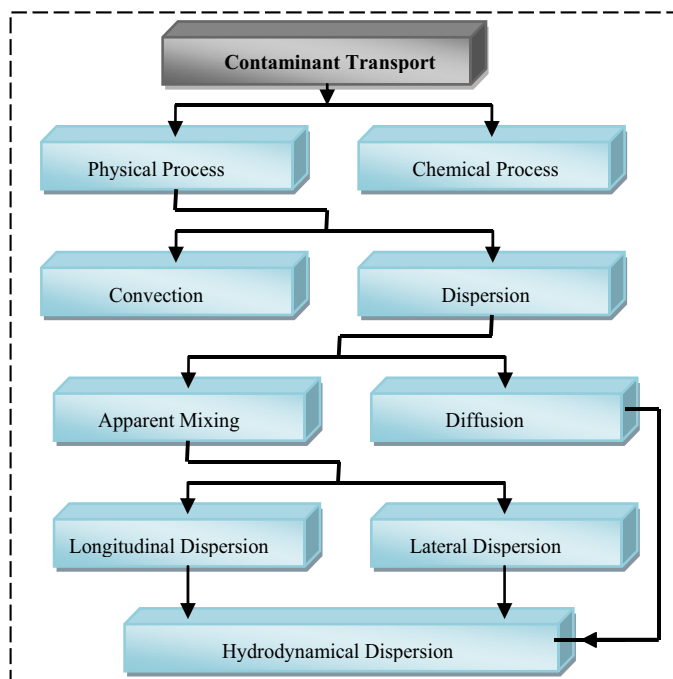


Fig. 4. Chemical and physical processes affecting the fate and transport of a pollutant

### Pyrite oxidation mechanism

Pyrite oxidation can be expressed by a shrinking core model (Jaynes et al., 1984a, 1984b; Levenspiel, 1972). This model can be modified to take into consideration spherical pyritic grains and incorporating both surface reaction kinetics and oxidant diffusion into the particles containing pyrite (Cathles & Apps, 1975):

$$\frac{\partial X}{\partial t} = \frac{-3X^{2/3}}{6\tau_{D[O_2]}X^{1/3}(1-X^{1/3}) + \tau_{C[O_2]}} + \frac{-3X^{2/3}}{6\tau_{D[Fe^{3+}]}X^{1/3}(1-X^{1/3}) + \tau_{C[Fe^{3+}]}} \quad (7)$$

where,

$X$  = fraction of pyrite remaining within the particle (Kg/Kg);

$t$  = time (s);

$\tau_c$  = total time required for complete oxidation of pyrite within a particle if the oxidation process is only controlled by the decreasing surface area of pyrite (s);

$\tau_D$  = total time required for full oxidation of pyrite within a particle assuming the oxidation rate is solely controlled by oxidant diffusion into the particles (s);

$[O_2]$  and  $[Fe^{3+}]$  = oxygen and ferric iron concentrations.

In Equation 7, both oxygen and ferric iron participate in the pyrite oxidation process.  $\tau_D$  and  $\tau_c$  are expressed by Equations 8 and 9 (Levenspiel, 1972):

$$\tau_D = \frac{\rho_{Py} R^2}{6bD_{[Ox]}C_{[Ox]}} \quad (8)$$

$$\tau_c = \frac{\rho_{Py} R}{b K_{[Ox]} \alpha_{Py}^{rock} \lambda C_{[Ox]}} \quad (9)$$

where,

$\rho_{Py}$  = density of pyrite in the particle ( $mol / m^3$ );

$R$  = particle radius (m);

$b$  = stoichiometric ratio of pyrite to oxidant consumption (mol/mol);

$D_{e[Ox]}$  = effective diffusion coefficient of oxidant in oxidised rim of the particle ( $m^2 / s$ );

$K_{[Ox]}$  = first-order surface reaction rate constant (m/s);

$\alpha_{Py}^{rock}$  = surface area of pyrite per unit volume of particle ( $m^{-1}$ );

$\lambda$  = thickness of the particle in which pyrite oxidation occurs (reaction skin depth) (m);

$C_{[Ox]}$  = concentration of oxidant in the water surrounding the particle ( $mol / m^3$ ).

### Enthalpy model

A simple enthalpy balance is employed to model the heat transfer using Equation 10 (adopted from Cathles & Apps, 1975):

$$\rho_b C_p \frac{\partial T}{\partial t} = K_T \left( \frac{\partial^2 T}{\partial x_j^2} \right) - \rho_w C_w u_{xjw} \frac{\partial T}{\partial x_j} + \frac{3(1-\phi) B^{-1} \rho_s X^{\frac{2}{3}}}{6 \tau_{Do_2} X^{\frac{1}{3}} \left( 1 - X^{\frac{1}{3}} \right) + \tau_{CO_2}} + \frac{3(1-\phi) B'^{-1} \rho_s X^{\frac{2}{3}}}{6 \tau_{D_{Fe^{3+}}} X^{\frac{1}{3}} \left( 1 - X^{\frac{1}{3}} \right) + \tau_{C_{Fe^{3+}}}} \quad (10)$$

where,

$T$  = temperature ( $^{\circ}C$ );

$\rho_b$  = bulk density of the spoil ( $Kg / m^3$ );

$\rho_s$  = molar density of pyrite in spoil ( $mol / m^3$ );

$\phi$  = porosity of spoil;

$K_T$  = thermal conductivity ( $J / m^{\circ}C s$ );

$C_p$  = specific heat capacity of the spoil ( $J / Kg^{\circ}C$ );

$\rho_w$  = density of water in the spoil ( $Kg / m^3$ );

$u_{xjw}$  = water velocity ( $m / s$ );

$C_w$  = heat capacity of water ( $J / Kg^{\circ}C$ );

$B$  = moles of pyrite consumed in pyrite-oxygen reaction per heat generated ( $mol / J$ );

$B'$  = moles of pyrite consumed in pyrite- $Fe^{3+}$  reaction per heat generated ( $mol / J$ ).

### Oxygen balance

Oxygen has an important role in pyrite oxidation within the spoils of an open cut mine. Oxygen is transported within the spoils by the process of diffusion. It is consumed by the pyrite oxidation reaction, chemical oxidation of ferrous iron and Thiobacillus ferrooxidans bacteria (Jaynes et al., 1984a). The governing equation of oxygen transport incorporating the volumetric consumption terms reduces to:

$$\phi_a \frac{\partial u}{\partial t} = D_e \left( \frac{\partial^2 u}{\partial x_j^2} \right) - S_{K_{Py-O_2}} - S_{K_{Fe^{2+}-O_2}} - S_{K_{B-O_2}} \quad (11)$$

where,

- $\phi_a$  = air-filled porosity of the spoil ( $m^3 / m^3$ );
- $u$  = gaseous concentration of oxygen in the spoil pore spaces ( $mol / m^3$ );
- $D_e$  = effective diffusion coefficient ( $m^2 / s$ );
- $S_{KPy-O2}$ ,  $S_{KFe^{2+}-O2}$ ,  $S_{KB-O2}$  = volumetric oxygen consumption terms ( $mol / m^3 s$ ) by the pyrite oxidation reaction, chemical oxidation of ferrous iron and oxygen consumption by bacteria. The oxygen consumption terms can be found in Jaynes et al. (1984a).

### Transport equation

This model assumes that the oxidation products are transported through the groundwater flow system after leaching from the spoils. The governing transport equation can be expressed as follows (Freeze & Cherry, 1979; Rubin & James, 1973):

$$\phi \frac{\partial C_i}{\partial t} + \rho_b \frac{\partial \bar{C}_i}{\partial t} = D \frac{\partial^2 C_i}{\partial x_j^2} - q_j \frac{\partial C_i}{\partial x_j} + q_{re} C_i \pm S \quad i = 1, 2, \dots, n_c \quad (12)$$

where,

- $C_i$  = solute concentration in aqueous phase ( $mol / m^3$ );
- $\bar{C}_i$  = solute concentration in adsorbed form ( $mol / Kg$ );
- $\rho_b$  = bulk density of the flow medium ( $Kg / m^3$ );
- $q_{re}$  = surface recharge ( $m / s$ );
- $S$  = sink and source terms representing the changes in aqueous component concentrations due to the chemical reactions ( $mol / m^3 s$ );
- $q_j$  = vector components of the pore fluid specific discharge ( $m / s$ );
- $D$  = hydrodynamic dispersion coefficient ( $m^2 / s$ );
- $n_c$  = number of dissolved species.

### The $H^+$ - spoil interaction

The interaction between  $H^+$  produced by oxidation reactions and spoil was incorporated by a simple empirical relationship (Jaynes et al., 1984a):

$$\frac{H^+}{H_{Gen}^+} = \{ 1.0 - EXP(G_A - pH) \} \quad (13)$$

where,

- $H^+$  = Hydrogen ion in solution ( $mol / m^3$ );
- $H_{Gen}^+$  =  $H^+$  generated through chemical reactions ( $mol / m^3$ );
- $G_A$  = an empirical constant that defines the buffer system.

Equation 13 was slightly modified to calculate the  $H^+$  consumption per cubic metre of spoil per unit time as given below:

$$\frac{\partial H^+}{\partial t} = - \frac{H_{Gen}^+}{\Delta t} \exp(G_A - pH) \quad (14)$$

where,

- $\Delta t$  = simulation time step (s).

Equation 14 was incorporated as a sink term in the governing transport equation for the hydrogen ion. In this particular case the solution pH was maintained above 2.5.

#### 4.1.2 Model parameters

The model input data were taken from Cathles & Apps (1975), Lide, (1998) and Jaynes et al., (1984b). A one-dimensional simulation was conducted to verify modelling accuracy. A two-dimensional simulation was then carried out when the reasonable output results were obtained in comparison with those results obtained from the POLS finite difference model developed by Jaynes et al., (1984a, 1984b). The model input parameters are given in Table 1.

| Model parameter   | Value   | Unit                              | Reference            |
|---|---|-----------------------------------|----------------------|
| Pyrite fraction   | 0.0025  | Kg pyrite/ Kg spoil               | Jaynes et al., 1984b |
| Fraction of coarse particles containing pyrite                            | 75  | %                                 |                      |
| The bulk density of spoil   | 1650  | $Kg / m^3$                        |                      |
| The porosity of the spoil   | 0.321   | -                                 |                      |
| Water-filled porosity   | 0.225   | -                                 |                      |
| Surface area of pyrite per unit volume of spoil                           | 80  | $cm^{-1}$                         | Cathles & Apps, 1975 |
| Radius of particles   | 2   | $cm$                              | Jaynes et al., 1984b |
| Diffusion coefficient of oxidant in water                                 | $1.0 \times 10^{-11}$                                     | $m^2 / s$                         |                      |
| Molar density of pyrite within particle                                   | 23  | $mol / m^3$                       |                      |
| First-order rate constant for $Fe^{3+}$                                   | $4.4 \times 10^{-8}$                                      | $m / s$                           |                      |
| First-order rate constant for oxygen                                      | $8.3 \times 10^{-10}$                                     | $m / s$                           |                      |
| Recharge value  | 0.5   | $m / yr$                          |                      |
| constants for chemical oxidation of $Fe^{2+}$                             | $K_1 = 1.3 \times 10^{-10}$<br>$K_2 = 1.7 \times 10^{-9}$ | $mol^2 / (m^3)^2 (s)$<br>$s^{-1}$ |                      |
| Effective diffusion coefficient for oxygen transport                      | $1.0 \times 10^{-7}$                                      | $m^2 / s$                         |                      |
| Enthalpy of Reaction (1)  | $-1.45 \times 10^6$                                       | $J / mol$                         | Lide, (1998)         |
| Enthalpy of Reaction (3)  | $-1.78 \times 10^4$                                       | $J / mol$                         | Lide, (1998)         |
| Moles of pyrite consumed per heat generated in $FeS_2 - O_2$ reaction     | $6.9 \times 10^{-7}$                                      | $mol / J$                         |                      |
| Moles of pyrite consumed per heat generated in $FeS_2 - Fe^{3+}$ reaction | $5.6 \times 10^{-5}$                                      | $mol / J$                         |                      |
| Thermal conductivity  | 2.1   | $J / m^\circ CS$                  |                      |
| Specific heat capacity  | 2500  | $J / Kg^\circ C$                  |                      |

Table 1. Parameters used for simulation (Cathles & Apps, 1975; Jaynes et al., 1984b; Lide, 1998)

### 4.1.3 Model calibration

A one-dimensional simulation was carried out to calibrate the model and verify its capability for simulation of pyrite oxidation and leaching process associated with open cut coal mines. To perform the simulation, a 10-metre spoil column was simulated as 20 equal size control volumes. The influx and background concentrations of dissolved species and pH are listed in Table 2.

| Aqueous components | Concentration ( $mol / m^3$ ) |                 |
|--------------------|-------------------------------|-----------------|
|                    | Influx data                   | Background data |
| $Fe^{2+}$          | 0                             | 0.5             |
| $Fe^{3+}$          | 0                             | 0               |
| $SO_4^{2-}$        | 50                            | 50              |
| $pH$               | 5                             | 5               |

Table 2. Influx and background chemistry (Jaynes et al., 1984b)

### 4.1.4 Boundary conditions

A first type boundary condition was assigned at the top of the spoil profile for the oxygen transport model equal to its atmospheric concentration ( $8.9 mol / m^3$ ). The spoil column initially contained no oxygen concentration. A zero-gradient boundary condition was considered at the profile base.

The spoil temperature was initially set at  $15^\circ C$  for the enthalpy model. The top surface of the spoil profile was specified as a first type boundary condition equal to  $15^\circ C$ .

A constant recharge of  $2 \times 10^{-8} m / s$  was maintained at the profile top surface. A dispersivity of  $0.005 m$  was applied for the transport model in order to achieve consistency with the POLS model. The main reason of selecting a small value of dispersivity is that the mechanism of the leaching process used in the POLS model is different from the present finite volume model. The POLS model did not consider the processes of diffusion and hydrodynamic dispersion effects.

The following boundary and initial conditions were specified for the transport of the pyrite oxidation products:

- The top boundary of the model was assigned as first type with respect to concentration of solutes
- The background solute concentrations were simulated by specifying an initial boundary condition
- A zero concentration gradient boundary condition was specified at outflow boundary.

### 4.1.5 One-dimensional simulation results

For one-dimensional simulation, the effective diffusion coefficient for oxygen transport was selected to be  $1.0 \times 10^{-7} m^2 / s$  and air-filled porosity of 0.1 was set for the simulation. The temperature rise due to the pyrite oxidation reactions was ignored and a constant temperature equal to  $15^\circ C$  was considered for modelling purposes. The iron-oxidising

bacteria were allowed to be active in the spoil profile where the conditions were favourable. The mathematical expressions describing the role of bacteria were taken from Jaynes et al., (1984a) and relevant FORTRAN codes were supplied in the GROUND subroutine accessible by the user of the PHOENICS package.

Figure 5 shows the total iron-discharging rate as a function of time predicted in the water leaving the spoil profile for two different cases. In Case 2 the iron-oxidising bacteria are active and the interaction between the spoil and  $H^+$  is incorporated. In Case 1 no bacteria are allowed to be present but in this case the effective diffusion coefficient for oxygen transport is four times greater than that in Case 2. A comparison was made with those results predicted by the POLS model (dots). The iron-leaching rate showed a similar pattern with time for both cases and the maximum rate occurred between 1750 to 2100 days. As Figure 5 shows, the leaching rate in Case 1 is greater than in case 2 due to bigger in the effective diffusion coefficient.

The  $H^+$  - spoil interaction increased the pH of the solution. It caused an increase in the bacterial activity therefore more ferric iron was produced. Consequently, the pyrite oxidation rate increased considerably over time (Figure 6).

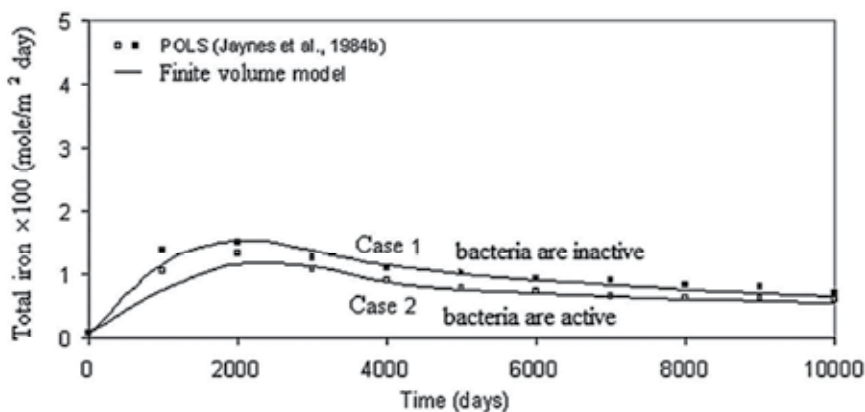


Fig. 5. Total iron leaching rate versus time in the water leaving the spoil profile for Cases 1 and 2

As Figure 6 shows, about 36 % of the pyrite was oxidised after 10000 days of the simulation. For this time, the POLS model predicted that 39 % of pyrite was consumed. The difference between the finite volume modelling predictions and those predicted by the POLS model can be explained in that unlike the POLS model, the ferric complexation reaction was not incorporated in the finite volume model. The complexation reaction increases the ferric concentration. Consequently the rate of pyrite oxidation increases.

The mole fraction of oxygen within the spoil profile versus depth was illustrated in Figure 7. Oxygen decreased linearly with depth. As Figure 7 shows, oxygen diffusion was limited in the surface elements of the spoil profile up to about 3 metres from the spoil surface. Bacterial activity ( $S_{K_{B-O_2}}$  in Equation 11) was the main reason for this sharp reduction of oxygen concentration within the surface layers of the spoil profile, consuming most of the oxygen over this part of the profile (Case 2). In Case 1, oxygen diffused over entire profile because no bacteria were active to consume the oxygen.



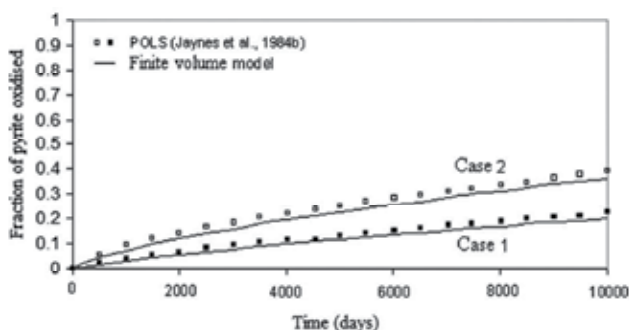


Fig. 6. Comparison of the POLS results (dots) with the PHOENICS results (solid lines) for the pyrite oxidised vs. time over entire spoil column with and without  $H^+$ -spoil interaction

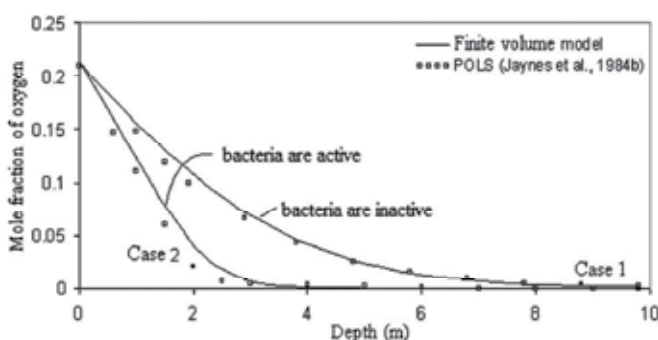


Fig. 7. Comparison of the POLS modelling results (dots) with the finite volume simulated results (solid lines) for oxygen mole fraction as a function of depth for 5-year period

#### 4.1.6 Two-dimensional simulation

Two-dimensional simulations were also performed to demonstrate the capability of the finite volume model for prediction of the long-term pyrite oxidation and transportation of the oxidation products from backfilled open cut coal mines. Except for few, all other model parameters are almost similar to those input data used for one-dimensional simulation (Table 1). Chemical species considered in the two-dimensional simulations are the same as those in the one-dimensional model. Slight modifications were made to their influx and background concentrations (Table 3).

| Aqueous components | Concentration ( $mol / m^3$ ) |            |
|--------------------|-------------------------------|------------|
|                    | Source                        | Background |
| $Fe^{2+}$          | 0.6                           | 0.6        |
| $Fe^{3+}$          | $2.1 \times 10^{-5}$          | 0          |
| $SO_4^{2-}$        | 55                            | 55         |
| $pH$               | 4                             | 5          |

Table 3. Source and background concentrations of aqueous components used for two-dimensional simulations

The two-dimensional cross-sectional dimensions are 50 m horizontally by 20 m vertically and this domain is discretised into  $40 \times 20$  control volumes of size 1.25 m horizontally  $\times$  1 m vertically. The groundwater flow system was assumed to be steady. The difference head between the left and the right boundaries was maintained at 0.1 m. An average recharge value of 0.5 m/yr was considered for the upper boundary (spoil surface). For the simulation it was assumed that reactive pyrite was contained only in a 12.5-m-wide segment of the unsaturated zone of the spoil (Figure 8).

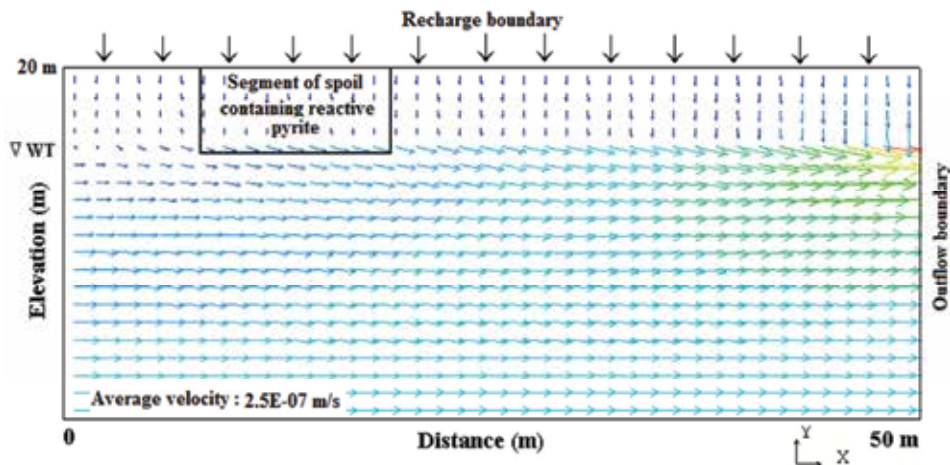


Fig. 8. Two-dimensional simulation cross-section showing velocity vectors and the segment of the spoil where oxidation reactions take place

The upper 4 m of the grid was assumed to be unsaturated and the remainder fully saturated with a constant porosity of 0.321. For simplicity the horizontal component of the velocity was ignored in the unsaturated zone and flow was only assumed to be vertical in this zone. Horizontal and vertical hydraulic conductivities of  $1.40 \times 10^{-5}$  m/s and  $1.40 \times 10^{-6}$  m/s were used for the simulation. Horizontal and vertical dispersion coefficients of  $7.0 \times 10^{-9}$  m<sup>2</sup>/s and  $5.0 \times 10^{-9}$  m<sup>2</sup>/s were specified for the model. The steady state flow system in terms of velocity vectors is shown in Figure 8.

The spoil temperature was assumed constant at 20 °C and the temperature rise in pore water due to the oxidation reactions was predicted using the enthalpy balance. An effective diffusion coefficient of  $9 \times 10^{-8}$  m<sup>2</sup>/s was assigned for the oxygen transport model. The bacterial action and the interaction between  $H^+$  and the spoil were also considered for two-dimensional simulation. The spoil surface was maintained as a first-type boundary condition for oxygen equal to its atmospheric concentration ( $8.9 \text{ mol} / \text{m}^3 \approx 0.21 \text{ mol} / \text{mol}$ ). First - type boundary conditions were specified above the water table for the oxygen transport model. The spoil solution initially contained no oxygen. To avoid non-linearity problems, no ferric complexation reactions were allowed to take place. An oxidation period of 10000 days ( $\approx 27$  years) was considered for the simulation. 100 time steps were considered for the simulation.

The pH of the system was not allowed to drop below 3.0. The interaction between  $H^+$  and the spoil and also maintaining the pH closer to the optimum pH required for the maximum

activity of the iron-oxidising bacteria ( $\approx 3.0$ ), caused more ferric iron to be produced by the bacterially mediated oxidation of ferrous iron. Consequently more pyrite was oxidised. Figure 9 shows the oxygen concentrations for simulation times of 5 and 10 years. In the segment where chemical reactions take place, more oxygen was consumed due to bacterial activity. As time progresses, more oxygen is being diffused to the reaction site.

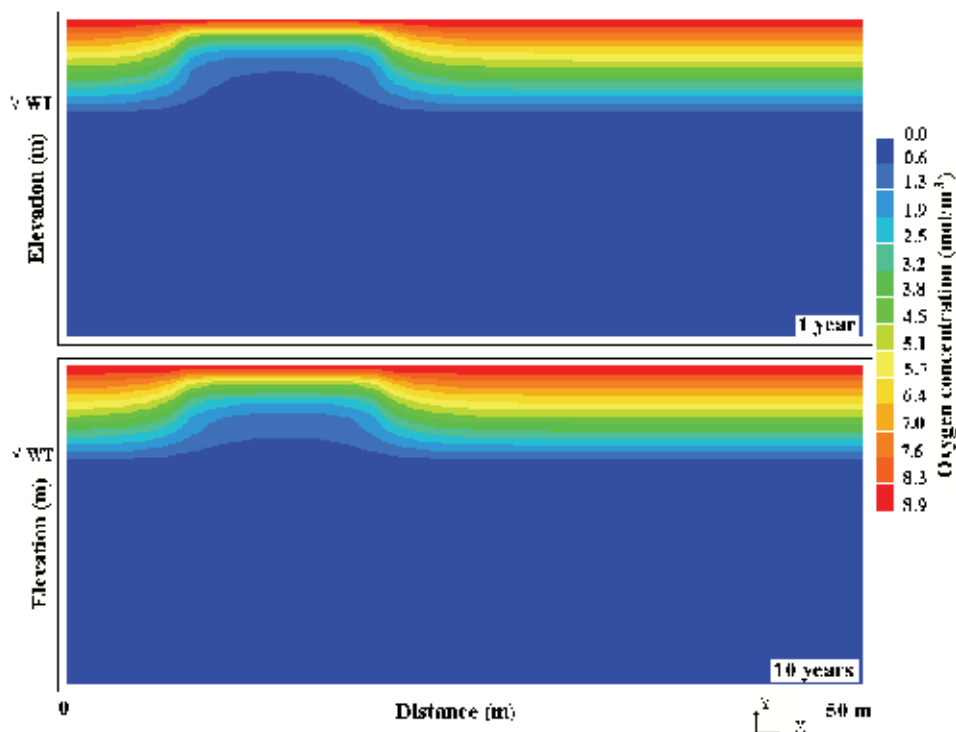


Fig. 9. Oxygen concentration after: (a) 5 years; (b) 10 years of simulation

The ferrous iron concentrations for simulation times of 5, 10, 12 and 15 years are illustrated in Figure 10. After 5 years of the simulation (Figure 10a), pH reached about 3.3, a favourable pH required for bacterial activity. The bacteria catalysed the ferrous iron oxidation reaction and more  $Fe^{2+}$  converted to  $Fe^{3+}$ . Therefore, the ferrous iron concentration decreased in the unsaturated zone whereas the ferric iron concentrations increased considerably in this zone. At 10 years (Figure 10b),  $Fe^{2+}$  is almost removed from the unsaturated zone due to ferrous-ferric oxidation reaction and a downward recharge water flow. Therefore, An  $Fe^{2+}$  peak (greater than  $1.05 \text{ mol/m}^3$ ) reached to the saturated zone. In the saturated zone,  $Fe^{2+}$  spreads by groundwater flow. By 12 years (Figure 10c), the  $Fe^{2+}$  peak moved further down into the saturated zone.

After 15 years of the simulation (Figure 10d), pH is still in the range that is favourable for bacterial activity; therefore, ferric concentration is dominant in the unsaturated zone and  $Fe^{2+}$  peak moved further down into the saturated zone.

Figure 11 shows the solution pH for simulation times of 5, 10, 12 and 10 years. As pyrite oxidation takes place the pH dropped significantly (average pH is 3.3 in the unsaturated

zone) but it never drops below about 3.2 due to taking into account the reaction between the spoil and  $H^+$ . By 15 years the average pH is about 3.5 in the unsaturated zone due to the transport of hydrogen ions downward by the water flow.

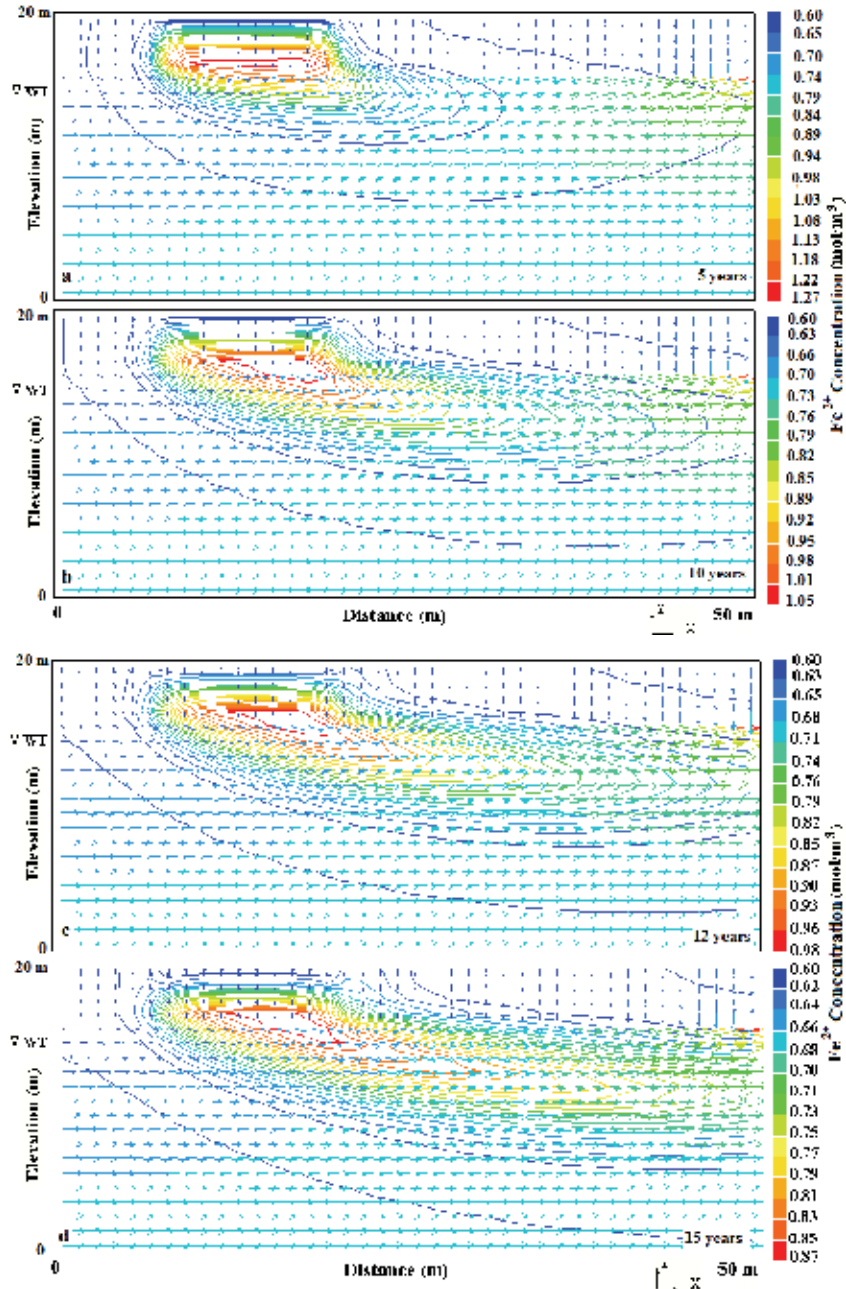


Fig. 10.  $Fe^{2+}$  concentration after: (a) 5 years; (b) 10 years; (c) 12 years; (d) 15 years of simulation

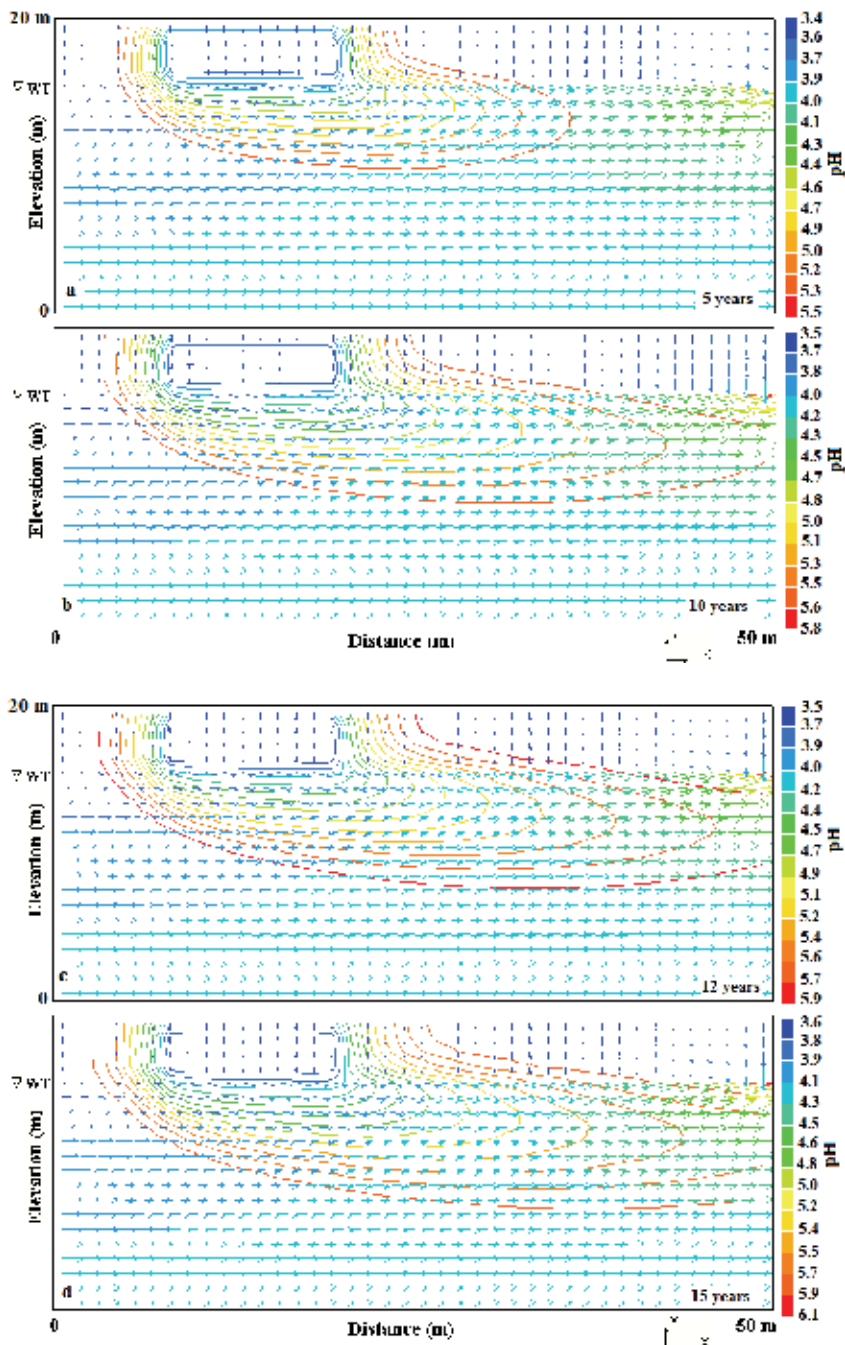


Fig. 11. pH after: (a) 5 years; (b) 10 years; (c) 12 years; (d) 15 years of simulation

Figure 12 shows the ferric iron concentrations after 5, 10, 12 and 15 years of simulation. The concentrations of  $Fe^{3+}$  are high in the unsaturated zone where oxygen is available and the conditions for maximum bacterial activity are favourable. The ferric concentrations are

limited to the unsaturated zone, but as time progresses, some is being transported below the water table. In the case where pyrite is present below the water table,  $Fe^{3+}$  is converted back into  $Fe^{2+}$  through the  $Fe^{3+}$  - pyrite reaction.

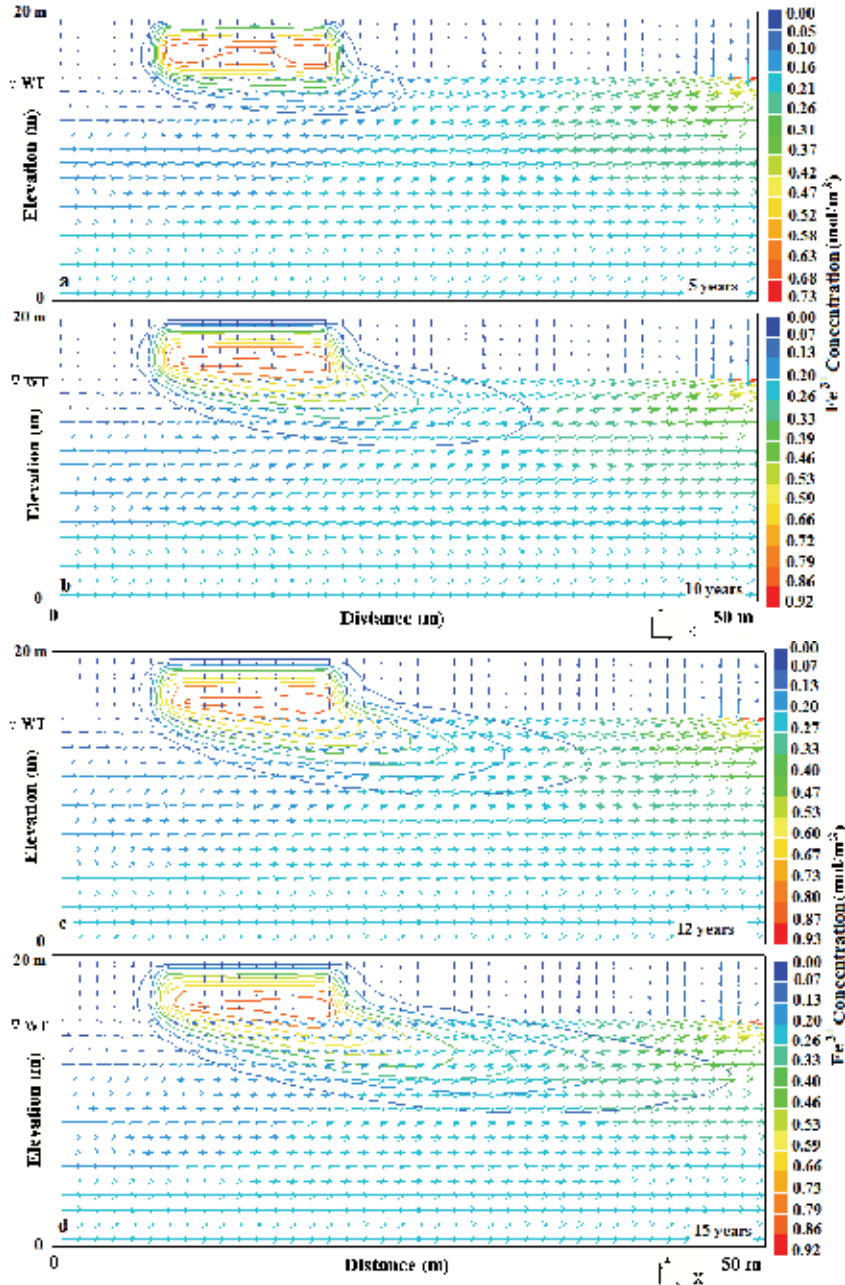


Fig. 12.  $Fe^{3+}$  concentration after: (a) 5 years; (b) 10 years; (c) 12 years; (d) 15 years of simulation



Figure 13 shows  $SO_4^{2-}$  concentrations for time periods of 5, 10, 12 and 15 years. Both oxygen and  $Fe^{3+}$  react with pyrite and produce  $SO_4^{2-}$ .

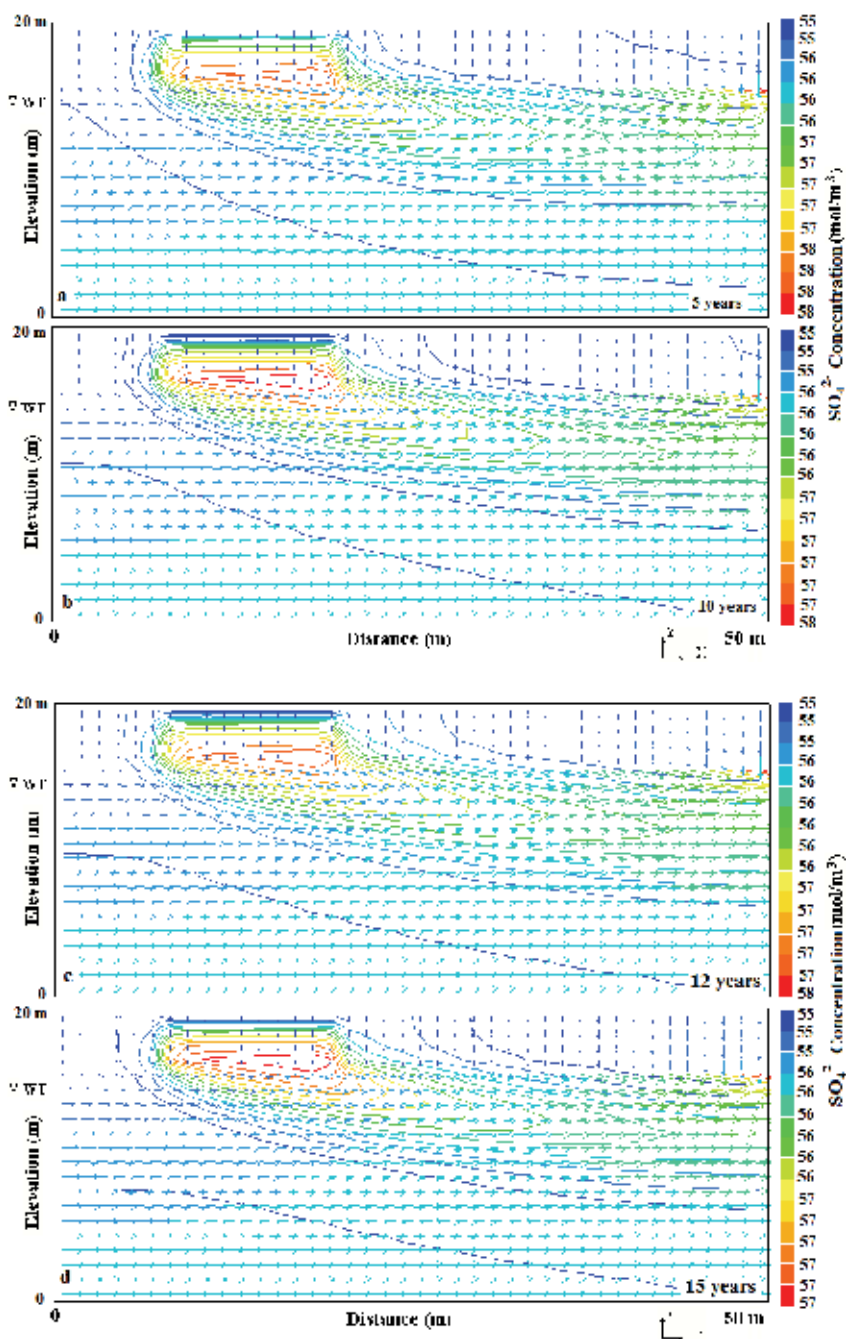


Fig. 13.  $SO_4^{2-}$  concentration after: (a) 5 years; (b) 10 years; (c) 12 years; (d) 15 years of simulation

Although not illustrated, early in the simulation the  $SO_4^{2-}$  peak occurs in the unsaturated zone. Pyrite-oxygen reaction is recognised to be the only important source for  $SO_4^{2-}$  production at the beginning of the simulation.

At 5 years (Figure 13a), an  $SO_4^{2-}$  peak (greater than  $58 \text{ mol} / \text{m}^3$ ) occurred in the saturated zone due to a downward recharge water flow. In the saturated zone,  $SO_4^{2-}$  spreads by groundwater flow. As time progresses (Figure 13b-d), the  $SO_4^{2-}$  peak moved further down into the saturated zone whereas  $SO_4^{2-}$  concentrations in the unsaturated zone began to decrease. No significant concentrations of  $SO_4^{2-}$  were produced in the saturated zone by the reaction between ferric iron and pyrite, because, for two-dimensional simulations, it was considered that only pyrite in a 12.5 m wide segment of the unsaturated zone participates in the oxidation reaction.

#### **4.2 Problem 2- modelling of pollutants transportation associated with AMD in Shour River at Sarcheshmeh copper mine, Iran**

During the past years there was a major public interest concerning the management of water resources. A hot spot of this field is the availability of water of acceptable quality under circumstances of pollutant discharge in rivers. The water quality management in such situations requires fast decisions based on knowledge related to the distribution of pollutant concentration along the river downstream of the releasing source.

The second problem deals with the modelling of transportation of metallic pollutants associated with AMD in the Shour River at Sarcheshmeh copper mine, Iran. This case attempts to numerically model the water pollution problems in the Shour River passing near the Sarcheshmeh copper mine. This river has been seriously affected by AMD emanated from the Sarcheshmeh mine, sulphide wastes and acidic leachates from heap leaching facilities in the study area.

Sarcheshmeh is a large open pit mine in the Kerman Province of Iran and considered to be one of the largest copper deposits in the world. Sarcheshmeh complex contains substantial amounts of molybdenum, gold and other rare metals. Approximately 40,000 tons of ore at 0.9 % Cu and 0.03 % molybdenum is extracted per day in Sarcheshmeh mine (Banisi & Finch 2001). The Sarcheshmeh copper mine is located about 160 km southwest of Kerman and 50 km south of Rafsanjan. Sarcheshmeh ore body, situated in the central part of Zagros ranges, consists of folded and faulted early tertiary volcano- sedimentary rocks. The mine is recognized with latitude of  $29^\circ 58'$  and a longitude of  $53^\circ 55'$ . The average annual precipitation at the site varies from 300 to 550 mm. The temperature varies from  $+35^\circ \text{C}$  in summer to  $-20^\circ \text{C}$  in winter (Bani Asadi et al., 2008; Doulati Ardejani et al., 2008a). Production units of Sarcheshmeh Copper Complex involve the mine itself, concentrator, smelter, refinery, foundries and heap leaching facilities. Different aspects of the Sarcheshmeh copper deposit have been previously described by Aftabi & Atapour (2000), Atapour & Aftabi (2007), Bani Asadi et al., (2008), Banisi & Finch (2001), Bazin & Hubner (1969), Doulati Ardejani et al., (2005), Doulati Ardejani et al., (2008a), Ghorashizadeh (1978), Majdi et al., (2007), Shayestehfar et al., (2007).

Mining operation has placed many low grade waste dumps and has posed many environmental problems. AMD is a serious problem in Sarcheshmeh copper mine which has a detrimental impact on groundwater and surface water quality. Sulphide minerals oxidation in particular pyrite and subsequence discharge of acidic drainages containing



toxic metals into Shour River and groundwater aquifer is the major source of water pollution.

AMD is generally formed due to the oxidation of sulphide minerals in particular pyrite. When pyritic minerals are exposed to air, their rapid oxidation occur which produces acidic drainage (Atkins & Pooley, 1982; Ricca & Schultz, 1979; Rubio & Del Olmo, 1995).

The impacts of AMD on the quality of the surface and groundwater were investigated by sampling in the Shour River and analysing them for hydrogeochemical parameters in particular toxic metals. The concentration of  $\text{SO}_4^{2-}$  in both surface and groundwater samples were high. The pH of the water samples in Shour River varies from 2 to 3.9. However, the pH of groundwater samples (6.3-7.2) was found within the permissible limit (Bani Asadi et al., 2008; Doulati Ardejani et al., 2008a).

Numerical modelling of metallic pollutants transport is necessary to predict their migration through the Shour River. Modelling the metallic pollutants fate and transport can help in the design of a mining operation to minimize the various effects on the environment during the activities. The effects of AMD may remain for long times after mine closure, hence careful environmental management is a necessary task during mining operations and a basic mine closure strategy has to be developed to prevent the subsequent generation of AMD. Simulation of long-term pyrite oxidation and the transportation of oxidation products in particular metallic pollutants provide useful information which can be used for the design of efficient remediation programs.

#### 4.2.1 Sampling

Water samples were collected from the Shour River. The Shour River is the main stream flows in the study area. The Sarcheshmeh mine drainages enter the Shour River. Figure 14 shows this river and the sampling locations. The water samples were collected in February 2006. Sampling locations consist of upstream of the Shour River, coming from the Sarcheshmeh mine in the upstream of heap facility, in the entrance of acidic leachate of heap structure to the river, run-off of leaching solution into the river and river downstream (Table 4). The water samples were immediately acidified to less than  $\text{pH}=2$  using pure  $\text{HNO}_3$ . Analysis results of samples are shown in Table 5. The pH of the samples was measured using a portable pH meter. Concentrations of dissolved metals in the water samples were determined using an atomic adsorption spectrometer (AA220) in water Lab of the National Iranian Copper Industries Co (Bani Asadi et al., 2008).

Concentrations of heavy metals and  $\text{SO}_4^{2-}$  in water decrease with distance from upstream to downstream of the Shour River due to a dilution effect by uncontaminated waters, adsorption process with suspended fine particles in river water and riverbed sediments and also due to precipitation effect resulting from increase in pH. Such processes can be well described by mathematical models for transport and fate of pollutants in rivers (see Ani et al., 2010).

pH of the Shour River water plays an important role in the transportation of heavy metals. In the Shour River, Fe is the most rapidly depleted from aqueous phase. pH varies from 2.0 (leaching solution run-off) to 4.3 (Shour River diluted water). This range of pH is lower than the acceptable values of pH from any surface mine site (Stiefel & Busch, 1983). Due to low pH, the heavy metals remain in dissolved state in river water for long distances. Subsequently, this leads to potential environmental damages in the study area. Furthermore, high concentrations of heavy metals and low pH cause the death of aquatic life.

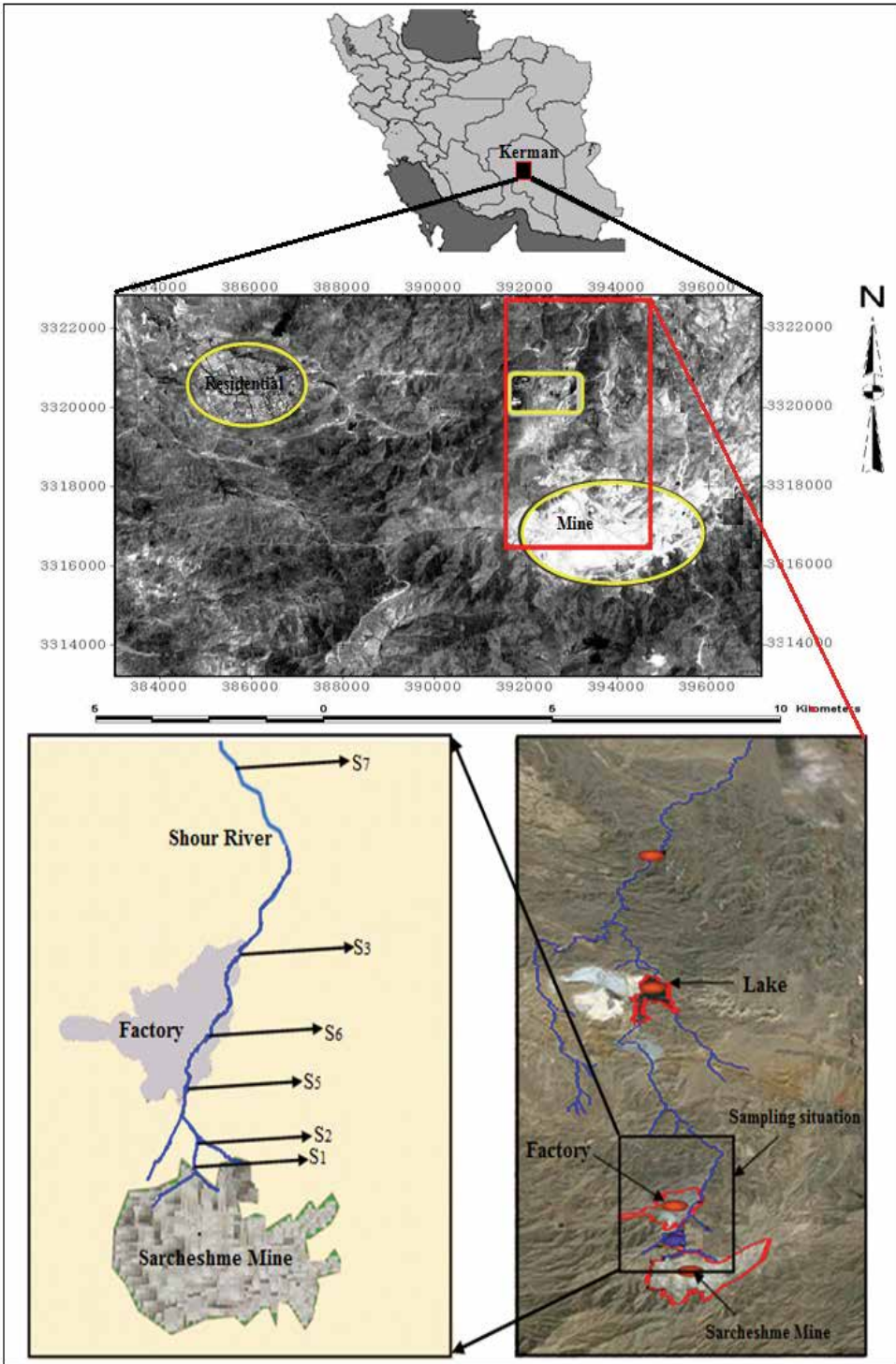


Fig. 14. Sampling locations in Shour River, from Sarcheshmeh porphyry copper mine

| Station        | Y (m)   | X (m)  | Sampling place  |
|----------------|---------|--------|---|
| S <sub>1</sub> | 3315792 | 339809 | leaching factory overflow (leaching solution run-off) |
| S <sub>2</sub> | 3315734 | 389737 | river water (downstream of the leaching factory)      |
| S <sub>3</sub> | 3315095 | 390234 | acidic leachate of heap No.2                          |
| S <sub>5</sub> | 3315422 | 390013 | river water mixed with heap leachate                  |
| S <sub>6</sub> | 3315320 | 390013 | river water (crusher downstream)                      |
| S <sub>7</sub> | 3314578 | 339765 | river water (crusher upstream)                        |

Table 4. Sampling details from Shour River. Sample S<sub>4</sub> was removed from Table 1 due to analysing error

| Sample         | Distance (m) | (ppm) |      |      |      |      |      |      |      |                 | pH  |
|----------------|--------------|-------|------|------|------|------|------|------|------|-----------------|-----|
|                |              | Cu    | Mn   | Fe   | Cd   | Pb   | Cr   | Mo   | Zn   | SO <sub>4</sub> |     |
| S <sub>1</sub> | 0            | 410   | 1050 | 4800 | 3.8  | 1.8  | 1.3  | 0.6  | 475  | 3500            | 2   |
| S <sub>2</sub> | 69.9         | 215   | 360  | 1515 | 1.7  | 1    | 0.7  | 0.3  | 185  | 3400            | 2.3 |
| S <sub>5</sub> | 357          | 225   | 62.5 | 2.1  | 0.17 | 0.22 | 0.07 | 0.1  | 25   | 3300            | 3.9 |
| S <sub>6</sub> | 414          | 32    | 5.5  | 0.5  | 0.02 | 0.18 | 0.05 | 0.01 | 1.51 | 1023            | 4.3 |
| S <sub>3</sub> | 696          | 570   | 215  | 38   | 0.45 | 0.4  | 0.2  | 0.1  | 67   | 3000            | 3.4 |
| S <sub>7</sub> | 1200         | 83    | 4.2  | 0.12 | 0.01 | 0.1  | 0.05 | 0.01 | 1.13 | 626             | 4.3 |

Table 5. Chemical analysis of water samples from Shour River

Variations in pH strongly control the mobility of dissolved heavy metals with a typical inverse relationship (Dinelli et al., 2001). The heavy metals are significantly elevated in water sampled at the nearest points of river to the heap structure. Concentrations of heavy metals in water decrease with distance from the heap facility due to a dilution effect by uncontaminated waters and due to an increase in pH. This shows that high concentrations of metals are greatly influenced by leachates from heap structure. The concentrations of most metals are significantly higher than their standard limits found in potable water (WHO, 2008).

#### 4.2.2 Governing equation of pollutant transport through the Shour River

In this section, a CFD model incorporating the finite volume discretisation scheme is presented to simulate pollutants transportation processes through the Shour River at Sarcheshmeh copper mine. It is assumed that the adsorption is the main process occurred during the course of the physical transportation of the pollutants in river. This process may take place between dissolved pollutants and suspended fine particles in river water and riverbed sediments. The model incorporates the Langmuir isotherm expression to describe the non-linear adsorption process in the Shour River. The governing equations of the model were numerically solved using PHOENICS software. The field data presented in this study were compared with those results predicted by the numerical model.

The Langmuir isotherm can be expressed as follows (Doulati Ardejani et al., 2007; Gokmen & Serpen, 2002; Hachem et al., 2001; Shawabkeh et al., 2004; Sheng & Smith, 1997):

$$q = \frac{Q_0 K_L C}{1 + K_L C} \quad (15)$$

where,  $q$  is the adsorbed concentration,  $C$  is the equilibrium concentration,  $Q_0$  denotes the maximum absorption capacity and  $K_L$  is the Langmuir constant.

The second-order partial differential equation that expresses the pollutant transport at the surface rivers and groundwater aquifer and consist of both physical (advection and dispersion) and chemical (adsorption) processes can be rewritten as:

$$\phi \frac{\partial C}{\partial t} + \rho_b \frac{\partial q}{\partial t} = D \frac{\partial^2 C}{\partial x_j^2} - v_j \frac{\partial C}{\partial x_j} \pm S \quad (16)$$

where,

$x_j$  = Cartesian coordinates ( $m$ );

$D$  = dispersion coefficient ( $m^2 / s$ );

$\phi$  = porosity;

$v_j$  = vector components of the specific discharge ( $m/s$ );

$t$  = time ( $s$ );

$\rho_b$  = bulk density ( $kg/m^3$ );

$S$  = sink and source term representing the change in aqueous component concentrations due to the chemical reactions.

The concentration of any chemical species in the aqueous system can be related to its sorbed concentration in the solid phase using the following equation:

$$\frac{\partial q}{\partial t} = \frac{\partial q}{\partial C} \frac{\partial C}{\partial t} \quad (17)$$

Substituting Equation 17 into Equation 16 yields the following equation:

$$\phi \frac{\partial C}{\partial t} + \rho_b \left( \frac{\partial q}{\partial C} \frac{\partial C}{\partial t} \right) = D \frac{\partial^2 C}{\partial x_j^2} - v_j \frac{\partial C}{\partial x_j} \pm S \quad (18)$$

where,

Differentiating the Langmuir isotherm expression with respect to the concentration  $C$  gives:

$$\frac{\partial q}{\partial C} = \frac{Q_0 K_L}{(1 + K_L C)^2} \quad (19)$$

Substituting Equation 19 into Equation 18 yields the following equation:

$$\phi \frac{\partial C}{\partial t} + \rho_b \frac{Q_0 K_L}{(1 + K_L C)^2} \frac{\partial C}{\partial t} = D \frac{\partial^2 C}{\partial x_j^2} - v_j \frac{\partial C}{\partial x_j} \pm S \quad (20)$$

Equation 20 can now be rewritten as:

$$\phi \frac{\partial C}{\partial t} = D \frac{\partial^2 C}{\partial x_j^2} - v_j \frac{\partial C}{\partial x_j} - \rho_b \frac{Q_0 K_L}{(1 + K_L C)^2} \frac{\partial C}{\partial t} \pm S \quad (21)$$

The rearrangement of Equation 21 yields:

$$\frac{\partial C}{\partial t} = D \frac{\partial^2 C}{\partial x_j^2} - v_j \frac{\partial C}{\partial x_j} + (1 - \phi) \frac{\partial C}{\partial t} - \rho_b \frac{Q_0 K_L}{(1 + K_L C)^2} \frac{\partial C}{\partial t} \pm S \quad (22)$$

where, terms in  $\partial C/\partial t$  have been added to both sides of Equation 21.

For a continuous system and assuming that the adsorption is the only mechanism taking place during pollutant transportation, Equation 22 reduces to:

$$\frac{\partial C}{\partial t} = D \frac{\partial^2 C}{\partial x_j^2} - v_j \frac{\partial C}{\partial x_j} - \rho_b \frac{Q_0 K_L}{(1 + K_L C)^2} \frac{\partial C}{\partial t} \quad (23)$$

In Equation 23,  $\rho_b = 1$  and  $\phi = 100\%$

Equation 23 contains one additional source term, which can be evaluated by FORTRAN99 codes located in GROUP 13 of GROUND routine in PHOENICS software. Given appropriate boundary conditions and an initial condition, the non-linear partial differential Equation 23 is solved numerically using PHOENICS software for each dissolved pollutant.

In the case of a single-phase problem, the partial differential equation solved by PHOENICS has the following general form (Spalding, 1981):

$$\frac{\partial}{\partial t} (\rho \psi) + \frac{\partial}{\partial x_j} \left( \rho u_j \psi - \Gamma_\psi \frac{\partial \psi}{\partial x_j} \right) = S_\psi \quad (24)$$

where,

$\psi$  = any of the dependent variable;

$t$  = time;

$\rho$  = PHOENICS-term for density;

$u_j$  = velocity component in the  $x_j$  direction;

$\Gamma_\psi$  = diffusive exchange coefficient for  $\psi$ ;

$S_\psi$  = source rate of  $\psi$ .

#### 4.2.3 Modelling setting and input data

In order to model the transport process, a one-dimensional modelling was performed using PHOENICS software. The Shour River was simulated as a finite volume model with a length, a width and a depth of 1200, 1 and 1 m respectively. The model was divided into 1500 equal size control volumes and considered as a continuous system in which the pollutants transport take place. An average water velocity of 1 (m/s) was considered. 30 time steps with a power law distribution (power=1.5) were assigned. The modelling time was 1200 seconds. Total iteration of 3500 was assigned to the simulation. A grid distribution with geometric pressure was used with a power/ratio of 1. An upwind differencing scheme was considered (Figure 15).

A hydrodynamic dispersion equal to 1.5 m<sup>2</sup>/s was assigned. Table 6 gives the Langmuir isotherm constants and bulk density of the flow medium used in pollutant transport model. In this paper, the results predicted by the finite volume model were compared with the field data. Figures 16 to 25 compare the numerical modelling results to the field data for Cu<sup>2+</sup>, Mn<sup>2+</sup>, Fe<sup>2+</sup>, Cd<sup>2+</sup>, Pb<sup>2+</sup>, Cr<sup>2+</sup>, Mo<sup>2+</sup>, Zn<sup>2+</sup> and SO<sub>4</sub><sup>2-</sup> concentrations distributions and pH in the

Shour River. A close agreement between the results of numerical model and field data explains that the adsorption process is well described by the Langmuir isotherm in the Shour River.

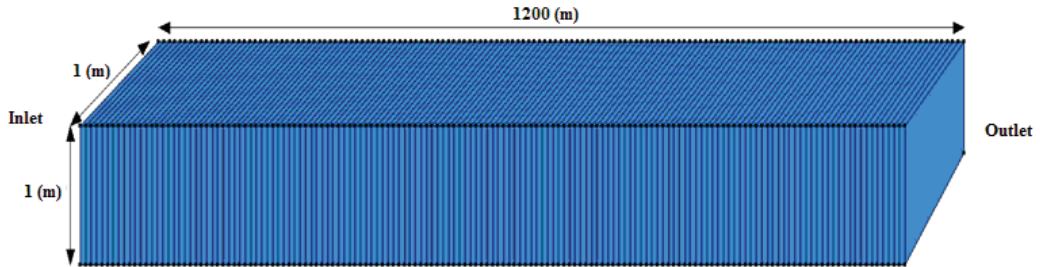


Fig. 15. Finite volume model for Shour River

| Metallic pollutant | $K_l(L/mg)$ | $Q_0(mg/g)$ | $\rho_b(kg/m^3)$ | References                      |
|--------------------|-------------|-------------|------------------|---------------------------------|
| Cu                 | 2.103       | 8.598       | 1                | Doulati Ardejani et al., (2011) |
| Mn                 | 0.347       | 2.381       | 1                | Doulati Ardejani et al., (2011) |
| Fe                 | <b>1.90</b> | 7.15        | 1                | Not published data              |
| Cd                 | 2.05        | 3.65        | 1                | Not published data              |
| Pb                 | 1.45        | 5.63        | 1                | Not published data              |
| Cr                 | 0.65        | 3.30        | 1                | Not published data              |
| Mo                 | 2.0         | 6.20        | 1                | Not published data              |
| Zn                 | 2.25        | 6.15        | 1                | Not published data              |
| SO <sub>4</sub>    | 1.65        | 8.75        | 1                | Not published data              |
| H <sup>+</sup>     | 1.93        | 5.75        | 1                | Not published data              |

Table 6. Langmuir isotherm constants and bulk density of the flow medium used in the simulation

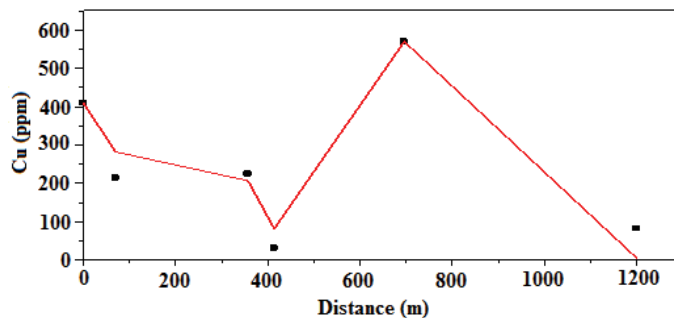


Fig. 16. Comparison of model predictions (—) and field data (■) for Cu<sup>2+</sup> concentrations versus distance in the Shour River

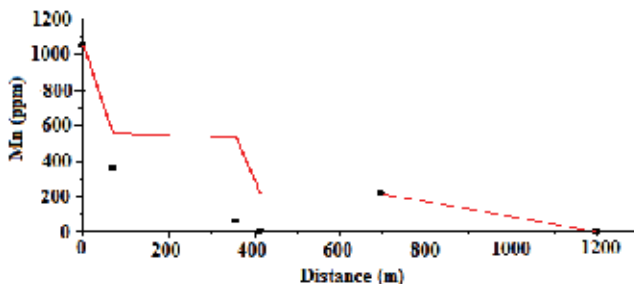


Fig. 17. Comparison of model predictions (—) and field data (■) for Mn<sup>2+</sup> concentrations versus distance in the Shour River

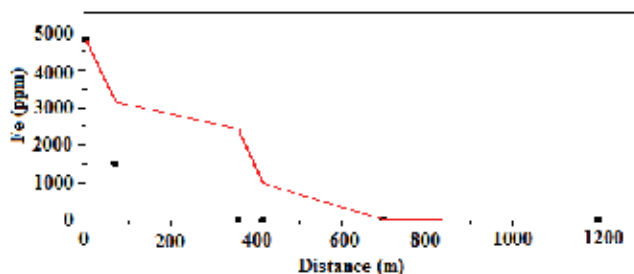


Fig. 18. Comparison of model predictions (—) and field data (■) for Fe<sup>2+</sup> concentrations versus distance in the Shour River

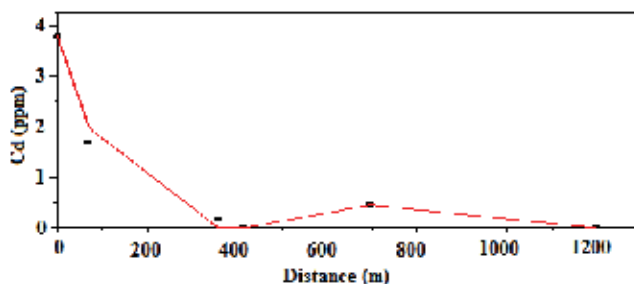


Fig. 19. Comparison of model predictions (—) and field data (■) for Cd<sup>2+</sup> concentrations versus distance in the Shour River

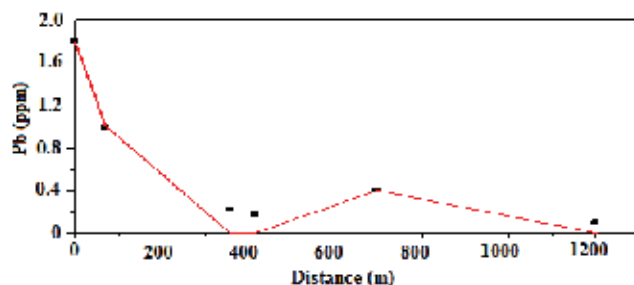


Fig. 20. Comparison of model predictions (—) and field data (■) for Pb<sup>2+</sup> concentrations versus distance in the Shour River

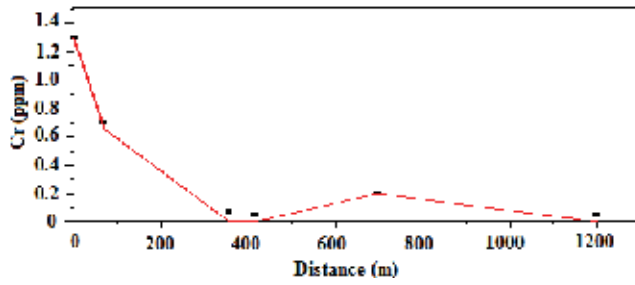


Fig. 21. Comparison of model predictions (—) and field data (■) for Cr<sup>2+</sup> concentrations versus distance in the Shour River

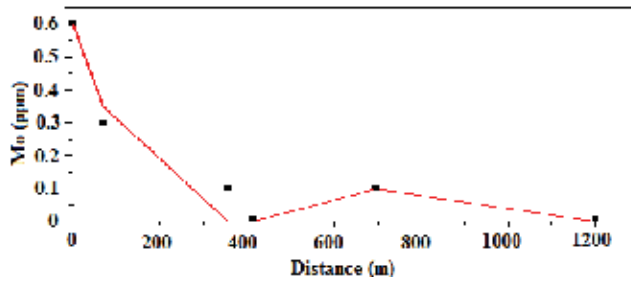


Fig. 22. Comparison of model predictions (—) and field data (■) for Mo<sup>2+</sup> concentrations versus distance in the Shour River

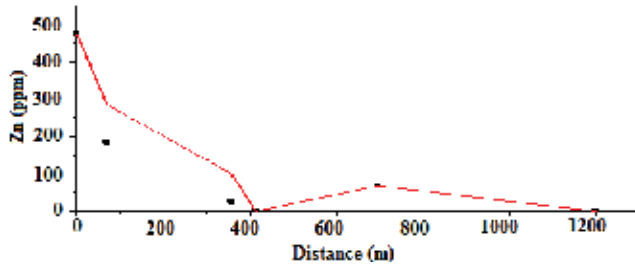


Fig. 23. Comparison of model predictions (—) and field data (■) for Zn<sup>2+</sup> concentrations versus distance in the Shour River

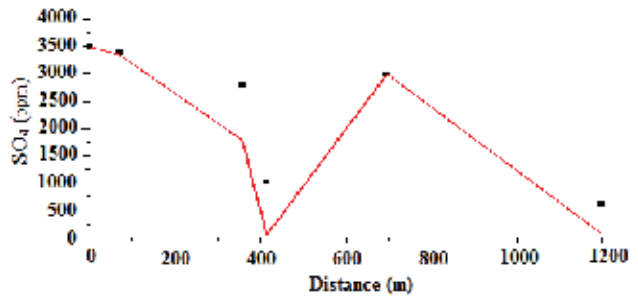


Fig. 24. Comparison of model predictions (—) and field data (■) for SO<sub>4</sub><sup>2-</sup> concentrations versus distance in the Shour River



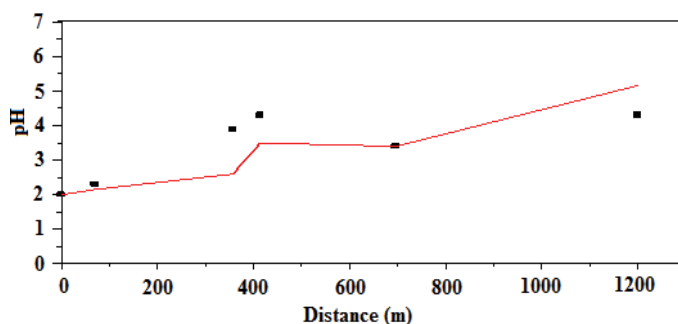
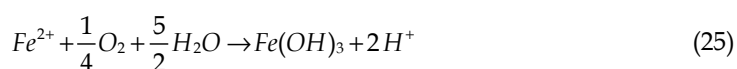


Fig. 25. Comparison of model predictions (—) and field data (■) for pH versus distance in the Shour River

#### 4.2.4 Reactive transport modelling of Fe (II) and pH including ferrous iron oxidation and ferric iron hydrolysis reactions

The design of water management policies and water use technologies as well as management of mine drainages can only be conducted properly when it is based on appropriate mathematical models (Kaden & Luckner, 1984). For more accurate prediction of Fe (II) and pH fate and transport in Shour River, it is necessary to incorporate hydrolysis of Fe (III) reaction.  $Fe^{3+}$  produced by the oxidation of ferrous iron may be hydrolysed and precipitated as amorphous ferrihydrite according to Equation 25:



Equation 25 is important in the Shour River and it entirely depends on pH. Reduced conceptual water quality models have been developed for the concentrations of  $[Fe^{2+}]$  and  $[H^+]$  in mine water treatment plants, rivers and remaining pits (Hummel et al., 1985). The typical chemical reactions for all models in the one-phase system 'water' are the oxidation reactions of Fe (II) and the hydrolysis of Fe (III). According to Hummel et al., (1985), the following assumptions are necessary to be considered when such models are used for surface water bodies.

- The chemical reactions are considered as non-equilibrium reactions with complete stoichiometric turnover of the initial substances.
- Oxygen is enough for oxidation processes in the surface water bodies and the partial pressure is constant ( $P_{O_2} = 0.21 \text{ bar}$ ).
- The transport processes are one dimensional.
- All the ferrous hydroxide formed is restricted within the reaction time; no mathematical modelling is therefore necessary to reflect the sedimentation processes.

The kinetics of the chemical oxidation of  $Fe^{2+}$  have been previously studied and the necessary rate expression was found. Singer & Stumm (1970) proposed the following rate law:

$$r_{Fe} = \frac{\partial[Fe^{2+}]}{\partial t} = -k[OH^-]^2 P_{O_2} [Fe^{2+}] = \frac{-k P_{O_2} K_w [Fe^{2+}]}{[H^+]^2} \quad (26)$$

where,

$k$  = rate constant ( $\text{mol}^{-2} \text{L}^2 \text{min}^{-2} \text{bar}^{-1}$ );

$[OH]$  = Concentration of hydroxyl ions;

$[Fe^{2+}]$  = Concentration of ferrous ions;

$[H^+]$  = Concentration of hydrogen ions.

Equation 26 can be rewritten as follow:

$$r_{Fe} = -\frac{\partial[Fe^{2+}]}{\partial t} = k_1[Fe^{2+}] \quad (27)$$

$$k_1 = \frac{-k P_{O_2} K_w}{[H^+]^2} = \frac{k^*}{[H^+]^2} \quad (28)$$

$k_1$  has the unit of inverse time ( $1/t$ ) and it varies between  $1.6 \times 10^{-13}$  and  $13 \times 10^{-13}$  (quoted in Hummel et al., 1985). Substituting Equation 28 into Equation 27 yields the following equation:

$$r_{Fe} = -\frac{\partial[Fe^{2+}]}{\partial t} = \frac{k^*[Fe^{2+}]}{[H^+]^2} \quad (29)$$

Based on the Equation 25, the stoichiometric ratio between protons and ferrous mass formation rate,  $K_{Fe}$ , is:

$$K_{Fe} = \frac{[H^+]}{[Fe^{2+}]} = 3.58 \times 10^{-2} \left( \frac{\text{mol } H^+}{\text{gr } Fe^{2+}} \right) \quad (30)$$

Considering Equation 30, the rate expression for  $H^+$  may be expressed as:

$$r_{H^+} = k_{Fe} \frac{\partial[Fe^{2+}]}{\partial t} \quad (31)$$

Incorporating the kinetics expressions 29 and 31, the following transport equations can then be written to describe reactive transport of  $Fe^{2+}$  of  $H^+$  in the Shour River.

$$\frac{\partial[Fe^{2+}]}{\partial t} = D_x \frac{\partial^2[Fe^{2+}]}{\partial x^2} - v \frac{\partial[Fe^{2+}]}{\partial x} - \frac{k}{[H^+]^2} [Fe^{2+}] \quad (32)$$

$$\frac{\partial[H^+]}{\partial t} = D_x \frac{\partial^2[H^+]}{\partial x^2} - v \frac{\partial[H^+]}{\partial x} - \frac{k^* k_{Fe}}{[H^+]^2} [Fe^{2+}] \quad (33)$$

The values of  $k_{Fe}$  and  $k$  are  $0.0385$  and  $2 \times 10^{-13}$ , respectively.

Equations 32 and 33 can now be solved by defining the appropriate initial and boundary conditions. Figures 26 and 27 compare the results of numerical model with the field data. The hydrolysis reaction of Fe (III) was incorporated.

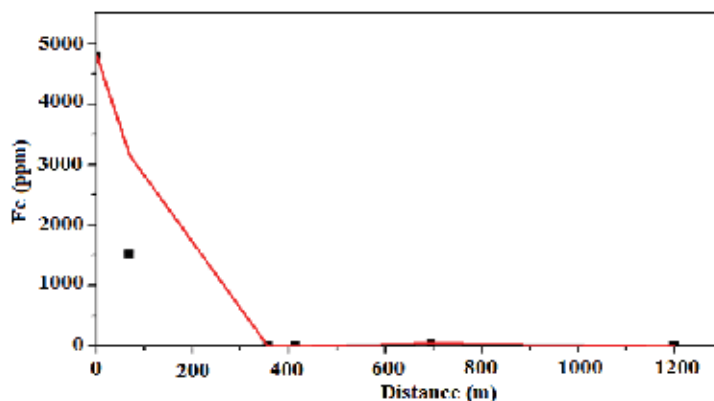


Fig. 26. Comparison of model predictions (—) and field data (■) for  $Fe^{2+}$  concentrations versus distance in the Shour River. The hydrolysis reaction of Fe (III) was incorporated

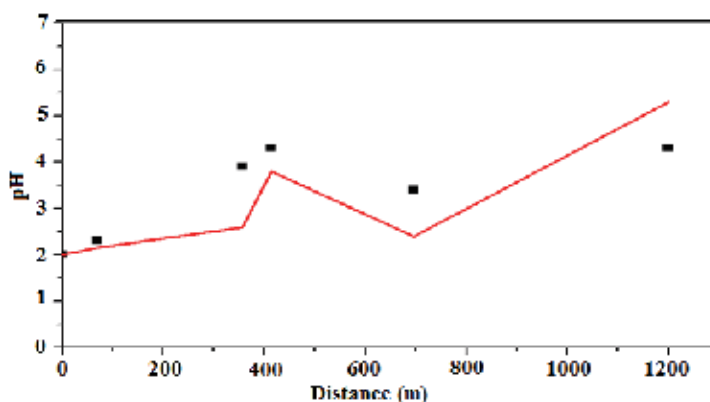


Fig. 27. Comparison of model predictions (—) and field data (■) for pH versus distance in the Shour River. The hydrolysis reaction of Fe (III) was incorporated

As Figures 26 and 27 show, the results predicted by the finite volume model for  $Fe^{2+}$  and  $H^+$  agreed closely with the field data. The reason is that, the oxidation of Fe (II) and the hydrolysis of Fe (III) reactions removed ferrous iron from the solution phase in the direction of the water flow.

## 5. Conclusion

In this chapter the general features of the CFD analysis and the fundamentals of the finite volume numerical technique were described. PHOENICS as a CFD package, its features, capabilities and applications were briefly reviewed. Finite volume discretisation of the surface and groundwater flow and transport equations is presented. The basic principles of the finite volume method can be easily understood and it is particularly strong on coarse non-uniform meshes. One important advantage of the finite volume method over other numerical methods is its strong capability in dealing with boundary conditions and specific source terms. This feature of the finite volume method is very important for acid mine drainage cases associated with production (source) and consumption (sink) terms for many

chemical components and the specification of different boundary and initial conditions. The applications of CFD analysis in the modelling of the environmental problems have been considered by the simulation of two different problems. A numerical finite volume model using PHOENICS as a general-purpose CFD package has been developed.

The first problem deals with the simulation of long-term pyrite oxidation and pollutant generation within the spoil of an open cut mine. In this first modelling, the following conclusions were made:

- Gaseous diffusion process is an important source for supplying oxygen to the reaction site.
- Both oxygen and ferric iron produced by bacterially mediated oxidation of ferrous iron participate in the oxidation of pyrite.
- It was found that a pyrite oxidation model in the backfilled site of an open cut mine should take into consideration the role of iron oxidising bacteria.
- Bacterial activity caused a sharp depletion of oxygen in the vadose zone.
- In the absence of bacteria, oxygen is the only important oxidant of pyrite and the oxidation rate is highly dependent on the effective diffusion coefficient.
- The oxidation of only a small fraction of pyrite is enough to generate an acid mine drainage load. Considerable pyrite presence creates a long-term source of acid mine drainage.
- The lowering of pH in the range between 2.5 to 3.5, results in the bacterial oxidation of pyrite being enhanced. Subsequently the bacterial action produces more  $Fe^{3+}$ ,  $SO_4^{2-}$ ,  $H^+$ , and  $Fe^{2+}$ .
- The results of two-dimensional simulations clearly indicate that the most of dissolved ferric iron remains above water table while a ferrous iron peak appears below it, in the saturated zone.
- Sulphate initially generated by the pyrite-oxygen reaction and subsequent production from the  $Fe^{3+}$  - pyrite reaction due to bacterial action mainly appears below the water table.

The second problem deals with the modelling of transportation of metallic pollutants associated with acid mine drainage in the Shour River at Sarcheshmeh copper mine, Iran. Acid mine drainage production and heavy metals release and transportation have created many environmental problems. The results show that the mechanical dispersion and advection are the main pollutant transport mechanisms through river water. The results further show that the adsorption is the main mechanism for metal removal from river water. Moreover, this process fits well the Langmuir non-linear isotherm. A better agreement was achieved between the field data and model predictions when ferrous iron oxidation and hydrolysis of ferric iron processes were considered.

The numerical models presented here can help to design, optimise and predict the performance of field remediation and polluted waters treatment programs. The results obtained from this study can be used for developing an appropriate environmental management program in order to monitor surface and groundwater pollution problems and to have a better understanding of the pollution transport mechanisms.

## 6. Acknowledgment

The authors would like to thank the Faculty of Mining, Petroleum and Geophysics, Shahrood University and Technology, School of Civil, Mining and Environmental

Engineering, University of Wollongong, Australia and National Iranian Copper Industries (N.I.C.I.Co.) for supporting this research.

## 7. References

- Ani, E.C. Hutchins, M.G. Kraslawski, A., & Agachib, P.S. (2010). Assessment of pollutant transport and river water quality using mathematical models. *Revue Roumaine de Chimie*, Vol. 55, No. 4, pp. 285-291
- Ani, E.C. Wallis, S. Kraslawski, A., & Serban Agachi, P. (2009). Development, calibration and evaluation of two mathematical models for pollutant transport in a small river. *Environmental Modelling & Software*, Vol. 24, pp. 1139-1152
- Atkins, A.S., & Pooley, F.D. (1982). The effects of bio-mechanisms on acidic mine drainage in coal mining. *International Journal of Mine Water*, No. 1, pp.31-44
- Balusu, S.R. (1993). Design and development of a multi-scrubber dust control system for longwall faces: Experimental and modelling studies. Ph.D. Thesis, University of Wollongong, pp.188-246.
- Bani Assadi, A., Doulati Ardejani, F. Karami, G.H., Dahr Azma, B., Atash Dehghan, R., & Alipour, M. (2008). Heavy metal pollution problems in the vicinity of heap leaching No. 3 of Sarcheshmeh porphyry copper mine, *10th International Mine Water Association Congress*, pp. 355-358, Karlovy Vary, Czech Republic, 2-5 June 2008
- Banisi S., & Finch J.A. (2001). Testing a floatation column at the Sarcheshmeh copper mine. *Mineral Engineering*, Vol. 14, No. 7, pp. 785-789
- Barovic, G., & Boochs, P.W. (1981). Two- and Three-dimensional mathematical models of contaminant movement in groundwater. *Studies in Environmental Science*, Vol. 17, pp. 849-855
- Bignoli, G., & Sabbioni, E. (1981). Long-term prediction of the potential impact of heavy metals on groundwater quality as a result of fertilizer use. *Studies in Environmental Science*, Vol. 17, pp. 857-862
- Binning, P., & Celia, M.A. (1996). A finite volume Eulerian-Lagrangian localized adjoint method for solution of the contaminant transport equations in two-dimensional multiphase flow systems. *Water Resources Research*, Vol. 32, No. 1, pp.103-114
- Cathles, L.M., & Apps, J.A. (1975). A model of the dump leaching process that incorporates oxygen balance, heat balance and air convection. *Metallurgical Transactions B*, Volume 6B, pp.617-624
- CHAM (2008). The PHOENICS On-Line Information System, [http://www.cham.co.uk/phoenics/d\\_polis/polis.htm](http://www.cham.co.uk/phoenics/d_polis/polis.htm)
- Lide, D.R. (Ed.). (1998). *Handbook of chemistry and physics*, 78th edition, CRC press LLC, Boca Roton, New York
- Dinelli, E. Lucchini, F, Fabbri, M., & Cortecchi, G. (2001). Metal distribution and environmental problems related to sulfide oxidation in the Libiola copper mine area (Ligurian Apennines, Italy). *Journal of Geochemical Exploration*, Vol. 74, pp. 141-152
- Doulati Ardejani, F. (2003). Hydrogeological investigation of backfilled Surface of Coal Mine Site, PhD Thesis, University of Wollongong, Australia, 435 p.
- Doulati Ardejani, F. Badii, Kh. Yousefi Limaee, N. Mahmoodi, N.M. Arami, M. Shafaei, SZ., & Mirhabibi, AR. (2007). Numerical modelling and laboratory studies on the

- removal of Direct Red 23 and Direct Red 80 dyes from textile effluents using orange peel, a low-cost adsorbent. *Dyes and Pigment*, Vol. 73, No. 2, pp.178-185
- Doulati Ardejani, F. Karami, G.H. Bani Assadi, A., & Atash Dehghan, R. (2008a). Hydrogeochemical investigations of the Shour River and groundwater affected by acid mine drainage in Sarcheshmeh porphyry copper mine, *10th International Mine Water Association Congress*, pp. 235-238, Karlovy Vary, Czech Republic, 2-5 June 2008
- Doulati Ardejani F., Jodieri Shokri B., Moradzadeh A., Soleimani E., & Ansari Jafari M. (2008b). A combined mathematical-geophysical model for prediction of pyrite oxidation and pollutant leaching associated with a coal washing waste dump. *International Journal of Environmental Science and Technology*, Vol. 5, No. 4, pp.517-526
- Doulati Ardejani F., Jodieri Shokri B., Bagheri M., & Soleimani E. (2010). Investigation of pyrite oxidation and acid mine drainage characterization associated with Razi active coal mine and coal washing dumps in the Azad Shahr-Ramian region, northeast Iran. *Environmental Earth Sciences*, Vol. 61, pp. 1547-1560
- Doulati Ardejani F., Marandi, R., & Soleimanifar H. (2011). Biological extraction of copper and manganese ions from acid mine drainage using the fungal species *Aspergillus niger*. *Journal of Environmental Science and Technology* (Persian version), accepted for publication.
- Edwards, J.S. Ren, T.X., & Jozefowicz, R. (1995). Using computational fluid dynamics (CFD) to solve mine safety and health problems, *Technical Proceedings, Application of Computers and Operations Research in the Minerals Industries, APCOM xxv 1995*, pp.41-47, Brisbane, Australia, 9-14 July 1995
- Fried, J.J. (1981). Groundwater pollution mathematical modelling: important or stagnation. *Studies in Environmental Science*, Vol. 17, pp. 807-822
- Gokmen, V., & Serpen, A. (2002). Equilibrium and kinetic studies on the adsorption of dark colored compounds from apple juice using adsorbent resin. *Journal of Food Engineering*, Vol. 53, pp.221-227
- Green, S.R., & Clothier, B.E. (1994). Simulation water and chemical movement into unsaturated soils. *The PHOENICS Journal of Computational Fluid Dynamics & Its Applications*, Vol. 7, No.1, pp.76-92
- Hachem, C. Bocquillon, F. Zahraa, O., & Bouchy, M. (2001). Decolourization of textile industry wastewater by the photocatalytic degradation process. *Dyes and Pigments*, Vol. 49, pp.117-25
- Harvard, L., Thomas, H.P. & David, W.Z. (1999). *Fundamentals of Computational Fluid Dynamics*, NASA Ames Research Center, 267p.
- Hummel, J. Fischer, R. Luschnner, L., & Kaden, S. (1985). Submodels of water quality for the analysis of regional water policies in open-pit lignite mining area, *Mine Water Proceeding of the second International Congress*, No. 2, pp.673-684, Granada, Spain, 1985
- Jaynes, D.B., Rogowski, A.S., & Pionke, H.B. (1984a). Acid mine drainage from reclaimed coal strip mines, 1, Model description. *Water Resources Research*, Vol. 20, No. 2, pp.233-242
- Jaynes, D.B., Rogowski, A.S., & Pionke, H.B. (1984b). Acid mine drainage from reclaimed coal strip mines, 2, Simulation results of model. *Water Resources Research*, Vol. 20, No. 2, pp.243-250

- Kachiashvili, K. Gordeziani, D. Lazarov, R., & Melikdzhaian, D. (2007). Modeling and simulation of pollutants transport in rivers. *Applied Mathematical Modelling*, Vol. 31, pp.1371-1396
- Kaden, S., & Luckner, L. (1984). Groundwater management in open-pit lignite mining area, *International Symposium, Montreal, Canada*, Proc. Vol. I, pp. 69-78, 21-23 May 1984
- Kerdijk, H.N. (1981). Groundwater pollution by heavy metals and pesticides from a Dredge spoil dump. *Studies in Environmental Science*, Vol. 17, pp. 278-285
- Levenspiel, O. (1972). *Chemical reaction engineering*, John Wiley, New York
- Murthy, J.Y. (2002). Numerical Methods in Heat, Mass, and Momentum Transfer, School of Mechanical Engineering Purdue University, 196p.
- Nawalany, N. (1981). Observation of aquifer pollution state. *Studies in Environmental Science*, Vol. 17, pp.985-990
- Patankar, S. (1980). *Numerical heat transfer and fluid flow*, Taylor & Francis, USA
- Pickens, J.F., & Lennox, W.C. (1976). Numerical simulation of waste movement in steady groundwater flow systems. *Water Resources Research*, Vol. 12, No. 2, pp.171-180
- Pinder, G.F. (1973). A Galerkin-finite element simulation of groundwater contamination on Long Island, New York. *Water Resources Research*, Vol. 9, No. 6, pp.1657-1669
- Putti, M., Yen, W.W.G., & Mulder, W.A. (1990). A triangular finite volume approach with high-resolution upwind terms for the solution of groundwater transport equations. *Water Resources Research*, Vol. 26, No. 12, pp.2865-2880
- Rabbani, M.G., & Warner, J.W. (1994). Shortcomings of existing finite element formulations for subsurface water pollution modelling and its rectification: One-dimensional case. *SIAM Journal on Applied Mathematics*, Vol. 54, No. 3, PP.660-673
- Ricca, V.T., & Schultz, R.R. (1979). Acid mine drainage modelling of surface mining. Mine Drainage, *Proceedings of The First International Mine Drainage Symposium*, G.O. Argall, Jr. C.O. Brawner (Eds.), pp. 651-670, Miller Freeman Publications, Inc., U.S.A, 1979
- Shawabkeh, R., Al-Harashsheh, A., & Al-Otoom, A. (2004). Copper and zinc sorption by treated oil shale ash. *Separation and Purification Technology*, Vol. 40, pp. 251-257
- Sheng, D., & Smith, D.W. (1997). Analytic solutions to the advective contaminant transport equation with non-linear sorption, Research report No. 158.12.1997, ISBN 0 7259 10194, Department of civil, surveying and environmental engineering, The University of Newcastle, Australia
- Singer, P.C., & Stumm, W. (1970). Acidic mine drainage: The rate determining step. *Science*, Vol. 167, pp.1121-1123
- Singh, R.N., & Doulati Ardejani, F. (2004). Finite volume discretisation for solving acid mine drainage problems. *Archives of Mining Science*, Vol. 49, No. 4, pp.531-556
- Spalding, DB. (1981). A general purpose computer program for multi-dimensional one- and two-phase flow. *Mathematics and Computers in Simulation*, Vol. 23, No. 3, pp.267-276
- Stiefel, R.C., & Busch, L.L. (1983). Surface water quality monitoring, In: *Surface Mining Environmental Monitoring and Reclamation Handbook*, L.V.A. Sendlein, H. Yazicigil and C.L. Carlson (Eds.), pp. 189-212, Elsevier Science Publishing Co., Inc., New York
- Svensson, U. (1997). Modeling ground- water flow on a regional scale. *The PHONICS Journal: Computational fluid Dynamics and Its Applications*, Vol. 10, No. 4, pp.442-450

- U.S. Environmental Protection Agency. (1994). Acid mine drainage prediction. Technical document, office of solid waste, special waste branch, EPA530-R-94-036, NTIS, PB94-201829, 48p.
- Versteeg, H.K., & Malalasekera, W. (1995). *An introduction to computational fluid dynamics, the finite volume method*, Prentice Hall, UK
- WHO, (2008). Guidelines for drinking-water quality, 3rd edition, Vol. 1, Recommendations, 3rd edition incorporating 1st and 2nd addenda.
- Wunderly, M.D., Blowes, D.W., Frind, E.O., & Ptacek, C.J. (1996). Sulfide mineral oxidation and subsequent reactive transport of oxidation products in mine tailings impoundments: A numerical model. *Water Resources Research*, Vol. 32, No. 10, pp.3173-3187
- Zhi-Qiang, D., & Hoon-Shin, J. (2009). Scaling dispersion model for pollutant transport in rivers. *Environmental Modelling & Software*, Vol. 24, pp. 627-631



# Computational Flow Modelling of Multiphase Reacting Flow in Trickle-bed Reactors with Applications to the Catalytic Abatement of Liquid Pollutants

Rodrigo J.G. Lopes and Rosa M. Quinta-Ferreira  
*GERSE – Group on Environmental, Reaction and Separation Engineering*  
*Department of Chemical Engineering, University of Coimbra*  
*Portugal*

## 1. Introduction

The contemporary status of computational flow modelling encourages strongly the application of modern CFD codes on the design and investigation of process equipment and aims to accomplish novel and stringent environmental regulations on the decontamination of high strength wastewaters. The application of CFD is envisaged as a prevailing tool to gain more control in the delivery of reactants or energy and in the removal of products since any chemical or physical transformation process requires the addition or removal of different materials and energy. Therefore, the distribution of materials as well as the energy within the process vessel is improved noticeably if one has the capability to predict and control fluid dynamics by means of CFD. Instead of extensive and costly experimentation, CFD models allow the optimization of process equipment to maximize industrial benefit following rigorous environmental regulations. CFD enable the establishment of quantitative relationships between the throughput and operating flow regime avoiding a massive number of empirical parameters. Transport parameters such as heat- mass-transfer coefficients and several hydrodynamic parameters including film structures and thicknesses, boundary layer geometries, pressure drop, wetted area or even the residence time distribution are investigated and optimized for multiple process configurations. Consequently, CFD aids in the identification of most appropriate process configurations from the large selection of alternatives.

In fact, in the realm of environmental reaction engineering, major improvements on active and stable heterogeneous catalyst are intended to be realized in the near future. This fact will allow substantial enhancements of catalytic wet oxidation technology to become economically and environmentally feasible in comparison to most of the conventional treatments. In this ambit, agro-food processing wastewaters will be undertaken as an example of non-biodegradable and phytotoxic effluents. Polyphenolic compounds deserve particular attention in what concerns the process performance at different levels as follows: total organic carbon reduction, intermediate compounds formation, catalyst stability and kinetic modelling. The kinetic parameters will be obtained taking into account the

generalized lumped kinetic model and this information will be further integrated into a hydrodynamic model developed by means of CFD where the reaction aspects as well as the transport mechanisms were accounted for a high-pressure trickle-bed reactor. Two multiphase CFD frameworks - Euler-Euler and Volume-of-Fluid - will be evaluated for either cold flow or reacting flow conditions. Axial and radial profiles of hydrodynamic and reaction parameters will be thoroughly evaluated at different operating conditions. The influence of gas and liquid flow rates as well as the effect of temperature and pressure will be investigated in terms of total organic carbon conversions.

## 2. Literature review

In the field of environmental reaction engineering, long-established technologies have been intensified during the last decade to demonstrate new potentialities and hindrances from a process viewpoint. Having recognized the effect of technological threats generated by dangerous substances on the environment, it is possible to identify a gap of knowledge on how to provide consistent remediation technologies of contaminated air, soil and water. In this regard, multiphase reactors such as trickle-bed reactors (TBRs) can then be evaluated on its further deployment for the catalytic abatement of moderate- to high-strength wastewaters if one takes into account modern and advanced simulation tools as CFD codes. The specialized literature identified various dynamic circumstances in TBRs as a new breed potential for performance enhancement arising from the interaction between the gas and liquid phases in supplying reactants to the catalyst surface and pores. This fact is even reinforced due to the multifaceted relationship between fluid dynamics, catalyst wetting and chemical reaction. Multiphase reactors such as TBRs have been commonly designed and operated under steady-state mode in the industrial applications. However, novel operating modes under transient conditions has generated an emergent interest in view of the significant performance enhancement encompassing chemical conversion and products selectivity (Dudukovic et al., 1999; Boelhouwer et al., 2002; Silveston & Hanika, 2002, 2004). The transient operation of TBR revealed key characteristics reinforced by the dynamic nature of gas-liquid flow over the catalyst packing, which ultimately leads to the cumbersome non-linearity behaviour of trickle beds (Khadilkar et al., 2005). Here, we pursue our prior efforts to provide new insights on environmentally-based TBRs to detoxify hazardous polluted liquid streams. This task is sought to be accomplished by the experimental work devoted to investigate the suitability of this methodology as well as by state-of-the-art simulation tools considered by CFD codes. The case study encompasses the application of a trickle-bed reactor to the detoxification of phenolic wastewaters through a series of experimental runs accompanied and validated by a multiphase Volume-of-Fluid (VOF) model formerly reported (Lopes & Quinta-Ferreira, 2009). At a first glance, a brief prospect of literature on trickle-bed reactor modelling and validation is presented at reaction conditions. Then, the application of CFD is reinforced by its investigation on the minimization of hazardous materials. Iliuta et al. (2006) investigated how plugging affect hydrotreating performance by simulating simultaneous fines deposition under catalytic in hydrodesulfurization in TBRs. The three-phase heterogeneous model developed to simulate the trickle bed performance incorporates the concentration gradients inside the catalyst particle and solid deposit. The model correctly handled the effect of the fine particles deposition process being identified the bed plugging and the increase of the resistance to two-phase flow. Ayude et al. (2005)

presented a phenomenological approach to interpret the effect of liquid flow modulation in TBRs at the particle scale. Dynamic reactant profiles inside the catalytic particle were obtained for different cycling and system conditions being the experimental trends explained with this approach. Liu et al. (2005) examined the periodically operated TBR for ethylanthraquinones hydrogenation. A dynamic model was verified by simulating the effect of cycle period and split on the conversion and the selectivity enhancement and compared with the experimental results. An experimental and theoretical study of forced unsteady-state operation of TBR was presented by Lange et al. (2004) in comparison to the steady-state operation. The simulation studies demonstrate that the liquid flow variation has a strong influence on the liquid hold-up oscillation and on the catalyst wetting efficiency. Rajashekharan et al. (1998) developed a TBR model for the hydrogenation of 2,4 dinitrotoluene with experimental verification. The model incorporates the contributions of partial wetting and stagnant liquid hold-up effects in addition to external and intraparticle mass transfer resistances for a complex consecutive/parallel reaction scheme under consideration represented by Langmuir-Hinshelwood kinetics.

On the investigation of CFD for the risk assessments related to industrial environments, Calay & Holdo (2008) have modelled the dispersion of flashing jets in where gas is kept in liquid form under high-pressure. The authors presented reproducible results to those phenomena related to turbulence, droplet transport, evaporation, break-up and coalescence events. Gavelli et al. (2010) presented a reliable method to quantify and bound LNG vapour dispersion hazard distances for regulatory purposes. The mathematical models encompass conservative assumptions in the derivation of the LNG vapour source term. It is suggested that sophisticated models could be used to predict the flow and vaporization of LNG by numerical integration of the shallow water equations. Pontiggia et al. (2010) have assessed the consequences of hazardous gas releases in urban areas through CFD simulations. Once again, CFD has demonstrated its versatility to represent realistically such complex geometries in detailed simulation models leading to three-dimensional flow fields that strongly influence gas dispersion. The authors have pointed out that integral models can both overestimate and underestimate the magnitude of consequences related to hazardous material releases in urban areas.

From the above survey, CFD models can be trustfully applied in different frameworks, nevertheless such approach has scarcely been reported to predict the reaction behaviour of trickle beds. Apart from the hydrodynamic models evolved at cold flow conditions, we extend our previous VOF model to gain further insight on how process parameters such as liquid velocity, surface tension and wetting phenomena affect the multiphase flow in high-pressure trickle-bed reactor. A Volume-of-Fluid model was developed to simulate the multiphase reactive flow in the catalytic wet oxidation of mimicked agro-industry effluents. As long as the temperature and liquid flow rate play a major role on the decontamination rate of liquid pollutants, several computational runs have to be validated accordingly and performed under transient conditions. This methodology provides a more fundamental understanding of flow environment and TBR chemical behaviour.

### 3. Mathematical models

#### 3.1 Governing flow equations

A trickle bed based on a cylindrical geometry ( $50 \text{ mm}_{\text{ID}} \times 1.0 \text{ m}_{\text{length}}$ ) was modelled with a specified void fraction and a set of fluid physical properties. The computational geometry

was designed so that a distance gap of about 3% of the sphere diameter facilitates the grid generation avoiding numerical difficulties that arise in the calculation of convective terms as described elsewhere (Lopes & Quinta-Ferreira, 2008; Nijemeisland & Dixon, 2001). The VOF method was used to compute velocity field, liquid volume fraction distributions as well as the total organic carbon concentration that was used to quantify the mineralization degree of liquid pollutants. The multiphase flow is assumed to be vertical downward and incompressible, with the mathematical description based on the Navier-Stokes equations for momentum and mass conservation of a viscous fluid flow through a three-dimensional catalytic bed. The variable fields are shared by both phases and correspond to volume-averaged values knowing the volume fraction,  $a_{q,t}$  of each phase,  $q$ , in the entire computational domain. The volume fraction equation for the phase  $q$  is given by:

$$\frac{\partial}{\partial t}(\alpha_q \rho_q) + \nabla \cdot (\alpha_q \rho_q \mathbf{U}_q) = 0 \quad \text{with } q = g \text{ or } l \quad (1)$$

where  $g$  and  $l$  denote, respectively, the gas and liquid phases,  $t$ , being the time, and through the resolution of the momentum equation shared by the two considered fluids:

$$\frac{\partial}{\partial t}(\alpha_q \rho_q \mathbf{U}_q) + \nabla \cdot (\alpha_q \rho_q \mathbf{U}_q \mathbf{U}_q) = -\alpha_q \nabla p + \alpha_q \rho_q \mathbf{g} + \nabla \cdot \alpha_q \left( \overline{\overline{\tau}_q} + \overline{\overline{\tau}_{t,q}} \right) + \mathbf{I}_q \quad \text{with } q = g \text{ or } l \quad (2)$$

where  $p$ ,  $\mathbf{g}$  and the physical properties (density,  $\rho$ ; and viscosity,  $\mu$ ) being determined by volume-weighted averages.  $\mathbf{I}_q$  is the interphase momentum exchange term and  $\overline{\overline{\tau}_q}$  and  $\overline{\overline{\tau}_{t,q}}$  are, respectively, the viscous stress tensor and the turbulent stress tensor, defined as follows:

$$\overline{\overline{\tau}_q} = \mu_q \left( \nabla \mathbf{U}_q + \nabla \mathbf{U}_q^t \right) + \left( \lambda_q - \frac{2}{3} \mu_q \right) \nabla \mathbf{U}_q \overline{\overline{I}} \quad (3)$$

and

$$\overline{\overline{\tau}_{t,q}} = \mu_{t,q} \left( \nabla \mathbf{U}_q + \nabla \mathbf{U}_q^t \right) - \frac{2}{3} \left( k_q + \mu_{t,q} \nabla \mathbf{U}_q \right) \overline{\overline{I}} \quad (4)$$

### 3.2 Free surface model: surface tension and wall adhesion

The continuum surface force model proposed by Brackbill et al. (1992) has been used to compute the surface tension. The pressure drop across the surface depends upon the surface tension coefficient,  $\sigma$ , and the surface curvature as measured by two radii in orthogonal directions,  $R_1$  and  $R_2$ , as expressed by Eq. 5.

$$p_2 - p_1 = \sigma \left( \frac{1}{R_1} + \frac{1}{R_2} \right) \quad (5)$$

where  $p_1$  and  $p_2$  are the pressures in the two fluids on either side of the interface. The surface curvature is computed from local gradients in the surface normal at the interface.  $n$  is the surface normal, defined as the gradient of  $a_i$ :  $n = \nabla a_i$ . The curvature,  $\kappa$ , is defined in terms of the divergence of the unit normal,  $\hat{n}$ :  $\kappa = \nabla \cdot \hat{n}$  where  $\hat{n} = n/|n|$ . The forces at the surface are expressed as a volume force using the divergence theorem assuming the form of Eq. 6.

$$F_j = \sum_{\text{pairs } ij, i < j} \sigma_{ij} \frac{\alpha_i \rho_i \kappa_j \nabla \alpha_j + \alpha_j \rho_j \kappa_i \nabla \alpha_i}{\frac{1}{2}(\rho_i + \rho_j)} \quad (6)$$

### 3.3 Species continuity and energy equations

The predicted flow field including velocities and volume fractions of both phases was further used to solve species transport equations in the catalytic wet air oxidation of a model phenolic solution in the trickle-bed reactor. These equations are expressed in the mass balance equation for any species,  $i$ :

$$\frac{\partial \alpha_q \rho_q C_{q,i}}{\partial t} + \nabla \cdot (\alpha_q \rho_q u_q C_{q,i}) = \nabla \cdot (\alpha_q \rho_q D_{i,m} \nabla C_{q,i}) + \alpha_q \rho_q S_{q,i} \quad (7)$$

where,  $C_{q,i}$  is the concentration of species  $i$  in the  $q^{\text{th}}$  phase (gas or liquid),  $\rho_q$  and  $\alpha_q$  is the density and volume fraction of the  $q^{\text{th}}$  phase.  $S_{q,i}$  is the source for species  $i$  in phase  $q$ . Volume averaged properties of fluids were used for calculating the flux across the control cell. Two-film theory was used for accounting mass transfer and the resistance in gas-liquid film was considered as the rate limiting resistance (Bhaskar et al., 2004). Mass transfer coefficient was computed according to the Satterfield et al. (1978) correlation and heat transfer coefficient was calculated according to the correlation developed by Boelhouwer et al. (2001) as expressed by equations 8 and 9, respectively.

$$Sh = 0.815 Re^{0.822} Sc^{1/3} \quad (8)$$

$$Nu = 0.111 Re^{0.8} Pr^{1/3} \quad (9)$$

The energy equation, also shared among the phases, is shown in equation 10:

$$\frac{\partial}{\partial t}(\rho E) + \nabla \cdot (\bar{v}(\rho E + p)) = \nabla \cdot (k_{eff} \nabla T) + S_h \quad (10)$$

The VOF model treats energy,  $E$ , and temperature,  $T$ , as mass-averaged variables:

$$E = \frac{\sum_{q=1}^n \alpha_q \rho_q E_q}{\sum_{q=1}^n \alpha_q \rho_q} \quad (11)$$

where  $E_q$  for each phase is based on the specific heat of that phase and the shared temperature. The properties  $\rho$  and  $k_{eff}$  (effective thermal conductivity) are shared by the phases. The source term,  $S_h$ , contains contributions from volumetric reaction heat sources, which is given by the product  $\Delta H \times \rho \times r_{TOC}$ .

### 3.4 Two-phase k-ε turbulence model

Taking into account that the Reynolds numbers range for the gas phase is wide (min: 10, max: 2500), the mixture  $k$ - $\epsilon$  approach is used for turbulence modelling (Elghobashi et al., 1984). For incompressible flows, the turbulence parameters are calculated from equations 10-11:

$$\frac{\partial}{\partial t}(\rho_m \varepsilon) + \nabla \cdot (\rho_m u'_m k) = \nabla \cdot \left( \frac{\mu_{t,m}}{\sigma_k} \nabla k \right) + G_{k,m} - \rho_m \varepsilon \quad (12)$$

$$\frac{\partial}{\partial t}(\rho_m \varepsilon) + \nabla \cdot (\rho_m \bar{u}_m \varepsilon) = \nabla \cdot \left( \frac{\mu_{t,m}}{\sigma_k} \nabla \varepsilon \right) + \frac{\varepsilon_m}{k_m} \times (C_{1\varepsilon} G_{k,m} - C_{2\varepsilon} \rho_m \varepsilon) \quad (13)$$

and the turbulent viscosity  $\mu_{t,m}$  and the production of turbulence kinetic energy,  $G_{k,m}$  are computed from Eq. 14.

$$\begin{aligned} \mu_{t,q} &= \rho_q C_\mu \frac{k_q^2}{\varepsilon_q} \\ G_{k,m} &= \mu_{t,m} \left( \nabla \bar{u}_m + (\nabla \bar{u}_m)^T \right) : \nabla \bar{u}_m \end{aligned} \quad (14)$$

$C_\mu$  is equal to 0.09 and  $C_{1\varepsilon}$  and  $C_{2\varepsilon}$  are the constants of standard  $k$ - $\varepsilon$  model: 1.44 and 1.92, respectively, whereas  $\sigma_k$  and  $\sigma_\varepsilon$  are the turbulent Prandtl numbers for  $k$  and  $\varepsilon$ , 1.0 and 1.3, respectively.

### 3.5 Numerical simulation

The interstitial space of the trickle-bed reactor was designed through a tetrahedral mesh representing that was created using the integrated solid modelling and meshing program GAMBIT (2005) mimicking the characteristic dimensions of commercial catalyst N-140 supplied by the Süd-Chemie Group, Munich. The VOF method simulates free-surface flow by means of a fluid fraction function, which has a value between unity and zero. The discretization of the governing equations is done by the finite-volume method. The grid independency was established after the evaluation of different mesh natures and apertures in order to isolate mesh related discretization errors. All transport equations were discretized to be at least second order accurate in space. A segregated implicit solver available in commercial CFD package FLUENT 6 (2005) was employed to evaluate the resulting linear system of equations. The conditions required for grid convergent results are based on a 1% relative error criterion and the simulations accuracy has been assessed by comparisons to experimental data available in the literature. At the interface, the additional interaction conditions depend on interfacial velocity and gradient of the surface tension.

The CWAO kinetic parameters for the commercial catalyst N-140 were similarly derived to the work developed by Lopes et al. (2007). The right-hand side term of Eq. 7,  $S_{i,q}$ , include the reaction rates in terms of the total organic carbon concentration of the lumped species  $A$ ,  $B$  and  $C$  as represented by Eq. 15:

$$\begin{aligned} -r_{TOCA} &= -\frac{dC_{TOCA}}{dt} = (k'_1 + k'_2) C_{TOCA} \\ -r_{TOCB} &= -\frac{dC_{TOCB}}{dt} = k'_3 C_{TOCB} - k'_2 C_{TOCA} \end{aligned} \quad (15)$$

where first order reactions were assumed for each mechanism step of the Generalized Kinetic Model. GKM considers three types of compounds: easier degraded reactants ( $A$ ); intermediates with difficult degradation ( $B$ ) and desired end products, namely carbon dioxide and water ( $C$ ). In the oxidation process of the phenolic solutions with N-140 catalyst,

phenol and acetic acid were formed as intermediate compounds, being totally degraded during the treatment and the overall TOC practically reduced to zero. After integrating these equations a mathematical expression for TOC evolution is obtained in Eq 16:

$$\frac{C_{TOC}}{C_{TOC_0}} = \frac{k'_2}{k'_1 + k'_2 - k'_3} e^{-k'_3 t} + \frac{k'_1 - k'_3}{k'_1 + k'_2 - k'_3} e^{-(k'_1 - k'_2)t} \quad (16)$$

The activation energies and the pre-exponential factors were calculated by using the Arrhenius plot for the N-140 kinetic studies. These values were used in the corresponding expressions of the reaction rate constants  $k'_1$ ,  $k'_2$ ,  $k'_3$  as a function of temperature, according to Arrhenius law as described in Eq 17:

$$\begin{aligned} k'_1 &= 452 \cdot \exp\left(-\frac{3.121 \times 10^3}{T}\right) \text{min}^{-1}; \\ k'_2 &= 28.1 \cdot \exp\left(-\frac{3.612 \times 10^3}{T}\right) \text{min}^{-1}; \\ k'_3 &= 4.32 \times 10^6 \cdot \exp\left(-\frac{9.814 \times 10^3}{T}\right) \text{min}^{-1} \end{aligned} \quad (17)$$

The trickle-bed reactor studies have been carried out in pilot plant as illustrated in Fig. 1 comprising a cylindrical reactor in stainless steel (SS-316) with 50 mm of internal diameter and 1.0 m length and the experimental procedure has been described elsewhere (Lopes & Quinta-Ferreira, 2010).

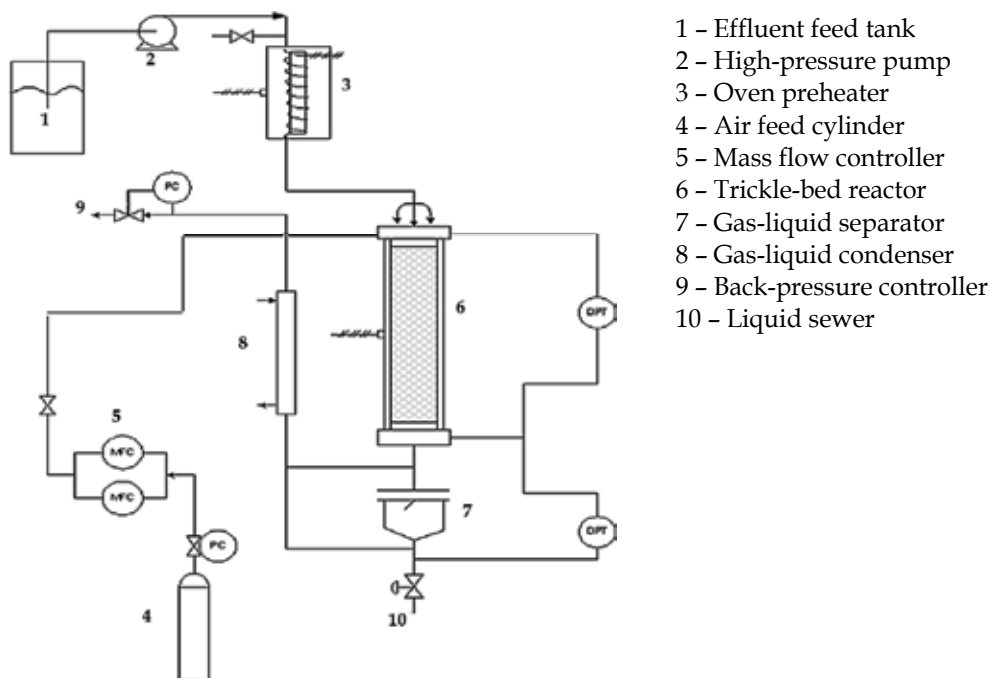


Fig. 1. Schematic diagram of trickle-bed reactor experimental set-up

## 4. Results and discussion

### 4.1 Mesh and time sensitivity tests

To check grid independence, several computational runs were carried out to figure out the mesh density with different apertures. An introductory parametric optimization was also accomplished querying the effect of different differencing schemes on the momentum and volume fraction balance equations. High-order differencing schemes based on Compressive Interface Capturing Scheme for Arbitrary Meshes (CICSAM) and High Resolution Interface Capturing (HRIC) schemes were found to agree better with the experimental data from the literature given that its formulation includes inherently the minimization of artificial numerical dissipation as described elsewhere (Lopes & Quinta-Ferreira, 2009).

We begin with a base case querying the influence of numerical solution parameters including different mesh apertures. The refinement is performed in eight levels: four levels for the coarser meshes with  $2 \times 10^5$ ,  $6 \times 10^5$ ,  $1 \times 10^6$ ,  $1.4 \times 10^6$  of tetrahedral cells and four levels for the finer meshes with  $1.8 \times 10^6$ ,  $2.2 \times 10^6$ ,  $2.6 \times 10^6$  and  $3 \times 10^6$  of tetrahedral cells. Figure 2 displays the influence of the number of tetrahedral cells on the total organic carbon concentration profile when the catalytic abatement of phenolic wastewaters was simulated at  $L=6 \text{ kg/m}^2\text{s}$ ,  $G=0.3 \text{ kg/m}^2\text{s}$  and  $T=200 \text{ }^\circ\text{C}$ ,  $P=30 \text{ bar}$ .

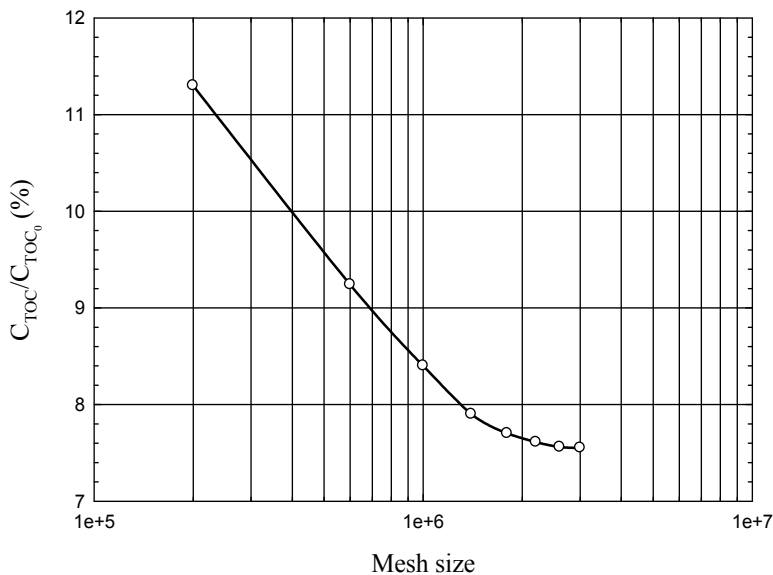


Fig. 2. Comparison of CFD predictions on normalized Total Organic Carbon concentration for different mesh resolutions ( $L = 6 \text{ kg/m}^2\text{s}$ ,  $G = 0.3 \text{ kg/m}^2\text{s}$ ,  $P = 30 \text{ bar}$ ,  $d_p=2 \text{ mm}$ )

As can be seen from Fig. 2, the increase of mesh density led to an asymptotic solution as one increases the number of cells from  $2.2 \times 10^6$  onwards. Low mesh density characterized by  $2 \times 10^5$  of tetrahedral cells at particle surface led to erroneous solutions due to an incorrect definition of boundary layer. As long as the mesh density increases, the theoretical predictions of total organic carbon conversion improve noticeably. Concerning the mesh sensitivity analysis, several computational runs were additionally performed changing the mesh density in the catalyst particle surface to properly capture the boundary layer



now on the temperature profile. The effect of mesh aperture on the thermal behaviour of the trickle-bed reactor is portrayed in Fig. 3 at  $L=6 \text{ kg/m}^2\text{s}$ ,  $G=0.3 \text{ kg/m}^2\text{s}$  and  $T=200 \text{ }^\circ\text{C}$ ,  $P=30 \text{ bar}$ .

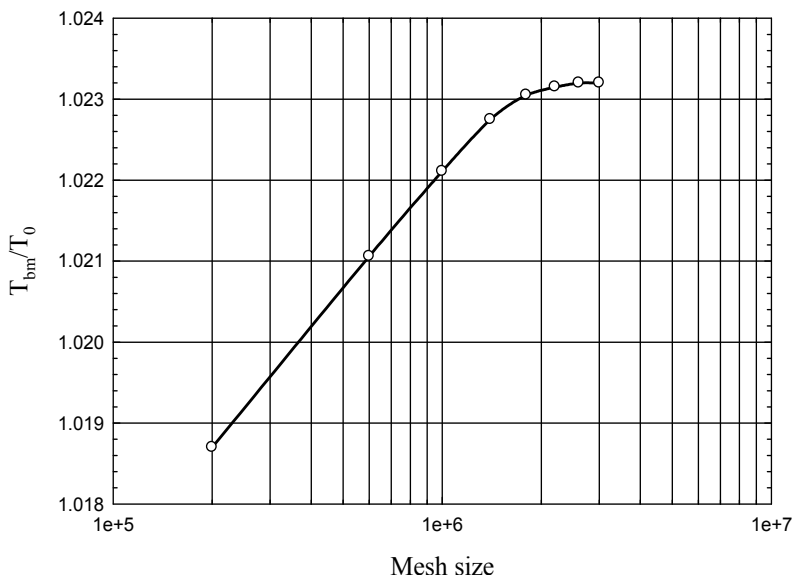


Fig. 3. Comparison of CFD predictions on normalized bulk temperature for different mesh resolutions ( $L = 6 \text{ kg/m}^2\text{s}$ ,  $G = 0.3 \text{ kg/m}^2\text{s}$ ,  $P = 30 \text{ bar}$ ,  $d_p=2 \text{ mm}$ )

Once again, the CFD predictions converged as soon as we used a computational grid comprising 2.2 million of tetrahedral cells. Another mathematical output information revealed by Figs. 2 and 3 is related to the monotony of the total organic carbon conversion and temperature profiles. As evidenced by the mesh sensitivity analysis, the asymptotic demeanour of total organic carbon profile is monotonically decreasing until the final conversion approaches the experimental value at steady-state. On the contrary, the temperature profile is a monotonically decreasing function as one increases the density of the computational grid. Provided that the catalytic wet oxidation follows the Arrhenius's law, the higher conversions or lower percentages of the ratio  $C_{\text{TOC}}/C_{\text{TOC}0}$  are accompanied with increasing values of the bulk phase temperature, see Fig. 3.

The numerical integration encompassed by the CFD model is also dominated by the time-stepping methodology. In the CFD multiphase calculations, we employed first-order and second-order time discretization methods. This latter scheme was found to give confident computed results in comparison to the former one as long as the second-order time-accurate scheme achieves its accuracy by using an Euler backward approximation in time. This fact can in all likelihood be ascribed to the fully implicit methodology which highlighted an unconditional stability. A fair implementation of one of these methods for solving the scalar transport equation entails more than the time-stepping formula. Additionally, we have investigated the time step in the range:  $10^{-5}$ ,  $10^{-4}$ ,  $10^{-3}$  and  $10^{-2} \text{ s}$ . Figure 4 plots the CFD computations of total organic carbon conversions attained with those values at  $L=6 \text{ kg/m}^2\text{s}$ ,  $G=0.3 \text{ kg/m}^2\text{s}$  and  $T=200 \text{ }^\circ\text{C}$ ,  $P=30 \text{ bar}$ .

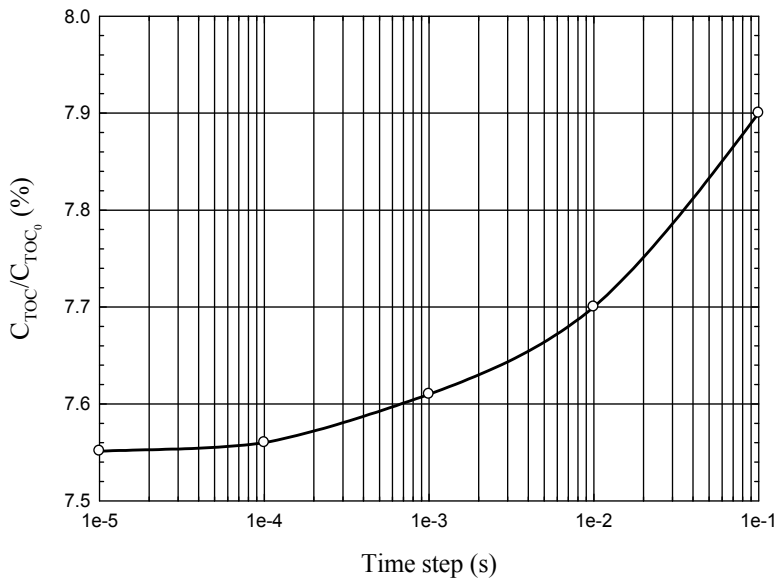


Fig. 4. Effect of time step on normalized Total Organic Carbon concentration ( $L = 6 \text{ kg/m}^2\text{s}$ ,  $G = 0.3 \text{ kg/m}^2\text{s}$ ,  $P = 30 \text{ bar}$ ,  $d_p = 2 \text{ mm}$ )

A similar asymptotic trend was depicted in Fig. 4 so we have identified a time step of  $10^{-5} \text{ s}$  which agreed better with the experimental data. Concomitantly, the analysis of the temperature profile obtained at  $L=6 \text{ kg/m}^2\text{s}$ ,  $G=0.53\text{kg/m}^2\text{s}$  and  $T=200 \text{ }^\circ\text{C}$ ,  $P=30 \text{ bar}$  reinforced the above-mentioned selection on the time step assessment, see Fig. 5.

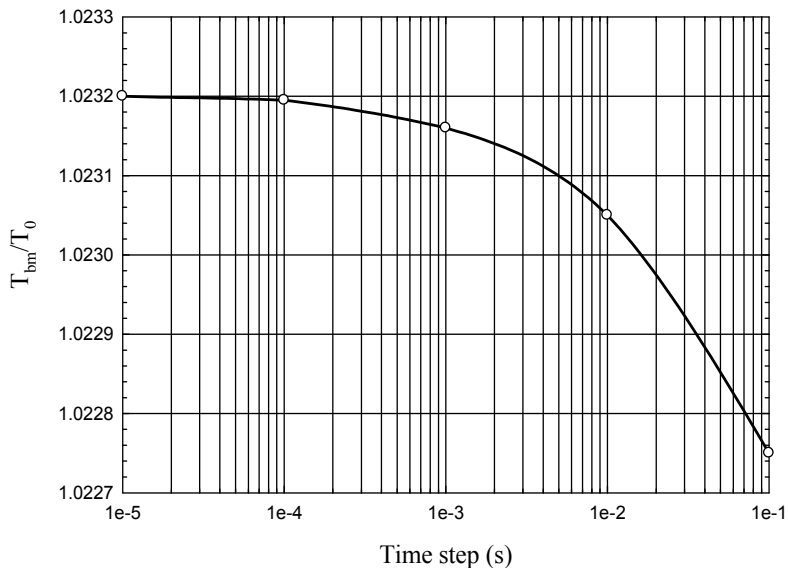


Fig. 5. Effect of time step on normalized bulk temperature ( $L = 6 \text{ kg/m}^2\text{s}$ ,  $G = 0.3 \text{ kg/m}^2\text{s}$ ,  $P = 30 \text{ bar}$ ,  $d_p = 2 \text{ mm}$ )

It is worthy to notice the reverse behaviour that featured the total organic carbon concentration and temperature profiles illustrated in Figs. 4 and 5. As discussed earlier on the monotonic nature of mesh density functions, this suggests again the Arrhenius's temperature dependence of the rate constant for the chemical oxidation reaction.

#### 4.2 Effect of temperature

At  $L=2 \text{ kg/m}^2\text{s}$ ,  $G=0.3\text{kg/m}^2\text{s}$ ,  $P=30 \text{ bar}$ , the VOF computations of total organic carbon conversion along the axial coordinate of trickle-bed reactor are shown with experimental data at different temperatures in Fig. 6.

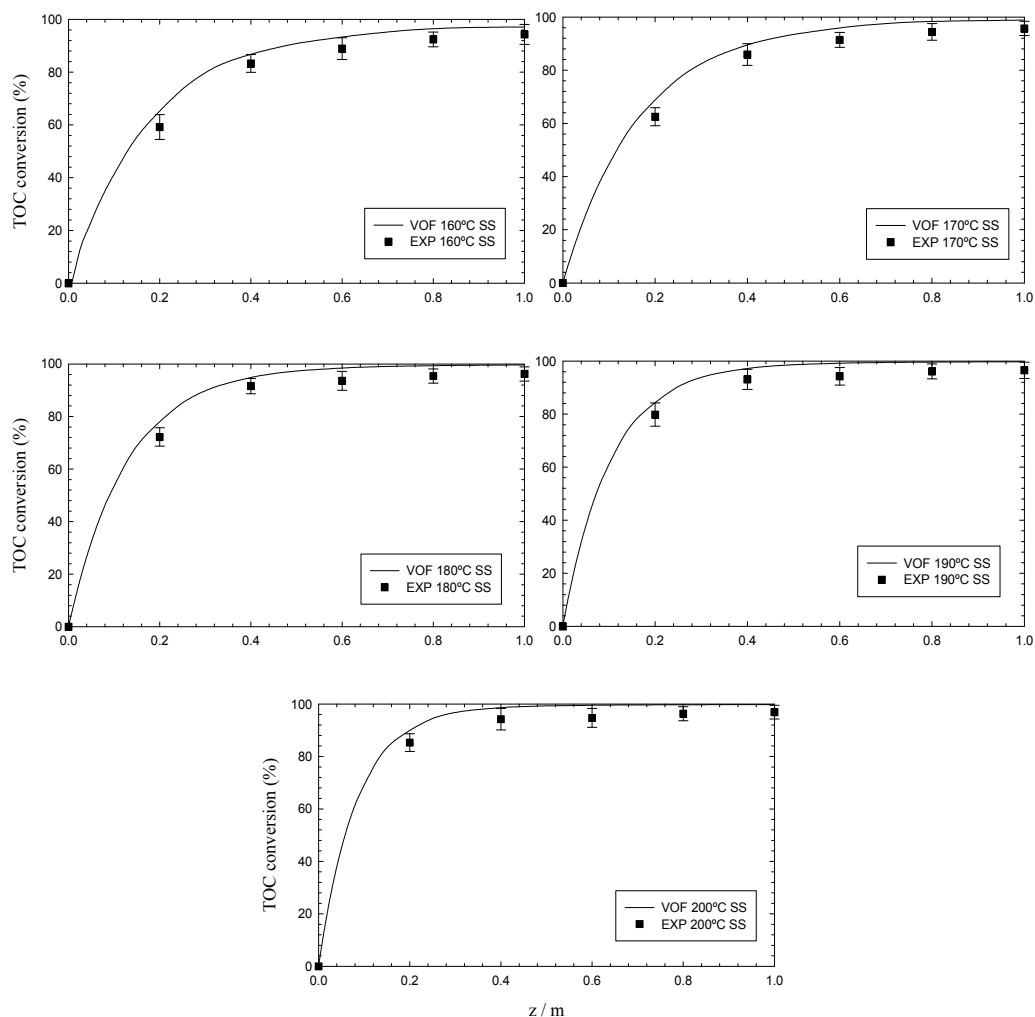


Fig. 6. Mean bulk total organic carbon conversion profiles for axial coordinate at different temperatures ( $L = 2 \text{ kg/m}^2\text{s}$ ,  $G = 0.3 \text{ kg/m}^2\text{s}$ ,  $P = 30 \text{ bar}$ ,  $d_p=2 \text{ mm}$ )

In the range 160-200°C, five characteristic temperatures of catalytic wet oxidation have been used to query the effect of this reaction parameter on organic matter decontamination. As

expected, conversion is favoured by increasing the temperature, hence we have the complete mineralization of organic matter after one half of reactor length when the simulation was carried out at the highest temperature (200°C), see Fig. 6e. However, none experimental measure on total organic carbon concentration has indicated that we have an absolute depletion of organic pollutants from the liquid phase. Examination of successive plots of Fig. 6, provides the ability to compare quantitatively CFD model predictions with the corresponding experimental conversion either through the averaged relative or absolute errors. At the lowest temperature ( $T=160^{\circ}\text{C}$ , see Fig. 6a), the averaged relative errors obtained at  $z=0.2, 0.4, 0.6, 0.8$  and  $1\text{m}$  were 16.2, 24.6, 43.1, 46.4 and 44.8%, respectively. Despite these values are remarkably increasing, the averaged absolute errors are decreasing and we had achieved 5.9, 3.6, 3.8, 2.9, 2.1 for  $z=0.2, 0.4, 0.6, 0.8, 1\text{m}$ , respectively. In fact, the magnitude of the relative errors can be explained by the narrow range of TOC concentrations that were obtained at the reactor egress. At  $z=0.6$  and  $0.8\text{m}$  the TOC conversions were higher than 90% which produced very low concentration ratios  $C_{\text{TOC}}/C_{\text{TOC}0}$  as illustrated in Fig. 6. This behaviour on the complementary nature of both averaged relative and absolute errors warned that every validation accomplished with VOF multiphase model should follow a systematic comparison between those rating parameters. Indeed, at  $T=170^{\circ}\text{C}$  the averaged relative errors obtained with CFD model were 18.6, 30.6, 57.8, 64.1 and 65.9% for  $z=0.2, 0.4, 0.6, 0.8$  and  $1\text{m}$  whereas the averaged absolute errors were 6.4, 3.8, 4.1, 2.9, 2.1, respectively. Moreover, at the highest temperature the magnitude of the averaged relative errors was enlarged hastily to 32.5, 78.4, 90.6, 90.9 and 91.4% albeit the averaged absolute errors kept almost the same intensity that was early identified at lower temperatures as 4.1, 3.9, 3.8, 2.9 and 2.4 for  $z=0.2, 0.4, 0.6, 0.8$  and  $1\text{m}$ , respectively.

According to all VOF computations that have been carried out at  $L=2\text{ kg/m}^2\text{s}$ ,  $G=0.3\text{kg/m}^2\text{s}$ ,  $P=30\text{ bar}$ , one was able to identify the recurring overestimation of total organic carbon conversion for every simulated temperature. Generally, it can be seen from Fig. 6 that computed results agreed better with experimental data at the lower temperatures. This fact has been explained by the formulation of enthalpy balance meaning that a separate enthalpy equation for each phase in Eulerian models is more efficient on the prediction of temperature, which is used to compute the species concentration, against the shared formulation for enthalpy and temperature variables accounted by the current VOF model.

At  $L=2\text{ kg/m}^2\text{s}$ ,  $G=0.3\text{kg/m}^2\text{s}$ ,  $P=30\text{ bar}$ , the averaged axial temperature profiles are depicted by Fig. 7. The thermal behaviour exhibited by the trickle-bed reactor is a distinguishing feature of exothermic reactions. As long as the catalytic wet air oxidation of phenolic pollutants releases energy available from the lower enthalpy of reaction products in comparison to the higher enthalpy of reactants, the chemical conversion of those compounds into water and carbon dioxide is responsible by the temperature increase of bulk phase. This fact led to the heating of catalyst particles more pronounced in the first one fourth of trickle-bed length as portrayed in the thermal profiles of Fig. 7. The higher the inlet temperature was the stronger the increase of bulk phase temperature was attained at steady-state. The averaged relative errors at the lowest temperature were -1.7, -0.5, -0.4, -0.4 and -0.5% for  $z=0.2, 0.4, 0.6, 0.8$  and  $1\text{m}$ , respectively. These averaged relative errors were almost identical to the ones obtained at  $T=170^{\circ}\text{C}$  and they have become lower when the catalytic wet oxidation was performed at the highest temperature giving -1.1, -0.5, -0.6, -0.5, and -0.3% for  $z=0.2, 0.4, 0.6, 0.8$  and  $1\text{m}$ , respectively.

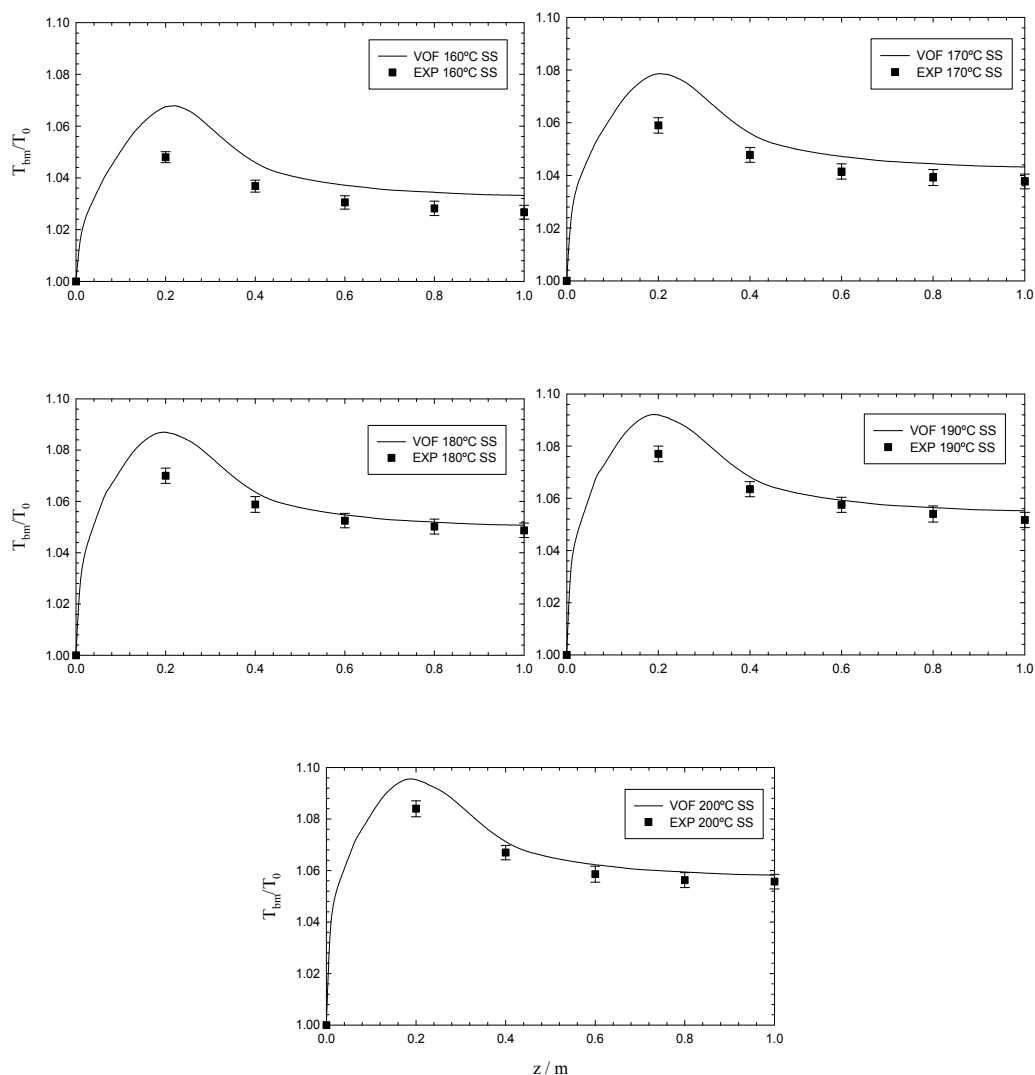


Fig. 7. Mean bulk temperature profiles for axial coordinate at different temperatures ( $L = 2 \text{ kg/m}^2\text{s}$ ,  $G = 0.3 \text{ kg/m}^2\text{s}$ ,  $P = 30 \text{ bar}$ ,  $d_p = 2 \text{ mm}$ )

Having analysed quantitatively these findings, it can be argued that the VOF computations of total organic carbon conversion agreed better with experimental data at lower temperatures, whereas the computed VOF predictions of temperature profiles managed better at higher ones.

#### 4.3 Effect of liquid flow rate

The VOF multiphase model has also been used to query the effect of liquid flow rate on total organic carbon conversion within the above-mentioned temperature range, 160-200°C. Figure 8 shows the axial profiles of total organic carbon conversion attained theoretically and experimentally at  $L = 6 \text{ kg/m}^2\text{s}$ ,  $G = 0.3 \text{ kg/m}^2\text{s}$ ,  $P = 30 \text{ bar}$ .

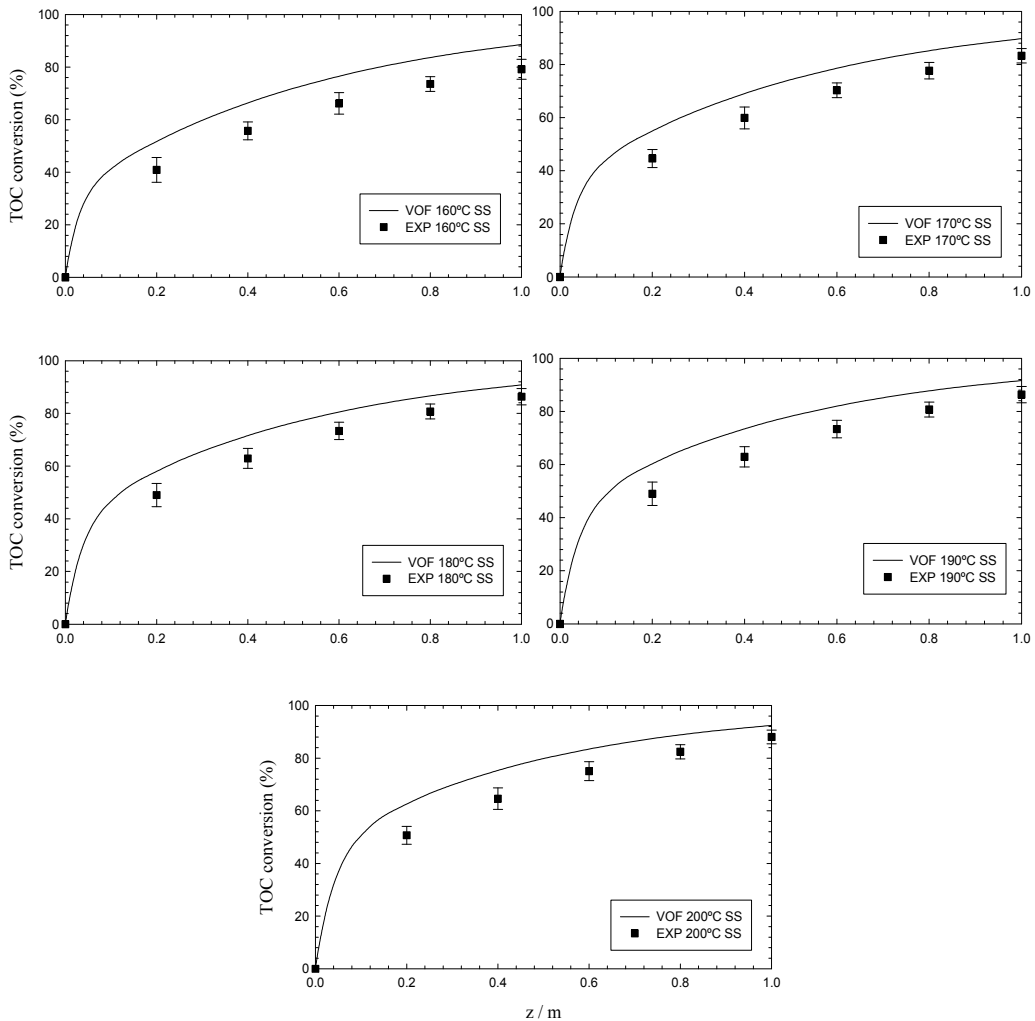


Fig. 8. Mean bulk total organic carbon conversion profiles for axial coordinate at different temperatures ( $L = 6 \text{ kg/m}^2\text{s}$ ,  $G = 0.3 \text{ kg/m}^2\text{s}$ ,  $P = 30 \text{ bar}$ ,  $d_p = 2 \text{ mm}$ )

A fivefold increase on liquid flow rate led to lower decontamination rates as it can be observed from Fig. 8. This behaviour can be explained by the lower residence time of liquid phase which limited the mineralization degree expressed by reminescent total organic carbon concentration. The maximum conversion was obtained at the highest temperature giving 90.7% while 85.1% was achieved at  $T=160^\circ\text{C}$ . Once again, the higher the inlet temperature is, the improved the total organic carbon conversion become at steady-state. When one increases the liquid flow rate up to  $L=6 \text{ kg/m}^2\text{s}$ , the VOF multiphase model also overestimated the decontamination rate as already categorized at lower liquid flow rates. The five series of simulated temperatures illustrated in Fig. 8 were additionally employed on the calculation of both averaged relative and absolute errors. At the lowest temperature, the averaged relative errors attained at  $z=0.2, 0.4, 0.6, 0.8$  and  $1\text{m}$  were 18.2, 25.4, 32.1, 30.9 and 30.2%, whereas the averaged absolute errors were 10.1, 10.7, 10.8, 9.1 and 5.9,

respectively, see Fig. 8a. Increasing the temperature up to  $T=180^{\circ}\text{C}$ , the averaged relative errors became 20.7, 27.8, 33.2, 29.6 and 23.7% while the averaged absolute errors turned out to be 10.9, 10.3, 8.7, 5.1 and 3.3 for  $z=0.2, 0.4, 0.6, 0.8$  and  $1\text{m}$ , respectively. If one increases even further the reactor temperature up to  $T=200^{\circ}\text{C}$ , the computed averaged relative errors were 24.7, 31.3, 35.7, 29.5 and 18.4 whereas the averaged absolute errors happened to be 11.8, 10.7, 8.8, 4.7 and 2.1, see Fig. 8e. This in return translates into an unbiased trend of deviations between the computed results and experimental data in dissimilarity with previous results obtained at the lower liquid flow rate,  $L=2\text{ kg/m}^2\text{s}$ , keeping invariable the gas flow rate and operating pressure ( $G=0.3\text{ kg/m}^2\text{s}$ ,  $P=30\text{ bar}$ ).

Figure 9 shows the computed results and experimental data of the temperature profiles attained axially when the catalytic wet oxidation has been performed at the same five-valued temperature series and at  $L=6\text{ kg/m}^2\text{s}$ ,  $G=0.3\text{ kg/m}^2\text{s}$ ,  $P=30\text{ bar}$ .

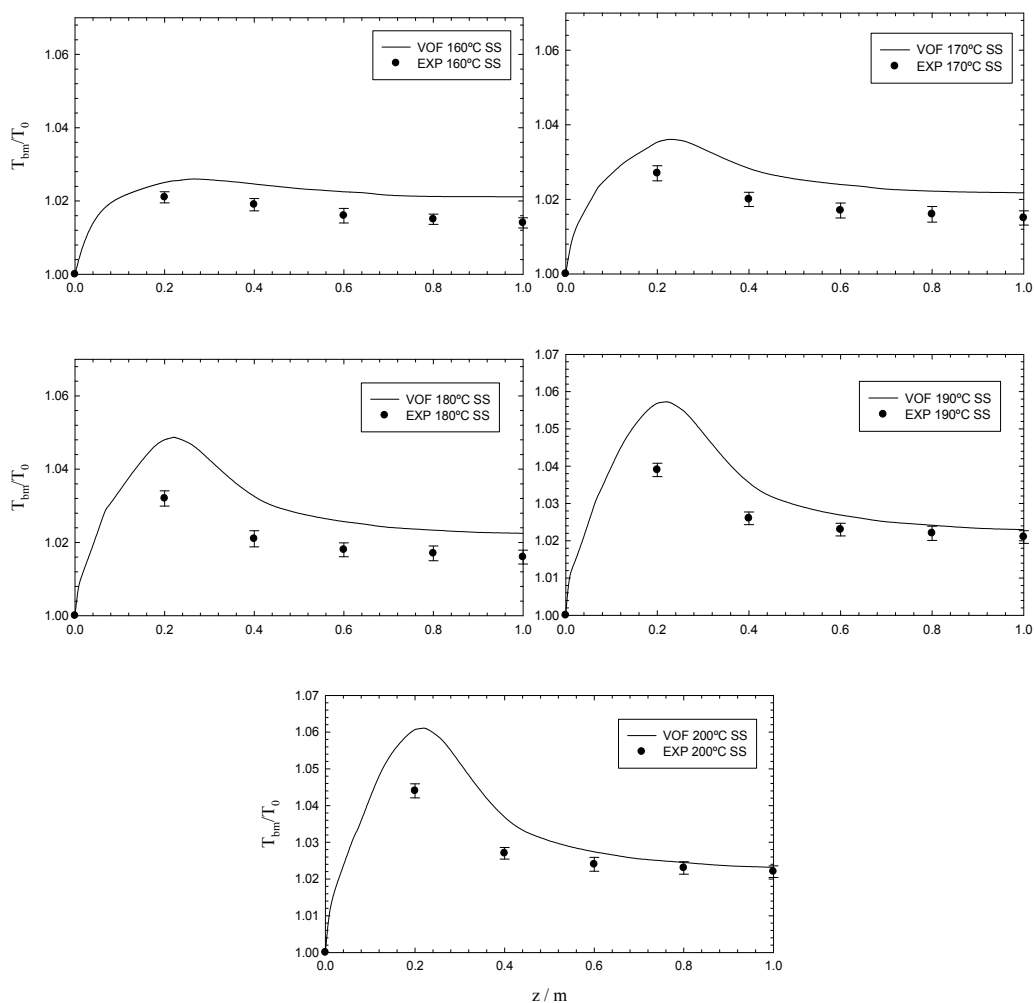


Fig. 9. Mean bulk temperature profiles for axial coordinate at different temperatures ( $L = 6\text{ kg/m}^2\text{s}$ ,  $G = 0.3\text{ kg/m}^2\text{s}$ ,  $P = 30\text{ bar}$ ,  $d_p=2\text{ mm}$ )

As suggested from the simulations displayed in Fig. 9, the temperature increase predicted by the VOF multiphase model was always higher than the experimental value. As the reactor operation is now simulated at higher liquid flow rate, one should expect a reduction on the maximum temperature increase along the trickle-bed reactor. Indeed, the maximum temperature increase obtained at  $L=2 \text{ kg/m}^2\text{s}$  was 8.9% whereas it became 5.2% at  $L=6 \text{ kg/m}^2\text{s}$  meaning that a lower residence time did not allow for such heating degree as one observed for higher liquid phase residence time. At the lowest temperature, the averaged relative errors were -0.2, -0.3, -0.5, -0.5 and -0.6% for  $z=0.2, 0.4, 0.6, 0.8$  and  $1\text{m}$ , respectively. The magnitude of these decreased from the hotspot zone onwards with higher temperatures so we obtained -0.2, -0.1 and -0.2% for  $z=0.6, 0.8$  and  $1\text{m}$ .

#### 4.4 Evaluation of reaction map fields

Prominent research on continuous catalytic wet oxidation of hazardous compounds has identified that hydrodynamics such as phase holdup, pressure drop, and liquid distribution are fundamental criteria for the efficient design of trickle beds. In this ambit and as long as the multiphase flow environment in trickle-bed reactors is strongly influenced by the local phase distribution and the velocity of the gas and the liquid contained in them, here we attempt to examine computationally the interstitial flow in environmentally-based trickle-bed reactors given the inherent difficulties of conventional measurement methods which mainly confer a global view on the trickle bed performance.

Two representative computational mappings of interstitial flow environment are depicted by Figs. 10 and 11 at  $L=6 \text{ kg/m}^2\text{s}$ ,  $G=0.3 \text{ kg/m}^2\text{s}$ , and  $P=30 \text{ bar}$ .

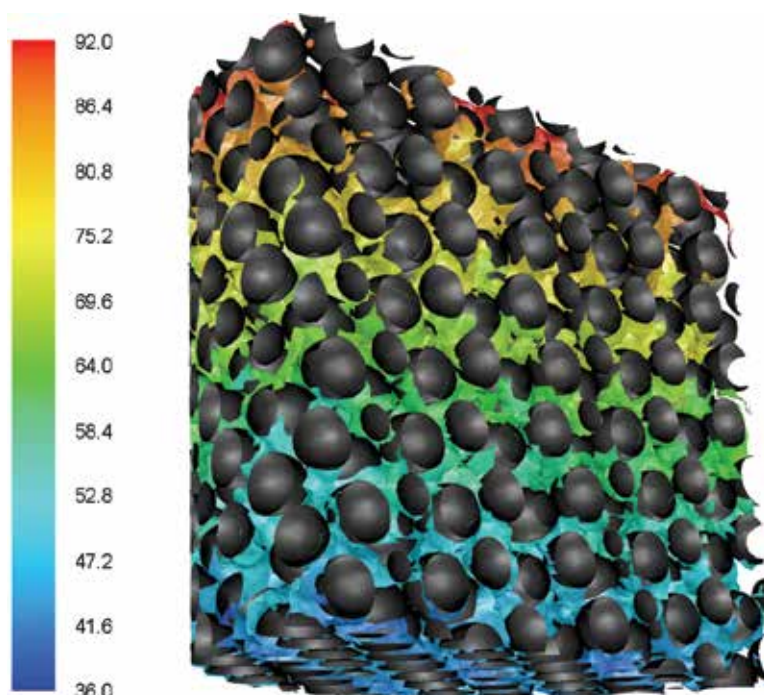


Fig. 10. Instantaneous snapshot of liquid phase distribution coloured by total organic carbon concentration ( $L=6 \text{ kg/m}^2\text{s}$ ,  $G=0.3 \text{ kg/m}^2\text{s}$ ,  $P=30 \text{ bar}$ ,  $T=200^\circ\text{C}$ ,  $d_p=2 \text{ mm}$ )



The former map corresponds to an instantaneous snapshot of liquid phase distribution coloured by total organic carbon concentration while the latter one shows an instantaneous snapshot of liquid phase distribution coloured by temperature at the same operating conditions.

The three-dimensional mappings allow us to ascertain the liquid flow consisting of rivulets and films, the former exhibiting poor liquid-solid contacting regions and the latter being good liquid-solid contacting. Indeed, this computational behaviour was experimentally observed by several authors who have systematized the rivulet/film classification in liquid distribution studies using computer-assisted tomography (Lutran et al., 1991; Ravindra et al., 1997).

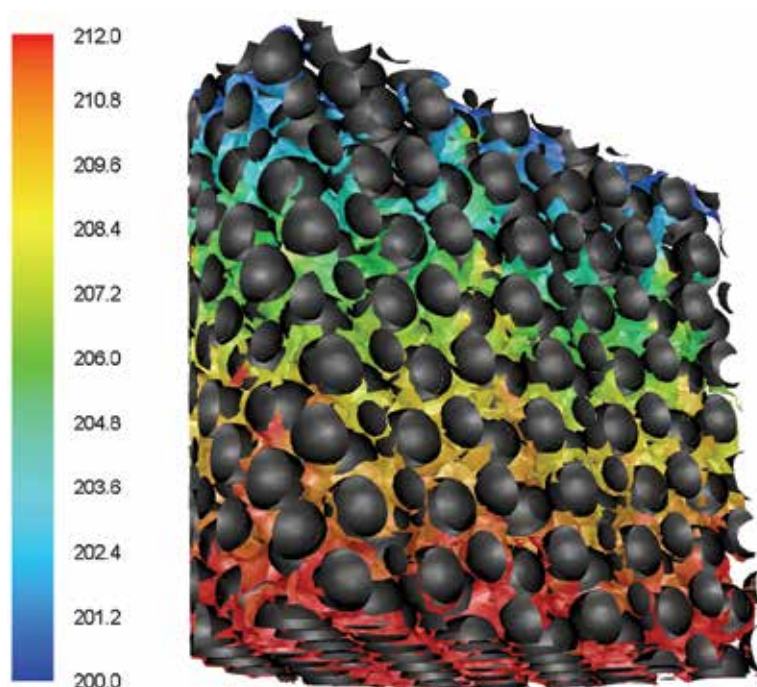


Fig. 11. Instantaneous snapshot of liquid phase distribution coloured by liquid temperature ( $L=6 \text{ kg/m}^2\text{s}$ ,  $G=0.3 \text{ kg/m}^2\text{s}$ ,  $P=30 \text{ bar}$ ,  $T=200^\circ\text{C}$ ,  $d_p=2 \text{ mm}$ )

As one can observe, the liquid distribution is not uniform at the catalyst scale which identified computationally the so-called flow maldistribution of trickle beds. These strong axial and radial heterogeneities were observed experimentally by means of a magnetic resonance imaging technique to directly measure the flow in a pore space of a packed bed (Suekane et al., 2003) that in turn affected the spatial distribution of reaction parameters such as the ones illustrated in Figs. 10 and 11.

## 5. Conclusions

Advanced CFD simulation codes can be used to intensify and demonstrate new potentialities and shortcomings in the field of modern environmental detoxification technologies. In this work, we have developed an integrated experimental and theoretical

framework to give further insights into consistent, safer and cleaner remediation technology of wastewaters contaminated with hazardous compounds by catalytic wet oxidation.

First, our case study encompassed the development of a CFD multiphase model which accounts for the chemical kinetics and interphase coupling hydrodynamics in the constitutive equations. On the optimization of mesh density and time step, the CFD model correctly handled the effect of these numerical solution parameters on the computations of TOC conversion and temperature. Second, particular attention was paid to the axial profiles of temperature and TOC depletion rates. The CFD simulations have shown promising results on how fluid dynamics can be correlated with chemical reaction, namely on the prediction of total organic carbon conversions functionalized by nominal liquid flow rates and attained at different temperatures. Finally, the interstitial flow was analysed by three-dimensional computational mappings of gas-liquid distribution as well as TOC and thermal representations highlighting the inhomogeneous reactive flow environment within the trickle-bed reactor. This methodology encompassed a novel integrated tool which empowered a secure estimation of reaction properties on the simulation of hazardous and complex multiphase flows with adjustable parameters.

## 6. Acknowledgment

The authors gratefully acknowledged the financial support of *Fundação para a Ciência e Tecnologia*, Portugal.

## 7. References

- Ayude, M. A.; Cassanello, M. C.; Martínez, O. M. & Haure, P.M. (2005). Phenomenological approach to interpret the effect of liquid flow modulation in trickle bed reactors at the particle scale. *Chemical Engineering Science*, Vol.60, pp.6262-6269, ISSN 0009-2509.
- Bhaskar, M.; Valavarasu, G.; Sairam, B.; Balaraman, K. S. & Balu, K. (2004). Three-Phase Reactor Model to Simulate the Performance of Pilot-Plant and Industrial Trickle-Bed Reactors Sustaining Hydrotreating Reactions. *Industrial and Engineering Chemistry Research*, Vol.43, pp.6654-6669, ISSN 0888-5885.
- Boelhouwer, J. G.; Piepers, H. W. & Drinkenburg, A. A. H. (2001). Particle-Liquid Heat Transfer in Trickle-Bed Reactors. *Chemical Engineering Science*, Vol.56, pp.1181-1187, ISSN 0009-2509.
- Boelhouwer, J. G. & Piepers, H. W.; Drinkenburg, A. A. H. (2002). Advantages of forced non-steady operated trickle-bed reactors. *Chemical Engineering Technology*, Vol.25, pp. 647-650, ISSN 0930-7516.
- Brackbill, J. U.; Kothe, D. B. & Zemach, C. (1992). A Continuum Method for Modeling Surface Tension. *Journal of Computational Physics*, Vol.100, pp.335-354, ISSN 0021-9991.
- Calay, R. K. & Holdo, A. E. (2008). Modelling the dispersion of flashing jets using CFD. *Journal of Hazardous Materials*, Vol.154, pp.1198-1209, ISSN 0304-3894.
- Dudukovic, M. P.; Larachi, F. & Mills, P. L. (1999). Multiphase reactors – revisited. *Chemical Engineering Science*, Vol.54, pp.1975-1995, ISSN 0009-2509.

- Elghobashi, S.; Abou-Arab, T.; Rizk, M. & Mostafa, A. (1984). Prediction of the Particle-Laden Jet with a Two-Equation Turbulence Model. *International Journal of Multiphase Flow*, Vol.10, pp.697-710, ISSN 0301-9322.
- FLUENT 6.1. User's Manual to FLUENT 6.1. (2005). Fluent Inc. Centerra Resource Park, 10 Cavendish Court, Lebanon, USA.
- GAMBIT 2. User's Manual to GAMBIT 2. (2005). Fluent Inc. Centerra Resource Park, 10 Cavendish Court, Lebanon, USA.
- Gavelli, F.; Chernovsky, M. K.; Bullister, E. & Kytomaa, H. K. (2010). Modeling of LNG spills into trenches. *Journal of Hazardous Materials*, Vol.180, pp.332-339, ISSN 0304-3894.
- Iliuta, I.; Ring, Z. & Larachi, F. (2006). Simulating simultaneous fines deposition under catalytic hydrodesulfurization in hydrotreating trickle beds—does bed plugging affect HDS performance? *Chemical Engineering Science*, Vol.61, pp.1321-1333, ISSN 0009-2509.
- Khadilkar, M. R.; Al-Dahhan, M. H. & Dudukovic, M. P. (2005). Multicomponent flow-transport-reaction modeling of trickle bed reactors: application to unsteady state liquid flow modulation. *Industrial and Engineering Chemistry Research*, Vol.44, pp.6354-6370, ISSN 0888-5885.
- Lange, R.; Schubert, M.; Dietrich, W. & Grünewald, M. (2004). Unsteady-state operation of trickle-bed reactors. *Chemical Engineering Science*, Vol.59, pp.5355-5361, ISSN 0009-2509.
- Liu, G.; Duan, Y.; Wang, Y.; Wang, L. & Mi, Z. (2005). Periodically operated trickle-bed reactor for EAQs hydrogenation: Experiments and modeling. *Chemical Engineering Science*, Vol.60, pp.6270-6278, ISSN 0009-2509.
- Lopes, R. J. G.; Silva, A. M. T. & Quinta-Ferreira, R. M. (2007). Screening of Catalysts and Effect of Temperature for Kinetic Degradation Studies of Aromatic Compounds During Wet Oxidation. *Applied Catalysis B: Environmental*, Vol.73, pp.193-202, ISSN 0926-3373.
- Lopes, R. J. G. & Quinta-Ferreira, R. M. (2008). Three-Dimensional Numerical Simulation of Pressure Drop and Liquid Holdup for High-Pressure Trickle-Bed Reactor. *Chemical Engineering Journal*, Vol.145, pp.112-120, ISSN 1385-8947.
- Lopes, R. J. G. & Quinta-Ferreira, R. M. (2009). VOF based Model for Multiphase Flow in High-Pressure Trickle-Bed Reactor: Optimization of Numerical Parameters. *AIChE Journal*, Vol.55, pp.2920-2933, ISSN 1547-5905.
- Lopes, R. J. G. & Quinta-Ferreira, R. M. (2010). Assessment of CFD Euler–Euler method for trickle-bed reactor modelling in the catalytic wet oxidation of phenolic wastewaters. *Chemical Engineering Journal*, Vol.160, pp.293-301, ISSN 1385-8947.
- Lutran, P. G.; Ng, K. M. & Delikat, E. P. (1991). Liquid distribution in trickle-beds. An experimental study using computer-assisted tomography. *Industrial and Engineering Chemistry Research*, Vol.30, pp.1270-1280, ISSN 0888-5885.
- Nijemeisland, M. & Dixon, A. G. (2001). Comparison of CFD Simulations to Experiment for Convective Heat Transfer in a Gas-Solid Fixed Bed. *Chemical Engineering Science*, Vol.82, pp.231-246, ISSN 0009-2509.
- Pontiggia, M.; Derudi, M.; Alba, M.; Scaioni, M. & Rota, R. (2010). Hazardous gas releases in urban areas: Assessment of consequences through CFD modelling. *Journal of Hazardous Materials*, Vol.176, pp.589-596, ISSN 0304-3894.

- Rajashekharam, M. V.; Jaganathan, R. & Chaudhari, R. V. (1998). A trickle-bed reactor model for hydrogenation of 2,4 dinitrotoluene: experimental verification. *Chemical Engineering Science*, Vol.53, pp.787-805, ISSN 0009-2509.
- Ravindra, P. V.; Rao, D. P. & Rao, M. S. (1997). Liquid flow texture in trickle-bed reactors: an experimental study. *Industrial and Engineering Chemistry Research*, Vol.36, 5133-5145, ISSN 0888-5885.
- Satterfield, C. N.; van Eek, M. W. & Bliss, G. S. (1978). Liquid-Solid Mass Transfer in Packed Beds with Downward Concurrent Gas-Liquid Flow. *AIChE Journal*, Vol.24, pp.709-717, ISSN 1547-5905.
- Silveston, P. L. & Hanika, J. (2002). Challenges for the periodic operation of trickle-bed catalytic reactors. *Chemical Engineering Science*, Vol.57, pp.3373-3385, ISSN 0009-2509.
- Silveston, P. L. & Hanika, J. (2004). Periodic operation of three-phase catalytic reactors. *Canadian Journal of Chemical Engineering*, Vol.82, pp.1105-1142, ISSN 1939-019X.
- Suekane, T.; Yokouchi, Y. & Hirai, S. (2003). Inertial flow structures in a simple-packed bed of spheres. *AIChE Journal*, Vol.49, pp.10-17, ISSN 1547-5905.

# Simulating Odour Dispersion about Natural Windbreaks

Barrington Suzelle, Lin Xing Jun and Choiniere Denis

*Department of Bioresource Engineering, Macdonald Campus of McGill University,  
Consumaj inc.  
Canada*

## 1. Introduction

Worldwide, population and economic growth has reduced the distance separating residential areas and odour sources. Annoyance can result from not only obnoxious odours but also prolonged pleasant odours such as produced by a chocolate or frying factory. Odours indirectly affect human health through stress (Evans & Cohens, 1987) and their impact is greater when humans are exposed to a continuous rather than an intermittent source. People with a problem coping style (seeking a solution to the odour problem) can become more annoyed by odours than those using comforting cognition (telling themselves that the situation will improve) or having an emotional oriented style (those looking for a diversion) because the solution is often out of hand (Cavalini et al., 1991). Although pleasant odours can become annoying when too concentrated or persistent, malodours are perceived as unpleasant under most if not all conditions. Malodours are also known to activate a different area of the brain, as compared to pleasant odours (Zald & Pardo, 2000). According to Jacob et al. (2003), the response of humans to malodours is quite consistent and it differs compared to that of pleasant odours which produce a wider range of response. Furthermore, Jacob et al. (2003) found that the detection of any odour increases with dose and duration, but that the change in response of humans is much more important for small increases of malodour concentrations when presented at a low level just above their detection threshold.

Accordingly, odour dispersion models must take into consideration the olfactory response of humans. Noxious odours are likely much easier to model because most humans will classify them as an annoyance, as opposed to pleasant odours where the response is more variable. Furthermore, the human olfactory sense will detect the presence of an odour at a low level and if noxious, will immediately classify it as a nuisance. As the air concentration of the odorous gas increases, the relative level of annoyance does not increase as quickly. Furthermore, at a specific odorous gas air concentration, the response becomes intolerable and increasing the concentration any further will not increase the level of annoyance. To be accurate, this type of response must be incorporated into an odour dispersion model.

The use of separation or setback distances for odour sources conveniently insures the dilution of malodours to acceptable levels in the vicinity of neighbours (Redwine & Lacey, 2000). Nevertheless, conventional separation distances rely on the generalized odour

emission associated with a given operation regardless of management issues. Accordingly, separation distances do not provide satisfactory legislation against nuisance in many instances (Jacobston et al., 2005). Effective separation distances need to consider a greater number of factors pertaining to odour emission rate and character, and subsequent dispersion before reaching the neighbours. Furthermore, management practices can change the cleanliness of the operation, the frequency and intensity of odour emissions and the location of the source on the property (Li & Guo, 2008; Le et al., 2005; Lim et al. 2001). Physical and climatic factors constitute other factors, namely topography and buildings, and atmospheric stability, air temperature, and wind velocity and direction (Schauberger et al., 1999; Zhu et al. 2000; Lin et al., 2007c, 2009a,b).

To improve the calculation of separation distances, several industrial models were modified for agricultural applications. The first models were steady state and Gaussian based (Chen et al., 1998; Smith & Watts, 1994) with a normally distributed exponential function extrapolated to ground level. Examples of such models are the ISCST3 and AUSPLUME. Later, McPhail (1991) and Gassman (1993) suggested that odours should be modelled as a series of puffs, to produce cycles of strong followed by weaker odour concentrations. An example of such models is INPUFF2, which is Gaussian based and is capable of simulating the release of odours over short intermittent periods. Zhu et al. (2000) tested this model in the Canadian Prairie Provinces with swine operations and resident panellists trained to compare odour annoyance against the n-butanol scale (ASTM 1999). Whereas the accuracy was relatively high up to a distance of 300 m from the source, INPUFF2 performed poorly at distances exceeding 400 m, where simulation was critical in determining the annoyance limit of the odour plume. Furthermore, the odour source emission rate needed to be scaled up by a factor of 35 and 10, for odours from livestock shelters and manure storages, respectively. CALPUFF is another Gaussian dispersion model simulating the dispersion of odours released over short time intervals, but with the added advantage of a Lagrangian function simulating the effect of spatially variable wind conditions. Xing et al. (2006) evaluated CALPUFF along with three other models, using once more panellists trained to recognize odour intensity using the n-butanol scale. The agreement between measured field data and the four models ranged between 37 and 50 %.

Computational Fluid Dynamics models have successfully simulated gas dispersion in complex spaces (Riddle et al., 2004), such as ammonia distribution in barns (Sun et al., 2002) and spray droplet transport in fields (Ucar & Hall, 2001). Lin et al. (2007b, 2009a, b) produced a model based on Computational Fluid Dynamics (CFD) to simulate odour dispersion downwind from natural windbreaks. The model was calibrated with field odour observations using panellists trained to associate odour concentration with an odour annoyance scale of 0 to 10, where 10 is the maximum level of annoyance. The CFD model required as input, the exponential equation correlating odour annoyance and concentration, as perceived by the panellists in an olfactory laboratory, after each morning of field measurements. The  $R^2$  exceeded 0.75 when all the data beyond 150 m was considered, as these observation points corresponded to odour concentration below  $117 \text{ OU m}^{-3}$  and within the annoyance scale of 1 to 10. For odour concentrations exceeding  $117 \text{ OU m}^{-3}$ , the panellists were assigning the maximum annoyance level of 10, irrespective of the odour concentration value. In contrast, the n-butanol scale uses an odour intensity scale of 1 for  $25 \text{ OU m}^{-3}$ , of 2 for  $72 \text{ OU m}^{-3}$ , and so on up to  $1834 \text{ OU m}^{-3}$  for a scale of 5 (Guo et al., 2001). Accordingly, the n-butanol scale is designed to measure high odour concentration levels

whereas the method used by Lin et al. (2007b, 2009a, b) is designed to measure odour levels in the vicinity of the threshold values. In determining separation distances, the threshold values can be most useful.

Windbreaks were suggested in the late 1990's as a possible odour dispersion technique. Based on Asian research demonstrating the successful reduction of odours, North American livestock producers have used natural and artificial windbreaks on the fan side of livestock shelters to reduce odours emissions. The effect of a porous wall was studied by means of smoke emitters and simulated using a Gaussian model (Bottcher et al., 2000; Bottcher et al., 2001). The porous wall was found to vertically divert the odours from the exhaust fans and promote mixing with the wind flowing over the building, but not to be as effective as tall stacks. In Asia, solid walls have been used around livestock barns to precipitate dust released by the ventilation system (Bottcher, 2000). Dust has been shown to carry odours (Das et al., 2004). Such application requires a windbreak with a high porosity capable of reducing wind velocity and turbulence. The same principle has been applied to control snow and sand accumulation, reduce pesticide drift, increase crop yield and reduce heat losses from animals and buildings (Plate, 1971; Heisler & Dewalle, 1988; Wang & Takle, 1997; Ucar & Hall, 2001; Guan et al., 2003; Vigiak et al., 2003; Wilson & Yee, 2003a). Accordingly, several North American cooperative extension services offer information on planting natural windbreaks or tree shelter belts, suggesting a high porosity in the absence of solid scientific testing.

The objective of the present chapter is therefore to present the development of a model simulating the dispersion of odours or the size of the odour plume formed downwind from a natural shelter belt or windbreak located at a specific distance from an odour source. The purpose of the model was to identify the best management practices for the implementation of natural windbreaks minimizing the size of the odour plume; best management practices pertain to the properties of the windbreak itself, its location with respect to the odour source and the general climatic environment for the given region. The model uses Computational Fluid Dynamics (CFD) to estimate the size and intensity of the odour plume to establish the necessary separation distance between the source and the neighbouring receptor susceptible to annoyance. The model development includes the selection of a computational method capable of handling conditions of high turbulence, the addition of an olfactory perception equation and finally the output validation.

In summary and with the windbreak dispersion model developed, this Chapter will examine the features of natural windbreaks which enhance atmospheric dispersion and maximize the reduction in odour plume length. Finally, this Chapter will examine the effect of various climatic conditions on the performance of windbreak and their effectiveness in shortening odour plumes.

## **2. Field acquisition of calibrating and validating data**

Field odour dispersion data was required to calibrate and validate the model. As well, typical natural windbreak characteristics were required to establish equations for its physical description. The field work therefore consisted in producing an odour generator which could generate an odorous air stream from a single point. Then, 5 sites were used to measure odour plumes under different climatic conditions: 1 control site without a windbreak, and 4 sites where the windbreaks offered different combinations of tree type, dimension and porosity. The distance between the odour generator and the windbreak were

also varied. In all, 39 different field tests were conducted to obtain data for the calibration and validation of the model.

### 2.1 The field instruments

A mobile odour generator was designed and built to be able to produce, in the field, a controllable level of odour emissions during the experiment (Lin et al., 2006). The odour generator consisted of a 500 L tank filled with swine manure (Fig. 1). A pump provided a consistent flow of manure over a vertical porous filter through which air was blown at a rate of  $1.65 \text{ m}^3 \text{ s}^{-1}$ . The odour generator offered an air/liquid contact surfaced of  $76.8 \text{ m}^2$ .

During all field tests, the released odorous air was sampled at regular 30 minute intervals using Alinfan® bags. A laboratory forced choice dynamic olfactometer was then used to establish the threshold dilution value of each air samples by the same 12 trained panellists who observed the field odour plume dispersion. Odour concentration (OC) was expressed as "odour units per cubic meter" ( $\text{OU m}^{-3}$ ) (CEN, 2001; Schaubberger et al., 2002; Zhang et al., 2002). The rate of odour production,  $\text{OU s}^{-1}$ , was computed using the air flow rate of the odour generator.



Fig. 1. The odour generator carried on a truck to be positioned at specific distances upwind from the windbreak (Lin et al., 2006)

During each field test and installed on a 7.6 m high tower, a weather station was positioned 200 m upwind from the windbreak to avoid disturbance. At one minute intervals, a



computer recorded the temperature, wind direction and wind speed. The wind direction was measured before hand to estimate the range of the field odour plume and to direct panellists into the odour plume zone. Air stability values were obtained from the weather station at the Pierre Elliott Trudeau Airport (Montreal, Canada) located 50 km north of the field sites. This weather station was the nearest measuring Pasquill-Gifford atmospheric stability conditions.

## 2.2 The experimental windbreaks

This experiment was conducted using 4 uniform single row natural windbreaks located at least 5 km away from any livestock operation to eliminate interferences (Table 1; Fig. 2). The porosity of each windbreak was optically evaluated by measuring the percentage of open surface visible through the windbreak (Heisler and Dewalle, 1988; Guan et al., 2003).

Each natural windbreak was different in terms of porosity, tree type and height (Lin et al., 2006). The optical porosity of the windbreaks on sites 1 and 3 was 0.55 compared to 0.35 for those on sites 2 and 4 (Table 1). The windbreaks on sites 1 and 2 were of deciduous trees as compared to conifers for those on sites 3 and 4. All sites were located on farm land with a relatively flat and consistent slope of 0.1 % and the vegetation did not exceed a height of 0.7 m. Tree height was the other parameter which varied among windbreaks, sites 1 and 4 offering windbreaks with a height exceeding 15 m compared to sites 2 and 3 offering windbreaks with a height under 10 m. A control site (site 5) without windbreak was selected to also observe odour dispersion. This site consisted of relatively flat (0.1 % uniform slope) land without trees or fences, where a cereal crop had been freshly harvested.

## 2.3 The panelists and the olfactomètre

For the field tests and the laboratory olfactory work, three groups of four panellists were trained by requiring them to detect n-butanol at concentrations of 20 to 80 ppb and to show consistency in their individual measurements (Choinière and Barrington, 1998; Edeogn et al., 2001). In the field, the panellists were trained to evaluate the hedonic tone (HT) of the ambient air using a scale of 0 to -10, where 0 to -2 is tolerable, -2 to -4 is unpleasant, -4 to -6 is very unpleasant, -6 to -8 is terrible and -8 to -10 is intolerable. For each day of field testing, HT evaluations were translated into OC ( $\text{OU m}^{-3}$ ) by asking the panellists in the laboratory, to evaluate the HT of various dilutions of the odorous air samples collected at the generator and at known OC strengths. The reading of each panellist forming a group of four was averaged to convert the field HT observations into OC.

The laboratory forced choice dynamic olfactometer used in this experiment was fully automated and capable of analyzing 4 contaminated air samples in 20 minutes, using 12 panellists. The olfactometer is unique because of its level of automation and speed suitable to evaluate air samples (Choinière and Barrington, 1998).

## 2.4 The field testing operation

Before each field test, the odour generator and weather station tower were checked and installed upwind from the windbreak. During the tests, the odour generator was positioned upwind from the windbreak, at a distance of 15, 30, 49 or 60 m. Each three groups of four panellists was assigned evaluation points organized in a zigzag pattern over part of a 25 ha area (500 m x 500 m downwind from the windbreak or odour generator) and given a GPS to keep track of their exact field position. Panellist paths were also designed to overlap each other.

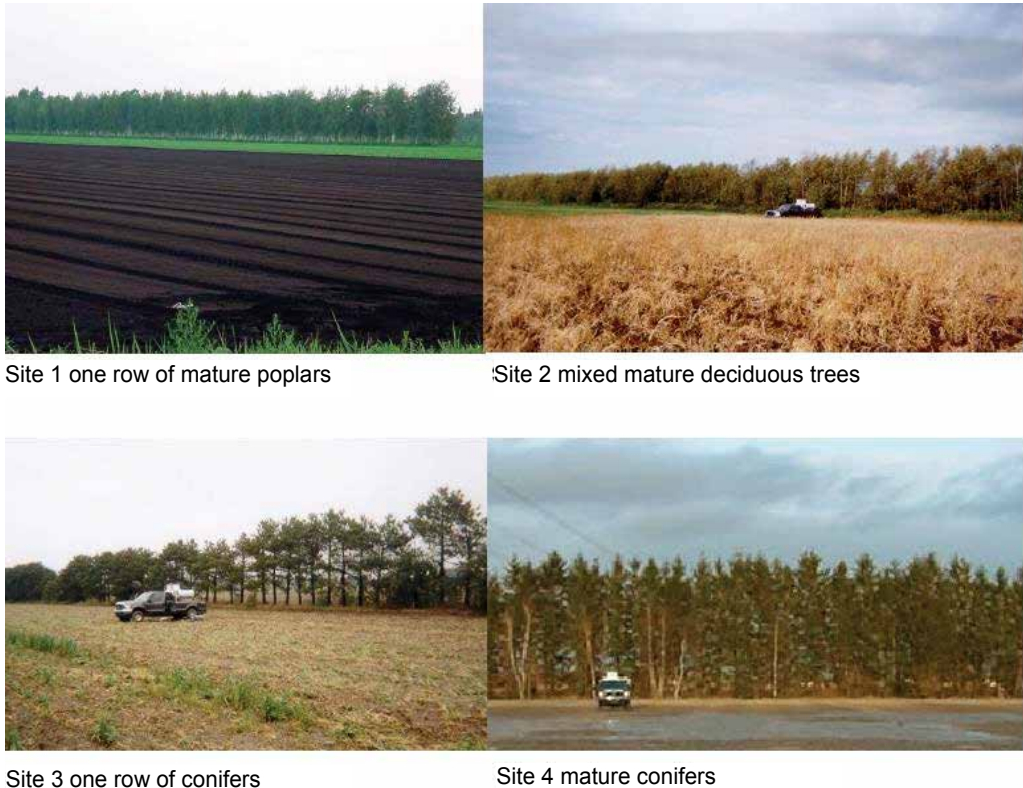


Fig. 2. The four experimental windbreaks each offering a different type of tree and/or porosity (Lin et al., 2006)

After operating the odour generator for 15 minutes, the groups of panellists would start covering their specified overlapping zigzagged path and measure the odour plume. At each measurement point, the group would stop walking, removed their face masks and evaluate for one minute the hedonic tone (HT) of the ambient air using the scale of 0 to -10. An odour point was defined as a point in the field where at least 50 % (2 out of 4) of the panellists detected an odour. The HT of the ambient air at an odour reading point was averaged from the four panellist evaluations.

During each test day, the odour plume was observed in the morning by 12 trained panellists. Then, in the afternoon, the same 12 panellists evaluated the air samples collected at the odour generator using the laboratory olfactometer. This laboratory work served two purposes: measure the odour concentration (OC in  $\text{OU m}^{-3}$ ) of each odorous air sample, and; correlate the measured field hedonic tone (HT) observed by the panellists with odour concentration values. This correlation was then used to translate the HT plumes into OC plumes.

During 18 days between the end of August and the beginning of December 2003, 39 different tests were conducted on the 4 windbreak sites and the single control site (Lin et al., 2006). On the control site without a windbreak, 6 repeated tests were conducted on 4 different days. Then, 33 tests were conducted on the 4 windbreak sites. A total of 12, 11, 9 and 1 tests were conducted with the odour generator located 15, 30, 60 and 49 m upwind

from the windbreak, respectively. Tests on site 4 were conducted in December 2003, because of delays in finding a suitable windbreak site.

During each test, the odour generator emitted a decreasing odour level and, from one test to other, the odour level varied. Each odour plume was therefore standardized for purposes of comparison. Thus, the odour concentration measured at every station by each group of panellists, at a given period in time, was divided by the odour concentration of the generator at that time, and multiplied by the average odour level of 471.6 OU m<sup>-3</sup> calculated from all 39 tests.

| Description                       | Site        |                        |           |            |
|-----------------------------------|-------------|------------------------|-----------|------------|
|                                   | 1           | 2                      | 3         | 4          |
| Tree type                         | poplar      | mixed mature deciduous | conifers  | conifers   |
| Windbreak                         |             |                        |           |            |
| - length (m)                      | 2100        | 1050                   | 405       | 380        |
| - height (m)                      | 18.3        | 9.2                    | 7.6       | 15.2       |
| - depth (m)                       |             | 7                      |           | 6          |
| - optical porosity (fraction)     | 0.55        | 0.35                   | 0.55      | 0.35       |
| - porosity at the base (fraction) | 0.70        | 0.30                   | 0.70      | 0.40       |
| Location                          | Sherrington | St Chrysostome         | St Amable | St Charles |

Table 1. Description of experimental windbreak sites with tree type. All locations are located within 50km of the Island of Montreal, Canada, in the south west region

## 2.5 The statistical analysis of panelist performance and windbreak dispersion

In the laboratory, the panellists HT as observed in the field needed to be translated into an odour concentration value (OC) using the forced choice dynamic olfactometer. During the 39 tests conducted over 18 days, the odorous air released by the odour generator was samples 78 times or once every 30 minutes. From these 78 samples, 56 were used to have the panellists produced sets of HT and corresponding OC readings. Based on these data sets, a regression equation was produced to correlate OC with HT using SAS (SAS Institute Inc., 2001).

Based on the field data, the effect of the windbreak on the size of the odour plume was tested statistically. A 2 OU m<sup>-3</sup> contour for each measured odour plume was plotted and enclosed within a rectangle to define its length and width equal to the side of the rectangle parallel and perpendicular to the average wind direction, respectively. The statistical classification and covariance models were used to analyze the various factors affecting the size of the odour plume (length and width). The covariance model is the combination of the regression and classification models in the same analysis of variance model (SAS Institute Inc., 2001). The distance between the windbreak and the odour generator (DWO), atmospheric stability (AS), and windbreak porosity were fixed factors used for the classification, and wind speed, wind angle against the windbreak (90° being perpendicular), odour emission rate (OER) and temperature (T) were the continuous factors used for the regression analysis. Tree height and type were not considered in the analysis.

### 3. Model development

The Computational Fluid Dynamic used for this modelling was based on the SST  $k-\omega$  model capable of considering a high level of turbulence (Fluent inc., 2005). The model development respected the following steps: 1) determining the governing equations; 2) meshing the computational domain; 3) selecting the solver capable of defining the fluid properties and its components such as the windbreak, and; 4) setting boundary conditions.

#### 3.1 Governing equations

The air flow moving from one computational cell to the next must respect the governing equations of mass, momentum, energy and species conservation expressed as:

$$\frac{\partial \rho}{\partial t} + \frac{\partial}{\partial x_i}(\rho u_i) = 0 \quad (1)$$

$$\begin{aligned} \frac{\partial}{\partial t}(\rho u_i) = & -\frac{\partial}{\partial x_j}(\rho u_i u_j) - \frac{\partial p}{\partial x_i} + \frac{\partial}{\partial x_j} \left[ \mu \left( \frac{\partial u_i}{\partial x_j} + \frac{\partial u_j}{\partial x_i} - \frac{2}{3} \delta_{ij} \left( \frac{\partial u_1}{\partial x_1} + \frac{\partial u_2}{\partial x_2} + \frac{\partial u_3}{\partial x_3} \right) \right) \right] \\ & + \frac{\partial}{\partial x_j} \left( -\rho \overline{u_i' u_j'} \right) + \rho g_i - \frac{\mu}{\alpha} u_i - \frac{1}{2} C_{ir} \rho u_{mag} u_i \end{aligned} \quad (2)$$

$$\frac{\partial}{\partial t}(\rho E) + \frac{\partial}{\partial x_j} [u_j (\rho E + p)] = \frac{\partial}{\partial x_j} \left( k_{eff} \frac{\partial T}{\partial x_j} - \sum_i h_i J_i + u_i (\tau_{ij})_{eff} \right) + S_h \quad (3)$$

$$\frac{\partial}{\partial t}(\rho Y_i) + \nabla \cdot (\rho u Y_i) = -\nabla \cdot J_i \quad (4)$$

where  $\rho$  is fluid density;  $t$  is time;  $u_i$  ( $i=1, 2, 3$ , indicating  $x, y$ , and  $z$  direction) is the mean velocity  $u$  in  $i$ th direction;  $u_i'$  is the fluctuating component of the instantaneous velocity;  $\mu$  is fluid viscosity;  $\delta_{ij}$  is the unit tensor;  $p$  is the static pressure;  $g_i$  is the gravitational acceleration constant in the  $i$ th direction;  $a$  is the aerodynamic porosity or permeability of the windbreak;  $a^{-1}$  is the viscous resistance coefficient;  $C_{ir}$  is the inertial resistance coefficient caused by the windbreak;  $u_{mag}$  is the magnitude of the velocity (Hinge, 1975; Saatjian, 2000);  $E$  is the total energy;  $k_{eff}$  is the effective thermal conductivity;  $S_h$  represents all volumetric heat sources such as those of chemical reactions;  $T$  is temperature, and;  $(\tau_{ij})_{eff}$  is the effective deviatoric stress tensor.

The coefficients  $Y_i$ ,  $J_i$  and  $h_i$  are the mass fraction, diffusion flux and the sensible enthalpy of the  $i$ th atmospheric species (Bird et al., 2002; Fox & McDonald, 1992). The term  $-\rho u_i' u_j'$  is called the Reynolds stresses.

In Eq. (4), the diffusion flux  $J_i$  of the atmospheric species  $i$ , arises due to concentration gradients. The diffusion flux for turbulent flow is:

$$J_i = -(\rho D_{i,m} + \frac{\mu_t}{Sc_t}) \nabla Y_i - D_{T,i} \frac{\nabla T}{T} \quad (5)$$

where  $Y_i$  is mass fraction of the species  $i$ ;  $D_{i,m}$  is the diffusion coefficient for species  $i$  in the mixture; and  $D_{T,i}$  is the thermal diffusion coefficient;  $Sc_i$  is the turbulent Schmidt number generally equal to 0.7, and;  $\mu_t$  is the turbulent viscosity (Saatjian, 2000; Bird et al., 2002).

### 3.2 Describing the windbreak

A windbreak is a porous medium resisting wind or air flow and therefore constituting a momentum sink. This resistance can be introduced in the momentum equation in terms of viscous and inertial resistance:

$$F_i = -\frac{\mu}{\alpha} u_i - \frac{1}{2} C_{ir} \rho u_{mag} u_i \tag{6}$$

where  $F_i$  is the resistance to wind flow;  $\mu$  is fluid viscosity;  $\alpha$  is the aerodynamic porosity or permeability of the windbreak;  $\alpha^{-1}$  is the viscous resistance coefficient;  $C_{ir}$  is the inertial resistance coefficient caused by the windbreak;  $u_{mag}$  is the magnitude of the average velocity, and;  $u_i$  ( $i=1, 2, 3$ , indicating x, y, and z direction) is the mean velocity  $u$  in  $i$ th direction. The term  $\mu u_i / \alpha$  in Eqn (6) is Darcy’s law for porous medium which calculates the resistance exerted by the windbreak due to fluid viscosity (Bird et al., 2002). The term  $(C_{ir} \rho u_{mag} u_i / 2)$  in Eqn (6) computes the inertial loss of the fluid flowing through the windbreak, which varies over the height of the tree depending on its shape (Wang & Takle, 1995; Wilson, 2004; Wilson, 1985). Poplars offer dense foliage at their top compared to conifers which offer more foliage at their base. Accordingly, a valid simulation uses an inertial resistance coefficient which varies over tree height.

In this project, the simulated windbreak was designed as a cubic volume with a specific width, height, length and optical porosity, positioned at a specific distanced  $x$  downwind from the odour source. The optical porosity was used to compute the aerodynamic porosity representing the exact amount of air flowing through the foliage of the windbreak. The aerodynamic porosity, or permeability, is defined as the ratio of wind speed perpendicular to the windbreak, immediately downwind and averaged over the full height of the windbreak, to that upwind from the windbreak (Guan et al., 2003; Wang & Takle, 1995):

$$\alpha = \frac{\int_{0@windbreak}^H u_1 dz}{\int_{0@inlet}^H u_1 dz} \tag{7}$$

The relationship between optical and aerodynamic porosity is defined according to the wind tunnel measurements of Guan et al. (2003):

$$\alpha = \beta^{0.4} \tag{8}$$

where  $\alpha$  is the aerodynamic porosity and  $\beta$  is the optical porosity. Accordingly, an optical porosity of 0.35 results in an aerodynamic porosity of 0.66, implying that 66 % and 34 % of the air flows through and over the windbreak, respectively.

To calibrate and validate the model, the field work in this project observed the effect of tree types (poplar and deciduous, Fig. 3) and size forming the windbreaks using sites 1, 2 and 3 (Table 1). On site 1, the windbreak consisted of mature deciduous trees offering an averaged optical porosity of 0.35 but the optical porosity at its base was 0.30 while that over the rest of its profile was 0.40. Therefore, the inertial resistance  $C_{ir}$  was defined as proportional to the density (1.0 minus its porosity) of the windbreak:

$$C_{ir} = \begin{cases} w_1 - \frac{w_1 - w_2}{h_1} z & z \leq h_1 \\ w_2 - \frac{w_2 - w_3}{H - h_1} (z - h_1) & h_1 < z \leq H \end{cases} \quad (9)$$

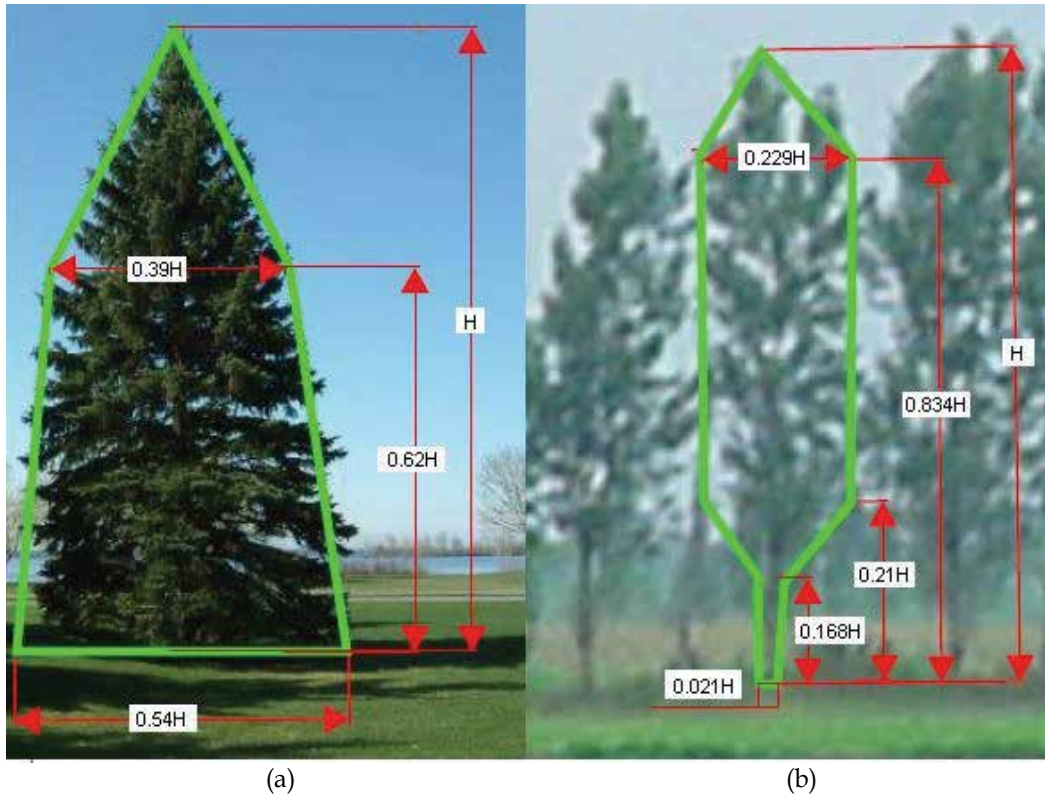


Fig. 3. The structure of the trees forming the windbreak, where  $H$  is the total height; a) conifer; b) poplar (Lin et al., 2007b)

where  $z$  is the coordinate value in the vertical direction;  $H$  is the height of the windbreak;  $h_1$  is the height at which the porosity of the windbreak changes ( $0 < h_1 < H$ ), and;  $w_1$ ,  $w_2$ , and  $w_3$  are three constants corresponding to the thickness of the real windbreak, set in the simulation to allow 66 % of the air to pass through.

For the windbreak on site 2, the averaged optical porosity was 0.35: the optical porosity at the base was 0.40; that between heights of 3 to 14 m was 0.3, and; above 14 m, the porosity was gradually increased from 0.3 to 1.0. Therefore  $C_{ir}$  was:

$$C_{ir} = \begin{cases} w_1 - \frac{w_1 - w_2}{h_1} z & z \leq h_1 \\ w_2 & h_1 < z \leq h_2 \\ w_2 - \frac{w_2 - w_3}{H - h_2} (z - h_2) & h_2 < z \leq H \end{cases} \quad (10)$$

where  $w_1$ ,  $w_2$ , and  $w_3$  were set at 0.27, 0.39 and 0.05, and;  $h_1$ ,  $h_2$  and  $H$  were set at 3, 14 and 15 m, respectively. Again, such conditions allowed 66 % of the air to pass through the windbreak. The windbreak on site 3 offered an average optical porosity of 0.55. Its porosity was assumed to be 0.7 at a height of 1.0 m, to linearly decrease to 0.47 at a height of 3 m, to remain constant between the height of 3 to 15 m, and; then, to increase to 1.0 at the tree top. These conditions produced an average air permeability of 0.79 and a  $C_{ir}$  calculated as:

$$C_{ir} = \begin{cases} w_1 & z \leq h_1 \\ w_1 + \frac{w_2 - w_1}{h_2 - h_1}(z - h_1) & h_1 < z \leq h_2 \\ w_2 & h_2 < z \leq h_3 \\ w_2 - \frac{w_2}{H - h_3}(z - h_3) & h_3 < z \leq H \end{cases} \quad (11)$$

where  $w_1$  and  $w_2$  were set at 0.1 and 0.205, and;  $h_1$ ,  $h_2$ ,  $h_3$  and  $H$  were set at 1, 3, 15 and 18 m, respectively.

### 3.3 Computational domain

The computational domain was designed as a volume measuring 690 m in length ( $75 H$ ,  $H$  being the height of the windbreak of 9.2 m), 184 m ( $20 H$ ) in width and 73.6 m ( $8 H$ ) in height (Fig. 4). The left and right faces of the space were the wind inlet and outlet, located 138 and 552 m from the origin, respectively. The front, back and top faces of the volume were set to have an open or undisturbed wind velocity and were positioned at 92, -92 and 73.6 m from the origin, respectively. The bottom face of the volume was the ground surface.

The odorous air was introduced into this computational volume by a single source opening measuring 1.5 m  $\times$  0.376 m  $\times$  1.75 m in  $x$ ,  $y$ ,  $z$  directions with the right face positioned at  $x = 0$  m and the front face at  $y = -0.188$  m. The centre of the odour emission surface was positioned at  $x = 0$  m,  $y = 0$  m and  $z = 1.562$  m. Odours were blown from the right-up rectangular face (the red zone in Fig. 4) measuring 0.376  $\times$  0.376 m. The windbreak (green zone in Fig. 4) was designed as a porous cubic volume.

For computational purposes, the computational volume was meshed into 228, 81, and 46 segments in the  $x$ ,  $y$  and  $z$  coordinates, respectively, and the size of the rectangular cells gradually increased from the odour generator towards the outward faces of the system. For the odour inlet, 64 rectangles were meshed over an area of 0.376  $\times$  0.376 m<sup>2</sup> to effectively transfer the odour mass fraction to other cells.

### 3.4 Numerical solver

The Reynolds stresses in Eq. (8) can be computed using the Boussinesq Hypothesis based on the mean velocity gradients:

$$-\rho \overline{u'_i u'_j} = \mu_t \left( \frac{\partial u_i}{\partial x_j} + \frac{\partial u_j}{\partial x_i} \right) - \frac{2}{3} \left( \rho k + \mu_t \frac{\partial u_i}{\partial x_i} \right) \delta_{ij} \quad (12)$$

where  $\mu_t$  is the turbulent viscosity, and;  $k$  is the turbulence kinetic energy.

Selected to perform the simulations, the SST  $k$ - $\omega$  model of the Fluent software uses two different transport equation to express the turbulence kinetic energy  $k$  and the specific

dissipation rate  $\omega$ . The SST k- $\omega$  accounts for the principal turbulent shear stress and uses a cross-diffusion term in the  $\omega$  equation to blend both the k- $\omega$  and k- $\epsilon$  models and to ensure that the model equations behave appropriately in both the near-wall and far-field zones. Thus, the SST k- $\omega$  model offers a superior simulation performance as compared to the individual k- $\omega$  and k- $\epsilon$  models (Menter et al., 2003).

The Fluent 6.2 steady 3-dimension segregated solver was used to solve the SST k- $\omega$  model through second and quick orders of discretisation schemes converting the governing equations into algebraic equations solved numerically while increasing the calculation accuracy. The second order scheme was used to compute the pressure, the second order upwind scheme was used to compute odour dispersion and the quick scheme was used to compute momentum, turbulence kinetic energy, turbulence dissipation rate and energy. The SIMPLE method was applied to the velocity and pressure coupling (Fluent inc., 2005).

### 3.5 Fluid properties

Livestock manures emit over 168 odorous compounds and six of the ten compounds with the lowest detection thresholds contained sulphur (O'Neil & Phillips, 1992). Hydrogen sulphide ( $H_2S$ ) was selected as odour and presumed to flow along with clean dry air. Therefore, the modelled fluid was defined as clean air and  $H_2S$  and its mass fraction at the odour source was:

$$Y_2 = \frac{OC_g \bullet m_{H_2S}}{\frac{P_a M_1}{RT} + OC_g \bullet m_{H_2S}} \quad (13)$$

where  $Y_2$  is the odour mass fraction (OMF) at the odour inlet, or the ratio of the odour mass to the total air and odour mass in 1.0 m<sup>3</sup>, dimensionless;  $P_a$  is the atmospheric pressure of 101325 Pa at sea level;  $T$  is temperature in K;  $M$  is the molecular weight of dry air or 0.028966 kg mol<sup>-1</sup>;  $R$  is the universal gas constant or 8.31432J mol<sup>-1</sup> K<sup>-1</sup> (ASHRAE, 2009);  $OC_g$  is the odour source concentration, in OU m<sup>-3</sup>, and;  $m_{H_2S}$  is the mass of  $H_2S$  required to produce one odour unit, expressed as kg OU<sup>-1</sup> and  $m_{H_2S} = 7.0 \times 10^{-9}$  kg OU<sup>-1</sup> (Blackadar, 1997).

| Description                     | Unit                               | Mixture                     | Air  | H <sub>2</sub> S                                    |
|---------------------------------|------------------------------------|-----------------------------|--|---|
| Density                         | kg m <sup>-3</sup>                 | Impressible-ideal-gas law   |  |   |
| Cp                              | J kg <sup>-1</sup> K <sup>-1</sup> | Mixing law                  | 1005.422                                   | 1005.333  |
| Thermal conductivity            | W m <sup>-1</sup> K <sup>-1</sup>  | Mass-weighted-mixing-law    | 0.0260411                                  | 0.0137023   |
| Viscosity                       | kg m <sup>-1</sup> s <sup>-1</sup> | Mass-weighted-mixing-law    | 1.458E-6 T <sup>1.5</sup><br>/ (T + 110.1) | -1.4839E-6<br>+ 5.1E-8T<br>-1.26E-11 T <sup>2</sup> |
| Mass diffusivity                | m <sup>2</sup> s <sup>-1</sup>     | -1.3497E-5<br>+ 1.05772E-7T |  |   |
| Thermal diffusivity coefficient | kg m <sup>-1</sup> s <sup>-1</sup> | Kinetic-theory              |  |   |
| Molecular weight                | kg kgmol <sup>-1</sup>             |                             | 28.966                                     | 34.07994  |

Table 2. Properties of clean air and  $H_2S$  used in the simulation where T is temperature in K, and for a temperature range of 283 to 313 K



The modelled fluid was defined using the physical properties of clean dry air and H<sub>2</sub>S, including density, specific heat capacity, thermal conductivity, viscosity, mass and thermal diffusion coefficients for the mixture and individual species. The modelled fluid was considered incompressible and its density varied with temperature but not with pressure because of a Mach number under 10 %. The fluid's specific heat capacity, thermal conductivity and viscosity were calculated using the mass mixing-law and the thermal diffusion coefficient was calculated using the kinetic-theory (Table 2).

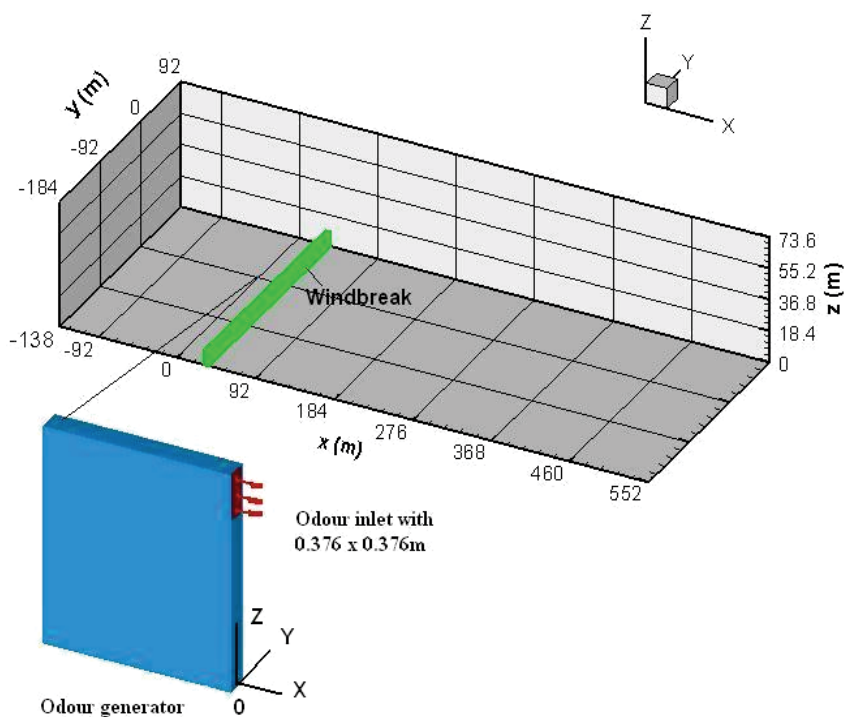


Fig. 4. The computational volume schematics used to predict odour dispersion. In this case, the  $z$  coordinate is magnified 2 times and the windbreak optical porosity is 0.35. The green bar represents the windbreak and the odour emission surface centre of the odour generator is located at  $x = 0$ ,  $y = 0$  and  $z = 1.562$  m

### 3.6 Boundary conditions

The boundary conditions define the faces of the computational volume and the velocity inlet of the clean air and odorous gas. The bottom face of the odour dispersion system (ODS) was assumed to be no slip requiring as input only temperature and roughness length. As air inlet velocity, the inputs included the vertical profile of the horizontal wind velocity, temperature, turbulence kinetic energy and specific dissipation rate.

The odour dispersion around the windbreak was assumed to occur in the homogeneous plat terrain of the surface layer of the atmosphere, and the approaching wind flow was assumed not to change the vertical direction of horizontal velocity and to satisfy the assumption of the Monin Obukhov similarity theory. Atmospheric stability was determined by the Monin Obukhov length  $L_{MO}$ :

$$L_{MO} = -\frac{u_*^3 \rho C_p T}{k_a g H_F} \quad (14)$$

where  $u_*$  is the friction velocity;  $k_a$  is the von Karman constant ranging from 0.35 to 0.43 and usually equal to 0.4;  $T$  is the surface temperature;  $C_p$  is the specific heat of air;  $H_F$  is the vertical heat flux;  $\rho$  the air density, and;  $g$  is the gravitational acceleration constant (Schnelle, 2000). When the convective heat flux is upward,  $L_{MO}$  is negative and the air is unstable. When the earth absorbs heat energy, the heat flux is negative,  $L_{MO}$  is positive and hence the air is stable. However, when the heat flux is zero,  $L_{MO}$  is infinite and the air stability conditions are neutral.

The vertical profile of the horizontal mean wind velocity is calculated by:

$$u_{mag}(z) = \begin{cases} \frac{u_*}{k_a} \ln \frac{z}{z_0} & h_{ABL} / L_{MO} = 0 \text{ neutral} \\ \frac{u_*}{k_a} \left( \ln \frac{z}{z_0} - \ln \frac{(1+x)^2 (1+x^2)}{(1+x_0)^2 (1+x_0^2)} + 2 \tan^{-1}(x) - 2 \tan^{-1}(x_0) \right) & h_{ABL} / L_{MO} < 0 \text{ unstable} \\ \frac{u_*}{k_a} \left( \ln \frac{z}{z_0} + \frac{5(z-z_0)}{L_{MO}} \right) & h_{ABL} / L_{MO} > 0 \text{ stable} \end{cases} \quad (15)$$

$$\text{where} \quad x = \left( 1 - \frac{16z}{L_{MO}} \right)^{\frac{1}{4}} \quad (16)$$

$$x_0 = \left( 1 - \frac{16z_0}{L_{MO}} \right)^{\frac{1}{4}} \quad (17)$$

where  $u_{mag}$  is the magnitude of the horizontal mean wind velocity at height  $z$  above the surface ( $z \geq z_0$ );  $z_0$  is the roughness length of the surface,  $h_{ABL}$  is the height of the atmospheric boundary layer, and  $L_{MO}$  is the Monin Obukhov length (Panofsky & Dutton, 1984; Blackadar, 1997; Jacobson, 1999).

Assuming that the potential temperature is equal to the temperature at  $z_s$ , the vertical temperature profile  $T(z)$  can be calculated as (Panofsky & Dutton, 1984):

$$T(z) = \begin{cases} -\gamma_d(z - z_s) + T_s & h_{ABL} / L_{MO} = 0 \text{ neutral} \\ -\gamma_d(z - z_s) + T_s \left( 1 + \frac{u_*^2}{\kappa_a^2 g L_{MO}} \left( \ln \frac{z}{z_s} - 2 \ln \frac{1 + \sqrt{1 - \frac{16z}{L_{MO}}}}{1 + \sqrt{1 - \frac{16z_s}{L_{MO}}}} \right) \right) & h_{ABL} / L_{MO} < 0 \text{ unstable} \\ -\gamma_d(z - z_s) + T_s \left( 1 + \frac{u_*^2}{\kappa_a^2 g L_{MO}} \left( \ln \frac{z}{z_s} + \frac{5(z - z_s)}{L_{MO}} \right) \right) & h_{ABL} / L_{MO} > 0 \text{ stable} \end{cases} \quad (18)$$

where  $z_s$  is a height of 1.35 m above ground;  $T_s$  is the temperature at height  $z_s$ ;  $g$  is the gravitational acceleration constant, and;  $Y_d$  is the dry adiabatic lapse rate of  $0.01 \text{ K m}^{-1}$ . The vertical turbulence kinetic energy profile within the surface atmospheric layer can be defined as:

$$k(z) = \frac{1}{2} (\sigma_u^2 + \sigma_v^2 + \sigma_w^2) \quad (19)$$

where  $k(z)$  is the turbulence kinetic energy (TKE), and;  $\sigma_u$ ,  $\sigma_v$  and  $\sigma_w$  are turbulence components in the x, y, z coordinates.

For neutral conditions,  $h_{ABL}/L_{MO} = 0$ , TKE linearly decreased with height, and at the top of the atmospheric boundary layer, equals 20 % of its value at the ground level (Carruthers & Dyster, 2006). The TKE for neutral condition is:

$$k(z) = 5.97 u_*^2 T_{WN}^2 \quad (20)$$

where

$$T_{WN} = 1 - a_s \frac{z - z_0}{h_{ABL} - z_0} \quad (21)$$

where  $a_s = 0.8$ .

For unstable conditions ( $h_{ABL}/L_{MO} < 0$ ), the TKE is:

$$k(z) = 5.97 u_*^2 T_{WN}^2 + w_*^2 (0.3 + 0.2 T_{WC}^2) \quad (22)$$

where

$$T_{WC} = 2.1 \left( \frac{z - z_0}{h_{PBL} - z_0} \right)^{\frac{1}{3}} T_{WN} \quad (23)$$

$$w_* = u_* \left( \frac{h_{ABL} - z_0}{k_a |L_{MO}|} \right)^{\frac{1}{3}} \quad (24)$$

where  $w_*$  is the mixing layer velocity scale.

For stable conditions ( $h_{ABL}/L_{MO} > 0$ ), TKE is expressed as:

$$k(z) = 5.97 u_*^2 T_{WN}^{\frac{3}{2}} \quad (25)$$

and  $a_s = 0.5$  for roughness length  $z_0 \geq 0.1 \text{ m}$ .

The vertical turbulence specific dissipation rate  $\omega(z)$  is:

$$\omega(z) = \frac{k(z)^{\frac{1}{2}}}{0.09^{\frac{1}{4}} l} \quad (26)$$

where  $l$  is the turbulence length scale set as twice the height of the ground surface roughness length ( $2z_0$ ) based on a calibration of the horizontal velocity recovery rate downwind from the windbreak (Schnelle, 2000; Menter, 2003).

The parameters defining the surface layer conditions in the SST model, namely  $z_0$ ,  $L_{MO}$ ,  $h_{ABL}$ ,  $u^*$  and  $T_s$  are determined according to the simulation conditions. Corresponding to the physical conditions of the ground surface,  $z_0$  was 0.13 m (Lin et al., 2007b). The coefficient  $L_{MO}$  was estimated from the Pasquill atmospheric stability categories. When  $z_0$  was 0.13 m, the average  $L_{MO}$  was -20 m for the Pasquill stability category B, and was 20 for the stability category F (Golder, 1972). The coefficient  $h_{ABL}$  was designated as the average rural mixing height for each stability category measured at the weather station. Once  $z_0$ ,  $L_{MO}$  and  $h_{ABL}$  were determined,  $u^*$  and  $T_s$  were calculated from the temperature and wind velocity measured at a height of 10 m and using Eqs. (15) and (18), respectively.

### 3.7 Simulating the effect of weather conditions

The effect on odour plume length of climatic factors was tested through 21 simulations (Table 3): simulations 1 to 9 for wind velocity; simulations 10 to 12 for air temperature; simulations 13 to 19 for wind direction, and; simulations 20 and 21 for atmospheric stability. Simulations 1 to 12, 20 and 21 respected an odour dispersion system (ODS) as shown in Fig. 4, and presumed a constant odour concentration at the source of 300 OU m<sup>-3</sup>. For simulations 13 to 19, the ODS measured 460 m × 414 m × 73.6 m, and the odour concentration at the source was 550 OU m<sup>-3</sup>. For all simulations, the surface roughness length was 0.13 m, the odour generator emitted odorous air at a rate of 1.6 m<sup>3</sup> s<sup>-1</sup> and the natural windbreak consisted of a single row of conifers, measuring 7.0 m in width and 9.2 m in height and offering an aerodynamic porosity of 0.4 with a coefficient  $C_{ir0}$  equal to 0.08706. The windbreak was located 30 m downwind from the odour source.

Simulations 1 to 9 tested the effect on odour dispersion of the wind velocity for unstable (category B), neutral (category D) and stable (category F) atmospheric conditions for their average  $T$ ,  $L_{MO}$  and  $h_{ABL}$  values. The wind velocity ranges were measured in September 2003 at PE Tudeau airport by Environment Canada for stability category B, D and F. For simulations 1, 2 and 3 under stability category B, the averaged values of  $T$ ,  $L_{MO}$  and  $h_{ABL}$  were 293 K, -20 m and 1390 m and the velocities were 1.0, 1.8 and 3.0 m s<sup>-1</sup>, respectively (Table 8.2). For simulations 4, 5 and 6 under stability category D, the averaged  $T$ ,  $L_{MO}$  and  $h_{ABL}$  were 291 K, infinity ( $\infty$ ) and 2090 m, and the velocities were 3.0, 5.4 and 6.4 m s<sup>-1</sup>, respectively. Finally, for simulations 7, 8 and 9 under stability category F, the averaged  $T$ ,  $L_{MO}$  and  $h_{ABL}$  were 287 K, 20 m and 1811 m, and the velocities were set at 1.0, 1.9 and 3.0 m s<sup>-1</sup>, respectively.

Temperature effects were tested under unstable, neutral and stable atmospheric stability categories, using simulations 10, 11 and 12 with average December 2003 temperatures of 269, 270 and 265 K, and simulations 2, 5 and 8 with average September temperature of 293, 291 and 287 K.

Simulations 13 to 19 tested the effect of the wind direction, measured from the positive x-axis and set at 0, -15, -30, -45, -60, -75 and -90°, respectively. The weather atmospheric stability category D was assumed and  $T$ ,  $L_{MO}$ ,  $h_{ABL}$  and wind velocity were 291 K,  $\infty$ , 2090 m and 5.4 m s<sup>-1</sup>, respectively.

The effect of the atmospheric stability was tested twice. Simulations 2, 5 and 8 compared average values of wind velocity, atmospheric boundary layer height and temperature. Simulations 4, 20 and 21 were also similar except for their respective stability categories B, D and F. For these three simulations, wind velocity,  $h_{ABL}$  and  $T$  were set at 3.0 m s<sup>-1</sup>, 2090 m and 291 K, respectively, which are mean values for the atmospheric stability categories B, D and F.

| Test | Weather condition    |              |            |               |          |           | Computed results |             |             |       |        |
|------|----------------------|--------------|------------|---------------|----------|-----------|------------------|-------------|-------------|-------|--------|
|      | $u_{mag}$<br>at 10 m | T<br>at 10 m | Wind       | Atm.<br>Stab. | $L_{MO}$ | $h_{ABL}$ | Length<br>1      | Length<br>2 | Length<br>3 | Width | Height |
| Unit | $m\ s^{-1}$          | $^{\circ}K$  | $^{\circ}$ | A-F           | m        | m         | m                | m           | m           | m     | m      |
| 1    | 1                    | 293          | 0          | B             | -20      | 1390      | 394              | 353         | 323         | 48    | 67     |
| 2    | 1.8                  | 293          | 0          | B             | -20      | 1390      | >552             | 465         | 404         | 48    | 41     |
| 3    | 3                    | 293          | 0          | B             | -20      | 1390      | >552             | 397         | 268         | 38    | 17     |
| 4    | 3                    | 291          | 0          | D             | infinite | 2090      | >552             | 395         | 271         | 47    | 18     |
| 5    | 5.4                  | 291          | 0          | D             | infinite | 2090      | 444              | 235         | 170         | 34    | 16     |
| 6    | 6.4                  | 291          | 0          | D             | infinite | 2090      | 379              | 205         | 151         | 32    | 18     |
| 7    | 1                    | 287          | 0          | F             | 20       | 1811      | >552             | >552        | 552         | 48    | 25     |
| 8    | 1.9                  | 287          | 0          | F             | 20       | 1811      | >552             | 474         | 349         | 46    | 19     |
| 9    | 3                    | 287          | 0          | F             | 20       | 1811      | >552             | 343         | 253         | 10    | 17     |
| 10   | 1.8                  | 269          | 0          | B             | -20      | 1390      | >552             | 463         | 404         | 44    | 41     |
| 11   | 5.4                  | 270          | 0          | D             | infinite | 2090      | 443              | 235         | 170         | 34    | 16     |
| 12   | 1.9                  | 265          | 0          | F             | 20       | 1811      | >552             | 475         | 351         | 44    | 19     |
| 13   | 5.4                  | 291          | 0          | D             | infinite | 2090      | 301              | 168         | 129         | 31    | 15     |
| 14   | 5.4                  | 291          | -15        | D             | infinite | 2090      | 231              | 135         | 102         | 60    | 15     |
| 15   | 5.4                  | 291          | -30        | D             | infinite | 2090      | 198              | 117         | 77          | 67    | 15     |
| 16   | 5.4                  | 291          | -45        | D             | infinite | 2090      | 187              | 103         | 92          | 74    | 15     |
| 17   | 5.4                  | 291          | -60        | D             | infinite | 2090      | 248              | 150         | 118         | 40    | 15     |
| 18   | 5.4                  | 291          | -75        | D             | infinite | 2090      | 342              | 219         | 180         | 24    | 15     |
| 19   | 5.4                  | 291          | -90        | D             | infinite | 2090      | >322             | >322        | 301         | 18    | 11     |
| 20   | 3                    | 291          | 0          | B             | -20      | 2090      | >552             | 394         | 266         | 39    | 19     |
| 21   | 3                    | 291          | 0          | F             | 20       | 2090      | >552             | 344         | 251         | 39    | 17     |

Table 3. Simulation test plan for weather conditions and computed results : Length 1 for the length of the odour plume for the 1 OU m<sup>-3</sup>, Length 2 for the 2 OU m<sup>-3</sup>, and Length 3 for the 3 OU m<sup>-3</sup>

### 3.8 Generating the simulated odour plumes

An odour plume is expressed by a series of odour concentration (OC) contours within a plane. In the field and at various locations, the trained panellists detected the odour hedonic tone (HT) which is the degree of pleasant or unpleasant smells, expressed using a scale 0 to -10, where 0 is neutral and -10 is extremely unpleasant (Lin et al., 2007b). In the laboratory, the panellists were then asked to detect the HT and OC of 56 odour samples, which produced the following correlation:

$$OC = \begin{cases} 0 & AHT = 0 \\ 1.3e^{0.45AHT} & 1 \leq AHT \leq 10 \end{cases} \quad (27)$$

where OC is odour concentration in OU m<sup>-3</sup>, and; AHT is an absolute value of HT ranging from 0 to 10. From Eq. (27), the maximum AHT is 10 and the corresponding OC is 117 OU m<sup>-3</sup>. Hence, when OC exceeds 117 OU m<sup>-3</sup>, AHT is still defined as 10, because panellists still feel an extremely unpleasant odour.

To plot the odour plume reflecting HT, the computed dimensionless odour mass fraction (OMF) for all point of the ODS needs to be transformed into a simulated odour mass concentration (SOMC):

$$SOMC = \frac{OMF}{\frac{Y_2}{OC_g}} m_{H_2S} \times 10^9 \quad (28)$$

where SOMC is simulated odour (H<sub>2</sub>S) mass concentration in µg m<sup>-3</sup>; OMF is the odour (H<sub>2</sub>S) mass fraction computed by the model for a given point in space, dimensionless; Y<sub>2</sub> and OC<sub>g</sub> are the odour mass fraction and odour concentration at the odour source as defined by Eq. (28), which are respectively dimensionless and in OU m<sup>-3</sup>, and; m<sub>H<sub>2</sub>S</sub> is the mass of H<sub>2</sub>S required to produce 1.0 OU m<sup>-3</sup> in kg OU<sup>-1</sup> as described by Eq. (28).

Secondly, the SOMC were transformed into SAHT by correlating the 5 field test AHT (absolute HT readings) with SOMC:

$$SAHT = \begin{cases} 0.57SOMC^{0.46} & SOMC \leq 506.5 \text{ } \mu\text{g m}^{-3} \\ 10 & SOMC > 506.5 \text{ } \mu\text{g m}^{-3} \end{cases} \quad (29)$$

where SAHT is simulated absolute hedonic tone, and; SOMC is defined by Eq. (29). The field test correlation indicated a statistically significance (P < 0.01) relationship between AHT and SOMC (Lin et al., 2007b). In this procedure, the odour mass fraction of 506.5 µg m<sup>-3</sup> results in AHT of 10 for an OC of 117 OU m<sup>-3</sup>.

## 4. Results and discussion

The following sections will start by characterizing the panellists, on which all results were based, and then providing a comparison for windbreak performance as observed from the field data. The modelling section will follow, starting with the model calibration using literature data, and then model application to identify the windbreak characteristics having the most influence on odour plume length, followed by the effect of climate. In all results presented, the length of the odour zone or plume is measured from the odour source. Furthermore, the strength of the odour was standardized using an average odour source emission of 471.6 OU m<sup>-3</sup>; this standardization compensated for the variability in odour generation between field tests.

### 4.1 Odour interpretation

The relationship between hedonic tone (HT) and odour concentration (OC) for the 56 samples measured during the field tests is presented in Figure 5. Collected in the morning during the odour plume observation, the field odour samples produced by the odour

generator were evaluated for their threshold dilution and hedonic tone by the same 12 panellists in the afternoon using the olfactometer. There was a dual purpose to this exercise: evaluate the odour concentration (OC) of the sample collected at the odour generator, and; obtain a correlation between odour concentrations (OC) in OU m<sup>-3</sup> and hedonic tones (HT) measured in the field while sizing the odour plume.

Several interesting aspects can be concluded from Fig. 5: correlation between the odour concentration (OC) and the hedonic tone (scale of 0 to -10) is quite variable although typical of panellist response (Edeogn et al., 2001); the present panellist response differs from that of Lim et al. (2001) and Nimmermark (2006), despite the n-butanol rating of all panellists before hand, according to standards (ECN, 2001; ASTM 1997a, b). This difference resulted from culture, tolerance, and previous historical exposure to odorous situations, and; above the observed OC of 117 OU m<sup>-3</sup>, the response in HT reached its peak value of -10, explaining the larger variability in reported OC value.

**4.2 Field windbreak odour dispersion**

The odour plumes observed in the field are far from being regular, as illustrated by Fig. 6, rather the odour plumes are formed of odour puffs resulting from the oscillating wind speed and direction. Nevertheless in terms of modelling, it will be assumed that the OC profile parallel to wind direction follows an average trend.

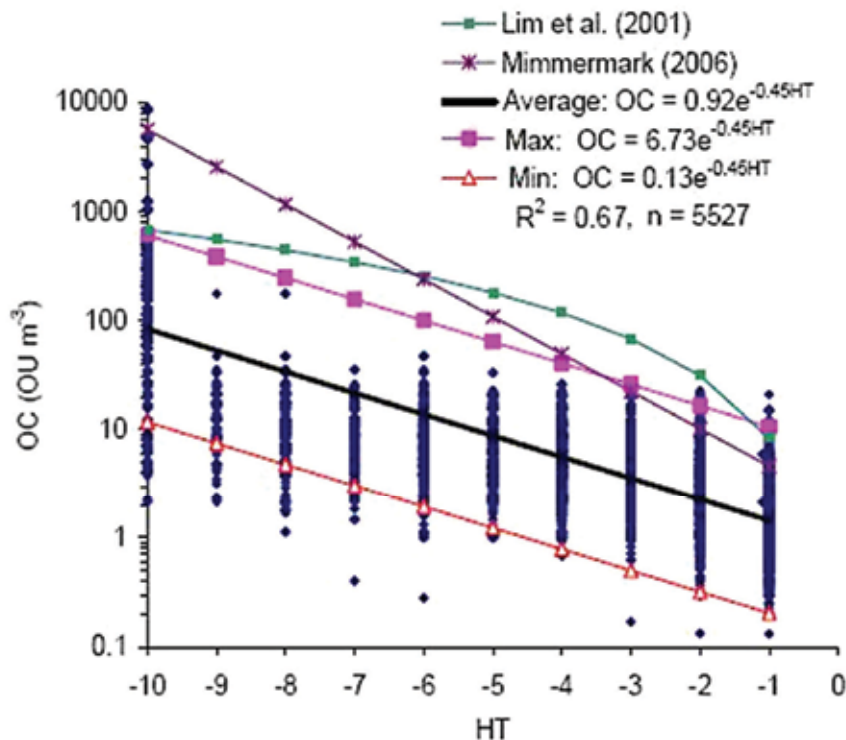


Fig. 5. Compared to data collected by Lim et al. (2001) and Nimmermark (2006), typical relationship between hedonic tone (HT) and odour concentration (OC) for the 56 air sample (minimum, average and maximum) curves (Lin et al., 2007b)

The control without a windbreak (field tests 37, 38 and 39 on site 5) is compared (Fig. 6a) to that of site 2 with a mature deciduous windbreak (field tests 5, 8, 12 and 16, on site 2) and the odour generator located 30 m upwind (Fig. 6b). The average air temperature was 26.4 and 22.6°C, respectively, for the control and windbreak sites. On site 2, the wind direction ranged between 20 to 90° with respect to the windbreak, 90° being perpendicular. Both odour plumes were observed in late August and early September under similar landscape and weather conditions.

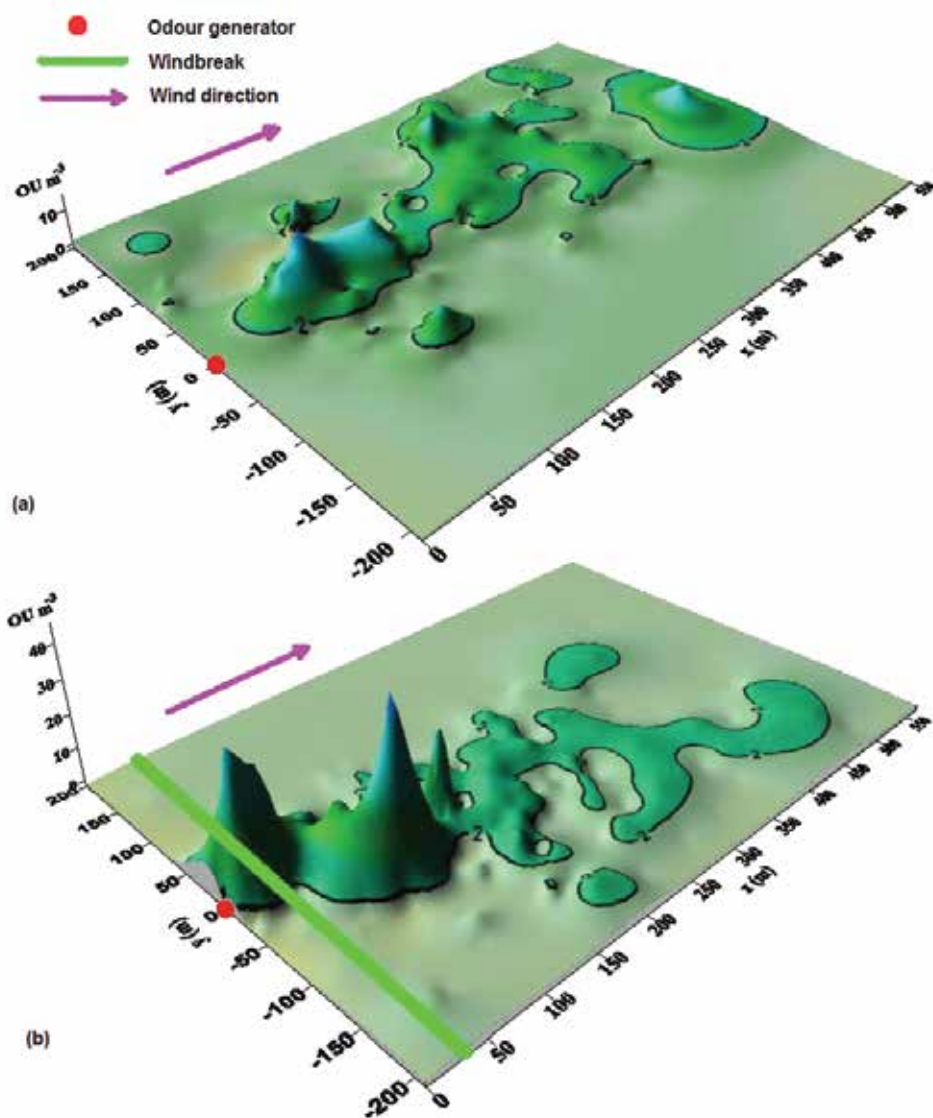


Fig. 6. Odour plumes on field sites 2 and 5 with and without a windbreak. (a) without a windbreak (tests 37, 38 and 39); (b) with windbreak on the site 2 (tests 5, 8, 12 and 16). An odour concentration of 2 OU m<sup>-3</sup> is used to draw the final contour of the odorous zones (Lin et al., 2006)



Fig. 6 demonstrates that the plume developed without a windbreak reached a much longer distance downwind, compared to that developed with the windbreak. Measured furthest away, the windbreak created an odour zone of  $2.0 \text{ OU m}^{-3}$  ending at 500 m away from the source, compared to the same level of odour extending beyond 550 m for the control site. Without a windbreak, the control produced an odour plume with a maximum odour peak of  $16 \text{ OU m}^{-3}$  at a distance of 69 m while the windbreak produced a plume with a peak of  $50 \text{ OU m}^{-3}$  at a distance of 117 m. Accordingly, the windbreak is observed to concentrate or trap the odours on its leeward position before further dispersion.

The most significant parameter affecting the length of the odour plume was found to be the foliage porosity (Fig. 7). Despite the greater tree height on site 1, the more open foliage (optical porosity of 0.55) produce a longer odour plume covering 150 m in width by 600 m in length, compared to that of the windbreak on site 2 with a porosity of 0.35, generally covering a width of also 150 m but a shorter length of 300 m.

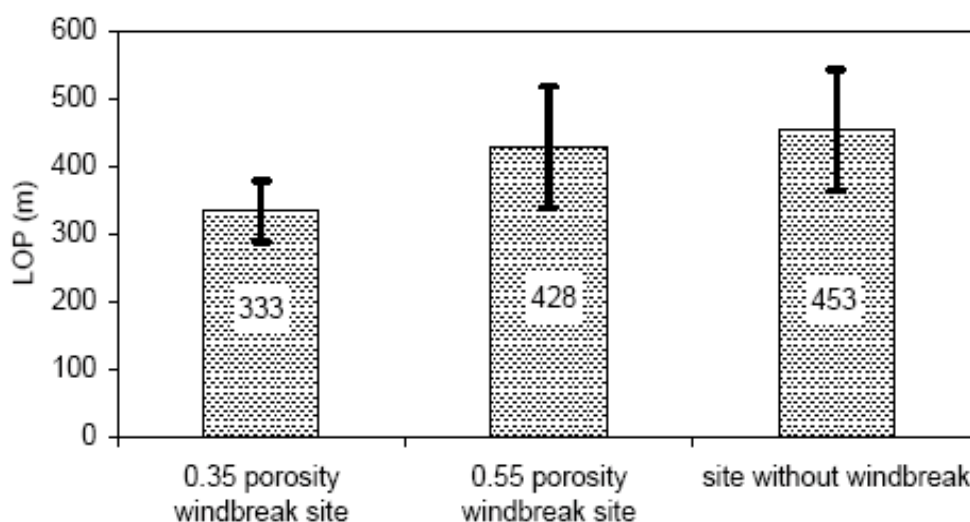


Fig. 7. The mean length of the odour plume (LOP) for the 4 field sites with a windbreak and the single control site without a windbreak; the error bars illustrates the standard error of  $\pm 1.96$  meter (Lin et al., 2007c)

The furthest measured odour concentrations for the windbreak optical porosity of 0.55 and 0.35 had values of  $3.2$  and  $4.0 \text{ OU m}^{-3}$  at a respective distance of 601 and 281 m. However, the windbreak optical porosity of 0.55 produced a maximum odour peak of  $22 \text{ OU m}^{-3}$  at a distance of 138 m while that with an optical porosity of 0.35 produced a maximum odour peak of  $50 \text{ OU m}^{-3}$  at a distance of 117 m. Again, the smaller odour plume corresponded to a more intense odour trapping in the leeward position of the windbreak.

In summary and for the field observation, the more open windbreak produce an odour plume similar to that of the control without a windbreak, likely because a porous windbreak produces less turbulent energy and therefore less odour mixing and odour dilution, compared to a denser windbreak. The denser windbreak with a foliage porosity of 0.35 was

able to reduce the length of the odour plume by 25 %, as compared to no windbreak, but the peak odour concentration was several times higher immediately downwind from the windbreak.

### 4.3 Calibrating the dispersion model

For the model to reproduce adequate wind velocities about windbreaks, the standard  $k-\epsilon$  model was calibrated using field data measured at half height around a natural windbreak 2.2 m tall and offering an optical porosity of 0.55 (Eimern et al., 1964). The model parameter  $C_\mu$  (a constant used to quantify the level of turbulent viscosity  $\mu_t$ ) and  $C_{2\epsilon}$  (a constant used to define the turbulent dissipation rate  $w$ ) were adjusted from the default of 0.09 and 1.92, to 0.12 and 2.2, respectively. Also, the inertial resistance parameter of the windbreak was set at  $10.3 \text{ m}^{-1}$ . Once calibrated, the differences between the simulated and measured wind speeds were (Fig. 8): from -10 to  $0H$ , lower by 4.5 %; from 0 to  $30H$ , slightly greater by 0 to 10 %, and; at  $30 H$ , negligible. An  $R^2$  value of 0.97 was obtained between the measured and simulated velocity values from -10 to  $30 H$ .

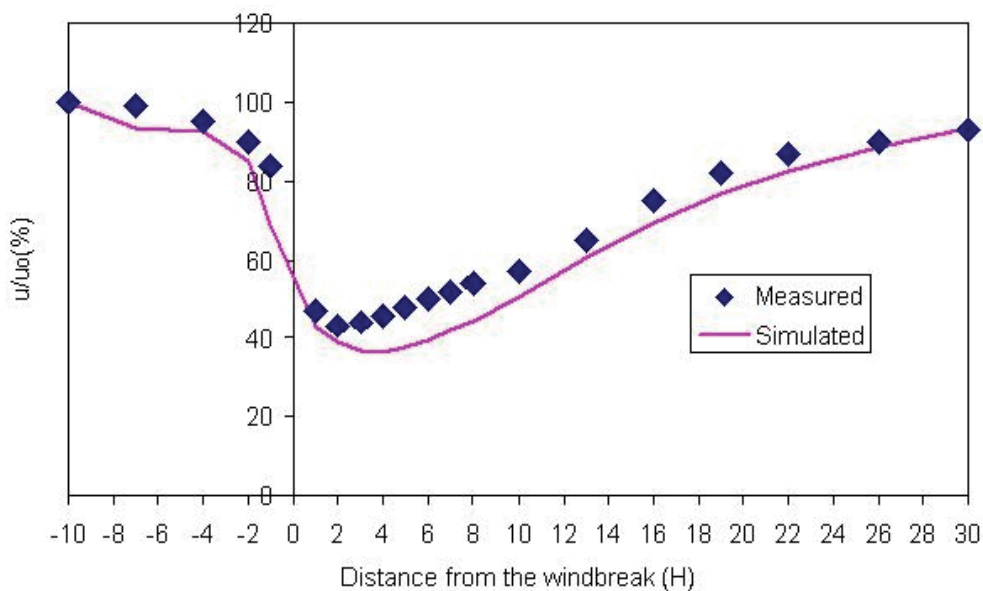


Fig. 8. Comparison of the simulated and measured wind speeds at windbreak half height where  $u$  is the wind speed,  $u_0$  is the undisturbed wind speed, and  $H$  is the height of the windbreak (Lin et al., 2007a). The measured wind speed is taken from Eimern et al. (1964)

The model was also validated for odour concentration simulation (Fig. 9). The correlations between MAHT and SAHT for the 11 tests, as a function of distance from the source, were found to be statistically significant ( $P = 0.01$ ), implying that the standard  $k-\epsilon$  model can accurately predicts odour HT downwind from windbreaks. As illustrated in Figure 5 a, c, e, and g for tests 2, 5, 7, and 8, the simulated lines are found in the centre of the range of MAHT, which is a good indication that the model can reproduce the observations. Depending on the test, the  $R^2$  value ranged between 0.48 and 0.90. If all values within 150 m

of the windbreak are excluded to remove the odour puff effect, then  $R^2$  exceeds 0.75 for all simulations.

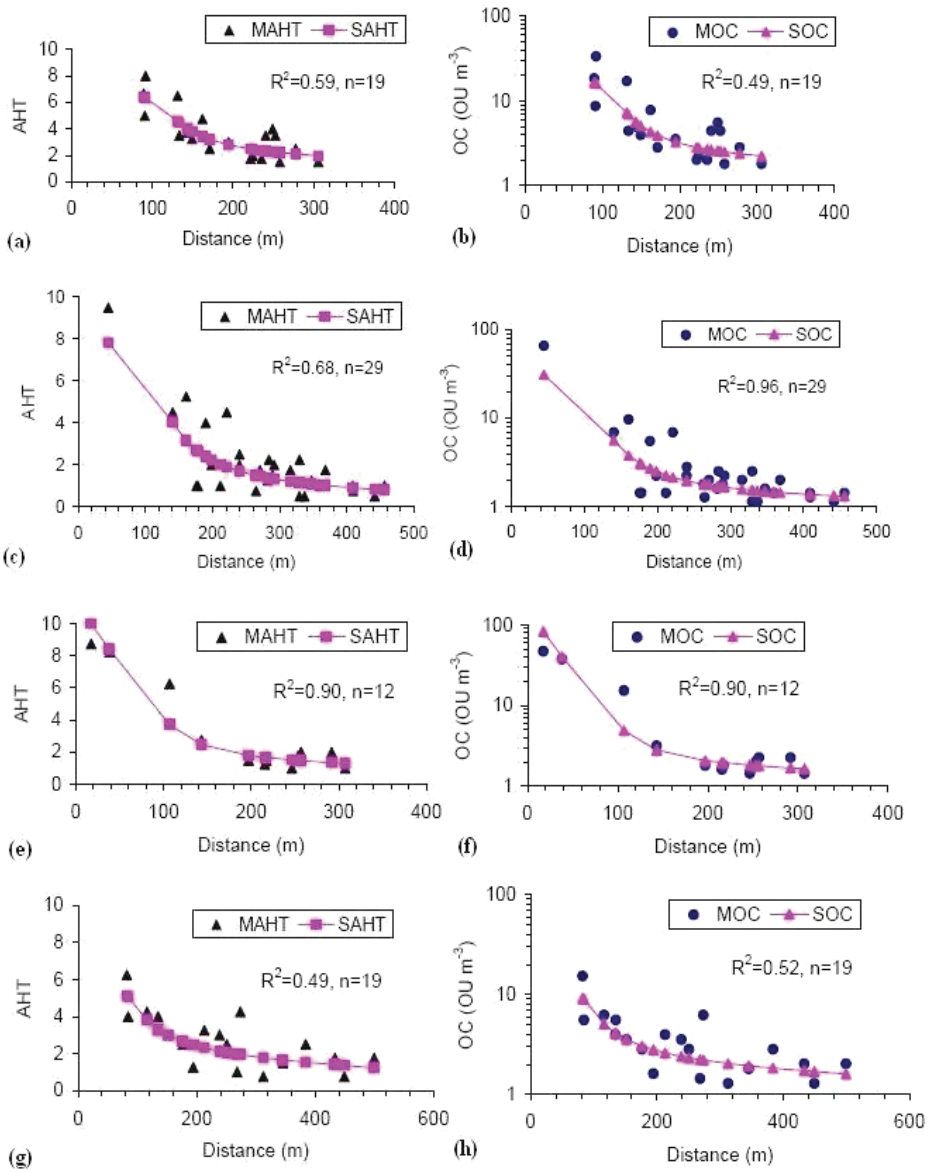


Fig. 9. For the field tests 2, 5, 7 and 8, a, c, e, g give the measured and simulated absolute hedonic tone where *AHT* is the absolute hedonic ton, *MAHT* and *SAHT* are the measured and simulated hedonic tone, respectively,  $R^2$  is the correlation coefficient between the *MAHT* and *SAHT* and *n* is odour points measured; b, d, f, h give the measured and simulated odour concentration where *OC* is odour concentration, *MOC* and *SOC* are respective measured and simulated *OC*, and  $R^2$  is the correlation coefficient between *MOC* and *SOC*. The *x* axis indicates the distance from the odour source (Lin et al., 2009a)

#### 4.4 Simulated effect of windbreak characteristics on odour dispersion

When establishing a natural windbreak to improve odour dispersion, the tree belt characteristics must be optimized in terms of porosity, height and distance from the source. The following sections will present results of simulations designed to identify the windbreak characteristics minimizing the size of the odour plume.

##### 4.4.1 Windbreak porosity, tree type and height

The porosity is the main factor governing the amount of air flowing through the windbreak as determined by the inertial resistance coefficient  $C_{ir}$ , for given  $H$ ,  $h_1$ ,  $w_1$ ,  $w_2$ , and  $w_3$  values (Eqn 9, 10 and 11).

The following values were used to simulate conditions establishing optimal windbreak porosity:  $H$  and  $h_1$  of 9.2 and 6.9 m; an aerodynamic porosity  $\alpha$  of 0.2, 0.3 and 0.66 resulting in respective  $w_1$ ,  $w_2$ , and  $w_3$  values of 4.508, 3.864 and 0.644 for  $a = 0.2$ , values of 1.204, 1.032 and 0.172 for  $a = 0.4$ , and values of 0.38, 0.2598 and 0.16 for  $a = 0.66$ , and; an odour source 30 m upwind from the windbreak.

The simulation indicated that aerodynamic porosity is the main factor governing odour trapping behind the windbreak, and accordingly, odour dispersion and odour plume shortening (Fig. 10). As compare to  $\alpha$  of 0.2 dropping the odour concentration to 2 OU m<sup>-3</sup> at a distance of 217 m,  $a$  of 0.4 required a distance of 292 m to drop the odour concentration to the same level. For  $a$  of 0.66, a distance of over 452 m was required to reach the same OC of 1 OU m<sup>-3</sup>. Furthermore and for aerodynamic porosities of 0.2, 0.4 and 0.6, the odour plume width measured 73, 37 and 30 m, respectively. Thus, lower aerodynamic porosities produced shorter but wider odour plumes, because of the trapping of more odours immediately downwind from the windbreak. Fig. 6 shows the effect of windbreak aerodynamic porosity on the profile of the odour dispersion plume. Again, the lower density windbreak produced a higher OC immediately downwind, confirming the enhanced trapping of odours before dispersion.

The tree type had a slight impact on odour plume length, for the same aerodynamic porosity. For example, a single row conifer produced an OC of 2 OU m<sup>-3</sup> at 320 m, as compared to 310 m for the poplars. The velocity gradient created by the conifer windbreak gradually increased with height especially above 6.4 m as a result of the drop in horizontal tree section area, explaining its slightly poorer performance.

As for a tree height of 4.6 and 9.2 m, for a windbreak offering the same aerodynamic porosity of 0.4, an OC of 3 OU m<sup>-3</sup> was reached at 225 and 407 m, respectively. The size of the low turbulence zone is thus directly related to the windbreak tree height.

##### 4.4.2 Windbreak distance from the source

The simulations demonstrated that the shorter the distance between the source and the windbreak, the faster the odours are trapped to be concentrated and then dispersed. For the 15 m distance, the 2 OU m<sup>-3</sup> contour occurred at a distance of 309 m from the source or 287 m from the windbreak, including its thickness. The 2 OU m<sup>-3</sup> contour appeared for the 60 m distance, at a distance of 411 m from the source and 347 m from the windbreak. The 15 and 60 m distance between the source and windbreak resulted in simulated OC upwind from the windbreak of 228 and 73 OU m<sup>-3</sup> respectively, at a height  $z = 1.5$  m.

When the odour is released from a building ventilated naturally, the windbreak should be positioned at least 24 m away, a condition which does not necessarily optimise odour dispersion.

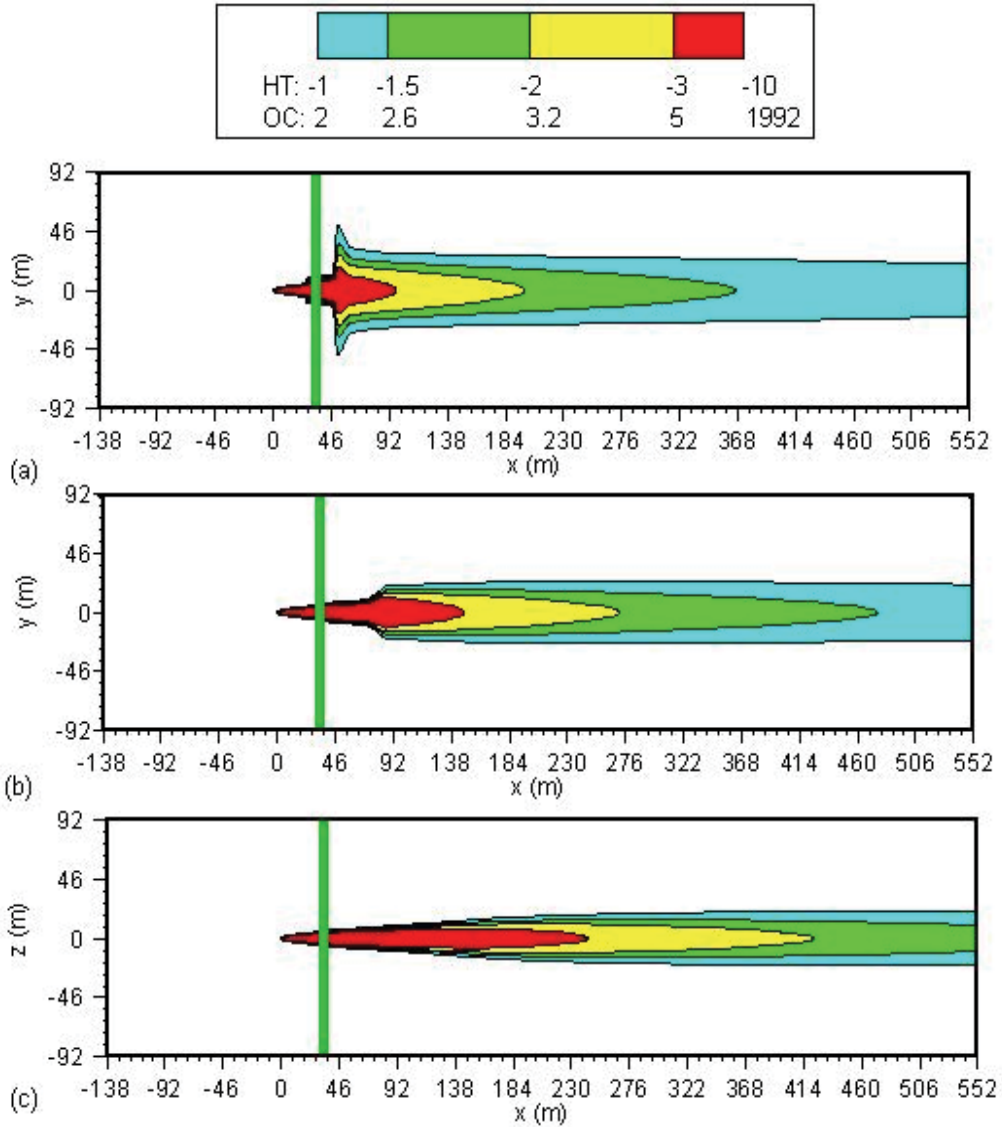


Fig. 10. Contours of the odour plume ( $z = 1.5$  m) for an aerodynamic porosity of (a) 0.2, (b) 0.4 and (c) 0.66, respectively. The green bar is the windbreak and the unit of the odour concentration is  $\text{OU m}^{-3}$  (Lin et al., 2009a)

**4.5 Simulated effect of climatic conditions on windbreak odour dispersion**

Weather conditions certainly vary in time and affect the dispersion performance of a windbreak. Furthermore, atmospheric stability impacts the effect of climatic factors since it

represents the degree of air convection or air movement in the vertical direction. It can compete against wind and it defines air temperature gradient with height. Accordingly and when simulating the effect of the main climatic factors of wind velocity and air temperature, atmospheric stability must be examined in parallel.

#### 4.5.1 Effect of wind velocity and direction

For unstable atmospheric stability conditions (Category B), wind velocities of 1.0, 1.8 and 3.0  $\text{m s}^{-1}$  produced simulated odour plume length of 321 m, 406 m and 268 m for a 2 OU contour (Fig. 11). Accordingly, low wind velocity (1.0  $\text{m s}^{-1}$ ) could not counteract the air lifting effect of unstable conditions, as opposed to stronger winds carrying odours further. Similarly, the height of the odour plume decreased from 43 to 17 and 15 m with increasing wind velocities 1.0, 1.8 and 3.0  $\text{m s}^{-1}$ , respectively.

For neutral atmospheric stability conditions (Category D) with wind velocities of 3.0, 5.4 and 6.4  $\text{m s}^{-1}$ , the odour plume length decreased from 272 m to 121 and 102 m (Fig. 11) respectively, for a 2 OU  $\text{m}^{-3}$  contour. Wind velocities for neutral atmospheric conditions are normally higher than those associated with unstable conditions and produce a higher turbulence kinetic energy at the windbreak which enhances odour dispersion (Lin et al., 2007b). This is also reflected in terms of odour flux which is accelerated by the turbulence viscosity proportional to turbulent kinetic energy.

For stable atmospheric stability conditions (Category F) with typical wind velocities of 1.0, 1.9 to 3.0  $\text{m s}^{-1}$ , the odour plume length dropped from 552 to 350 and 253 m, respectively. Under stable atmospheric conditions with limited upward convection, as compared to unstable conditions, vertical forces are not as strong and less air is projected upwards at the windbreak, resulting in lower wind velocities, weaker turbulent kinetic energy at the windbreak and therefore a longer odour plume.

Wind direction affects the orientation and shape of the odour plume. On the horizontal plane  $z = 1.5$  m and for wind directions varying from 0 to  $-90^\circ$ , the shape of the odour plume followed wind direction (Fig 12). The length of the odour plume decreased from 281 to 176 m for a wind direction changing from 0 to  $-45^\circ$  and then increased from 176 to 321 m for a wind direction changing from  $-45$  to  $-90^\circ$ , for a 2 OU contour. The odour plume developed a fin immediately downwind from the windbreak when the wind direction ranged between  $-15$  and  $-75^\circ$ . This fin was generated when sufficient air flowed parallel to the windbreak and when the windbreak could sufficiently reduce the x-component of the air flow. At a distance of 28 m downwind from the windbreak, the wind streamlines were observed to sharply change direction and become parallel to the windbreak. As a result, the fin reached its maximum length when the wind direction was  $-45^\circ$ .

#### 4.5.2 Effect of atmospheric stability

Atmospheric stability condition had a major impact on odour plume length because it establishes wind velocity range and temperature gradient as well as the strength of the convective air forces. Assuming an average wind velocity, temperature and atmospheric boundary layer height, the odour plume length for an odour contour of 2 OU, measured 406, 170 and 350 m for unstable, neutral and stable atmospheric stability conditions (Categories B, D and F), respectively. Hence, OPL increased from Category D to B and

then F, because Categories B and F generally exhibit lower wind speeds compared to Category D.

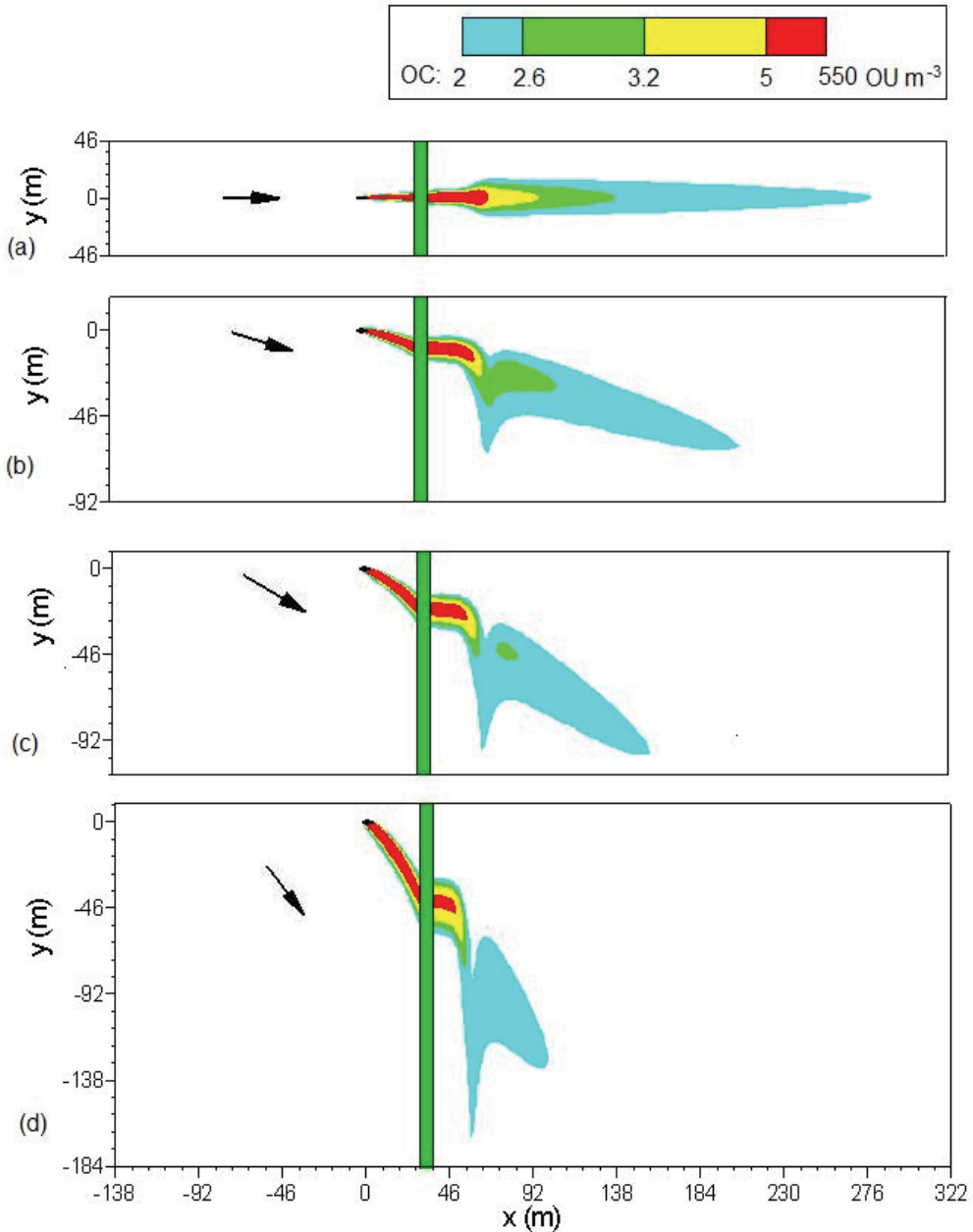


Fig. 11. Effect of wind velocity for: upper) unstable atmosphere for wind velocities of (a) 1.0  $\text{m s}^{-1}$ ; (b) 1.8  $\text{m s}^{-1}$ , and; (c) 3  $\text{m s}^{-1}$ ; lower) neutral atmosphere for wind velocities (a) 3  $\text{m s}^{-1}$ ; (b) 5.4  $\text{m s}^{-1}$ , and; (c) 6.4  $\text{m s}^{-1}$ . The green bar is the windbreak; the odour concentration is in  $\text{OU m}^{-3}$  (Lin et al., 2009b)

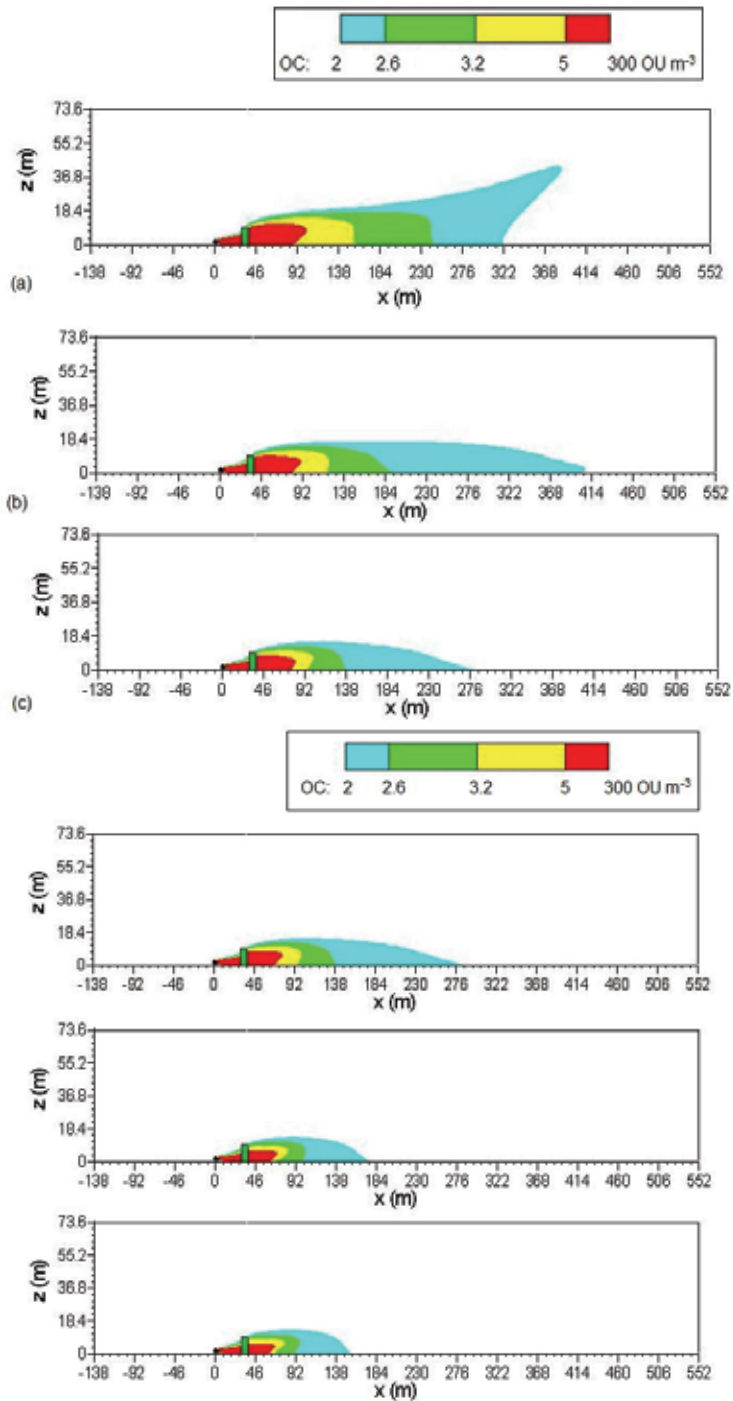


Fig. 12. Effect of wind direction on the odour plume for an horizontal plane at  $z = 1.5$  m, when the wind direction from the positive x-axis is (a)  $0^\circ$ ; (b)  $15^\circ$ ; (c)  $30^\circ$ , and; (d)  $45^\circ$ . The green bar is the windbreak (Lin et al., 2009b)



For the same atmospheric boundary layer height, and wind velocity and air temperature at a height of 10 m, but for Stability Categories B, D and F, odour plumes measured in length 267, 272 and 253 m, respectively because of a different typical profile for wind velocity, temperature and turbulence. The turbulent kinetic energy on the upwind side of the windbreak decreases from Stability Category B, to that of D and then F but then increases in the opposite order on the downwind side of the windbreak, thus shortening the odour plume (Lin et al., 2007b).

For Stability Categories B, D and F, the vertical wind velocity profile was different for  $3 \text{ m s}^{-1}$  at a 10 m height. Stability Category B produced a profile slightly smaller than that obtained with Category D, but for Categories B and D, the profile was much smaller than that for Category F.

For a temperature of 291 K at a 10 m height, the vertical temperature profile was quite different for Stability Categories D, B and F. For Stability Category D (neutral conditions), this profile decreased with height at a rate  $0.01 \text{ K m}^{-1}$ , but for that of B (unstable conditions), it dropped much faster over a height of 0 to 10 m and then decreases at a slower rate but still faster than that obtained with Stability Category D. The temperature profile for Stability Category F (stable conditions) increased with height and produced the inverse of stable effects. Because Stability Category F produced larger profile differences for wind velocity and temperature, between heights of 0 and 73.6 m in the computational domain, compared to D and B, the resulting odour plume was shorter.

Generally, the odour plume length for neutral atmospheric conditions (Category D) was shorter than that for unstable (Category B) and stable conditions (Category F), because of the corresponding different wind velocity. However, when all the conditions were the same except for atmospheric stability conditions, Category F produced a slightly shorter odour plume compared to that under neutral and unstable conditions.

#### 4.5.3 Effect of air temperature gradient

In general, the ground air temperature had limited effect on odour plume size, when associated with a specific atmospheric condition. On a horizontal plane with  $z = 1.5 \text{ m}$ , same length odour plumes were obtained at temperatures of 293 and 269 K under unstable neutral and stable atmospheric conditions.

The phenomenon can be explained by the fact that the odour diffusion flux is proportional to  $(\Delta T/T)$  or the rate of change of temperature  $T$ . For neutral atmospheric conditions,  $T$  dropped with height at  $0.01 \text{ K m}^{-1}$ , but the rate of change of  $T$  over a 0 to 20 m height was similar in both cases at 0.069 % and 0.074 %, respectively. The differences for Simulations 2 and 10, and 8 and 12 of 0.006 % and 0.005 %, respectively, were too small to influence odour dispersion. Hence, the same odour plumes were observed for the different temperatures under the same atmospheric stability condition.

## 5. Conclusions

The objective of the project was to develop a model from the Computational Fluid Dynamics method based on SST  $k-\omega$  computations (Fluent inc., 2005) to simulate odour dispersion around windbreaks and then to use this validated model to observe the effect on odour plume size of windbreak characteristics and climatic factors. The model was calibrated for odour dispersion using field data measured by panellists.

The simulations produced the following conclusions:

1. After calibration, the SST  $k-\omega$  model simulated the velocity recovery rate observed downwind from a 2-dimensional windbreak with an  $R^2$  factor of 0.95 for distances of 0 to  $30H$ , where  $H$  is the height of the windbreak;
2. The SST  $k-\omega$  model predicted odour concentration with an  $R^2$  value generally above 0.75 for values over 150 m away from the windbreak, which is considered quite acceptable for odour simulations.
3. A less porous or denser windbreak (aerodynamic porosity of 0.2 versus 0.4 and 0.66) produced a shorter, wider and more intense odour plume;
4. Assuming that the air flow resistance was proportional to the square of the tree diameter, the tree type had almost no effect on the size of the odour plume. As opposed to the conifer, the poplar windbreak created a slightly shorter odour plume for the same aerodynamic porosity;
5. A taller windbreak resulted in a shorter odour plume, by creating a taller low turbulence zone downwind from the windbreak, where more odours were trapped and retained for dispersion;
6. When close to odour source, the windbreak produces a shorter odour plume.
7. In terms of climatic factors, atmospheric stability was the governing element since it generally establishes wind speed and air temperature gradient; under low wind speeds weaker than convective forces, the odour plume was shorter but under low convective forces, higher wind speeds created more turbulences and shorter odour plumes.

## 6. Nomenclature

$AHT$  is absolute hedonic tone

$AS$  is atmospheric stability

$a_s$  is a factor involved in determining TKE

$C_{ir}$  is the inertial resistance coefficient

$C_{ir0}$  is the constant

$C_p$  is specific heat of air

$D_1$  and  $D_2$  are the tree diameters

$D_{i,m}$  is the diffusion coefficient for species  $i$  in the gaseous mixture

$D_{T,i}$  is the thermal diffusion coefficient for species  $i$  in the gaseous mixture

DWO is the distance between the windbreak and the odour source

$E$  is the total energy

$F_i$  is the resistance to wind flow

$g$  is acceleration of gravity

$g_i$  is the component of the gravitational vector in the  $i$ th direction

$H$  is the total height of the windbreak

$H_F$  is the vertical heat flux

$h_i$  is the height at which the rate of the gradient of the tree diameter changed at the  $i$ th height

$h_{ABL}$  is the height of the atmospheric boundary layer

$H_i$  is the sensible enthalpy of  $i$ th species

HT is the odour hedonic tone

$J_i$  is the diffusion flux of species  $i$

$k_a$  is the van Karman constant ranging from 0.35 to 0.43, and normally equal to 0.4

$k$  is the turbulence kinetic energy  
 $k_{eff}$  is the effective thermal conductivity  
 $k(z)$  is the turbulence kinetic energy (TKE)  
 $l$  is the turbulence length scale  
 $L_{MO}$  is the Monin Obukhov length  
 $M$  is the molecular weight of dry air ( $0.028966\text{kg mol}^{-1}$ )  
 $m_{H_2S}$  is the mass of hydrogen sulphide in one odour unit  
 $OC$  is the odour concentration in  $\text{OU m}^{-3}$   
 $OC_g$  is the odour concentration at odour generator in  $\text{OU m}^{-3}$   
 $ODS$  is the odour dispersion system used for simulations  
 $OER$  is the odour emission rate  
 $OMF$  is odour mass fraction, dimensionless  
 $p$  is the static pressure  
 $P_a$  is the atmospheric pressure at sea level  
 $R$  is the universal gas constant ( $8.31432\text{J mol}^{-1}\text{K}^{-1}$ )  
 $SAHT$  is simulated absolute hedonic tone  
 $Sc_t$  is the turbulent Schmidt number generally equal to 0.7  
 $Sh$  is the heat of chemical reaction and other volumetric heat sources  
 $SOC$  is simulated odour concentration in  $\text{OU m}^{-3}$   
 $SOMC$  is odour mass concentration in  $\mu\text{g m}^{-3}$   
 $T$  is temperature  
 $TKE$  is turbulence kinetic energy  
 $T_s$  is the temperature at the  $z_s$   
 $T_{(z)}$  is the vertical temperature profile  
 $T_{WC}$  is a factor to control the convective energy varied with height  
 $T_{WN}$  is a factor controlling the drop in TKE with height within the atmospheric boundary layer  
 $t$  is time  
 $u$  is instantaneous wind velocity  
 $u$  and  $u'$  are mean and fluctuating component of instantaneous velocity  
 $u^*$  is the friction velocity  
 $u_i$  ( $i=1, 2, 3$ ) is scalar component of the mean velocity in  $i$ th direction, indicating in  $x, y, z$  direction in Cartesian coordinate system, respectively  
 $u_i'$  ( $i=1, 2, 3$ ) is the fluctuating component of the instantaneous velocity  $i$ th direction, indicating in  $x, y, z$  direction in Cartesian coordinate system, respectively  
 $u_{mag}$  is magnitude of the mean velocity  
 $u_0$  is the undisturbed wind velocity  
 $w^*$  is the mixing layer velocity scale  
 $w_{(z)}$  is the vertical turbulence specific dissipation rate  
 $w_1, w_2, w_3$  are constant describing the tree shape and resistance to wind flow at a height  $h_1, h_2, h_3$  respectively  
 $x$  is the coordinate for the axis perpendicular to the windbreak  
 $y$  is the coordinate for the axis parallel to the windbreak  
 $z$  is the coordinate for the vertical axis  
 $z_0$  is roughness length

$z_s$  is a height of 1.35 m above surface  
 $Y_i$  is the mass fraction of the species  $i$  in a mixture of gases  
 $Y_2$  is the odour mass fraction  
 $z$  is a coordinate in the vertical direction  
 $a$  is the aerodynamic porosity, or permeability  
 $a^{-1}$  is the viscous resistance coefficient  
 $\beta$  is the optical porosity  
 $\mu$  is viscosity of mixture of the air and odorous gases  
 $\mu_t$  is the turbulence kinetic viscosity  
 $\rho$  is fluid density  
 $\omega$  is the specific dissipation rate  
 $\delta_{ij}$  is the unit tensor  
 $(\tau_{ij})_{eff}$  is the effective deviatoric stress tensor  
 $\sigma_u, \sigma_v$  and  $\sigma_w$  are the turbulence components in  $x, y, z$  coordinates  
 $Y_d$  is dry adiabatic lapse rate of  $0.01 \text{ K m}^{-1}$

## 7. Acknowledgment

The authors wish to acknowledge the financial contribution of Consumaj inc., CDAQ, the Livestock Initiative Program, Agriculture and Agro-Food Canada and the Natural Sciences and Engineering Research Council of Canada.

## 8. References

- ASHRAE. (2009). *Handbook of Fundamentals*. American Society of Heating, Refrigeration and Air Conditioning, Atlanta, Georgia, U.S.A, pp.13.1-13.6.
- ASTM (1997a). *Standard Practice for Defining and Calculating Individual and Group Sensory Thresholds from Forced-Choice Data Sets of Intermediate Size*. E1432-91. West Conshohocken, PA, American Standards of Testing and Measurement International.
- ASTM (1997b). *Standard Practice for Determination of Odour and Taste Thresholds by a Forced-Choice Ascending Concentration Series Method of Limits*. E679-91. West Conshohocken, PA, American Standards of Testing and Measurement International.
- ASTM (1999). *Standard practice for referencing supra-threshold odour intensity*. E544-75. Philadelphia, Pa, USA, American Standards of Testing and Measurement International.
- Bird, R.B.; Stewart, W.E & Lightfoot, E.N. (2002). *Transport phenomena*. John Wiley, New York, USA.
- Blackadar, A.C. (1997). *Turbulence and diffusion in the atmosphere: lectures in environmental sciences*. Springer Berlin Publishers, New York, USA.
- Bottcher, R.W.; Munilla, R.D.; Baughman, G.R. & Keener, K. M. (2000). Designs for windbreak walls for mitigating dust and odour emissions from tunnel ventilated swine buildings. In: *Swine Housing, Proc. of the 1st International Conference*, Oct. 9-11, 2000, Des Moines, Iowa. American Society of Agricultural Engineers, 2950 Niles road, St. Joseph, Mi. USA. pp. 174-181.

- Bottcher, R.W.; Munilla, R.D.; Keener, K.M. & Gates, R.S. (2001). Dispersion of livestock building ventilation using windbreaks and ducts. 2001 ASAE Annual International Meeting, paper 01-4071. 2950 Niles Road, St. Joseph, Mi. USA.
- Carruthers, D.J. & Dyster, S.G. (2006). *Boundary layer structure specification*. ADMS 3 P09/01T/03 <http://www.cerc.co.uk/software/pubs/3-1techspec.htm> visited in April 2006.
- Cavalini, P. M.; Koeter-Kemmerling, L. G. & Pulles, M. P. J. (1991). Coping with odour annoyance and odour concentrations: three field studies. *Journal of Environmental Psychology*, Vol. 11, pp.123-142.
- CEN (2001). *Air quality - determination of odour concentration by dynamic olfactometry*. prEN13725. 36 rue de Stassart, B-1050 Brussels, European Committee for Standardization.
- Chen, Y. C.; Bundy, D. S.; Hoff, S. (1998). Development of a model of dispersion parameters for odour transmission from agricultural sources. *Journal of Agricultural Engineering Research*, Vol. 69, pp. 229-238.
- Choinière, D. & Barrington, S. (1998). The conception of an automated dynamic olfactometer. CSAE/SCGR paper 98-208. Winnipeg, Manitoba, Canada.
- Das, K.C.; Kastner, J.R. & Hassan, S.M. (2004). Potential of particulate matter as a pathway for odour dispersion. *ASAE paper 04-4125*. American Society of Agricultural Engineering, St Joseph, Michigan, USA.
- Edeogn, I.; Feddes, J.J.R.; Qu, G.; Coleman, R. & Leonard, J. (2001). *Odour measurement and emissions from pig manure treatment/storage systems*. Final report, University of Alberta, Edmonton, Canada.
- Eimern, J.V.; Karschon, R.; Razumova, L.A. & Robertson, G.W. (1964). *Windbreak and shelter belts*. Report of a working group of the Commission for Agricultural Meteorology, World Meteorological Organization, Technical note 59, Secretariat of the World Meteorological Organization, Geneva, Switzerland.
- Evans, G. W. & Cohen, S. (1987). *Environmental stress*. In D. Stokols & I. Altman Eds., *Handbook of Environmental Psychology*, New York: Wiley, pp. 571-610.
- Fluent inc. (2005). *Fluent 6.2 user's guide*. Fluent Inc., Centerra Resource Park, Lebanon, NH, USA.
- Fox, R.W. & McDonald, A.T. (1992). *Introduction to fluid mechanics*. John Wiley, New York, USA.
- Gassman, P. W. (1993). Simulation of odour transport: A review. *ASAE Paper 92-4517*. St Joseph, Michigan, USA, American Society of Agricultural Engineering.
- Golder, D. (1972). Relations among stability parameters in the surface layer. *Boundary-Layer Meteorology*, Vol. 3, pp.47.
- Guan, D.; Zhang, Y. & Zhu, T. (2003). A wind-tunnel study of windbreak drag. *Agriculture, Ecosystem & Environment*, Vol. 118, pp.75-84.
- Guo, Y.; Jacobson, L. D.; Schmidt, D. R. & Nicolai, R. E. (2001). Calibrating INPUFF-2 model by resident-panellists for long-distance odour dispersion from animal production sites. *Transactions of the ASAE*, Vol. 17, pp.859-868.
- Heisler, G.M. & Dewalle, D.R. (1988). Effects of windbreak structure on wind flow. *Agriculture, Ecosystems and Environment*. Vol. 22-23, pp.41-69.
- Hinze, J.O., 1975. *Turbulence*, McGraw-Hill, New York, USA.

- Jacob, T. J. C.; Fraser, C.; Wang, L.; Walker, V. & O'Connor, S. O. (2003) Psychophysical evaluation of responses to pleasant and mal-odour stimulation in human subjects; adaptation, dose response and gender differences. *International Journal of Psychophysiology*, Vol. 48, pp.67-80.
- Jacobson, L. D.; Guo, H.; Schmidt, D. R.; Nicolai, R. E.; Zhu, J. & Janni, K. A. (2005). Development of the OFFSET model for determination of odour annoyance free setback distances from animal production sites: Part I. Review and experiment. *Transactions of the ASAE*, Vol. 48, pp.2259-2268.
- Jacobson, M.Z. (1999). *Fundamentals of atmospheric modeling*. Cambridge University Press, Cambridge, UK.
- Le, P. D.; Aarmink, A. J. A.; Ogink, N. W. M. & Versteegen, M.W. A. (2005). Effect of environmental factors on odour emission from pig manure. *Transactions of the ASAE*, Vol. 48, pp.757-765.
- Li, Y. & Guo, H. (2008). Evaluating the effect of computational time steps on livestock odour dispersion using a CDF model. *Transactions of the ASABE*, Vol. 50, pp.2199-2204.
- Lim, T.T.; Heber, A.J.; Ni, J.Q.; Sutton, A.L. Sutton & Kelly, D.T.(2001). Characteristics and emission rates of odour from swine nursery buildings. *ASBE Transactions*, Vol. 44, pp. 1275-1282.
- Lin, X.-J.; Barrington, S.; Nicell, J. & Choinière, D. (2009). Evaluation of standard k- $\epsilon$  model for the simulation of odour dispersion downwind from windbreaks. *Canadian Journal of Civil Engineering*. Vol. 36, pp. 895-910.
- Lin, X.J.; Choinière, D. & Prasher, S. & Barrington, S. (2009b). Effect of weather on windbreak odour dispersion. *Journal of Wind Engineering and Industrial Aerodynamics*, Vol 97, pp.487-496. ISSN: 0167-6105.
- Lin, X.-J.; Nicell, J.; Choinière, D.; Vézina, A. & Barrington, S. (2006). Field odour dispersion plume produced by different natural windbreaks. *Journal of Agriculture, Ecosystems & Environment*, Vol. 116, pp. 263-272. ISSN: 0167-8809.
- Lin, X.-J.; Nicell, J.; Choinière, D. & Barrington, S. (2007b). Simulation of the effect of windbreak characteristics on odour dispersion. *Biosystems Engineering*, Vol. 98, pp. 347-363. ISSN: 1537-5110.
- Lin, X.-J.; Nicell, J.; Choinière, D. & Barrington, S. (2007c). Effect of natural windbreaks on maximum odour dispersion distance. *Journal of Canadian Biosystems Engineering*, Vol. 49, pp.6.21-6.32.
- Lin, X.-J.; Nicelle, J.; Choinière, D. & Barrington, S. (2007a). Livestock odour dispersion as affected by natural windbreaks. *Journal of Soil, Water and Air Pollution*, Vol 182, pp.263-273.
- McPhail, S. (1991). Modeling the dispersion of agricultural odours . *Proceedings of a workshop on agricultural odours*. Toowoomba, Queensland, Australia. AMLRDC Report No. DAQ 64/7. Feedlot Services Group, Queensland Department of Primary Industries. Toowoomba, Queensland, Australia.
- Menter, R.R.; Kuntz, M. & Langtry, R. (2003). Ten years of industrial experience with the SST turbulence model. In: K. Hanjalic, Y. Nagano and M. Tummers (Editors), *Turbulence, Heat and Mass Transfer 4*. Begell House Inc, Redding, CT, pp.625-632.
- Nimmermark, S. (2006). *Characterization of odour from livestock and poultry operation by the hedonic tone*. Paper number 064157. In: ASABE Annual International Meeting,

- American Society of Agricultural and Biological Engineering, St Joseph, Michigan, USA.
- O'Neill, D.H. & Phillips, V.R. (1992). A review of the control of odour nuisance from livestock buildings: Part 3, properties of the odorous substances which have been identified in livestock wastes or in the air around them. *Journal of Agricultural Engineering Research*, Vol. 53, pp.23-50.
- Panofsky, H.A. & Dutton, J.A. (1984). *Atmospheric turbulence: models and methods for engineering applications*. Wiley, New York, USA.
- Plate, E.J., 1971. The aerodynamics of shelter belts. *Agricultural Meteorology*, Vol. 8, pp203.
- Redwine, J. S. & Lacey, R. E. (2000). A summary of state-by-state regulation of livestock odour. In: *Proceedings of the Second International Conference on Air Pollution from Agricultural Operations*, St. Joseph, Michigan, ASBE.
- Riddle, A.; Carruthers, D.; Sharpe, A.; McHugh, C. & Stocker, J. (2004). Comparisons between FLUENT and ADMS for atmospheric dispersion modelling. *Atmospheric Environment*, Vol. 38, pp.1029-1038.
- Saatdjian, E.B. (2000). *Transport phenomena: equations and numerical solutions*. John Wiley, New York, USA.
- Sarkar, U.; Longhurst, P. J. & Hobbs, S. E. (2002). Community modeling: a tool for correlating estimates of exposure with perception of odour from municipal solid waste landfills. *Journal of Environmental Management*, Vol. 68, pp.153-160.
- SAS Institute Inc. (2001). *SAS (r) Proprietary Software Release 8.2*. SAS, Cary, NC, USA.
- Schauberger, G.; Piringer, M. & Petz, E. (1999). Diurnal and annual variation of odour emission from animal houses: a model calculation for fattening pigs. *Journal of Agricultural Engineering Research*, Vol. 74, pp.251-259.
- Schnelle, K.B. & Dey, P.R. (2000). *Atmospheric dispersion modeling compliance guidelines*. McGraw-Hill, New York, USA.
- Smith, R. J. & Watts, P. J. (1994). Determination of odour emission rates from cattle feedlots: Part 1, A review. *Journal of Agricultural Engineering Research*, Vol. 57, pp.145-155.
- Sun, H.; Stowell, R.R.; Keener, H. M. & Michel, F.C. (2002). Comparison of predicted and measured ammonia distribution in a high-rise™ hog building (HRHB) for summer conditions. *Transactions of the ASAE*, Vol. 45, pp.1559-1568.
- Ucar, T. & Hall, F.R. (2001). Review windbreaks as a pesticide drift mitigation strategy: a review. *Pest Management Science*, Vol. 57, pp.663-675.
- Vigiak, O.; Sterk, G.; Warren, A. & Hagen, L.J. (2003). Spatial modeling of wind speed around windbreaks. *Catena*, Vol. 52, pp.273-288.
- Wang, H. & Takle, E.S. (1997). Momentum budget and shelter mechanism of boundary-layer flow near a shelterbelt. *Boundary-Layer Meteorology*, Vol. 82, pp.417-435.
- Wang, H.; Takle, E. S. & Takle, A. (1995). Numerical simulation of boundary-layer flows near shelterbelt. *Boundary-Layer Meteorology*, Vol. 75, pp.141-173.
- Wilson, J.D. & Yee, E. (2003). Calculation of winds distribution by an array of fences. *Agricultural and Forest Meteorology*. Vol. 115, pp. 31-50.
- Wilson, J.D. (1985). Numerical study of flow through a windbreak. *Journal of Wind Engineering and Industrial Aerodynamics*, Vol. 21, pp.119-154. ISSN: 0167-6105.

- Wilson, J.D. (2004). Oblique, stratified winds about a shelter fence. Part II: Comparison of measurements with numerical models. *Journal of Applied Meteorology*, Vol. 43, pp.1392-1409.
- Xing, Y.; Guo, Y.; Feddes, J. & Shewchuck, S. (2006). Evaluation of air dispersion models using swine odour plume measurement data. *CSAE Paper 06-172*. Canadian Society of Agricultural Engineering, Winnipeg, Manitoba, Canada.
- Zald, D. H. & Pardo, J. V. (2000). Functional neuroimaging of the olfactory system in humans. *International Journal of Psychophysiology*, Vol. 36, pp.1165-1181.
- Zhang, Q.; Feddes, J.; Edeogu, I.; Nyachoti, M.; House, J.; Small, D.; Liu, C.; Mann, D. & Clark, G. (2002). *Odour production, evaluation and control*. Manitoba Livestock manure Management Initiative Inc., Winnipeg, Manitoba, Canada.
- Zhang, Q.; Zhou, X. J.; Cicek, N. & Tenuta, M. (2007). Measurement of odour and greenhouse gas emissions in two swine farrowing operations. *Canadian Biosystems Engineering*, Vol. 49, pp.6.13-6.20.
- Zhu, J.; Jacobson, L. D.; Schmidt, D. R. & Nicolai, R. (2000). Evaluation of INPUFF-2 model for predicting downwind odours from animal production facilities. *Applied Engineering in Agriculture*, Vol. 16, pp.159-164.



## **Part 3**

### **CFD in Industrial**



# Simulation of Three Dimensional Flows in Industrial Components using CFD Techniques

C. Bhasker  
Hyderabad-500020  
India

## 1. Introduction

### 1.1 Description of power/process plant

The schematic of coal fired power plant for electricity generation is shown in Fig-1, wherein fuel preparation is being made in grinding mills. The fuel from the mill outlet tubes will be transported to corner fired furnace as shown in Fig-2. The coal combustion in the furnace will take place at 1500 deg C, wherein the tubes carrying water convert to saturated steam and enters in steam-drum. This steam in turn subjected turbine cylinders at different pressures through reheater/superheater, will generate electric power. Due to presence of high ash content in Indian coals, fluid transport devices often fail to perform with expected efficiencies. To troubleshoot these failures, industries are expected to integrate key technologies for design process through CAE-PLM concepts as suggested by Efim Korytnyi (1988). The traditional approach of taking a product from laboratory scales to pilot plants and then to develop the better efficient product is no longer attractive. While measurement probes provide point data, field information at multiple locations are often required to diagnose a problem fully. Success in this challenging environment hinges on leveraging the latest technology system based on CAE and multi-disciplinary coupled simulations as indicated by Pordal, et.al (2001) and Tylor B Thompson, et.al (1999).

## 2. CFD process

Today's design processes must be more accurate, while minimizing development costs to compete in a world economy. This forecast engineering companies to take advantage of design tools, which augment existing experience with empirical data. While minimizing cost, one tool which excels under these conditions are through CFD as discussed in technology road map towards chemical industries by Christopher Riff (2004). In general, CFD methods are used to understand the overall flow behavior of single/multi-component assemblies involves several steps like geometry modeling, computational mesh generation, and description of flow physics with turbulence, incorporating two-phase flow effects and visualization besides extending to multi-disciplinary areas like FSI and aero acoustics. CFD simulations are highly dependent on CAD model, which can be generated from programming/assembly drawings, are expected to be error free for evaluation of meaningful flow characteristics. Creation of component from simple to complex parts are generated using several commercial CAD software or programming is illustrated in Fig-3.

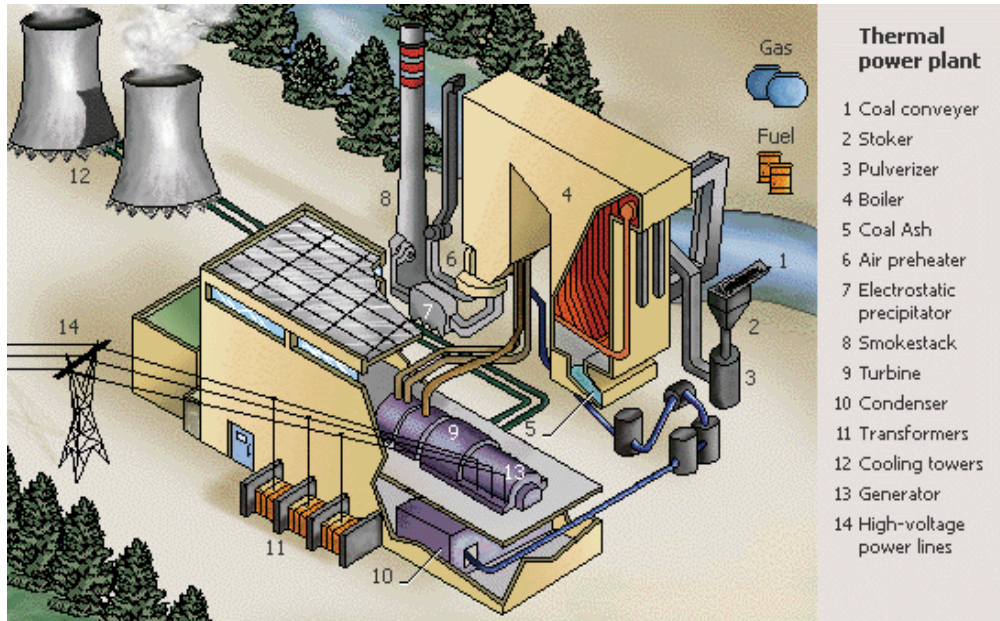


Fig. 1. Schematic of Coal fired Power Plant

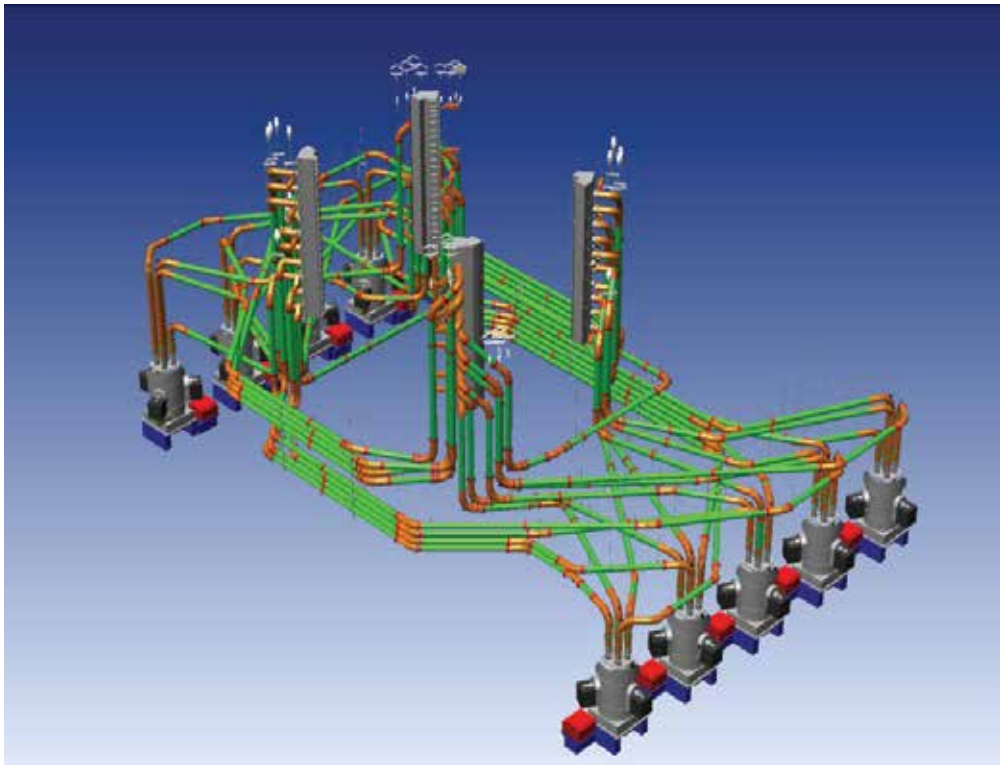


Fig. 2. Arrangement of fuel from mills to the furnace

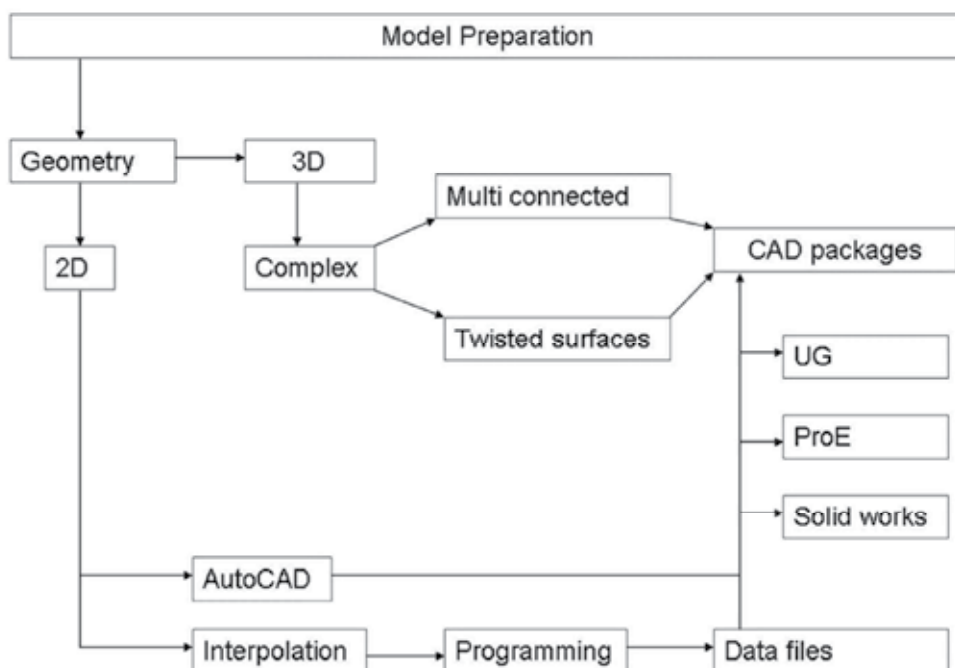


Fig. 3. Approach for creation of component geometries

The geometric shapes like cylinders, aerofoil and straight ducts can be generated through high level programming languages while linking its output to grid generation/flow simulation as discussed by C.Bhasker (2000). The disadvantage of this approach is of limited use and lacks graphic user interfaces for visualization of the component. If the geometries are complex assemblies involving complicated surface irregularities, solid modeling software provides effective tools for generation of three dimensional models accounting every detail of the component. The CAD software has powerful geometric engine provide variety of definition tools including fillet, shell, draft and feature based primitive icons to generate part modeling interactively were comprehensively discussed by Delli P (2007). CAD softwares includes powerful tools for capturing design intent in part features, which are easily edited and updated to support real-time modification processes. Using solid modeller softwares SDRC - I-DEAS and UG NX, several three dimensional component assemblies are created and exported to third party softwares for extraction of fluid portion for computational mesh generation.

### 3. Computational grid generation

At the core of CFD, computational grid is central element, which often considered as most important and time consuming part in simulation projects. The quality of the grid plays a direct role on the quantification of flow results, regardless of the flow solver used for simulation. The mesh generation concepts were comprehensively discussed by Thomson, JF (1985) and reviewed by Mazumdar, S (1994) has resulted to several commercial softwares which are being extensively used for several industrial components by Bhasker, C (2010a) was shown in Fig-4. The quality of mesh interms of size and density influences the accuracy,

convergence and speed of the numerical solution of fluid flow equations. As described in Fig-4 the computational mesh for component volume can be generated through unstructured, structured and hybrid method.

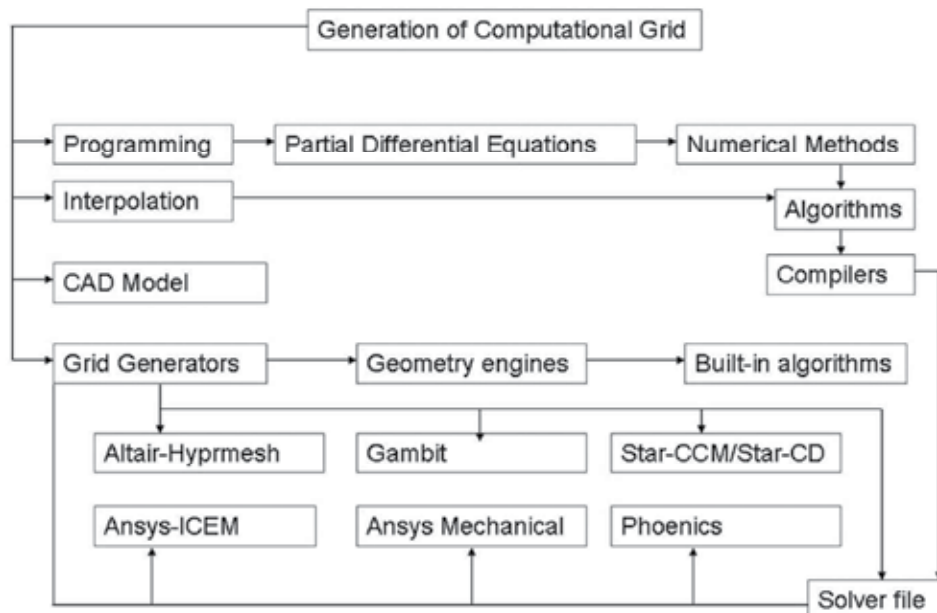


Fig. 4. Schematic of computational mesh generation

Unstructured grid methods utilize an arbitrary collection of elements to fill the domain automatically requires the volume bounded by error free surfaces. The unstructured mesh with tetra-hedral elements will have problems associated with large memories and lacks mesh refinement tools at desired locations in the computational domain is still preferred technique for the complex geometries. Using this type of mesh, parametric mesh generation for check valve has been developed by Iyer VK (2009) to estimate pressure drop under different opening conditions. In structured grid methods the grid is laid out in a regular repeating pattern called a block. These types of blocks utilize quadrilateral elements in 2D and hexahedral elements in 3D. Depending upon geometrical shape of the object, hexahedral elements with the combination of tetrahedral elements are generated in two different blocks of topologically connected boundaries. The accomplishment of computational meshes through high level programming requires numerical solutions to differential equation using interpolation or discretization using Finite volume/difference methods. To this effect, among several commercial grid generators, provides 2D/3D single and multiblock structured and unstructured meshing tools with the direct interface to popular flow solvers and applications are discussed in subsequent sections.

### 3.1 Structured grid generation using body fitted coordinates

The block grids using quadrilateral elements in 2D and hexahedral elements in 3D volume are generated through numerical solution to differential equations. If the geometries are not irregular, generation of body fitted coordinate grids are extensively discussed by Schuh

(1990) using the transformations from physical to computational domain as shown in the Fig-5.

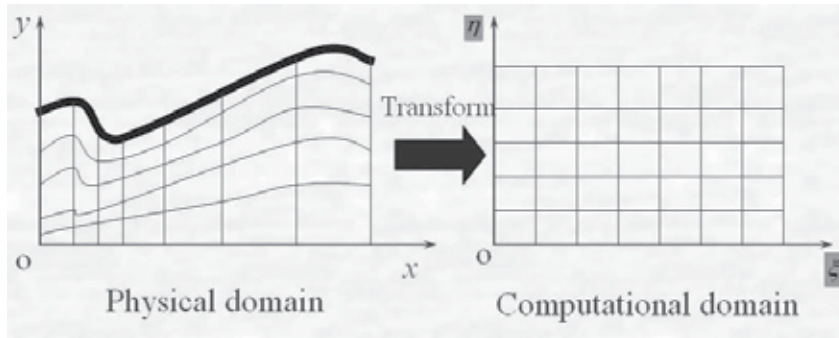


Fig. 5. Transformation of physical domain to computational domain

In the two-dimensions, the transformations in the mathematical form are represented as -

$$\frac{\partial f}{\partial x} = \frac{\partial f}{\partial \xi} \frac{\partial \xi}{\partial x} + \frac{\partial f}{\partial \eta} \frac{\partial \eta}{\partial x} = \xi_x \frac{\partial f}{\partial \xi} + \eta_x \frac{\partial f}{\partial \eta} \quad (1)$$

$$\frac{\partial f}{\partial y} = \frac{\partial f}{\partial \xi} \frac{\partial \xi}{\partial y} + \frac{\partial f}{\partial \eta} \frac{\partial \eta}{\partial y} = \xi_y \frac{\partial f}{\partial \xi} + \eta_y \frac{\partial f}{\partial \eta} \quad (2)$$

Substitution of these derivatives in the Poisson equation, the transformed equation will results to -

$$\alpha \frac{\partial^2 \xi}{\partial x^2} + 2\beta \frac{\partial x}{\partial \xi \partial \eta} + \gamma \frac{\partial^2 \eta}{\partial x^2} = -J^2 \left( P \frac{\partial x}{\partial \xi} + Q \frac{\partial x}{\partial \eta} \right) \quad (3)$$

$$\alpha \frac{\partial^2 \xi}{\partial y^2} + 2\beta \frac{\partial y}{\partial \xi \partial \eta} + \gamma \frac{\partial^2 \eta}{\partial y^2} = -J^2 \left( P \frac{\partial y}{\partial \xi} + Q \frac{\partial y}{\partial \eta} \right) \quad (4)$$

$$\alpha = \frac{\partial^2 x}{\partial \xi^2} + \gamma \frac{\partial^2 x}{\partial \eta^2} \quad ; \quad \gamma = \frac{\partial^2 y}{\partial \xi^2} + \gamma \frac{\partial^2 y}{\partial \eta^2} \quad (5)$$

$$J = \frac{\partial(x, y)}{\partial(\xi, \eta)} = \frac{\partial x}{\partial \xi} \frac{\partial y}{\partial \eta} - \frac{\partial x}{\partial \eta} \frac{\partial y}{\partial \xi} \quad (6)$$

and the control functions  $P, Q$  in terms of transformed coordinates are written as

$$P(\xi, \eta) = \sum_{i=1}^N -a_i \text{sign}(\xi - \xi_i) e^{-c_i(\xi - \xi_i)} - \sum_{j=1}^M b_j \text{sign}(\xi - \xi_j) e^{-d \left[ (\xi - \xi_j)^2 + (\eta - \eta_j)^2 \right]^{\frac{1}{2}}} \quad (7)$$

$$Q(\xi, \eta) = \sum_{i=1}^N -a_i \text{sign}(\eta - \eta_i) e^{-c_i(\eta - \eta_i)} - \sum_{j=1}^M b_j \text{sign}(\eta - \eta_j) e^{-d \left[ (\eta - \eta_j)^2 + (\xi - \xi_j)^2 \right]^{\frac{1}{2}}} \quad (8)$$

Where a,b,c,d are positive integers which control the magnitude of attraction towards line and point. Negative value of a and b result in the repulsion from the lines and points. Boundaries of cylinder and aerofoil are seen in the Fig-6. To account curvature and spacing, the derivatives of control functions are written as -

$$P(\xi,\eta) = -\frac{\frac{\partial x}{\partial \xi} \cdot \frac{\partial^2 x}{\partial \xi^2}}{\left|\frac{\partial x}{\partial \xi}\right|^2} - \frac{\frac{\partial x}{\partial \xi} \cdot \frac{\partial^2 x}{\partial \eta^2}}{\left|\frac{\partial x}{\partial \eta}\right|^2} ; \left|\frac{\partial x}{\partial \xi}\right| = \left[\frac{\partial x}{\partial \xi} \cdot \frac{\partial x}{\partial \xi}\right]^{\frac{1}{2}} \quad (9)$$

$$Q(\xi,\eta) = -\frac{\frac{\partial y}{\partial \eta} \cdot \frac{\partial^2 y}{\partial \eta^2}}{\left|\frac{\partial y}{\partial \eta}\right|^2} - \frac{\frac{\partial y}{\partial \eta} \cdot \frac{\partial^2 y}{\partial \xi^2}}{\left|\frac{\partial y}{\partial \xi}\right|^2} ; \left|\frac{\partial y}{\partial \eta}\right| = \left[\frac{\partial y}{\partial \eta} \cdot \frac{\partial y}{\partial \eta}\right]^{\frac{1}{2}} \quad (10)$$

The effect of control functions P, Q with attraction of points (fine grid points) towards the boundaries. Such types of grids close to solid boundaries are essential in CFD simulation for accurate estimation of viscous losses. In order to generate body fitted computational mesh, elliptic partial differential equations with control functions are solved numerically using finite volume techniques. The control functions clusters the mesh points towards solid boundaries very closely to account viscous losses. An interactive program has been developed for generation of body fitted coordinated grid for cylinder and aerofoil whose output has been visualised in the graphic software Tecplot3D. The body fitted computational mesh data from the program for a rod-aerofoil with boundary layer thickness towards solid boundaries are shown in Fig-6 and the detailed derivations and program code structure is available in the presentation material by Bhasker (2010b).

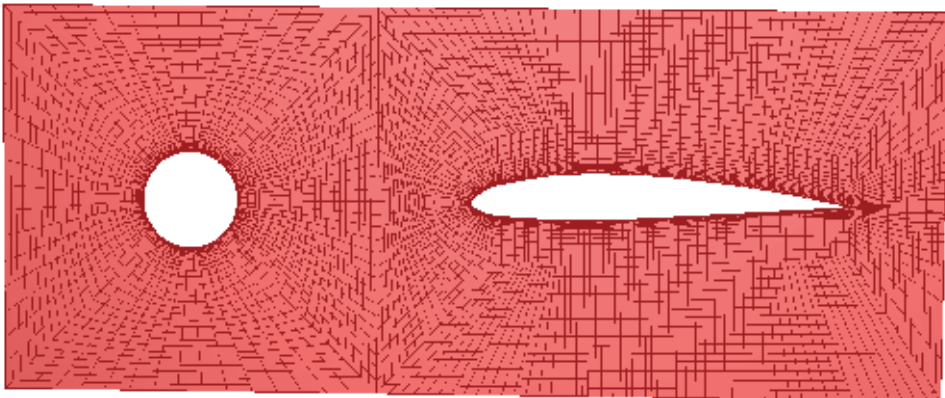


Fig. 6. Body fitted CFD mesh for rod-aerofoil using programming approach

When the geometries are irregular and multi-connected, the programming approach is limited usage and algorithms for multiblock structured grid generation schemes were developed by Spekrijse (1966) are implemented in commercial software, which provides more user friendly under Graphic User Interface - GUI environment with powerful geometric engine for CAD repair and multi-block grid generation, with choice of elements and different distribution laws for mesh density.



### 3.2 Structured multi-block grid generation

The geometry of fuel preparation device called beater wheel mill used for power generation has been considered from the experimental investigation by Founti (1995) for flow simulation using multiblock structured grid generation. The geometrical details and block decomposition around solid objects like impeller vanes baffle plates in the classifier, wherein flow is subjected to impeller blades for crushing the coals into fine particles. The flow from the impeller outlet enters mill chamber travels upwards through convergent duct and enters in the classifier region from baffle plates. In order to carry out flow simulation, mill geometry in 2D plane has been created and decomposed for mesh generation using commercial grid generator as shown in Fig 7(a).

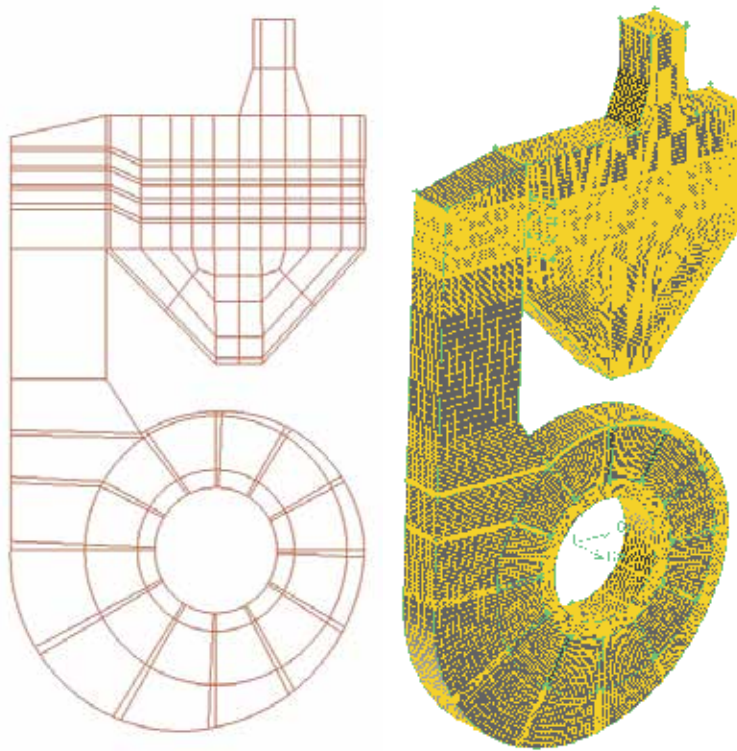


Fig. 7. (a-b) Multiblock structured grid for industrial component

In order to generate computational mesh for the mill geometry shown, the component has grouped into three parts impeller, converging duct and classifier which can be toggled through blank and unblank options. In the computational domain, 2d mesh generation has been started from the small cell using quad elements. To avoid mixed elements, mesh style algorithms are properly chosen to map rectangular mesh. In order to have uniform mesh at neighboring cell, mesh density is varied in the flow direction. In this process, the mesh densities at mating edge across two cells are equivalenced. In this process, 2d quad elements at all the cells present in the computational domain are filled and equivalenced the edges so that no duplicate nodes are present across mating edges of cells. After checking the mesh quality, computational mesh was dragged in z direction for specified distance to generate

three dimensional meshes as shown in the Fig 7(b). The flow simulation through CFD coarse grid was extensively discussed by Anagnostopoulos J (1997) for partial geometry of the mill, which in turn was extended for detailed investigation by Bhasker (2008) to simulate the air flow from mill inlet to classifier outlet location.

### 3.3 Emerging trends in grid generation

Structured grid forms through building blocks, which will have six neighbor cells possess excellent numerical properties, when the flow is aligned with the grid. Hexahedral elements, which are efficient at filling space, support a high amount of skewness and stretching before the solution is significantly effected. Alternatively, computational mesh can be generated for complex shaped object through automatically using tetrahedral element, which has four neighbor cells. But, the triangle and tetrahedral elements have the problem that they do not stretch or twist well, therefore, the grid is limited to be isotropic, i.e. all the elements have the same size and shape. Ideally, flow should be perpendicular to the element surfaces. Hence, tetrahedrons are the least ideal computational cell and they are inefficient at filling space. Though volume mesh with tetra-hedral elements generates faster, but the simulation of flow equations require more memory and have longer execution times than structured grid solvers. Hexahedra elements are an improvement, but they are difficult and expensive to generate for complex geometries.

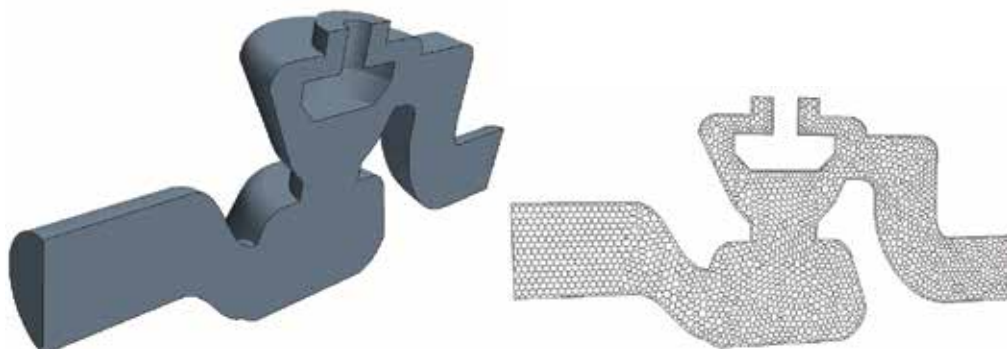


Fig. 8. Polyhedral Mesh for the valve (a) geometry (b) Mesh

To overcome these difficulties, CFD solvers have developed new type of element is called polyhedral as discussed by Stephen Ferguson (2005). Polyhedral cells possess excellent numerical properties including good accuracy using finite volume discretizations and well connections with neighboring cells. Polyhedral mesh cell counts are much smaller than tetrahedral meshes with equivalent accuracy. The flow solvers Star-CCM and Fluent use polyhedral meshes for flow simulation. In order to generate polyhedral meshes for CFD flow simulation, the geometry of control valve is shown in Fig.8 (a) was imported. On visualization, it is observed that surface representation of geometry through triangle definition was coarsely faceted.

In order to improve surface quality, the solid boundary surfaces are need to be broken so that mesh refinements/clustering can be created at desired locations. Using this option, geometry of component was split at an angle of  $45^\circ$  to obtain several boundary surfaces. These boundaries are carefully visualized and grouped into the regions like inlet, exit, valve body and symmetry surfaces. In order to improve/generate the surface/volume mesh

quality, the suitable inputs related to surface curvature, growth rate, proximity, base size, number of prism layers, prism layer stretching and relative thickness values are defined. For the provided flow conditions, flow simulation has been carried out on this polyhedral mesh shown in Fig-8(b) for several flow characteristics and estimation of pressure drop evaluation across control valve inlet/exit locations by Bhasker (2010c).

#### 4. Fluid mechanics – effect of turbulence

The transport of fluid comprises gases/liquid from one component to other in power/process equipment are described through mass, moment and energy conservation principles. The Navier Stokes (transport) equations are derived from these principles are discussed by Hoffman, K.A [1993) are represented mathematically as-

$$\frac{\partial \rho \phi}{\partial t} + \text{div}(\rho \phi \vec{u}) = \text{div}(\Gamma \text{grad} \phi) + q_{\phi} \quad (11)$$

The terms on Left Hand Side - LHS defines acceleration of flow over time with inertia depends on the sum of the external forces, diffusion and sources acting on the fluid element. If the value of  $\phi$  is 1, the eqn. (11) results to continuity equation. The value of  $\phi$  is either  $u$  or  $v$  or  $w$ , the above eqn. describes momentum equation in  $x$ ,  $y$ ,  $z$  directions. The value of  $\phi$  is  $h$  then the above eqn. yields to energy equation. Two important material properties of fluid i.e., density and viscosity, whose ratio times characteristic flow velocity and length are defined as Reynolds number. This non-dimensional quantity is the ratio of inertial forces to viscous forces, whose magnitude depends upon flow disturbances can changes from laminar to turbulent. In other words, if the Reynolds Number is small, then the flow will be laminar and the flow progresses in layers. If the Reynolds Number is large flow then the flow will be turbulent and there will be a mixing of flow layers with large eddies are illustrated through cigarette smoke in Fig-9 by Sodja, J (2007).

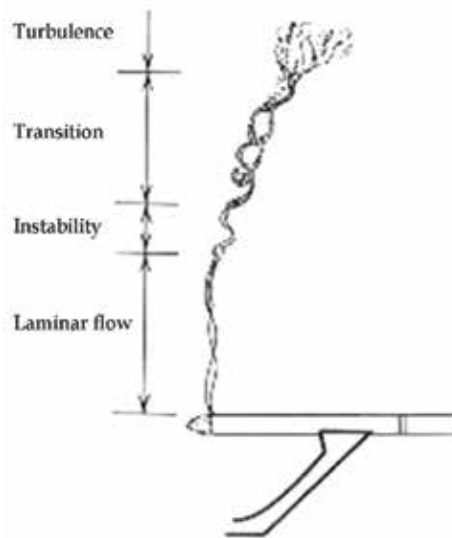


Fig. 9. Illustration of turbulent flow from cigarette smoke

The flow consists of a spectrum of different scales in turbulent flow, largest eddies are the order of geometry scales and breaks into smaller as time progress. At the other end of the spectra, the smallest eddies by viscous forces are dissipated into internal energy. Even though turbulence is chaotic, its characteristics are determined through Navier-Stokes equations. The turbulent is dissipative, which means that kinetic energy in the small eddies are transformed into internal energy. The small eddies receive the kinetic energy from slightly larger eddies. The slightly larger eddies receive their energy from even larger eddies and so on. In order to resolve wide spectrum of scales in turbulent eddies, normally two approaches are employed and are discussed in detail by Zhiqiang Z (2007). The first approach is Direct Numerical simulation - DNS, wherein the range of eddy size varies as small as the Kolmogorov scale in turbulent flow. This requires dense mesh points for proper resolution and its solution depends on heavy computational resources, expensive, time consuming process and very rarely used simulation technique. The other approach generally used for most of the applications are Reynolds' averaging process described by Shao (2009), wherein flow variables are decomposed into mean and fluctuating components as -

$$u_i = \bar{u}_i + u_i' \quad (12)$$

Where  $i=1,2,3$  denotes in  $x, y, z$  direction. Like wise the pressure and other scalars can be expressed as

$$\phi = \bar{\phi} + \phi' \quad (13)$$

Substituting flow variables in the form into the instantaneous continuity and momentum equations and taking a time (or ensemble) average (and dropping the overbar on the mean velocity) yields to

$$\frac{\partial \rho}{\partial t} + \frac{\partial}{\partial x_i}(\rho u_i) = 0 \quad (14)$$

$$\frac{\partial}{\partial t}(\rho u_i) + \frac{\partial}{\partial x_j}(\rho u_i u_j) = -\frac{\partial p}{\partial x_i} - \frac{\partial}{\partial x_j} \left[ \mu \left( \frac{\partial u_i}{\partial x_j} + \frac{\partial u_j}{\partial x_i} - \frac{2}{3} \delta_{i,j} \frac{\partial u_k}{\partial x_k} \right) \right] + \frac{\partial}{\partial x_j} (\overline{-\rho u_i' u_j'}) \quad (15)$$

Eqn (14-15) are called (RANS) equations. The term  $\overline{\rho u_i' u_j'}$  in the eqn (15) results from averaging process is called Reynolds' Stress. With the help of Boussinesq hypothesis to relate the Reynolds stresses, choosing Kronecker delta  $\delta=1$  if  $i=j$  and  $\overline{u_i' u_i'} = 2k$  the Reynold's stress term in the eqn (15) is rewritten as -

$$\overline{-\rho u_i' u_j'} = \mu_t \left( \frac{\partial u_i}{\partial x_j} + \frac{\partial u_j}{\partial x_i} \right) - \frac{2}{3} \left( \rho k + \mu_t \frac{\partial u_k}{\partial x_k} \right) \delta_{i,j} \quad (16)$$

Where  $\mu_t$  is turbulent viscosity. To resolve turbulence viscosity and Reynolds' stresses, eddy viscosity models based on Boussinesq hypothesis will leads to zero, one and two equation turbulence models and Reynolds's Stress models - RSM. The strength and weakness of these models for prediction of turbulence effects are extensively reviewed by Davidson (2003). Whenever non-isotropic effects in turbulence are important use of higher

models like  $v^2-f$  is preferable to predict separation near the wall. When the fluid flow is subjected to rotating components, Large Eddy Simulation -LES or Detached Eddy Simulations - DES are employed to evaluate flow characteristics as a function of turbulence viscosity and energy dissipation. These models are based on filtered equations, still require finer meshes and solve RANS calculations in transient mode. In the simulation of turbulent flows, accurate estimation of pressure drop infact highly dependent on usage of turbulence model with smooth/rough wall functions. The variation of pressure influence surfaces roughness and can alter structural stresses. Description of these models are highly mathematical nature and its detailed derivations are available in the technical paper by Durbin P.A. (1995) and text book by Wilcox (1999). An application of turbulent flows in complex components of industrial equipments are discussed in the case study -1 & 2.

## 5. CFD Solvers – Finite Volume Algorithms (FVM)

As discussed in the previous section, whether working fluid is a compressible or incompressible and laminar or turbulent, its dynamics are described by mass, momentum and energy equations. However its complexities depends upon consideration of the external forces due to presence of discrete particles, fluid-solid interactions and aero acoustics besides incorporating thermal phenomena involving different modes of heat transfer mechanism in the simulation. FVM is used to discretize Navier Stokes equations (11) numerically to solve for several flow variables on high speed digital devices as discussed by Petersburg (2004). The integration of transport equation over the control volume, after applying Gauss divergence theorem can be written as

$$\int_{CV} \frac{\partial \rho \phi}{\partial t} dV + \oint_S (\rho \phi \bar{u}) \cdot \bar{n} dS = \int_S (\Gamma \text{grad} \phi) \cdot dS + \int_{CV} q_\phi dV \quad (17)$$

The control volume  $_{CV}$  of typical cuboids with P as its center are surrounded by six faces defined as n - North, s - South, e-East, w-West, t-Top and b-Bottom. The face centers n, s, e, w, t and b are located at the intersection of the lines joining the midpoint of the opposite edges. All variables are stored either in collocated or staggered nodes in the finite volume cell to address pressure-velocity coupling. If the flow is steady, in the LHS of eqn (17) first term vanishes. On RHS of above eqn. if  $q$  is constant in the source term and linear, then the volume integral can be approximated about  $p$  as

$$\int_{CV} q_\phi dV = \bar{q} \text{Vol}(CV) \approx q_p \text{Vol}(CV) \quad (18)$$

If  $q$  is bilinear, interpolation of  $q$  at more points of control volume can is approximated as

$$\int_{CV} q_\phi dV = \frac{\Delta x \Delta y}{36} [16q_p + 4q_s + 4q_n + 4q_e + 4q_w + q_{se} + q_{sw} + q_{ne} + q_{nw}] \quad (19)$$

Now to approximate surface integral on LHS of eqn (17), the net flux through CV boundary is the sum of integrals over the faces implies

$$\int_S (\rho \phi \bar{u}) \cdot \bar{n} dS = \int_S f \cdot \bar{n} dS = \sum_k \int_{S_k} f dS \quad \text{where } f = \rho \phi \bar{u} \quad (20)$$

Considering east face, assuming dependent variables like velocity/density ( $f$ ) at cell points and if the points  $n_e$ ,  $e$  and  $s_e$  known, the function  $f$  with unknown variable  $\phi$  can be approximated through Simpsons rule as

$$\int_S f dS \approx \frac{S_e}{6} (f_{n_e} + 4f_e + f_{s_e}) \tag{21}$$

To determine  $f$  with the unknown  $\phi$ , interpolations like, unwind - (UDS), central differencing-(CDS) and quadratic upwind interpolation-(QUICK) techniques are shown in Fig-10 are used to develop the algorithms. In the case of upwind difference, the value of  $\phi$  at location  $e$  will be

$$\phi_e = \begin{cases} \phi_p & \text{if } (\vec{u} \cdot \vec{n})_e > 0 \\ \phi_e & \text{if } (\vec{u} \cdot \vec{n})_e < 0 \end{cases} \tag{22}$$

this scheme is of first order, the solution is numerically diffusive and generally not recommended. The approximation of  $\phi$  at location  $e$  in the case of central difference scheme is.

$$\phi_e = \phi_e \lambda_e + \phi_p (1 - \lambda_p) \tag{23}$$

Which is a second order, still produce oscillations.

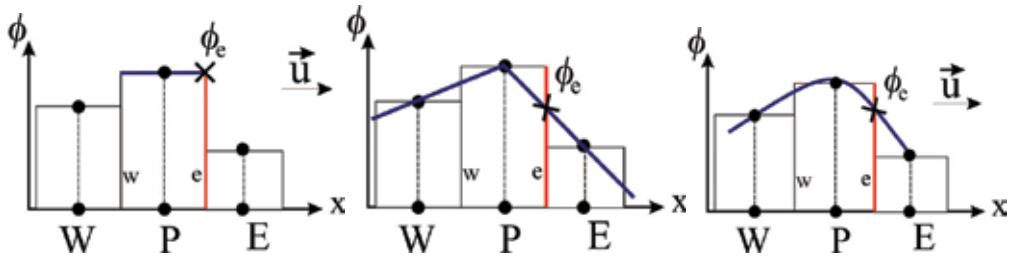


Fig. 10. Illustration of UDS, CDS and QUICK Interpolation Schemes

The approximation using QUICK

$$\phi_e = \begin{cases} \phi_p + g_1(\phi_e - \phi_p) + g_2(\phi_p - \phi_w) & \text{if } u_x > 0 \\ \phi_e + g_3(\phi_p - \phi_e) + g_4(\phi_e - \phi_p) & \text{if } u_x < 0 \end{cases} \tag{24}$$

Where  $g$  is coefficients in terms of nodal coordinates and the scheme is third order and aimed to provide accurate estimates. In the QUICK scheme, one adds one point in each direction and calculates the derivative using the cubic polynomial drawn through the four involved points. The approximation to surface and volume integrals in eqn (24) generates algebraic system of equations for control volume as -

$$A_p \phi_p + \sum_I A_I \phi_I = Q_p \quad \text{which in matrix form are represented as} \tag{25}$$

$$[A] \cdot [\phi] = [Q] \tag{26}$$

Where [A] is sparse matrix and the coefficient matrix values are updated which depends upon boundary conditions and initial guess and above equality will not hold. The imbalance called residual R defined as -

$$R_p = A_p \phi_p + \sum_l A_l \phi_l - Q_p \quad (27)$$

Will reduce over the increase in iteration is called convergence. The target value for Root Mean Square - RMS or maximum RMS of the order 1.0e-04 is generally used for convergence criteria based on discretization schemes used for flow equations. Acceleration of convergence also depends on the scheme of matrix inversion techniques employed. It may be noted that level maximum RMS error are always lower than RMS errors and it will take more execution time.

## 6. Particulate laden flows – erosive wear by particle impacts

Many engineering problems involves the study of multiphase flow mixtures with the combination of gas-solid, liquid-solid phases and its effects were extensively reviewed by Humphrey JAC (1990). Prediction of flows with dispersed phase involves the separate calculation of each phase with source terms to account the interaction between two phases. The flow of the continuous phase is predicted using a discretized form of the Navier Stoke's equations. The particles motion as a function flow velocities/temperatures are predicted using the discrete approach, wherein each individual particle is treated on Lagrangian scale. The most widely applied method available to determine the behavior of the dispersed phase is to track several individual particles through the flow field. Acceleration of particle in the flowing fluid under the assumptions a) Particle/particle interactions are not included in the model. b) Particle interactions may be important in flows, where the discrete phase volumetric concentration is greater than 1% c) there are no particle source terms to the turbulence equations, and therefore turbulence is not modulated by the discrete phase and d) Only inert, spherical particles are considered, are described mathematically as--

$$m_p \frac{dv_p}{dt} = 3\pi\mu d C_d (v_f - v_p) + \frac{\pi d^3 \rho_f}{6} \frac{dv_f}{dt} + \int_{t_0}^t \frac{\pi d^3 \rho_f}{12} \left( \frac{dv_f}{dt} - \frac{dv_p}{dt} \right) + F_e \quad (28)$$

$$\frac{3}{2} d^2 \sqrt{\pi \rho_f \mu} \int_{t_0}^t \frac{\frac{dv_f}{dt} - \frac{dv_p}{dt}}{\sqrt{t-t'}} dt' - \frac{\pi d^3}{6} (\rho_p - \rho_f) \omega \times (\omega \times \bar{R}) - \frac{\pi d^3 \rho_p}{3} \omega \times v_p$$

Detailed derivation of for acceleration of particle and its simplification was discussed by Routhiainen, P.O (1970). The terms on the left-hand side is acceleration of particle motion is the summation of all forces acting on it describes in above equation. The first term indicates viscous drag of fluid over the particle surface according to Stokes law. The second term is the force applied on the particle due to the pressure gradient in the fluid surrounding the particle caused by fluid acceleration. The third term is the force to accelerate the virtual mass of the fluid in the volume occupied by the particle. This term is important, when the displaced fluid mass exceeds the particle mass, such as in the motion of bubbles. The fourth term is an external force which may directly affect the particle such as gravity or an electric field. The fifth term is the Basset force or history term, which accounts for the deviation in

flow pattern from steady state. This term increases the instantaneous flow resistance, when the particle is accelerated at a high rate by an external force and can be significant only when the fluid density is equal or exceeds the particle density. The last two terms are the centrifugal and coriolis forces, present only in a rotating frame of reference. In the eqn (28) third and fifth terms are insignificant, as particle density is higher than fluid density. As a result, the eqn (28) further reduces to

$$\frac{\pi d^3 \rho_p}{6} \frac{dv_p}{dt} = 3\pi \mu d C_d (v_f - v_p) + F_e - \frac{\pi d^3}{6} (\rho_p - \rho_f) \omega \times (\omega \times \vec{R}) - \frac{\pi d^3 \rho_p}{3} \omega \times v_p \quad (29)$$

The drag coefficient  $C_d$  is obtained experimentally based on size and Reynolds' number of particle. The calculation of the instantaneous fluid velocity,  $v_f$ , depends on the flow regime and the type of particle tracking desired. In laminar flows or in flows, where mean particle tracking is calculated,  $v_f$  is equal to the mean local fluid velocity,  $\bar{v}_f$  surrounding the particle. Prediction of particle motion requires an accurate estimation of turbulent behavior and velocity fluctuations. Turbulent flows consist cascade of eddies, which transport and dissipate the energy. These eddies have a spectrum of characteristic sizes and life times. A particle travelling through a turbulent flow would be exposed to this entire spectrum of eddies, interacting with each for some characteristic time or distance. The particle trajectory calculations are carried out through numerical integration of eqn (29) in the flow filed upto the point of impact. When the particles are flowing through the fluid, its conditions at various locations are defined as follows:

| Boundary condition       | Action   |
|--------------------------|--|
| wall                     | escapes the domain, reflects, collects, reacts |
| symmetry plane           | reflects                                       |
| inlet                    | escapes the domain                             |
| outlet                   | escapes the domain                             |
| periodic                 | particle translated and velocity rotated       |
| grid embedding interface | search for new flux element                    |

The magnitude and direction of the impact velocity relative to the wall surface, for a large number of particles constitute the essential data for the evaluation of erosive wear. To this effect the velocity of a rebounding particle is calculated using the restitution coefficients, which are measured by experiments. When the particle impact/rebound from the wall surfaces, normal/tangential velocity before/after impact of the wall relating to coefficients of restitution, are calculated by using following relations:

$$V_{2t} = e_t V_{1t} \quad (30)$$

$$V_{2n} = e_n V_{1n}$$

The restitution ratios are determined experimentally based on flow velocity, particle and target material. The coefficient restitutions are calculated using

$$e_t = 1 - 2.12\beta_1 + 3.0775\beta_1^2 + 1.1\beta_1^3 \quad (31)$$

$$e_n = 1.0 - 0.4159\beta_1 + 0.49943\beta_1^2 - 0.293\beta_1^3 \quad (32)$$



Where  $\beta$  is impact angle in radian. With the values of coefficient restitution, impact angle and velocity, the erosive wear can be estimated with the following relation:

$$E = AV \beta \quad (33)$$

User need to specify the inputs for particle resident times, coefficient of restitution, particle material, density etc to calculate erosive wear by particle impacts. In turbo machinery applications, these particles under two phase flow conditions, experience different degrees of turning, as they flow through blade channels. The damage due to particle impacts are manifested by pitting and cutting of the blade leading and trailing edges are compressively discussed by Tabbakoff (1983). The overall effect of the phenomena from the aerodynamic point of view is an increase in total pressure loss across the blade row. However, the particulate laden flow simulation and its effect in the recyctic cyclone used in power generation are discussed at length under the case study-3.

## 7. Structural deformations due to flow pressure loads – FSI

The mathematical formulations to simulate structural deformations and stresses on the component surfaces are extensively discussed by Mustafa (2006). To determine the deformations, governing equations are mathematically represented as -

$$\rho \ddot{u} = \nabla \cdot \sigma + b \quad (34)$$

Where  $\ddot{u}$  is displacement,  $\sigma$  is stress field depends on strain, internal variable,  $b$  - body force. the expression for strain in terms of displacement can be expressed as

$$\bar{\varepsilon} = \frac{1}{2} (\nabla \ddot{u} + \nabla \ddot{u}^T) \quad (35)$$

The finite volume form and after integration by parts, the eqn (34) can be written as

$$\int_V \rho \ddot{u} dV = \int_A \sigma ds + \int_V b dV \quad (36)$$

For all cells  $i$  in the domain  $V$ , the discrete form of the momentum equation becomes:

$$\rho_i \ddot{u}_i V_i = \sum_{j \in f(i)} f_j + b_i V_i \quad \text{where } f_j = \sigma_j \cdot s_j; \quad s - \text{surface vector} \quad (37)$$

Dropping inertial terms and considering some of the forces acting on the body is zero for a static case, the eqn (37) can be re-written as -

$$r_j = \sum_{j \in f(i)} f_j + b_i V_i \quad (38)$$

In order to compute the stress tensor  $\bar{\varepsilon}$  on the centroids of the faces, it is required to establish the discrete form of the strain tensor and the deformation gradient  $\nabla \ddot{u}$ . The deformation gradient is computed at cell centers based on the difference in displacement between neighboring points. The approximation of stiffness matrix can be accumulated over all faces are -

$$K_{ik} = -\frac{\partial r_i}{\partial u_k} = -\sum_{j \in f(i)} \frac{\partial f_j}{\partial u_k} \quad \forall_{i,k} \in N(i) \quad (39)$$

With the help of Newton method to correct displacement Eqn (38) further simplifies to

$$K_{i,k} \nabla \ddot{u}_k = r_i^n \quad ; \quad \nabla \ddot{u}_k = \ddot{u}_k^{n+1} - \ddot{u}_k^n \quad (40)$$

To obtain structural deformations, pressure/heat flux loads are normally obtained from CFD solver using finite volume approximations and deformations/stresses are obtained through finite element techniques. However, in the current versions of few flow solvers, flow and thermal stress based on finite volume techniques can provide FSI characteristics of industrial components. A detailed discussion of a case related to transition duct used in gas-turbine application is presented under the case study-4.

## 8. Pressure waves – generation of aerodynamic noise

Aerodynamic noise results from the propagation of disturbances through the fluid flows at some point in time and space. Whether the disturbance is caused by an object or the fluid itself, fluctuations in fluid pressure propagate outwards from the source at the speed of sound relative to the fluid. Theory associated to noise as function of flow pressure was discussed by Alan Powel (1994) and the size of the pressure fluctuation relative to the pressure is called the sound pressure level. The sound intensity  $I$  defined as -

$$I = \frac{p'}{2\rho c} \quad (41)$$

where  $p'$  is fluctuating pressure,  $\rho$  - density of fluid and  $c$  - is speed of sound. Pressure and velocity fluctuations are simulated from CFD simulations in the near field noise. The near field will likely include the locations, where the maximum noise levels occur. For most CFD simulations the extent of the computational domain is usually such that near field/far field noise can be estimated.

The near field pressure and velocity fluctuations play a key role in determining far field noise, which occurs at some distance by acting as a localized source of noise. The influence of turbulence modeling on the broad band noise simulation for complex flow simulation by Greshchner (2004) has provided valuable insights to predict overall sound pressure and power for an application to rod-aerofoil. In many practical applications involving turbulent flows, noise does not have any distinct tones, and the sound energy is continuously distributed over a broad range of frequencies. Assuming that the fluid is a perfect gas, homogeneous wave equation is solved using noise sources taken from CFD are defined as -

$$\frac{\partial^2 \rho'}{\partial t^2} - c^2 \frac{\partial^2 \rho'}{\partial x_i^2} = \frac{\partial^2 \overline{T_{i,j}}}{\partial x_i \partial x_j} \quad (42)$$

Where  $\overline{T}$  is Lighthills tensor,  $\rho'$  is density fluctuation with respect to ambient condition. It assumes that the ambient fluid is an isothermal polytropic gas so that the pressure fluctuation is directly proportional to the density fluctuation. As a result, the eqn (42) can be

written in terms of either pressure or density variation. The Lighthill tensor has three components defined as

$$\bar{T}_{i,j} = \rho u_i u_j + p_{i,j} - c^2 \rho' \delta_{i,j} \tag{43}$$

Where the first term Reynolds stresses and  $p_{i,j}$  is the stress tensor. One approach is to solve Lighthill equation to predict the noise source strength on a separate acoustic mesh, which is normally much coarser than CFD mesh. This approach significantly reduces the cost of solving for the far field noise using turbulent compressible Navier Stoke’s equations, accounting the effects like reflections, diffraction or absorption besides frequency analysis. The noise sources present due to turbulent flows shown in Fig-11 are extensively discussed by Sandeep Sovan (2005)

In terms of noise sources, the eqn (42-43) can be re-written as -

$$\frac{\partial^2 \rho'}{\partial t^2} - c^2 \frac{\partial^2 \rho'}{\partial x_i^2} = \frac{\partial}{\partial t} \{ \rho_0 v_n \delta(f) \} - \frac{\partial}{\partial x_i} \{ p_{i,j} \delta(f) \} + \frac{\partial^2 \bar{T}}{\partial x_i \partial x_j} \tag{44}$$

Where  $\delta(f)$  describes the source of geometry,  $v_n$  normal velocity and  $p_{i,j}$  stress tensor is given by

$$p_{i,j} = p \delta_{i,j} - \mu_{eff} \left( \frac{\partial u_i}{\partial x_j} + \frac{\partial u_j}{\partial x_i} \right) - \frac{2}{3} \mu_{eff} \frac{\partial u_k}{\partial x_k} \delta_{i,j} \tag{45}$$

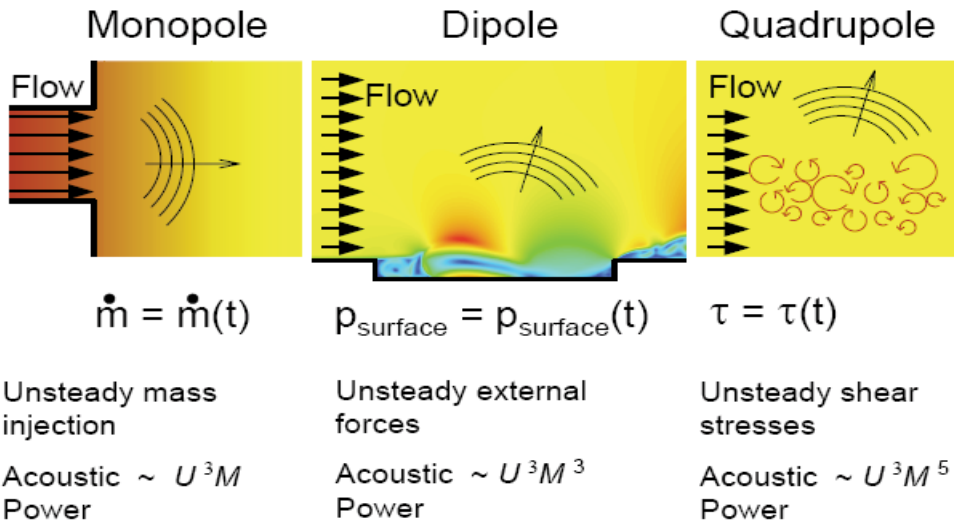


Fig. 11. Illustration of aerodynamic noise sources

In the right hand side of the eqn (45), first, second and third terms indicates mono/dipole/quadro poles noise sources respectively. The eqns (44-45) are called aero acoustic formulation by Ffowcs Williams and Hawkins. In CFD software, the noise resulting from unsteady pressure fluctuations can be computed in several ways. Transient LES

predictions for surface pressure can be converted to a frequency spectrum using the built-in Fast Fourier transform (FFT) tool in most of the flow solvers. The Ffowcs Williams-Hawkings acoustics whose derivation was extensively discussed by Ffowcs W J E and Hawkings D L (1969) are used to model the propagation of acoustic sources for objects ranging from exposed bluff bodies to rotating fan blades. Broadband noise source models allow acoustic sources to be estimated based on the results of steady-state simulations provides practical tools for interpretations of noise sources. More comprehensive analysis for predicting sound directivity, reflections and radiations can be analyzed through CFD commercial software like CFX, Fluent and Star-CD even though simulation needs special purpose commercial software like Sysnoise/ Actron for comprehensive investigations for far field noise. The typical simulation has attempted to compute different noise source strengths and frequency analysis for an axial fan using RANS equations are discussed under case study-5.

### 9. Flow simulation in coal pulveriser – case study: 1

Fuel preparation for the boilers through grinding the coal has been made in the pulverizers. The grinding mills can be different types like ball, impact and the roller mill is also called bowl mill is extensively used in Indian coal fired power station. The need to design more efficient grinding elements are necessary to increase thermal efficiency of boiler auxiliaries. If the coal fails to burn as required, the alternatives available to pulverize operators are limited and results in combustion inefficiency in the boiler, was reported in the technical paper by Mechthild Angleys et.al (1998). The Electric Power Research Institute has reported that 1% of plant availability is lost on average due to malfunctioning of pulverizer internals.

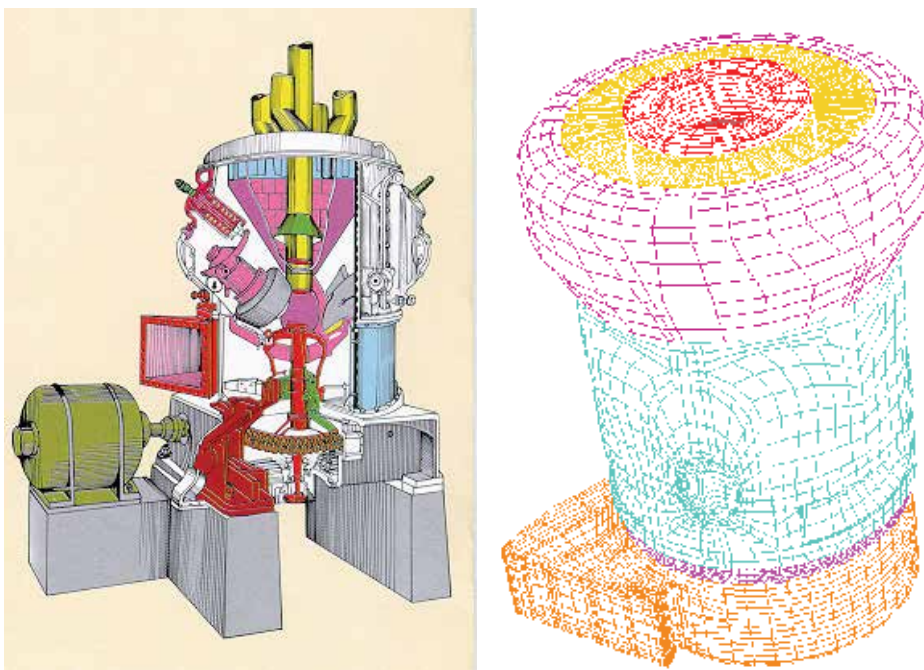


Fig. 12. (a) Isometric view of the mill (b) Computational grid

To understand the flow pattern inside the different types of pulverizers, numerical simulations were described by Mechthild Angleys (1998) and CAJ Fletcher (1993). Based on these works, CFD analysis in the roller mill was discussed by C.Bhasker (2001) whose isometric view in three dimensions are shown in Fig-12(a). This mill is used to separate coal particles based on centrifugal forces due to spinning motion of bowl. However, due to bowl rotation, particles are moved away to clearance, where rollers crush them into fine powder with the pressure forces by the springs attached to it. The air flow enters tangentially through inlet duct vanes lift these particles towards classifier vanes and exit pipes connected to boiler. The coarse particles, which are not separated will fall back to bowl for re-grinding. Flow around different internals present inside the pulverizer is complex and are prone to secondary and tertiary swirl motion.

The flow travels in the mill around stationary and rotating internals crosses bowl rim, rollers, vanes at inlet, classifier vanes and exit coal outlets have geometrical complexities involving steep curvatures and steps. CAD modeling from the assembly of manufacturing drawings with all internals has been carried out and extracted the flow passage. The flow passage around the solid objects is further decomposed to generate high quality structured computational meshes in different parts. The computational mesh shown in Fig-12(b) in different parts are imported in the flow solver for flow simulation. The grid-interfaces between parts of the meshes are created to remove duplicate elements at mating surfaces. The computational mesh of 120,000 point data has been generated in 307 grid blocks with several connections between blocks to avoid the prevention of flow due to presence of artificial walls. The CFD software TASCflow from AEA Technology/Canada based on finite volume method has been employed to solve 3-dimensional RANS equations for incompressible flow. Turbulent effects are accounted through  $k-\varepsilon$  model with standard wall functions. The mass flow of 29.6 kg/s is assumed to be entering in the pulverizer through inlet fixed with five vanes and leaves through exit locations, at which static pressure of order 6.16 ata has been specified for flow simulation.

The convergence of equation residuals for simulation of flow in the pulverizer along its internals depends on proper initial guess and under-relaxation factors. The optimum value of time step, which is based on trial and error method was provided to accelerate the convergence for flow simulation. Besides time step, dropping of error in the equation residuals also requires proper inputs for turbulence intensity and length scales at inlet location. With suitable initial guess values for flow momentum, pressure and turbulence quantities and under-relaxation factors in control parameters, the simulation took about 300 iterations for completion of flow simulation on 256 MB RAM Compaq Pentium-III 450 MHz work station. After completion of simulation, with the help of result files, several planes across the mill height and horizontal directions are created from the grid block nodes using region manager available in solver post processor. The flow visualization in terms of velocity vectors/contours different cross-section of device and streak lines from the inlet of mill chamber are generated to understand the flow distribution. The velocity vectors in the planes over the height of the mill are described in Fig-13(a) wherein the flow path is highly non-uniform and exhibits recirculating flow especially in the inlet region. As a result, flow in the mill exit locations are leaving with unequal velocity as seen in Fig -13(b). The air flow in terms streak lines drawn from the inlet of mill indicates that its paths are not reaching to classifier with required intensities due to flow recirculation observed at several locations in the mill. The observations from the simulation have shown significant impact on existing designs for improving the flow distribution by small changes in the geometries.

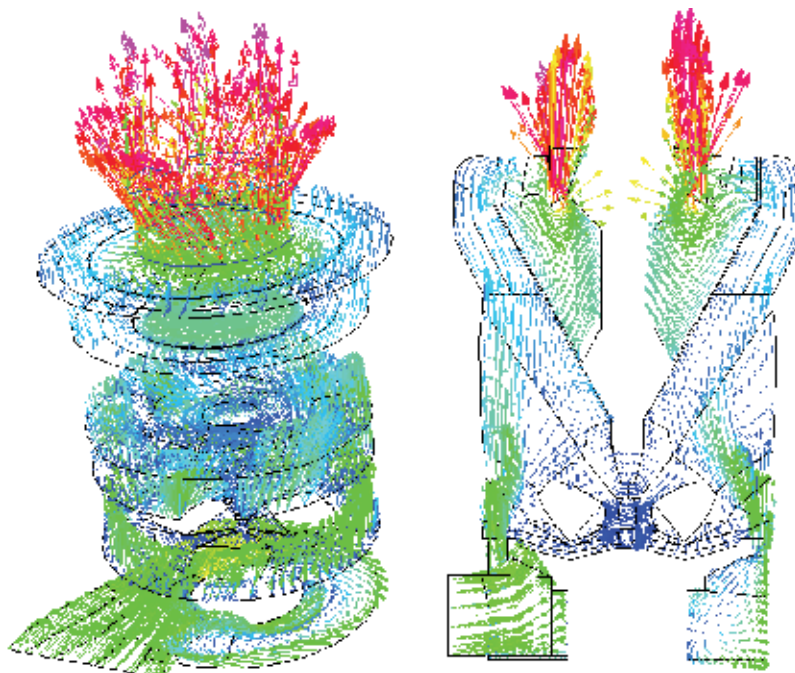


Fig. 13. Velocity vectors in the mill (a) over height [b] horizontal plane

### 9.1 Flow analysis in electrostatic precipitator – case study: 2

Electrostatic precipitators are extensively used to collect particulate emissions from the power production units. Although the performance of the precipitators are high, their collection efficiency is strongly dependent on the electro hydrodynamic behavior of two-phase flow inside the chamber. The problems faced in the operation of ESPs depend on many factors such as gas volume, particle size distribution, gas-temperature, mechanical conditions, etc., Indian coals have high ash content, can affect electrical resistivity and particle size distribution besides disturbing uniform flow pattern, as discussed by Srinivasan (1996).

The gas velocity characteristics with an electrostatic precipitator play an important role in overall ESP performance. If local gas velocities are too high, then the aerodynamic factors depends upon the particles can overwhelm the electrostatic forces generated by the collecting surfaces and electrodes. This leads to degradation in collection efficiency and techniques to improve its performance was outlined in the paper by Dumont (2001). If the local velocities are too low, the collecting surfaces are not being utilized and the potential of particulate deposition. In view of these problems, proper design of flow control devices within ESPs are critical. Construction of physical model includes turning vanes, baffles and perforated plates in several combinations are complex task for development of ESP. The analysis of ESP flow characteristics through physical scale model was only the choice until now are expensive and time consuming process, as the change in configuration will limit to use of existing models.

Many CFD studies as an alternative have been made to understand the flow distribution in ESP especially using skew gas flow technologies by Schmitz (2001). The multi-disciplinary

flow simulation influencing the flow distribution towards emitting electrode by Gallimberti (1998) and Varonos (2002) are the major contributions for improving the efficiency. However, still there is a need to understand the following parameters, which influences performance degradation in ESP.

- Resistivity
- Ash quality
- Ash distribution
- Gas composition
- Gas temperature
- Gas distribution
- Duct geometry
- Inlet geometry
- Electro-static forces
- Electrode geometry
- Collection plate geometry
- Rapping

Depending upon power station rating, the configuration of ESP varies in terms of fields and length, height, width of chambers. The ESP chamber also can be single or multiple pass connecting to one or two chimneys varies based on power plant layout. The entrainment of flue gases in the ESP chamber from the air-preheater is subjected to several internals like inlet funnels, gas distribution screens, outlet funnels and induced draft fans to stack. The prediction of uniform flow from the air-pre heater to ESP chamber through several flow control devices placed in the ducts, splitter vanes, gas distribution screens involves complicated process, as modeling the gas distribution screens placed in the ESP inlet and exit location will an important issue.

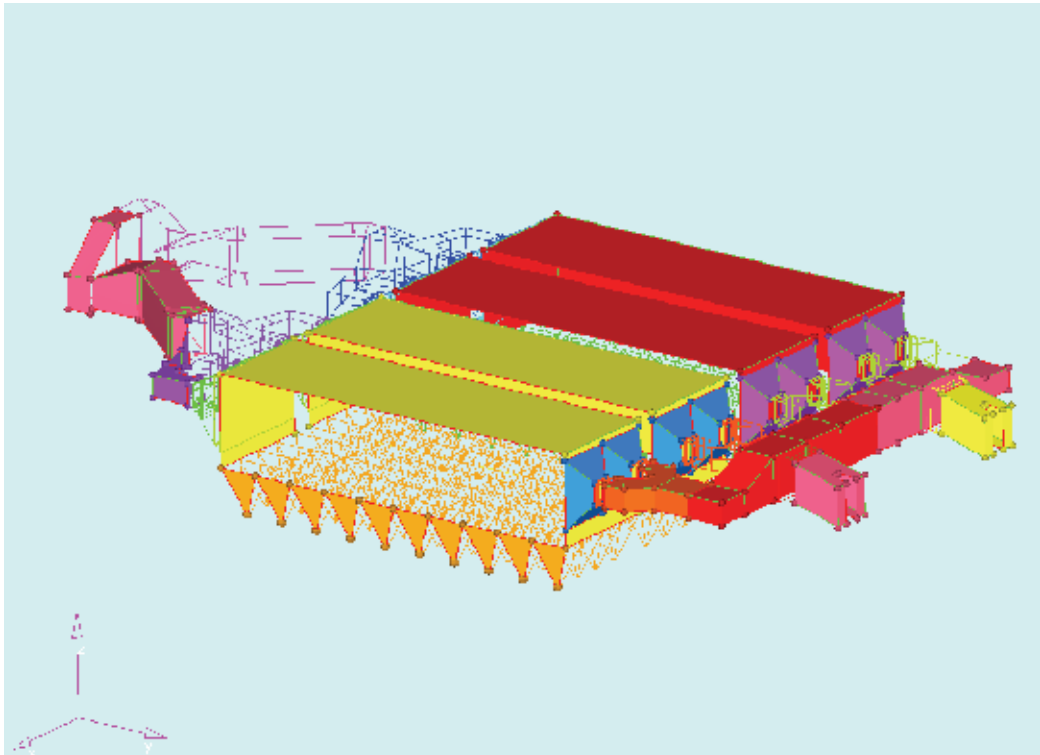


Fig. 14. Isometric view of four pass ten field ESP configuration

As suggested by Nielsen (2001) gas distribution screens are simulated by two different methods a) that of porous baffle computational cells, which are effectively zero thickness



may be placed between any two fluid cells b) use of source term model which requires experimental input. Both the models implement the forces from the screens acting on the flow without modeling the geometrical details of the screens. Accurate modeling of the gas distribution screen geometries comprises several thousands of holes are time consuming process with even large and fast computers. To overcome this, the momentum equations with the lift and drag sources are introduced, wherein its coefficients depends on angle of attack and screen design. Using above approaches, flow through four fields single pass ESP as part of retrofit for the power producing unit was analyzed by Bhasker (2005) and estimated the pressure drop across this cleaning device. This work has renewed the interest to know the flow uniformity at inlet duct outlet of higher rating ESP, whose isometric view is shown in Fig: 14.

In order to study the flow distribution in the inlet duct portion of four pass two ESP configuration connected to two ID fans, IGES file from CAD model has been imported in CFD pre-processor. The geometry of inlet duct with flow control devices shown in Fig-15(a) is considered to develop the flow pattern inside the duct around flow control devices. Accordingly the computational domain was discretized into number of blocks past the turning vanes present in the duct. The computational domain is divided through number of blocks in such way that grid points are captured on turning vane surfaces. In the process at several places, triangular shape portion forms in the domain and computational mesh from upstream blocks disturbs element node connectivity. To over come this, triangular shape blocks present in the domain are further divided into Y type blocks to make uniform topological connections between grid blocks. After checking the edges discontinuity between grid blocks in the computational domain using solid mesh options available in grid generator, mesh has been filled firstly in smallest volume. In order to ensure topological connection between grid points in neighboring volumes, hex elements are filled in the smallest block while varying the node distribution in flow direction. The computational grid for the ESP inlet duct with turning vanes comprises 445071 nodes generated is shown in Fig-15(b). After generation of grids, duplicate elements are removed through check edge option, adjusting the default tolerance values. Software has several other quality checks especially Jacobians and face checks. Any negative Jacobians will indicate distortion of elements leads to negative volumes and such grid data cannot be accepted by flow solvers. Face check indicates computational grid inside the flow volume is free from duplicate/distorted elements. Using this face grid collector, several boundary conditions regions are created and exported to several flow solvers like, TASCflow, Fluent, CFX and Star-CD for benchmarking the simulation.

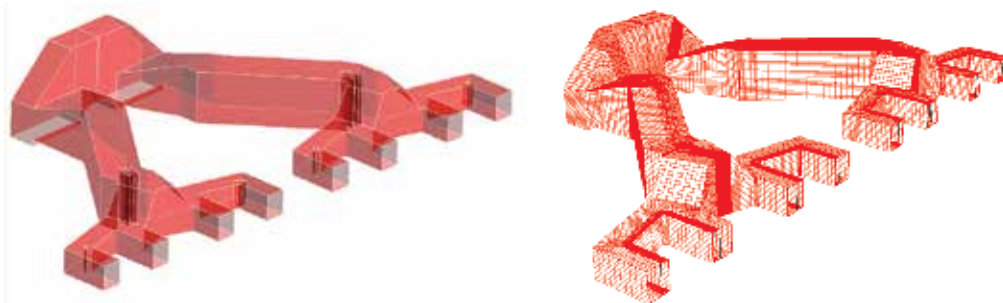


Fig. 15. ESP Duct (a) Geometry (b) Computational Mesh



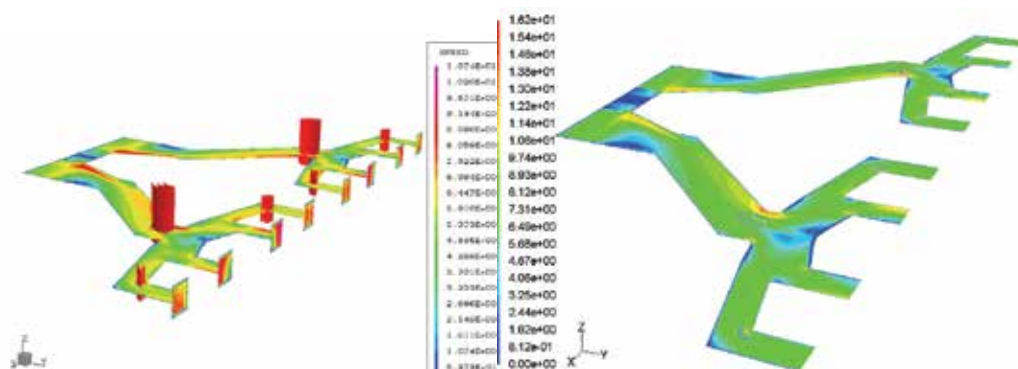


Fig. 16. Velocity in the middle plane a) TASCflow b) Fluent flow solvers

The flow pattern in the middle plane of the duct using TASCflow and Fluent solvers is shown in Fig-16(a-b). It is observed that flow separation in the case of fluent solver is better than the same obtained using TASCflow solver. However, CFX and Star-CD solvers comprises robust multi-grid algorithms along with advanced post-processing features provides excellent visualizations and estimation of averaged flow quantities at duct outlet. The velocity pattern in form of streamlines are better predicted separation regions near corners using CFX and Star-CD. All the solvers have predicted that that flow at eight ducts outlet are not uniform and required to be improved by adding more flow control devices. This bench mark study with more details available in the paper by C.Bhsker (2011) also reveals that fluent-3D can be best choice for feel of results quickly. CFX and Fluent along with several pre/post processors all merged with Ansys are available under current version through workbench to study multi-disciplinary simulations including fluid-solid interactions even with electro fluid dynamic effects. The Cd-Adapco's current version or star-ccm solver with similar features provides another alternative on polyhedral cells for flow visualization and quantification of results. The cross comparison presented in this work proves that the basic numerical techniques through multiple flow solvers are reliable and deliver the expected performance in terms of accuracy and convergence.

### 9.2 Particulate laden flows in cyclone collector – case study: 3

The cross sectional view of cyclone separator along with other components used in Circulating Fluidized Bed Combustion - CFBC plant for supply of electricity to paper manufacturing unit is shown in Fig-17. Flue gas produced out of the solids used in the combustor enters to refractory lined cyclone. The cyclone collects more than 99% of the incoming solids, which travel down the conical bottom to the sealpot blower and are eventually siphoned back into the combustor as detailed by Rajaram (1999).

The flue gas leaves the cyclone top flows on to a convective pass containing three stages of super-heater and economizer. A tubular air heater forms the last heat recovery surface and preheats the primary/secondary air streams separately with the air flowing inside the tubes and gas flowing outside them. The flue gas is then enters in an electrostatic precipitator and leaves towards stack through induced draft fans. Although the operation of the plant with varied load is successful, there were problems related to flue gases, which are coming from the cyclone outlet are settling on the super-heater tubes, concern the plant efficiency.

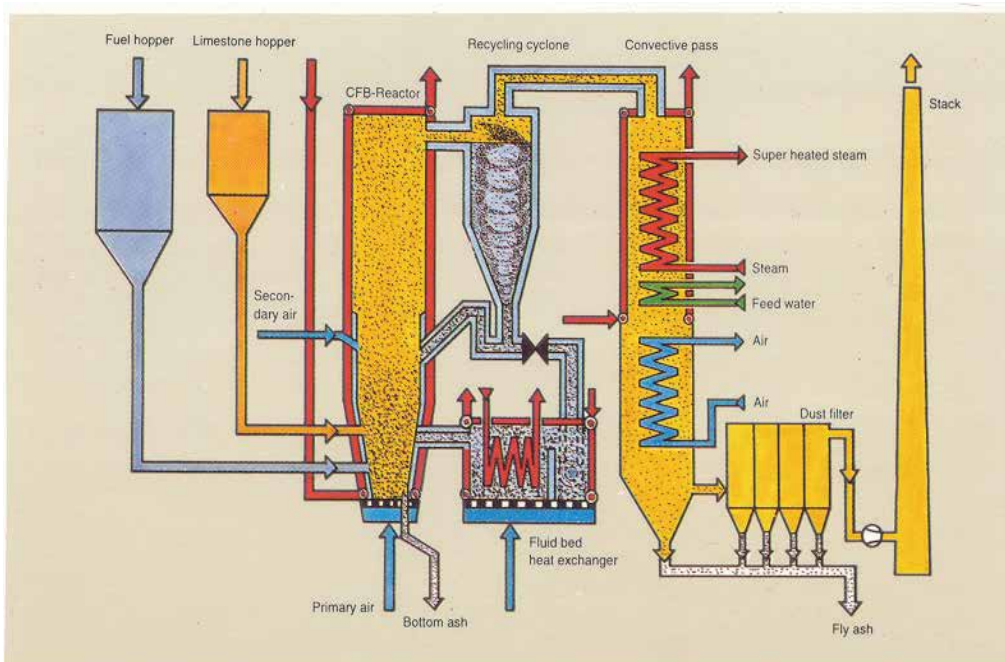


Fig. 17. Location of Recycle cyclone in CFBC power plant

The flow in cyclone separator is highly turbulent due to swirl motion and several investigations are carried out by Slack (2000) and Fraser (1997) using advanced numerical techniques. The geometry of cyclone separator used in paper manufacturing industry considered for flow and particle trajectories are different from the conventional cyclone separator, as it is placed between boiler and tube banks of power plant. However, its basic geometry resembles with conventional one, the orientation of inlet and exit duct attached to it are different. The cyclone collector considered consists of an upper cylindrical part, with a tangential inlet and lower part with an exit at the apex. They are used to separate dispersed heavy substance from a fluid of lower density, the suspension to be separated being injected with high velocity tangentially into the cyclone. These results in high spin velocities within the cyclone, which produce a large centrifugal force field. The separated material leaves the cyclone at its apex, while clean fluid is discharged at the top through the overflow pipe.

The geometrical model of cyclone has been created from assembly drawing using CAD modeler I-DEAS and its output is exported to CFD pre-processor for extraction of flow passage. ICEM CFD pre-processor has flexible tools for mesh generation with several surface repair options. In order to proceed for mesh generation, initialized block is placed on the computational domain and the same has been divided through horizontal and vertical directions using splitting options, according to geometry shape and internals. The resulting block edges are aligned to geometrical edges using project/associate commands. With this referenced block, using its face selection, topologically connected blocks are constructed for rest of the geometrical part. To obtain the computational mesh in three dimensions, nodes to master linking to slave edges are to be specified. Software provides several distribution laws for clustering the nodes on boundary surfaces. The pre-view of the nodes on the master and

slave edges with direction arrows provides the first insight for the proper mesh distribution on the geometrical part. The activation of volume mesh, under mesh generation option provides three dimensional meshes for the specified solver format. After completion of mesh generation in different parts, the assembled mesh has been imported in flow solver is shown in the Fig-18(a) with grid interfaces between parts so that no artificial walls present in the volume grid.

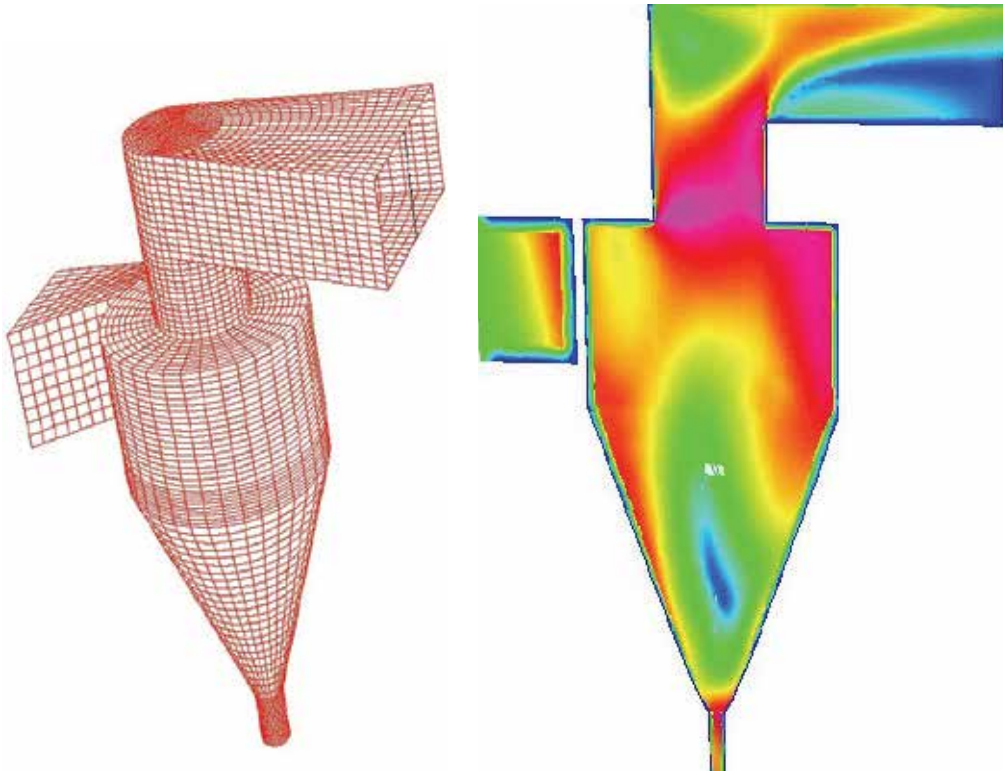


Fig. 18. Cyclone Collector (a) Computational Mesh b) Velocity Contours

After description of fluid properties in flow solver, boundary conditions for the velocity and pressure are prescribed at inlet and exit locations. In order to capture the viscous effects, two equation turbulence model based on intensity and length scale with standard wall functions are employed. Since the flow inside the cyclone collector is highly rotational and the option of covariant velocity in normal direction has been used as an initial guess for flow simulation. From the simulation results it is observed that the velocity distribution from inlet of cyclone leaves through one side of the outlet duct indicating that flue gas comprises particles settles on super heater tube bank surfaces. Simulation of flow in the existing configuration of cyclone separator also indicates that particles are unable to reach with required velocity magnitude in the outlet duct region due to large flow recirculation.

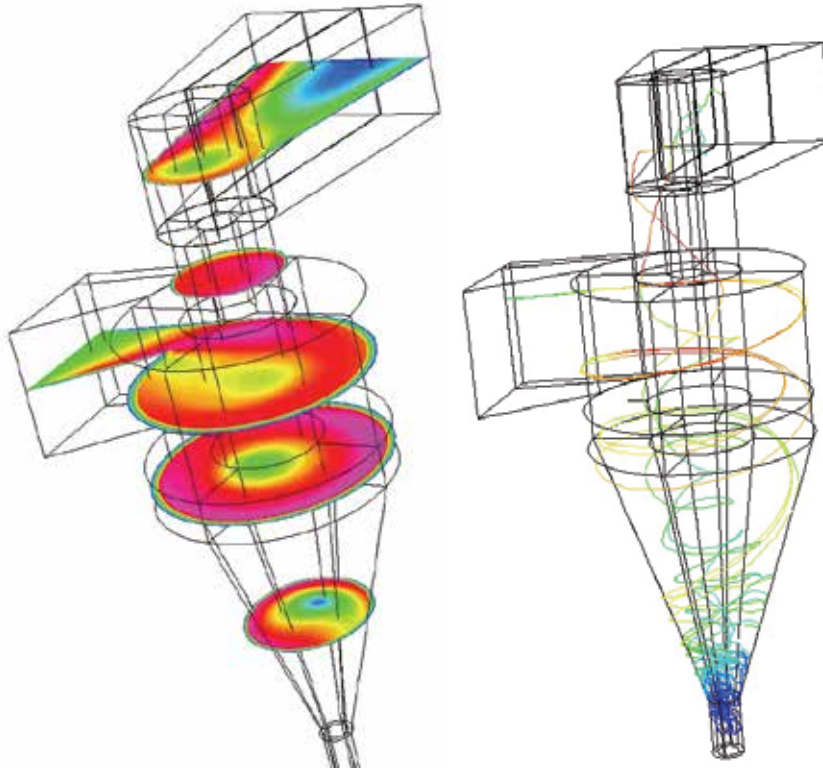


Fig. 19. Improved geometry (a) Velocity pattern (b) Particle trajectories

To improve the velocity distribution, geometrical changes with two baffle plates in the outlet duct of the cyclone separator are provided in the CAD model. Multi-block hexahedral element mesh has been re-generated and imported in the flow solver. After obtaining successful flow simulation, discrete phase of particulate media has been added to working fluid to track the particle trajectories in the cyclone collector. The inputs like particle resident times, particle material and particle sizes according to distribution laws are defined for two-phase gas-solid particle flow simulation. The velocity contour plots over height of the modified cyclone separator is shown in the Fig-19 (a), wherein it is noticed that presence of partition plates reduces the flow recirculation in the outlet duct and thus decreases the settling of particles on super heater tubes. From the particle trajectories plot Fig-19(b), it is observed that the particle size 10 microns follows air flow along the wall of vortex tube finder to gas exit. Bigger size particle of 100 micron released from the inlet of cyclone separator moves along the outer conical wall. This is because the particles have low inertia and associated drag force decelerates the fluid motion. It also follows the recirculation gas flow back into the cyclone body, where it is captured into the vortex core and moves upward to the outlet gas. The larger particle of 1000 micron size captured in a particle rope and later follows the recirculating flow to the vortex finder and separated from the fluid stream towards cyclone bottom outlet. The detailed simulation of flow in cyclone collector with formulations are comprehensively discussed in the paper by C.Bhasker (2010).



### 9.3 FSI studies on gas-turbine transition duct – case study: 4

In order to achieve higher net power outputs and thermal efficiencies, turbine inlet temperatures (TITs) have to be as high as possible in compliance with technological limits. As a consequence, hot gas path parts (HGPPs) are exposed to severe thermal conditions leading to high metal temperature, which are responsible for the deterioration of hot gas carrying parts. They include all components associated with the combustion process liners, fuel nozzles, transition pieces, buckets, shrouds, etc. In a gas turbine combustion chamber, the transition piece carries the hot gases from its outlet to turbine first stage, as shown in Figs 20(a-b) to the turbine.

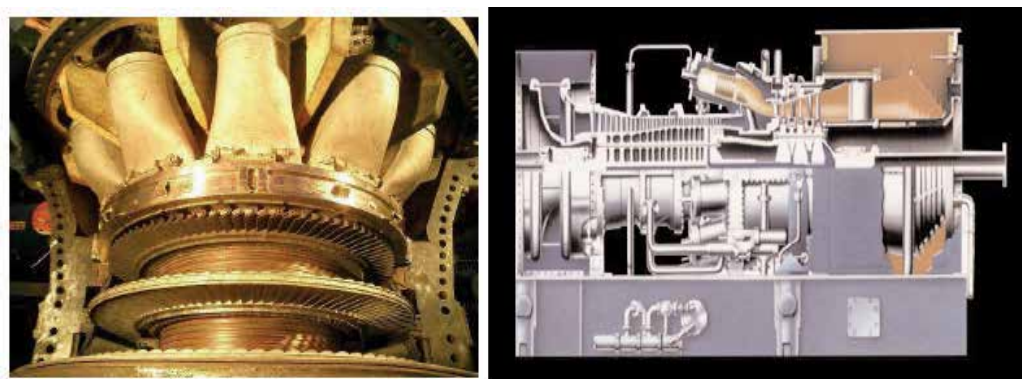


Fig. 20. (a) Transition Duct (b) Location of Transition duct in Gas-Turbine

The gas turbine field engineering team has reported that unscheduled engine outages can occur as a result of premature part failure in the gas turbine flow path. As a consequence, initiatives were launched to address these fleet-wide combustion and turbine hardware field issues. The efforts were initiated at user request after a large number of 501F machines began exhibiting chronic transition duct failures across the fleet, causing forced outages, which significantly affect the revenue generation as reported in the publication by Jeff Benoit (2007). The duct in which cross sectional shape often follows a circle to rectangular transition with stream wise curvature and combined effects of viscosity/geometry produce a secondary flow in the form of stream wise vortices. These vortices significantly affect the overall performance of the system, for instance, the pressure drop and flow uniformity. Due to presence of steep curvature in stream wise direction, prediction of turbulent structure at near wall region is very critical.

In design context geometric constraints will often dictate the use of possible shortest possible duct for the given cross sectional shapes at inlet and outlet. In this case, the level of separation and severity of flow distortion at the duct exit due to transverse vertical motion are function of aspect/length ratio and cross sectional variation in the transition portion. The design of this duct contains an inlet was subjected to laboratory model for measurements by Davies (1991) later several flow simulations was carried out by Richard Cavicchi H (1999) and Sugiyama H (1999). Based on these investigations, Bhasker (2009) has undertaken comprehensive fluid solid interaction studies on transition duct, which has a sharp transition from circular to rectangular arcs over a short axial and radial distance. The circular to rectangular duct based on inlet dia, exit aspect ratio, length of the transition duct

was constructed. At each stream wise location, the cross-sectional shape is defined by the elliptic equation –

$$\left(\frac{y}{a}\right)^n + \left(\frac{z}{b}\right)^n = 1 \quad (46)$$

The parameters  $a$ ,  $b$  and  $n$  are functions of stream wise coordinate  $x$ . The cross-sectional shape of these transition ducts constructed in six sections becomes more rectangular as the value of the exponent  $n$  increases, but they never truly rectangular. In the Fig-21(a), section-1 is inlet diameter upstream of the start of transition (section-2), section-3 and 4 are in the mid-region of transition, section-5 is at the end of transition and section-6 is 2 times of inlet diameters downstream of the duct, with a flanged juncture between station 5 and 6. The ratio of major to minor axis lengths at the duct exit is referred as aspect ratio. For fixed  $x/D$ , using the polynomial coefficients for  $a$ ,  $b$  and  $n$ , the profile for the duct are generated through a computer program and decomposed into several blocks for computational mesh generation shown in 21(b).

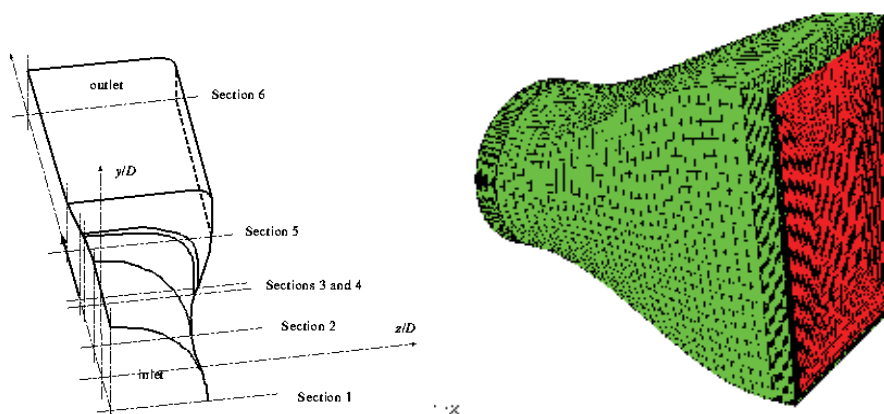


Fig. 21. Transition Duct (a) Geometry (b) Computational grid

The grid shown above comprises 127623 nodes along with face grid was created using commercial grid generator. It has been ensured that elements present between block to block at mating surfaces are one-one so that volume grid is free from any artificial walls. Simulations were carried out using commercial flow solver fluent and the flow pattern obtained in the horizontal planes are shown in the Fig-22(a). The velocity magnitude reduces along the stream wise direction towards the duct exit. This is more pronounced in the flow downstream close to exit location. This is because of the flow expansion due to the enlargement of the duct.

Moreover, the deceleration of the flow in the radial direction is more significant close to the outer casing. Consequently, fluid close to outer casing attains lower velocity with turbulent eddies. This is because of the axial momentum is considerably higher than that occurring in the radial direction. The flow in stream wise direction near wall planes at central portion is smooth. In view of secondary flow pattern prevailing in the duct, it is observed that the flow distribution at its exit location exhibits highly non-uniform. Fig-22(b) shows the

pressure distribution on transition duct surface. In general, the wall static pressure is a function of cross sectional area, wall curvature and viscous forces in the flow. Concave curvature along the upper wall induces positive pressure gradient which influences maximum pressure near exit wall surfaces. Conversely convex curvature along the side walls induces negative pressure gradient resulting minimum pressure. Also the radius of curvature of walls at changes signs between stations 3 and 4, which causes maximum and minimum pressure along the side and upper walls respectively. It is also noticed from the figure that undulations exist in the distribution due to vortex flow in close proximity.

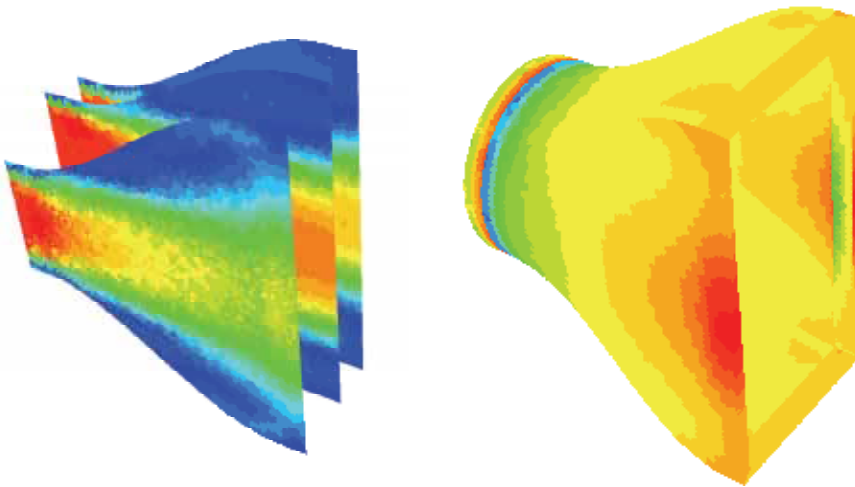


Fig. 22. (a) Velocity in duct planes (b) Pressure on wall surface

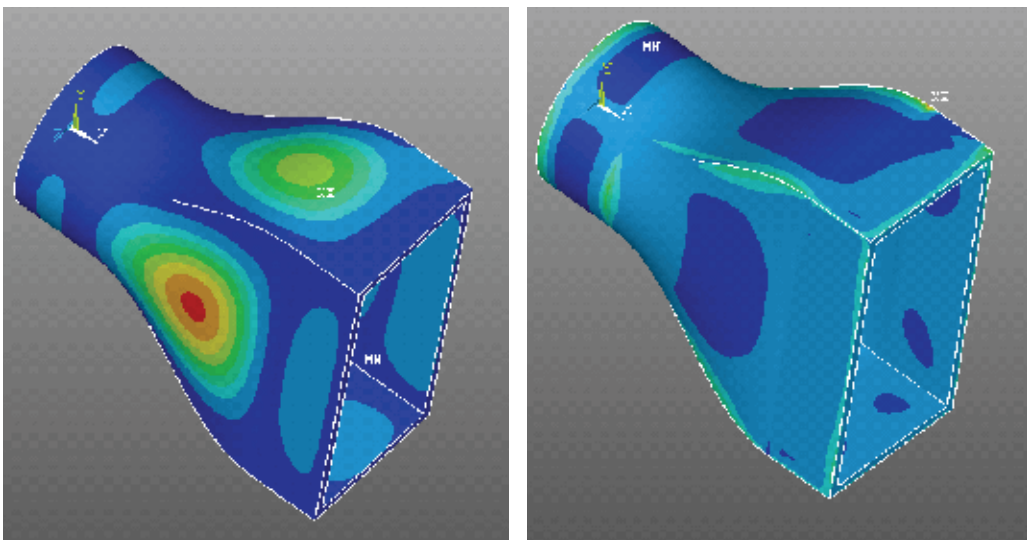


Fig. 23. (a) Displacement (b) Von-Mises Stresses

From the physical point of view fluid structure interactions are a two field problem; one is related to flow simulation, and another is related to structural stress determination. These fields are coupled via the so-called wet surface where the pressure and friction forces caused by the fluid are acting on the structure. Due to these loads the component structure is subjected to deformations and these changes can affect the equivalent stresses.

In order to understand the component deformations due to influence of pressure gradients of transition duct inner profile, static structural analysis has been carried out using the Ansys Mechanical Solver. Computational mesh for transition duct was created using solid element. After specifying material and elastic properties, displacement and pressure loads are transferred from CFD solvers to obtain the displacement and equivalent stresses on the transition duct. The magnitude of maximum displacement is observed in Fig-23(a) at station 4 of transition duct and high stresses are noticed at transition edges as shown in Fig 23(b) are not high enough to produce severe material damages.

#### 9.4 Aerodynamic noise prediction from axial fan – case study: 5

Fans are extensively used to transport the air from one device to other in coal fired power station. Outages of these components due to operational problems are concern the efficiency of critical equipment. Two kinds of fans are normally employed i.e., centrifugal/axial fans; in the former one air accelerates radially outward in a rotor blades in the scroll casing. The fluid is accelerated to parallel to the fan axis in the case of axial fan. Fan performance is best expressed in the form of fan curves between static pressure, horsepower, and efficiency as a function of volumetric flow rate. Axial fans are employed in Induced Draft – ID fans which will have unique characteristics called stall. Stall is the aerodynamic phenomena, which occurs when it is operated beyond its performance limits and flow separation occurs around the blade. If this happens, the fan becomes unstable and no longer operates on its normal performance curve. Extended operation in the stall region should be avoided for excessive noise levels as reported by Subramnian (1984). The poorly designed inlet or a sharp turn just upstream can affect the performance of fan.

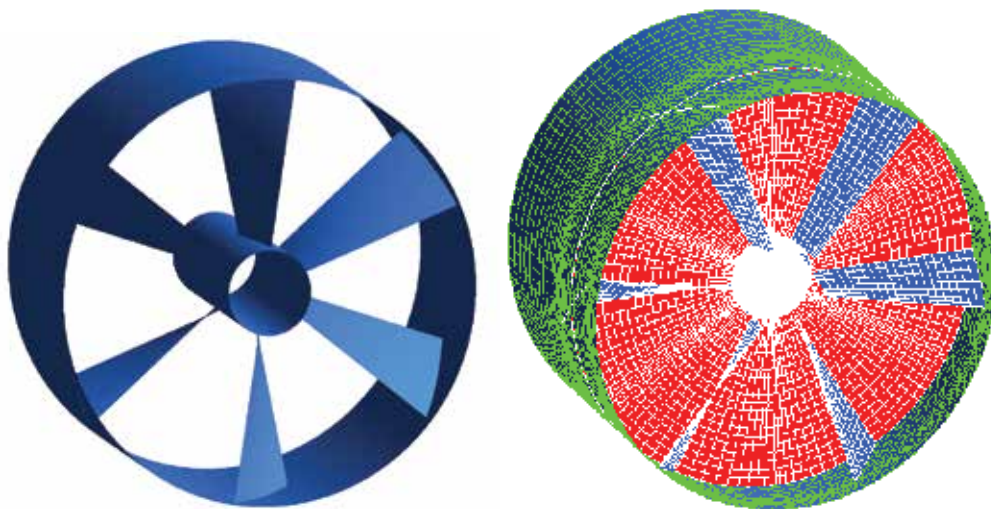


Fig. 24. a) Axial Fan model b) Computational grid



Dozohme (2006) has reported rotating components like fans and blowers contribute to the tonal component, which is very unpleasant. The tonal noise is influenced by the rotational speed of the fan, the number of blades, fan size and mass flow rate through the fan. Tight tolerances between the blades and casing improve overall efficiency. This improved efficiency in turn reduces the overall sound levels; the asymmetrical blade locations reduce the blade passing frequency tones, while generating a smoother sound spectrum. The choice of different hub diameters, hub/tip ratios along with variations in blade span, ensures the economical performance. Focusing on noise analysis, Shao-Yi Hsia (2009) has suggested that there are several paths through which noise may be radiated from the fluid machine require to be controlled.

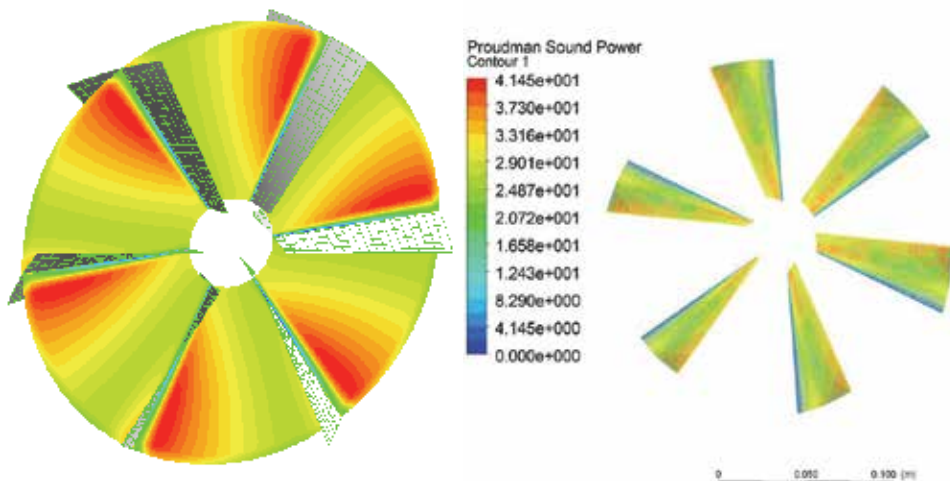


Fig. 25. a) Velocity b) Sound power

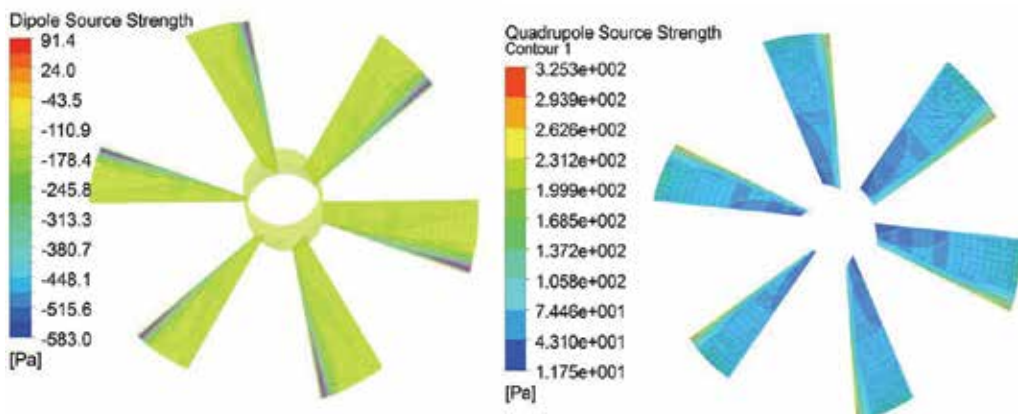


Fig. 26. a) Dipole b) Quadrupole noise source strength

The methodology used is applicable to low Mach number in unsteady flows, where the radiated noise is a small byproduct of the flow that is not altered by it. This assumption is central to Lighthill's formulation of aerodynamic sound generation, which implies that

sound characteristics are obtained in two stages. Turbulent flow fields are predicted at CFD stage followed by sound post-processing stage. One of the objectives of this study is to select turbulence modeling technique that is computationally affordable and yet capable in producing appropriate data for acoustic characteristics.

In order to predict flow and far field noise for the enclosed fan assembly with six blades shown in Fig 24(a) is rotating with 2000 rpm. In order to simulate the flow, a computational grid has been generated for the fan shown in fig 24(b) with boundary condition regions inlet, exit, hub, shroud, blade surfaces, and periodic surfaces in the pre-processor Hypermesh.

The flow simulation has been carried out with defined flow conditions and blade rotations to predict the efficiency of fan. The velocity pattern and sound power on blade surfaces obtained are shown in the Fig-25(a-b). Due to presence of turbulent flow field and blade rotations the dipole and quadruple noise strength variations on the blade surfaces are shown in Fig 26(a-b) using F-W wave equation as a function of flow pressure. From the frequency analysis, it is estimated that overall sound level pressure and sound power are 54.68 dB at 200 Hz respectively are measured at one meter distance from the component. The fan efficiency the ratio between the power transferred to the airflow (outlet – inlet) and the mechanical power consumed by the rotating blades for defined flow conditions are calculated is about 76%. Fan efficiency can be further improved using shape optimization of blades in conjunction with CFD.

## 10. Optimisation – advance tools in CAD-CFD

Turbo machinery design is a complex task that involves many objectives and constraints coming from different disciplines. Many optimization algorithms have been reported to date with varying degree of success. One of the approaches used for optimization of puffer valve was extensively discussed by C.Srikanth (2009) through unsteady flow simulation with mesh morphing techniques. This technique involves good skills for scripting the moving boundaries in computational model and expensive to perform unsteady state simulations for complex components. In the recent developments more automated methods of shape optimization along with CFD solvers are providing robust tools are discussed by Sheldon Imaoka (2006) through design of experiments using Response Surface Method - RSM. RSM attempts to substitute for the optimizations using iterative flow simulations for variations in geometries by Design of Experiments - DOEs using response surfaces. RSM basically works with linear and non-linear coefficients uses Monte-Carlo simulations for global approximations. Global approximations are very beneficial in case of multi-objective problems; they are built and reformulated based on shapes and constraints. In order to increase marginal efficiency of axial fan, an investigation has been undertaken to simulate the flow inside the fan using mesh morphing, shape optimization and DOE on RSM is under progress based on approach discussed by Nixing Chen (2007). Once the user determines that the generated response surface provide a useful representation of the input-output relationship, goal driven optimization, six sigma analysis or robust design studies then can be performed instead of running time consuming flow simulations for every changed geometry.

## 11. Concluding remarks

The failures of power plant components used in terms of flow losses, erosive wear by particle impacts, cleaning devices performance due to non-uniform flows and effect of

turbulence in rotating machinery for excessive noise generation are extensively discussed. The alternative approaches are explored to understand the flow behavior involving multiphysics are through CAE for virtual product development. State of art approaches are covered for modeling and grid generation in simple/complex situations with help of programming and commercially available software. Mathematical descriptions for body fitted coordinates, presence of Reynolds's stress due to turbulent flow for development of pressure based algorithms to simulate incompressible fluid flows are briefly outlined. The formulations related to coupled fluid-solid stress and aerodynamic noise is also highlighted to predict structural stresses and far field noise. The case study related to grinding mill has been discussed and also suggested as how the flow recirculation pattern observed in air housing can be minimized by adding two inlet ducts. Complex multiblock grid generation to simulate the turbulent flow through inlet duct with turning vanes of ESP was detailed for flow uniformity using several CFD solvers in second case study. The simulation of fluid-particles present in the cleaning device is outlined in third case study to provide remedies for preventing the flow from one side of the outlet towards convective pass of CFBC power plant used in paper manufacturing unit. A case study of transition duct used in gas turbine is highlighted for flow pattern and its pressure loads on structural stresses/displacements. Pressure fluctuations in turbo machinery components generates excessive noise and the methodology to predict far field noise from an axial fan is described in final case study. RSM with DOE through mesh morphing techniques in conjunction with CFD are suggested as alternatives for optimization to obtain high efficient devices used in power and process equipment.

## 12. References

- Alan Powel, How do vortices generate sound? Acoustic Radiation and Wave Propagation, ASME, NCA vol 17, 1994
- Anagnostopoulos J et.al, Numerical Investigation of the grinding process in a beater wheel with classifier, *ASME Journal of Engineering for Gas Turbines and Power*, pages, 1997
- Bhasker C et.al, Air Flow Simulation in Electrostatic Precipitator, *BHEL Journal*, Vol 26, No.4, PP:56-61, 2005
- Bhasker C, Flow simulation in ESP Duct with turning vanes, revised paper submitted for *Advances in Software Engineering Journal*, Elsevier, UK, 2011.
- Bhasker C., CFD applications for Industrial Flow Simualtions - Invited talk, *SONIC-10 Conference, International Institute of information Technology, Pune, India, 2010(a)*
- Bhasker C., Flow Analysis in Lignite Grinding Mill, *Procs of 34<sup>th</sup> National Conference on Fluid Mechanics and Fluid power*, BITS, Ranchi, India, pp 698-702
- Bhasker C., Grid Generation for complex industrial components - Lecture notes for a training program on CFD for practicing engineers, IIT, Roorkee, 2010(b).
- Bhasker C., Numerical simulation of turbulent flow in complex geometries used in power plants, *Advances in Engineering Software*, vol. 33, pp 71-83, 2001.
- Bhasker C., Troubleshooting Steam Turbine By-pass Valves Role of CFD as a Key Analytical Tool Pumps, *Valve and Systems Industrial magazine*, Ahemdabad, India, 2010 (c)
- Bhasker, C, Flow simulation in industrial cyclone separator, *Advances in Engineering Software*, Vol 41, issue 2, pp 220-228, 2010
- Bhasker, C., Post Doctoral research report on high performance computing, Engineering Research Center, Mississippi State University, Strakville, USA, 2000

- Bobcock GH et.al, *Steam and its generation & use*, 41<sup>st</sup> edition, Chapter-12 Bobcox and Wilcox publishers, USA. 2005
- Christopher Riff, *Computational Fluid Dynamics Modeling, Laboratory Product/Process Design*, University of Chicago, USA, 2004
- Davies, D.O et.al. Experimental investigation of turbulent flow through circular to rectangular transition duct, NASA Report TM105210, 1991.
- Delli P et.al, *Unigraphics for engineering design*, Dept. of Mechanical and Aerospace Engineering, Rolla, Missouri, 2007
- Dozolme A et. al, Electronics cooling fan noise prediction, *Nice Cote d' Azur seminar*, France, 2006.
- Dumont J et.al, *Computational Fluid Dynamic Modeling of Electro-static Precipitators*, *Procs of 8<sup>th</sup> Internation Conference on Electro-static Precipitation*, 2001.
- Durbin P.A.: Separated Flow Computations with the  $k-\epsilon-v^2$  Model, *AIAA Journal*, V33, N4, PP659-664, 1995
- Efim Korytnyi, et.al, Computational fluid dynamic simulations of coal-fired utility boilers: An engineering tool, *International Journal – Fuel*, paper under press, 2008
- Ffowcs W JE, Sound Generation by Turbulence and surfaces in arbitrary motion, *Procs of Royal Society*, Vol 264, 1969.
- Fletcher CAJ, Gas particle industrial flow simulation using RANSTAD, *Sadhana*, Vol 18, Parts 3&4, pp 657-681, 1993
- Fraser S M, et. al, Computational and experimental investigations in a cyclone dust separator, *Procs. of Institution of Mechanical Engineers*, UK, 1997.
- Gallimberti, I, Recent advancements in the physical modeling of electrostatic precipitators, *Journal of electrostatics*, vol.43, pp 219-217, 1998
- Greschner B et.al, Influence of turbulence modeling on the broadband noise simulation for complex flows, AIAA paper No:902, 2004
- H'ausser J et.al, *Modern Introduction to Grid Generation*, Short course Notes, EPF Lausanne, Dept. of Parallel Computing Center of Logistics/Expert Systems Salzgitte, Deutschland, 1996
- Hoffman, K.A et al, *Computational Fluid Dynamics for Engineers*, in two volumes, *Engineering Education System*, Wichita, KS, 67208-1078. 1993.
- Humphery JAC, Fundamentals of fluid motion in erosion by solid particle impact, *Int.Jrnl. Heat & Mass Transfer*, Vol.11, p170, 1990
- Iyer VK et. al , Flow Studies through Quick Closing Non-return Valves, *Procs. 2<sup>nd</sup> Nat. Conf. on CFD applications in Power & industry sectors*, BHEL, Hyderabad, pp 152-155, 2009
- Jeff Benoit, Enhancing Gas Turbine Power Plant Profitability Chronic transition piece and turbine part failures. *Power engineering*, Penwel publishers, USA, 2007
- Jun Shao, et.al, *Turbulence Modeling in Computational Fluid Dynamics (CFD)*, lecture notes, Maxwell Stanley Hydraulics Laboratory The University of Iowa, 2009
- Mandechthild Angleys, Development of modern EVT Bowl Mill, *VGB Power Technology*, Vol 9, pp 60-66, 1998
- Maria A et.al, Experimental investigation, of particle motion in a model of a beater wheel mill, *Proceedings, 2<sup>nd</sup>. Inter. Conf. on Multiphase Flow*, Kyoto, Ja, Vol. 3 PT4, pp. 9-18, 1985

- Mustafa A.H, et al, Thermal Stress analysis in annular duct resembling as turbine transition piece, *Journal of Materials processing Technology, Elsevier Publishers*, Vol.131, pp283-294, 2006.
- Naixing Chen, et.al, Blade Parameterization & Aerodynamic Design optimization, *Procs. of 8<sup>th</sup> Int. Symp., exp. Comp., aero-thermo dynamics paper ISAI8-8021*, Lyon, 2007.
- Nielsen N F et.al, Numerical modelling of gas distribution in electro-static precipitators, *Procs of 8<sup>th</sup> International Conference on Electrostatic Precipitators*, 2001.
- Pordal H.S et.al. Computational fluid dynamics a key analytical tool, *Hydrocarbon processing*, pp 85-91, 2001
- Rajaram S., Design features and operating experience of circulating fluidized bed boilers firing high ash coals in India. *Procs. of the 15<sup>th</sup> ASME conf. on fluidised bed combustion*; 1999.
- Richard H C, Application of the RNS3D Code to a circular -rectangular Transition duct, NASA Report TM 209394, 1999
- Routhiainen, P.O et.al, On the Deposition of small particles from Turbulent Streams, *ASME Jr of Heat Transfer*, pp 169-178, 1970
- Sandeep Sovani, Acoustic modeling, *CFD Summit 2005*, Fluent Inc., Hampton, USA.
- Schmitz W et.al, Computational Fluid Dynamics modeling of Collection Dynamics, *Procs of 8<sup>th</sup> International Conference on Electro-Static Precipitation*, 2001.
- Schuh MJ, Numerical predictions of fluid and particle motion in flows past tubes, Ph.D thesis, Univ. of California, USA, 1987.
- Shao-Yi Hsia et al , Sound field analysis and simulation for fluid machines, Vol.40, *Advances in Engineering Software*, pp pp 15-22, 2009, Elsevier publishers, UK.
- Shekar Majumdar, Pressure based finite volume algorithm for viscous flow computation, Lecture Notes, *CFD Advances and Applications*, NAL, Bangalore, India, 1994
- Sheldon Imaoka, Generating Response Surfaces in Ansys DesignXplorer, *Ansys Solutions*, Vol 7, pp 38-39, 2008
- Slack .M.D et al, Advances in cyclone modeling using unstructured grids, *Trans IChemE Vol 78, Part A*, 2008
- Sodja, J, Turbulence Models in CFD, Internal Report, Department of Physics, University of Ljubljana, 2007.
- Spekreijse, S.P et.al, Multiblock grid generation Part I: Elliptic grid generation methods for structured grids, *27<sup>th</sup> CFD Course*, VonKarman Institute for fluid dynamics, Belgium, 1996
- Srikanth C et.al, Flow analysis in valve with moving grids through CFD Techniques Vol.40, *Advances in Engineering Software*, 2009, Elsevier publishers, UK
- Srinivas RK , Status of electrostatic precipitator technology usage in India, *Teri inf. Monitor on env. science*, Vol.,pp:1-12, 1996.
- St. Petersburg, Introduction to numerical simulation of fluid flows, Lecture notes, University of Munich, Germany, 2004
- Stephen Ferguson, Polyhedra: Nature's answer to Meshing, *CD-Aadapco, Dynamics Vol 25*, pp 8-9, 2005.
- Suagiyama H, et. al, Numerical Analysis of Turbulent Structure through a circular to Rectangular transition duct, *Procs of 5<sup>th</sup> Jnt. Thermal Engineering Conf*, USA, Pap.AJTE99-6385, 1999.

- Subramanian SA et.al, Operating Experience of PA, ID & FD Fans affecting the plant load factors of 200/210 MW power plant units, *Seminar on Fans*, Paper No.15, New Delhi, 1984
- Tabakoff, W., Performance deterioration of Turbomachinery with presence of solid particles, *Procegs., of AIAA/ASME Joint d heat transfer conference*, St Louis, Missouri, USA, 1982
- Thompson T B et.al, Chemical Industry of the Future, Technology Road map for Computational Fluid Dynamics, 1996
- Thomson, J.F et.al, Numerical Grid Generation - Foundations and Applications, North Holland, Amsterdam, 1985
- Varonos A A et.al, Prediction of the cleaning efficiency of an electrostatic precipitator, *Journal of electrostatics*, vol.55, Vol.55, pp 111-133, 2002.
- Wilcox, D.C, Turbulence modelling for CFD, *DCW Industries*, California, USA, 1993
- Zhiqiang Zhai, et.al, Evaluation of Various Turbulence Models in Predicting Airflow and Turbulence in Enclosed Environments, *HVAC&R Research*, 13(6).2007

# Computational Fluid Dynamics Analysis of Turbulent Flow

Pradip Majumdar

*Department of Mechanical Engineering, Northern Illinois University, Illinois  
U.S.A*

## 1. Introduction

One important characteristics of a turbulent flow is that the velocity and pressure may be steady or remain constant at a point, but still may exhibit irregular fluctuations over the mean or average value. The fluid elements which carry out fluctuations both in the direction of main flow and at right angles to flow are not individual molecules but rather are lumps of fluid of varying sizes known as eddies. The fluctuating components may be a few percent of the mean value, but it is the controlling factor in describing the flow. A turbulent fluid flow is then characterized as the main flow stream super-imposed with localized rotational eddies, where motion are three dimensional, unstable, and random. Turbulent eddies have a wide range of sizes or length scales. These eddies form continuously and disintegrate within few oscillation periods, and hence have very small time scales. In general, the frequencies of the unsteadiness and the size of the scales of motion span several orders of magnitude.

The governing equations for fluid flow for a general linear Newtonian viscous fluid are Navier-Stokes equations given by the following set of equations:

$$\frac{\partial \rho}{\partial t} + \frac{\partial}{\partial x_i}(\rho u_i) = 0 \quad (1)$$

$$\frac{D(\rho u_i)}{Dt} = \rho g - \nabla p + \frac{\partial}{\partial x_j} \left[ \mu \left( \frac{\partial u_i}{\partial x_j} + \frac{\partial u_j}{\partial x_i} \right) + \delta_{ij} \lambda \text{div} V \right] \quad (2)$$

Where  $u_i$  and  $u_j$  are the mean velocities of water,  $P$  is the pressure,  $\rho$  is the density of the water and  $\mu$  is the dynamic viscosity.

In principle, the time dependent three dimensional Navier-Stokes equations can fully describe all the physics of a given turbulent flow. This is due to the fact that turbulence is continuous process which consist of continuous spectrum of scales ranging from the largest one associated with the largest eddy to the smallest scales associated with the smallest eddy, referred as *Kolmogorov micro-scale*, a concept brought by the theory of turbulence statistics. These eddies overlap in space, larger one carrying the smaller ones. The process can be characterized as a cascading process by which the turbulence dissipates its kinetic energy from the larger eddies to the smaller eddies through vortex stretching. The energy is finally

dissipated into heat through the action of molecular viscosity in the smallest eddies. These larger eddies randomly stretch the vortex elements that compress the smaller eddies cascading energy to them. The cascading process give rise to the important features such as apparent stresses and enhanced diffusivity, which are several orders of magnitude larger than those in corresponding laminar flows. The scales of motion or wave lengths usually extend all the way from a maximum size comparable to the characteristic length of the flow channel to a minimum scale corresponding to the smallest eddy fixed by the viscous dissipation. The range of these scales or the ratio of minimum to maximum wave lengths varies with characteristic flow parameter such as Reynolds number of the flow.

## 2. Computational model for turbulence flow

In the computational simulation of turbulent flow, it is important to decide how finely we should resolve these eddies in the computational model as it has a direct effect on the accuracy of the prediction as well as computer time. Methods available for simulating turbulent fluid flow are *Direct Numerical Simulation (DNS)* based on direct solution of Navier-Stokes Equations and *Averaged or Filtered Simulation* based on averaged solution of Navier-Stokes Equations. A brief description of these methods is described as follows:

### 2.1 Direct Numerical Simulation (DNS)

A computational model based on the micro-scale discretization is called Direct Numerical Simulation (DNS). It involves complete resolution of the flow field by a direct solution of unsteady Navier-Stokes Equations resolving all active scales of motion in the flow field without using any approximation and models. The grid spacing and time steps should be fine enough to capture the dynamics of all scales down to the smallest scale associated with the smallest eddy, which is established by the *Kolmogorov microscale*. The smallest eddy based on *Kolmogorov micro-scale* decreases with the increase in flow Reynolds number in proportion to the value of  $Re^{3/4}$  and could be as small as 0.1-1 mm. Also, the computational domain should be large enough to include the largest scale of the flow dynamic, which is established by the characteristic dimension such as the height and width of the flow domain. Resolving all scales and frequencies of turbulent eddies based on the *Kolmogorov microscale* requires excessively large number of nodal points and excessively large computational time, and faces serious obstacles even with the most powerful supercomputers available today.

There are two basic requirements that a DNS model must meet to represent turbulence. These are: 1. It must represent a solution of Navier-Stokes equations resolving all scales of motion (viscous dissipation scales) adequately by the computational mesh, and 2. It should provide adequate statistical resolution (large samples or smaller time steps) of the set of all possible fluid motions allowed by the Navier-Stokes equations. These two requirements for a turbulence simulation conflict. The sample improves as the energy moves to smaller scales, but the viscous resolution is degraded. As a result, a DNS model of three-dimensional time dependent Navier-Stokes Equations for all important scales of turbulence has posed a great challenge for computer and numerical techniques in the past due to the requirement of extremely fine mesh size distribution and very small time steps to capture the essential details of the turbulent structures. Such requirements had limited the past DNS studies to very low Reynolds numbers. More detail descriptions of DNS method are given



by Eswaran and Pope (1988), Rai and Moin (1991, Kim et. al. (1997), Rogallo (1981) and Deb and Majumdar (1999).

## 2.2 Averaged or filtered simulation

In order to overcome the computational difficulties in terms grid size limitation imposed by *Kolmogorov microscale*, a simplified approach based on the solution of average Navier-Stokes Equations is most often used for turbulent fluid flow. An averaging or filtering operation is employed over the Navier-Stokes equation in order to smooth out certain range of high frequency variation of flow variables or smaller scales of turbulent eddies. This *averaging* or *filtering operation*, also known as *coarse graining* leads to a new set of flow governing equations that represents only the larger scale eddies or lower frequencies of flow variable. Because of the smoother variation of the flow variables, the smallest scale are no longer of the order of *Kolmogorov microscale*, but rather limited by the cut-off scale used in the averaging or filtering method and this results in a considerable reduction in the number of grid points and savings in computational time. So in the averaged or filtered simulation, only large scale of turbulence eddies are resolved, and an average affects of small scale eddies on the resolved scales are taken into account by the use of statistical average model, known as turbulence closure models. Turbulence modeling is designed to simulate the averaged flow Field, named as *coarse graining* instead of the original flow field. In this coarse graining process, small scale eddies that are difficult to resolve are neglected. The small eddies that are neglected in coarse graining are included in the simulation through the *turbulence modeling*.

Options available for analyzing turbulent flows are either a time-averaged approach using Reynolds Averaged Navier-Stokes (RANS) equations along with turbulence closure models, or a space-averaged approach using Large Eddy Simulations (LES) that takes into account of only large scale eddies and uses turbulence closure model for the smaller eddies, but require large amounts of computational time as well.

### 2.2.1 Large Eddy Simulation (LES)

In order avoid the limitation of the DNS method to resolve all scales of turbulence eddies in terms of smallest mesh size refinements, large eddy simulation (LES) are used. In large eddy simulation, the unsteady nature of turbulent eddies and only large scale eddies are resolved. The large scale eddies are anisotropic in nature and responsible for the driving physical mechanism such as production and major carrier of the turbulent kinetic energy. The small scale eddies are only responsible for viscous dissipation of small fraction of kinetic energy that they carry. The small scale eddies are modeled based on assuming an isotropic or a direction independent nature of eddies that follow a statistically predictive behavior for all turbulent flows. As small scale eddies are not resolved, LES methods are computationally less expansive than DNS method in which all scales or turbulence eddies are resolved. Nevertheless, LES method still requires finer mesh size distributions and computationally more expansive than RANS model.

### 2.2.2 Reynolds Averaged Navier-Stokes (RANS) model

Reynolds Averaged Navier-Stokes (RANS) model is the next level of approximation in which no attempts are made to resolve the unsteady nature of any sizes of turbulence

eddies. The increased level of mixing and dissipation caused by the turbulent eddies is taken into account through the turbulence closure models. In this approximation, the turbulence itself is not directly computed, but rather its average effect on mean flow is modeled by describing the turbulent motion in terms of time averaged form of Navier-Stokes equation referred to as the Reynolds-Averaged Navier-Stokes Equations. As described before instantaneous turbulent flow quantities are composed of two different types of motions: mean motion and a fluctuating motion as described by the following expressions for the instantaneous velocity components and pressure as

$$\mathbf{u} = \bar{\mathbf{u}} + \mathbf{u}', v = \bar{v} + v', w = \bar{w} + w' \text{ and } p = \bar{p} + p' \quad (3)$$

The mean velocity components are represented as  $\bar{u}$ ,  $\bar{v}$  and  $\bar{w}$ . The fluctuating (time dependent) components  $u'$ ,  $v'$  and  $w'$ , when added with the mean (time-independent)  $\bar{u}$ ,  $\bar{v}$  and  $\bar{w}$  components gives the instantaneous velocity components. The time mean of a quantity  $\phi$  is described as

$$\bar{\phi} \equiv \lim_{T \rightarrow \infty} \frac{1}{T} \int_{t_0}^{t_0+T} \phi \, dt \quad (4)$$

The velocity fluctuations produce mean rates of momentum transfer in addition to those produced by the mean velocity components. Substituting all fluctuating flow quantities given by equation (3) into in the Navier-Stokes equation (1-2) and performing the time averaged integration, the Reynolds-averaged Navier-Stokes equation is obtained as

$$\frac{\partial \rho}{\partial t} + \frac{\partial}{\partial x_i} (\rho u_i) = 0 \quad (5)$$

$$\frac{\partial}{\partial t} (\rho u_i) + \frac{\partial}{\partial x_j} (\rho u_i u_j - T_{ij}) = -\frac{\partial P}{\partial x_i} + \rho g_i + F_i \quad (6)$$

Where

$$T_{ij} = \left[ \mu \left( \frac{\partial u_i}{\partial x_j} + \frac{\partial u_j}{\partial x_i} \right) \right] - \frac{2}{3} \mu \frac{\partial u_k}{\partial x_k} \delta_{ij} - \overline{\rho u_i' u_j'} \quad (7)$$

The time averaged Navier-Stokes equation is complicated by the inclusion of the new turbulent term  $T_{ij} = -\overline{\rho u_i' u_j'}$ , which represents nine additional turbulent shear stress components caused by the cross-products of the fluctuating velocity components and are referred to as the Reynolds stress components. The nine components Reynolds stress tensor can be summarized by the following:

$$T_{ij} = -\overline{\rho u_i' u_j'} = \rho \begin{vmatrix} \overline{u'^2} & \overline{u'v'} & \overline{u'w'} \\ \overline{u'v'} & \overline{v'^2} & \overline{v'w'} \\ \overline{u'w'} & \overline{v'w'} & \overline{w'^2} \end{vmatrix} \quad (8)$$

The total stress is written as the sum of laminar viscous shear and turbulent Reynolds stress as

$$T_{ij} = -\overline{\rho u_i' u_j'} + \mu \left( \frac{\partial u_i}{\partial x_j} + \frac{\partial u_j}{\partial x_i} \right) \quad (9)$$

The new nine-component turbulent stress tensor depend not only on the fluid properties but also on the flow conditions such as geometry, velocity surface roughness and the up stream conditions, and defined based on the turbulence structure, which needs to be defined as well. Major challenge is to express Reynolds stress tensor in terms mean flow. Two approaches to evaluate the Reynolds stresses in terms of mean flow variables are 1. Boussinesq Eddy viscosity concept and Prandtl Mixing Length model and 2. Reynolds Stress Transport Model.

### Boussinesq eddy viscosity concept and Prandtl mixing length model

In an effort to mathematically describe turbulent stress in terms of mean flow quantities, Boussinesq (1877) introduced the concept of *eddy viscosity* using the analogy with the Newtonian viscous linear stress and strain rate relationship. Boussinesq assumption relates Reynolds turbulent stresses to the mean flow and strain rate in similarity with laminar linear shear-stress – strain relation as follows:

$$\tau_t = -\overline{\rho u' v'} = \mu_t \left( \frac{du}{dy} + \frac{dv}{dx} \right) \quad (10)$$

Where  $\mu_t$  is term as the turbulent viscosity or eddy viscosity and the total stress is given as

$$\tau_t = (\mu + \mu_t) \left( \frac{du}{dy} + \frac{dv}{dx} \right) \quad (11)$$

This leads to general expression for the Reynolds stress tensor expressed as

$$T_{ij} = \left[ \mu_t \left( \frac{\partial u_i}{\partial x_j} + \frac{\partial u_j}{\partial x_i} \right) \right] - \frac{2}{3} \mu_t \frac{\partial u_k}{\partial x_k} \delta_{ij} \quad (12)$$

and the total stress is expressed as the sum of laminar and turbulent stress

$$T_{ij} = \left[ \mu_{tot} \left( \frac{\partial u_i}{\partial x_j} + \frac{\partial u_j}{\partial x_i} \right) \right] - \frac{2}{3} \mu_{tot} \frac{\partial u_k}{\partial x_k} \delta_{ij} \quad (13)$$

Where  $\mu_{tot} = \mu + \mu_t$  = total viscosity, which is the sum of the molecular dynamic viscosity,  $\mu$  and turbulent or eddy viscosity,  $\mu_t$ .

Turbulent or eddy viscosity value is generally several order of magnitude higher than the molecular dynamic viscosity depending on the order of magnitude of the turbulence in the flow. Another important characteristic of turbulent or eddy viscosity is that it depends not only on the fluid, but it varies throughout the flow domain and depends strongly on fluid flow characteristics, geometry, roughness and upstream conditions. Prandtl in 1925 introduced the concept of mixing length ( $l_m$ ) theory that closely relates to eddy viscosity

concept and form the basis for all turbulent modeling effort. The Prandtl mixing length is defined as the average distance travelled by a lump of fluid or the fluid eddy in the normal direction to the flow in similarity with the mean free path length of molecules. Based on this concept, the turbulent stress and turbulent eddy viscosity are expressed in terms of Prandtl mixing length as follows:

$$\tau_t = -\rho \overline{u'v'} = \rho l_m^2 \left( \frac{\partial u}{\partial y} \right)^2 \quad (14)$$

and

$$\mu_t = \rho l_m^2 \left( \frac{\partial u}{\partial y} \right) \quad (15)$$

#### Different classes of turbulence closure models:

Turbulence closure models take into account the statistical average effect of small scale eddies on the time averaged mean flow that only resolves large scale eddies. In order to define the turbulent eddy viscosity, it is necessary to determine a suitable velocity scale and a length scale. The mixing length model is considered as an algebraic model or a zero-equation turbulence model. Subsequently, additional classes of turbulence models were developed based on the number of additional equations to describe the turbulent viscosity. An  $n$ -equation turbulence model requires the solution of  $n$  additional transport equations for additional variables used to describe the length and velocity scales used in the estimation of turbulent viscosity. In *one-equation* turbulence model, *turbulence kinetic energy* ( $k$ ) was introduced to describe the velocity scale. Subsequently, in *two-equation model*, an additional variable like the rate of dissipation of turbulence kinetic energy was introduced to represent the length scale of turbulence. The estimation of turbulent viscosity in terms of turbulence kinetic energy ( $k$ ) and turbulence dissipation rate ( $\epsilon$ ) is given by the Prandtl-Kolmogorov relation:

$$\mu_t = \rho C_\mu k^2 / \epsilon \quad (16)$$

Turbulence models are classified into the following several divisions and subdivisions:

#### i. Algebraic turbulence or Zero-equation model

Algebraic turbulence models are zero-equation turbulence models that do not require the solution of any additional equation, and are calculated directly from the flow variables. As a consequence, zero equation models do not take into account the history effects of the turbulence, such as convection and diffusion of turbulent energy and are often adequate for simpler flow geometries. Some of the most popular algebraic zero-equation turbulence models are a) Cebeci-Smith model, b) Baldwin-Lomax model and c) Johnson-King model. Algebraic models are simple, quite robust and computationally less expensive. Major limitations of algebraic turbulence are that they are semi-empirical with weak physical bases and so not applicable to flow problems that are significantly different from flow problems for which the empirical constants are derived.

#### ii. One-equation model

One equation turbulence models include i) Prandtl's one-equation model, ii) Baldwin-Barth model and iii) Spalart-Allmaras model

- Spalart – Allmaras model

The model proposed by Spalart and Allmaras is a one-equation model that solves for kinematic eddy viscosity from the transport equation. It is the preferred model for problems involving no separation or weak separation and it is widely used in turbomachinery applications. The transport equation is given by

$$\frac{\partial}{\partial t}(\rho \tilde{\nu}) + \frac{\partial}{\partial x_i}(\rho \tilde{\nu} u_i) = G_\nu + \frac{1}{\sigma_\nu} \left[ \frac{\partial}{\partial x_j} \{ \mu + \rho \tilde{\nu} \} \frac{\partial \tilde{\nu}}{\partial x_j} \right] + C_{b2} \rho \left( \frac{\partial \tilde{\nu}}{\partial x_j} \right)^2 - Y_\nu \quad (17)$$

Where  $G$  is the production of turbulent viscosity and  $Y_\nu$  is the destruction of turbulent viscosity that occurs in the near-wall region. The turbulent viscosity ( $\mu_t$ ) is computed as

$$\mu_t = \rho \tilde{\nu} f_{\nu 1} \quad (18a)$$

Where  $f_{\nu 1}$  is the viscous damping function given by

$$f_{\nu 1} = \frac{\chi^3}{\chi^3 + C_{\nu 1}^3}, \chi = \frac{\tilde{\nu}}{\nu} \quad (18b)$$

$$G_\nu = C_{b1} \rho \tilde{S} \tilde{\nu} \quad (18c)$$

$\tilde{S}$  is a function of mean rate of rotation tensor and viscous damping function.

$$Y_\nu = C_{w1} \rho f_w \left( \frac{\tilde{\nu}}{d} \right)^2 \quad (18d)$$

Where  $f_{w1}$  is a function of vorticity and  $d$  is the distance from the wall.

### iii. Two-equation model

Two equation turbulence models include two extra transport equations to represent the turbulent properties of the flow that accounts for convection and diffusion of turbulent energy. Most often one of the transported variables is the **turbulent kinetic energy**,  $k$ . The second transport variables varies, however, with different two-equation models. Most common choices are the **turbulent dissipation**,  $\varepsilon$ , or the **specific dissipation**,  $\omega$ . While the **turbulent kinetic energy**,  $k$  represents the energy in the turbulence, the **turbulent dissipation**,  $\varepsilon$ , or the **specific dissipation**,  $\omega$  represents the turbulence length-scale. A list of some of these widely used two-equation turbulence models is given here:

**$k-\varepsilon$  Turbulence models:**  $k-\varepsilon$  High Reynolds turbulence model,  $k-\varepsilon$  Low Reynolds turbulence model, Realisable  $k-\varepsilon$  model,  $k-\varepsilon$  Renormalization Group (RNG) turbulence model,  $k-\varepsilon$  Chen turbulence model,  $k-\varepsilon$  Standard Quadratic High Reynolds Turbulence model,  $k-\varepsilon$  Suga Quadratic High Reynolds Turbulence models

**$k-\omega$  Turbulence models:**  $k-\omega$  Standard High Re,  $k-\omega$  Standard Low Re,  $k-\omega$  SST High Re and  $k-\omega$  SST Low Re

### iv. Reynolds Stress Model (RSM)

Reynolds stress model (RSM) discarded the eddy viscosity approach and computes the Reynolds stresses directly. It is a higher level more elaborate turbulent model, which

introduces exact Reynolds stress transport equations to compute the Reynolds stresses directly and accounts for the directional effects of Reynolds stress field. Some of the most popular RSM model are RSM/Gibson-Launder (wall Reflection: Standard), RSM/Gibson-Launder (wall Reflection: Craft) and RSM/Speziale, Sarkar and Gatski.

### 2.2.3 The Standard $k-\varepsilon$ model

The standard  $k-\varepsilon$  turbulence model is the most widely used one, which is also known as  $k-\varepsilon$  High Reynolds turbulence model. It includes two transport equations to define the turbulence scales. The  $k$  denotes the turbulent kinetic energy ( $\text{m}^2/\text{s}^2$ ), whereas  $\varepsilon$  denotes the dissipation rate ( $\text{m}^2/\text{s}^3$ ). The model proposed by Launder and Spalding [1974] is based on the transport equations for the turbulent kinetic energy,  $k$  and its rate of dissipation,  $\varepsilon$  as follows.

$$\frac{\partial}{\partial t}(\rho k) + \frac{\partial}{\partial x_i}(\rho k u_i) = \frac{\partial}{\partial x_j} \left[ \left( \mu + \frac{\mu_t}{\sigma_k} \right) \frac{\partial k}{\partial x_j} \right] + G_b - \rho \varepsilon - Y_M + S_k \quad (19)$$

$$\frac{\partial}{\partial t}(\rho \varepsilon) + \frac{\partial}{\partial x_i}(\rho \varepsilon u_i) = \frac{\partial}{\partial x_j} \left[ \left( \mu + \frac{\mu_t}{\sigma_\varepsilon} \right) \frac{\partial \varepsilon}{\partial x_j} \right] + C_{1\varepsilon} \frac{\varepsilon}{k} (C_{3\varepsilon} G_b) - C_{2\varepsilon} \rho \frac{\varepsilon^2}{k} + S_\varepsilon \quad (20)$$

The generation of turbulent kinetic energy due to buoyancy is

$$G_b = -g_i \frac{\mu_t}{\rho \text{Pr}_t} \frac{\partial \rho}{\partial x_i} \quad (21)$$

The fluctuating dilatation in compressible turbulence to the overall dissipation rate

$$Y_M = \frac{2\rho\varepsilon\kappa}{a^2} \quad (22)$$

Where,  $a$  = Speed of sound.

The turbulent viscosity is computed by combining  $k$  and  $\varepsilon$  as

$$\mu_t = \rho C_\mu \frac{k^2}{\varepsilon} \quad (23)$$

Where,  $C_\mu = 0.09$ ,  $C_{1\varepsilon} = 1.44$ ,  $C_{2\varepsilon} = 1.92$  and,  $C_{3\varepsilon} = 0.09$  are model constants.  $\sigma_k = 1.0$  and  $\sigma_\varepsilon = 1.3$  are the turbulent Prandtl numbers for  $k$  and  $\varepsilon$  respectively.  $S_k$  and  $S_\varepsilon$  are user-defined source terms.

A two-equation  $k-\varepsilon$  model could be quite suitable for flow in straight channels without the presence of any large scale flow separations and adverse pressure gradient or in problems where only average parameters are to be determined without the requirement of resolving detail turbulence quantities. This model is found to be quite adequate for many industrial applications.

### 2.2.4 Low Reynolds $k-\varepsilon$ turbulence model

The failure of standard  $k-\varepsilon$  model to predict the low-Re and separated flows, introduces the  $k-\varepsilon$  Low-Re turbulence model {Lam and Bremhorst (1981), Jones and Launder (1972)

and Majumdar and Deb (2003)], which has a special near-wall treatment for proper prediction of the flow at a region very near to the wall, referred to as the laminar sub-layer. It is well known that the turbulent kinetic energy distribution reaches to its peak value in the near-wall region. Though  $\varepsilon$  increases in this region,  $k$  also increase and  $k^2$  plays a very important role by changing the  $\mu_t$  by a large extent. On the other hand, at a location very close to the wall,  $k^2$  suppresses  $\mu_t$ . To counteract these effects, two approaches have been taken:

- The wall-function method, where an empirical wall function has been introduced along with  $k$  and  $\varepsilon$  equations. However, it is not suitable for many flows.
- The low-Reynolds-number method, where the wall boundary conditions are directly applied to the equations without introducing any wall functions.

Jones and Launder [11] extended the standard k- $\varepsilon$  model to the low Reynolds number model, which allows calculation through the viscous sub-layer to the wall without using wall function formulas. Additional terms were included in the equations for dissipation rate. The equations for the rate of dissipation and the turbulence kinetic energy included viscous diffusion term to ensure that the total dissipation rate is non-zero at the wall and modified terms containing C's to make them dependent upon Reynolds number of turbulence. The  $k$  equation for this TM is the same as equation (19), except the expression of the term  $\mu_t$ , which is defined as

$$\mu_t = f_\mu \frac{C_\mu \rho k^2}{\varepsilon} \quad (24)$$

where

$$f_\mu = \left[ 1 - e^{-0.0198 \text{Re}_y} \right] \left[ 1 + \frac{5.29}{\text{Re}_y} \right] \quad (25)$$

$\varepsilon$  equation:

$$\begin{aligned} \frac{\partial}{\partial t}(\rho\varepsilon) + \frac{\partial}{\partial x_j} \left[ \rho u_j \varepsilon - \left( \mu + \frac{\mu_t}{\sigma_\varepsilon} \right) \frac{\partial \varepsilon}{\partial x_j} \right] = C_{\varepsilon 1} \frac{\varepsilon}{k} \left\{ \mu_t (P + P_{NL} + P') - \frac{2}{3} \left( \mu_t \frac{\partial u_i}{\partial x_j} + \rho k \right) \frac{\partial u_i}{\partial x_j} \right\} + \\ C_{\varepsilon 3} \frac{\varepsilon}{k} \mu_t P_B - C_{\varepsilon 2} (1 - 0.3e^{-R_i^2}) \rho \frac{\varepsilon^2}{k} + C_{\varepsilon 4} \rho \varepsilon \frac{\partial u_i}{\partial x_j} \end{aligned} \quad (26)$$

The additional term  $P'$  is given by

$$P' = 1.33 (1 - 0.3e^{-R_i^2}) \left[ P + P_{NL} + 2 \frac{\mu}{\mu_t} \frac{k}{y^2} \right] e^{-0.00375 \text{Re}_y^2} \quad (27)$$

Where  $\text{Re}_y = \frac{y\sqrt{k}}{\nu}$ ,  $y$  = a normal distance to the nearest wall and  $R_i = \frac{k^2}{\nu\varepsilon}$  = Turbulent Reynolds Number.

### 2.2.5 k - $\varepsilon$ Chen turbulence model

The Chen model has been introduced to have a better response of the energy transfer mechanism of turbulence towards the mean strain rate. It does not take into account of the compressibility and buoyancy effects explicitly.

**Equation for  $k$  :**

$$\frac{\partial}{\partial t}(\rho k) + \frac{\partial}{\partial x_j} \left[ \rho u_j k - \left( \mu + \frac{\mu_t}{\sigma_k} \right) \frac{\partial k}{\partial x_j} \right] = \mu_t (P + P_B) - \rho \varepsilon - \frac{2}{3} \left( \mu_t \frac{\partial u_i}{\partial x_j} + \rho k \right) \frac{\partial u_i}{\partial x_j} \quad (28)$$

**Equation for  $\varepsilon$  :**

$$\begin{aligned} \frac{\partial}{\partial t}(\rho \varepsilon) + \frac{\partial}{\partial x_j} \left[ \rho u_j \varepsilon - \left( \mu + \frac{\mu_t}{\sigma_\varepsilon} \right) \frac{\partial \varepsilon}{\partial x_j} \right] = & C_{\varepsilon 1} \frac{\varepsilon}{k} \left[ \mu_t P - \frac{2}{3} \left( \mu_t \frac{\partial u_i}{\partial x_j} + \rho k \right) \frac{\partial u_i}{\partial x_j} \right] + \\ & + C_{\varepsilon 3} \frac{\varepsilon}{k} \mu_t P_B - C_{\varepsilon 2} \rho \frac{\varepsilon^2}{k} + C_{\varepsilon 4} \rho \varepsilon \frac{\partial u_i}{\partial x_j} + C_{\varepsilon 5} \frac{\mu_t^2 P^2}{\rho k} \end{aligned} \quad (29)$$

### 2.2.6 Suga's High Reynolds number $k$ - $\varepsilon$ turbulence model:

In Suga's  $k$ - $\varepsilon$  model  $\tilde{\varepsilon}$  is solved instead of  $\varepsilon$ , which is the isotropic part of  $\varepsilon$  and is zero at the wall. The  $k$  equation for this TM is same as equation (19) and the dissipation equation is given as

**Equation for  $\varepsilon$  :**

$$\frac{\partial}{\partial t}(\rho \tilde{\varepsilon}) + \frac{\partial}{\partial x_j} \left[ \rho u_j \tilde{\varepsilon} - \left( \mu + \frac{\mu_t}{\sigma_\varepsilon} \right) \frac{\partial \tilde{\varepsilon}}{\partial x_j} \right] = \rho C_{\varepsilon 1} \frac{\tilde{\varepsilon}}{k} P_k - \rho C_{\varepsilon 2} + C_{\varepsilon 3} \frac{\tilde{\varepsilon}}{k} \mu_t P_B + C_{\varepsilon 4} \rho \tilde{\varepsilon} \frac{\partial u_i}{\partial x_j} \quad (30)$$

Where

$$P_B \equiv \frac{g_i}{\sigma_{h,t}} \frac{1}{\rho} \frac{\partial \rho}{\partial x_j}, \quad P_k = -\overline{u_i u_j} \frac{\partial u_i}{\partial x_j}, \quad \tilde{R}_t = \frac{k^2}{v \tilde{\varepsilon}}, \quad \tilde{\varepsilon} = \varepsilon - 2\nu \left[ \frac{\partial \sqrt{k}}{\partial x_i} \right]^2$$

Turbulent viscosity  $\mu_t$  is defined as

$$\text{does not take into account of} \quad \mu_t = f_\mu \frac{C_\mu \rho \cdot k^2}{\varepsilon} \quad (31)$$

Where

$$f_\mu = 1 - \exp \left[ - \left( \frac{\tilde{R}_t}{90} \right)^{\frac{1}{2}} - \left( \frac{\tilde{R}_t}{400} \right)^2 \right] \quad (32)$$

### 2.2.7 The Renormalization Group (RNG) $\kappa$ - $\varepsilon$ model

The renormalization group (RNG)  $\kappa$ - $\varepsilon$  model [Choudhury, D. (1993)] originated from the instantaneous Navier-Stokes equations, utilizing a mathematical technique called renormalization group (RNG) method. This derivation results in additional terms and functions in transport equations of  $k$  and  $\varepsilon$ .



### Transport equation for the RNG $\kappa$ - $\varepsilon$ model

The RNG  $\kappa$ - $\varepsilon$  model has similar form to the standard  $\kappa$ - $\varepsilon$  model:

$$\frac{\partial}{\partial t}(\rho k) + \frac{\partial}{\partial x_i}(\rho k u_i) = \frac{\partial}{\partial x_i}(\sigma_k u_{\text{eff}} \frac{\partial k}{\partial x_j}) + G_b - \rho \varepsilon - Y_M + S_k \quad (33)$$

$$\frac{\partial}{\partial t}(\rho \varepsilon) + \frac{\partial}{\partial x_i}(\rho \varepsilon u_i) = \frac{\partial}{\partial x_i}(\sigma_\varepsilon u_{\text{eff}} \frac{\partial \varepsilon}{\partial x_j}) + C_{1\varepsilon} C_{3\varepsilon} G_b - C_{2\varepsilon} \rho \frac{\varepsilon^2}{k} - R_\varepsilon + S_\varepsilon \quad (34)$$

The RNG theory results in a differential equation for *turbulent viscosity*:

$$d\left(\frac{\rho^2 k}{\sqrt{\varepsilon \mu}}\right) = 1.72 \frac{\hat{v}}{\sqrt{\hat{v}^3 - 1 + C_v}} d\hat{v} \quad (35)$$

Where  $\hat{v} = \frac{\mu_{\text{eff}}}{\mu}$  and  $C_v \approx 100$

Turbulent quantities change considerably with the effect of swirl in the mean flow direction. To incorporate the swirl effect the turbulent viscosity is calculated form

$$\mu_t = \mu_{t0} f\left(\alpha_s, \Omega, \frac{\kappa}{\varepsilon}\right) \quad (36)$$

Where  $\mu_{t0}$ , is the turbulent viscosity calculated without swirl modification from equation (35),  $\alpha_s = 0.05$ , for moderately swirl flow,  $\Omega$  swirl number. For higher Reynolds numbers equation turbulent viscosity is calculated by equation (16) and  $c_\mu = 0.0845$ . The default model constants are  $C_{1\varepsilon} = 1.42$ ,  $C_{2\varepsilon} = 1.68$ .

### 2.2.8 The Realizable $\kappa$ - $\varepsilon$ model

The Realizable  $\kappa$ - $\varepsilon$  model [Shih, T. and Liou, W. (1995)] includes additional mathematical constraints consistent with certain physics of the turbulent flow. It addresses the deficiencies of traditional  $\kappa$ - $\varepsilon$  models by adopting a new eddy-viscosity formula with a variable  $C_\mu$  and a new model equation for dissipation rate  $\varepsilon$  based on dynamic equations mean-square vorticity fluctuation. The transport equations in realizable  $\kappa$ - $\varepsilon$  model are

$$\frac{\partial}{\partial t}(\rho k) + \frac{\partial}{\partial x_i}(\rho k u_i) = \frac{\partial}{\partial x_i} \left[ \left( \mu + \frac{\mu_t}{\sigma_k} \right) \frac{\partial k}{\partial x_j} \right] + G_b - \rho \varepsilon - Y_M + S_k \quad (37)$$

$$\frac{\partial}{\partial t}(\rho \varepsilon) + \frac{\partial}{\partial x_j}(\rho \varepsilon u_j) = \frac{\partial}{\partial x_i} \left[ \left( \mu + \frac{\mu_t}{\sigma_\varepsilon} \right) \frac{\partial \varepsilon}{\partial x_j} \right] + \rho C_1 S \varepsilon - \rho C_2 \frac{\varepsilon^2}{\kappa + \sqrt{\nu \varepsilon}} + C_{1\varepsilon} \frac{\varepsilon}{k} C_{3\varepsilon} G_b + S_\varepsilon \quad (38)$$

Where  $C_1 = \max\left[0.43, \frac{\eta}{\eta + 5}\right]$ ,  $\eta = S \frac{k}{\varepsilon}$ ,  $C_{1\varepsilon} = 1.44$ ,  $C_2 = 1.9$ ,  $\sigma_k = 1.0$  and  $\sigma_\varepsilon = 1.2$  are the model constants. The eddy viscosity is calculated from equation (16), but

$$C_\mu = \frac{1}{A_0 + A_s \frac{kU^*}{\varepsilon}} \quad (39)$$

$$U^* \equiv \sqrt{S_{ij}S_{ij} + \tilde{\Omega}_{ij}\tilde{\Omega}_{ij}} \quad (40)$$

Where  $\tilde{\Omega}_{ij}$ , is the mean rate-of-rotation tensor viewed in the rotating reference frame with an angular velocity. Both the Realizable and RNG  $k-\varepsilon$  models have shown substantial improvements over the standard  $k-\varepsilon$  model where the flow features include strong streamline curvature, vortices, and rotation.

The realizable  $k-\varepsilon$  model provides superior performance for flows involving rotation, boundary layers under strong adverse pressure gradients, separation, and recirculation. The limitations of the realizable  $k-\varepsilon$  model are that it produces nonphysical turbulent viscosities in situations when the computational domain contains both rotating and stationary fluid zones, i.e., use of multiple reference frames or rotating sliding meshes.

### 2.2.9 Quadratic High Reynolds $k-\varepsilon$ turbulence model

Non-linear turbulence models are introduced to take into account of anisotropic turbulence characteristics present in many real flows by adopting non-linear relationships between Reynolds stresses and the rate of strain. For quadratic models, the constitutive relations for the Reynolds stresses are:

$$\begin{aligned} \rho \frac{\overline{u'_i u'_j}}{k} = & \frac{2}{3} \left( \frac{\mu_t}{k} \frac{\partial u_k}{\partial x_k} + \rho \right) \delta_{ij} - \frac{\mu_t}{k} S_{ij} + C_1 \frac{\mu_t}{\varepsilon} \left[ S_{ik} S_{kj} - \frac{1}{3} \delta_{ij} S_{kl} S_{kl} \right] + \\ & C_2 \frac{\mu_t}{\varepsilon} \left[ \Omega_{ik} S_{kj} + \Omega_{jk} S_{ki} \right] + C_3 \frac{\mu_t}{\varepsilon} \left[ \Omega_{ik} \Omega_{ik} - \frac{1}{3} \delta_{ij} \Omega_{kl} \Omega_{kl} \right] \end{aligned} \quad (41)$$

Where,  $\Omega_{ij}$  is the mean vorticity tensor given by

$$\Omega_{ij} = \frac{\partial u_i}{\partial x_j} - \frac{\partial u_j}{\partial x_i} \quad (42)$$

Coefficients are defined as,

$$C_1 = \frac{c_{NL1}}{(c_{NL6} + c_{NL7}S^3)C_\mu}, \quad C_2 = \frac{c_{NL2}}{(c_{NL6} + c_{NL7}S^3)C_\mu}, \quad C_3 = \frac{c_{NL3}}{(c_{NL6} + c_{NL7}S^3)C_\mu} \quad (43)$$

Where,

$$C_\mu = \frac{c_{A0}}{c_{A1} + c_{A2}S + c_{A3}\Omega}, \quad S = \frac{k}{\varepsilon} S^*, \quad \text{and} \quad \Omega = \frac{k}{\varepsilon} \Omega^*,$$

$$S^* = \sqrt{\frac{1}{2} S_{ij} S_{ij}} \quad \text{and} \quad \Omega^* = \sqrt{\frac{1}{2} \Omega_{ij} \Omega_{ij}}$$

| $c_{A0}$ | $c_{A1}$ | $c_{A2}$ | $c_{A3}$ | $c_{NL1}$ | $c_{NL2}$ | $c_{NL3}$ | $c_{NL6}$ | $c_{NL7}$ |
|----------|----------|----------|----------|-----------|-----------|-----------|-----------|-----------|
| 0.667    | 1.25     | 1.0      | 0.9      | 0.75      | 3.75      | 4.75      | 1000.0    | 1.0       |

 Table 1. Empirical coefficients for  $k - \varepsilon$  quadratic high Re turbulence model

### 2.2.10 $k - \omega$ SST (Shear Stress Transport Turbulence) model

An alternate approach to the  $k - \varepsilon$  model is the  $k - \omega$  model, where  $\omega$  is the specific dissipation rate, which is defined as

$$\omega = \varepsilon / C_\mu k \quad (44)$$

Equation for  $k$ :

$$\frac{\partial}{\partial t}(\rho k) + \frac{\partial}{\partial x_j} \left[ \rho u_j k - \left( \mu + \frac{\mu_t}{\sigma_k^\omega} \right) \frac{\partial k}{\partial x_j} \right] = \mu_t (P + P_B) - \rho \beta^* k \omega \quad (45a)$$

Equation for  $\omega$ :

$$\frac{\partial}{\partial t}(\rho \omega) + \frac{\partial}{\partial x_j} \left[ \rho u_j \omega - \left( \mu + \frac{\mu_t}{\sigma_\omega^\omega} \right) \frac{\partial \omega}{\partial x_j} \right] = \alpha \frac{\omega}{k} \mu_t P - \rho \beta \omega^2 + \rho S_\omega + C_{\varepsilon 3} \mu_t P_B C_\mu \omega \quad (45b)$$

Where,  $C_\mu$  and  $C_{\varepsilon 3}$  are empirical coefficients.

The coefficients are expressed as follows:

$$C_\phi = F_1 C_{\phi 1} + (1 - F_1) C_{\phi 2}$$

Where  $C_{\phi 1}$  and  $C_{\phi 2}$  are given by two separate coefficient sets and

$$F_1 = \tanh(\arg_1^4)$$

$$\arg_1 = \min \left[ \max \left( \frac{\sqrt{k}}{0.09 \omega y}, \frac{500 \nu}{y^2 \omega} \right), \frac{4 \rho k}{\sigma_{\omega 2}^\omega C D_{k\omega} y^2} \right]$$

$$C D_{k\omega} = \max \left( \frac{2 \rho}{\omega \sigma_{\omega 2}^\omega} \frac{\partial k}{\partial x_j} \frac{\partial \omega}{\partial x_j}, 10^{-20} \right)$$

Where

| $\sigma_{k1}^\omega$ | $\sigma_{\omega 1}^\omega$ | $\beta_1$ | $\beta_1^*$ | $\kappa$ |
|----------------------|----------------------------|-----------|-------------|----------|
| 1.176                | 2.0                        | 0.075     | 0.09        | 0.41     |

 Table 2. Coefficients for  $k - \omega$  SST turbulence model

With,

$$\alpha_1 = \frac{\beta_1}{\beta_1^*} - \frac{\kappa^2}{\sigma_{\omega 1}^\omega \sqrt{\beta_1^*}}$$

| $\sigma_{k2}^\omega$ | $\sigma_{\omega 2}^\omega$ | $\beta_2$ | $\beta_2^*$ | $\kappa$ |
|----------------------|----------------------------|-----------|-------------|----------|
| 1.0                  | 1.168                      | 0.0828    | 0.09        | 0.41     |

Table 3. Coefficients for  $k - \omega$  SST turbulence model

With,

$$\alpha_2 = \frac{\beta_2}{\beta_2^*} - \frac{\kappa^2}{\sigma_{\omega 2}^\omega \sqrt{\beta_2^*}}, \quad S_\omega = 2(1 - F_1) \frac{1}{\sigma_{\omega 2}^\omega} \frac{\partial k}{\partial x_j} \frac{\partial \omega}{\partial x_j}$$

The turbulent viscosity is defined as,

$$\mu_t = \rho \frac{a_1 k}{\max(a_1 \omega, \Omega^* F_2)}$$

Where,

$$a_1 = 0.31, F_2 = \tanh(\arg_2^2)$$

and

$$\arg_2 = \max\left(2 \frac{\sqrt{k}}{0.09 \omega y}, \frac{500 \nu}{y^2 \omega}\right)$$

Like standard  $k - \varepsilon$  model, the  $k - \omega$  model is also widely used in many industrial applications involving flow separation and recirculation.

### 2.2.11 Reynolds Stress Model

In the Reynolds stress model [Gibson and Launder (1978), Launder (1989) and Launder et al. (1975)], additional transport equations are used in the calculation of the Reynolds stresses. The stresses obtained are used to calculate the average momentum. Due the additional transportation equations, Reynolds stress model (RSM) model shows superior results with flows involving anisotropic turbulence. It includes seven additional equations and account for higher accuracy and however, require additional computational resources.

$$\frac{\partial}{\partial t}(\rho u_i) + \frac{\partial}{\partial x_j}(\rho u_i u_j) = \frac{\partial p}{\partial x_i} + \frac{\partial}{\partial x_j} \left[ \mu \left( \frac{\partial u_i}{\partial x_j} + \frac{\partial u_j}{\partial x_i} - \frac{2}{3} \delta_{ij} \frac{\partial u_l}{\partial x_l} \right) \right] + \frac{\partial}{\partial x_j} \left( -\rho \overline{u_i u_j'} \right) \tag{46a}$$

$$\begin{aligned} \frac{\partial}{\partial t} \left( \rho \overline{u_i u_j'} \right) + \frac{\partial}{\partial x_k} \left( \rho u_k \overline{u_i u_j'} \right) &= \frac{\partial}{\partial x_k} \left[ \rho \overline{u_i u_j' u_k'} + p \left( \delta_{kj} \overline{u_i'} + \delta_{ik} \overline{u_j'} \right) \right] \\ &+ \frac{\partial}{\partial x_k} \left[ \mu \frac{\partial}{\partial x_k} \left( \overline{u_i' u_j'} \right) \right] - \rho \left( \overline{u_i' u_k'} \frac{\partial u_j}{\partial x_k} + \overline{u_j' u_k'} \frac{\partial u_i}{\partial x_k} \right) - \rho \beta \left( g_i \overline{u_j' \theta} + g_j \overline{u_i' \theta} \right) \\ &+ p \left( \frac{\partial \overline{u_i'}}{\partial x_j} + \frac{\partial \overline{u_j'}}{\partial x_i} \right) - 2\mu \frac{\partial \overline{u_i'}}{\partial x_k} \frac{\partial \overline{u_j'}}{\partial x_k} - 2\rho \Omega_k \left( \overline{u_j' u_m'} \varepsilon_{ikm} + \overline{u_i' u_m'} \varepsilon_{jkm} \right) \end{aligned} \tag{46b}$$

Like any other transport equation the Equation (46b) for the Reynolds stress transport includes number of terms including convection, turbulent diffusion, molecular diffusion, buoyancy, stress production, and rotation production, pressure strain, viscous dissipation and user defined source term. Some of the most commonly used RSM models are i. Gibson and Launder model and ii) Speziale, Sarker and Gatski model.

A RSM model is generally required in problems involving strong anisotropic effects.

Usually one would start with the simplest model such as the standard model with wall function or a low Reynolds number model with fine mesh size near the wall to see if reasonably acceptable engineering results are obtained. In order to narrow down the choice of turbulence model in terms of stable converging solutions, each class of turbulence models are to be compared among themselves first before comparing all models with the experimental data or DNS/LES.

### 2.3 Boundary condition for turbulence quantities

One of the major requirements for the solution of turbulent flow is the specification of turbulence quantities such as turbulence kinetic energy and turbulence dissipation rate or the mixing length or the ratio of turbulence viscosity to molecular viscosity at the inlet. While results are not strongly influenced by the inlet turbulence level for problems with inlet located far away from the region of interest, the specified values have a significant effect on the resulting flow solution for problems with smaller entry length. So, one approach is to assign directly the values of turbulent kinetic energy and turbulent dissipation rate. However, specification of turbulence quantities such as turbulence kinetic energy and turbulence dissipation rate at inlet can be quite difficult and often rely on engineering judgments. It is always, however, preferred to assign experimentally measured values of turbulence quantities. If such data are not available, then values can be prescribed based on engineering assumptions and a numerical sensitivity study must be performed to understand the sensitivity of inlet turbulence conditions on the solutions.

For the specification of the turbulent kinetic energy, appropriate values can be specified through *turbulence intensity* ( $I$ ), which is defined by the ratio of the fluctuating components of the velocity to the mean velocity. In general, the inlet turbulence is a function of the upstream flow conditions. Approximate values for the turbulence kinetic energy can be determined according to the following relationship:

$$k_{inlet} = \frac{3}{2} (U_{inlet} I)^2 \quad (47a)$$

Inlet dissipation rate can be specified based on length scale as

$$\epsilon_{inlet} = \frac{C_{\mu}^{3/4} k^{3/2}}{l} \quad (47b)$$

Where  $l = 0.1D_H$

In external aerodynamic flows over airfoils, the turbulence intensity level is typically 0.3%. For atmospheric boundary layer flows, the level can be as high as two orders of magnitude - 30%. The range of turbulence intensity for a moderately turbulent flow is around 1-10%.

The turbulence intensity at the core of a fully developed duct flow is estimated from the following formula:

$$I = 0.16(\text{Re}_{DH})^{1/8} \quad (48)$$

### Near-wall region modeling

Another important aspect of using some of the turbulence closure models are that they are valid only in the fully turbulent region due to the laminarization of flow or the presence of laminar viscous sub-layer near the wall. In regions close to the wall, viscous effects dominate over turbulence effects due to the small local Reynolds number of turbulence. The near-wall modeling consists of two approaches. The *first approach* involves modifying the turbulence models such as low Reynolds number models and by using an appropriate fine grid to resolve the near-wall viscous effects. In low Reynolds number modeling methods  $k$  and  $\epsilon$  equations are modified such that they are valid throughout the laminar, semi-laminar and fully turbulent regions

In the *second approach*, the viscosity-affected region is not resolved and *wall functions* are used to bridge the viscosity-affected region between the wall and the fully turbulent region. The standard high Reynolds number turbulence models need not be modified if the wall functions are used to account for the presence of walls. The two most popular types of wall functions are the standard wall functions and non-equilibrium wall functions.

In the wall function method the grid size distribution is selected in such a way that the adjacent grid point P is sufficiently remote from the wall. This causes local Reynolds number of turbulence at point P to be much greater than one, so that the viscous effects are dominating in this region. The standard wall functions proposed by Launder and Spalding [17] relate the non-dimensional distance ( $y^+$ ) to the distance of the nearest cell point P ( $y_p$ ) from the wall as

$$y^+ = \frac{\rho C_\mu^{1/4} k_p^{1/2} y_p}{\mu}$$

Where  $k_p$  is the turbulent kinetic energy at point P and  $\mu$  is the dynamic viscosity of the fluid.

In addition, the momentum and heat flux between the wall and the adjacent grid point P is assumed to obey certain relations in the numerical calculations. The refined mesh size distribution near the wall is limited by satisfying  $y^+$  requirement, which defines the minimum distance of the computational cell from the wall boundary. Having the correct  $y^+$  value for the cells next to the wall is extremely important to obtain the correct velocity, pressure and shear stress values. Also for using turbulence models with wall functions, the  $y^+$  value of the near wall cells is a basic requirement that has to be satisfied. All computational turbulence studies starts with an initial search for the correct cell size to satisfy the  $y^+$  requirement for the turbulence model used. For example, in the study of  $k - \epsilon$  high Reynolds number turbulence closure model with standard wall function the  $y^+$  value are required to be kept within 30 - 120.

Non-equilibrium wall functions solve for mean velocity near the wall region incorporating pressure gradient effects. The non-equilibrium wall function employs a two-layer concept in computing the turbulence kinetic energy at the wall-adjacent cells. The standard wall

functions are generally used for high Reynolds number wall bounded flows and for satisfying equilibrium conditions for production and dissipation of turbulent kinetic energy at the wall. For flows that involve adverse pressure gradient, rotation, and strong streamline curvature, the flow conditions depart from equilibrium. The non-equilibrium wall functions take into account of the effects of pressure gradient and departure from equilibrium conditions and are generally involve severe pressure gradient.

### 3. Case study examples

#### 3.1 Case – I: Computational fluid dynamic analysis of turbulent flow in blade passages of centrifugal fan impeller

The objective of the present study is to analyze the three-dimensional turbulent flow in a single blade passage of a centrifugal fan impeller at design and off-design conditions. Numerical calculations are performed using commercial code FLUENT. A computational treatment of turbulent flow in a single blade passage of the centrifugal fan impeller is considered in this study. The geometric description of the impeller used for CFD simulation is presented in form of Pro/E solid model with different views describing the centrifugal fan geometrical features is shown in Figure 1. The assembly consists of a hub mounted on a back plate. The back plate is flat and circular with blades arranged in circular symmetry. The shroud is tapered from inlet to outlet with higher cross-sectional area at the inlet. The blades are straight and radial and their sectional width extends from the back plate all the way to the shroud, thus making the size of the tip gap region reduce to zero.

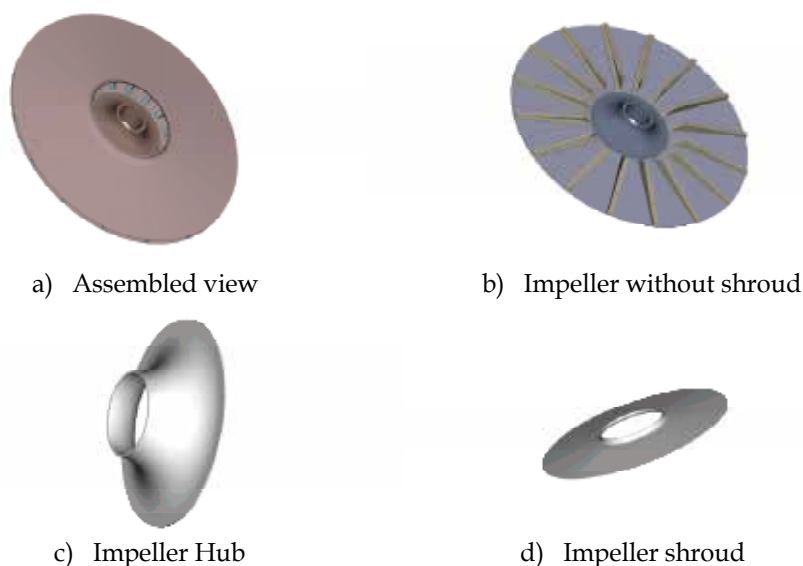


Fig. 1. Solid model of the impeller design

##### 3.1.1 Physical representation of the problem

A three-dimensional flow in a single blade passage of the centrifugal fan impeller is considered, taking into account of the cyclic nature of the flow and impeller geometry. The computational domain is depicted in Figure 2. Periodic boundaries are assumed at the inlet,

blade surface, and outlet. The flow includes important features like: Flow separation at the blade leading edge and Secondary flows arising in the channel due to centrifugal forces and Coriolis forces acting on the working fluid.

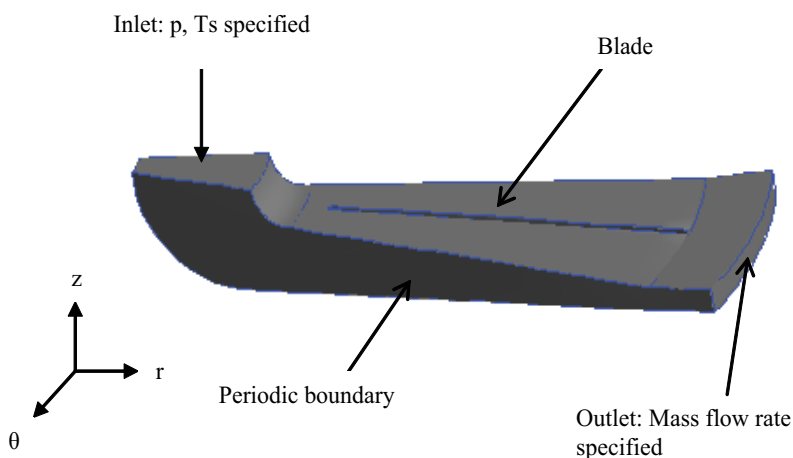


Fig. 2. Computational domain

A mathematical model for the flow field with associated boundary conditions and turbulence models are discussed

### 3.1.2 Governing equations

The RANS model for steady-state, turbulent, compressible flow in a rotating frame expressed in cylindrical coordinate system has been considered. Due to the rotation effects, the centrifugal forces and Coriolis forces act on the fluid. These effects are incorporated in the relative velocity formulation of the governing equations. The Reynolds turbulent stresses which arise due to the fluctuating velocity components are related to the mean flow variables calculated through different turbulence models. Turbulence closure model considered are 1. Spalart - Allmaras Model, 2. The Standard  $\kappa-\epsilon$  Model, 3. *The Realizable  $\kappa-\epsilon$  Model* and 3. *The RNG  $\kappa-\epsilon$  Model* The near-wall modeling is performed considering both the standard wall function and the non-equilibrium wall function. After initial evaluation of all turbulence models using both the wall functions, final results in the present study are presented with the standard wall functions in the RNG and standard  $\kappa-\epsilon$  models, and the non-equilibrium wall functions are used for the realizable  $\kappa-\epsilon$  model.

#### 3.1.2.1 Boundary conditions

**Inlet:** Static pressure is specified at the channel inlet.

**Outlet boundary condition:** The mass flow outlet adjusts the exit pressure such that a target mass flow rate (i.e., mass flow at the inlet) is obtained at convergence. This type of approach is used in problems where the outlet static pressure is unknown at the beginning of solution.

**Turbulence:** The turbulent intensity and hydraulic diameter were specified at the inlet. The turbulent intensity is calculated based on Eq. (48).

Periodic boundary conditions are imposed between the channel inlet and outlet as the flow field is symmetric from blade to blade and the boundary conditions are uniform in circumferential direction. In the periodic boundary condition, each surface of the periodic



pair is treated as an internal surface. The pressure jump across the periodic boundaries was specified to be zero.

### 3.1.2.2 Flow Parameters

#### *Reynolds number*

The incoming flow into the impeller is from a circular pipe. Therefore the Reynolds number at the channel inlet is defined by

$$Re_{in} = \frac{\rho v D}{\mu} \quad (48)$$

Where  $v$  is the velocity of the fluid,  $D$  is the hydraulic diameter  
The Reynolds number at the channel exit is defined as

$$Re = \frac{\rho C V_{\theta}}{\mu} \quad (49)$$

Where  $C$  is the chord length of the blade and  $V_{\theta}$  is the tip speed of the impeller. For the base case ( $\omega = 3300$  RPM), the Reynolds number typically varies from 301900 to 1760000.

### 3.1.3 Computational model

A computational model based on the mathematical model presented is developed in GAMBIT. The edge set required to form the turbo volume was imported from Pro/E assembly file with edge set consisting of the hub, blade, and the casing cross-sections. Only a single blade passage was modeled assuming 22.5-degree ( $2\pi/Z$ ) as the rotationally periodic conditions, Since there is no relative velocity difference between the fluid zone and the different wall zones (hub, blade, shroud), the whole geometry was modeled as a single rotating reference frame with the axis of rotation directed along the  $z$ -axis. After constructing the turbo volume, H template decomposition is adopted to split the volume bounded by the hub and casing with the surfaces representing the pressure and suction sides of the blades, and this results in four volumes as shown in Figure 3.

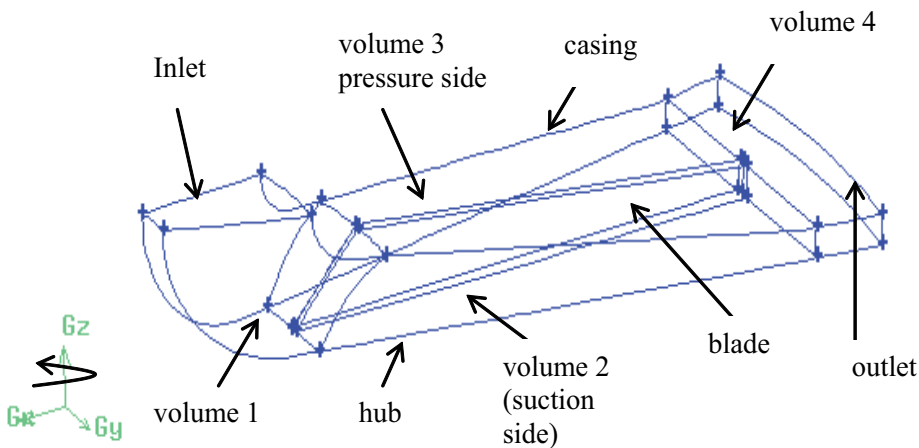


Fig. 3. Domain decomposition of turbo volume

### 3.1.3.1 Meshing the geometry

The mesh for the prescribed control volume shape and regulated order of spacing is achieved through a mapped meshing and using a combination of 8-node hexagonal brick volumes and 10-node clipped cube volumes. A soft nonuniform grading scheme is used for edge meshing. The turbo decomposition divides the impeller region into four volumes, each of which could be mapped with hexahedral structured mesh. It sets the interval count and grading on the edges and also sets face vertex types for the volume to be meshed. Hexahedral elements developed in the streamline direction of expected flow helps in improving the convergence of solution. The mesh for single blade passage grid is shown in Figure 4.

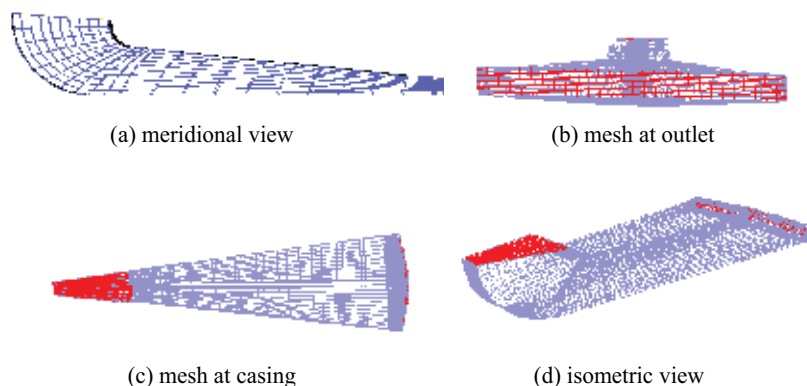


Fig. 4. Single passage grid modeling

The grid system for the bases case consists of  $78 \times 40 \times 30$  hexahedral elements in pitch, axial and radial directions respectively. The impeller region is meshed with  $78 \times 140 \times 30$  hexahedral elements along pitch, meridional, and span-wise directions respectively. The model uses segregated solver in which all the equations are solved sequentially along with the second-order upwind discretization scheme for convective terms in momentum, energy, turbulence kinetic energy and the rate of dissipation of turbulent kinetic energy. A linear interpolation scheme is used to estimate the cell face pressure as the average of all the pressure values in the adjacent cells. The density interpolation scheme is based on upwind interpolation of density at the cell faces for compressible flow calculations. The pressure-velocity coupling method is based on SIMPLE algorithm and a point implicit Gauss-Seidel linear equation solver is used in conjunction with the algebraic multigrid (AMG) method to solve the resultant scalar system of equations for the dependent variable in each cell with a specified convergence limit of  $1 \times 10^{-6}$ .

Fluid flow characteristics in the single blade passage of the centrifugal fan impeller are analyzed in this section. The distribution of pressure and velocity field and its impact on the losses inside the channel are studied. The results presented in this section include implementation of two numerical approaches for turbo modeling, and performance of different turbulence models.

### 3.1.3.2 Turbulence modeling

A turbulence model study is conducted on the single blade passage of the impeller in order to understand the flow characteristics and pressure losses occurring due to flow separation

and circulatory flows. The different turbulence models considered are the Spalart-Allmaras model, which is a one-equation model; the two-equation model, namely the standard  $k-\epsilon$  model; realizable  $k-\epsilon$  model with non-equilibrium wall functions, and the RNG model. Since the maximum losses occur at around  $x/c=0.3$  location in meridional direction along the passage, the performance of turbulence models is compared in this region to predict the flow behavior for the base case.

### 3.1.4 Analysis of flow field

Figure 5 shows the static pressure distribution for all the turbulence models considered for the base case. Results show similar static pressure distribution on the pressure side of the blade. However, there is a significant variation of static pressure distribution and the size of the low-pressure region on the blade suction side predicted by the different turbulence models. Figure 6 shows the distribution of dynamic pressure at the blades leading edge.

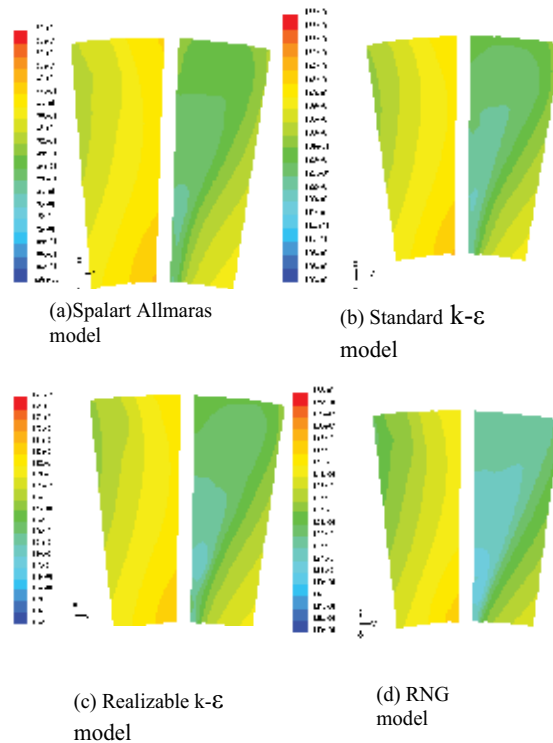


Fig. 5. Static pressure at  $x/c = 0.3$

It can be seen that all the models predict large recirculation regions on the blade suction side. On the pressure side of the blade, low-pressure region is developed at the hub-pressure side corner and on the suction side at the suction-casing corner. The vector plot of relative velocity vectors in the meridional view, as presented in Figure 7, reveal large areas of low velocity regions on the blade suction side. The flow separation region is developed close to suction-casing corner due to the flow turning from the axial direction to radial direction. It can be seen that the RNG model predicts larger area of flow separation compared to other turbulence models considered.

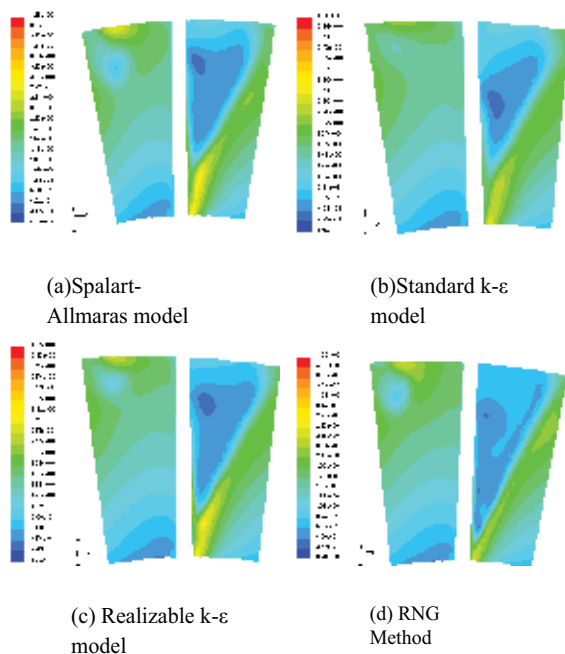


Fig. 6. Dynamic pressure distribution at  $x/c = 0.3$

Plots of relative velocity vectors both at the critical section and at the mid-span region are presented in figures 7 and 8.

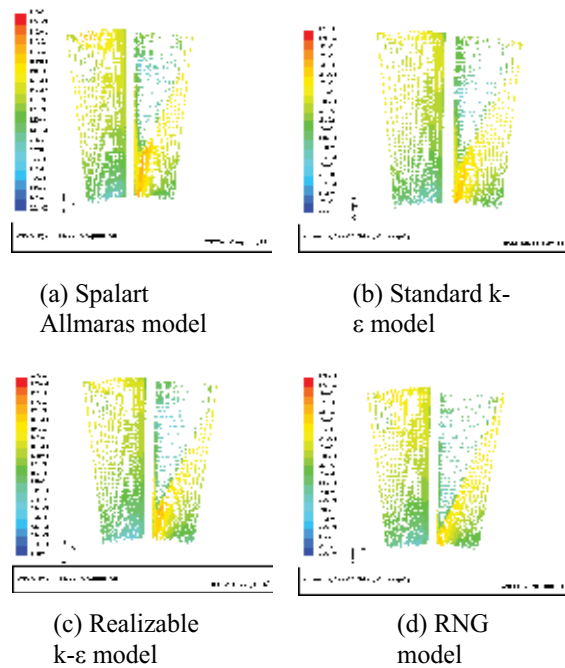


Fig. 7. Relative velocity vectors magnitude at  $x/c = 0.3$

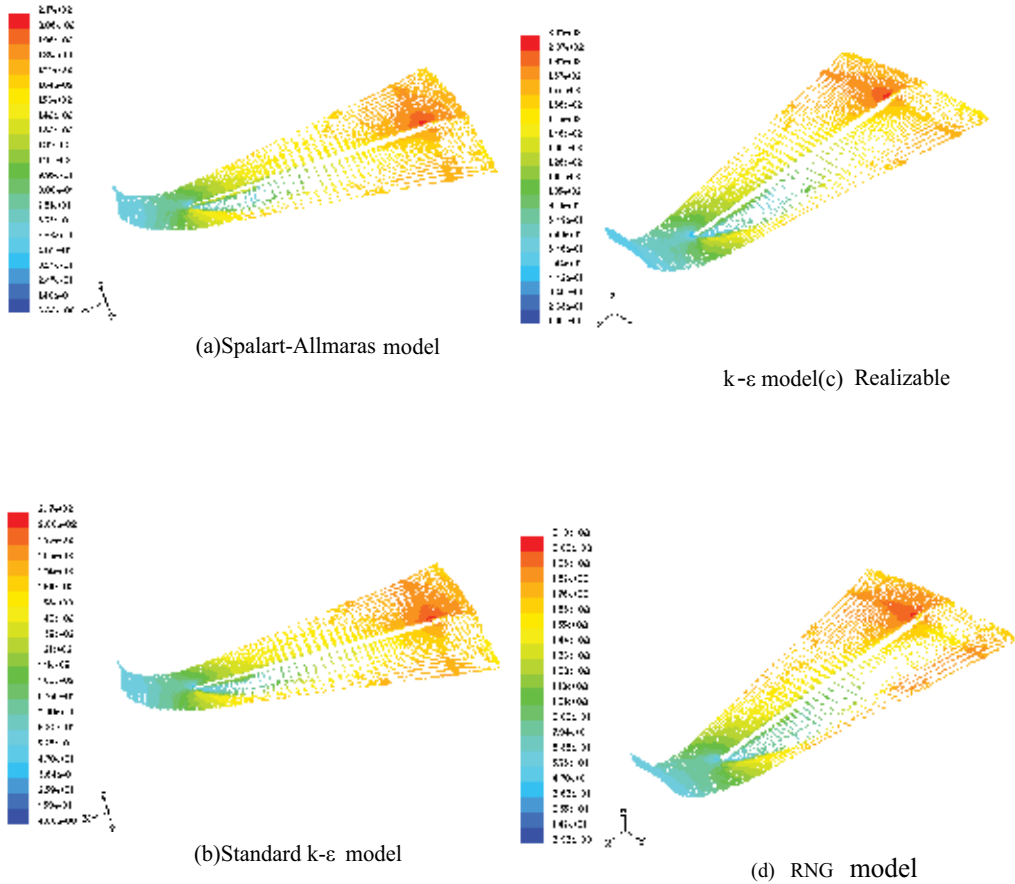
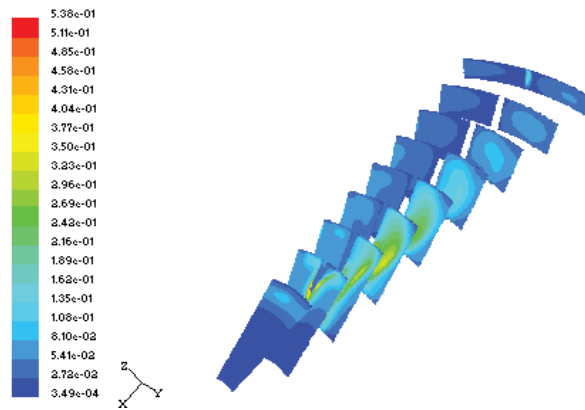
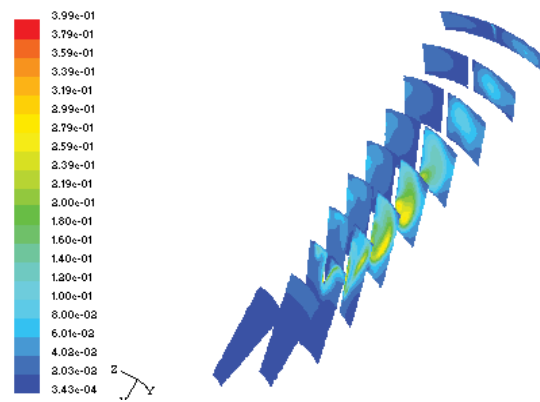
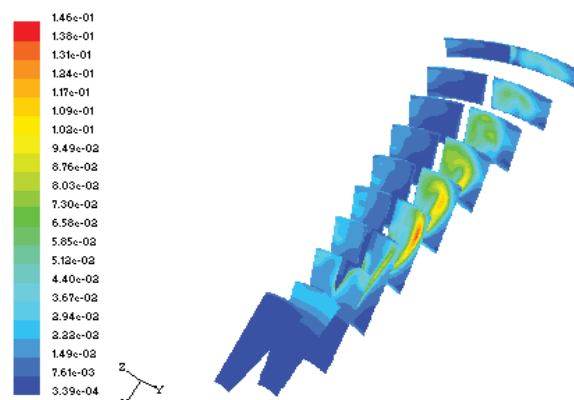


Fig. 8. Relative velocity vectors magnitude at mid-span

The plot of velocity vectors at mid-span of the passage, as given by Figure 8, shows flow separation on the blade suction side close to the leading edge. The realizable k-ε model and RNG model predict higher flow separation region compared to the Spalart-Allmaras and the standard k-ε models. Figure 9 shows the shadow graph plots of the normalized turbulent kinetic energy distribution along the blade passage. It can be seen from the contour plots of turbulent kinetic energy that the turbulence is stronger on the blade suction side due to the presence of higher momentum fluid. The realizable k-ε model and the RNG model show a better resolution of the turbulence compared to the standard k-ε model.

Results in figure 10 at the mid-span show that the turbulence structure predicted by the RNG model spreads from the blade leading edge on suction side to about 70% of the passage distance which is higher than the structure predicted by the realizable k-ε model and the standard k-ε model, but the intensity of the turbulence magnitude predicted decreases from the standard k-ε model to realizable k-ε model and to the RNG model.

(a) Standard  $k-\epsilon$ (b) Realizable  $k-\epsilon$  model

(c) RNG

Fig. 9. Normalized turbulent kinetic energy contours along the passage

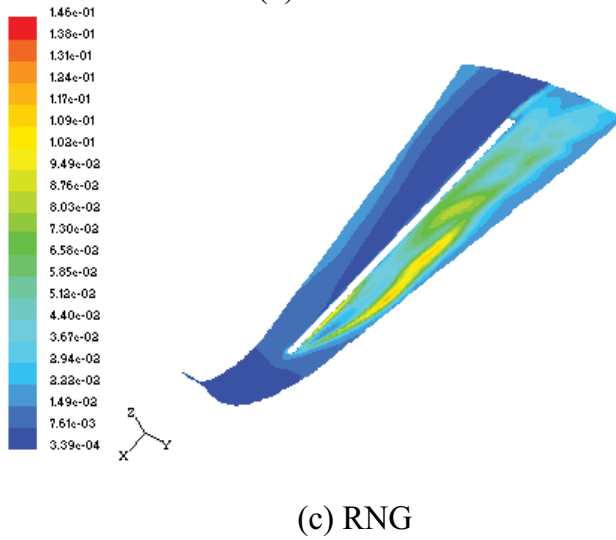
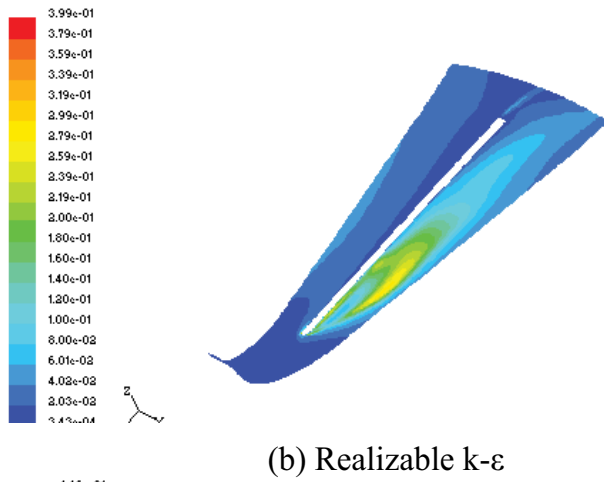
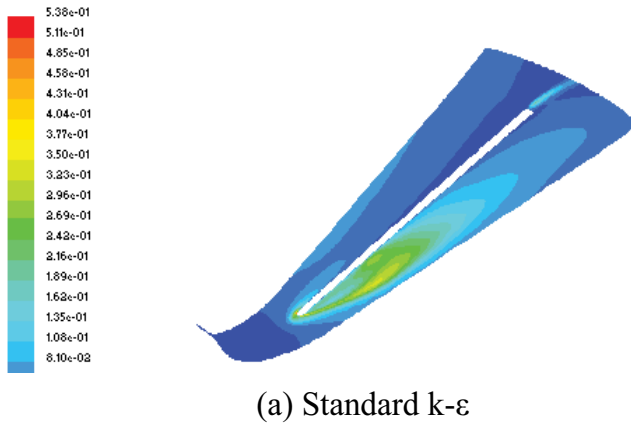


Fig. 10. Normalized turbulent kinetic energy contours at mid-span

The variation of area-averaged normalized turbulent kinetic energy and dissipation rate is shown in Figures 11 and 12 respectively. The turbulent dissipation rate is normalized with respect to the inlet velocity and the blade chord length.

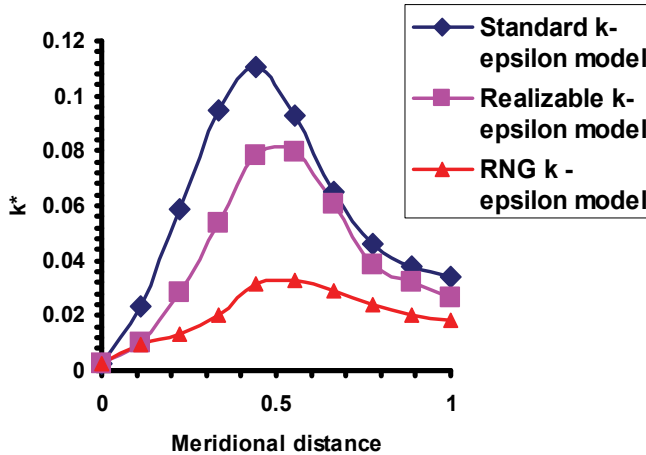


Fig. 11. Variation of normalized turbulent kinetic energy along the passage

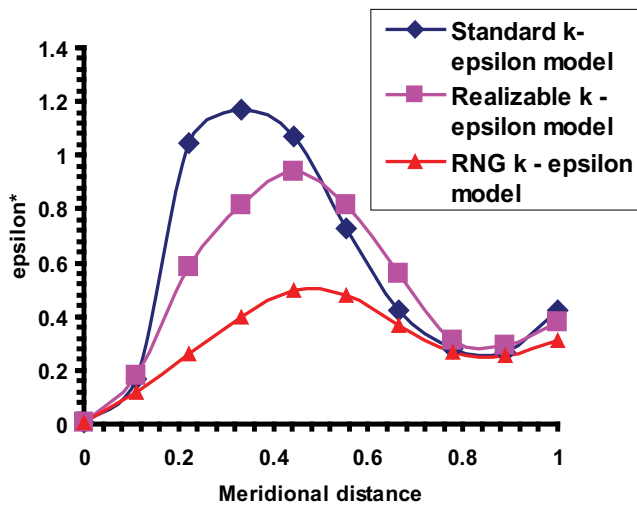


Fig. 12. Variation of normalized dissipation rate along the passage

From figure 11 it is observed that the turbulence kinetic energy develops from the inlet and rises to a peak value at approximately the center of channel. The standard  $k-\epsilon$  model over predicts the turbulent kinetic energy more than the other Realizable and RNG models. From figure 12 it can be seen that the realizable  $k-\epsilon$  model predicts less dissipation rate than the standard  $k-\epsilon$  model because the transport equation for dissipation rate is based on the dynamic equation of mean square vorticity fluctuation. The RNG model predicts the least dissipation rate of the other two turbulent models since it contains additional terms in the



transport equation for  $k$  and  $\epsilon$ , which are more suitable for flows with high streamline curvature and high rapid strain rate.

Following are the conclusions of the study:

1. The computational model demonstrated the secondary flow or slip losses in blade passages due to varying velocity gradient between the blade pressure side and suction side.
2. The RNG turbulence model gave more detailed resolution of flow separation and recirculation in the intake region. However, in terms of total pressure rise, the results predicted by the RNG model and the standard  $\kappa$ - $\epsilon$  models were within 0.6%.
3. Further design analysis of centrifugal fan impeller can be performed using standard  $\kappa$ - $\epsilon$  model along with standard wall function to resolve near wall region.

### 3.2 Case –II: numerical simulation of turbulent fluid flow over a surface-mounted

Fluid flow and heat transfer over a block in square tubes; ducts and channels have an extensive application in electronics cooling and heat exchanger design. The objective of this work is to study three-dimensional turbulent flow over a surface mounted block in a channel with adverse pressure gradient giving rise to flow separation and reattachment. The study focuses on evaluating different turbulence models for simulating turbulence and flow statistics using FLUENT commercial code. Computational solution is compared with existing experimental data in the literature. A parametric study is also conducted to analyze the flow separation, turbulence statistics and pressure coefficient with varying geometrical parameters over a range of Reynolds number. Figure 1 gives the schematic representation of the problem.

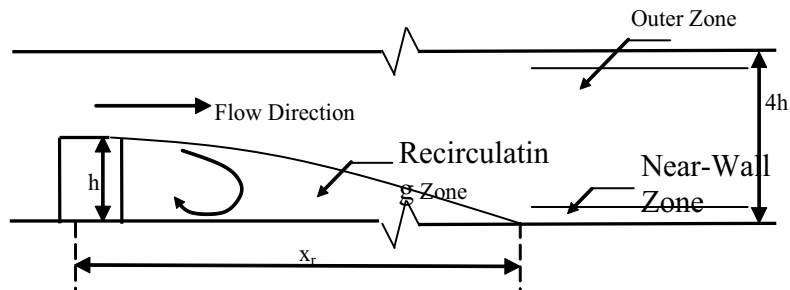


Fig. 13. Schematic representation of the problem

#### 3.2.1 Governing equations

RNS flow equation with Reynolds stresses expressed via the eddy viscosity concept has been used. Turbulence closure model considered are 1. High Reynolds number  $\kappa$ - $\epsilon$  turbulent model, 2. The RNG  $\kappa$ - $\epsilon$  model, 3. The Reynolds Stress model.

##### 3.2.1.1 Mesh generation

Volumetric mesh with regulated spacing of the control volume is done using mapped meshing technique as shown in figure 14. A soft non-uniform grading scheme is used for edge meshing. Near wall meshing is performed based on the distance established by wall function treatment. Mesh size distribution near wall is selected based on satisfying wall function requirement and keeping the values of  $y^+$  along the wall surfaces within 30 to 60.

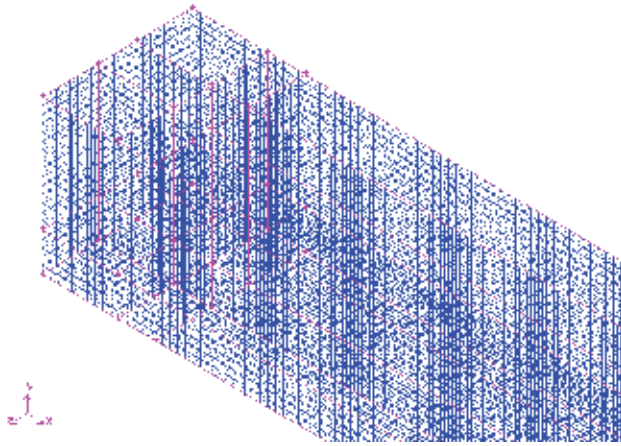


Fig. 14. Mesh size distribution

Core mesh is refined until the percentage relative error of the centerline velocities decreases and the maximum percentage relative error is below 0.003413 %. Typical mesh of the model is with 201895 cells, 62876 faces, 222604 nodes, 1 cell zones, and 5 face zones. Mesh is refined along  $x$ ,  $y$  and  $z$  directions and the velocity variation is studied for different kinds of mesh generated. The element used in the mesh generation is an 8-node hexahedron volume element. In order to validate the accuracy of turbulence models, results are compared with the experimental data obtained from the test case of Kasagi and Matsunga [1993]. The test case is the flow over a backward facing step involving adverse pressure gradient and boundary layer separation. The schematic representation of the flow field is show in the figure 15. A steam-wise fully developed flow passes over the backward-facing step with an expansion ratio of 1.504. The hydraulic Reynolds number flow as defined by the step height is 5540. The experiment was conducted in a closed-loop water channel flow facility. Numerical simulations with different turbulent model are compared with the experimental data.

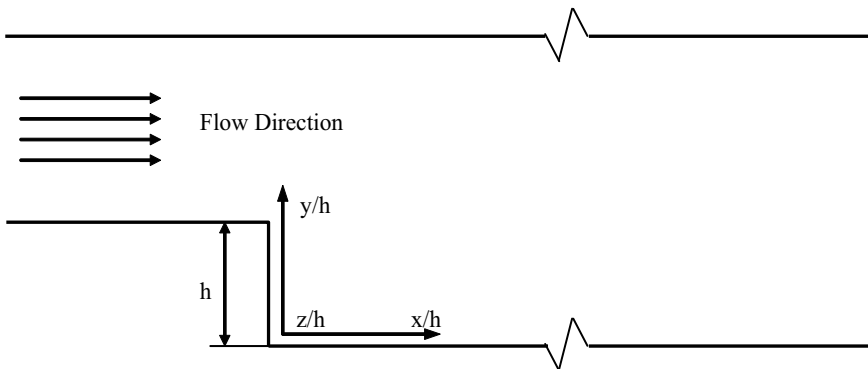
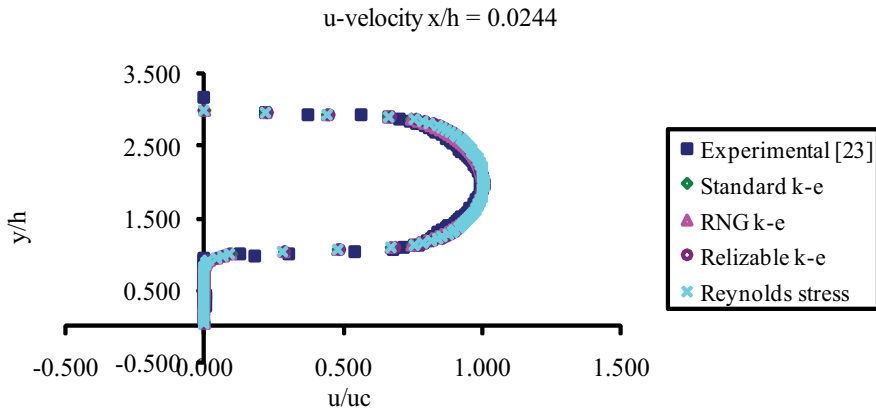
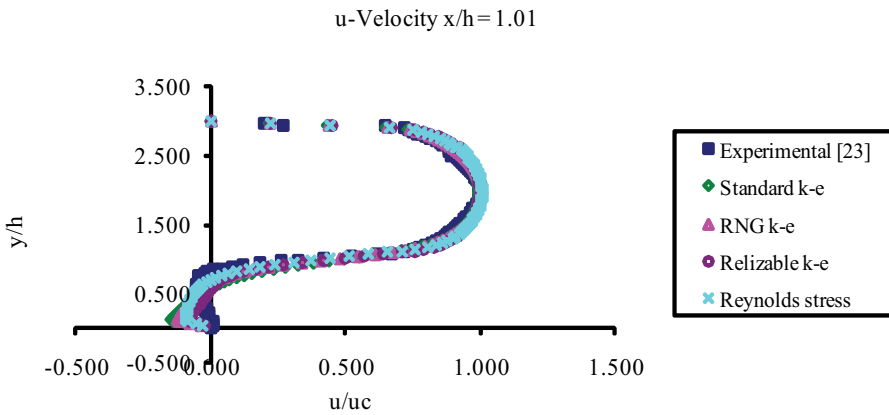


Fig. 15. Schematic representation of the experiment conducted by Kasagi and Matsunga [1993]

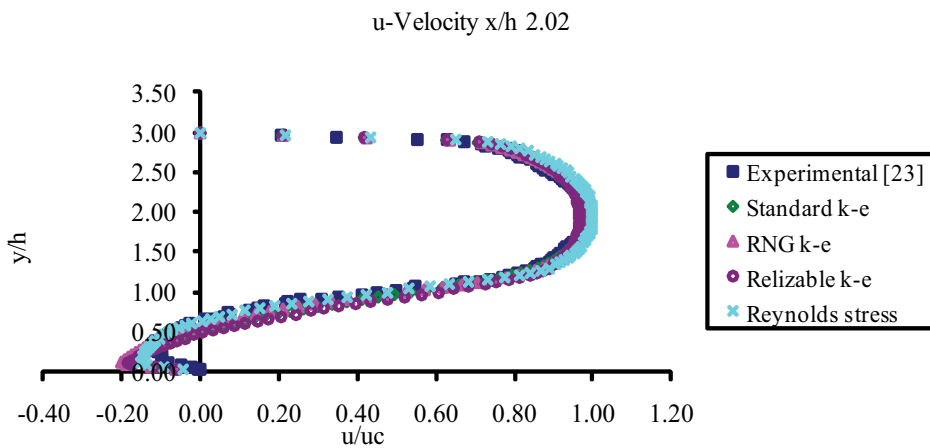
The non-dimensional  $x$ -velocity profile at the center of the channel at different  $x$ -locations is shown in the Fig. 16. As it can be seen that the velocity distribution at a distance of  $0.0244h$  is closely predicted by all four models. However prediction is exceptionally accurate for Reynolds stress model. Since the flow in this region is primarily a core turbulent flow.



(a) Comparison at  $x = 0.0244h$



(b) Comparison at  $x=1.01h$



(c) Comparison at  $x = 2.02h$

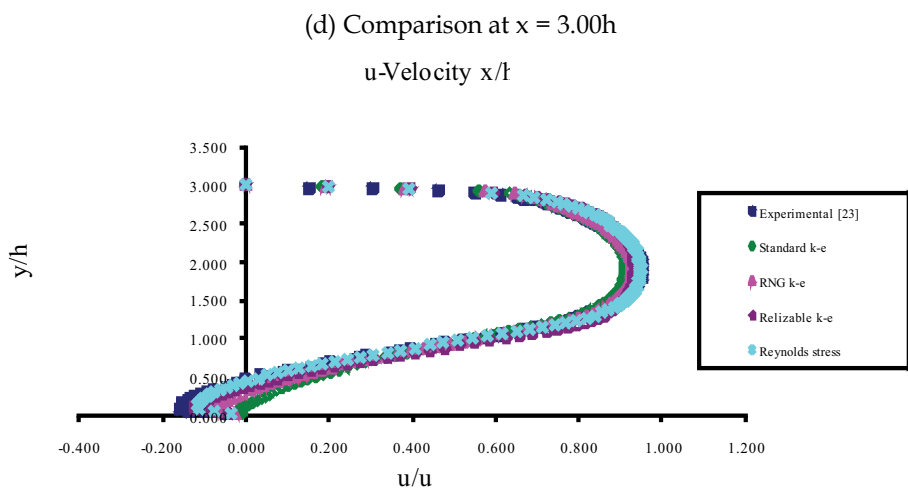
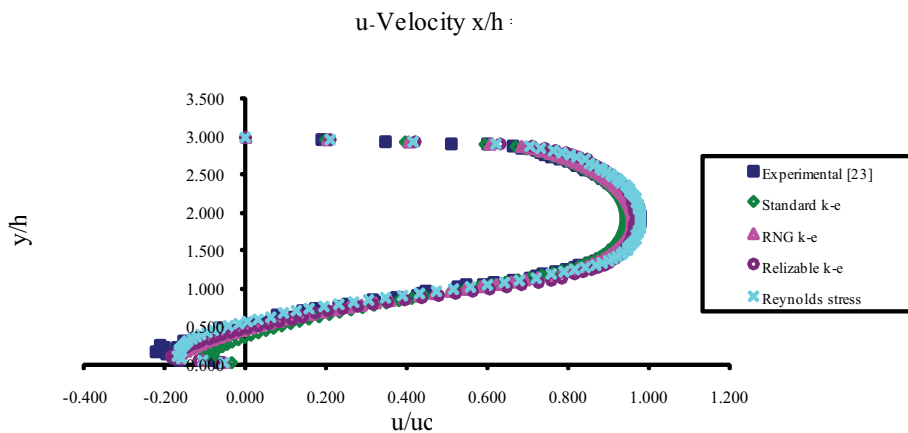


Fig. 16. Comparison with experimental data

Fluid flow after the step height is highly unsteady for many reasons. Distortion of boundary layer, adverse pressure gradient, normal shear stress and, secondary or backflow are some of the reason. At  $x/h = 1.01$ , a reverse flow is observed (as shown in Figure: 16b). All the turbulent models predict the reversed flow. But, magnitudes of the reversed flow are different form the experimental data. This portion fall under the core of the recirculation zone, where maximum deviation between the numerical and experimental data is observed. As we move away from this region representation of the recirculation region is more accurate as discussed in the following section. The intensity of the back flow decreases as we traverse along the flow direction. The secondary flow and effect of swirl on the flow decrease. In figures 16c-e, the x component of velocity at different locations in the recirculation is compared. The deviation form the experimental data decreases as the flow becomes to stabilize. A better prediction is observed as we move away from the wall and the recirculation zone. The major contribution of this may be due to the numerical computation

given by different turbulent closure model. The seven equations, Reynolds stress model predicts better results in comparison with the other turbulent models used.

Velocity contours plots at the center plane of the flow regime are presented for the range of Reynolds number in Fig. 17. Two critical points are observed. The obstruction in the direction of the fluid flow causes in an increase in the thickness of boundary layer followed by the point of detachment. The recirculation of the flow right after the obstruction is evident from the figures. The number of contours in the recirculation zone increases as the Reynolds number increase, signifying the increase in the recirculation strength.

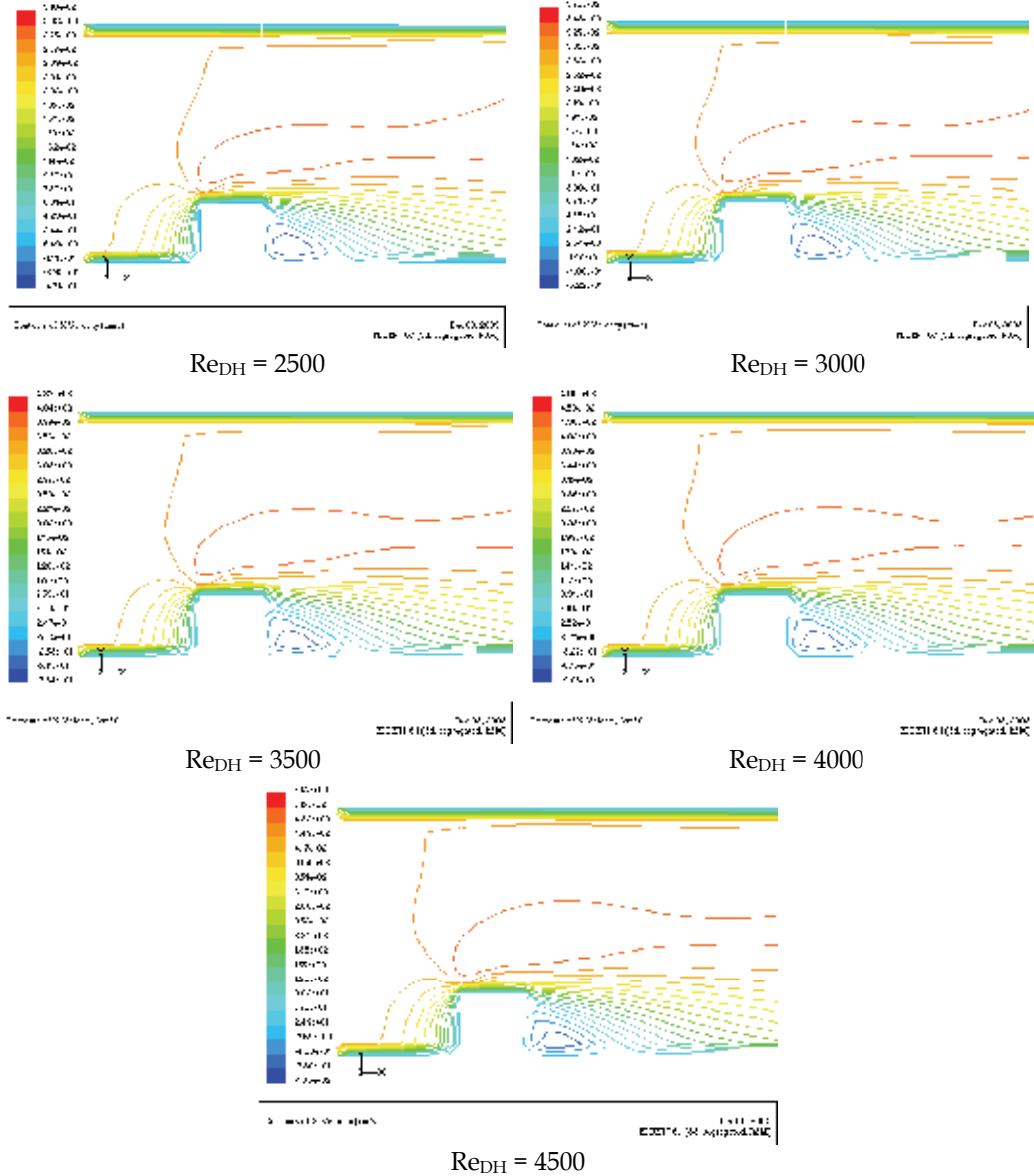


Fig. 17. Velocity contour plot at the center plane

The pressure coefficient ( $C_p$ ) along the flow direction at the center of the flow is plotted for different Reynolds numbers ranging from 2500–4500 in the Fig. 18. The detachment of the boundary layer causes adverse pressure gradients.  $C_p$  decrease as the velocity at the inlet increases. With the increase in  $Re_{DH}$ , the pressure drop increases. The comparison of static pressure at  $x = 1.75$  cm on the center plane with different Reynolds numbers is shown in Fig. 18. If the pressure gradient continues to increase, the velocities eventually come to zero and reversal of the flow will occur (backflow). To compensate the effect of the pressure gradient, the flow velocity decelerates to maintain the continuity of the domain

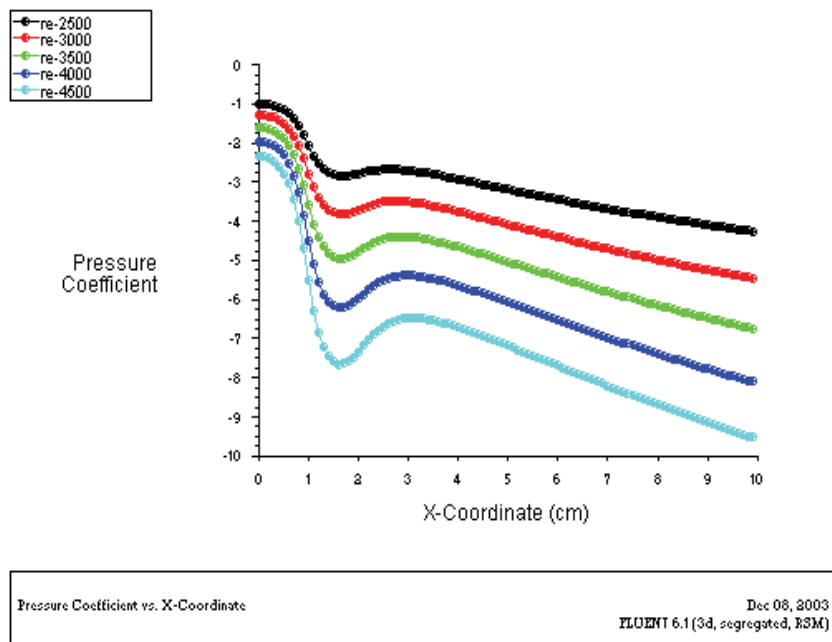


Fig. 18. Comparison of  $C_p$  with different Reynolds numbers

Velocity vector plots are presented in Fig. 19. It is evident that the size of the recirculating eddy as well as the magnitude of reversed flow (i.e. the negative velocities) increases as the Reynolds number increases.

Backflow is also a result of turbulent statistics moving upstream for some distance, then reversing and being convected downstream. The rate at which this phenomenon occur increase as the detachment location is approached. Velocity vector along the x-direction, at the mid-section of the block along the flow direction, for different Reynolds numbers are shown in the following Fig. 20. As the Reynolds number increases the swirl velocity and the eddy formation around the block dramatically increases.

The turbulent flow consists of production, convection, diffusion and, dissipation of turbulent energy. Dissipation and production play crucial role on turbulent energy in order to minimize the pressure gradient in the region far away from the wall. In the recirculating region, turbulent intensity increases as the Reynolds number increases. The turbulent viscosity, kinetic energy and, its dissipation rate along the y-axis at the  $x = 1.75$  cm on the center plane are plotted in the Fig. 21. In the recirculating region, viscosity decreases as the Reynolds number increases. It can be observed that as the velocity of the fluid field increase,

the pressure in the recirculating zone decreases and the turbulent properties such as turbulent kinetic energy, its dissipation rate increases, but the turbulent viscosity decreases.

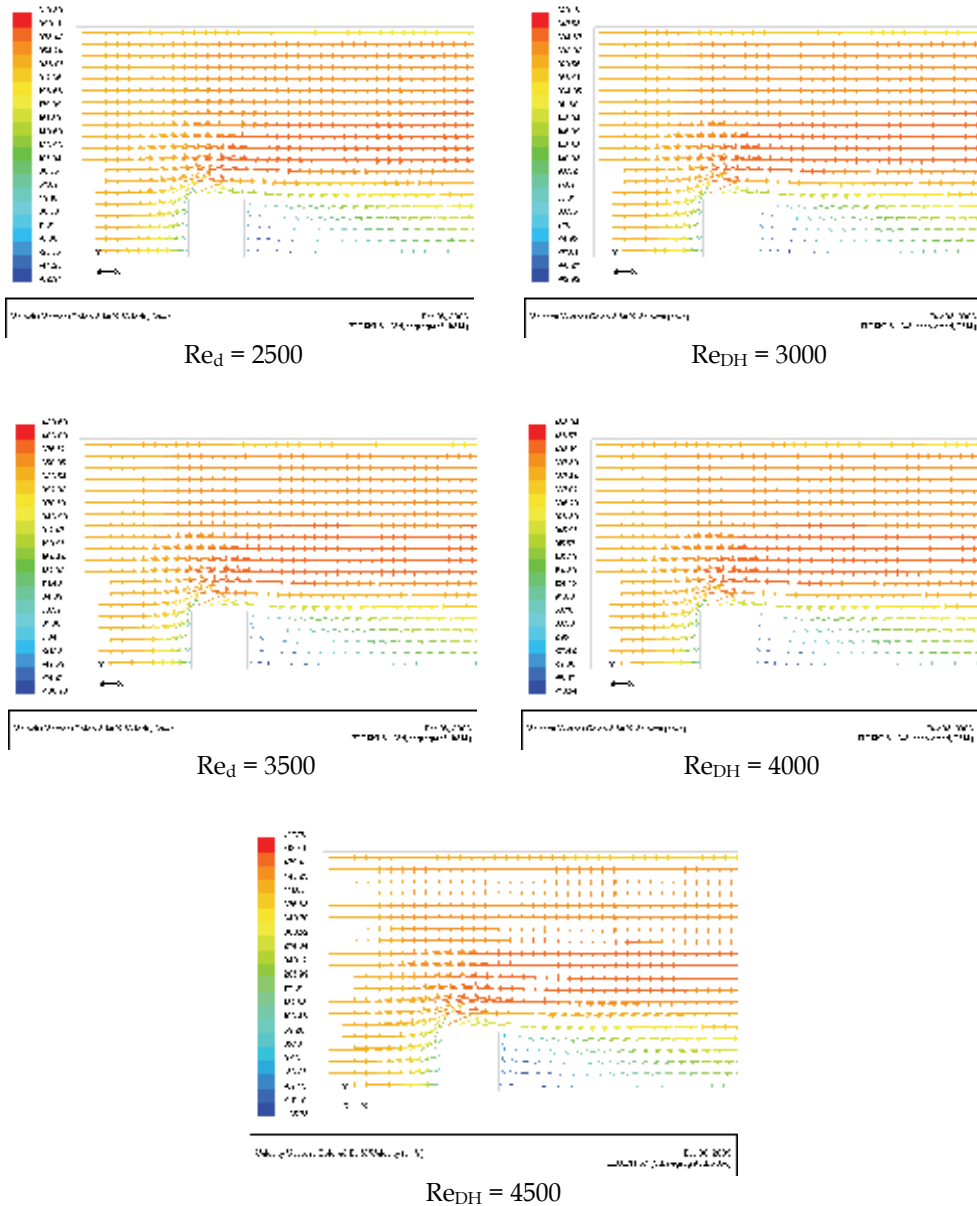


Fig. 19. Velocity vectors along the x-direction at the center plane

The reattachment length ( $x_r$ ), is the distance from the point of detachment of the fluid from solid to the point of attachment. The change in reattachment over varying Reynolds number is studied. The reattachment length is a critical quantity because the re-development of the

boundary layer and pressure recovery starts at this point. Since the maximum reattachment is observed at the center due to the effect of the y and z velocities the center plane is chosen. Figure 22 shows that the reattachment point moves along the flow direction with increase in Reynolds number.

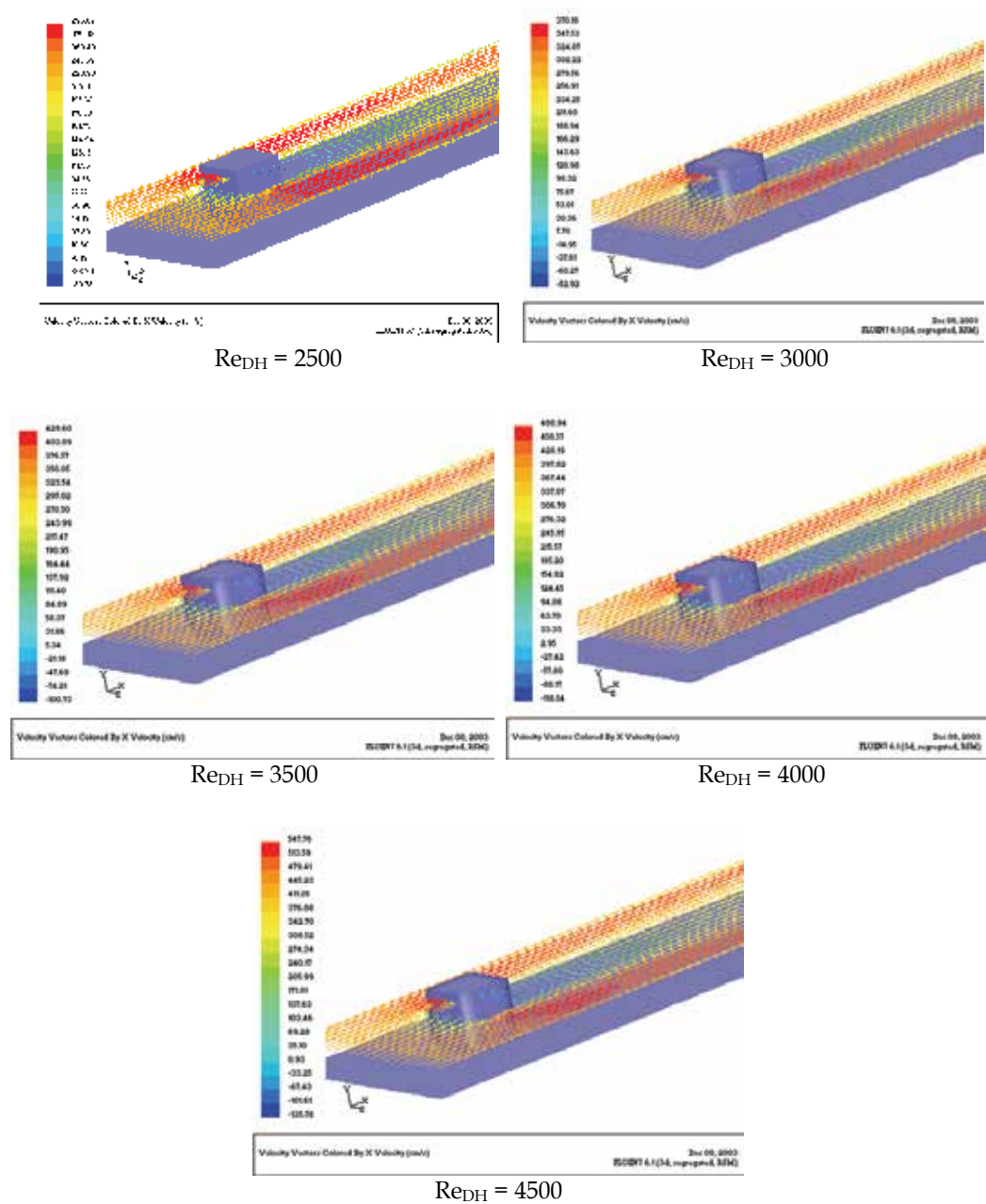


Fig. 20. Velocity vectors around the block



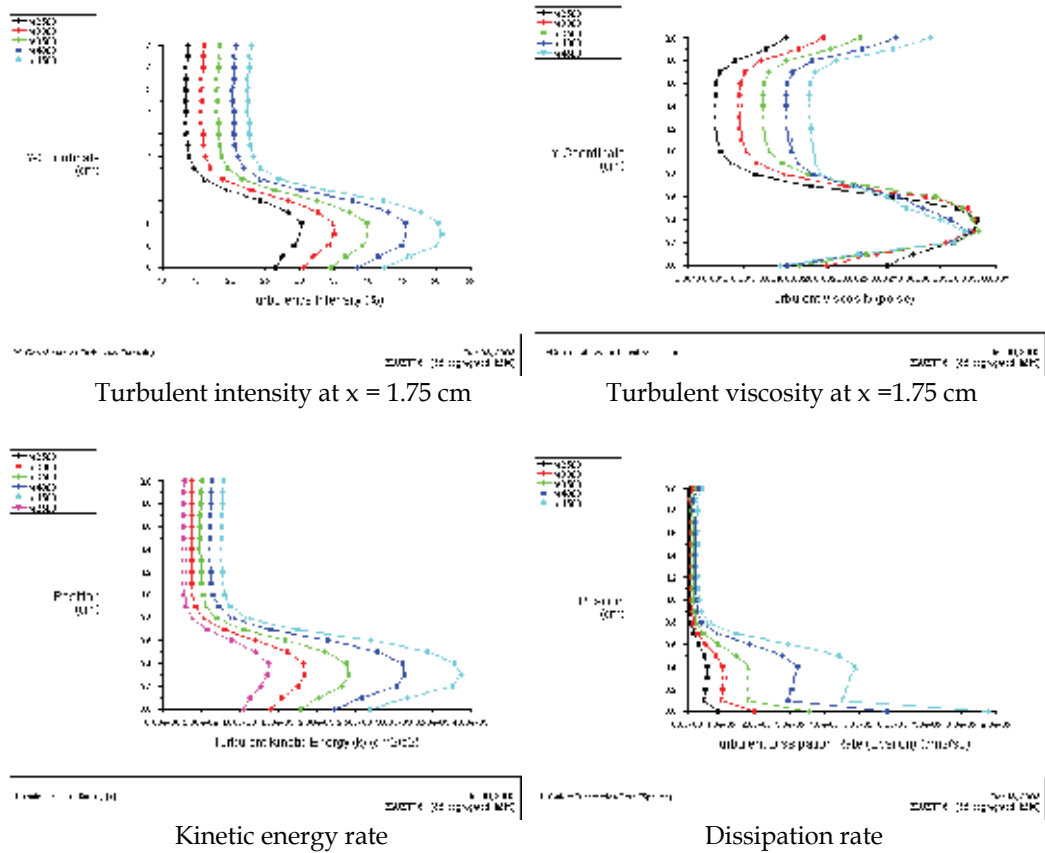


Fig. 21. Comparison of turbulent quantities at  $x = 1.75$  cm with varying Reynolds number

#### 4. Conclusion

A description of computational fluid dynamics analysis methods for turbulent fluid flow in number engineering problems is discussed. While a brief description of different turbulent modeling approaches such as Reynolds Averaged Navier-Stokes (RANS) equations, Large Eddy Simulations (LES) and Direct Numerical Simulation (DNS) is given, a more detail consideration is given to the of RANS method with turbulence closure models and to the computational challenges such as the selection of appropriate turbulence closure model, wall function treatment, inlet turbulent and application to number of engineering problems. Four different classes of turbulence closure models such as i) algebraic zero-order equation  $k-\epsilon$  turbulence models including low Reynolds number models, iv)  $k-\omega$  turbulence models, and v) Reynolds Stress Model (RSM) and. their selection of an appropriate model for a specific application is considered. Examples are drawn from practical industrial applications, and results from extensive numerical experimentations and validations with experimental data are presented to demonstrate the challenges in turbulent flow simulations.

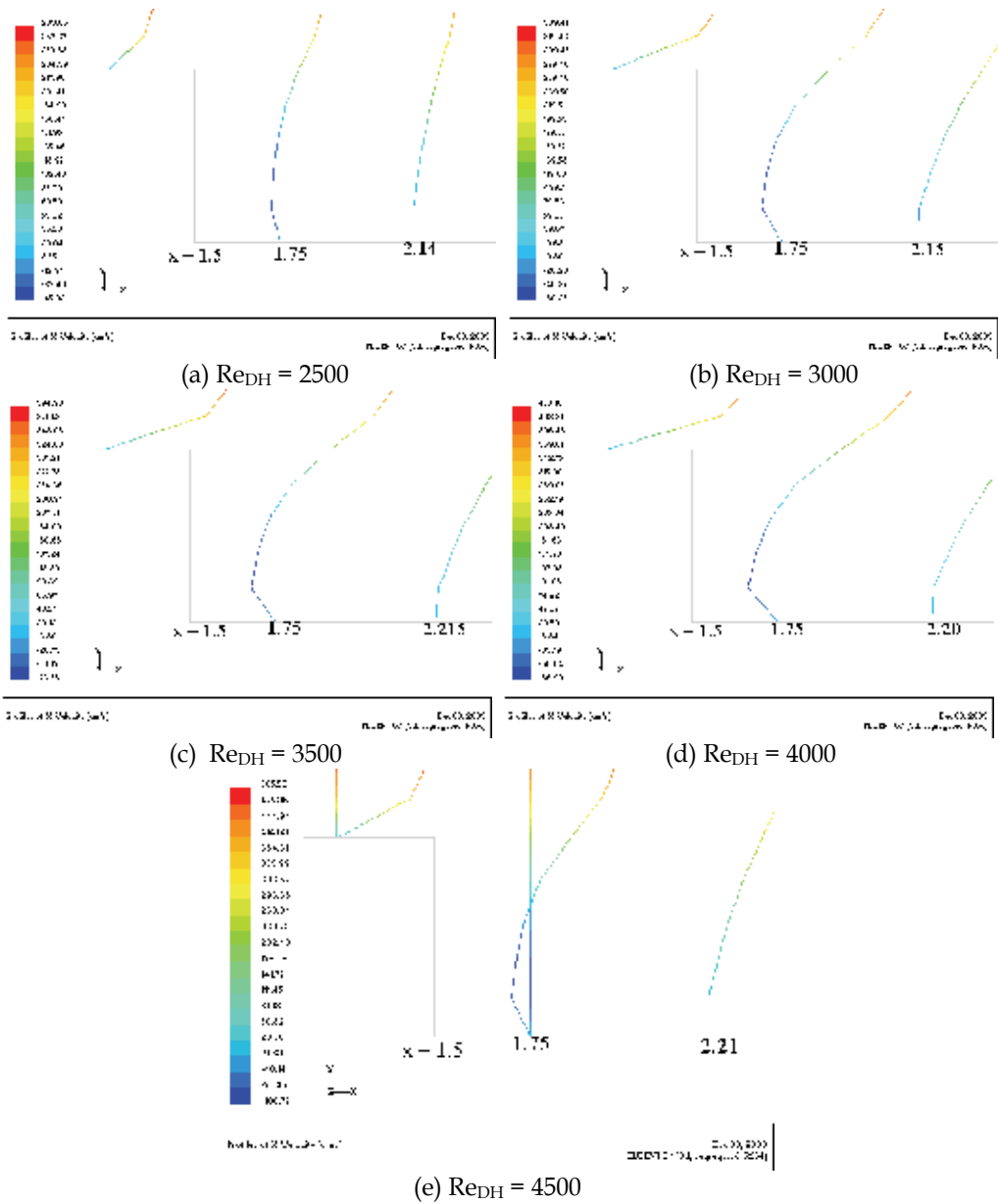


Fig. 22. Flow separation and reattachment at different Reynolds number.

**5. References**

Agonafer, D., Moffatt, D. F. (1990). Numerical Modeling of Forced Convection Heat Transfer for Modules Mounted on Circuit Boards. *ASME*, Vol. 112, pp. 112-333.

Asaka, Y. and Mohammad Faghri (1995). Prediction of Turbulent Heat Transfer in the Entrance of an Array of Heated Blocks using Low-Reynolds-Number  $k-\epsilon$  model. *Numerical Heat Transfer, Part A*, 28:263-277.

- Choudhury, D. (1993). Introduction to the Renormalization Group Method and Turbulence Modeling. Fluent Inc. Technical Memorandum TM-107.
- Chung, B. T. F., & Li, H. H. (1992). Forced Convective Cooling Enhancement of Electronic Modules through a Double Layer Cavity Design. *Fundamentals of Forced Convection Heat Transfer*. ASME, Vol. 210.
- Cotton, M. A., Jackson, J. D. (1989). Vertical Tube Air Flow in the Turbulent Mixed Convection Region Calculated using a Low-Reynolds-Number  $k$ - $\epsilon$  Model. *International Journal of Mass and Heat Transfer*, Vol. 33, No. 2, pp. 275-286.
- Deb P. and Majumdar Pradip, Direct Numerical Simulation of Mixing of a Passive Scalar Decaying Turbulence, *Proceedings of the 1999 International Mechanical Engineering Congress and Exhibition (IMECE)*, Nov. HTD-Vol.364-3, pp. 299- 306, 1999.
- Deb, P and Pradip Majumdar, Numerical Investigation of the Effect of Variable Viscosity on Decaying Turbulence Flow Field using DNS technique Paper NoNHTC2000-12085. *Proceedings of NHTC'00, 34<sup>th</sup> ASME National Heat Transfer Conference, Pittsburgh, August, 2000*
- Deb, Prasanta and Majumdar, P., (2000), Turbulence Flow and Heat Transfer Over Heated Modules for a Wide Range of Reynolds Numbers and Module Size, *Journal of Electronics Manufacturing*, Vol. 10, No. 4, pp. 263-269, 2000.
- Deb, Prasanta and Pradip Majumdar. Numerical Investigation of Fluid Flow and Heat Transfer Over Distributed Heated Modules with the Standard  $k$ - $\epsilon$  model and a low Reynolds Number Model, *Proceedings of the 33<sup>rd</sup> ASME National Heat Transfer Conference, Albuquerque, NHTC'99*, pp. 1-7, 1999.
- Dogruoz, M., B. CFD Benchmark Testing of Selected Laminar Flow Problems. Department of Aerospace and Mechanical Engineering, Experimental and Computational Heat Transfer Group, The University of Arizona. Available [Online]: <<http://w3.arizona.edu/~thermlab/>>
- Dutta, S. and S. Acharaya (1993). Heat Transfer and Flow Past a Backstep with the Nonlinear  $k$ - $\epsilon$  Turbulence Model and the Modified  $k$ - $\epsilon$  Turbulence Model. *Numerical Heat Transfer, Part A*, Vol. 23, pp. 281-301.
- Eswaran, V and Pope, S. B, (1988), Direct Numerical Simulations of the Turbulent Mixing of a Passive Scalar, *Physics of Fluids*, v. 31, p.506.
- Gibson, M. & Launder, B. (1978). Ground Effects on Pressure Fluctuations in the Atmospheric Boundary Layer, *Journal of Fluid Mech.* pp. 491-511.
- Gibson, M. and Launder, B. (1978). Ground Effects on Pressure Fluctuations in the Atmospheric Boundary Layer, *Journal of Fluid Mech.* pp. 491-511.
- Kang, S., Hirsh, Sh. (1999) Numerical investigation of the three dimensional flow in NASA low speed centrifugal compressor impeller. *Proceedings of the Fourth International Symposium on Experimental and Aerothermodynamics of Internal Flows, Germany, Aug. 31 - Sept. 2, 1999.*
- Kasagi, N and Matsunaga, A. (1995). Three-dimensional Particle-tracking Velocimetry Measurement of Turbulence Statistics and Energy Budget in a Backward-facing Step Flow. *International Journal of Heat and Fluid Flow*, Vol. 16, pp. 477-485.
- Kasagi, N., & Matsunaga, A. (1993). Turbulence Measurement in a Separated and Reattaching Flow Over a Backward-Facing Step with the Aid of Three-Dimensional Particle Tracking Velocimetry, *Journal of Wind Engineering and Industrial Aerodynamics*, Vol. 46 & 47, pp. 821-829.
- Lakshminarayana, B. (1996) *Fluid Dynamics and Heat Transfer of Turbomachinery*, John Wiley & Sons, Inc.

- Larosiliere, L.M., Skoch, G.J., Prahst, P.S. (1997) Aerodynamic synthesis of a centrifugal impeller using CFD and measurements. NASA TM - 107515, AIAA- 97-2878, July 1997.
- Launder, B. (1989). Second-Moment Closure, *International Journal of Heat and Fluid Flow*, Vol. 10, pp. 282-300.
- Launder, B. (1989). Second-Moment Closure, *International Journal of Heat and Fluid Flow*, Vol. 10, pp. 282-300.
- Launder, B., E. and Spalding, D. B., (1974). Numerical Computation of Turbulent Flows, *Comp. Methods in Appl. Mech, and Engg.*, 3, 269-289.
- Launder, B., Reece, G. and Rodi, W. (1975). Progress in the Development of a Reynolds-Stress Turbulence Closure, *International Journal of Heat and Fluid Flow*, Vol. 68, pp. 537-566.
- Launder, B., Reece, G. and Rodi, W. (1975). Progress in the Development of a Reynolds-Stress Turbulence Closure, *International Journal of Heat and Fluid Flow*, Vol. 68, pp. 537-566.
- Launder, B.E and Spalding, D.B. (1972) *Lectures in Mathematical Models of Turbulence*, Academic Press, London, England.
- Lehmann, G. L., Wirtz, R. A. (1985). The Effect of Variation in Stream-wise Spacing and Length on Convection from surface Mounted Rectangular Components. *ASME Winter Annual Meeting*, Denver, HTD Vol. 48, pp. 39-47.
- Majumdar, P., and Deb, P. (2003). Computational Analysis of Turbulent Fluid Flow and Heat Transfer over an Array of Heated Modules using Turbulence Models. *Numerical Heat Transfer*, Part A, Vol. 43, pp. 1-21.
- Majumdar, P., *Computational Methods for Heat and Mass Transfer*, Taylor & Francis Publisher, 2005.
- Majumdar, Pradip and Prasanta D., (2000), Numerical Prediction of Fluid Flow and Heat Transfer Over Heated Modules using the Standard k- $\epsilon$  Model and Low Reynolds Number Models Paper No. NHTC2000-12257, pp- 1-8, *Proceedings of the NHTC'00, 34<sup>th</sup> ASME National Heat Transfer Conference*, Pittsburgh, August, 2000
- Mawlood, K., Asrar, W., Omar, A., and Basri, S. (2002). Flow Past a Backward-Facing Step: Fourth-Order Compact Finite-Difference Results. *32<sup>nd</sup> AIAA Fluid Dynamics Conference and Exhibit*, pp. 24-25
- Piller, M., Nobile, E. (2002). Direct Numerical Simulation of Turbulent Heat Transfer in a Square Duct. *International Journal for Numerical Methods for Heat & Fluid Flow*, Vol. 12, pp. 658-686.
- Rai, M. M and Moin, P., (1991), Direct Simulation of Turbulent Flow Using Finite Difference Schemes, *J. Comp. Physics*, Vol. 96, p. 15, 1991.
- Rogallo, R. S., (1981), Numerical Experiments in homogeneous Turbulence, NASA Report NO: N81-31508.
- Shih, T. and Liou, W. (1995). A New  $k-\epsilon$  Eddy- Viscosity Model for High Reynolds Number Turbulent Flows - Model Development and Validation. *Computers Fluids*. pp. 227-238.
- Wagner, C., T. Huttli and P. Sagaut, Large-Eddy Simulation for Acoustics, Cambridge University Press, 2007
- Wilcox, David C. (1993). *Turbulence Modeling for CFD*. DCW Industries, Inc. La Canada, California.
- Xiadong, B., Xudong, T., Zhichi, Z. (2000) Application of numerical simulation of flow field of centrifugal impellers for fan design. *Tsinghua Science and Technology*, Vol.5, No.1, pp. 82-88.

# Autonomous Underwater Vehicle Propeller Simulation using Computational Fluid Dynamic

Muhamad Husaini<sup>1</sup>, Zahurin Samad<sup>2</sup> and Mohd Rizal Arshad<sup>1</sup>

<sup>1</sup>*Underwater Robotic Research Group, School of Electric & Electronic Engineering, Engineering Campus, Universiti Sains Malaysia, Penang*

<sup>2</sup>*School of Mechanical Engineering, Engineering Campus, Universiti Sains Malaysia, Penang Malaysia*

## 1. Introduction

Recently AUV development was stressed on improving the operation range and time. To achieve this requirement sufficient energy to propel and operate the device must be taken into consideration. However, the AUV power mainly supply by on board battery (Neocleous, and Schizas, 1999). Thus, the range of operation only depends on how much power it has. There are two options in order to improve the operation time, the first is developing very efficient battery and the second is optimized the AUV system either electrically or mechanically. For the first option, it takes time in order to develop very efficient battery. Then for time being, the second option is always selected by the researcher in order to improve the operation range of the AUV. Takinaci and Atlar, (2002) improved the energy power management in order to optimized the power consumption. Olsen, (2004) develops the optimum design of propeller that has less energy consumption but high thrust. Beside that Husaini, et al. (2009) work on AUV hull design by using numerical method to reduce the drag.

As mentioned by Takekoshi, et al., (2005) AUV speed was affected by resistance force along the body. This resistance was due to drag force. Stanway and Stefanov-Wagner (2006) reported that the thrust produced by the propeller was quadratically by increasing in propeller speed. This phenomenon can be understood by reviewing lifting line theory in Carlton, (2007). Although the thrust was increase in rotational speed, the torque also shows the same behavior Chen and Shih,(2007). In electrical point of view, this torque represents the shaft torque of the motor. This torque will introduced power output of the motor.

From the theory that explained before, power consumption can be minimized by optimizing the propeller speed during operation. As mentioned in Olsen (2004) the power increases by increasing in speed. This is because to increase the speed of the vehicle more, thrust is needed. To increase the thrust, propeller speed must be increased. Thus, the power increases because the torque will be rise due to increasing in propeller speed. By knowing the power and thrust relationship, the developer is able to design the specific control system algorithm for certain task.

Objective of this study is to analyse the performance of the propeller using finite volume method. By predicting the performance using simulation, the experiment number can be minimized. This will lead to reduction in cost and time of developing control system. In this paper the torque, thrust, and efficiency of the propeller was extracted from the simulation. Further this data can be manipulated by the researcher to develop optimum control system. However, in this paper the result manipulation or relationship mapping for developing control system was not covered.

## 2. Literature survey

With an increasing demand for optimum propeller designs, propeller behavior becomes even more important. This situation has accelerated researchers desire to understand the behavior of fluid around the propeller during its operation. To do this with low cost and less effort, the computational fluid dynamic (CFD) approach was introduced in propeller modeling. This section will review some of the previous works related to propeller simulation by using CFD. The review will only cover the application of CFD in specific propeller problems, such as; cavitations effect and the unsteady simulation of propeller behavior.

In order to highlight the significance of blade element theory in propeller performance prediction, Benini (2004) made the comparison between combined momentum-blade element theory (CMBET) with the three dimensional Navier-Stokes calculation. The CMBET representation of the propeller model was validated with a four blade Wageningen B series propeller. Fluid flow around the same type of propeller geometry was simulated by using FLUENT 6.2 software. Furthermore, the result of the CMBET and CFD simulations were compared with theoretical explanations. The result showed that CMBET was only true to experimental values if the fluid-flow was in 2D, but for CFD the performance of the propeller can still be predicted, with certain degrees of agreement with the experiment, even though the flow is 3 dimensional.

Rhee and Joshi (2003) conducted a study to validate the flow around a marine propeller using unstructured mesh based on the Navier-Stokes solver. The study was conducted based on the P5168 propeller type with a diameter of 0.402 metres, which were designed at the David Taylor Model Basin. For computational study the propeller blades were simply mounted on an infinitely long constant radius cylinder, which served as the hub. There are two types of computational domains developed, which are; base domain and extended domain. The purpose of these two different domains is to examine the influence of exit boundary distance from the blade. For the baseline domain, the upstream is 0.5D from blade, downstream at 0.72D and the outer boundary is 1.43D. While the extended domain upstream and outer boundary remained unchanged, but the downstream was extended to 2D. To minimize the computational cost, only one blade was simulated with the domain divided into 4 parts of 72 degrees each. To model the turbulent flow, there are two turbulent flows applied in this study, which are k-omega and RTSM. Commercial software Fluent 6.2 was used to solve the Navier-Stokes equation and gambit as mesh generator.

The major problem of the marine propeller study is the cavitation effect, where in conventional modeling, such as momentum theory and blade element theory, this effect was ignored (Wald, 2006). However, Young and Shen (2007) showed that there is some change in the performance of the propeller due to the cavitation effect. Therefore, the modeling of propeller must consider this effect to ensure that the performance of the propeller can be

predicted accurately. CFD can significantly predict the thrust and torque of the propeller under the influence of cavitation. For the steady simulation, the domain geometry was the same as that of Rhee and Joshi (2003) where only one blade was simulated. But for the unsteady domain, a complete propeller was simulated with an infinite cylinder in the middle of the blade to serve as a hub. Two types of propeller were investigated in this study, which were the MP017 and Sien Maru propellers. For both cases, the turbulent model (k omega) was used to model the turbulent flow. The solver was segregated, the pressure velocity coupling was SIMPLE and the discretization method was QUICK scheme. To solve the problem FLUENT 6.2 software code was implemented.

Besides the propeller itself, the performance of the propeller was also investigated by the presence of the stator. The stator in front of, or at the back of, the propeller will increase the efficiency of the propeller (Kerwin, 2001). The stator will act by cancelling the swirl at the hub, which will increase the torque of the propeller. The study of the propeller stator interaction, using CFD, was presented by (Guo et al., 2004). In their study, 3D incompressible RANS equations were solved on the non-orthogonal multi-blocked grid system to analyze the flow of ducted marine propulsion. 3D incompressible code was validated with a turbine blade, where the experiment result was already available. The time averaged pressure coefficient was compared with the experiment and a fairly good agreement was obtained. After the code validation, the flow field around the single-stage ducted marine propulsion was simulated, followed by the plotting of pressure distributions, streamlines and changes of velocity components. The hydrodynamic coefficients and propulsive efficiency were also obtained. The main contribution of Guo et al. (2004) is that the CFD code can be used to study the behavior of the fluid around the propeller in the presence of other structures.

Ideally, turbulence is the phenomena, where the fluid flow was not following the laminar flow behavior. The study of turbulence started in the 18th century, after Reynolds introduced the study of fluid behavior in a tube channel. Reynolds differentiates between these two types of fluid behavior by using the Reynolds numbers. These numbers actually represent the ratio between inertia and viscous forces. At low Reynolds numbers, the inertia force is smaller than the viscous force. In this case, the disturbances are dissipating and the flow remained laminar. At high Reynolds numbers, the inertia force is sufficiently large to amplify the disturbances, and turbulence occurs.

In the CFD simulation of the propeller, the selection of the turbulent model was crucial in order to get an accurate result of the propeller's behavior. Batten et al. (2008) solved the Navier-Stokes equation for viscous flow around the propeller and used a K epsilon turbulent model to represent turbulence behavior. Later, Celik and Gunner (2007) and Phillips et al. (2009) also used a K epsilon turbulence model to solve the turbulent flow around the propeller. However, Li (2006) applied a K omega to model the turbulence flow. From literature, both of these turbulent models give a good agreement with experiments. The simulations carried out by the researchers above were in both steady and unsteady domains. This shows that the K epsilon and K omega are also available for unsteady simulations. Beside these two turbulent models, Vysokhlyd and Mahesh (2006 and 2007) was specifically working on unsteady simulation and proved that the Large Eddy Simulation (LES) was also good for modeling the turbulent flow around a propeller.

From the review, the performance of the propeller was studied by the previous researchers by using numerical method. This approach is to ensure the design propeller can give

desired result in real situation (Young and Shen, 2007). Many such as Rhee and Koutsavdis (2005), Vysohlid and Mahesh (2006), Celik and Gunner (2007) and Guo et al. (2009) used finite volume method to simulated the behavior of the propeller in various cases. Li (2006) showed CFD simulation can represent the propeller during it operation with small error compare with experimental result. From the review, the simulation of propeller operation by using CFD will be used in this researched in order to reduce the numbers of experiment. Beside that from the previous work there is only few researchers (Singhal et al., 2002; Phillips et al., 2009) simulated the small scale propeller by using the CFD. Rhee and Joshi (2006), Batten et al. (2008), and Ghassemi and Ghadimi (2008) studied the behavior of the fluid around the propeller.

### 3. Computational fluid dynamic

Propeller performance in open water was calculated in the design stage. The thrust and torque coefficient will be computed using CFD. Because of difficulty in testing the propeller under axial flow, CFD was used to get the performance of the propeller when the water was moving. However, to confirm that the CFD model is correct, a bollard pull test was run to validate the CFD simulation. Yoger (1999) stated that the efficiency of the propeller varies in different advanced ratios. Although the performance of the propeller was already calculated by using the vortex lattice method, this value is purely theoretical and based on the assumption that the efficiency of the propeller was 98 percent of the actuator disc efficiency. This assumption was not correct for real conditions, where the fluid flow was not necessarily moving straight and hitting the disc surface. Therefore, CFD analysis is required to resolve this problem.

In this study, the speed of the propeller varies from 500 to 1500 rpm. The maximum speed was set at 1500 rpm in order to match the PVL propeller design speed. The advanced ratios, was varied from 0.6 to 1.2. Advanced ratios  $J_s$  can be calculated using the equation below:

$$J_s = \frac{V_s}{nD} \quad (1)$$

$V_s$  is the vehicle velocity,  $n$  is the rotations per second and  $D$  is the propeller's diameter. Thus, in FLUENT the value of inlet velocity must be set based on the vehicle velocity ( $V_s$ ) that can be calculated using Equation (1). The rotational speed of the propeller was set to 500 rpm, 1000rpm and 1500 rpm.

The simulation process was started by importing the STEP file of the propeller from the CAD to the pre-processor, called Gambit. The two main steps carried out in Gambit were domain and mesh generation. The model was then exported to the solver software; in this study, FLUENT 6.2 was used. FLUENT is a finite volume based software that is commercially available to run numerical simulations. The flow field was predicted by solving the 3D incompressible Navier-Stokes equation. Gambit, Fluent package, turbulence model, solver setup and solution control will be briefly explained in the next section.

#### 3.1 Numerical method

For the simulation, a second-order implicit formulation was chosen for temporal discretization and a central-differencing scheme was chosen for spatial discretization. The



solution for continuity and velocity equations continued until the flow became statistically steady throughout monitoring the torque of the propeller. The computations were carried out using FLUENT 6.2, which is general purpose CFD software. The governing equations are written for mass and momentum conservation, such that;

$$\frac{\partial \rho}{\partial \tau} + \nabla \cdot (\rho \bar{v}) = 0 \quad (2)$$

$$\frac{\partial}{\partial t}(\rho \bar{v}) + \nabla \cdot (\rho \bar{v} \bar{v}) = -\nabla \rho + \nabla \cdot (\bar{\tau}) \quad (3)$$

where  $\bar{v}$  is the velocity vector in the Cartesian coordinate system,  $\rho$  is the fluid density and  $\bar{\tau}$  is the stress tensor - given by;

$$\bar{\tau} \equiv \mu \left[ (\nabla \bar{v} + \nabla \bar{v}^T) - \frac{2}{3} \nabla \cdot \bar{v} \right] \quad (4)$$

where  $\mu$  is the molecular viscosity and the second term, on the right hand side, is the effect of volume dilation. Once the Reynolds averaging approach for turbulence modeling is applied, the Navier–Stokes equations can be written in Cartesian tensor form as follows;

$$\frac{\partial \rho}{\partial \tau} + \frac{\partial}{\partial x_j}(\rho u_i) = 0 \quad (5)$$

$$\frac{\partial}{\partial t}(\rho u_i) + \frac{\partial}{\partial x_j}(\rho u_i u_j) = -\frac{\partial p}{\partial x_i} + \frac{\partial}{\partial x_j} \left[ \mu \left( \frac{\partial u_i}{\partial x_j} + \frac{\partial u_j}{\partial x_i} - \frac{2}{3} \delta_{ij} \frac{\partial u_k}{\partial x_k} \right) \right] + \frac{\partial}{\partial x_j}(-\rho \overline{u_i' u_j'}) \quad (6)$$

Where  $\delta_{ij}$  is the Kronecker delta, and  $-\rho \overline{u_i' u_j'}$  is the Reynolds stresses. The Reynolds stress term is related to the mean velocity gradients, i.e., turbulence closure, by the Boussinesq hypothesis as;

$$-\rho \overline{u_i' u_j'} = \mu_\tau \left( \frac{\partial u_i}{\partial x_j} + \frac{\partial u_j}{\partial x_i} \right) - \frac{2}{3} \left( \rho k + \mu_\tau \frac{\partial u_i}{\partial x_i} \right) \delta_{ij} \quad (7)$$

The k-omega model is one of the most widely used turbulence models for external aerodynamic and hydrodynamic flows and has shown a better potential to predict the key features of vertical/ separated flows than other models. In this study, CFD code employs a cell-centred finite-volume method, which allows use of computational elements with arbitrary triangulation shapes. Convection terms are discretized using the second-order accurate upwind scheme, whilst diffusion terms are discretized using the second-order accurate central differencing scheme. It should be noted here that the thrust of the present study is the application of the unstructured dynamic meshing techniques and efforts are being made to enable higher order accurate schemes for dynamic meshing. The velocity-pressure coupling and overall solution procedure is based on a SIMPLE type segregated algorithm, adapted to an unstructured grid. The discretized equations are solved using point-wise Gauss-Seidel iterations, and an algebraic multi-grid method accelerates the solution convergence.

### 3.2 CFD control data setup

In order to develop the thruster control system for AUV applications, the relationship between the speed of the propeller and the thrust must be determined. Common practice in AUV development is that the control system must be developed in parallel due to time constraints. For this reason, the CFD simulation is required to give the relationship between speed and thrust of the propeller. For this study, the speed of the propeller was varied and the axial flow was set constant. This test is also known as a bollard pull test, where the water is static and the propeller rotates. In addition to studying the relationship between thrust and speed, this experiment importantly validates the CFD simulation.

### 3.3 Simulation procedure

There are many constraints to consider when completing this simulation. One of them is model development. The model was generated in the pre-processor stage, where the mesh type was selected from either a structured or unstructured mesh. In the case of the propeller, the unstructured mesh must be selected due to the complexity of the geometry. After meshing process, the boundary conditions for each surface must clearly be defined. An accurate setup for boundary conditions is important for any numerical solutions, to ensure the accuracy of the solution. The mesh process was finished with the export of the mesh file into the solver software. The solver should recognize the mesh as being set in the pre-processor software.

The mesh model, generated previously, will be solved by the solver software. Before the solver starts to solve the problem, the quality of the mesh was evaluated. If the mesh quality was poor, then it has to be refined. In the solver, the turbulence model and material properties were selected in order to predict the fluid behavior in the system. After that, the boundary condition values and solution control parameters are specified. Then the problem is ready for initialization step, which will stop when the calculations are computed. Finally, the results of the computation will be analyzed.

### 3.4 Pre-processing

In the pre-processing stage, the propeller model with a scale of 1:1 was imported into GAMBIT for the meshing process. The propeller model was saved as a para-solid file in SolidWorks to ensure that the propeller profile is maintained when exported into Gambit. Another option was to save as STP, IGES or STL file format. But this option is not suggested because it will lead to some geometry lost. If the file is in IGES, imported files will have numbers on the edge that are not required in the meshing process. This edge finally needs to be reconnected in Gambit. This process consumed unnecessary time for the grid process.

GAMBIT was used as the pre-processor for geometry modeling due to several of its advantages. GAMBIT is very user friendly in terms of generating a mesh. Besides that, this software has broad options for CAD modeling that it accepts. Important considerations when selecting the pre processor software were that the generated mesh file must be accepted by the solver that will be used. GAMBIT has no problems with this issue, because it is easily accepted by many main commercial solvers such as FLUENT, FIDAP, RAMPANT, NEKTON, POLYFLOW and GENERIC.

### 3.5 Geometry setup

This section presents details of the model geometry development. In real situations, the propeller will operate in water. For the simulation, water was developed and declared as a

domain. Domain size was importantly studied, because it is related to computational accuracy and machine capability. If the domain is too large, the time consumed in calculation is longer, but if the domain is too small, it will not represent real situations of the phenomena. The domain size in this study was referring to (Vysohlid and Mahesh, 2006). The domain was given in terms of propeller diameter.

For the propeller, the mesh must be smaller in comparison to the domains mesh. This step reduces errors of discretization, due to the complexity of the propeller's geometry. Besides that, the fine domain around the propeller can be used to rotate the water whilst the simulation is in process. Referring to Vysohlid and Mahesh (2006) domains, the computation was in a cylindrical form. From the scale that mentioned by Vysohlid and Mahesh (2006), the cylinder with a diameter of 0.5 meters and length 1 meter has been created. And for the smaller domain around the propeller, the diameter was set to 0.15 meters and length was 0.2 meters.

### 3.6 Grid generation

The computational grid was divided into three parts for this study. The parts were named as; domain, rotation part and propeller geometry. As shown in Figures 1 and 2. To minimize computational time, the numbers of cell must be decreased. To achieve this, the simulation domain must be split into three sub-domains, as shown in Figure 2. The main cylinder was divided into 120 degree sections. Only one blade was considered in this simulation and assumes that the other blade will performed as a key blade. The reason to create a smaller cylinder around the propeller in this study was that the propeller was fixed but the water surrounding it was rotating. Without this small cylinder, the rotation of the water must include all the water inside the domain.

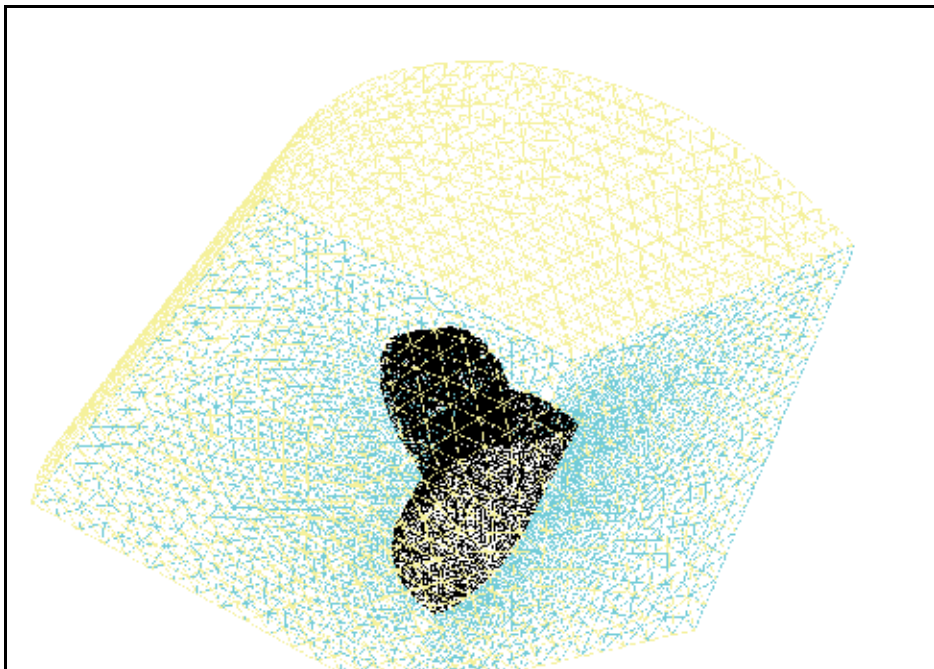


Fig. 1. Rotation part of domain

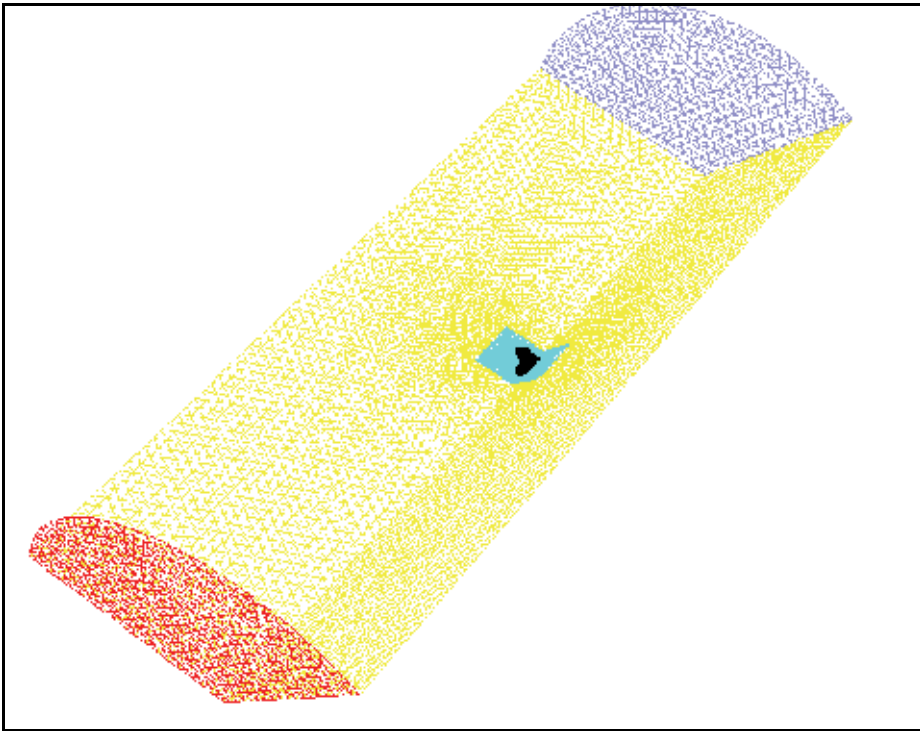


Fig. 2. Computational domain

This is a totally wrong situation, where the water in the far field (main domain) must be moving axially or static, depending on input. Boundary conditions were set to simulate the flow around a rotating propeller in open water: on the inlet boundary, the velocity components of uniform stream with a given inflow speed were imposed; on the exit boundary, the static pressure was set to a constant value - zero in non-cavitating cases, while other variables were extrapolated; on the outer boundary, a slip boundary condition was imposed, i.e., zero normal velocity component with extrapolated tangential velocity components and static pressure; on the blade and the hub surface, the no slip condition was imposed; and on the periodic boundaries, rotational periodicity was ensured.

### 3.7 Boundary condition

For the validation process, the velocity inlet was set to zero. This condition was chosen to represent the bollard pull condition, where the water is static and the propeller didn't move. After the validation process, the velocity inlet was varied to represent the advanced speed of the underwater vehicle. The variation of the velocity inlet was used to study the performance of the propeller under various vehicle speeds. In this simulation the gauge pressure was set to zero. Back flow direction specification method was set to normal to boundary. To ensure that the water in the pill box domain and the main domain interact, the surface of the pillbox must be set as an interface. The blade surface was set as a non slip wall. Because the domain was divided into 3, the surface must be set symmetrically. This set up can be utilized to avoid redundant calculations in other identical parts.

### 3.8 Grid dependency study

In the CFD simulation, the grid setup made a big impact to the accuracy of the simulation. Versteeg and Malalasekera (2007) listed three main factors that lead to simulation errors. The three errors that have been listed are; numerical, coding and user errors. Amongst these three errors, the numerical error was directly related to the geometry setup. For numerical errors, three types of error were recognized, namely; round off, iterative convergence and discretization errors. In theory, discretization errors can be minimized by a reduction of the timing step and space mesh size. However, by doing this the computing time and amount of memory required also increased. Here, grid sensitivity takes place to find the optimum setup between memory and computational time against the accuracy of the result.

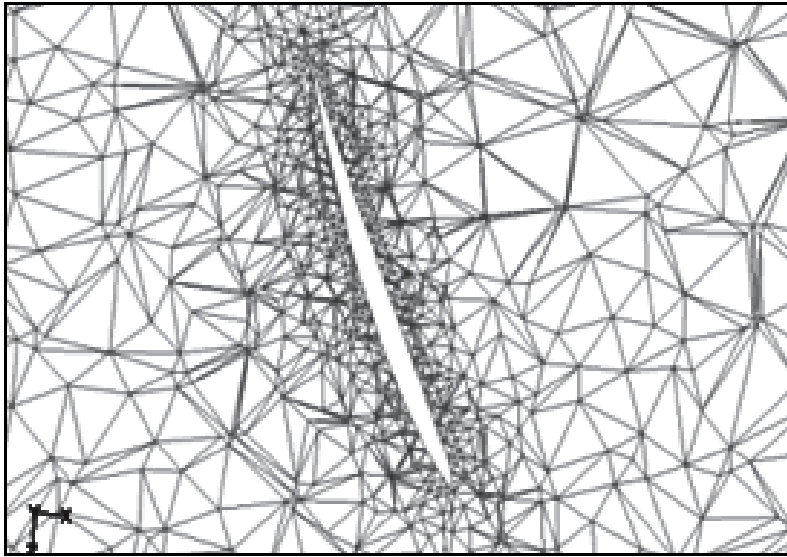


Fig. 3. Coarse meshes surround the blade

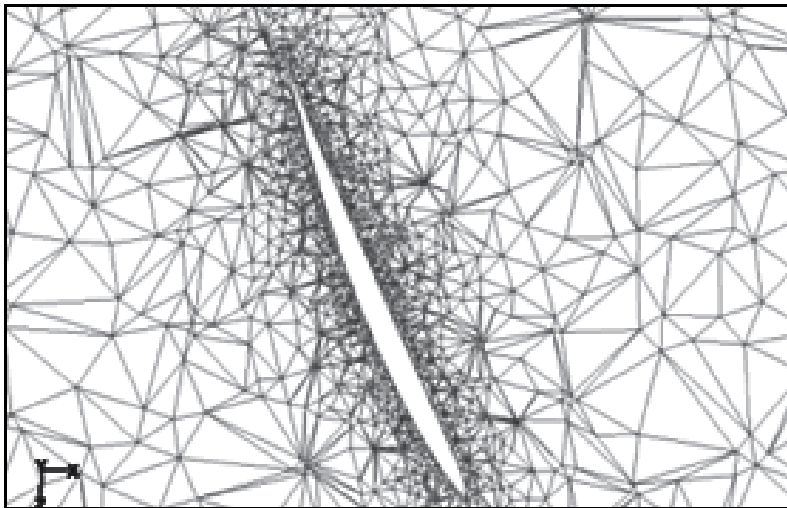


Fig. 4. Medium meshes surround the blade

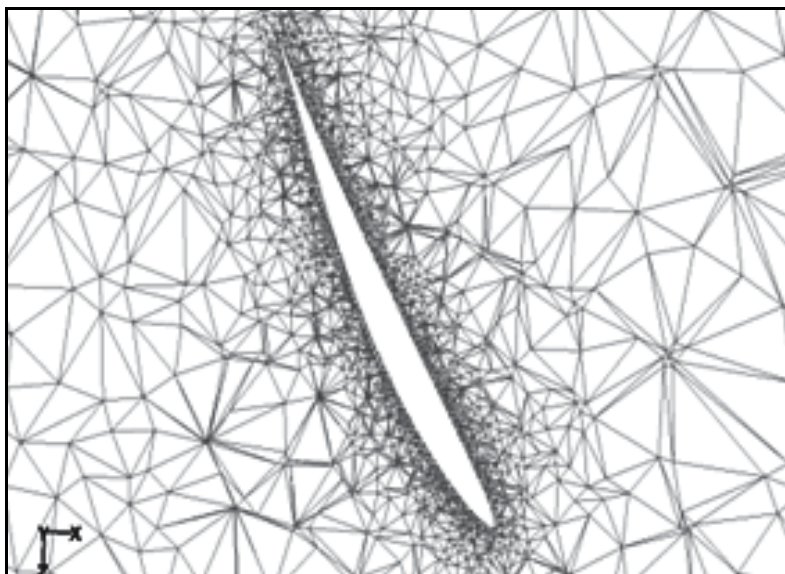


Fig. 5. Fine meshes surround the blade

For the grid sensitivity study, the same domain geometry was kept with three different kinds of mesh. The meshed grids were named as; coarse mesh, medium mesh and fine mesh. For coarse mesh, 154649 numbers of cells were used. For medium mesh, the number of cells was increased 2 times to 378784. Finally, for fine mesh, the number of cells was increased 2 times that of medium mesh, to become 620415. Figures 3, 4 and 5, show different size of meshes around blade boundary.

## 4. Result and discussion

In the previous section, the performance analysis method of the propeller was shown. However, the experiment run was only in bollard pull conditions. In real applications, the propeller will move together with the vehicle. Due to experimental limitations, CFD was used to study the performance of the propeller by giving an advanced speed. The test results above will be used to validate the CFD simulation.

### 4.1 Grid Independency

As mentioned in section 3, the model geometry was meshed in three types, namely; fine, medium and coarse mesh. Table 1 shows the simulation results of the four types of mesh. The thrust value of the propeller was taken at 1500 rpm, and the water was static. The results from simulation were compared with the experiments results. The percentage error was calculated with subtract the simulation result from the experiment result then divided with the experiment result. The experiment thrust recorded at this speed was 14.6 Newton.

The simulation results were compared to the experiment result. This comparison was made because in this study, CFD was used as a tool to measure the performance of the propeller in real cases. From the grid dependency study, errors were reduced by increase the numbers of cells. The Table 1 above also shows the simulation errors. By applying the

medium mesh, the errors for the simulation were 5.41%. This error value was considered small, and the CFD result was valid for further analysis. The graph in Figure 6 shows the plot of both the CFD result and the experiment for power input. From the graph, the patterns were similar. This shows that CFD can predict the behavior of the propeller within small errors. However, from the graph, the errors of CFD were increased by the increase in speed. One of the reasons for this limitation is due to the limitation of CFD in predicting turbulent flow. When the rotation of the propeller increased, the Reynolds number also increased. Therefore, the turbulent intensity also increased and the flow became more chaotic and unpredictable.

#### 4.2 Thrust coefficient

The graph in Figure 7 shows the thrust coefficient against advance ratio. These  $K_t$  values actually represent the thrust behavior. The trend clearly shows that the  $K_t$  values decrease when the advance ratio increases. This phenomenon can be explained by the momentum theory, which was introduced by Rankine in 1865, even though this theory does not consider the geometry of the propeller (Carlton, 2007). In this case, the propeller system can be modeled by this approach, in order to simplify the explanation. In this theory, thrust was calculated by using equation (8) below:

$$T = m(v_c - v_a) \quad (8)$$

Where,  $T$ ,  $m$ ,  $v_c$  and  $v_a$  is thrust, mass of fluid, incoming velocity and accelerated velocity. From the equation, it can be seen that the difference in velocity affects thrust generation. Referring back to the graph in Figure 6, the thrust was decreased by increasing in the speed of the axial velocity. This is correct, because at a low axial velocity, the difference of velocity is greater. This occurs because, at this axial velocity, the water surrounding the propeller will be accelerated from a low velocity. At the higher advanced velocity, water surrounds the propeller, which is already moving at a high velocity. Therefore, the propeller makes less change to the water velocity.

| Mesh   | Predicted thrust (N) | Cell numbers | Percentage error |
|--------|----------------------|--------------|------------------|
| Coarse | 11.3974              | 154649       | 21.93%           |
| Medium | 13.81                | 378784       | 5.41%            |
| Fine   | 14.12                | 620415       | 3.28%            |

Table 1. Grid dependency study results

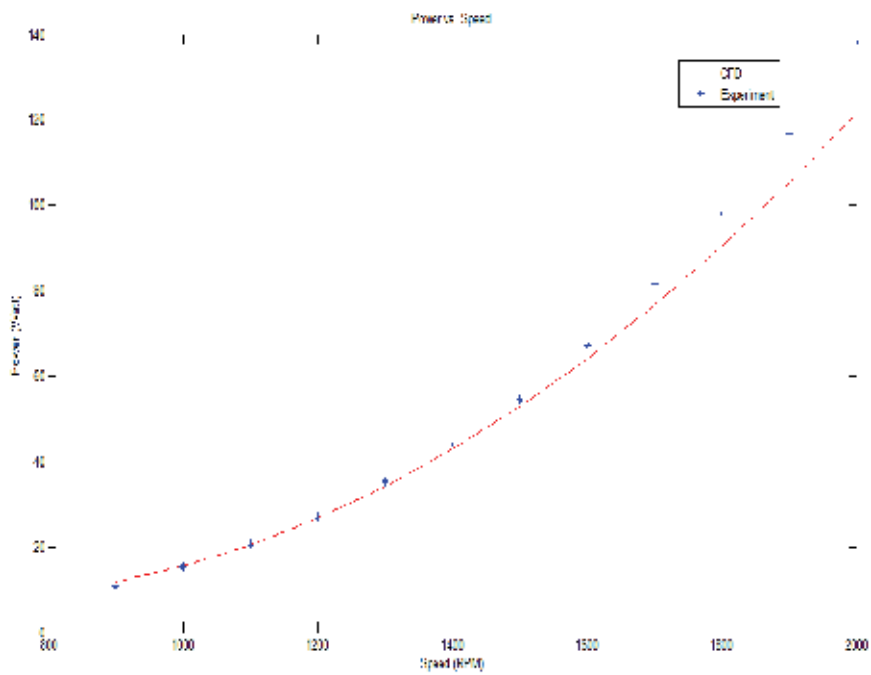


Fig. 6. Plot of power input against propeller speed

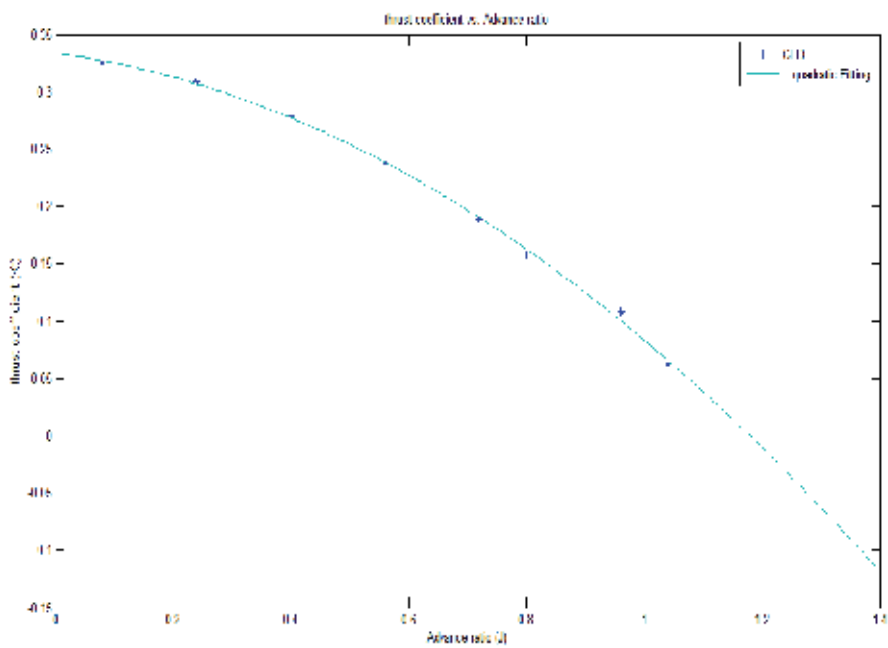


Fig. 7. Plot of Thrust co-efficient against advanced ratio



### 4.3 Torque coefficient

The graph in Figure 8 shows the relationship between Torque coefficients and advanced ratios. The trend of this graph is similar to the thrust coefficient against advance ratio. This graph shows the behavior of propeller torque under different advanced ratios. From the graph, it can be seen that the torque decreases by increasing the advance ratio. This phenomenon occurs due to a decreasing drag force on the blade surfaces. According to aerofoil theory the propeller torque is calculated by a summation of all drag forces along the blades surface (Wald, 2006).

When the water is almost static, or at a low velocity, the propeller consumed more torque in order to accelerate the water. This is because, at the low speed, the water pressure surrounding the blade was high, which contributes as pressure drag on the blade surface. However, when the water started moving with a higher velocity, this pressure will drop slowly and subsequently, the pressure drag also drops. Compared to viscous drag, pressure drag gives a more significant value to the propellers overall drag. Therefore, by increasing the advance ratio, the torque of the propeller will reduce, as the pressure drag affecting the blade surface drops.

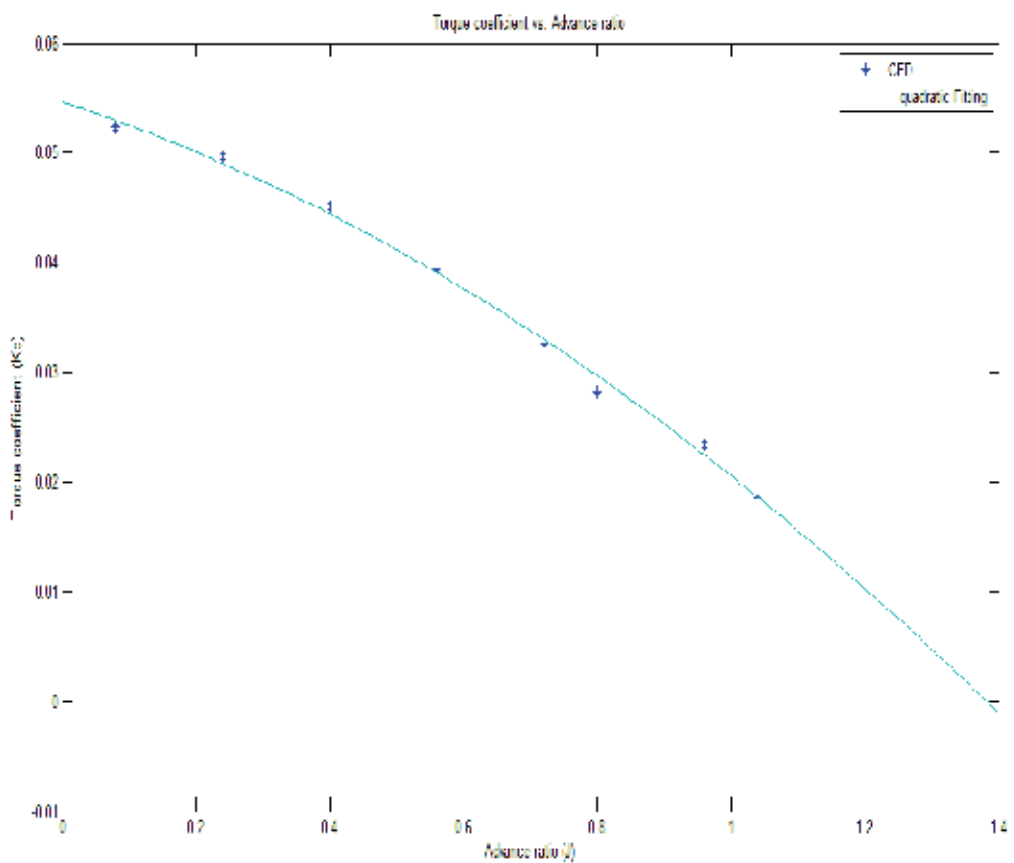


Fig. 8. Plot of torque coefficient vs. advance ratio

#### 4.4 Efficiency vs. advanced speed

The graph in Figure 9 shows the plot of efficiency against advance coefficient. From the graph, it is clear that the peak occurs at efficiency equal to 64.54 %. At this efficiency the advance coefficient was 0.85. During the design stage, the highest propeller efficiency was predicted to occur at an advance ratio equal to 0.8. This shows that the highest efficiency occurred at a different advance coefficient. The trend of the graph was close to the experiment shown by (Lin et al., 2009). However, the efficiency value was different to the design value within a 14 % margin. This error was due to the geometry of the propeller that was used in the simulation. Besides that, the predicted efficiency during the design process was a theoretical value only.

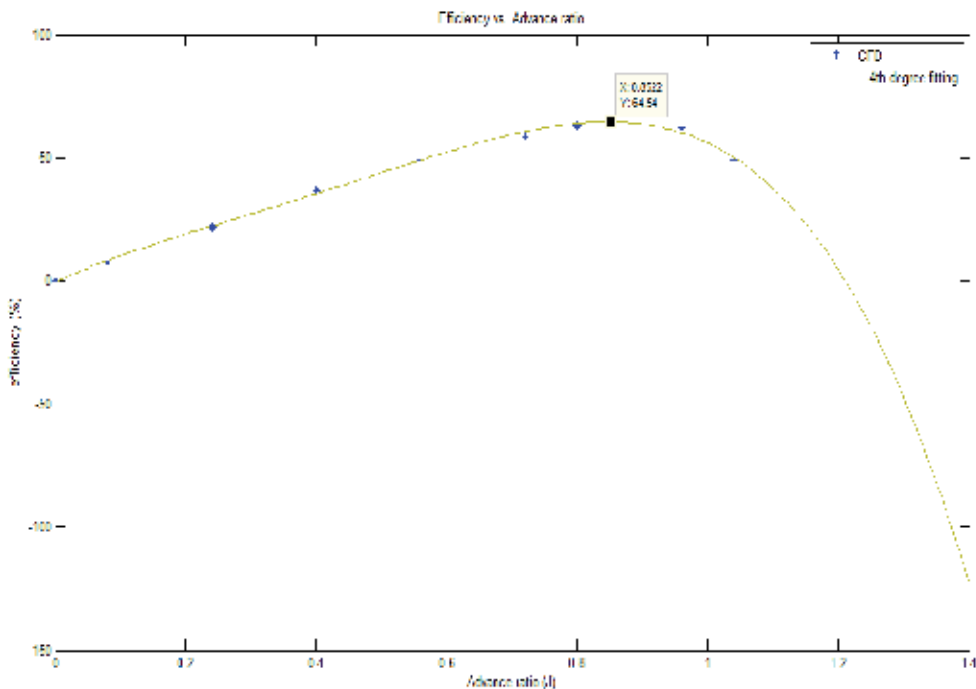


Fig. 9. Plot of efficiency vs. advance ratio

During the design stage, the hub effect was not considered, and the geometry did not have any changes. Nevertheless, in real applications, in order to suit the manufacturing process, the geometry must have a few changes. The CFD simulation utilized the geometry that contained some modification. Another factor of this error was that the theoretical calculations used in design process, contained a few assumption, such as no tangential velocity hitting the blade. The axial velocity was also assumed constant along the blades span. However, in real conditions, even small portions of tangential velocity will affect propeller performance. In the CFD, this tangential velocity was considered by solving the Navier-Stokes equation, where all fluid directions were taken into account. Additionally, the axial flows hitting the propeller are not constant along the blade span. There is always a variation of axial velocity along the blade span starting from the hub up to the blade tip. This variation was due to hub effect and reverse flow during the propellers operation. Some

of the water will be circulated back to the blade surface and then this type of flow will perturb the incoming water flow. Therefore, the axial inflow will be changing according to the perturbation.

In the CFD simulation, this water stream can be modeled with a high accuracy and the effect of this circulation can then be simulated. To fill the fabrication requirement, the tip of the blade must be cut off by 5%. This small change will affect the efficiency of the propeller. During the design process, the geometry was considered completely from the hub to the tip. Nevertheless, following the modification mentioned before, the geometry will be different. A CFD simulation used this geometry to obtain the real performance of the propeller. In Section 4.1, the CFD simulation showed a good agreement with the experiment results. This phenomenon occurred because in the CFD simulation the geometry and the operating conditions followed the experiments conditions. In this case, the CFD results can be used to predict the real performance of the propeller. The error between the design and the CFD simulation can be ignored because the goal of this research is to predict real performance of the propeller after fabrication by way of the cold forging process.

#### **4.5 Fluid behavior surrounding the blade**

Figures 10 and 11 show the velocity of the water around the blade at 0.7 radius. The propeller rotation was at 1500 rpm. In Figure 10, the water velocity was zero and in Figure 11 the water velocity was 2 m/s. In the bollard pull condition, the contour difference was evident, because the fluid was starting to move upwards from zero. However, for the advance coefficient 0.8, the velocity contour surrounding the blade showed no significant difference.

This behavior was due to the initial speed of the fluid, which was set at 2 m/s. Therefore, the fluid hitting the blade surface had initial speed and was not constant. Subsequently, the fluid direction, when it hits the surface, was normal to the surface. In the bollard pull condition, the water contour close to the blade also had a certain speed. This pattern of contour showed that the water was moving towards the propeller. Then this water is accelerated by the propeller in a backwards direction. This condition makes different velocities occur at the front and the backside of the propeller blade. The same phenomenon also occurred for fluid that had advance coefficient 0.8.

According to the Bernoulli principle, when the velocity is high, then the pressure will drop, and vice versa. As a result, the pressure surrounding the blade will be different between the back and front sides, as shown in Figures 12 and 13. This difference in pressure will create force on the blade, based on Pascal's rule, where the force is equal to pressure over an area. Because the pressure on the front side was higher than backside, the resulting force will push the propeller in one direction.

However, in Figures 12 and 13 the pressure contour between the two conditions has different patterns. In the bollard pull condition, the high-pressure contour was clearly seen, but in the advance coefficient condition, the lower pressure contour was clearer compared to high pressure. This pattern occurred because in the advance coefficient condition the water velocity hitting the blade surface was higher. Most of the water velocities are identical when they hit the blade surface. Therefore, the velocity contour for this area will have the same colour. For bollard pull conditions, the pressure contour was clear, because during this condition, the pressure behind the blade had an identical value along the blade. This is because the velocity of the water was only affected by the rotation of the blade. Besides that,

in advance coefficient conditions, the water that had velocity, will drag the water behind the propeller and move together. These circumstances make the velocity of the water behind the propeller increase and well distributed.

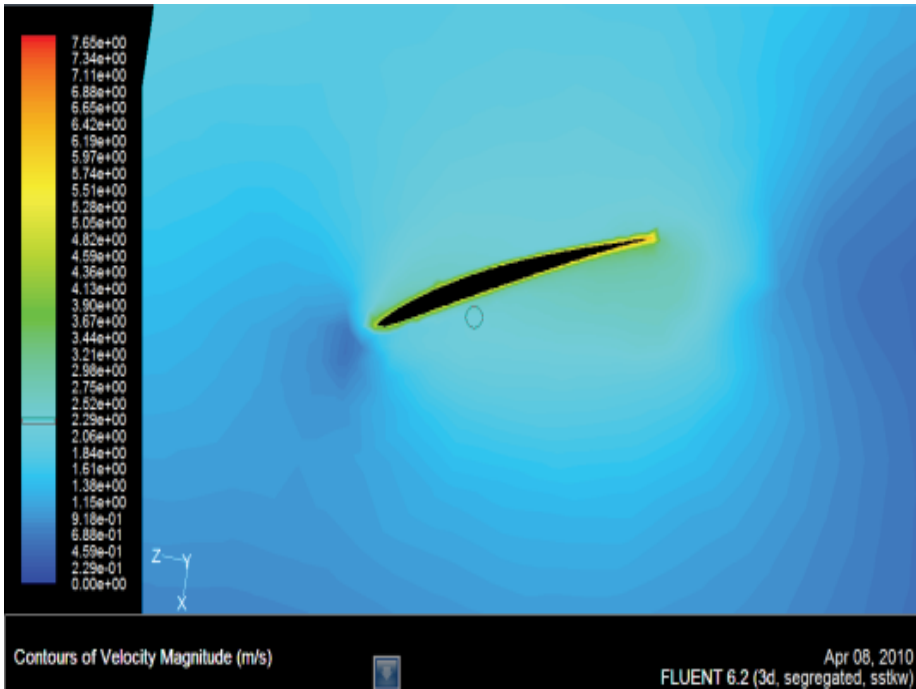


Fig. 10. Velocity contour surrounding the blade at 1500 rpm and bollard pull

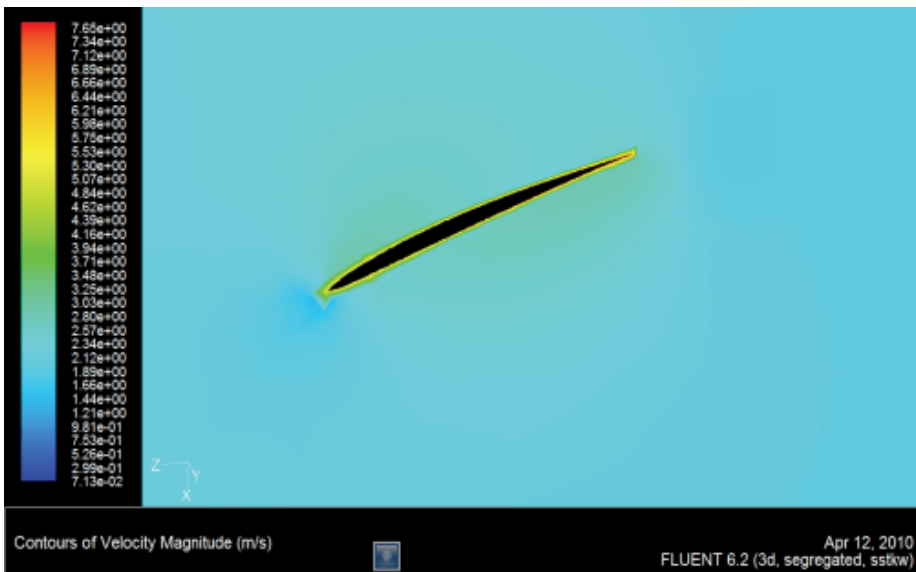


Fig. 11. Velocity contour surrounding the blade at 1500 rpm and 0.8 adv

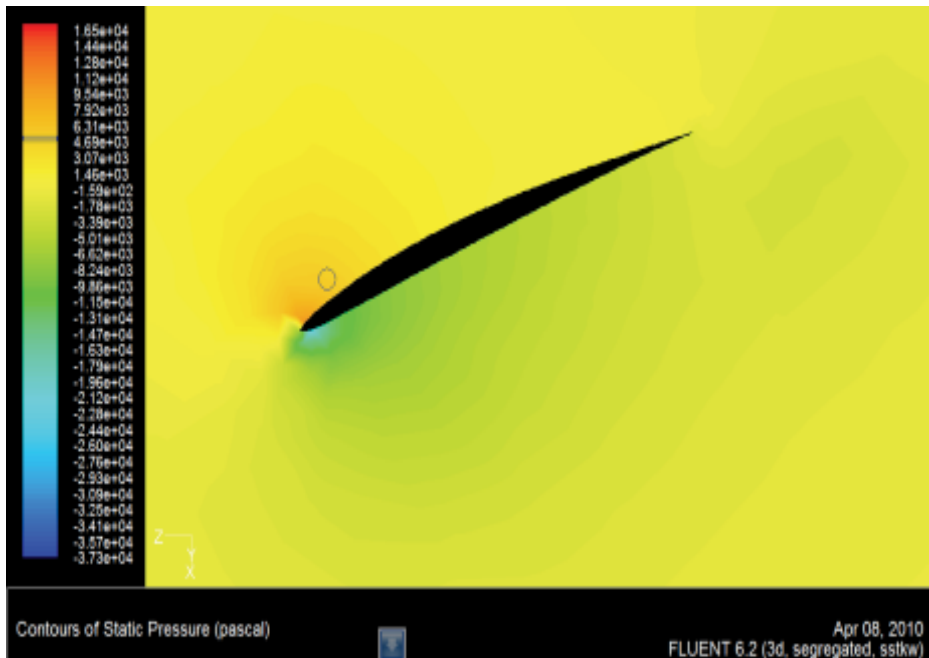


Fig. 12. Pressure contour surrounding the blade in bollard pull condition

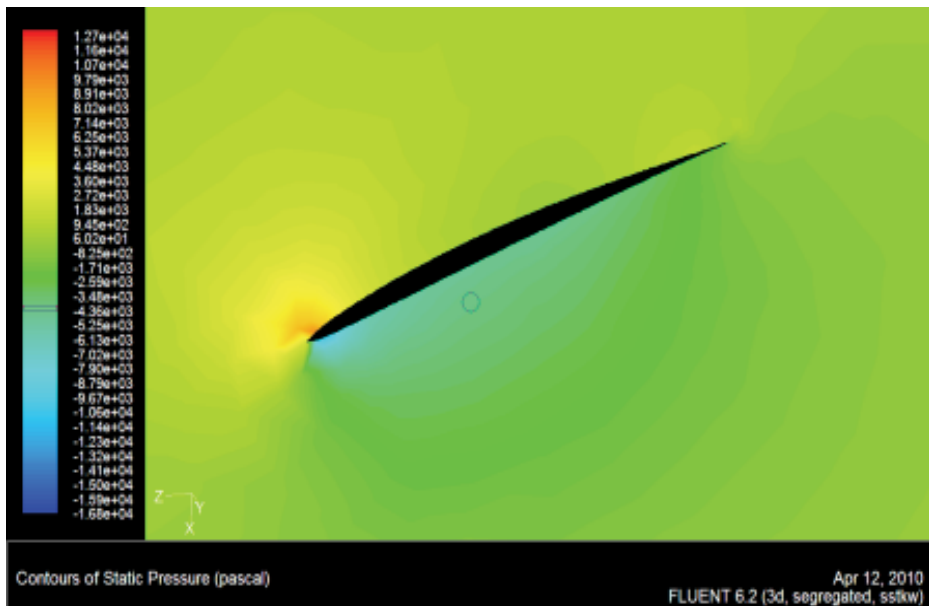


Fig. 13. Pressure contour surrounding the blade at 0.8 adv

#### 4.6 Pressure coefficient distribution along the blade at 0.8

Figures 14 and 15 show the pressure distribution along the blade. The result of this simulation was important in order to know the actions of pressure along the blade surface.

In the figures above, pressure was concentrated at the leading edge. This was also true for the backside of the propeller blade, with the lowest pressure occurring at the leading edge. The higher pressures occur at the 0.9 radius of propeller. This is because, at this radius, the

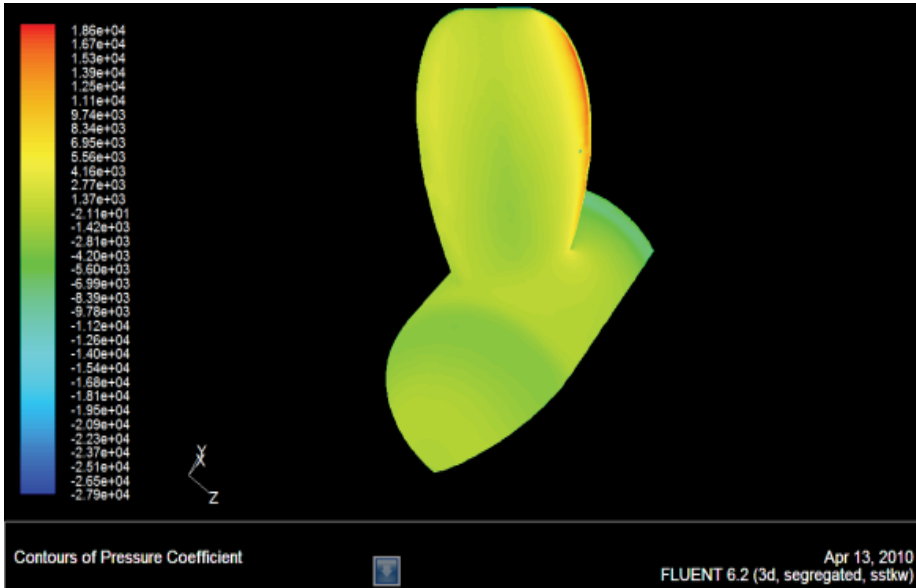


Fig. 14. Pressure coefficients on the back surface

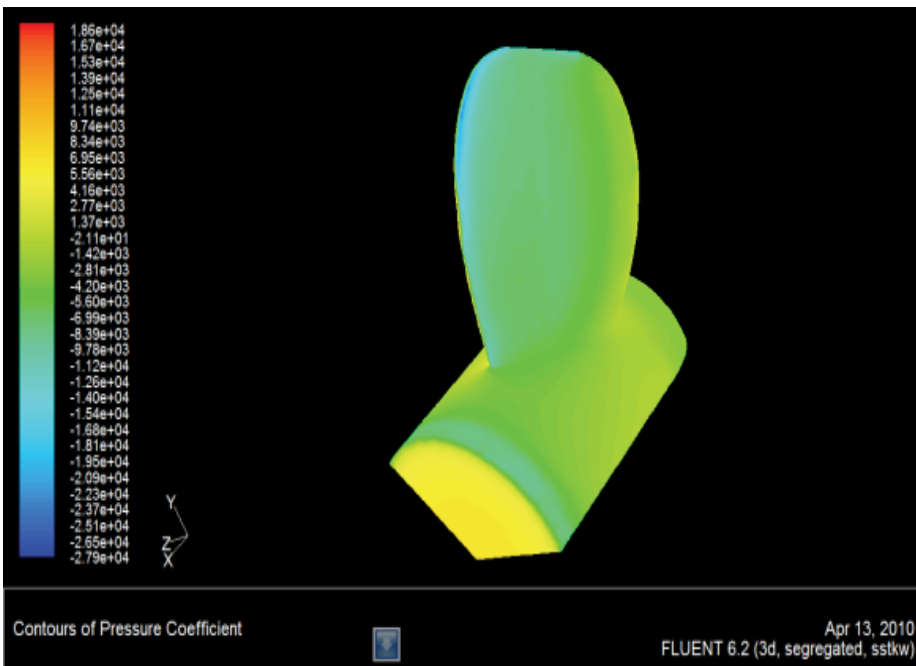


Fig. 15. Pressure coefficients at the front surface

chord length was higher compared to other radii. When the chord length higher, the water will hit this part first, before hitting other parts. The interaction between the blade and the water makes the fluid flow changing in direction and velocity. At the first interaction, water flow will separate into two directions. One will move through to the backside and another will move through to the front side. At radius 0.7 the water velocity will drop suddenly at the front side and increase at the backside. Then the water will face other parts of the propeller blade. At this stage, the water changing direction will already be absorbed by other parts of the propeller. This is the reason why, at the highest chord length, the pressure at the backside is higher and at the front side, it is lower.

From Figure 14 and 15, the force pattern along the blade can be measured. This behavior is important, because the force distribution will affect propeller performance. These pressure changes, as shown in Figures 14 and 15, were at their maximum on the leading edge. This is good for a propeller blade, because at the leading edge, the propeller blade was at its maximum. Therefore, the blade can exert force during operation without failure.

#### 4.7 Vehicle speed and propeller speed relationship

Any change in propeller speed will lead to a thrust change. Therefore, the vehicle speed will also affect propeller speed changes. Another relationship to be discovered, by using CFD, was vehicle speed and propeller speed. Graph in Figure 16 shows the relationship between vehicle speed and propeller speed. To plot the graph, the simulation was run and the thrust produced was recorded. The simulation was run for speeds equal to 0.5, 1, 1.5 and 2.

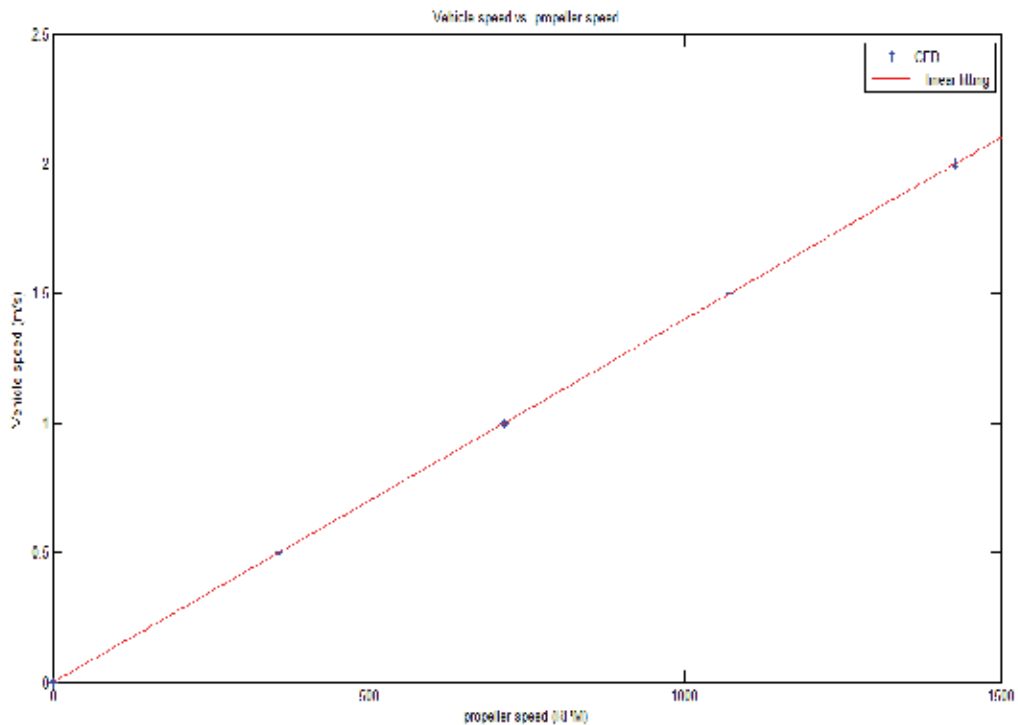


Fig. 16. Relationship between vehicle speed and propeller speed

From the graph in Figure 16, the relationship between speed and rpm can be matched to a linear function. This result was important, because in AUV applications, a precise control system must be developed. By knowing the map between vehicle speed and the propeller speed, a reference value for the control system can be set precisely. This approach will help to save energy consumed in propelling the vehicle. In other words, this method will avoid any waste of energy by randomly guessing the thrust required by the vehicle for a certain speed. This graph was plotted by using the results generated by the CFD simulation. For each speed, there are three levels of rpm to choose from and an approximation was made to find the value of thrust for the vehicles speed.

## 5. Conclusion

CFD results show the propeller was suitable to be used in AUV because it can give the required thrust. The CFD simulation has been successfully modeling the propeller behavior. In comparison between experiment and simulation for power input, the pattern for the graph was similar. The results show that the CFD can predict the relationship of thrust and torque coefficient for propeller in various advance ratio.

Finally this work has contributed CFD model for AUV propeller. In the literature, only few researchers have simulated AUV propeller. Most of the CFD models were works on marine propellers. Compare with AUV propeller the ship propeller have larger diameter. As mentioned in Carlton (2007) the propeller faces scaling effect when it was directly scale down from bigger size. Thus, to avoid this problem the specific numerical model must be developed in order to get real behavior of the AUV propeller. This research shows that the CFD simulation of AUV propeller was good in agreement with experiment.

In future unsteady CFD simulation of propeller simulation will be done. This study is needed to develop dynamic model of the propeller for precise control system. In this case, the CFD can be applied to support the system identification for nonlinear system such as propeller behavior. Finally, the study can be extended in term of developing the optimum control system that can minimize the energy consumption of AUV.

## 6. Acknowledgment

We are very grateful to National Oceanographic Directorate (NOD) and Ministry of Science, Technology and Innovation (MOSTI), Malaysia, for providing funding to pursue our research in underwater system technology.

## 7. References

- Benini, E. 2004. Significance of blade element theory in performance prediction of marine propellers. *Ocean Engineering*, 31, 957-974.
- Batten, W. M. J., Bahaj, A. S., Molland, A. F. & Chaplin, J. R. 2008. The Prediction of The Hydrodynamic Performance of Marine Current Turbines. *Renewable Energy*, 33, 1085-1096.
- Cairns, J., Larnicol, E., Ananthakrishnan, P., Smith, S. & Dunn, S. Year. Design of AUV propeller based on a blade element method. In: *OCEANS '98 Conference Proceedings*, 28 Sep-1 Oct 1998 1998. 672-675 vol.2.



- Carlton, J. S. 2007. Propeller design. *Marine Propellers and Propulsion (Second Edition)*. Oxford: Butterworth-Heinemann.
- Carlton, J.S., *Propeller design, in Marine Propellers and Propulsion (Second Edition)*. 2007, Butterworth-Heinemann: Oxford. p. 435-463.
- Celik, F. & Gunner, M. 2007. Energy saving device of stator for marine propellers. *Ocean Engineering*, 34, 850-855.
- Chen, J.H. and Y.S. Shih, *Basic design of a series propeller with vibration consideration by genetic algorithm*. Journal of Marine Science and Technology, 2007. 12(3): p. 119-129.
- Guo, C. Y., Ma, N. & Yang, C. J. 2009. Numerical Simulation of a Podded Propulsor in Viscous Flow. *Journal of Hydrodynamics*, 21, 71-76.
- Ghassemi, H. & Ghadimi, P. 2008. Computational hydrodynamic analysis of the propeller-rudder and the AZIPOD systems. *Ocean Engineering*, 35, 117-130.
- Henk Kaarle Versteeg & Weeratunge Malalasekera 2007. *An introduction to computational fluid dynamics*, Harlow, England, Addison Wesley Longman
- Hsu, T.H., et al., *An iterative coordinate setup algorithm for airfoil blades inspection*. International Journal of Advanced Manufacturing Technology, 2005. 26(7-8): p. 797-807.
- Kerwin, J. E. 2001. "Hydrofoils and Propellers" world wide available at: <http://ocw.mit.edu/course/mechanical-engineering/>.
- Li, D. Q. 2006. Validation of RANS predictions of open water performance of a highly skewed propeller with experiments. *Journal of Hydrodynamics*, 18, 520-528.
- Lin, C.-C., Lee, Y.-J. & Hung, C.-S. 2009. Optimization and experiment of composite marine propellers. *Journal of Composite Structure*, 89, 206-215.
- Muhamad Husaini, Zahurin Samad, and Mohd Rizal Arshad, CFD Simulation of Cooperative AUV Motion, *Indian Journal of Marine Science (IJMS)*, Vol.38(3), pp. 346-351, September 2009
- Neocleous, C. C. & Schizas, C. N. Year. Marine propeller design using artificial neural networks. In: Neural Networks, 1999. IJCNN '99. International Joint Conference on, Jul 1999 1999. 3958-3961 vol.6.
- Olsen, A.S., *Energy coefficients for a propeller series*. Ocean Engineering, 2004. 31(3-4): p. 401-416.
- Phillips, A. B., Turnock, S. R. & Furlong, M. 2009. Evaluation of manoeuvring coefficients of a self-propelled ship using a blade element momentum propeller model coupled to a Reynolds averaged Navier Stokes flow solver. *Ocean Engineering*, 36, 1217-1225.
- Rhee, S. H. & Joshi, S. Year. CFD validation for a marine propeller using an unstructured mesh based RANS method. In: Proceedings of the ASME/JSME Joint Fluids Engineering Conference, 2003. 1157-1163.
- Rhee, S. H. & Koutsavdis, E. 2005. Two-dimensional simulation of unsteady marine propulsor blade flow using dynamic meshing techniques. *Computers and Fluids*, 34, 1152-1172.
- Singhal, A. K., Athavale, M. M., LI, H. & Jiang, Y. 2002. Mathematical basis and validation of the full cavitation model. *Journal of Fluids Engineering, Transactions of the ASME*, 124, 617-624.
- Stanway, M.J. and T. Stefanov-Wagner. *Small-diameter ducted contrarotating propulsors for marine robots*. in OCEANS 2006. 2006.
- Takekoshi, Y., et al., *Study on the design of propeller blade sections using the optimization algorithm*. Journal of Marine Science and Technology, 2005. 10(2): p. 70-81.

- Takekoshi, Y., Kawamura, T., Yamaguchi, H., Maeda, M., Ishii, N., Kimura, K., Taketani, T. & Fujii, A. 2005. Study on the design of propeller blade sections using the optimization algorithm. *Journal of Marine Science and Technology*, 10, 70-81.
- Takinaci, A.C. and M. Atlar, *Performance assessment of a concept propulsor: the thrust-balanced propeller*. *Ocean Engineering*, 2002. 29(2): p. 129-149.
- Vysohldid, M. & Mahesh, K. 2007. Understanding crashback in marine propellers using an unsteady actuator disk model. In: *Collection of Technical Papers - 45th AIAA Aerospace Sciences Meeting*, 2007. 11133-11140.
- Vysohldid, M. and K. Mahesh. *Large Eddy Simulation of crashback in marine propellers*. in *Collection of Technical Papers - 44th AIAA Aerospace Sciences Meeting*. 2006.
- Wald, Q. R. 2006. The aerodynamics of propellers. *Progress in Aerospace Sciences*, 42, 85-128.
- Yoerger, D. R., Cooke, J. G. & Slotine, J. J. E. (1990) The influence of thruster dynamics on underwater vehicle behavior and their incorporation into control system design. *Oceanic Engineering, IEEE Journal of*, 15, 167-178.
- Young, Y. L. & Shen, Y. T. 2007. A numerical tool for the design/analysis of dual-cavitating propellers. *Journal of Fluids Engineering, Transactions of the ASME*, 129, 720-730.

## **Part 4**

### **CFD in Castle**



# Modelling and Simulation for Micro Injection Molding Process

Lei Xie<sup>1</sup>, Longjiang Shen<sup>2,3</sup> and Bingyan Jiang<sup>3</sup>

<sup>1</sup>*Institute of Polymer Materials and Plastics Engineering, Clausthal University of Technology,*

<sup>2</sup>*Institute of Mechanical Engineering, Clausthal University of Technology,*

<sup>3</sup>*College of Mechanical and Electronic Engineering, Central South University, Changsha*

<sup>1,2</sup>*Germany*

<sup>3</sup>*P.R.China*

## 1. Introduction

### 1.1 Micro injection molding process

Since end of 60s' last century, with the booming of the semi-conductive materials processing technologies related to IC (Integrated Circuits) industry, parts or components in micro-scale which is hard to see with naked eyes stepped into the attention of scientists. Thereafter, the various functional micro systems were rapidly widely used in different areas, such as watch and camera industry, printer ink jet, information storage, sensors and transducers, micro fluidic system, micro heat exchanger, micro reactor and so on (Madou M. J. 1997; Madou M. J. 2002). After impressive development, a new research scientific and engineering area was formed, named as Micro-Electronic-Mechanical systems (MEMs). Especially, in the last ten years, Micro optical electron system (MOEMS) and Bio- micro electron mechanical system (Bio-MEMS) played important roles in the Information Technology (IT) and Bio-Medical Engineering (BioM) fields (Yu L. Y.2002; Wilson K., Molnar P. & Hickman J. 2007; Spatz Joachim P. 2005; Pal, P. & Sato, K. 2009; Hecke M & Schomburg WK 2004).

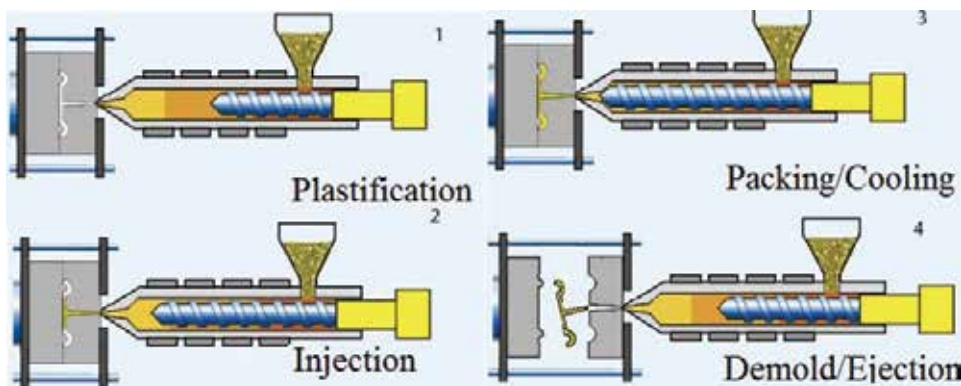


Fig. 1-1. Processing cycle of conventional injection molding process (Source: Veltkamp)

Today's micro system is longing for innovative products which are small, light, more powerful, faster and cheaper to produce than present products. Micro injection molding technology is perfectly satisfied with such requests. It evaluated from conventional injection molding process and can realize large-scale production of micro parts with polymeric materials and ceramic/metal powders with polymeric bonders.

However, micro injection molding process is not just a scaling down of the conventional injection process shown in Fig.1-1. It requires a rethinking of each step of the process, which indicates special requirements for the injection pressure, mold temperature, vacuum of cavity, shot size and cooling speed, which are remarked as red fonts in Fig.1-2.



Fig. 1-2. Micro injection molding processing steps

The polymer melts fill into micro scale cavity through small sized runners and gates with high speed and high pressure, which can induce its degradation, but will help shear-thin effects (Martyn M T et al. 2003). The fabrication of high aspect ratio micro features can be realized by using a mold temperature close to the softening temperature of polymer or even higher. In this way, some special structure sizes in the nano meter range also are able to be replicated [Mekaru H et al. 2004; Schiff H et al. 2000; Yao D. & Kim B. 2002; Liou A. C. & Chen R. H. 2006; Despa M. S., Kelly K. W. & Collier J. R. 1999).

## 1.2 Physical aspects and considerations

During micro injection molding process, the plastic material undergoes temperature and pressure increases, significant shear deformation, followed by rapid decay of temperature and pressure in the mold cavity, which leads to solidification, high residual stress, complex

molecular orientation, and other part properties that determine the molded part quality. The process design of micro injection molding involves the determination of a number of processing parameters, e.g., pressure (injection, holding, back and melt), temperature (coolant, nozzle, barrel, melt and mould), time (fill, holding, cooling and cycle), clamping force, injection speed, injection stroke, etc. In such process, the irregular geometry in micro scale and the complex thermo-mechanical history during the injection molding cycle, it is generally necessary to resort to numerical simulation methods to properly simulate the molding process and develop the capability of predicting the final configuration of the molded part, which is particularly important in precision injection molding operations.

However, due to those special processing features of micro injection molding process (micro scale parts dimension, high pressure/shear rate, high mold temperature, and fast cooling speed), the flowing behavior and phase transfer of polymer melts perform different as well. Therefore, comparing with numerical simulation of conventional injection molding process, there are some new physical aspects associated with the scale-down of forming parts need to consider, which are:

- Sliding of polymer frozen layer due to high shear stress near mold wall;
- High heat transfer rate of polymer melts in micro cavity resulting from micro mass/volume of materials;
- Complex rheological behaviour of polymer melts flowing in micro geometry, especially in sub-micro/nano dimensional cavities;
- Dominating of surface force related to surface effect and neglecting of volume forces contributed by viscous and interior because of the micro scale.

## 2. Software selection

Based on the criterion of technical performance, the selection of the CFD (computational fluid dynamics) software package for simulating micro injection molding process should consider the five aspects as following:

- Friendly User-Interface(UI) contributes to the easy start-up for beginner;
- Suitable mathematic models and efficient numerical solution method;
- Flexible user define function for mathematic models and boundary conditions;
- Convenient pre- and post- processing unit or interface;
- High capability-price rate.

Nevertheless, such software satisfied with all aspects is nearly possible, the users and customers need to make their decision depending on their stand and emphasis as for the application and project they are focusing on. The special commercial software for injection molding process are normally having human-based UI and powerful pre-/post- unit with smoothly operations, which make sure the beginner can drive the software in the short term, but such kind of software supplies less user defined functions limiting the software application in new technology development. In contrast, the general CFD packages open widely for user define ability in mathematic model, boundary condition, mesh elements type, numerical solution and multi-physical phenomena coupling, whereas they appear more complex and comprehensive operation interfaces which causes learning time-consuming.

### 2.1 Special commercial software for injection molding process

Since the first attempts to filling simulation of injection molding process, there have been numbers of commercial CAE software packages developed for injection molding process, in

which a couple of them have been maturely applied in industry and academics, such as MoldFlow®, Modex3D®, CADMOULD®, SIGAMA® etc.

Though these software packages are originally developed for the process simulation of traditional injection molding, the 3D module of them are often used in micro injection molding, especially for the macro injection molding components with micro features. On the other side, with the rapid development of micro injection molding technology, these traditional injection molding based software packages are trying to satisfy the requirements of micro injection molding process simulation by technology update and progress.

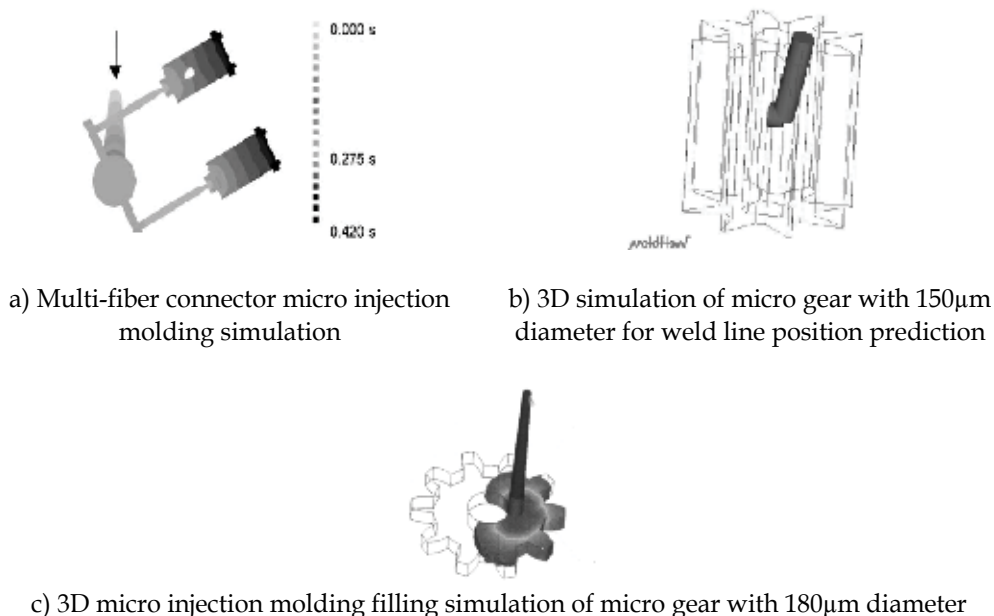


Fig. 2-1. Simulation of micro injection molding process with special commercial software

Researchers from Karlsruhe Research Center (now is Karlsruhe Institute Technology) studied the filling process of the multi-fiber connector in micro injection molding process in which the position of the weld line was predicted and the cavity numbers was optimized, shown in Fig.2-1a (Wallrabe U. et al 2002); Despa et al. investigated the micro injection molding processability of the micro-scale part with 100 µm diameter, and the results revealed the correlation between the processing conditions and processing ability (Despa M S, Kelly K W & Collier J R. 1998); W.N.P.Hung et al. used Moldflow and C mold to simulate the injection molding process of the micro gear with 150µm diameter in 2.5D/3D way and analyzed the weld line position, injection pressure and injection speed distribution during the process, shown in Fig.2-1b (Hung W.N.P., Ngothai Y., Yuan S., Lee C.W. & Ali M.Y. 2001); W. Michaeli et al. from IKV in TU Aachen simulated the 2.5D/3D micro injection molding process of the testing micro structures with ribs and corners by CADMOULD, MagmaSoft and Fidap. The results showed that 2.5D simulation is hard to describe the polymer melts flowing and filling behavior in ribs and corners (Kemmann O et al. 2000). The scientists from Taiwan are also very active in aspect of simulation of micro injection molding process, as the example, Y.K.Shen from Longhua University implemented the comprehensive studies for micro injection molding process by MoldFlow and C Mold as well as self-coded package,



Fig.2-1c shows their simulation results about the filling phase of the micro gear ( $120\mu\text{m}$  diameter) in micro injection molding process, in which the numerical simulation was carried out for 3 different polymers (PP, PA, POM) and based on Taguchi experimental method the significant influencing order of the processing parameter on filling performance was achieved (Y.K.Shen et al. 2002; Y.K.Shen et al. 2008).

With the commercial software package Moldflow Plastic Insight (MPI), the authors simulated the molding process of a micro columns array (the diameter of the column is  $200\mu\text{m}$ , the height is  $300\mu\text{m}$ ), shown as Fig.2-2. The mesh elements of the part's 3D model were processed by Hypermesh®. The simulation was not only carried out for filling process but the shrinkage and warpage of the part. Fig.2-3 and Fig.2-4 shows 3D meshes and the density distribution of part after packing respectively.

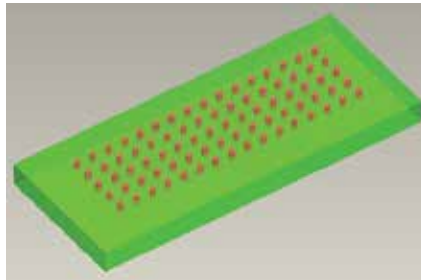


Fig. 2-2a. 3D model of a micro columns array

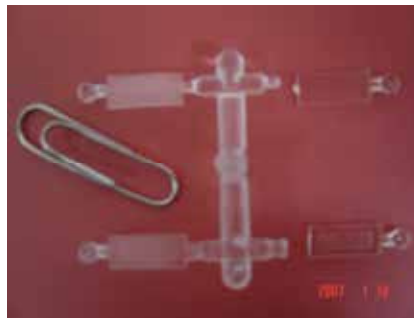


Fig. 2-2b. Injection molded micro columns array (including runner system)

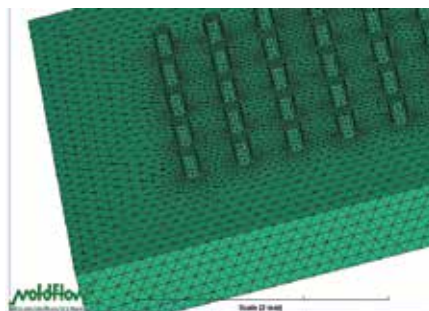


Fig. 2-3. 3D mesh of micro columns array

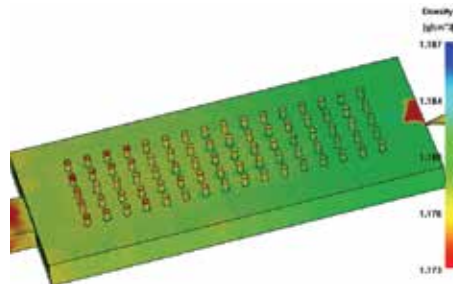


Fig. 2-4. The density distribution of part after packing

The main purpose of numerical simulation is to improve the replication fidelity of micro injection molded components by optimization of injection molding process parameters. Here, we define the replication fidelity as follows:

$$RF = \frac{\Omega_c \cup \Omega_p}{\Omega_c} \times 100\%$$

RF is replication fidelity,  $\Omega_c$  is the geometry domain of cavity,  $\Omega_p$  is the geometry domain filled by polymer. The weight of injection molded parts are used to characterize the replication fidelity of micro injection molded components quantitatively, it is not so accuracy but economy and simple as compared to the use of some very expensive equipments such as SEM to measure the geometry dimension of micro injection molded components.

Because the part weight is fixed after the packing phrase, so after the simulation of filling process and packing process of injection molding in Flow 3D module of MPI, the part weight will be calculated according to the two domain Trait equation. Fig.2-5. and Fig.2-6 shows the influence of packing time on the part weight in simulation and experiment respectively, the results from simulations and experiments are consistent. From the observation results of the image measuring apparatus, as shown in Fig.2-7, it was also discovered that the higher the part weight, the better the filling of the microstructures. The molding weight of the part can evaluate the replication fidelity of micro-feature structured parts primarily.

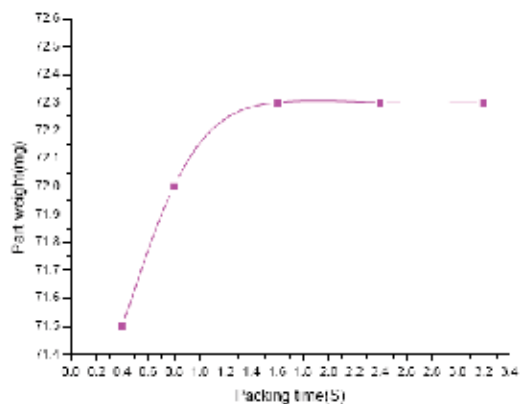


Fig. 2-5. Influence of packing time on the part weight in simulation

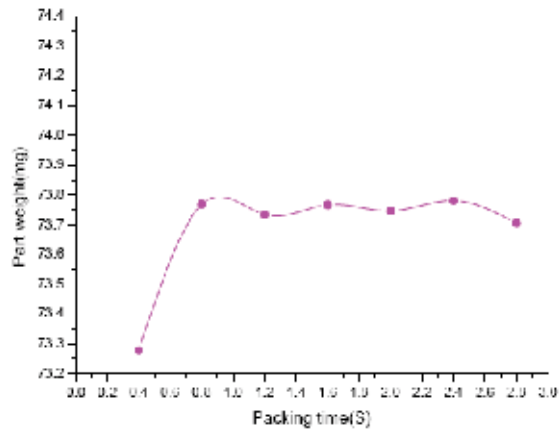


Fig. 2-6. Influence of packing time on the part weight in experiment

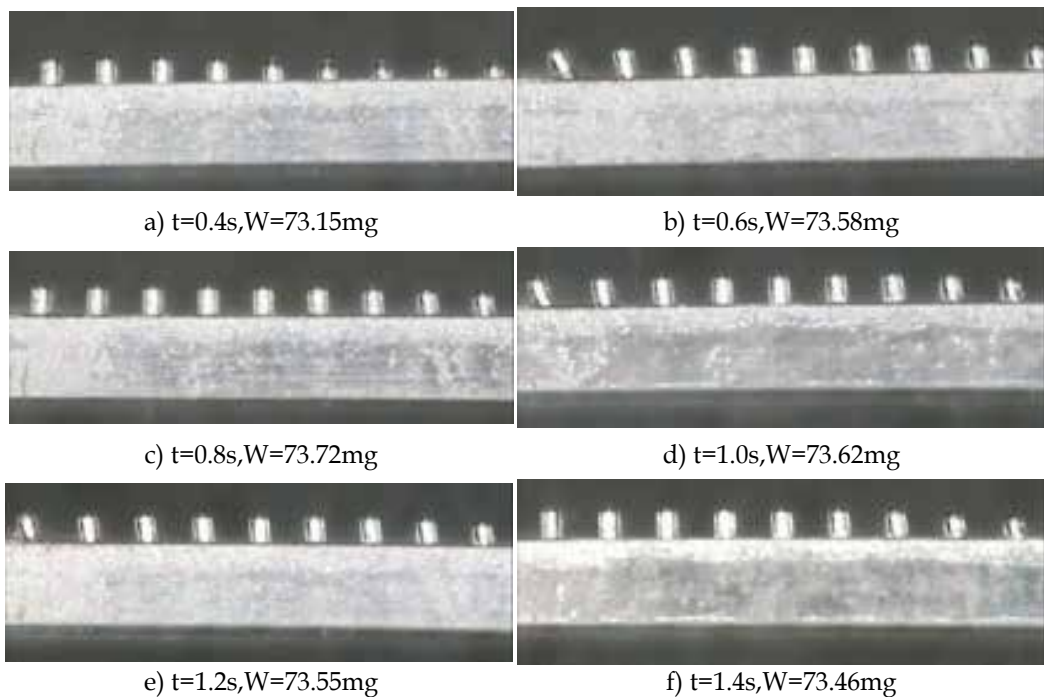


Fig. 2-7. Side view of molded parts vs. injection times ( $t$ -injection time,  $W$ -part weight)

There are still many attempts and investigations have been done in the similar way., like Guido Tosello et al. used MoldFlow simulate the micro injection molding process and applied the weld line flow marks in the formed parts for simulation verification and improvement(Guido Tosello et al.), N.C. Tham et al combined the Moldflow with pressure/temperature monitor transducer discussed the heat transfer mechanism and their relevant effect about the filling process of micro injection molding process(N. C. Tham et al.). the engineers in Moldex 3D Inc. successfully achieved the 3D simulation of the micro injection molding process with Moldex 3D and analyzed the temperature history and

distribution in micro features during micro injection molding (Moldex 3D). However, the research works based on special commercial software packages indicate that those simulation software based on conventional injection molding process can supply the characteristic analysis for micro injection molding process, but are not able to precisely perform the flow behavior of polymer melts in micro injection molding process, which is resulting from their mathematic model and boundary condition in background of macro fluid dynamics.

## 2.2 General CFD software

Restricted by the fixed mathematic model and boundary condition configuration, many researchers simulated the micro injection molding process based on general CFD software or self programming codes which offer more freedom in mathematic modeling and definition so that the simulation can be more precise by considering more micro scale phenomena which is neglected in normal commercial injection molding software.

Yu & Lee et al. presented that conventional Hele-Shaw 2.5D midplane simulation is unable to describe the flow pattern correctly. It tends to over-predict the effects of microstructures on global flow patterns. For the unidirectional flow, an x-z planar based on the general momentum equation is able to achieve better accuracy and to retrieve more detailed flow and heat transfer information around the microstructures. A hybrid numerical technique is developed, which can significantly reduce the nodes and computation time, and yet provide good flow simulation around the microstructures. The mold-melt heat transfer coefficient and injection speed are shown to be very important factors in determining the filling depth in microstructures. A decrease of the heat transfer coefficient and the occurrence of wall-slip are likely in microchannels (Yu, Liyong; Lee, L. James & Koelling Kurt W 2004).

Shi et al. were based on the particle tracking function of MIS (Mesh Free Micro Injection Simulation Code) to explore complex flow behavior. One of the mesh free methods, SPH, has been modified in MIS to simulate the course of micro injection molding. Mass points in various positions have been monitored to help understand melt flow behaviors. According to monitored tracks, mass points follow complex wave style routines. The findings of their study have provided some fundamental supports in understanding the fountain flow behavior in micro injection molding. However, the influence factors of fountain flow and the phenomenon caused by it were not comprehensively discussed (Shi F, Zhang X, Li Q & Shen C Y. 2010).

Su et al. characterized the flow behaviors of polymer melts in micro mold-cavities are by both simulation and experiments. In this study, among various process parameters, temperature was identified as the key factor that decisively determines the quality of injection-molded microstructures. Based on the collected experimental and simulation results, process optimization is performed to improve replication quality and to establish guidelines for potential applications (Su Y C, Shah J & Lin L W, (2004).

Based on SPH method, V Pottler et al. simulated the micro powder injection molding (M-PIM) process by discretion of a phenomenological model for shear induced particle migration in concentrated suspensions, which is firstly purposed by (Phillips et al. 1992). In this model, there are two effective fluxes parameters contributing to particle migration, named as  $J_c$  and  $J_v$ . The  $J_c$  represents a flow of solid particles towards the regions of least shear.  $J_v$  demonstrates a particle flux related to a spatially varying viscosity and is directed towards regions of lower viscosity. Generally, the viscosity supposes to increase with the

concentration of the solid powders in suspensions. Whereas, in their case,  $J_{-}$  is counteracting the effect of  $J_c$ , for an instance, for Poiseuille flow between two parallel plates, some steady state concentration profile will be reached, with a maximum in the centre of the channel. For the viscosity depending on the volume fraction of powders and binders, the Krieger rheological model (Krieger et al. 1972) is assumed and applied, with a saturation volume fraction of 0.68 by them. Building a test case, they took an injection molding test part with the geometry as depicted in Fig. 2-8a. The concentrated interesting area on the region is marked by the rectangle, and the gate of the mold geometry and the flow direction was illustrated by the arrows. Fig. 2-8b is a snapshot of an early stage of the injection, in which the distribution of the powders (or solids) load indicates an aggregation at convex corners and a decrease at concave corners. This result is consistent with intuitive understandings and theoretical commons since the shear in the proximity of convex corners should be lower than in the bulk of the geometry. On the other hand, concave corners are regions of large shear rates. In later stages of the filling the concentration in the part of the entrance volume behind the two arms is rather homogeneous and large. The concentration in the front part is a few percent lower because in this region the feedstock is still flowing towards the arms' areas. Inside the arms the average concentration is even lower, which means that a larger fraction of the solid powders prefers to stay in the entrance volume where shear rates and flow velocities are less pronounced. Additionally, the solids loading percent reaches the maximum in the centre of the arms contributed by the lower shear rates analogously to Poiseuille flow. In this stage, according to their results, the inhomogeneity from the initial stage start to disappear because they did not consider full or partial solidification of the feedstocks. If the feedstock material solidified at least partially in the entrance region, the inhomogeneous solids loading distribution would be frozen in (Piotter V. et al 2007; Piotter V. et al 2002);



Fig. 2-8. Schematic of Powder Injection Molding and the results

Hu applied a mesoscopic concurrent multiscale approach named CONNFESSIT ('Calculation of Non-Newtonian Flow: Finite Elements and Stochastic Simulation Technique') to solve this problem by combining the Brownian dynamics simulation (BDS) and the finite element method (FEM). In the simulation the simplest dumbbell model is used to mimic single linear polymer chain and has successfully achieved stable simulation results at a higher Weissenberg number than the conventional methods, which is commonly observed in polymer processing, especially in micro injection molding process (Hu et al 2005; Hu et al 2007).

Moguedet et al. developed a two phase flow approach by the use of Comsol Multiphysics to simulate the polymer melts filling micro cavities. In a first step, a Level Set model is applied to several configurations: Newtonian and non-Newtonian fluid (Cross viscosity law), coupled with a thermal equation and a thermal dependence of the viscosity (WLF law). They took into account the unsteady thermal behaviour of the mould while injecting the polymer into the cavity. The viscous thermal dissipation is also integrated in our calculations (shown in Fig.2-9). Finally, as air -trapping often occurs in the injection molding process, meanwhile they present some results considering a pseudocompression law (low Mach number) for the air. To conclude, they showed the ability of the Comsol model to simulate polymer filling in micro features (Moguedet et al. 2009).

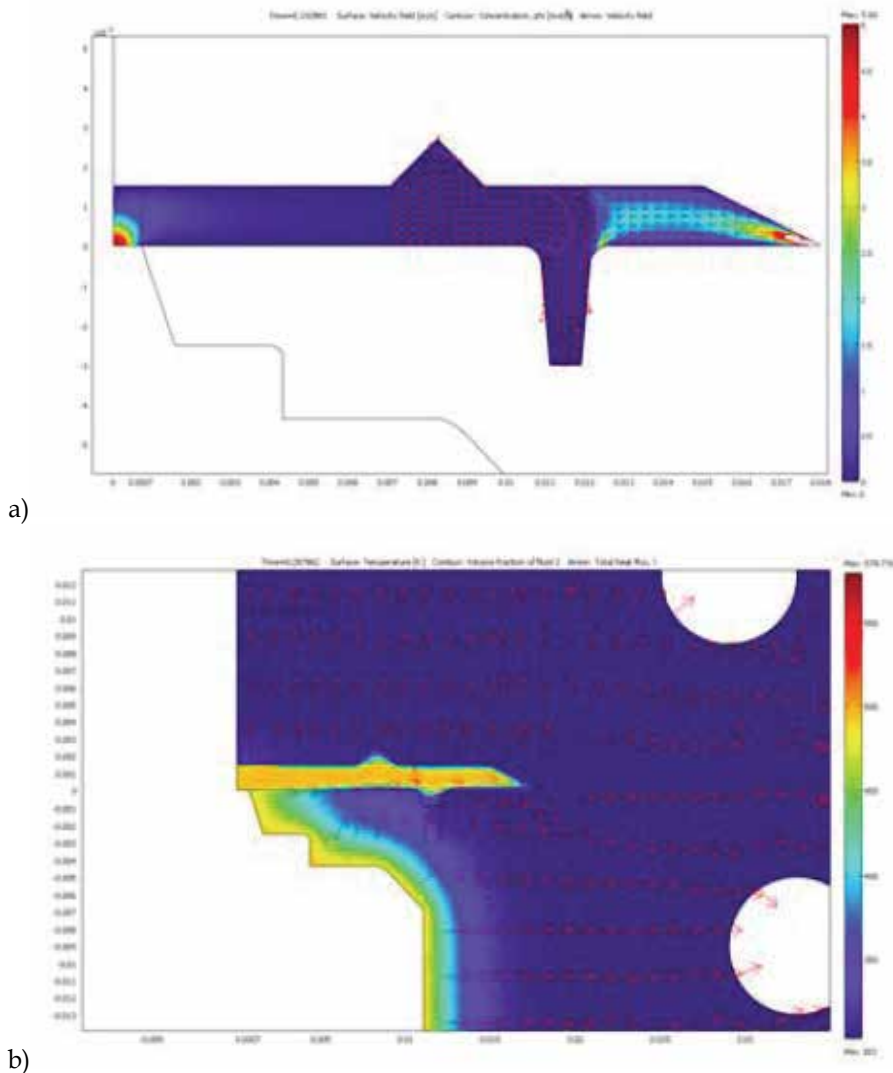


Fig. 2-9. a) Velocity field at 0.18s when vortices appear in the air; b) Temperature field in the mold and flow front position in the cavity (in red) at  $t = 0.29s$

The authors(Xie et al 2009) executed the simulation experiments for development of weld line in micro injection molding process respectively with specific commercial software (Mold Flow®) and general computational fluid dynamic (CFD) software (Comsol®Multiphysics), and the real comparison experiments were also carried out. The results show that during micro injection molding process, the specific commercial software for normal injection molding process is not valid to describe the micro flow process, the shape of flow front in micro cavity flowing which is important in weld line developing study and the contact angle due to surface tension are not able to be simulated. In order to improve the simulation results for micro weld line development, the general CFD software is applied which is more flexible in user defining function. The results show better effects in describing micro fluid flow behaviour. As a conclusion, as for weld line forming process, the numerical simulation method can give a characteristic analysis results for processing parameters optimizing in micro injection molding process, but for both kinds of software quantitative analysis cannot be obtained unless the boundary condition and micro fluid mathematic model are improved in the future.

According to the presented literatures on micro injection molding process simulation, it can be found that with general CFD software, the numerical simulation can be more precise than the case with special commercial software based on conventional injection molding process. However, it cannot realize the quantitative analysis for the process even with self defined CFD software, since there are still many phenomena and mechanism not clear yet for microfluidics, especially in such comprehensively complex processing conditions. Therefore, the improvement of modelling in physics and mathematics for microfluidics will be the key issue to reach the better numerical simulation results.

According to the presented literatures on micro injection molding process simulation, it can be found that with general CFD software, the numerical simulation can be more precise than the case with special commercial software based on conventional injection molding process. However, it cannot realize the quantitative analysis for the process even with self defined CFD software, since there are still many phenomena and mechanism not clear yet for microfluidics, especially in such comprehensively complex processing conditions. Therefore, the improvement of modelling in physics and mathematics for microfluidics will be the key issue to reach the better numerical simulation results.

### **3. Important issues in modelling and simulating of micro injection molding process**

Physical and mathematic modelling for the process or phenomena supposed to be simulated are always the most important issues and basement. The precise physical model with appropriate assumption and simplification will lower the complication of the mathematic description which is directly associated with the following solution efficiency. The next sections will discuss the aspects should be emphasized in micro injection molding simulation related to physical and mathematic points.

#### **3.1 Physical model and assumption**

The hele-shaw model (hieber & Shen 1982) is the typical physical model used in injection molding process simulation that provides simplified governing equations for non-isothermal, non-Newtonian and inelastic flows in a thin cavity, as shown in Fig.2-10. In

micro injection molding process, the model is also suitable when there is no special phenomena need to describe, like fountain flow, jetting, particle tracing and filler/matrix secretion etc. In Hele-shaw model, normally the following assumption were purposed and applied before mathematic modelling in the next step:

1. The thickness of the cavity is much smaller than the other dimensions, considered as thin cavity;
2. Polymer melts are incompressible and viscous fluid without elastics, whose flowing viscosity is shear dominated. Viscous force is much higher than inertia and gravitational forces;
3. Velocity in thickness direction is zero and in thickness direction the pressure gradient is zero as well;
4. The pressure in the flow front is zero and there is no fountain flow in the flow front;
5. There is no wall slides for frozen layer of polymers in the area near to mold walls;
6. The heat transfer between mold and polymer melts dominated by conductive way and inner of polymer melts transfer the heat by the convection.

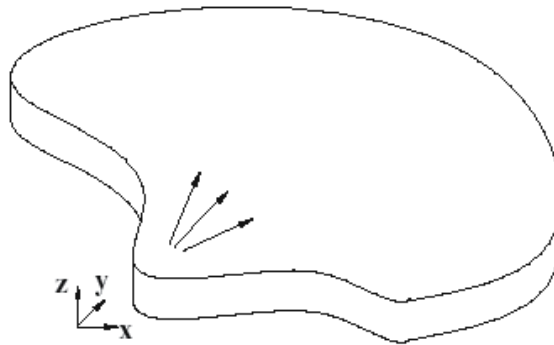


Fig. 2-10. Schematic of Polymer flows in Hele-Shaw cavity

Nevertheless, regarding the micro-scale effect, when Hele-shaw model applied for micro injection molding process, some assumptions need to change, like for assumption 4, the pressure in flow fronts might not be zero since the surface tension produced extra pressures there, or for assumption 5, the frozen layer of polymer melts near to mold wall may slide due to the high shear stress resulting from high shear rate and so on.

### 3.2 Mathematic models

Based on different approximation and physical models, the mathematic models for micro injection molding process could be various. In this section, the authors only discuss the simplified governing equations based on general Hele-Shaw models with somewhat micro scale considering.

The governing equations normally consist of three equations, named as Continuity Equation, Momentum Equation and Energy Equation, with formations as following:

Continuity Equation:

$$\nabla \cdot \mathbf{u} = 0 \quad (3)$$



Momentum Equation:

$$\rho \frac{D\mathbf{u}}{Dt} = -\nabla p + \nabla \cdot (2\eta \underline{\underline{\dot{\gamma}}}) + \rho \mathbf{g} \quad (4)$$

Energy Equation:

$$\rho C_p \left( \frac{\partial T}{\partial t} + \mathbf{u} \cdot \nabla T \right) = \nabla \cdot (k \nabla T) + 2\eta \underline{\underline{\dot{\gamma}}} : \underline{\underline{\dot{\gamma}}} \quad (5)$$

where  $\mathbf{u}$ ,  $\rho$ ,  $p$ ,  $\eta$ ,  $\underline{\underline{\dot{\gamma}}}$ ,  $\mathbf{g}$ ,  $C_p$ ,  $T$ ,  $k$  denote the velocity vector, density, pressure, non-Newtonian viscosity, strain rate tensor, body force vector, specific heat, temperature and thermal conductivity respectively.

During packing phrase, the melt compressibility and no longer be neglected, the governing equations for the compressible flow during the packing phrase are giving as follows:

$$-\nabla \cdot \mathbf{u} = \alpha \left( \frac{\partial p}{\partial t} + \mathbf{u} \cdot \nabla p \right) - \beta \left( \frac{\partial T}{\partial t} + \mathbf{u} \cdot \nabla T \right) \quad (6)$$

$$0 = -\nabla p + \nabla \cdot \left( 2\eta \underline{\underline{\dot{\gamma}}} - \frac{2}{3} \eta I \nabla \cdot \mathbf{u} \right) \quad (7)$$

$$\rho C_p \left( \frac{\partial T}{\partial t} + \mathbf{u} \cdot \nabla T \right) = \nabla \cdot (k \nabla T) + \beta T \left( \frac{\partial p}{\partial t} + \mathbf{u} \cdot \nabla p \right) + 2\eta \underline{\underline{\dot{\gamma}}} : \underline{\underline{\dot{\gamma}}} \quad (8)$$

Where  $I$  is the identity matrix,  $\alpha = \frac{1}{\rho} \left( \frac{\partial \rho}{\partial p} \right)_T$  is compressibility coefficient, and  $\beta = \frac{1}{\rho} \left( \frac{\partial \rho}{\partial T} \right)_p$  is the thermal expansion coefficient.

#### 4. Open challenges and future works

After the development in the last two decades, the modelling and simulation of micro injection molding process have been improved so decently that many meaningful results obtained are able to guide the real process optimization, micro parts design and tool constructions. However, the limits in the knowledge of microfluidics are restricting the further promotion of the simulation for micro injection molding process, which can be summarized as the following:

- The heat transfer ratio during the filling stage of polymer melts in micro injection molding process is extremely high than conventional case due to the high surface-volume ratio of micro cavity. Therefore, comprehensive understanding of the heat transfer phenomena in micro-scale is necessary for predicting the phase change and morphology evolution during the melts fill into the cavity;
- The interaction correlation between polymer molecules and micro dimensional geometry is inadequate investigated, which is related to rheological and morphological properties of polymer melts in micro injection molding process. Without correct and

precise description in these two properties, the filling process simulation cannot be processed in close- real way;

- The warpage and shrinkage analysis by micro injection molding simulations is still performed by traditional theoretical models, however the difference of thermal history and morphology development between micro and conventional injection molding process definitely will cause the totally deferent resulting shrinkage and inner residual stress distribution which is associated with mechanical properties prediction for micro injection molding parts in the following steps.

## 5. Acknowledgement

The authors would like to thank German Research Foundations (DFG) for financing support of the related works in this chapter.

## 6. References

- Despa M S, Kelly K W & Collier J R. (1998) Injection molding using high aspect ratio microstructures mold inserts produced by LIGA techniques. *Proc. SPIE*. Vol. 3512, PP. 286-294, ISBN-10: 0819429716, 21<sup>st</sup>. Sep., Santa Clara, CA, USA
- Despa M. S., Kelly K. W. & Collier J. R. (1999) Injection molding of polymeric LIGA HARMS, *Microsyst. Technol.* vol. 6, No.2, pp. 60-66, ISSN 0946-7076
- Heckele M & Schomburg WK (2004), Review on micro molding of thermoplastic polymers, *J. Micromech. Microeng.*, Vol 14, PP.1-14, ISSN 1361-6439
- Hieber C A & Shen S F (1982) A finite-element/finite-different simulation of the injection-molding filling process *J. Non-Newtonian Fluid Mech.* Vol.7, pp. 1-32, ISSN 0377-0257
- Hu X., Ding Z.& Lee L. J. (2005) Simulation of 2D Transient Viscoelastic Flow Using the CONNFESSIT Approach, *Journal of Non-Newtonian Fluid Mechanics*, Vol. 127, pp. 107-122, ISSN 0377-0257
- Hu X., Liu C., Xu G. & Lee L. J., (2007) Viscoelastic Flow in Micro-Injection Molding, *SPE ANTEC 2007*, V. 53. pp. 1612-161
- Hung W.N.P., Ngonthai Y., Yuan S., Lee C.W., and Ali M.Y. (2001) Micromolding of three-dimensional components. *The 10th International Conference on Precision Engineering*, PP.142-146, ISBN 792-37414-2, July 18-20,2001, Yokohama, Japan.
- Kemmann O, Weber L, Jeggy C & Magotte O. (2000) Simulation of the Micro Injection Molding Process. *Proceedings of the Annual Technical Conference, (ANTEC 2000)*, PP.576-580, ISBN 1566768551, Orlando, FL, USA.
- Krieger, I.M. (1972) Rheology of monodisperse lattices. *Adv. Colloid Interface Sci.*, Vol.3, pp. 111-136, ISSN 0001-8686.
- Liou A. C. & Chen R. H., (2006) Injection molding of polymer micro- and sub-micron structures with high aspect ratios *Int. J. Adv. Manuf. Technol.* Vol 28, PP.1097-1103, ISSN 0268-3768
- Madou M. J. (1997) *Fundamentals of Microfabrication*, ISBN 9780849308260, CRC Press, Boca Raton, FL, U.S.A.
- Madou M. J. (2002) *Fundamentals of Microfabrication: The Science of Miniaturization, 2nd ed.* ISBN-10: 0849308267, CRC Press, Boca Raton, FL, U.S.A.

- Martyn M T, Whiteside B, Coates P D, Allan P S, Greenway G & Hornsby P, (2003) Micromoulding: consideration of processing effects on medical materials, *SPE ANTEC Proc.* pp. 2582-2586
- Mekaru H, Yamada T, Yan S & Hattori T., (2004) Microfabrication by hot embossing and injection molding at LASTI, *Microsyst. Technol.* Vol10, PP.682-688, ISSN 0946-7076
- Moguedet M., Le Goff R., Namy P. & Béreaux Y. (2009) Level Set Method for Fully Thermal-Mechanical Coupled Simulations of Filling in Injection and Micro-Injection molding Process, *Proceedings of the COMSOL Conference 2009*, Milan, Italy
- Pal, P. & Sato, K. (2009) Silicon microfluidic channels and microstructures in single photolithography step, *Design, Test, Integration & Packaging of MEMS/MOEMS '09. Symposium*, PP.419-423, ISBN 978-2-35500-009-6, 2009,1-4, April, Rome, Italy
- Phillips, R.J.; Armstrong, R.C.; Brown, R.A.; Graham, R.L.; Abbott, J.R. (1992) A constitutive equation for concentrated suspensions that accounts for shear induced particle migration. *Phys. Fluids*, A 4, pp. 30-40, ISSN 1070-6631.
- Piotter V. et al. (2002) Performance and simulation of thermoplastic micro injection molding, *Microsyst. Technol.* vol. 8, No.6, pp. 387-390, ISSN 0946-7076
- Piotter V. et al., (2007) Micro injection moulding: special variants and simulation. *MiNaT :Internat.Fachmesse und Kongress für Feinwerktechnik, Ultrapräzision, Micro- und Nano-Technologien*, Stuttgart, 11.-15.Juni 2007
- Schift H, David C, Gabriel M, Gobrecht J, Heyderman L J, Kaiser W, Koepfel S & Scandella L., (2000) Nanoreplication in polymers using hot embossing and injection molding, *Microelectron. Eng.* Vol 53, PP.171-174, ISSN 0167-9317
- Shen Y. K., Chih-Yuan Chang, Yu-Sheng Shen, Sung-Chih Hsu & Ming-Wei Wu, (2008) Analysis for microstructure of microlens arrays on micro-injection molding by numerical simulation, *Int. Comm. Heat Mass Transfer*, Vol 35, No.6, PP. 723-727, ISSN 0735-1933
- Shen Y.K., Yeh S.L. & Chen S.H. (2002) Three-dimensional non-Newtonian Computations of Micro-Injection Molding with the Finite Element Method. *Int. Comm. Heat Mass Transfer*, Vol 29, No.5, PP. 643-652, ISSN 0735-1933
- Shi F, Zhang X, Li Q & Shen C Y. (2010) Particle tracking in micro-injection molding simulated MIS, *Computer Engineering and Technology (ICCET), 2010 2nd International Conference*, PP.313-317, Vol.5, ISBN: 978-1-4244-6347-3, 16-18 April 2010, Chendu, China
- Spatz Joachim P. (2005) Bio-MEMS: Building up micromuscles, *Nature Materials*, Vol 4, PP 115-116, ISSN 1476-1122
- Su Y C, Shah J & Lin L W, (2004) Implementation and analysis of polymeric microstructure replication by micro injection molding, *J. Micromech. Microeng.*, Vol 14, PP.415-4, ISSN 1361-6439
- Wallrabe U. et al (2002) Micromolded easy-assembly multi fiber connector: RibCon, c
- Wilson K., Molnar P. & Hickman J. (2007) Integration of functional myotubes with a Bio- MEMS device for non-invasive interrogation, *Lab on a Chip*, Vol 7, PP 920-922, ISSN 1473-0197
- Xie L, Ziegmann G & Jiang B Y, (2009) Numerical simulation method for weld line development in micro injection molding process, *Journal of Central South University of Technology*, Vol. 16, Nr. 5, pp. 774-780, ISSN 1005-9784
- Yao D. & Kim B. (2002) Injection molding high aspect ratio microfeatures, *J. Injection Molding Technol.* Vol 6, PP.11-17, ISSN 1533-905X

- Yu L. Y. (2004) *Experimental and numerical analysis of injection molding with micro features*, PhD Dissertation, Ohio State University, Ohio, U.S.A.
- Yu, Liyong, Lee, L. James & Koelling, Kurt W.(2004) Flow and heat transfer simulation of injection molding with microstructures, *Polymer Engineering and Science*, Vol 44, PP.1866–1876, ISSN1548-2634

# Simulation of Liquid Flow Permeability for Dendritic Structures during Solidification Process

S. M. H. Mirbagheri, H. Baiani, M. Barzegari and S. Firoozi  
*Amirkabir University of Technology*  
Iran

## 1. Introduction

Alloy solidification is a two stage process, which starts by nucleation and ends by growth of solid phases. Subsequently, number, distribution and morphology (dendritic or non-dendritic) of the grains are formed during the solidification. Some critical defects such as micro/macro segregation, micro/macro porosities and micro/macro shrinkage take place in the solidification stage. The micro-defects are located in the interdendritic space, which are micro-channels that fluid flow through them in the last stage of the solidification. Herein, the region in the grain growth stage is introduced as a mushy zone (or porous media), where the solid phase is constantly progressing; and the ability of fluid to flow into the mushy zone is known as permeability of interdendritic liquid. Therefore, formation of the micro-defects depends on controlling of the permeability factor. In a great number of studies micro/macro solidification models have been simulated based on the permeability factor using Darcy's law (Ganesan & Poirier, 1990; Nandapurkar et al., 1991; Poirier, 1987; Worster, 1991).

Interdendritic flow, in many CFD documents, is described using Darcy's law, which relates the fluid flow rate to the pressure gradient, fluid viscosity, and permeability of the porous medium. To obtain an expression for the permeability as a function of the porosity of the porous medium, one generally considers flow through an idealized medium geometry, since it is impractical to solve the flow equations for the complex flow between the particles. Fig. 1 presents two viewpoints for investigation of the permeability in the porous media: metallurgical view and non-metallurgical (or common) view.

As shown in Fig. 1a two of the most commonly used geometries for analytical models are capillaries (Carman, 1937; Chen et al. 1995; Williams et al., 1974) and an array of spaced particles. A more realistic approach will be introduced that assumes geometry of a periodic or random array of cylinders. Since it is not possible to solve analytically for this type of flow over the full range of porosities, two limiting closed form solutions are used for lubrication and point-particle (dilute) models in low and high porosities, respectively. Analysis of permeability for Stokes flow through periodic arrays of cylinders were done by Sangani & Acrivos (1982), Sparrow & Loefler (1959) and, Larson & Higdon (1986).

The effect of fluid inertia on pressure drop required to drive the flow is a function of Reynolds number. Several authors computed the fluid flow through periodic arrays of

cylinders as the function of Reynolds numbers for three ranges of low, moderate, and high Reynolds number (Cai & Berdichevsky, 1993; Edwards et al., 1990; Eidsath et al., 1983; Ghaddar, 1995; Koch & Ladd, 1997; McCartney, 1994; Nagelhout et al., 1995; Sangani & Mo, 1994; Sangani & Yao, 1988; Thom & Aplelt, 1961). Particularly noteworthy is the work of Koch & Ladd (1997) for modeling permeability and drag force based on Reynolds number using a Lattice-Boltzmann formulation. Also McCartney (1994) calculated the permeability in the range of low Reynolds numbers up to about 150 by Lattice Gas Cellular Automat (LGCA) model.

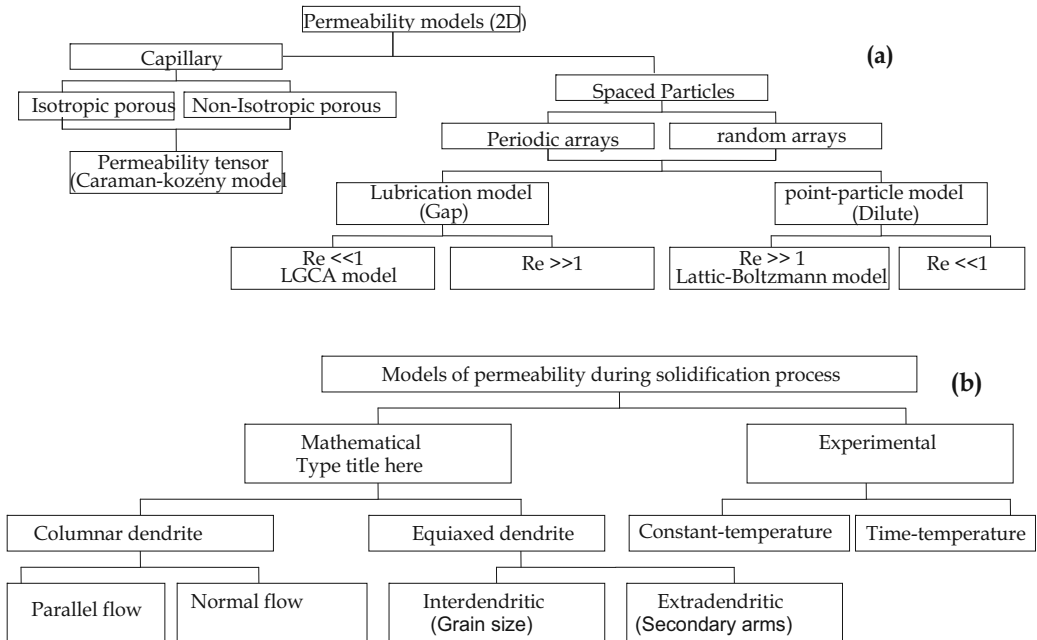


Fig. 1. Two categories of permeability models; a) Common permeability model; b) Metallurgical permeability model (solidification)

In the field of metallurgy, however, the models mentioned above had an important application in the mathematical modeling of flow through arrays of dendrites during the solidification of mushy alloys. Fig. 1b shows a schematic category for modeling of permeability during solidification process. There are many investigations for experimental measuring of permeability by variant methods during solidification process (Apelian et al., 1974; Duncan et al., 1999; Murakami et al., 1984; Murakami et al., 1983; Nielsen et al., 2001; Poirier & Ocansey, 1993; Streat & Weinberg, 1976). However, most of the experimental methods had two goals; 1) an experimental goal is to measure the permeability of an alloy at a constant temperature and to correlate the permeability with microstructures quantities. In this case, it is necessary to obtain a quantitative stereological characterization of the solid-phase morphology. This has been achieved by quenching of the mushy sample during the permeability experiment and subsequent metallography and image analysis, which distinguish between the phases that were solid and liquid during the experiment. 2) Another experimental goal is to measure the

permeability and the temperature of an alloy during solidification/re-melting and to correlate the permeability with the solid fraction, which can be estimated from the temperature-time curves. In this case, the composition of the interdendritic liquid varies throughout the experiment, which complicates the experimental design, the experiment method, and the data analysis (Nielsen et al., 2001).

The mathematical method includes two categories; 1) flow through a network of equiaxed grains, 2) flow through columnar dendrite networks with flows parallel and normal to the primary dendrites.

Piwonka & Flemings (1966), Apelian et al. (1974), Streat & Weinberg (1976), Liu et al. (1989) and Murakami et al. (1984) reported the permeability in equiaxed dendritic structures. In these investigations, however, the microstructural length scales were not reported or they could not be used to estimate permeability in a solidification model designed to calculate macro segregation. Ganesan & Poirier (1990) and Ocansey & Poirier (1993) measured and reported the permeability with inverse of the specific area of the solid selected as the length scale in equiaxed microstructures based on Kozeny-Carman model. There are at least two length scales associated with equiaxed dendritic solidification: the secondary dendrite arm spacing (or interdendritic flow) and the grain size (or extra-dendritic flow) (de Groh et al., 1993; Wang et al., 1995). Brown et al. (2002) developed a numerical model for the simulation of 3D flow through equiaxed dendrites of an Al13Cu3Si alloy and the determined the variation in permeability of structure as solidification progressed. The model involved the evolution of an equiaxed dendrite and the application of a CFD program to calculate permeability from Darcy's law.

Streat & Weinberg (1976), Poirier (1987), Ganesan & Poirier (1990), Nandapurkar et al. (1991) Worster (1991) reported the permeability in columnar dendritic structures for macroscopic scale. However, due to the very complex microstructure of the dendrites, permeability determination still remains a challenge. Indeed, the dendritic columnar region is characterized, first, by a strong anisotropy, which requires knowledge of the different components of the permeability tensor (Murakami et al., 1984; Murakami et al., 1983; Poirier, 1987) and, second, by the non-uniform macroscopic properties such as the liquid volume fraction, which continuously varies from unity in the melt to zero in the solid region. Ganesan et al. (1992) showed that the permeability for a flow parallel to primary dendritic arms is hardly dependent on the secondary dendrite arm spacing. In the columnar configuration, data in different dendritic structures have been summarized by Poirier (1987) and quantitative relationships for parallel and normal permeability have been derived using a regression analysis. In the range of liquid fraction considered ( $>0.66$ ) the regressions were in good agreement with the classical physical models, but the extrapolation beyond the upper limit failed. Numerical experiments for parallel and normal flow to the primary dendritic arms in columnar structures with a high liquid volume fraction ( $>0.6$ ) have been found to be more successful (Ganesan et al., 1992). Mirbagheri (2008; Mirbagheri & Khajeh, 2008) measured and simulated interdendritic flow for mushy alloy based on permeability factor and modeled some micro structural factors on the mushy alloys permeability. Bhat et al. (1995) calculated from digitized images, the permeability for flow normal to primary dendrite arm using a Navier-Stokes finite element solver.

As mentioned above, permeability for flow through transverse sections of columnar-dendritic alloy have modeled as flows through array of circles, rhombi, cruciform and schematic dendrites. These models used surface area to volume ratio of the solid for

normalizing permeability without predicting the effect of protuberance and radius of dendrite for a fixed fraction of solid as well the effect of angle of dendrite radius via liquid streamlines. In spite of these valuable researches in this field, determination of dendritic structural permeability due to the complex microstructure of the dendrites still remains a challenge in both fields of mathematical and experimental methods.

In this chapter, a numerical model has been introduced for determination of liquid flow permeability through dendritic solid phases during growth. The model includes three stages; first, numerical simulation of nucleation and growth of the equiaxed grains using a novel Cellular Automation Finite Difference (CAFD) method, and second, numerical simulation of micro fluid flow for interdendritic liquid alloys using Computational Fluid Dynamics (CFD) technique, and third, calculation of permeability based on Darcy's law by the pressure and velocity results of CFD code. Finally determining and modeling the permeability variations versus the cooling rate and the solidification rate during growth. This model can be linked as a module into a commercial macro fluid flow code in order to predict the micro-defects such as the micro porosities, shrinkages or micro-segregations.

## 2. Computation models

In the present work, two separate computation models of the nucleation and grain growth, and interdendritic liquid flow have been developed and coupled for modeling of permeability in mushy alloys.

This is achieved by combining sub-models for each of these processes, i.e., computation of nucleation and grain growth by using the CAFD, and the micro fluid flow by using the CFD model for calculation of the interdendritic permeability. The governing equations are described in details in the next sections.

### 2.1 Solid phase generation code

The solid phase generation code, which has been developed in this investigation is based on the CA and KGT model (Atwood & Lee, 2000; Lee et al., 2001). In other words, the solidification model is non-constrained nucleation and growth. The model comprises of: 1) Stochastic grain density based on local under-cooling, and 2) grain growth based on local thermal and under-cooling (Kurz et al., 2001; Kurz et al., 1986). However, in the present work, for a binary alloy system (Fig. 2) in the mushy zone, it is assumed that there is no constitutional under-cooling during growth phenomenon. Number, distribution, and morphology of nuclei as well as the growth rate are controlled by only thermal under-cooling, which is produced by Newtonian's heat transfer in a two dimensional (2D) space. In this condition, at the beginning, all the liquid have the same under-cooling (i.e., the gradient of the under-cooling or temperature is equal to zero). As shown in Fig. 3, once the nucleation takes place, temperature around of the nuclei is raised, because of the liberation of latent heat. Therefore, the temperature gradient around of the grains is negative.

After the solidification, the microstructure of the solidified alloy will consist of fully equiaxed grains and no columnar grains. Therefore, in this investigation, initial and boundary conditions for the simulation of heat transfer and liquid flow are based on the non-constrained solidification.



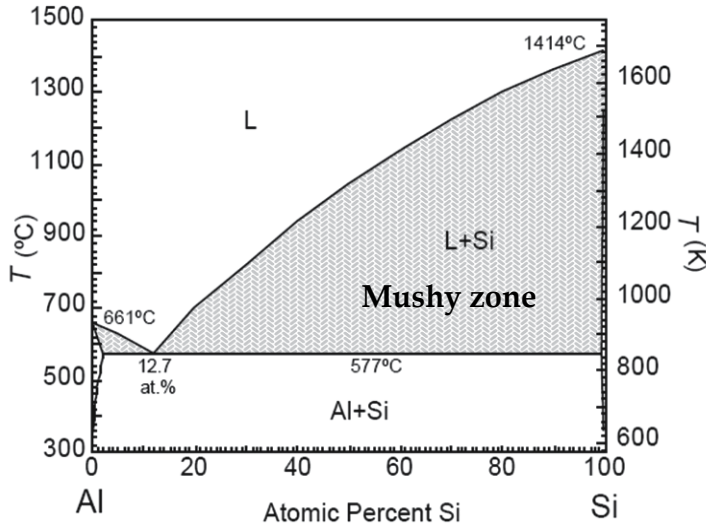


Fig. 2. Phase diagram of an Al-Si binary alloy system. The regions between the liquidus and the solidus temperatures are the mushy zone

### 2.1.1 Governing equations

#### i. Heat transfer equations

In solidification process, there are two terms of heat transfer and latent heat ( $H_f$ ). Interaction of these two terms affects the domain of thermal distribution. The heat transfer equation for the mushy zone may be written as:

$$\rho C_p \frac{\partial T}{\partial t} = \nabla \cdot (K \nabla T) + \rho H_f \frac{\partial f_s}{\partial t} \quad (1)$$

$$f_s = \frac{T_{liq} - T}{T_{liq} - T_{sol}} \quad (2)$$

where  $\rho$ ,  $C_p$  and  $K$  are the density, heat capacity and thermal conductivity, respectively;  $f_s$  is solid fraction and  $T_{sol}$ ,  $T_{liq}$  are solidus and liquidus temperature, respectively.  $\rho H_f (\partial f_s / \partial t)$  is the heat source term, which is a function of temperature in the mushy zone, and is written as follows:

$$\rho H_f \frac{\partial f_s}{\partial t} = \rho H_f \left( \frac{\partial f_s}{\partial T} \right) \left( \frac{\partial T}{\partial t} \right) \quad (3)$$

By differentiating Eq. 2, and substitution in Eq. 3:

$$\rho H_f \frac{\partial f_s}{\partial t} = \rho H_f \frac{\partial f_s}{\partial T} \frac{\partial T}{\partial t} = \rho H_f \left( \frac{-1}{T_{liq} - T_{sol}} \right) \left( \frac{\partial T}{\partial t} \right) \quad (4)$$

The fraction of solid in the mushy zone is estimated by Eq. 2. The release of latent heat between liquidus and solidus temperature is calculated by substituting Eq. 4 into the second term of Eq. 1. Therefore heat transfer equation is given by:

$$\rho \left[ C_p - H_f \left( \frac{-1}{T_{liq} - T_{sol}} \right) \right] \frac{\partial T}{\partial t} = \nabla \cdot (K \nabla T) \quad (5a)$$

$$\rho [C_p^{eq}] \frac{\partial T}{\partial t} = \nabla \cdot (K \nabla T) \quad (5b)$$

where  $C_p^{eq}$  can be considered as a quasi-specific heat given by:

$$C_p^{eq} = \left[ C_p - H_f \left( \frac{-1}{T_{liq} - T_{sol}} \right) \right] \quad (6)$$

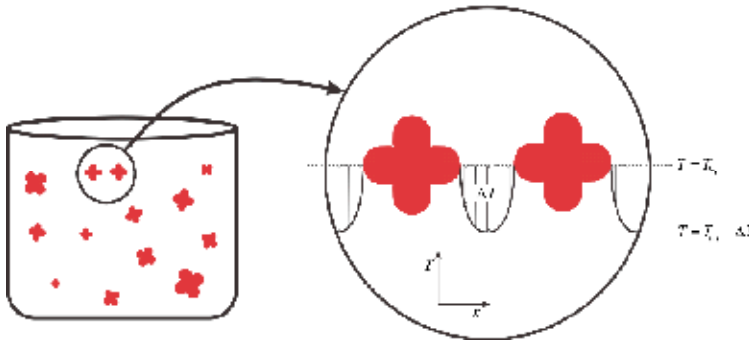


Fig. 3. Temperature distribution around the grains

Physical properties of the liquid and solid are assumed to be constant above  $T_{liq}$  and below  $T_{sol}$ , respectively. However, in the mushy zone, coefficients of heat conductivity and thermal capacity are presented as  $k_{mu} = f_L k_L + f_S k_S$ , and  $C_p^{mu} = f_L C_p^L + f_S C_p^S$  (Mirbagheri & Silk, 2007). In a case that the alloy composition has no solidification range (i.e.,  $\Delta T^0 = T_{liq} - T_{sol} = 0$ ), such as eutectic composition, the right hand side in Eq. 4 approaches infinity and as a result, a virtual solidification range of 0.1-1 °C is assumed.

#### ii. Nucleation equations

When the temperature falls below the liquidus temperature, nucleation begins. In this condition the number of nuclei at each temperature and time are calculated from Eq. 7, as follows:

$$N_s = N_{total} \exp \left( \frac{C_m T_{liq}^2}{T (T_{liq} - T)^2} \right) \quad (7)$$

After determining the number of nuclei in each time step, by assigning a random distribution function, nuclei are distributed in the liquid domain. In the next step, the latent heat of solidification is calculated to adjust the temperature.

#### iii. Growth equations

The final stage of solidification process is the growth simulation. As mentioned before, once a negative temperature gradient is present in liquid adjacent to the grains, equiaxed grains grow as shown in Fig 3. The direction of primary arms of the equiaxed dendrites depend on

crystal structure. Here, a B.C.C. crystal structure is assumed, in which each equiaxed dendrite has four perpendicular primary arms in 2D space, where they can grow in 48 crystalline directions (An et al., 2000). In order to simulate the morphology of the growth, a simple shape was used for grains based on Eq. 8 in polar coordinates.

$$r = R_d + P_d \cos(4(\theta + \theta_0)) \quad \text{if} \quad 0 < \frac{P_d}{R_d} < 1 ; \quad (R^*) < h \quad R^* = R_d + P_d \quad (8)$$

Fig. 4 shows a “cloverleaf” morphology for a dendrite section created based on Eq. 8, where  $P_d$  is perturbation,  $R_d$  radius of spherical nuclei prior to perturbation, and  $\theta$  angle between primary arm direction and stream line.

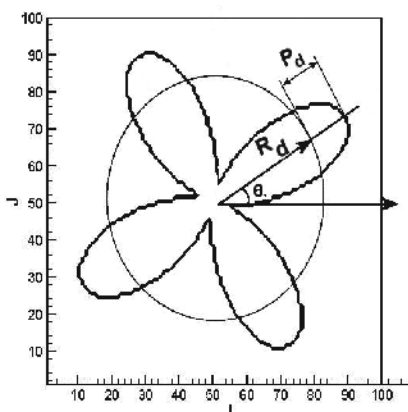


Fig. 4. Shape of a nucleus at the beginning of the growth

A function (Eq. 9) needs to be defined for the dendrites radius growth rate ( $dr$ ), which is added to the surface of existing grains in each time step of solidification stage.

$$r_{new} = r_{old} + dr ; \quad dr = \frac{df_s}{2\pi \sum r} \quad (9)$$

Finally, results of nucleation and growth simulation at each  $df_s$ , is used in the CFD code to calculate the permeability in domain.

### 2.1.2 CA-FD model

#### i. CA-FD model

The finite difference approximation of heat transfer equation is:

$$T_{i,j}^{n+1} = T_{i,j}^n - \Delta t \{ (UTX + VTY) + (DQX + DQY) \} \quad (10)$$

where UTX, DTXL, DTXR and DQX are defined as followed:

$$UTX = 0.5 \{ (1 + \alpha) U_{i-1,j} (DTXL) + (1 - \alpha) U_{i,j} (DTXR) \}$$

$$DTXL = \frac{T_{i,j} - T_{i-1,j}}{\Delta x} \quad DTXR = \frac{T_{i+1,j} - T_{i,j}}{\Delta x} \quad DQX = \frac{QXR - QXL}{\rho C_P \Delta x}$$

The terms of VTY and DQY are found in a similar way to UTX and DQX, respectively. If cells (i, j) and (i+1, j) are liquid:

$$QXR = -k_R \frac{T_{i+1,j}^n - T_{i,j}^n}{\Delta x}, \quad QXL = -k_L \frac{T_{i,j}^n - T_{i-1,j}^n}{\Delta x}$$

$K_R$  and  $K_L$  are thermal conductivity and found through the following equations:

$$K_R^{-1} = 0.5 \left( \frac{1}{k_{i,j}} + \frac{1}{k_{i+1,j}} \right), \quad K_L^{-1} = 0.5 \left( \frac{1}{k_{i,j}} + \frac{1}{k_{i-1,j}} \right)$$

If cell (i, j, k) contains a mixture of solid and liquid metal, the thermal conductivity of this cell is:

$$k_{i,j} = F_{S_{i,j}} k_{S_{i,j}} + F_{L_{i,j}} k_{L_{i,j}}, \quad F_{S_{i,j}} + F_{L_{i,j}} = 1$$

$$F_{L_{i,j}} = \frac{T_{i,j} - T_s}{T_l - T_s}; \quad T_s \leq T \leq T_l$$

In the freezing range the specific heat and liquid fraction of the mushy metal is found through the following equation:

$$C_p^{LS} = \frac{\Delta H_f}{T_l - T_s}; \quad T_s < T < T_l \quad (11)$$

where  $T_s$ ,  $T_l$  are solidus and liquidus temperatures respectively. In finite difference form,  $C_p$  is calculated as follows:

$$C_p = C_p^L; \quad T_{i,j}^n > T_{i,j}^{n+1} > T_l \quad (12a)$$

$$C_p = C_p^S; \quad T_{i,j}^{n+1} > T_{i,j}^n > T_s \quad (12b)$$

$$C_p = C_p^L \frac{T_{i,j}^n - T_l}{T_{i,j}^n - T_{i,j}^{n+1}} + C_p^{LS} \frac{T_l - T_{i,j}^{n+1}}{T_{i,j}^n - T_{i,j}^{n+1}}; \quad T_{i,j}^n > T_l > T_{i,j}^{n+1} > T_s \quad (12c)$$

$$C_p = C_p^{LS} \frac{T_{i,j}^n - T_s}{T_{i,j}^n - T_{i,j}^{n+1}} + C_p^S \frac{T_s - T_{i,j}^{n+1}}{T_{i,j}^n - T_{i,j}^{n+1}}; \quad T_l > T_{i,j}^n > T_s > T_{i,j}^{n+1} \quad (12d)$$

It should be noted that iteration is required here, because not only does  $T_{i,j}$  depends on  $C_p$ , but also  $C_p$  depends on  $T_{i,j}$ .

## ii. Direction of crystalline growth

For a solidifying cell, as the solid fraction within the cell becomes greater than zero, the local temperature of the particles is obtained using the phase diagram and the under-cooling is calculated accordingly. In each solidifying cell, the change in solid fraction is primarily determined by KGT model (Kurz et al., 1986), which calculates the maximum growth rate based on a given under-cooling at near absolute stability limit. The solid fraction is further corrected by diffusion-controlled growth once the solid fraction reaches a critical value; it

can grow into its neighboring liquid cells, providing the cells are under-cooled. Where the solid fraction of cells approaches unity, the cell is considered as fully solidified and the grain growth ends. A captured liquid cell by a growing neighboring cell is assigned the same grain orientation as its growing neighbor (Lee et al., 2001). Fig.5 shows the CA-FD algorithm of heat transfer during nucleation and growth

## 2.2 Inter-dendritic liquid flow code

### 2.2.1 Governing equations

#### i. Fluid flow equations

The Navier-Stokes and continuity equations are used to simulate flow of the interdendritic liquid through the network of dendritic solids. The Navier-Stokes equation for the incompressible liquid is given by the following equation (Bahat et al., 1995):

$$\rho_L \frac{D\vec{V}}{Dt} = -\nabla P + \rho_L \vec{g} + \mu \nabla^2 \vec{V} \quad (13)$$

Also, the mass continuity equation for the incompressible liquid is as follows:

$$\frac{\partial \rho}{\partial t} + \vec{\nabla} \cdot (\rho \vec{V}) = 0 \quad (14)$$

It is often desirable to reproduce large scale physical experiments in scaled-down and more manageable laboratory settings. Information on the flow is contained in the parameters which characterize it, such as dynamic viscosity, velocity and density. If these parameters are combined in a suitable way to yield dimensionless quantities, then these enable one to make the desired statements relating the flows on the large and small scales. By introducing the following dimensionless variables (Griebel et al., 1998):

$$\bar{x}^* = \frac{\bar{x}}{L}, \quad t^* = \frac{u_\infty t}{L}, \quad \bar{u}^* = \frac{\bar{u}}{u_\infty}, \quad \bar{g}^* = \frac{L}{u_\infty^2} \bar{g}, \quad p^* = \frac{p - p_\infty}{\rho_\infty u_\infty^2}, \quad \text{and} \quad \text{Re} = \frac{\rho_\infty u_\infty L}{\mu}$$

Navier-Stokes equation can be rewritten as the dimensionless form:

$$\frac{D\vec{V}}{Dt} = -\nabla P + \vec{g} + \frac{1}{\text{Re}} \nabla^2 \vec{V} \quad (15)$$

Thus by solving Eqs. 16a, 16b and 16c, one can get the, velocity and pressure fields for an incompressible viscous fluid:

$$\frac{\partial u}{\partial t} + \frac{\partial p}{\partial x} = \frac{1}{\text{Re}} \left( \frac{\partial^2 u}{\partial x^2} + \frac{\partial^2 u}{\partial y^2} \right) - \frac{\partial(u^2)}{\partial x} - \frac{\partial(uv)}{\partial y} + g_x \quad (16a)$$

$$\frac{\partial v}{\partial t} + \frac{\partial p}{\partial x} = \frac{1}{\text{Re}} \left( \frac{\partial^2 v}{\partial x^2} + \frac{\partial^2 v}{\partial y^2} \right) - \frac{\partial(uv)}{\partial x} - \frac{\partial(v^2)}{\partial y} + g_x \quad (16b)$$

$$\frac{\partial u}{\partial x} + \frac{\partial v}{\partial y} = 0 \quad (16c)$$

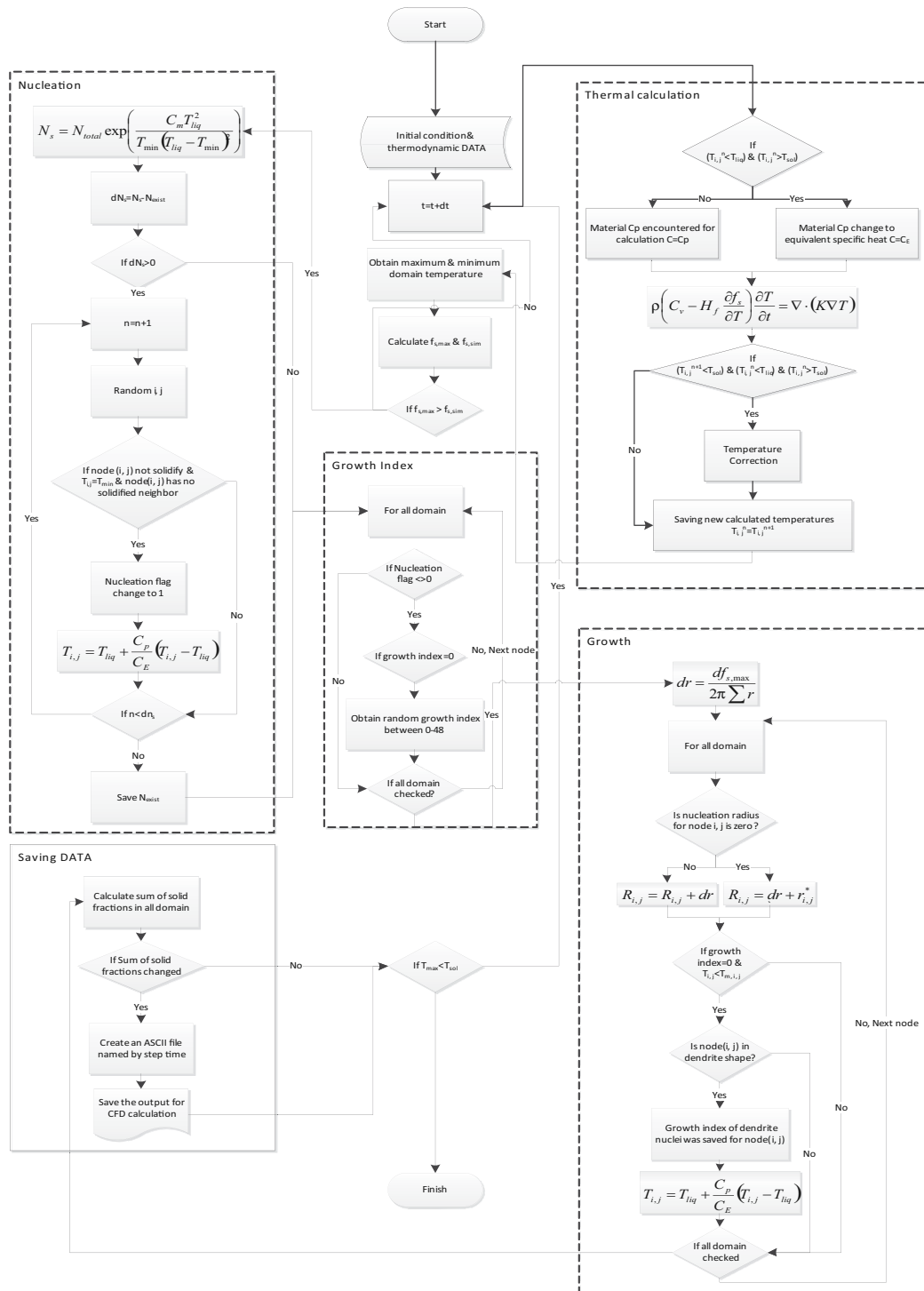


Fig. 5. CA-FD algorithm of heat transfer during nucleation and growth

Equation 15 can be written as two independent equations based on projection model as follows:

$$\frac{\partial(\delta\bar{V})}{\partial t} + \bar{V} \cdot \nabla \bar{V} = \frac{1}{\text{Re}} \nabla^2 \bar{V}; \quad \delta\bar{V} = V^* - \bar{V} \quad (17a)$$

$$\frac{\partial(\delta\bar{V})}{\partial t} + \nabla P = 0 \quad (17b)$$

Equation 17a is independent of pressure and by using the Poisson's equation (Eq. 18) the Navier-Stokes equation is solved implicitly.

$$\nabla^2 P = \frac{1}{\Delta t} \nabla \cdot V^* \quad (18)$$

After solution of the Navier-Stokes equations, the pressure and velocity fields can be calculated to obtain the permeability of the mushy zone in each growth sequence.

#### ii. Permeability equations

Permeability is a measure of the ability of a porous material to transmit fluids. Darcy's law is a simple proportional relationship between the instantaneous discharge rate through a porous medium ( $V$ ), the viscosity of the fluid ( $\mu$ ) and the pressure drop over a given distance. The law was formulated by Henry Darcy based on the results of experiments on the flow of water through beds of sand (Darcy, 1856).

$$V = -\frac{K}{\mu} \nabla P \quad (19)$$

where,  $K$  is permeability. The problem with this law is that it is not valid at high Reynolds number. As the velocity increases, inertia effects appear, which complicates the calculation of permeability. To overcome this weakness, several corrections have been applied to the Darcy's law by various researchers. In this investigation, the effective Darcy's law equation was used for calculation of permeability (Eq. 19).

$$V = -\frac{K}{\mu f_i} \nabla P \quad (19)$$

### 2.2.2 Numerical solution of the fluid flow governing equations

The main purpose of the permeability simulation in the solidification process is calculating the velocity profile for inter-dendritic space during equiaxed grains growth. Therefore, governing equations are solved by FDM. The numerical solution method can be considered in four steps: i) Meshing of the system, ii) Converting differential equations to finite difference approximation, iii) Solution of the finite difference approximations of momentum in order to calculate velocity profile, and iv) Calculation of permeability of the mushy zone by adding Darcy's law in each growth sequences.

#### i. Meshing

The computational domain is divided into a number of cells with  $\Delta X$ ,  $\Delta Y$  dimensions, and all cell dimensions are equal for all calculations. Curved boundaries of system are approximated by stepped boundaries. For example, if the solid phase fraction occupies more

than 0.9 volume of a cell, the cell is considered to be a complete solid cell. As shown in Fig. 6, domain is discretized as a staggered grid, i.e. the scalar and the vector variables are located at the centre and sides of the computational cell, respectively.

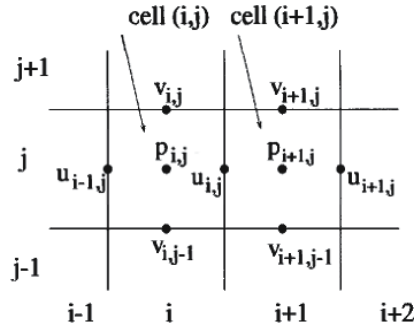


Fig. 6. Schematic of a staggered mesh and location of vector and scalar variables

The diffusive terms of the momentum equation is discretized using central differencing. The discretization of the convective terms of momentum equation has been done using the donor-cell scheme (Mirbagheri et al., 2003)

#### ii. Finite difference approximations

The finite difference approximation of momentum equations are:

$$U_{i,j}^{n+1} = U_{i,j}^n + \Delta t \left[ g_x - FUX - FUY + \frac{1}{\text{Re}} (VISX) \right] + \Delta t \left( \frac{P_{i,j}^{n+1} - P_{i+1,j}^{n+1}}{\Delta x} \right) \quad (20)$$

$$U_{i,j}^{n+1} = A_x^n + \Delta t \left( \frac{P_{i,j}^{n+1} - P_{i+1,j}^{n+1}}{\Delta x} \right)$$

$$V_{i,j}^{n+1} = V_{i,j}^n + \Delta t \left[ g_y - FVX - FVY + \frac{1}{\text{Re}} (VISY) \right] + \Delta t \left( \frac{P_{i,j}^{n+1} - P_{i,j+1}^{n+1}}{\Delta y} \right) \quad (21)$$

$$V_{i,j}^{n+1} = A_y^n + \Delta t \left( \frac{P_{i,j}^{n+1} - P_{i,j+1}^{n+1}}{\Delta y} \right)$$

$$A_x^n = U_{i,j}^n + \Delta t \left[ g_x - FUX - FUY + \frac{1}{\text{Re}} (VISX) \right] \quad (22)$$

$$A_y^n = V_{i,j}^n + \Delta t \left[ g_y - FVX - FVY + \frac{1}{\text{Re}} (VISY) \right]$$

$$FUX = \frac{U_{i,j}^n}{2\Delta x} [DUL + DUR + \alpha \text{Sign}(U_\alpha)(DUL - DUR)]$$

$$DUL = U_{i,j}^n - U_{i-1,j}^n ; DUR = U_{i+1,j}^n - U_{i,j}^n ; U_\alpha = (DUR + DUL) / 2$$



$$VISX = \left( \frac{U_{i+1,j}^n - 2U_{i,j}^n + U_{i-1,j}^n}{\Delta x^2} + \frac{U_{i,j+1}^n - 2U_{i,j}^n + U_{i,j-1}^n}{\Delta y^2} \right)$$

Other terms of the flux and the viscosity in x and y directions such as FUY, FVX, FVY, and VISY are obtained in a similar way as FUX and VISX terms, respectively. The finite difference approximation of Poisson's equation (Eq. 23) is

$$\frac{p_{i+1,j}^{n+1} - 2p_{i,j}^{n+1} + p_{i-1,j}^{n+1}}{(\delta x)^2} + \frac{p_{i,j+1}^{n+1} - 2p_{i,j}^{n+1} + p_{i,j-1}^{n+1}}{(\delta y)^2} = \frac{1}{\delta t} \left( \frac{A_{x,i,j}^n - A_{x,i-1,j}^n}{\delta x} + \frac{A_{y,i,j}^n - A_{y,i,j-1}^n}{\delta y} \right) \quad (23)$$

### iii. Solving and computing procedures

Various methods are available to adjust the pressure term in the Navier-Stokes equation (Hong, 2004; Versteeg & Malalasekera, 1995). Methods like SMAC (Amsden & Harlow, 1970) and SOLA (Hirt et al., 1975) use an explicit scheme to solve the pressure adjustment equation, which is based on divergence of pressure in each computational cell. The computational time are relatively long in these methods and are seldom used today due their low performance. Instead, other methods such as projection method are used to adjust the pressure term and compute new velocities that satisfy the continuity equation. Semi-implicit methods such as SIMPLE, SIMPLER and PISO are also frequently used (Versteeg & Malalasekera, 1995).

To solve the governing equations of fluid flow in a mushy zone for binary alloys, a new CFD code has been developed based on fundamentals presented by (Griebel, 2011). Therefore, to correct the pressures calculated from the Navier-Stokes momentum equation, the *Chorin's projection method* is used, and the resulting Poisson's equation is solved using Successive Over-Relaxation (SOR) iterative method.

Projection method uses an auxiliary velocity  $V^*$  to obtain a Poisson's equation for pressure. This equation can be solved using any solution algorithm such as the SOR or Gauss-Seidel methods. The momentum and continuity equations in time derivative form are:

$$\frac{V^{n+1} - V^n}{\Delta t} + V^n \cdot \nabla V^n + \nabla P^{n+1} = \frac{1}{Re} \nabla^2 V^n \quad (24)$$

$$\nabla V^{n+1} = 0 \quad (25)$$

The superscripts (n) and (n+1) denote old and new time level, respectively. In projection method  $V^{n+1}$  domain is calculated at each new time step. Using the auxiliary velocity, the momentum equation can be split to two independent equations with Eq. 26 with no pressure term and Eq. 27 with pressure term.

$$\frac{V^* - V^n}{\Delta t} + V^n \cdot \nabla V^n = \frac{1}{Re} \nabla^2 V^n \quad (26)$$

$$\frac{V^{n+1} - V^*}{\Delta t} + \nabla P^{n+1} = 0 \quad (27)$$

The divergence of Eq. 26 takes the form:

$$\frac{\nabla \cdot V^{n+1} - \nabla \cdot V^*}{\Delta t} + \nabla^2 P^{n+1} = 0 \quad (28)$$

Continuity equation (Eq. 25), requires that  $\nabla V^{n+1}$  to be zero, thus

$$\nabla^2 P^{n+1} = \frac{1}{\Delta t} \nabla \cdot V^* \quad (29)$$

The overall solution process is using Eq. 26 to obtain  $V^*$ , then to solving the Poisson's equation (Eq. 29) to find the adjusted pressure values and finally solving Eq. 27 to obtain  $V^{n+1}$ . Fig. 7 describes the algorithm used in the present code.

#### iv. Calculation of permeability

After obtaining the pressure and velocity fields, which is called herein as the temporary permeability subroutine, and using Darcy's law, coefficient of temporary permeability is calculated for domain in each solid fraction and their changes are saved until the end of solidification. This subroutine is showed at the lower part of the flowchart in Fig 7.

### 2.3 Validation of the present CFD code

The developed CFD code was validated by comparing the pressure gradient for an equiaxed grain with the Fluent code at the same initial and boundary condition. Fig. 8 shows four pressure fields adjacent to a single dendrite at solid fractions of 0.02, 0.08, 0.19, and 0.34, for and Al-6%wt.Si alloy. Fig. 9 shows comparison of the pressure gradient results between the present CFD code and the Fluent code based on data of Table 1. The CFD code predictions at high and low solid fractions are in good agreement with the corresponding Fluent code. Therefore, the present code could be valid for simulation of other domains.

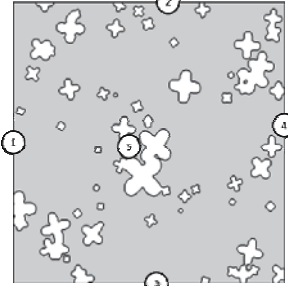
|   |   |
|---|---|
| Composition (%wt)                       | Al=92.50, Si=7.50   |
| Domain dimension (m)                    | $x = y = 1 \times 10^{-3}$  |
| Thermal conductivity (J/s.m.°C)         | $K_l = 121, K_s = 91$   |
| Heat of fusion (J/kg)                   | $\Delta H_f = 418600$   |
| Kinematic viscosity (m <sup>2</sup> /s) | $\nu = 2.3 \times 10^{-6}$  |
| Specific Heat (J/kg.°C)                 | $C_p^l = 963, C_p^s = 1084$   |
| Density (kg/m <sup>3</sup> )            | $\rho_L = 2385, \rho_S = 2605$  |
| Transformation temperature (°C)         | $T_L = 650, T_S = 577$  |
| Number elements of cavity               | $N = 40000$   |
| Dimension elements of cavity (cm)       | $\Delta X = \Delta Y = 5 \mu\text{m}$   |
| CPU time for Pentium IV (hr)            | 2   |
| Boundary condition at locations         |  <p>(1): Inlet<br/> (4): Outlet<br/> (2) and (3): Free-slip boundaries<br/> (5): No-slip boundaries for internal dendrites' surfaces<br/> No pressure gradient condition for all boundaries<br/> <math>U_{\text{Inlet}} = 0.16 \text{ mm/s}, V_{\text{Inlet}} = 0.</math><br/> Reynolds number (inlet) = 0.3</p> |

Table 1. Boundary conditions, thermo-physical properties, and initial condition for Fig 8 and Fig 10 to 13 domains

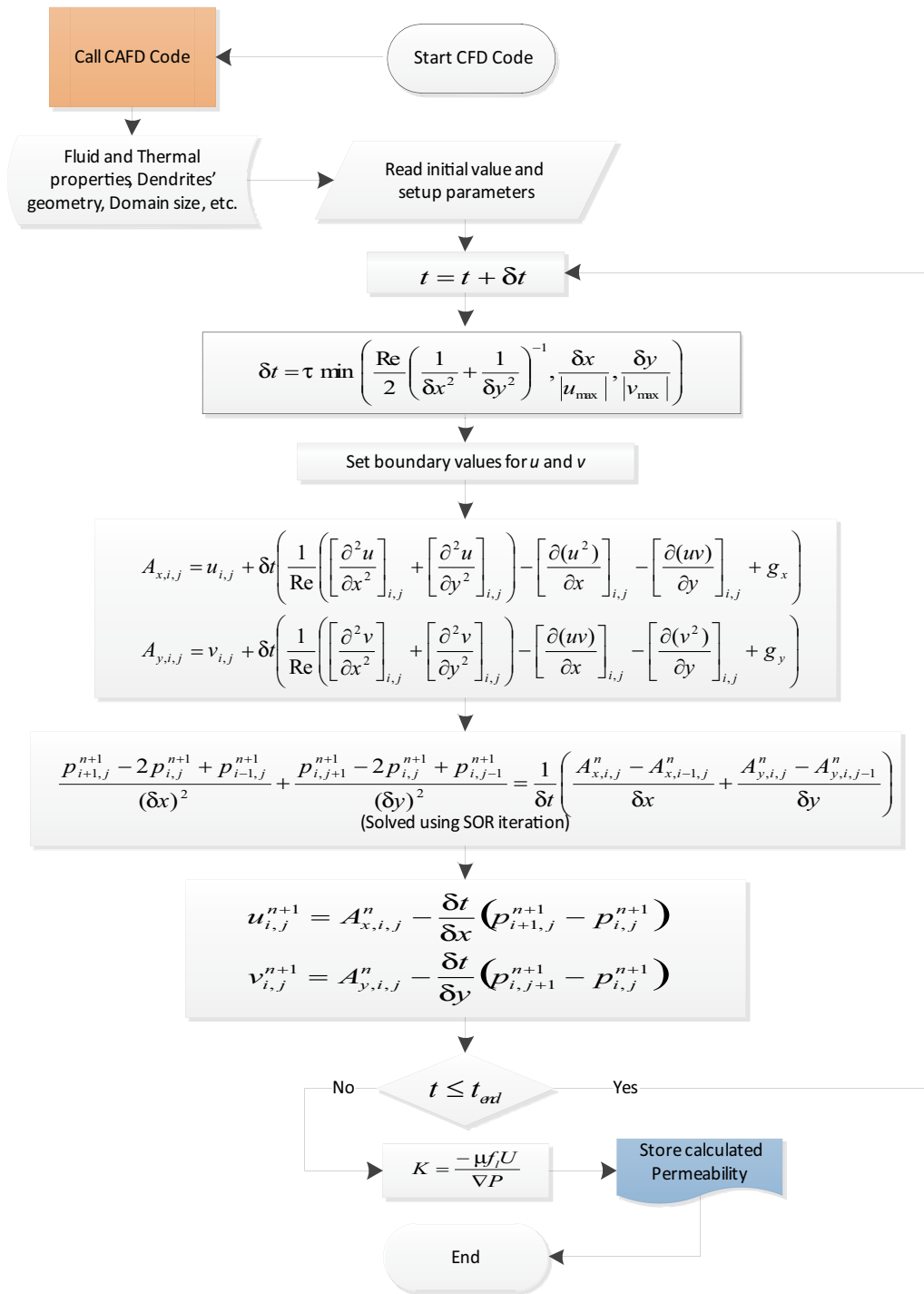


Fig. 7. Algorithm of the projection method for the present CFD code

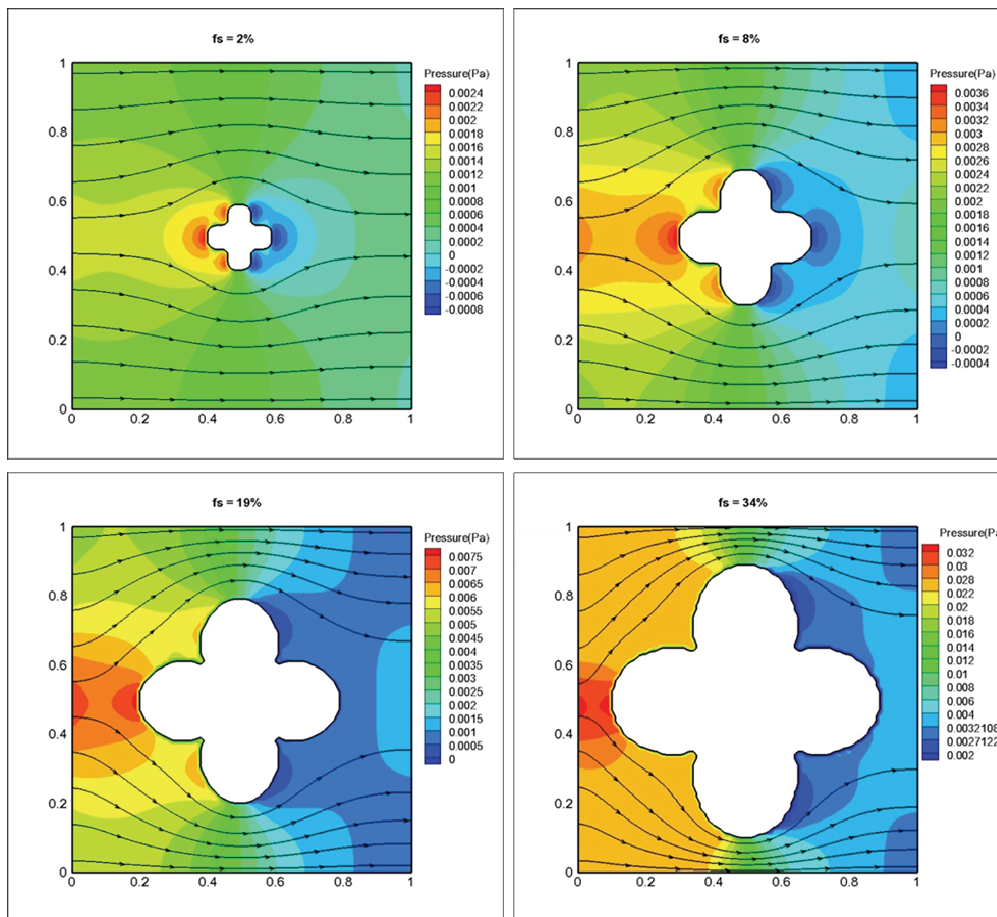


Fig. 8. Simulation of the pressure fields for 4 solid fractions during Al-6%wt.Si alloy grain growth based on Table 1 data

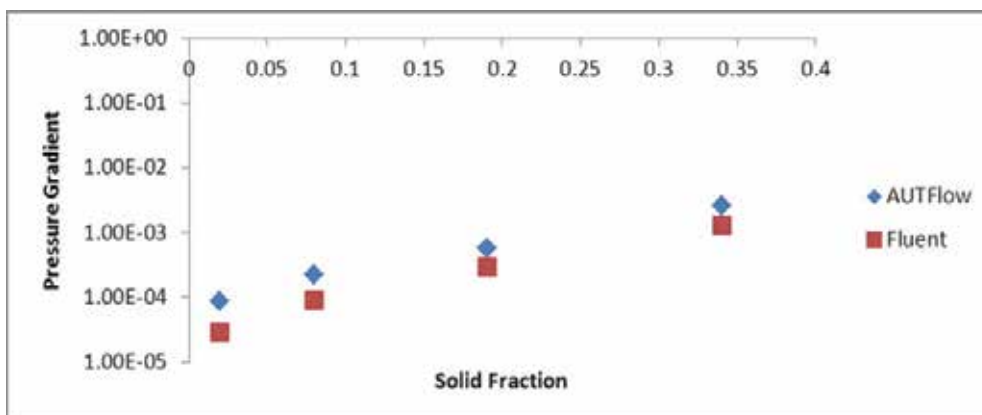


Fig. 9. Comparison of the pressure gradient results of Fig. 8 domain between Fluent and present code based of Table 1 data

### 3. Temporary permeability and effective parameters

It is clear that the permeability is a function of pressure gradient based on Darcy's law; therefore, the simulation of the pressure field in the mushy zone and the factors that affect it is our target. These factors such as, cooling rate, nucleation and growth rate, distribution of nucleus and grains, and morphology of grains, subsequently affects the permeability.

Since, in this investigation a Newtonian thermal condition is assumed; nucleation phenomena are entirely random. Therefore, the distribution of nuclei location could affect the behavior of the pressure field due to the drag force of nucleus on fluid flow. Figs. 10 to 12 show the effect of distribution of nuclei and grains on the pressure field for three constant solid fractions, 0.02, 0.10, 0.24, and 0.43 at a fixed cooling rate. Stream lines are substantially different in these figures, especial at high solid fractions (i.e.  $fs=0.43$ ), which are affected from the number and size of the grains as well as the distribution of nuclei and grains.

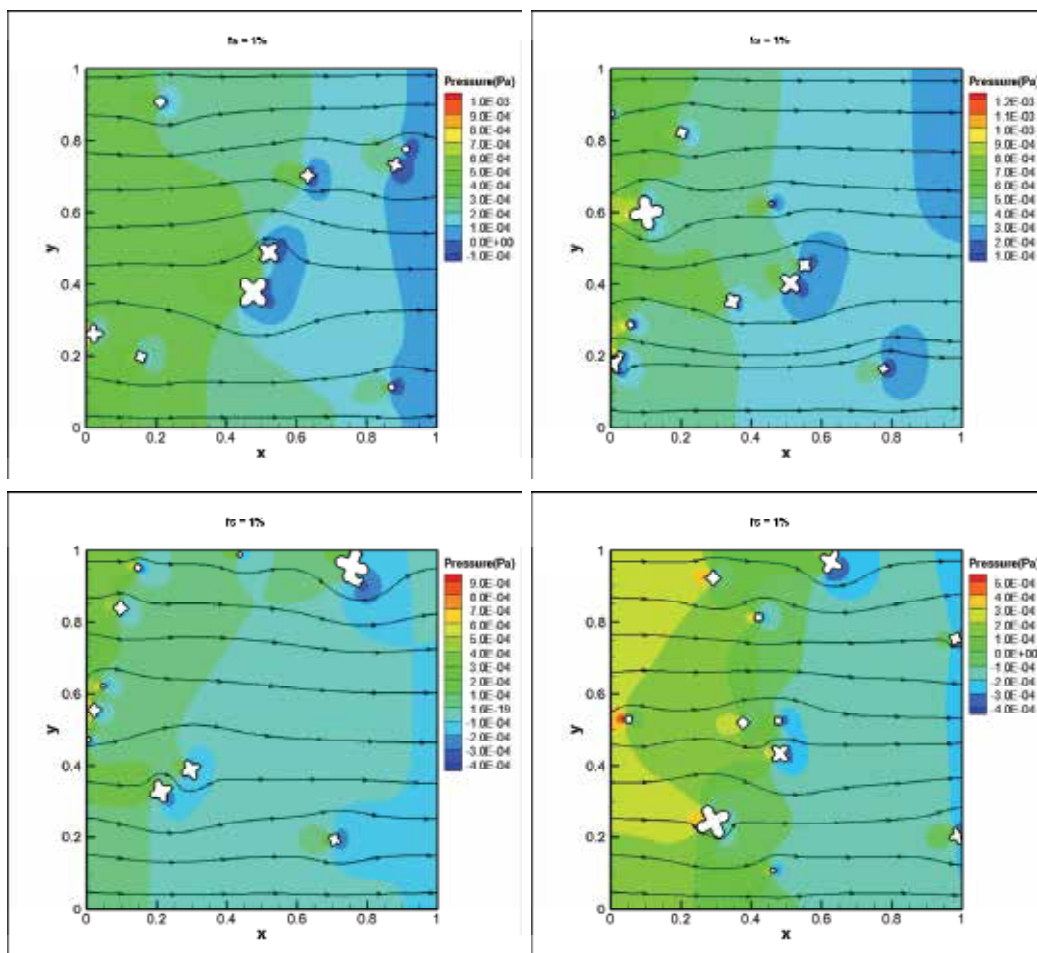


Fig. 10. Simulation of the pressure fields adjacent to 4 types of nucleus distribution with 1% solid fraction and cooling rate of 100 J in each time step. ( $dQ/dt = 1000 \text{ J/s}$ ,  $fs=0.1\%$ )

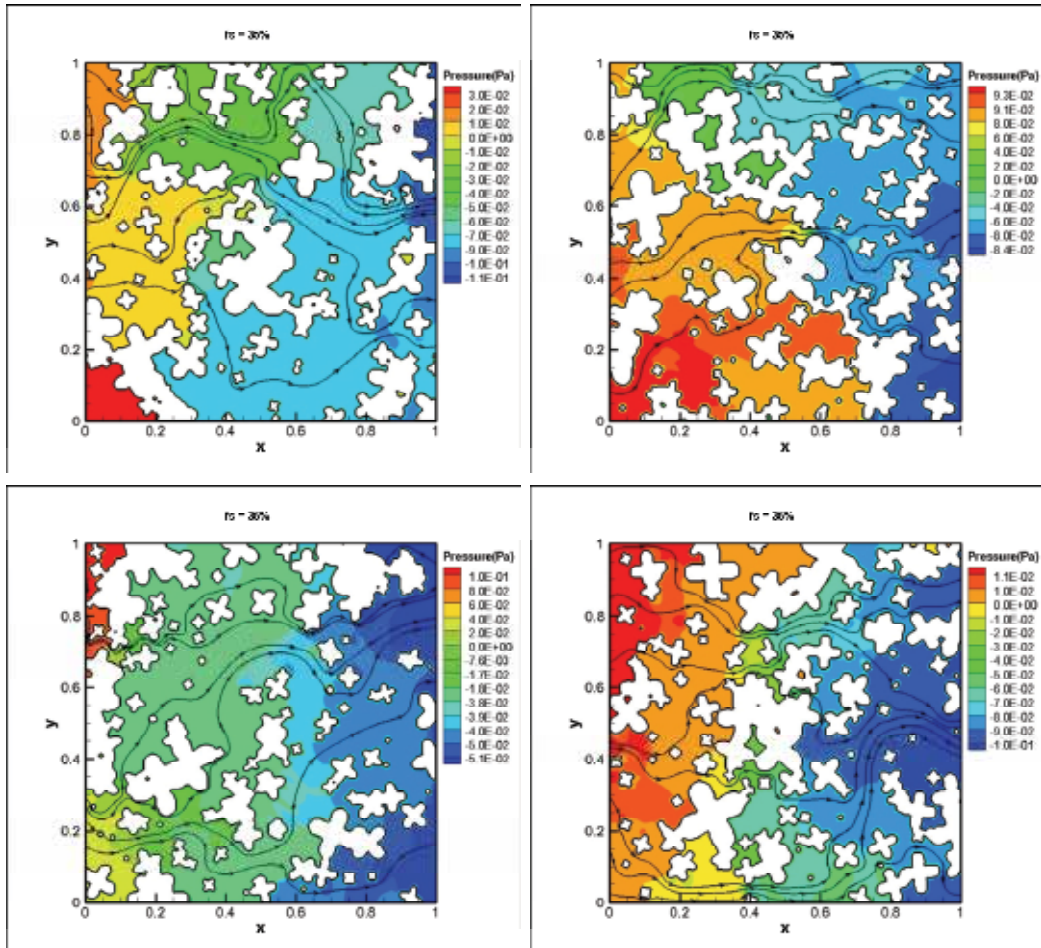


Fig. 11. Simulation of the pressure field adjacent to 4 types of nucleus distribution with 35% solid fraction and cooling rate of 100 J in each time step. ( $dQ/dt = 1000 \text{ J/s}$ ,  $f_s = 0.35\%$ )

Fig 13 shows the effect of cooling rate on the pressure field for a fixed solid fraction ( $f_s = 0.43\%$ ). Results show that by increasing the rate of heat extraction from the domain ( $dQ$ ), some parameter such as size, numbers, and distribution of nucleus and grains have changed and subsequently the pressure field has changed. For example at  $dQ = 70$ , grains are coarse and large, however at  $dQ = 300$ , grains are fine and small.

Fig 14 shows the temporary permeability that was calculated from the simulated pressure fields. In low solid fraction ( $f_s < 0.06$ ) and high solid fraction ( $f_s > 0.78$ ), the behavior of permeability is as asymptotic function, because of  $f_l$  factor in Eq. 19a. However between two solid fractions, behavior of the temporary permeability is almost linear. Markers,  $\blacksquare$ ,  $\bullet$ ,  $\blacktriangle$ , and  $\blacklozenge$ , demonstrate the effect of different grains distributions on the permeability coefficient, which do not show a significant effect, especially at low and high solid fractions.



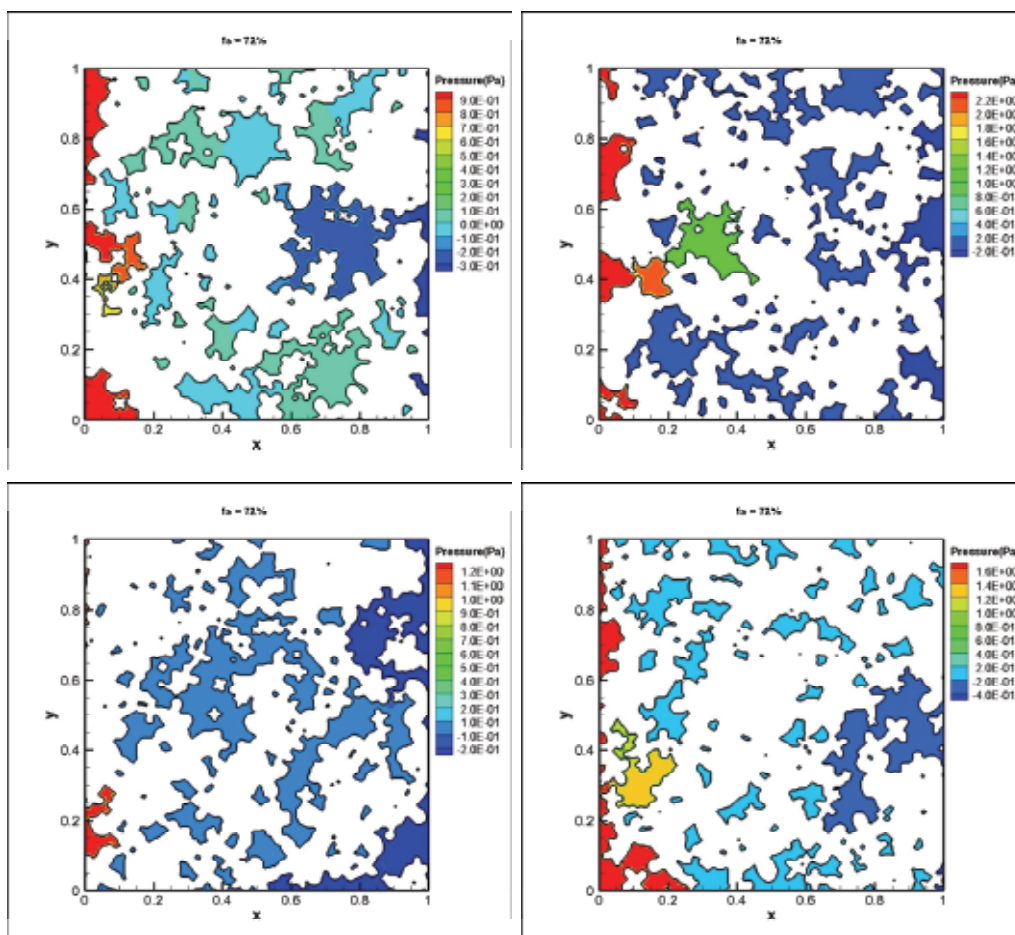


Fig. 12. Simulation of the pressure field adjacent to 4 types of nucleus distribution with 72% solid fraction and cooling rate of 100 J in each time step. ( $dQ/dt = 1000 \text{ J/s}$ ,  $f_s = 0.72\%$ )

#### 4. Conclusions

It is possible, especially in commercial codes, to obtain the thermal history in casting or solidification codes. In fact all numerical fluid flow and heat transfer software can save the cooling rate ( $\frac{\partial T}{\partial t}$ ), temperature gradient ( $G = \frac{Q}{k} = \frac{\partial T}{\partial x}$ ), and solidification rate ( $v = \frac{\partial f_s}{\partial t}$ ) for each location of the meshed domain. Therefore, in the present code if the interdendritic permeability is defined as a function of cooling rate, the micro-structure will be related to the thermal history in a macro scale, and the formation of micro defects could be predicted. In other words, the present code is capable of predicting the micro-defects based on thermal history. However, the cooling rate is not an independent variable and should be determined by the temperature gradient and the solidification rate, as follows:

$$\frac{\partial T}{\partial t} = \left( \frac{\partial T}{\partial x} \right) \left( \frac{\partial x}{\partial t} \right) = G \cdot v, \text{ for a single phase, and}$$

$$\frac{\partial T}{\partial t} = (k \cdot G) / (1 + \Delta H m \cdot v), \text{ during phase change}$$

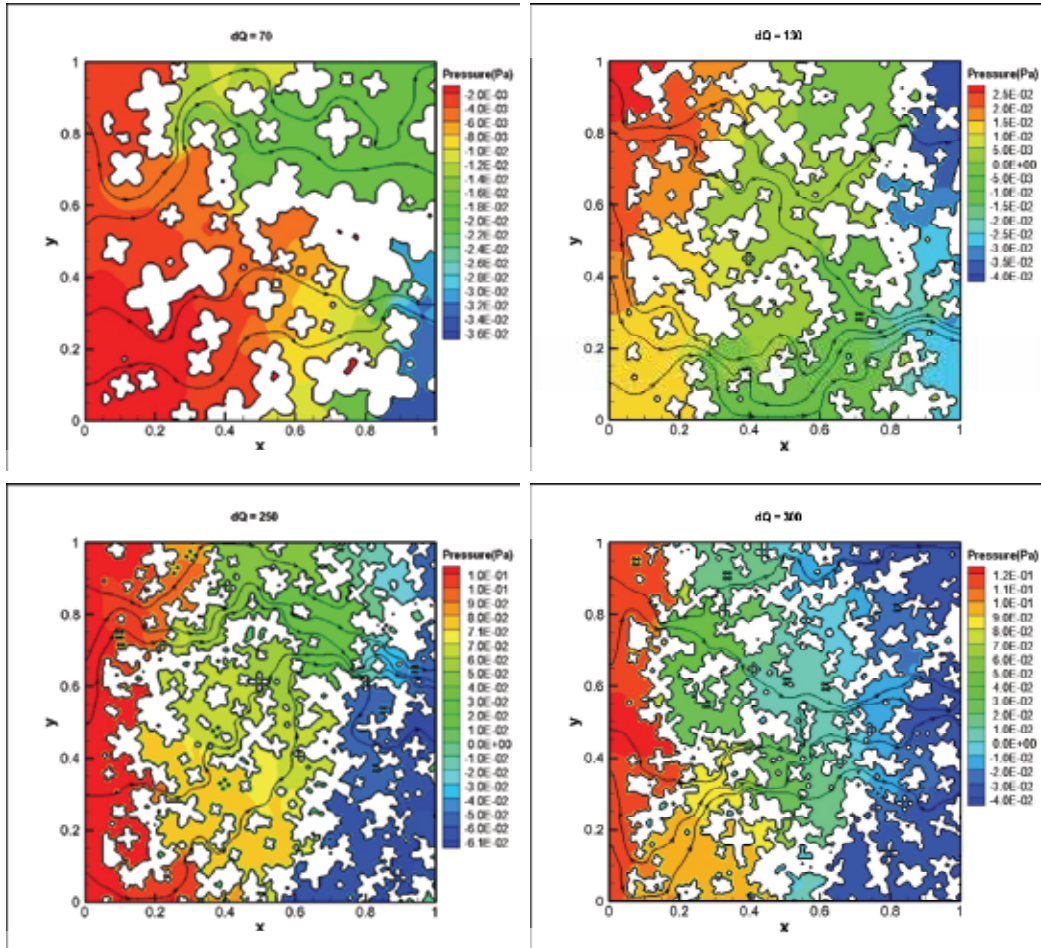


Fig. 13. Simulation of the pressure field adjacent to 4 types of nucleus distribution with 0.45% constant solid fraction and  $dQ$  equals to 70, 130, 250, and 300 J in each time step

It means that increasing the cooling rate results in an increase in the number of nuclei and the change of dendrite morphology from faceted surface to dendritic surface (cloverleaf grain) and that in turn affects the interdendritic permeability. Therefore, the effect of temporary solid fraction ( $df_s$ ) and heat extraction rate ( $dQ$ ) on the temporary permeability is modeled as an asymptotic function and plotted in Fig. 15 and 16. Results shown in Fig. 16 show that after formation of 0.72% solid, grains are inter-connected and join together. Consequently, there is no fluid stream into the mushy zone, but only some micro fluid flow



as a vortex of the entrapped liquid between the grains. It seems that the critical permeability for the formation of micro-porosity, in a mushy alloy such as Al-6%wt.Si, is less than  $1\text{E}-10$  to  $1\text{E}-11$  ( $\text{m}^2$ ). This is true, even at very high cooling rates of over  $3000$  J/s and different distributions of the equiaxed grains.

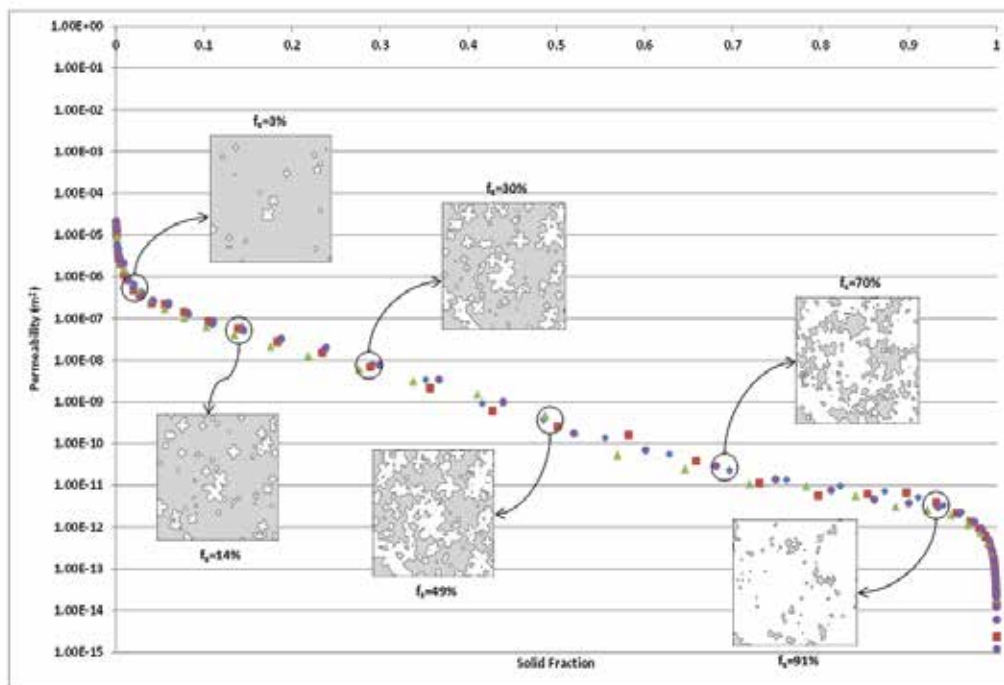


Fig. 14. Calculation of permeability based on simulation results of the present CFD and CA-FD codes during grain growth with 4 kinds of nucleus distribution ( $\blacksquare$   $\blacktriangle$   $\blacklozenge$   $\bullet$ ) versus solid fraction

In this investigation, the temporary permeability results, which were obtained based on the cooling and solidification rate, can be modeled as a 3-dimensional surface. The resulting equation of this 3D-surface, as given in Eq. 30, can be used in all casting simulation software.

$$-\text{Log}(\text{Permeability}) = 7.175f_s + 0.002dQ + 5.185 \quad (30)$$

Finally, the significant findings of this investigation can be phrased as follows:

- i. In this investigation, an algorithm was developed to calculate the permeability of mushy alloys. To simulate the permeability, CFD and CA-FD codes were coupled. The CA-FD code was used for nucleation and growth of the equiaxed dendrites, and the CFD code was used for simulation of the pressure and velocity fields adjacent to the nuclei and grains.
- ii. The temporary permeability was calculated based on the present codes (CFD and CA-FD)

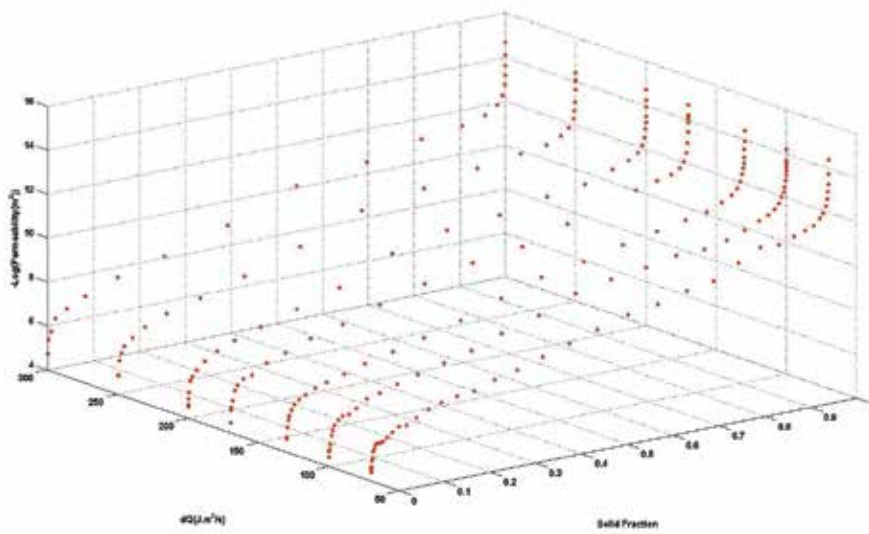


Fig. 15. Changes in permeability results in the Al-6%Si alloy

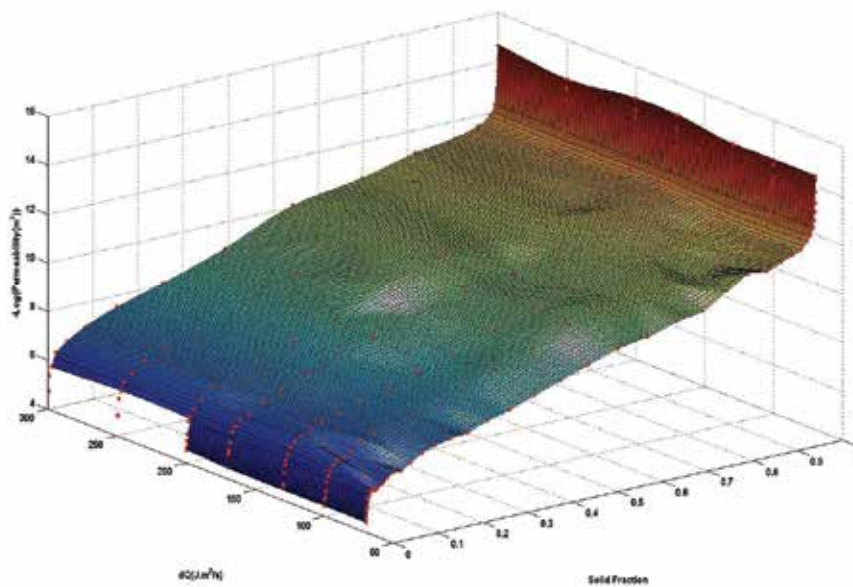


Fig. 16. Modeling of temporary permeability as a 3-D surface during equiaxed grain growth based on simulation results of the present code

- iii. Permeability simulation results showed that apart from low and high solid fractions,  $f_s < 0.06$  and  $f_s > 0.72$ , respectively, the temporary permeability versus the solid fraction during solidification has a linear behavior.

- iv. Results showed that the temporary permeability during nucleation and growth of the equiaxed grains depends on cooling and solidification rate.
- v. At high cooling and solidification rate fluctuations on temporary permeability was observed, which was presumably due to the perturbation of the grain surfaces or the evolution of semi-spherical grains to cloverleaf dendrites.
- vi. Permeability results of present code can be utilized in commercial casting and solidification software.

## 5. References

- Amsden, A. A. & Harlow, F. H. (1970). The SMAC method: A Numerical Technique for Calculating Incompressible Fluid Flows. *Los Alamos Scientific Laboratory Report LA-4370* New Mexico.
- An, S. U., Larionov, V., Monastyrski, V., Monastyrskaia, E., Grafas, I., Oh, J. M., Lim, O. D., Kim, S. H., Lee, J. H. & Seo, D. Y. (2000). The thermal analysis of the mushy zone and grain structure changes during directional solidification of superalloys. In: *Superalloys 2000*. Green, K. A., Pollock, T. M. & Kissinger, R. D., TMS.
- Apelian, D., Flemings, M. C. & Mehrabian, R. (1974). Specific permeability of partially solidified dendritic networks of Al-Si alloys. *Metallurgical and Materials Transactions B*. Vol. 5: pp. 2533-2537.
- Atwood, R. C. & Lee, P. D. (2000). A Combined cellular automaton and diffusion model for the prediction of porosity formation during solidification. *Modelling of casting welding and advanced solidification processing IX*, Aachen, Germany.
- Bahat, M. S., Poirier, D. R. & Heinrich, J. C. (1995). Permeability for cross flow through columnar-dendritic alloys. *Metallurgical and Materials Transactions B*. Vol. 26(5): pp. 1049-1056.
- Brown, S. G. R., Spittle, J. A. & Walden-Bevan, R. (2002). Numerical Determination of Liquid Flow Permeabilities for Equiaxed Dendritic Structures. *Acta Materialia*. Vol. 50: pp. 1559-69.
- Cai, Z. & Berdichevsky, A. L. (1993). Numerical simulation on the permeability variations of a fiber assembly. *Polymer Composites*. Vol. 14(6): pp. 529-539.
- Carman, P. C. (1937). Fluid flow through a granular bed. *Transactions of the Institution of Chemical Engineers*. Vol. 15: pp. 150-166.
- Chen, Y.-T., Davis, H. T. & Macosko, C. W. (1995). Wetting of fiber mats for composites manufacturing: I. *Visualization experiments*. Vol. 41(10): pp. 2261-2273.
- Darcy, H. (1856). *Les Fontaines Publiques De Ville de Dijon*, Paris.
- de Groh, H. C., Weidman, P. D., Zakhem, R., Ahuja, S. & Beckermann, C. (1993). Calculation of dendrite settling velocities using a porous envelope *Metallurgical and Materials Transactions B*. Vol. 24(5): pp. 749-53.
- Duncan, A. J., Han, Q. & Viswanathan, S. (1999). Measurement of liquid permeability in the mushy zones of aluminum-copper alloys *Metallurgical and Materials Transactions B*. Vol. 30(4): pp. 745-750.
- Edwards, D. A., Shapiro, M., Bar-Yoseph, P. & Shapira, M. (1990). The influence of Reynolds number upon the apparent permeability of spatially periodic arrays of cylinders. *Physics of Fluids A*. Vol. 2: pp. 45-60.

- Eidsath, A., R.G., C., Whitaker, S. & Herrmann, L. R. (1983). Dispersion in pulsed systems - III : Comparison between theory and experiments for packed beds. *Chemical Engineering Science*. Vol. 38: pp. 1803-1816.
- Ganesan, S., Chan, C. L. & Poirier, D. R. (1992). Permeability for flow parallel to primary dendrite arms. *Materials Science and Engineering A*. Vol. 151: pp. 97-105.
- Ganesan, S. & Poirier, D. R. (1990). *Metallurgical and Materials Transactions*. Vol. 21(B): pp. 173-81.
- Ganesan, S. & Poirier, D. R. (1990). Conservation of Mass and Momentum for the Flow of Interdendritic Liquid during Solidification. *Metallurgical and Materials Transactions B*. Vol. 21: pp. 173-181.
- Ghaddar, C. K. (1995). On the permeability of unidirectional fibrous media: A parallel computational approach. *Physics of Fluids A*. Vol. 7: pp. 2563-2585.
- Griebel, M. (2011). Retrieved 2011, from <http://www.ins.uni-bonn.de/institut/>.
- Hirt, C. W., Nichols, B. D. & Romero, N. C. (1975). SOLA - A Numerical Solution Algorithm for Transient Fluid Flows. *Los Alamos Scientific Laboratory Report LA-5852* New Mexico.
- Hong, C. P. (2004). *Computer modelling of heat and fluid flow in materials processing*, Taylor & Francis.
- Koch, D. L. & Ladd, A. J. C. (1997). Moderate Reynolds number flows through periodic and random arrays of aligned cylinders. *J. Fluid Mech*. Vol. 349: pp. 31-66.
- Kurz, W., Bezencon, C. & Gäumann, M. (2001). Columnar to equiaxed transition in solidification processing. *Science Technology and Advance Materials*. Vol. 2(1): pp. 185-191.
- Kurz, W., Giovanola, B. & Trivedi, R. (1986). Theory of Microstructural Development during Rapid Solidification. *Acta Metallurgica*. Vol. 34(5): pp. 823.
- Larson, R. E. & Higdon, J. J. L. (1986). Microscopic flow near the surface of two-dimensional porous media, Part 1. Axial flow. *Journal of Fluid Mechanics*. Vol. 166: pp. 449-472.
- Lee, P. D., Atwood, R. C., Dashwood, R. J. & Nagaumi, H. (2001). Modeling of Porosity Formation in Direct Chill Cast Aluminium-Magnesium Alloys. *Materials Science and Engineering*. Vol.: pp. Submitted.
- Lee, P. D., Chirazi, A. & See, D. (2001). Modeling Microporosity in Aluminum-Silicon Alloys: a Review. *Journal of Light Metals*. Vol. 1(1): pp. 15.
- Liu, C. Y., Murakami, K. & Okamoto, T. (1989). Permeability of dendrite network of cubic alloys. *Materials Science and technology*. Vol. 5(11): pp. 1148-1152.
- McCartney, J. F. (1994). Flow through arrays of cylinders: Lattice gas cellular automata simulations. *Physics of Fluids*. Vol. 6(2): pp. 435-437.
- Mirbagheri, S. M. H. (2008). Modeling of the equiaxed dendrite coarsening based on the interdendritic liquid permeability during alloy solidification. *Metallurgical and Materials Transactions B-Process Metallurgy and Materials Processing Science*. Vol. 39(3): pp. 469-483.
- Mirbagheri, S. M. H., Ashuri, H., Varahram, N. & Davami, P. (2003). Simulation of mould filling in lost foam casting process. *International Journal of Cast Metals Research*. Vol. 16(6): pp. 554-565.

- Mirbagheri, S. M. H. & Khajeh, E. (2008). Modelling and simulation of equiaxed dendritic structures permeability for Pb-Sn alloys. *Materials Science and Technology*. Vol. 24(12): pp. 1444-1451.
- Mirbagheri, S. M. H. & Silk, J. (2007). Simulation of Si concentration effect on the permeability for columnar dendrite structures during solidification of Al-Si alloy. *Materials & Design*. Vol. 28(1): pp. 356-361.
- Murakami, K., Shiraishi, A. & Okamoto, T. (1983). Interdendritic fluid flow normal to primary dendrite-arms in cubic alloys. *Acta Metallurgica*. Vol. 31: pp. 1417-1424.
- Murakami, K., Shiraishi, A. & Okamoto, T. (1984). Fluid flow in interdendritic space in cubic alloys. *Acta Metallurgica*. Vol. 32: pp. 1423-1428.
- Nagelhout, D., Bhat, M. S., Heinrich, J. C. & Poirier, D. R. (1995). Permeability for flow normal to a sparse array of fibres. *Materials Science and Engineering A*. Vol. 191(1-2): pp. 203-208.
- Nandapurkar, P., Poirier, D. R. & Heinrich, J. C. (1991). Momentum equation for dendritic solidification. *Numerical Heat Transfer*. Vol. 19A: pp. 297-311.
- Nielsen, O., Mo, A., Applolaire, B. & Combeau, H. (2001). Measurements and modeling of the microstructural morphology during equiaxed solidification of Al-Cu alloys. *Metallurgical and Materials Transactions A*. Vol. 32(8): pp. 12049-60.
- Piwonka, T. S. & Flemings, M. C. (1966). Part VIII - Pore Formation in Solidification. *Transactions of the Metallurgical Society of AIME*. Vol. 236: pp. 1157-1165.
- Poirier, D. R. (1987). Permeability for Flow of interdendritic liquid in columnar-dendritic alloys. *Metallurgical and Materials Transactions B*. Vol. 18: pp. 245-255.
- Poirier, D. R. & Ocansey, P. (1993). Permeability for flow of liquid through equiaxial mushy zones. *Materials Science and Engineering A*. Vol. 171: pp. 231-240.
- Sangani, A. S. & Acrivos, A. (1982). Slow flow past periodic arrays of cylinders with application to heat transfer. *International Journal of Multiphase Flow*. Vol. 8: pp. 193-206.
- Sangani, A. S. & Mo, G. (1994). Inclusion of lubrication forces in dynamic simulations. *Physics of Fluids*. Vol. 6: pp. 1653-62.
- Sangani, A. S. & Yao, A. (1988). Transport processes in random arrays of cylinders. II. Viscous flow. *Physics of Fluids*. Vol. 31(9): pp. 2435-42.
- Sparrow, E. M. & Loeffler, A. L. (1959). Longitudinal laminar flow between cylinders arranged in regular array. *AIChE Journal*. Vol. 5: pp. 325-330.
- Streat, N. & Weinberg, F. (1976). Interdendritic fluid flow in a lead-tin alloy. *Metallurgical and Materials Transactions B*. Vol. 7(3): pp. 417-23.
- Thom, A. & Aplett, C. J. (1961). *Field Computations in Engineering and Physics* Van Nostrand, London.
- Versteeg, H. & Malalasekera, W. (1995). *An Introduction to Computational Fluid Dynamics: The Finite Volume Method Approach*, Longman Group Ltd., Harlow.
- Wang, C. Y., Ahuja, S., Beckerman, C. & de Groh, H. C. (1995). Multiparticle interfacial drag in equiaxed solidification. *Metallurgical and Materials Transactions B*. Vol. 26(1): pp. 111-119.
- Williams, J. G., Morris, C. E. M. & Ennis, B. C. (1974). Liquid flow through aligned fiber beds. *Polymer Engineering & Science*. Vol. 14(6): pp. 413-419.

Worster, M. G. (1991). Natural convection in a mushy layer. *Journal of fluid mechanics*. Vol. 224: pp. 325-359.

# Numerical Modelling of Non-metallic Inclusion Separation in a Continuous Casting Tundish

Marek Warzecha  
*Czestochowa University of Technology*  
*Poland*

## 1. Introduction

Nowadays the cleanliness of steel plays a major role for steel producers. It is defined by the size and number of non-metallic inclusions in the final product. Today, the dominating method of global steel production is continuous casting. A continuous casting plant includes the ladle turret, several steel ladles, a tundish, and mould/moulds. Tundish buffers steel melt during the ladle change and distributes the steel melt to several strands. Tundish plays also an important role in removing non-metallic inclusions (i.e.  $\text{Al}_2\text{O}_3$  or  $\text{SiO}_2$ ), to the slag layer due to buoyancy force. The aluminium oxides are very hard and destroy steel structure during plastic formation process. Therefore strict steel quality conditions require a steady increase in the purity of steels and thus reducing the number and size of non-metallic inclusions is necessary.

Measurements of the melt flow and inclusions transport and separation in a steel mill, at working conditions, are nearly impossible due to the high temperatures and opacity of the fluid. The solution is using the physical and numerical simulations in this field of investigation. Water can be used for the physical simulation because the kinematic viscosities of liquid steel and water are comparable ( $\nu_{\text{st},1536^\circ\text{C}} = 8.26 \cdot 10^{-7} \text{ m}^2/\text{s}$ ,  $\nu_{\text{w},20^\circ\text{C}} = 10.0 \cdot 10^{-7} \text{ m}^2/\text{s}$ ), thus the flows of both fluids are similar. A wide review of such investigation was first done by Mazumdar and Guthrie (Mazumdar & Guthrie, 1999) and lately by Chattopadhyay et al. (Chattopadhyay et al., 2010). From this reviews it can be seen, that experimental measurements using water models are widely used, and considering the similarity laws, the results from water modelling can be transferred to the real process. Though, many publications are available with water model experiments, only a few experimental studies were done on particle separation in the tundish.

Tundish flow and accompanying inclusion separation process are strongly investigated with Computational Fluid Dynamics (CFD) models as well. Numerous studies can be found in literature. Present state of the CFD techniques allow to calculate the fluid flow in tundish with the satisfying accuracy. This is confirmed by a good agreement in flow fields predicted mathematically and measured by laser-optical method using water models (Braun et al., 2010). For turbulence modelling, the standard or realizable  $k-\epsilon$  models are mostly used, rather than Reynolds Stress Model (RSM) or Large-Eddy Simulations (LES). Results show that in many engineering problems, flow field is well described by steady-state numerical simulations using the Reynolds-Averaged Navier-Stokes (RANS) equations combined with the realizable  $k-\epsilon$  model.

On pre-calculated flow and turbulence field, the transport of disperse phase can be treated.

The weakness of mathematical model lies in defining boundary conditions for a disperse phase (inclusions). A lot of publications can be found where researchers investigate particle separation. However lots of assumptions have been made so far. Usually at boundaries like the fluid-fluid (liquid steel-slag interface, free surface) and fluid-solid (liquid steel-tundish lining) standard boundary conditions are used. It is assumed that if inclusion reaches one of these boundaries, it is either reflected or absorbed. In this way, the deposition of particles at these boundaries are not fully reproduced. A more detailed physical examination of inclusion separation is needed. Solutions, where a special model is applied for the melt surface or tundish walls belong to minorities (Zhang et al., 2000).

The aim of numerical studies should be focused on finding and implementing a proper boundary condition for modelling the particle separation at the covering slag and lining interface. Only after successful validation with experimental results, the mathematical model can be used to simulate the non-metallic inclusions movement in the liquid steel bath and separation at the steel-slag interface for industrial process conditions.

## 2. Tundish description

Investigated object is a six-strand continuous casting tundish operating in one of a Polish steel mill. The nominal capacity of the tundish is 15 Mg of liquid steel. The tundish is used for casting ingots intended for production of small cross-section rolled products. It is symmetrical with respect to its central cross-section. In its current configuration the tundish is furnished with an impact pad. The basic refractory lining is made up of andalusite tiles, and the working layer – a high-magnesite gunite mix. It is used for casting sequences composed of from several to more than ten heats. Figure 1 shows the geometry of the tundish with its major dimensions. The dimensions of the tundish are given in Table 1.

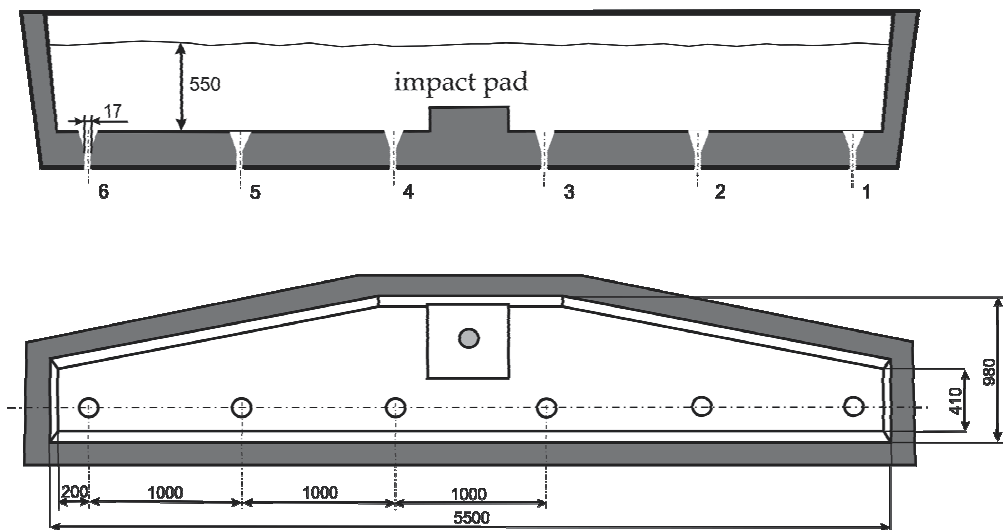


Fig. 1. Geometry of the investigated tundish



|                                   |       |
|-----------------------------------|-------|
| Nominal capacity (Mg)             | 15    |
| Tundish length (bottom) (m)       | 5.4   |
| Tundish width (bottom) (m)        | 0.82  |
| Inclination of the side walls (°) | 7     |
| Steel filling level (m)           | 0.55  |
| Number of nozzles (-)             | 6     |
| Nozzle diameter (m)               | 0.017 |

Table 1. Dimensions of the investigated tundish

Large differences in steel quality specified by the number of non-metallic inclusions, between individual strands for the former industrial six-strand tundish configuration have been the basis for undertaking the presented studies. The aim of the performed investigations were to improve the billets quality and to decrease observed differences in inclusion density in billets casted at individual strands. To improve the inclusion separation rate in the studied tundish, flow conditions have to be changed. It can be reached by installing a flow control device (FCD) in the tundish working space. FCD proposed here is a pair of dams (see Figure 2). For steelwork such device is cheap and easy solution from technical point of view.

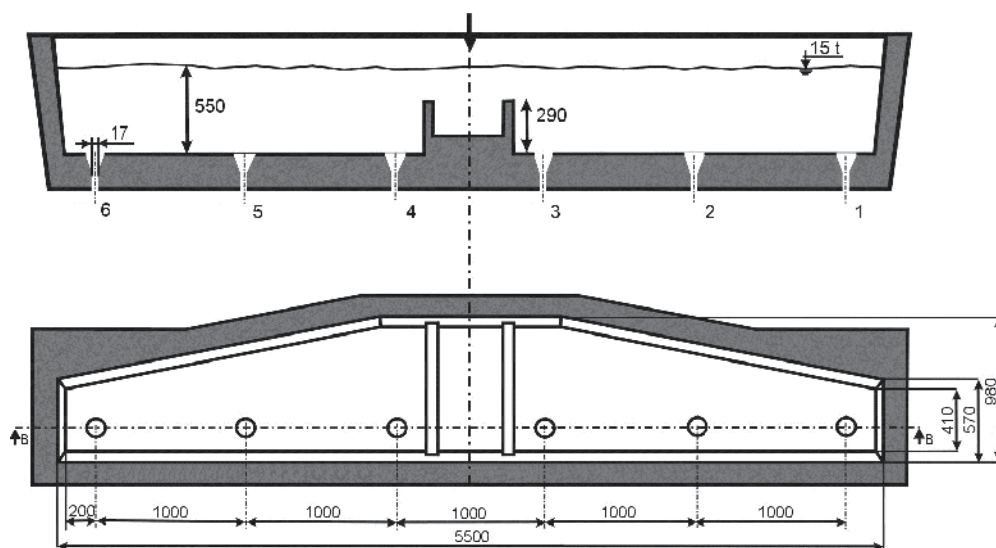


Fig. 2. Tundish configuration studied in presented work

### 3. Industrial investigation of inclusions distribution in the steel

Tests were carried out with industrial conditions at a continuous casting tundish working at one of a Polish steel mill. The investigation was performed to identify the distribution of non-metallic inclusions in steel ingot by analysing samples taken from billet casted in the investigated tundish. The study included quantitative and partly qualitative analysis of non-metallic inclusions found in square ingots (160x160 mm<sup>2</sup>) of BSt500S steel grade. The

analysis included samples cut from three billets (numbered: 1, 2 and 3), at the beginning and the end of casted ladle. The system of numbering of cc machine moulds in steelwork is shown in Figure 1. The samples were cut from the cross-section of the billets in the manner demonstrated in Figure 3. The surface of the samples was analysed using computerized image analysis system. For statistical reasons 10 fields (one field area of  $8.77 \cdot 10^5 \mu\text{m}^2$ ) on one sample were tested with a 200x magnification.

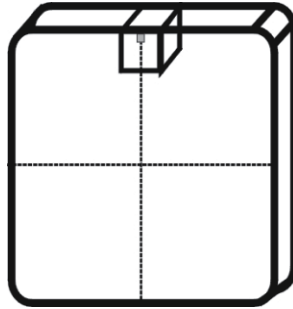


Fig. 3. Sampling method in billets

#### 4. Numerical model – equations, parameters and boundary conditions

The CFD numerical simulations were carried out on the basis of the RANS equations. The liquid phase Navier-Stokes equations for incompressible flow without source terms are as follows.

Continuity equation:

$$\frac{\partial u_i}{\partial x_i} = 0 \quad (1)$$

Momentum conservation equation:

$$\rho \frac{\partial u_i}{\partial t} + \rho u_j \frac{\partial u_i}{\partial x_j} = -\frac{\partial p}{\partial x_i} + \frac{\partial}{\partial x_j} \left[ \mu_{\text{eff}} \left( \frac{\partial u_i}{\partial x_j} + \frac{\partial u_j}{\partial x_i} \right) \right] + \rho g_i \quad (2)$$

where

$$\mu_{\text{eff}} = \mu + \mu_t \quad (3)$$

and where and:  $u_{i,j}$  is time-averaged fluid velocities in the  $i$ th and  $j$ th directions respectively,  $\rho$  is liquid density,  $p$  is pressure in the fluid,  $\mu$  is molecular viscosity of liquid,  $\mu_t$  is turbulent viscosity,  $\mu_{\text{eff}}$  is effective turbulent viscosity,  $g_i$  is gravitational acceleration in the  $i$ th direction,  $x_i, x_j$  are spatial coordinates in the  $i$ th and  $j$ th directions,  $i, j$  denote the three directions in the global Cartesian coordinate system.

Regarding heat transfer, the turbulent energy equation can be written as:

$$\frac{\partial}{\partial t}(\rho h) + \frac{\partial}{\partial x_i}(\rho h u_i) = \frac{\partial}{\partial x_j} \left[ \left( k + \frac{c_p \mu_t}{\sigma_t} \right) \frac{\partial T}{\partial x_j} \right] \quad (4)$$

where  $h$  is enthalpy,  $k$  is thermal conductivity,  $c_p$  is heat capacity of liquid water,  $\sigma_t$  is turbulent Prandtl number,  $T$  is temperature.

Turbulent flows occur during liquid steel flow through the tundish. When modelling the process a turbulence model has to be chosen. In practice, diffusion turbulence models of a simplified structure are used, which have been verified in many engineering applications with good results. For most tundish flows numerical calculations, the standard k- $\epsilon$  model is used. However some investigations (Solario-Diaz et al., 2004; Hou & Zou, 2005) demonstrate that this model does not give sufficient results for all cases. Investigations with water model (Braun et al., 2010) has shown that the overall flow phenomena in the tundish is well described by steady-state numerical simulations using RANS equations combined with the realizable k- $\epsilon$  model from Shih et al. (Shih et al., 1995). This model is a good compromise between accuracy and simulation time. The realizable k- $\epsilon$  model is based on the Boussinesq approximation, saying that the Reynolds stresses are a function of the mean gradients of velocity similar to the molecular stress. The unknown value is the turbulent viscosity:

$$\mu_T = \rho C_\mu \frac{k^2}{\epsilon} \quad (5)$$

which is a function of the turbulent kinetic energy  $k$  and the dissipation rate of the turbulent kinetic energy  $\epsilon$ .

In the realizable k- $\epsilon$  model  $C_\mu$  is a function of the gradients of velocity, whereby mathematical restrictions of the standard k- $\epsilon$  model are avoided. A further modification represents a new differential equation for the dissipation rate  $\epsilon$ .

Equation of the turbulent kinetic energy  $k$ :

$$\frac{\partial}{\partial t}(\rho k) + \frac{\partial}{\partial x_i}(\rho k u_i) = \frac{\partial}{\partial x_j} \left[ \left( \mu + \frac{\mu_t}{\sigma_k} \right) \frac{\partial k}{\partial x_j} \right] + G_k + G_b - \rho \epsilon \quad (6)$$

Equation of the dissipation rate of the turbulent kinetic energy  $\epsilon$ :

$$\frac{\partial}{\partial t}(\rho \epsilon) + \frac{\partial}{\partial x_j}(\rho \epsilon u_j) = \frac{\partial}{\partial x_j} \left[ \left( \mu + \frac{\mu_t}{\sigma_\epsilon} \right) \frac{\partial \epsilon}{\partial x_j} \right] + \rho C_{1\epsilon} S \epsilon - \rho C_2 \frac{\epsilon^2}{k + \sqrt{\nu \epsilon}} + C_{1\epsilon} \frac{\epsilon}{k} C_{3\epsilon} G_b \quad (7)$$

where  $G_k$  is generation of turbulence kinetic energy due to the mean velocity gradients,  $G_b$  is generation of turbulence kinetic energy due to buoyancy,  $C_1$ ,  $C_2$  and  $C_{1\epsilon}$ ,  $C_{3\epsilon}$  are constants,  $\sigma_k$  and  $\sigma_\epsilon$  are turbulent Prandtl numbers for  $k$  and  $\epsilon$  respectively.

The model constants are  $C_{1\epsilon} = 1.44$ ,  $C_2 = 1.9$ ,  $\sigma_k = 1.0$ ,  $\sigma_\epsilon = 1.2$ .

The flow field in tundish is calculated using commercial CFD software Fluent. The partial differential equations are solved with the help of mentioned below boundary conditions for all control volumes. To provide higher order accuracy a second order upwind scheme is used. SIMPLEC algorithm is used to resolve the pressure-velocity coupling in the momentum equation.

Because of symmetry plane only a half of the tundish is simulated. One half of a tundish working space is reproduced by a hybrid computational grid with about 0.4 to 0.5 million of control volumes, depending on tundish configuration.

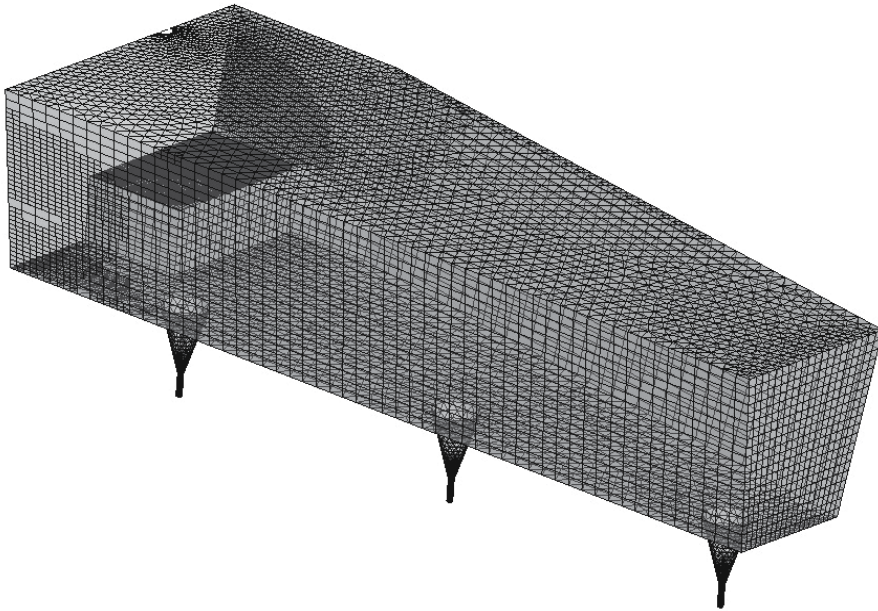


Fig. 4. Hybrid computational grid of the tundish working space

For inlet and nozzle outlet ports smaller grid spacing is used by applying mesh refinement. A symmetry boundary condition is given at a symmetry plane, which implies a zero gradient condition for all variables normal to the plane. Steel-slag interface is assumed to be flat and modeled as a frictionless wall. Deformations of the liquid steel surface can be neglected since its effect on the flow structure in the tundish is small. Side walls and bottom of the tundish as well as additional tundish equipment have stationary wall boundary condition for the velocity components and the turbulence quantities, so called "standard wall function". The inlet velocity of liquid steel is equal to 2.2 m/s, which is equivalent to billet casting speed in the order of 1.7 m/min. The velocity profile in the shroud is assumed to be flat with a turbulent intensity of 5%. The inlet temperature of the liquid steel stream is 1823 K. Heat losses along the slag cover and side walls/bottom of the tundish are taken from references (Joo & Guthrie, 1991; Chakraborty & Sahai, 1992) and are given in Table 2. At the outlets of the tundish a fixed pressure is applied.

On pre-calculated flow and turbulence field, the transport of disperse phase can be treated. There are two ways of modelling the discrete phase transport. First is the simple diffusion/convection approach. The particle concentration (defined as the number of particles per unit volume) and movement, due to turbulent transport and diffusion, is modelled by solving a transport equation, with the particle rise velocity as an extra convective component in the upward direction. The terminal rising velocity of particle is added when particle concentration is the dependent variable. The second approach is a full trajectory calculation. In this approach, each particle is treated separately and its trajectory is calculated by integrating local velocity. The differential equation, describing the motion of particles in the liquid, considers the different forces acting on particle, such as drag force, buoyancy force, added mass force and additional forces.

|   |       |
|---|-------|
| Liquid steel density (kg/m <sup>3</sup> )                                 | 7010  |
| Liquid steel dynamic viscosity (kg/m s)                                   | 0.007 |
| Inlet velocity (m/s)  | 2.2   |
| Inlet temperature (K)   | 1823  |
| Specific heat (J/kg·K)  | 821   |
| Thermal conductivity (W/m·K)  | 30.5  |
| Heat flux through side walls/bottom (kW/m <sup>2</sup> )                  | - 2.6 |
| Heat flux through slag cover (kW/m <sup>2</sup> )                         | - 16  |
| Inclusion density / Al <sub>2</sub> O <sub>3</sub> / (kg/m <sup>3</sup> ) | 3960  |

Table 2. Technological operating conditions of the tundish used in simulations

In presented studies full trajectory approach is applied. The inclusion movement is simulated in Fluent using the Discrete Phase Model (DPM). The differential equation describing the motion of inclusions in the liquid steel is:

$$\frac{d u_{inc.}}{d t} = \frac{3 \mu_{st} C_D Re_p}{4 \rho_{inc.} d_{inc.}^2} (u_{st.} - u_{inc.}) + \frac{g(\rho_{inc.} - \rho_{st.})}{\rho_{inc.}} + \frac{1}{2} \frac{\rho_{st.}}{\rho_{inc.}} \frac{d}{d t} (u_{st.} - u_{inc.}) + \frac{\rho_{st.}}{\rho_{inc.}} \frac{d u_{st.}}{d t} \quad (8)$$

where  $u_{inc.}$ ,  $u_{st.}$  are inclusion or liquid steel velocity,  $\rho_{inc.}$ ,  $\rho_{st.}$  are inclusion or liquid steel density,  $d_{inc.}$  is inclusion diameter,  $C_D$  is drag coefficient,  $Re_p$  is particle Reynolds number,  $g$  is gravitational constant,  $\mu_{st.}$  is molecular viscosity of the liquid steel.

The first term on the right hand side of equation (8) describes the drag force, the second term the buoyancy force, the third one the “virtual mass” force and the last one an additional force arising due to the pressure gradient in the fluid.

Inclusions travel through steady-state flow field. In industrial process non-metallic inclusions come to the tundish as deoxidization products together with steel from the ladle or are the product of tundish lining erosion or slag re-entering the melt. In this work only inclusions that originate as deoxidization products are considered. In the numerical simulations thus inclusions come to the tundish with liquid steel, with the same initial velocities as steel. Inclusions are spherical and their density ratio to liquid steel equals 0.56. Presented investigations concentrate on inclusion separation due to flotation. The results do not include other mechanisms of inclusion removal. Therefore inclusions are reflected from all solid surfaces and can come out only through one of the outlets or can be separated at the steel-slag interface (see Figure 5). Coalescence of inclusions is not considered here.

The transport equation is solved for each particle as it travels through the previously calculated flow field. A discrete random walk (DRW) model is applied to model the chaotic effect of the fluid turbulence on inclusion trajectories. In this model a fluctuant-random velocity vector is added to the calculated time average vector, in order to obtain the inclusion velocity at each time-step as it travels through the melt.

Based on the experimental results of the inclusions distribution in testing samples of steel, the numerical simulations have been performed for selected sizes: 2, 5, 10, 20, 30, 40 and 50  $\mu\text{m}$ . 1000 inclusions are released from the inlet surface and their trajectories are calculated with discrete random walk model. Injection of particles with one group size is repeated five times and the total separation rate is an average value form five probes.

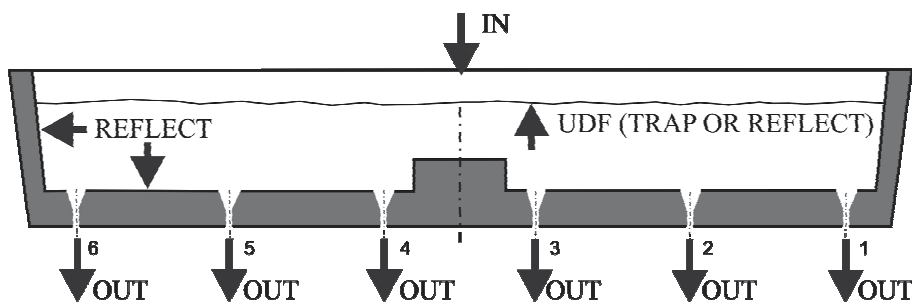


Fig. 5. Boundary conditions for the DPM model in numerical simulations

The separation rate is calculated from the number of inclusions injected to the tundish through the shroud ( $N_{in}$ ) and the number of inclusions counted at the outlets of the tundish ( $N_{out}$ ).

$$\beta = (N_{in} - N_{out}) / N_{in} \quad (9)$$

where:  $\beta$  is inclusion separation rate,  $N_{in}$  is number of inclusions which come into the tundish through the shroud,  $N_{out}$  is number of inclusions which come out through the outlets.

In this way inclusion separation due to flotation is considered. The other mechanisms are not considered in this work but flotation is the dominating mechanism of inclusions removal in tundishes.

## 5. Results and discussion

The results are presented in two sections. The first section focuses on the industrial estimations of inclusions composition and size distribution. The second section concentrates on numerical modelling. This section describes first the flow structure and its changes due to the tundish working space modification. In the second part inclusion separation from liquid steel and their distribution to the individual strands are analysed.

### 5.1 Industrial investigation

Based on the industrial measurements the chemical composition and quantity of inclusions in the analysed area were estimated. Non-metallic inclusions in samples taken from the billets were identified mainly as oxides and sulphides. Detailed statistical characteristics have been defined and on their basis the distribution of non-metallic inclusions have been determined depending on their diameter. The results are given in Table 3.

Based on the presented size distributions of non-metallic inclusions found in samples it can be concluded that the dominating share have the inclusions, which do not exceed the diameter of 15  $\mu\text{m}$ . It is only a little number of inclusions with diameter exceeding 50  $\mu\text{m}$ .

Similar results have been obtained by other plant investigations (Beskow et al., 2002; Zhang et al., 2003; EC Technical Report, 2005). These measurements performed also on aluminum killed steels have shown that the vast majority (about 90%) of the inclusions in tundishes and continuously casted ingots constitute spherical inclusions of small size. In case of oxide inclusions, the largest share (average 70-80%) is aluminum oxides.

| Inclusion diameters (μm) | Share of identified inclusions in size group (%) |        |                           |        |
|--------------------------|--|--------|---------------------------|--------|
|                          | billet casted at nozzle 1                        |        | billet casted at nozzle 2 |        |
|                          | Cast 1   | Cast 2 | Cast 1                    | Cast 2 |
| 0 ÷ 5                    | 60.5   | 63.2   | 53.1                      | 49.2   |
| 5 ÷ 15                   | 24.8   | 20.4   | 24.9                      | 27.9   |
| 15 ÷ 25                  | 3.4  | 8.1    | 10.7                      | 12.8   |
| 25 ÷ 35                  | 4.7  | 4.2    | 3.6                       | 3.1    |
| 35 ÷ 45                  | 2.0  | 0.1    | 2.2                       | 1.2    |
| 45 ÷ 60                  | 0.9  | 1.6    | 3.6                       | 2.8    |

Table 3. Non-metallic inclusions identified in the continuous casted billets during industrial experiment

## 5.2 Numerical investigations

Numerical simulations are used to calculate the liquid flow structure in the tundish and to predict the inclusion separation rates. First, the current tundish configuration has to be diagnosed. Then tundish equipped with dams is numerically investigated.

### 5.2.1 Flow structure and its influence on inclusion separation due to flotation

Analysis of the flow field and temperature distribution in the former tundish have been the topics of earlier studies published elsewhere (Jowša et al., 2006; Merder et al., 2007; Jowša et al., 2007). This research work revealed that the industrial tundish in its basic configuration is characterized by the unfavorable hydrodynamic casting conditions. Among other things, not much ascending streams can be found and they are essential for growing and separating inclusions due to their flotation.

Working space of the tundish has been equipped with dams. The main task of the dams is to reorient and direct the flow of the liquid steel stream. Installing dams in the inlet zone has created a space limited by them, which is a kind of container controlling the turbulence of the flow. Thanks to that the inlet zone is separated from the nozzle zone, which as a consequence should contribute to the reduction of the transient zone, increase of the share of dispersed plug flow and improve of the liquid steel inclusion refining conditions. Fluid flow topologies at the inlet region in the investigated tundish equipped with an impact pad (current configuration) and with dams (modified configuration) are shown in Figure 6.

Figure 7 shows that in the current tundish configuration a step between impact pad and bottom of the tundish direct liquid steel stream to the tundish bottom. It creates a short circuit between inlet and one of the outlet nozzles (number 3). A direct flow of the part of the liquid steel can be the reason of decreasing the quality of billet casted at this strand since small inclusions are transported with steel.

The situation is changing if incoming steel stream meets dams. In this case fluid is directed to the steel-slag interface helping to remove inclusions due to their flotation to the covering

slag. It is expected that dams help to improve steel quality and decrease the differences between individual strands.

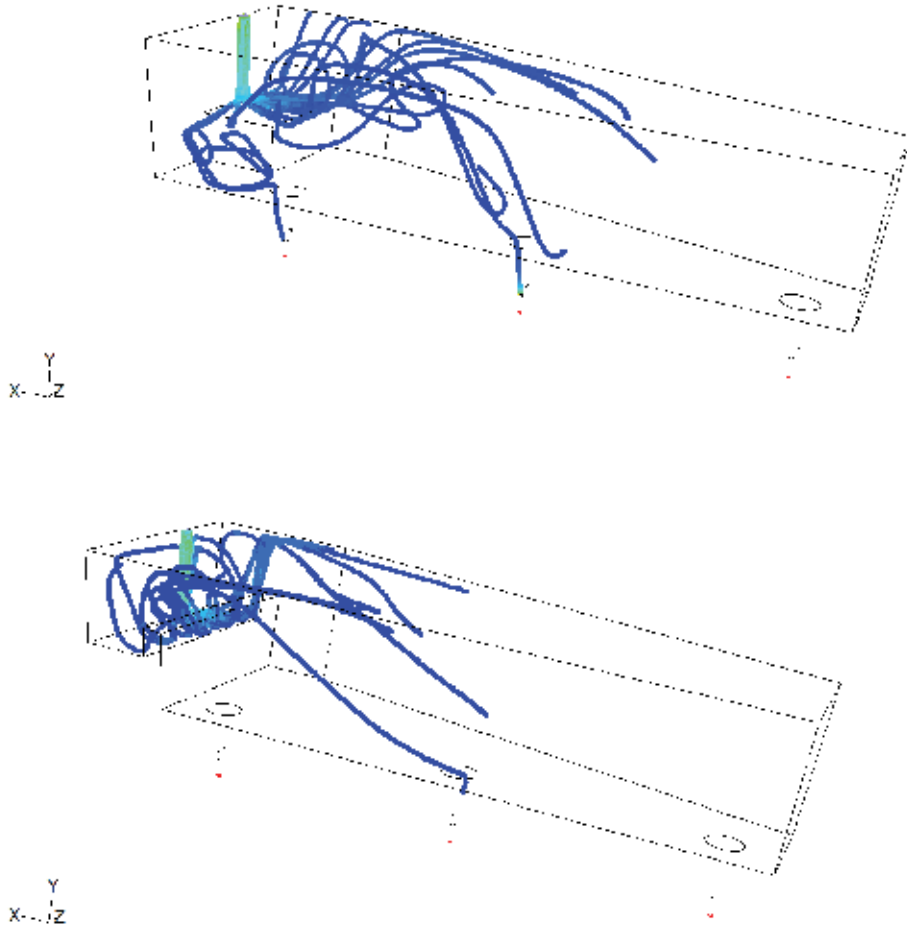


Fig. 6. A fluid flow topology at the inlet region in the investigated tundish equipped with an impact pad (top view, current configuration) and with dams (bottom view, modified configuration)

### 5.2.2 CFD predictions of inclusions separation in the tundish

Numerical simulations have been performed to calculate the inclusion separation rates in currently working tundish configuration. Predicted numerically separation rates are shown in Figure 7. In the first simulation a standard (trap) boundary condition is used for inclusion separation. Using trap condition, it is assumed that all inclusions which reach the covering slag surface are separated.



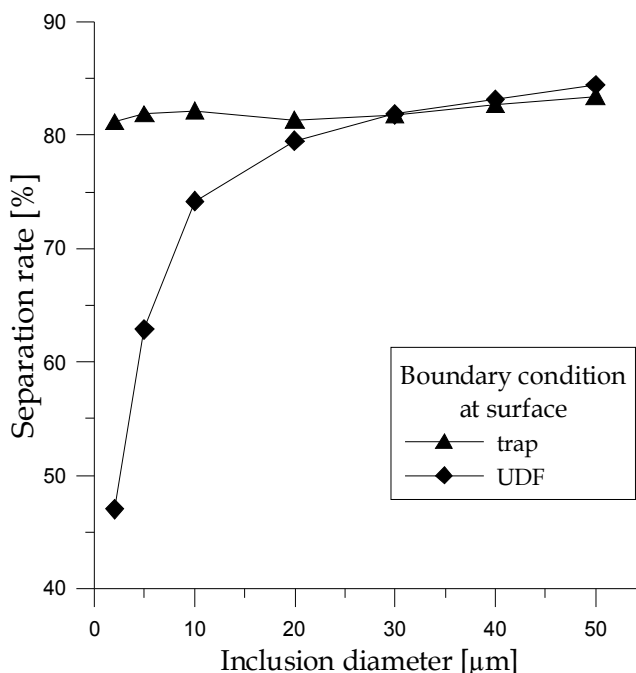


Fig. 7. Inclusions separation rate in the tundish with basic configuration

Figure 7 shows additionally the results obtained for the basic tundish configuration (with impact pad), calculated with modified boundary condition set at the steel-slag interface. It can be seen, that separation rate obtained with standard boundary condition is very high for all inclusion diameters. These results do not correspond to the values of inclusion numbers found in the billets. It is expected that the separation of the inclusions with considered diameters is much lower than predicted numerically.

Such a conclusion is confirmed additionally with results of particle separation performed using tundish water models (Martinez et al., 1986; Joo & Guthrie, 1993; Rogler et al., 2005). This results indicate that separation rate of modeled micro inclusions (diameter less than 30 μm), is very low, which means that they flow with the fluid and are nearly not separated at the water surface.

Rationales coming from industrial and laboratory investigations have been the reason for searching improved boundary condition describing the inclusion separation at the steel-slag interface. In its first approximation velocity of fluid in the vicinity of this border is considered. According to Engh (Engh et al., 1992) the critical velocity of fluid, above which the particle can be re-entrained to fluid, can be derived from a force balance. The shear force is calculated considering the drag force:

$$\tau_0 \pi r_{inc}^2 = \rho_{st} u_b^2 \varphi \pi r_{inc}^2 \quad (10)$$

where  $\tau_0$  is shear stress,  $r_{inc}$  is inclusion radius,  $u_b$  is the velocity outside the boundary layer,  $\varphi$  is an empirical friction factor, for a plane surface it is equal to:

$$\varphi = 0.03 (Re_x)^{-1/5} \quad (11)$$

with

$$\text{Re}_x = u_b x / \nu_{st.} \quad (12)$$

where  $x$  is the distance from the leading edge of the plane and  $\nu_{st.}$  is kinematic viscosity of liquid steel. With the approximation that the shear force and the gravity force are equal and opposite, the critical velocity can be described as:

$$u_b = \left[ \frac{4g(\rho_{st.} - \rho_{inc.})r_{inc.}x^{1/5}}{3\rho_{st.} \cdot 0.03\nu_{st.}^{1/5}} \right]^{5/9} \quad (13)$$

The velocity  $u_b$  has been included in the boundary condition at the surface via an UDF (User Defined Function). Velocity of the fluid in cell at the border where particle reach the surface is compared with the critical velocity. In case if the fluid velocity is lower than the critical velocity the particle is trapped, which means that the inclusion is absorbed by covering slag, otherwise particle come back to the computational domain which means that inclusion flows farther with the fluid.

More work need to be done to include additional forces. However the results obtained with the UDF function gave a better agreement with the experimental results and were a basis to use it also in simulations presented here. The numerical model with modified boundary condition has been previously validated with water model results obtained for the one-strand tundish model (Koitzsch et al., 2008).

This modified boundary condition is used to calculate the separation rates for tundish equipped with dams. The results showing the total separation rate values are shown in Figure 8 and the separation rate values for different strands are shown in Figures 9 and 10.

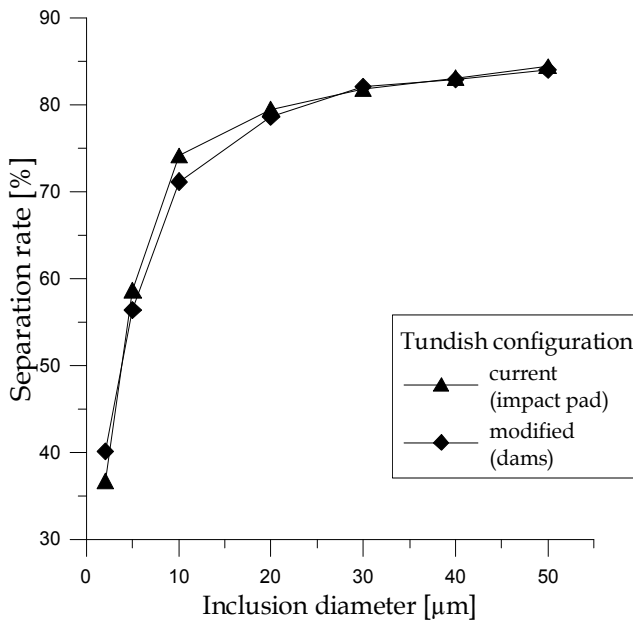


Fig. 8. Separation rate in current and modified tundish

From the results presented in Figure 8 it can be seen that installation of dams in tundish working space does not change the separation rates for none of the investigated inclusion diameters. In Figures 9 and 10 inclusions which flow out from the tundish through the nozzles are counted. Percentage share for each nozzle is calculated. Results shown in Figure 9 concerns tundish with current configuration. It can be seen that number of inclusions flowing out through the nozzle no. 3 is much higher than through the other ones. This confirms the findings from fluid flow structure investigations. In Figure 6 one can see the short circuit that transport the inclusions directly to the outlet nozzle no. 3. This can be the reason of differences in billet quality observed by the producer.

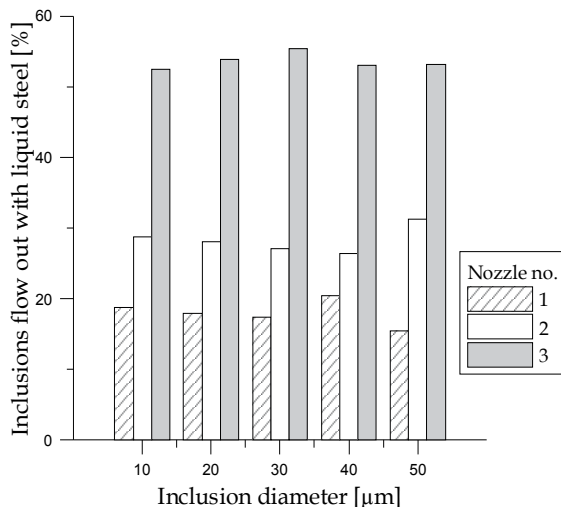


Fig. 9. Inclusions flowing with liquid steel through individual nozzles – tundish basic configuration

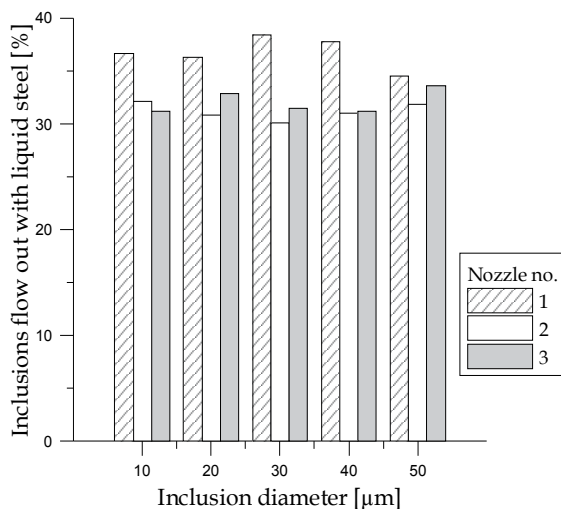


Fig. 10. Inclusions flowing with liquid steel through individual nozzles – tundish with dams

Situation has changed after installing dams. The results showing inclusions flowing out to individual strands are shown in Figure 10. Appearance of dams did not improve the separation rate of inclusions in the investigated tundish (see Figure 8) but what is very important, thanks to them the quality of all billets casted with modified tundish should be very similar.

## 6. Conclusion

This chapter presented the application of Computational Fluid Dynamics (CFD) supported by experimental results to simulate liquid steel flow through the continuous casting tundish and non-metallic inclusions separation process.

The basis of performed studies were to show the differences in billets quality between individual strands observed for the former industrial six-strand tundish configuration. The aim of the studies was to diagnose the current tundish and to decrease the differences in quality of the strands.

The numerical simulations of liquid steel flow through the tundish were carried out using a commercial Computational Fluid Dynamics software Fluent. On pre-calculated flow field, the non-metallic inclusion separation in the investigated tundish is numerically investigated. To validate the numerical results, plant estimations and measurements done previously with water model were used.

The presented results concern the evaluation of the changes in non-metallic inclusion separation due to modifications of the tundish working space. The results of numerical simulation show that dams installed in tundish working space significantly decreased the differences in separation rates at the individual strands.

Future research is currently being carried out to improve boundary condition describing inclusion separation at the steel-slag interface and to estimate the inclusion distribution at the tundish outlets for validation of numerical model in prediction of separation rates.

## 7. Acknowledgment

The author would like to thank Prof J. Jowsa from the Czestochowa University of Technology for his advice and support and to Dr T. Merder from the Silesian University of Technology for cooperation in research work.

## 8. References

- Beskow, K.; Jia, J.; Lupis, C.H.P.; Sicien, D. (2002). Chemical characteristics of inclusions formed at various stages during the ladle treatment of steel. *Ironmaking & Steelmaking*, Vol. 29, No. 6, (December 2002), pp. 427-435, ISSN 0301-9233
- Braun, A.; Warzecha, M.; Pfeifer, H. (2010). Numerical and Physical Modeling of Steel Flow in a Two-Strand Tundish for Different Casting Conditions. *Metal. and Mater. Trans. B*, Vol. 41, No. 3, (June 2010), pp. 549-559, ISSN 1073-5615
- Chakraborty, S.; Sahai, Y. (1992). Effect of holding time and surface cover in ladles on liquid steel flow in continuous casting tundishes. *Metal. Trans. B*, Vol. 23, No. 2, (February 1992), pp. 153-167, ISSN 1073-5615

- Chattopadhyay, K.; Isac, M.; Guthrie, R.I.L. (2010). Physical and mathematical modelling of steelmaking tundish operations: A review of the last decade (1999-2009). *ISIJ International*, Vol. 50, No. 3 (March 2010), pp. 331-348, ISSN 0915-1559
- Engh, T.A.; Simensen, C.J.; Wijk, O. (1992). *Principles of Metal Refining*, Oxford University Press, ISBN 0-19-856337-X, USA
- European Commission technical steel research report. (2005). Improved production control through rapid characterisation of non-metallic inclusions in steel, Final Report EUR 21627 EN, ISBN 92-894-9695-9
- Hou, Q.; Zou, Z. (2005). Comparison between standard and renormalization group  $k-\epsilon$  models in numerical simulation of swirling flow tundish. *ISIJ International*, Vol. 45, No. 3, (March 2005), pp. 325-330, ISSN 0915-1559
- Joo, S.; Guthrie, R.I.L. (1991). Heat flow and inclusion behaviour in a tundish for slab casting. *Canadian Metall. Quarterly*, Vol. 30, No. (1991), pp. 261-269, ISSN 1879-1395
- Joo, S.; Guthrie, R.I.L. (1993). Inclusion behavior and heat-transfer phenomena in steelmaking tundish operations: part 1 aqueous modeling. *Metal. and Mater. Trans. B*, Vol. 24, No. 5, (October 1993), pp. 755-765, ISSN 1073-5615
- Jowsa, J.; Boguslawski, A.; Garncarek, S.; Warzecha, M.; Merder, T.; Tyliczszak, A.; Cwudzinski, A. (2007). Research Report 3 T 08B 006 26
- Jowsa, J.; Derda, W.; Warzecha, M.; Merder, T.; Staniewski, I.; Cwudzinski, A. (2006). Numerical modelling of the mass, heat and momentum transfer during continuous casting of steel and in the ladle metallurgy processes. *Metallurgy – Metallurgical Engineering news*, No. 6, (June 2006), pp. 252-256, ISSN 1230-3534
- Koitzsch, R.; Warzecha, M.; Ruckert, A.; Pfeifer, H. (2008). Physical and mathematical simulation of the inclusion removal and determination of the deposition rate for the continuous casting process. *6th European Conference on Continuous Casting (ECCC 2008)*, Riccione, Italy, 4 – 6 June 2008
- Martinez, E.; Maeda, M.; Heaslip, L.J.; Rodriguez, G.; Mclean, A. (1986). Effects of fluid flow on the inclusion separation in continuous casting tundish. *Transactions ISIJ*, Vol. 26, No. 8, (August 1986), pp. 724-731, ISSN 0021-1583
- Mazumdar, D.; Guthrie, R. I. L. (1999). The physical and mathematical modelling of continuous casting tundish systems. *ISIJ International*, Vol. 39, No. 6, (June 1999), pp. 524-547, ISSN 0915-1559
- Merder, T.; Jowsa, J.; Warzecha, M.; Muchowicz, L.; Mendak, D.; Kalarus, L. (2007). Verification of the mathematical model of heat transfer in the continuous casting tundish. *Metallurgy – Metallurgical Engineering news*, No. 7, (July 2007), pp. 350-353, ISSN 1230-3534
- Rogler, J.P.; Heaslip, L.J.; Mehrvar, M. (2005). Physical modeling of inclusion removal in a tundish by gas bubbling. *Canadian Metall. Quarterly*, Vol. 44, No. 3, (July 2005), pp. 357-368, ISSN 1879-1395
- Shih, T.-H.; Liou, W.W.; Shabbir, A.; Yang, Z.; Zhu, J. (1995). A new  $k-\epsilon$  eddy-viscosity model for high Reynolds number turbulent flows – model development and validation. *Computers Fluids*, Vol. 24, No. 3, (March 1995), pp. 227-238, ISSN 0045-7930
- Solorio-Diaz, G.; Morales, R.D.; Palafax-Ramos, J.; Garcia-Demedices, L.; Ramos-Banderas, A. (2004). Analysis of fluid flow turbulence in tundishes fed by swirling ladle shroud. *ISIJ International*, Vol. 44, No. 6, (June 2004), pp. 1024-1032, ISSN 0915-1559

Zhang, F.; Taniguchi, S.; Cai, K. (2000). Fluid flow and inclusion removal in continuous casting tundish. *Metal. and Mater. Trans. B*, Vol. 31, No. 2, (April 2000), pp. 253-266, ISSN 1073-5615

Zhang, L.; Thomas, B.G.; Cai, K.; Zhu, L.; Cui, J. (2003). Inclusion investigation during clean steel production at Baosteel. *ISSTech 2003*, ISS, Warrandale, PA, (2003), pp. 141-156

# Numerical Simulation of Influence of Changing a Dam Height on Liquid Steel Flow and Behaviour of Non-metallic Inclusions in the Tundish

Adam Cwudziński

*Czestochowa University of Technology,  
Department of Metals Extraction and Recirculation  
Poland*

## 1. Introduction

The steel material is formed during the course of heterophase processes. During the smelting, ladle treatment and casting of steel efforts are made to obtain a homogeneous material that is free from any type of contaminants, which include both non-metallic inclusions (NMI) and gases. Among hazardous gases causing defects in steel material are oxygen, nitrogen, or hydrogen. NMI, on the other hand, include any types of oxides, sulphides and nitrides (Nuspl et al., 2004; Rocabois et al., 2003; Van Ende et al., 2009; Herrera-Trejo et al., 1998). The current state of knowledge enables steel products to be manufactured, which meet any requirements imposed on particular steel grades. However, the constant development of technology certainly enables searching for new standards and the production of even purer steel grades than those currently manufactured in production conditions. Due to the systematically depleting iron ore deposits, the electric arc process is more and more commonly used for steel production, which relies on scrap being the main carrier of impurities that might penetrate into the structure of steel material. Therefore it seems justifiable to develop and improve the processes of ladle treatment and continuous casting of liquid steel (Matsuura et al., 2007; Tanaka et al., 1994; Lachmund & Xie, 2003; Xie et al., 2005; Gupta & Chandra, 2004; Basu et al., 2004). Presently, the liquid metal as prepared on the ladle furnace stand has the required metallurgical purity and temperature allowing it to be cast by the continuous method. However, a number of interesting research works concerning tundishes have drawn the metallurgists' attention to this plant and contributed to perceiving the tundish also as an effective device assisting the liquid steel refining processes (Solorio-Diaz et al., 2005; Lopez-Ramirez et al., 2001; Hou et al., 2008; Bessho et al., 1992; Kuklev et al., 2004; Cwudziński, 2010). This results primarily from the fact that liquid steel resides in the tundish for a specific time, during which any phenomena that favour the refining process can be stimulated and intensified. The present chapter reports the results of studies on the behaviour of liquid steel and NMI in liquid steel as it flows through the tundish. The Ansys-Fluent® program was used for solved mathematical model of casting process.

Plotting of the RTD (residence time distribution) curve was possible by using a virtual tracer and introducing it to the numerical tundish model. As a result of computations, fields of liquid steel flow, fields of turbulence intensity, fields of steel temperature and non-metallic inclusions growth, residence time distribution type C and F curves were obtained. The facility under investigation is a tundish designed for casting slabs. This is a wedge-type tundish of a nominal capacity of 30 tons. The tundish incorporates a stopper rod system for controlling the outflow of liquid steel into the mould. Two novel constructional solutions concerning the change in the tundish working space were designed for the facility under examination. The dam being presently in use was made in two variants by changing the dam height. Thus, information about the influence of dam height variation on the process of NMI growth in the liquid metal and on liquid steel flow hydrodynamics was obtained. The description of the above-mentioned phenomenon is important, because the larger non-metallic inclusions, the easier they flow out to the liquid metal surface and can be assimilated by the tundish powder. However, the NMI growth generating the change in non-metallic inclusions size alone does not guarantee that the refining process will be effective. Therefore, the selection of the type of liquid steel flow control device to enhance the NMI take-out is of key importance. The intensification of liquid steel refining processes must also have rational justification in the costs incurred for this purpose. Therefore, the making of prototype flow control devices and their application in actual industrial conditions should be preceded by simulation studies carried out for a particular industrial facility, while maintaining the main technological parameters of the process being run.

## 2. Testing methodology

### 2.1 Numerical model

The mathematical model for the flow of steel in the tundish is described in detail in work (Cwudziński, 2010). The computer simulations were performed for unsteady and non-isothermal conditions. However for the simulation of the simultaneous flow of liquid steel and non-metallic inclusions and growth and aggregation of NMI in the liquid steel, the two-phase "mixture" model with population balance model in the turbulent motion condition was employed. For the description of the turbulence of liquid steel flow through the tundish, the k-ε turbulence model was adopted (Ilegbusi et al., 2000). In the population balance model, discrete method was employed for simulation of non-metallic phase behaviour within the working space of the tundish. The both model are described by the following equations:

$$\frac{\partial}{\partial t}(\rho_m) + \nabla \cdot (\rho_m \bar{v}_m) = 0 \quad (1)$$

$$\bar{v}_m = \frac{\sum_{k=1}^n \alpha_k \rho_k \bar{v}_k}{\rho_m} \quad (2)$$

$$\rho_m = \sum_{k=1}^n \alpha_k \rho_k \quad (3)$$



$$\frac{\partial}{\partial t}(\rho_m \bar{v}_m) + \nabla \cdot (\rho_m \bar{v}_m \bar{v}_m) = -\nabla p + \nabla \cdot \left[ \mu_m (\nabla \bar{v}_m + \nabla \bar{v}_m^T) \right] + \rho_m \bar{g} + \bar{F} + \nabla \cdot \left( \sum_{k=1}^n \alpha_k \rho_k K \bar{v}_{dr,k} \bar{v}_{dr,k} \right) \quad (4)$$

$$\mu_m = \sum_{k=1}^n \alpha_k \mu_k \quad (5)$$

$$\bar{v}_{dr,k} = \bar{v}_k - \bar{v}_m \quad (6)$$

$$\frac{\partial}{\partial t} \sum_{k=1}^n (\alpha_k \rho_k E_k) + \nabla \cdot \sum_{k=1}^n (\alpha_k \bar{v}_k (\rho_k h_k + p)) = \nabla \cdot (k_{eff} \nabla T) + S_E \quad (7)$$

where:  $t$  - time [s],  $\rho_m$  - mixture density [ $\text{kg}/\text{m}^3$ ],  $\bar{v}_m$  - mass averaged velocity [m/s],  $\alpha_k$  - volume fraction of phase  $k$  [-],  $\rho_k$  - density of phase  $k$  [ $\text{kg}/\text{m}^3$ ],  $\bar{v}_k$  - velocity of phase  $k$  [m/s],  $\rho_m$  - mixture density [ $\text{kg}/\text{m}^3$ ],  $p$  - pressure [Pa],  $\mu_m$  - viscosity of mixture [Pa·s],  $n$  - number of phases,  $g$  - gravitational acceleration [ $\text{m}/\text{s}^2$ ],  $\bar{F}$  - body force [N],  $\bar{v}_{dr,k}$  - drift velocity of phase  $k$  [m/s],  $\mu_k$  - viscosity of phase  $k$  [Pa·s],  $T$  - temperature [K],  $S_E$  - volumetric heat sources,  $k_{eff}$  - effective thermal conductivity [ $\text{W}/\text{m}\cdot\text{K}$ ],  $h_k$  - enthalpy for phase  $k$  [J/kg].

The relative velocity and drift velocity are presented by the following expressions:

$$\bar{v}_{pq} = \bar{v}_p - \bar{v}_q \quad (8)$$

$$c_k = \frac{\alpha_k \rho_k}{\rho_m} \quad (9)$$

$$\bar{v}_{dr,p} = \bar{v}_{pq} - \sum_{k=1}^n c_k \bar{v}_{qk} \quad (10)$$

where:  $\bar{v}_{pq}$  - slip velocity [m/s],  $\bar{v}_p$  - velocity of secondary phase [m/s],  $\bar{v}_q$  - velocity of primary phase [m/s],  $c_k$  - mass fraction for any phase  $k$  [-],  $\alpha_k$  - volume fraction of phase  $k$  [-],  $\rho_k$  - density of phase  $k$  [ $\text{kg}/\text{m}^3$ ],  $\rho_m$  - mixture density [ $\text{kg}/\text{m}^3$ ],  $\bar{v}_{dr,p}$  - drift velocity [m/s],  $\bar{v}_{qk}$  - velocity of phase  $k$  [m/s].

The relative velocity and drift velocity are presented by the following expressions:

$$\frac{\partial}{\partial t}(\rho_{NMI} \alpha_i) + \nabla \cdot (\rho_{NMI} u_i \alpha_i) + \frac{\partial}{\partial V} \left( \frac{G_v \rho_{NMI} \alpha_i}{V} \right) = \rho_{NMI} V_i (B_{ag,i} - D_{ag,i}) + 0^i \rho_{NMI} V_0 \dot{n}_0 \quad (11)$$

$$\alpha_i = N_i V_i, \quad i = 0, 1, \dots, N-1 \quad (12)$$

$$N_i(t) = \int_{V_i}^{V_{i+1}} n(V, t) dV \quad (13)$$

$$f_i = \frac{\alpha_i}{\alpha} \quad (14)$$

$$\frac{\partial}{\partial V} \left( \frac{G_v \rho_{NMI} \alpha_i}{V} \right) = \rho_{NMI} V_i \left[ \left( \frac{G_{v,i-1} N_{i-1}}{V_i - V_{i-1}} \right) - \left( \frac{G_{v,i} N_i}{V_{i+1} - V_i} \right) \right] \quad (15)$$

$$B_{ag,i} = \sum_{k=1}^N \sum_{j=1}^N a_{kj} N_k N_j x_{kj} \xi_{kj} \quad (16)$$

$$D_{ag,i} = \sum_{j=1}^N a_{ij} N_i N_j \quad (17)$$

$$a_{ij} = a(V_i, V_j) \quad (18)$$

$$\xi_{kj} = \begin{cases} 1 & \text{for } V_i < V_{ag} < V_{i+1}, \text{ where } i \leq N-1 \\ 0 & \text{otherwise} \end{cases} \quad (19)$$

$$V_{ag} = [x_{kj} V_i + (1 - x_{kj}) V_{i+1}] \quad (20)$$

$$x_{kj} = \frac{V_{ag} - V_{i+1}}{V_i - V_{i+1}} \quad (21)$$

where:  $\rho_{NMI}$  – density of non-metallic inclusions [kg/m<sup>3</sup>],  $\alpha_i$  – volume fraction of particle size  $i$  [-],  $\alpha$  – total volume fraction of the secondary phase [-],  $u_i$  – velocity magnitude of particle size  $i$  [m/s],  $V$  – volume [m<sup>3</sup>],  $G_v$  – particle volume [m<sup>3</sup>],  $V_i$  – volume of the particle size  $i$  [m<sup>3</sup>],  $B_{ag,i}$  – particle size  $i$  birth rates of aggregation [m<sup>3</sup>/s],  $D_{ag,i}$  – particle size  $i$  death rates of aggregation [m<sup>3</sup>/s],  $\dot{n}_0$  – nucleation rate [particles/m<sup>3</sup>/s],  $a_{ij}$  – aggregation kernel [m<sup>3</sup>/s],  $V_{ag}$  – particle volume resulting from the aggregation of particle  $k$  and  $j$  [m<sup>3</sup>],  $x_{kj}$  – contribution of particle  $k$  and  $j$  [-],  $N$  – number of bins.

The variation in the size of NMIs as a result of their mutual collisions caused by the turbulent motion of steel in the population balance model is expressed by the so called collision kernel ( $a_{ij}$ ) which is described by the following expressions:

$$a_{ij} = t_T \sqrt{\frac{8\pi}{15}} \dot{\gamma} \frac{(V_i + V_j)^3}{8} \quad (22)$$

$$\dot{\gamma} = \frac{\varepsilon^{0,5}}{\nu} \quad (23)$$

$$t_T = 0,732 \left( \frac{5}{N_T} \right)^{0,242} \quad (24)$$

$$N_T = \frac{6\pi\mu(V_i + V_j)^3 \dot{\lambda}}{8H} \quad (25)$$

$$\dot{\lambda} = \left( \frac{4\varepsilon}{15\pi\nu} \right)^{0.5} \quad (26)$$

where:  $t_T$  - capture efficiency coefficient of turbulent collision,  $\dot{\gamma}$  - shear rate,  $\varepsilon$  - turbulent energy dissipation rate [ $\text{m}^2/\text{s}^3$ ],  $\nu$  - kinematic viscosity [ $\text{m}^2/\text{s}$ ],  $N_T$  - ratio between viscous force and Van der Waals force,  $\dot{\lambda}$  - deformation rate,  $H$  - Hamaker constant for non-metallic inclusions  $2,3 \cdot 10^{-20}$ .

To build the virtual tundish models with an appropriate computational grid, Gambit software was used. The space of the virtual tundish models was formed by a computation grid made of 575-585 thousand tetrahedral elements. Tet/hybrid elements of Tgrid type were used to generate the computational grid. The grid made form such elements consisted primarily of tetrahedrons; but it could also contain cubes, pyramids and wedges. Computations of the flow of steel and NMIs (non-metallic inclusions) were performed in the Ansys-Fluent<sup>®</sup> program. Liquid steel flowed into the tundish at a velocity of 1.31 m/s. The values of  $k$  and  $\varepsilon$  for the steel flowing into the tundish were, respectively:  $0.017161 \text{ m}^2/\text{s}^2$  and  $0.064231 \text{ m}^2/\text{s}^3$ . The temperature of the liquid metal flowing into the tundish was 1827 K. The symmetry condition was assumed on the free surface of steel, whereas on the remaining surfaces describing the tundish and flow control device walls, the wall condition was assumed. No heat losses was assumed on the surface described by the symmetry condition, by assuming the ideal thermal insulation of the liquid metal. The heat loss on the tundish walls and bottom was assumed to be  $2600 \text{ W}/\text{m}^2$ , and on the flow control device wall describing surfaces and the immersible poring tube surfaces,  $1750 \text{ W}/\text{m}^2$ . For the description of the non-metallic phase, non-metallic inclusions of a density of  $3960 \text{ kg}/\text{m}^3$  were selected. The heat capacity and thermal conductivity of NMIs and liquid steel were, respectively:  $1364 \text{ J}/\text{kg}\cdot\text{K}$  and  $5,5 \text{ W}/\text{m}\cdot\text{K}$ , and  $750 \text{ J}/\text{kg}\cdot\text{K}$  and  $41 \text{ W}/\text{m}\cdot\text{K}$ . In addition, to describe the effect of temperature on the liquid steel, Bussinesq's description was used. For the employed description, the thermal expansion for steel was assumed to be at a level of  $0,0001 \text{ K}^{-1}$ . For the computation of tundish steel residence time curves, the scalar transfer equation, so called UDS user defined scalar, was used. It was thereby possible to introduce a virtual tracer to the system under analysis and to take the measurement of the variation of tracer concentration on the tundish outlet in time. Based on industrial experimental tests, the boundary conditions of the mathematical model were defined and an overall picture of non-metallic inclusion behaviour under industrial conditions was obtained. It was assumed in the simulation studies that the initial distribution in the form of 1, 1,2, 1,4, 1,7, 2, 2,5, 3, 3,6, 4,3  $\mu\text{m}$  diameter NMI fraction shares on the tundish inlet was, respectively: 0,55, 0,088, 0,088, 0,088, 0,088, 0,0033, 0,0033 and 0,0033. Variation in the share of NMI fractions in the size range from 1 to 11  $\mu\text{m}$ , i.e. NMI diameters of 1, 1,2, 1,4, 1,7, 2, 2,5, 3, 3,6, 4,3, 5,2, 6,3, 7,6, 9,1 and 11  $\mu\text{m}$ , was observed during computer simulation. In all of the simulation variants, only the possibility of NMI aggregation due to turbulence collisions was assumed. The system of equations forming the mathematical model of liquid steel flow with non-metallic inclusions secondary phase was solved by the method of control volumes by employing discretization of the second order upwind using the sequential solver. On the other hand "Quick" discretization was used for volume fraction. The algorithm SIMPLIC (Semi-Implicit Method for Pressure-Linked Equations-Consistent) was used for the description of the coupling of the pressure and velocity fields in the model being solved. The controlled level of residues was at a level of at least  $10^{-3}$ . The condition to comply with the impassable  $y^+$  parameter values (30+60) indicating the correct choice of the grid in the

wall boundary layers was also respected. The numerical computations were made with a so called 3ddp three-dimensional double precision solver. The simulations of steel flow in the tundish furnishing variants under consideration were performed on two 64-bit computational servers, each of them being equipped with two quad core 2.4 GHz processors and an operating memory of 12 GB RAM. The assessment of flow can already be done at the stage of analysis of the graphic distribution of the RTD curve E and F (qualitative analysis). From the obtained E-type time curve distributions, it is possible to determine the values that quantitatively define the hydrodynamic conditions in the tundish (Sahai & Emi, 2008; Mazumdar & Guthrie, 1999). Thus, the ranges of the stagnant, plug, and ideal mixing flows can be determined. In this method, the stagnant flow occurs in the regions, for which the value of the dimensionless time of steel residence in the tundish exceeds the value of 2. While, the plug flow is the sum of the values of the first and the maximum times of tracer appearances on the tundish nozzle divided by two. The plug flow is most favourable for the free NMI flotation from the liquid steel, whereas the stagnant flow may lead to drops in liquid steel temperature below the level permissible for a specific steel grade. In turn, the F curve is essential for the determination of the range of the transient zone that characterizes the hydrodynamic conditions existing in the tundish during the successive casting of steel grades differing in chemical composition. In the transient zone, there is a batch of liquid metal with a composition in between those of the steel grades being cast. Hence, this is a product which is difficult to be classified and subsequently processed in the Rolling Mill's departments. The model presented in work [Clark et al.] assumes that the transient zone exist between the values 0.2 and 0.8 of the dimensionless concentration of the tracer substance used for recording the curve in the system under examination. The F curve is described by relationship 27.

$$F = \frac{C_t - C_0}{C_\infty - C_0} \quad (27)$$

where:  $C_0$  - initial concentration of chemical element [kg],  $C_t$  - temporary concentration of a chemical element [kg],  $C_\infty$  - final concentration of a chemical element [kg].

## 2.2 Characterization of the test facility

The test object is a tundish designed for casting concast slab (fig.1a). Figure 1b shows the virtual geometry of the tundish with a line plotted, which indicates the distance by which the dam has been moved away from the tundish pouring zone. The nominal tundish capacity is 30 tons, but in the simulation variants examined it contained 25 Mg. This is a wedge-type tundish with a characteristic lowering of the bottom in the tundish stopper rod zone (the steel level in the tundish stopper rod zone is 0,92 m, and in the remaining tundish space, 0,7 m). Steel flows to the tundish through a ceramic ladle shroud of an inner diameter of 70 mm. In the tundish being currently operated in the industrial conditions, a notched dam and a system for controlling the flow of steel to the mould (stopper rod) have been mounted. The dimensions of the dam are shown in figure 2. The liquid steel flows to the mould through a ceramic submerged entry nozzle of an inner diameter of 70 mm.

For the modification of the direction of liquid steel flow within the tundish working space, a modified dam was employed, which is currently being used industrially. The modification of the dam consisted in the change of its height. In the first modification variant, the dam was elongated by 0,23 m up to 0,35 m, while in the second variant, by 0,38 m up to 0,5 m. Should favourable results from the point of view of conducting the CSC technology be

obtained, the proposed dam modification would be very simple to accomplish in the industrial conditions. The proposed change of the dam height does not need any interference in the design of the tundish working space. On the other hand, the modification involves an increase in the surface exposed to the liquid metal. Therefore, the modified dam should be made from refractory materials that will prevent any erosion from occurring during the casting process.

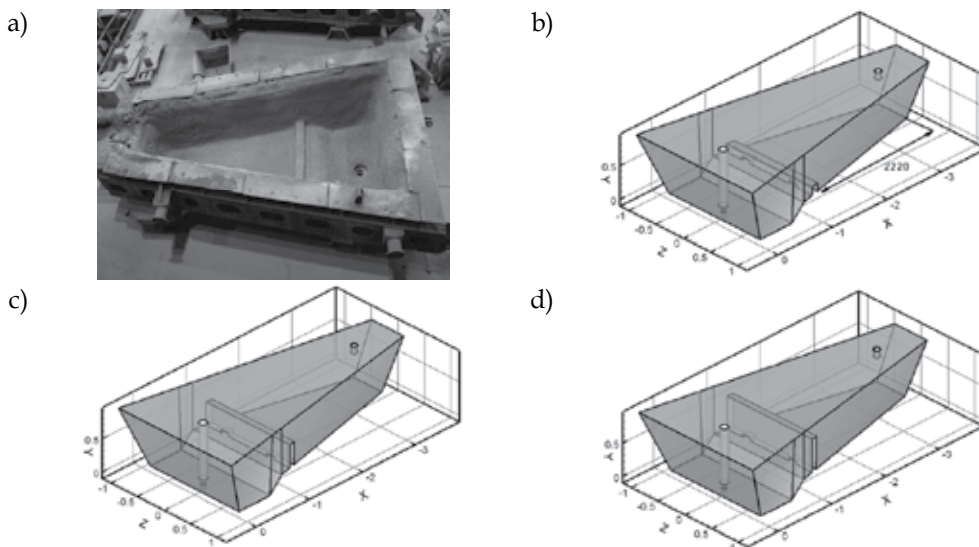


Fig. 1. Views of test facility: a) real tundish, b) virtual model of tundish with low dam, c) virtual model of tundish with medium dam, d) virtual model of tundish with high dam

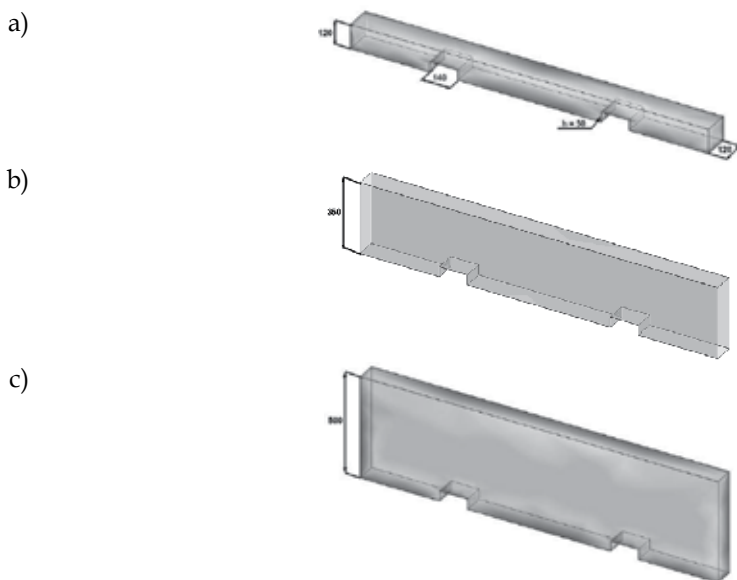


Fig. 2. Views of dam: a) low dam, b) medium dam, c) high dam

### 2.3 Description of industrial experiment

The industrial experiment was aimed at verifying the steel flow hydrodynamics, as well as the distribution of non-metallic inclusions in the steel. For the verification of the computer simulation results for steel flow, the measurement of chemical composition of the steel was employed, whereby so called lollipop samples were taken from the CSC machine mould. The measurements were taken from the moment of opening until the moment of closing the steelmaking ladle with a steel grade other than that existing in the tundish. Using a sampler, the operator sucked in liquid steel which, after solidification, was transferred to a quantometer where the steel was assayed for chemical composition. The samples were taken, on the average, every 1 minute (the first 9 samples) and every 3 minutes (the subsequent samples), depending on the casting speed (Cwudziński, 2008). Whereas, for the verification of non-metallic inclusion distribution in the liquid steel in the tundish during the CSC process, samples of the same type were taken from the upper part of the liquid metal under the tundish powder layer. The sampling area is indicated by the broken line in Figure 3. To define the initial conditions in the numerical model for NMI inclusion distribution in the liquid steel, lollipop samples were also taken from the steelmaking ladle located at the ladle furnace stand. A sample was taken from the steel prepared for casting immediately prior to the ladle departure from the ladle furnace stand. All the samples taken, after being freely cooled down, were prepared in the form of microsections for analysis on a scanning microscope to determine the distribution of NMIs and to measure their size in the metal batch taken. The measurement area on the prepared microsection surface was a surface area of 0.8 mm<sup>2</sup>. The industrial experiments were made during a sequence of casting 1500×225 dimension concast slabs at a speed of 0.9 m/min.

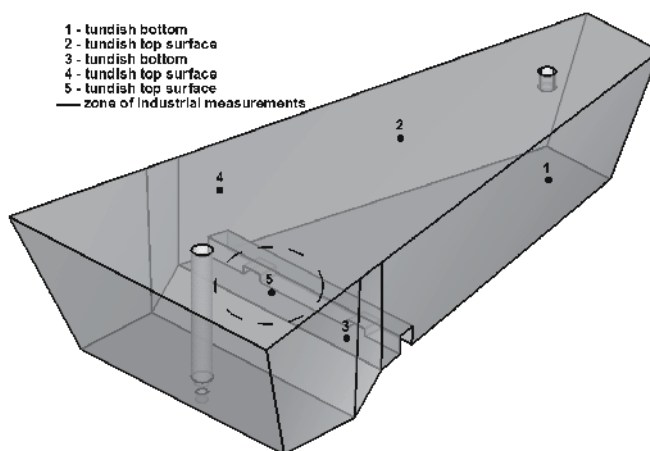


Fig. 3. View of tundish with measurement points and zone of industrial measurements

Figure 4 presents steel mixing curves for two melts differing in chemical composition, cast consecutively one after another. By recording the variation in the concentration of copper, niobium, carbon and chromium, points characterizing the process of steel mixing under real industrial conditions were obtained. The obtained industrial experiment results indicate satisfactory agreement between the computation results and the hydrodynamic conditions occurring during the course of the actual CSC process.

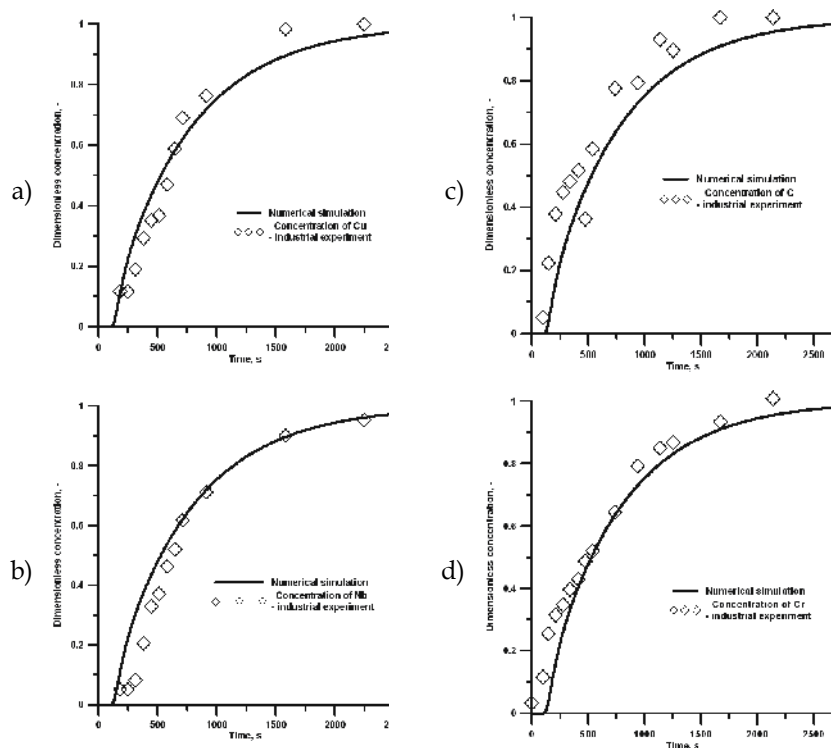


Fig. 4. Results of numerical simulation and industrial experiment: a) mixing curve calculated by numerical simulation and concentration of Cu measured during industrial experiment, b) mixing curve calculated by numerical simulation and concentration of Nb measured during industrial experiment, c) mixing curve calculated by numerical simulation and concentration of C measured during industrial experiment, d) mixing curve calculated by numerical simulation and concentration of Cr measured during industrial experiment

Figure 5 presents NMI growth curves computed numerically and juxtaposed with the industrial experiment results for three NMI size classes. The first size class concerned NMIs of a diameter of 1  $\mu\text{m}$ ; the second NMI size class comprised non-metallic inclusions in the size range from 1 to 3  $\mu\text{m}$ ; and the third NMI size class concerned non-metallic inclusions in the size range from 3 to 5  $\mu\text{m}$ . The division of NMIs into size classes was due to the fact that in the real industrial conditions non-metallic inclusions occur in very diverse size ranges, e.g. in the range from 1 to 2  $\mu\text{m}$  there occur NMIs of a size of 1, 1,1, 1,15 or 1,2 and 1,5  $\mu\text{m}$ , etc., up to 2  $\mu\text{m}$ . In the computer simulation, Class I was represented by NMIs of a size of 1  $\mu\text{m}$ ; Class II, by NMIs of a size of 1,2, 1,4, 1,7, 2 and 2,5  $\mu\text{m}$ ; while Class III, NMIs of a size of 3, 3,6 and 4,3  $\mu\text{m}$ . The NMI identification made on the basis of samples taken under industrial conditions showed that there were very few NMIs of a diameter above 5  $\mu\text{m}$ : on the average, 2 inclusions in the area examined, i.e. in a surface area of 0.8  $\text{mm}^2$ . In several samples, no NMIs of a size above 5  $\mu\text{m}$  were observed at all. Hence, Figure 5 concerns the three NMI size classes. In the numerical model, the possibility of NMI growth as a result of turbulent collisions was assumed. From the obtained results, no satisfactory agreement between the computer simulation results and the industrial experimental test results is

observed, especially for NMI size classes I and II. The numerical model does not foresee such a sharp change in NMI size from class I to class II, however it fairly well correlates with the results for class III of NMI size. The presented results indicate that the numerical model for NMI growth requires further improvement. Nevertheless, considering the complexity of the process of NMI growth in liquid steel and the difficulties involved with industrial tests (the high temperature of the CSC process), the proposed model can presently be used for the preliminary assessment of the influence of the flow control devices (FCD) on the process of NMI growth in the tundish.

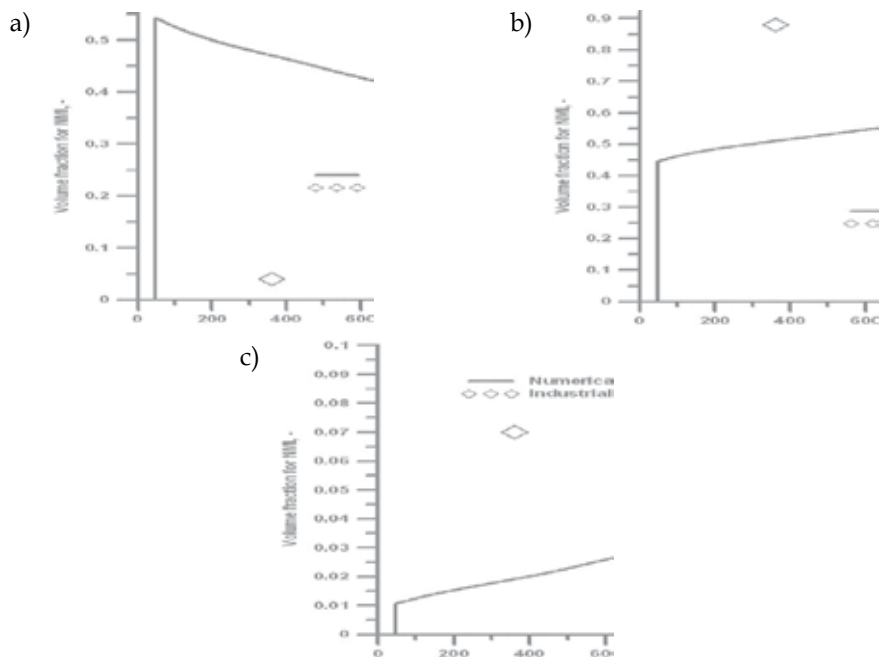


Fig. 5. Results of numerical simulation and industrial experiment: a) NMI growth curve calculated by numerical simulation and contribution of NMI (first class) in the liquid steel measured during industrial experiment, b) NMI growth curve calculated by numerical simulation and contribution of NMI (second class) in the liquid steel measured during industrial experiment, c) NMI growth curve calculated by numerical simulation and contribution of NMI (third class) in the liquid steel measured during industrial experiment

### 3. Computational results

Based on the performed computations, the fields of flow, turbulence intensity and steel temperature, among other things, have been obtained. Figure 6 presents the fields of steel flow in the central part of the tundish between the feed zone and the stopper rod system zone. When examining the presented figures it can be noticed that the change of the dam height does not cause any significant changes in the direction of steel flow in this tundish part. The tundish is divided into two regions. In the first region, between the tundish feed zone and the dam, metal circulations are observed in the central tundish part at the bottom. A back stream flowing in to this region from the stopper rod system zone can also be seen.



Whereas, in the second tundish region, after the dam, the steel stream makes its way toward the nozzle. In all of the tundish equipment variants, there are no ascending streams in the tundish region examined, which would intensify the flotation of NMIs to the slag phase. The reconstruction of the tundish does not cause any changes in the intensity of turbulence of the flowing steel (Fig. 7). The turbulence intensity is calculated from relationship (28) and take on values from 0 to 1.

$$I = \frac{\sqrt{\frac{2}{3}k}}{v_{ref}} \quad (28)$$

where:  $v_{ref}$  - reference velocity [m/s],  $k$  - kinetic energy of turbulence [ $m^2/s^2$ ]

Beyond the tundish feed zone, the turbulence intensity assumes values at a level of 0,01, which is indicative of a calm steel flow pattern. An parameter important from the SCS process viewpoint is liquid steel temperature. Each steel grade requires a specific casting temperature, and it is therefore important to assure that the proposed modernization of the plant's inner space will not impair the thermal conditions existing in the tundish. From the results represented in Figure 8, very good thermal stability of the plant is observed in all of the tundish equipment variants proposed. Figure 9 presents the residence time curves, C and F. The observation of hydrodynamic conditions prevailing in the tundish is possible thanks to the recording of tracer concentration variation as a function of time. On the axis of abscissae in Figure 9, the dimensionless time is expressed by the ratio of the actual time to the average tundish steel residence time. The steel movement maps, presented earlier, did not indicate any significant steel flow modification that might have been caused by the change of the dam height. Whereas, the shape of the RTD curves C and F describing the flow of steel on a macro scale, that is for the entire facility, does indicate a change in the steel flow pattern for particular tundish equipment variants. The increase in dam height causes a shift of the C curve peak from the axis of ordinates, which results in an increase in the share of plug flow in the overall flow structure. Moreover, a shortening of the line denoting the change of tracer concentration behind the peak is observed, which will be reflected in the developing of the extent of the stagnant flow share. Changes in the flow pattern are also visible in Figure 10b, as the position of the mixing curves changes at points 0,2 and 0,8 of the dimensionless tracer concentration.

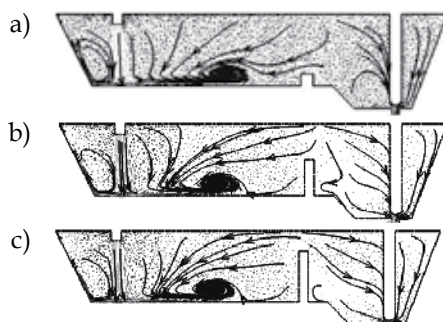


Fig. 6. Liquid steel flow in the central plane: a) tundish actually working in the steel plant, b) tundish with medium dam, c) tundish with high dam

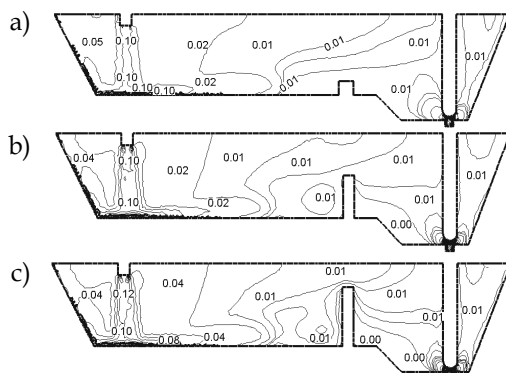


Fig. 7. Turbulence intensity of liquid steel in the central plane: a) tundish actually working in the steel plant, b) tundish with medium dam, c) tundish with high dam

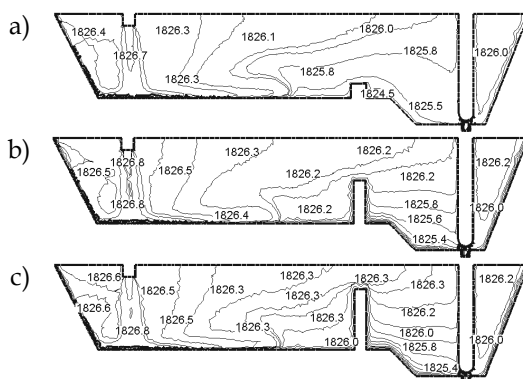


Fig. 8. Distribution of temperature fields of liquid steel in the central plane: a) tundish actually working in the steel plant, b) tundish with medium dam, c) tundish with high dam

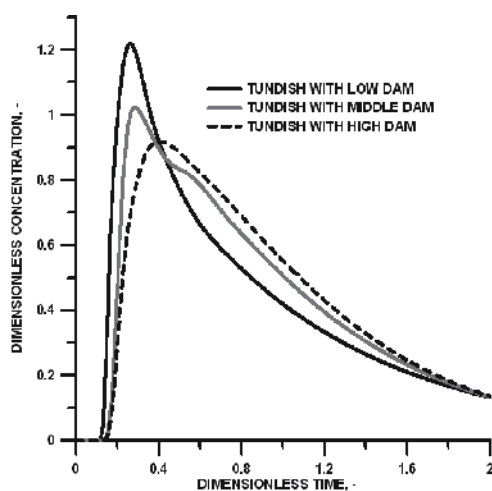


Fig. 9. Residence time distribution curve for consider variants of tundish

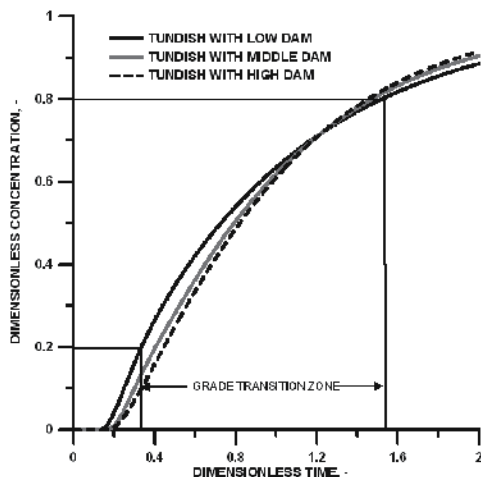


Fig. 10. Mixing curve for consider variants of tundish

For the quantitative analysis of the hydrodynamic conditions, it is necessary to calculate the shares of stagnant, plug and ideal mixing flows, as well as the quantity of metal existing in the transient zone. Table 1 provides the shares of particular flows, as calculated based on the C RTD curve. A successive increase in the dam height results in an increase in the plug flow share by 7% for the tundish with a high dam. In the case of the stagnant flow in the tundish with a high dam, a decrease in the share of this flow by 11% occurs. A positive effect of dam height change by up to 0.5 m is also visible for the transient zone extent. For this variant of tundish equipment, there is by 5 Mg less steel in the transient zone compared to the tundish variant being currently used in the industrial conditions.

| No. of tundish variant | Percentage contribution, % |           |                   |
|------------------------|----------------------------|-----------|-------------------|
|                        | Stagnant flow              | Plug flow | Ideal mixing flow |
| 1                      | 33,3                       | 13,2      | 53,5              |
| 2                      | 26,2                       | 14,2      | 59,6              |
| 3                      | 22,4                       | 20,2      | 57,4              |

Table 1. Steel flow characteristic for consider variants of tundish

| No. of tundish variant | Range of transition zone, [s] | Length of casting steel strand, [m] | Weight of casting steel strand, [Mg] | Reduction of grade transition zone, [Mg] |
|------------------------|-------------------------------|-------------------------------------|--------------------------------------|--|
| 1                      | 871                           | 13,06                               | 30,8                                 | -  |
| 2                      | 778                           | 11,67                               | 27,5                                 | 3,3                                      |
| 3                      | 729                           | 10,93                               | 25,7                                 | 5,1                                      |

Table 2. Characterization of grade transition zone for consider variants of tundish

Figures 11 to 16 represent the curves of fraction share change for NMIs of a diameter of 1, 2,5, 3,6, 5,2, 7,6 and 11  $\mu\text{m}$ . As NMIs in the size range of 1 to 11  $\mu\text{m}$  primarily follow the

liquid metal current, and their floatation onto the free steel surface depends chiefly on the steel flow direction, therefore the behaviour of NMIs in the liquid steel is represented during the average time of liquid metal residence in the tundish. For the metallurgical facility under consideration, the average liquid steel residence time, as expressed by the ratio of the mass of metal (kg) in the tundish to the flow rate of steel (kg/s), was 740 seconds. The change in the share of particular NMI fractions reflects the NMI growth process in the liquid metal. The NMI growth process was recorded at five measurement points located within the tundish and one point located at the tundish outlet. The results of computer simulation of NMI behaviour in the steel, shown in Figures 11 to 16, excellently not only depict the steel NMI growth process itself, but also illustrate their movement within the tundish working space. This is indicated by the shift of the fraction share change curves from the axis of ordinates, depending on the measurement point. The farther away from the tundish feed zone a point is situated, the later NMIs flow in there and the recording of their growth process occurs. An exception is the third point located behind one the notches in the dam. Here, NMIs appear latest, which is indicative of the complexity of the steel flow process. The position of curve peaks shown in Figures 11-16 illustrates also how NMIs start to change their size in the first steel casting phase (3 minutes from the start of the casting sequence). For NMIs of a size of 1  $\mu\text{m}$ , the value of the peak at successive measurement points is at a different level in the axis of ordinates, decreasing successively. For NMIs of a diameter of 2,5, 3,6, 5,2, 7,6 and 11  $\mu\text{m}$ , on the other hand, the curve peak attains a higher value at successive measurement points. After about 3 minutes, a stabilized NMI growth follows. For NMIs of a size above 5.2  $\mu\text{m}$ , or the 7,6 and 11  $\mu\text{m}$ -diameter NMIs, the share of fractions is contained in the range, successively, from  $1\text{e-}4$  to  $5\text{e-}11$  and from  $1\text{e-}3$  to  $3\text{e-}11$ , which suggest a very slow process of NMI growing up to sizes of around 7,6 and 11  $\mu\text{m}$ . The obtained picture refers to the testing results obtained from industrial experiment. Moreover, in the case of 7,6 and 11  $\mu\text{m}$ -size NMIs, the fraction share values are so small that the shape of the curves representing variations in the share of fractions, as observed in Figures 15 and 16, has no significance for the NMI growth process. The change in the dam height influences the NMI aggregation process. The higher the dam, the smaller the share of 1  $\mu\text{m}$ -diameter NMI fractions is, especially behind the dam towards the tundish outlet. The increase in the dam height intensifies the process of formation of increasingly large NMIs (Figs. 12-14). The most dynamic growth process of all NMIs examined was observed for NMIs of a diameter of 3.6  $\mu\text{m}$  (Fig. 12). The presented fraction share variation curves for particular NMIs, as recorded in different tundish regions, indicate little differences in the progress of the NMI growth process in a given size range. On the other hand, the observation of the NMI growth process in different tundish regions is important from the point of view of understanding of the behaviour of NMIs in different tundish regions. NMIs not assimilated by the tundish powder reach, together with steel, the tundish outlet and constitute a potential source of faults likely to occur in the concast slab. When examining the fraction share variation curves recorded at the tundish outlet, shown in Figures 11-16, one can notice that, in spite of the NMI growth process occurring in the liquid steel flowing into the mould, 1  $\mu\text{m}$ -diameter NMIs still constitute the vast majority of the NMI population. At the same time, a greater number of larger NMIs appear in the steel flowing to the mould, e.g. for 3,6  $\mu\text{m}$ -diameter NMIs, an increment in the fraction share at a level of 100% takes place.

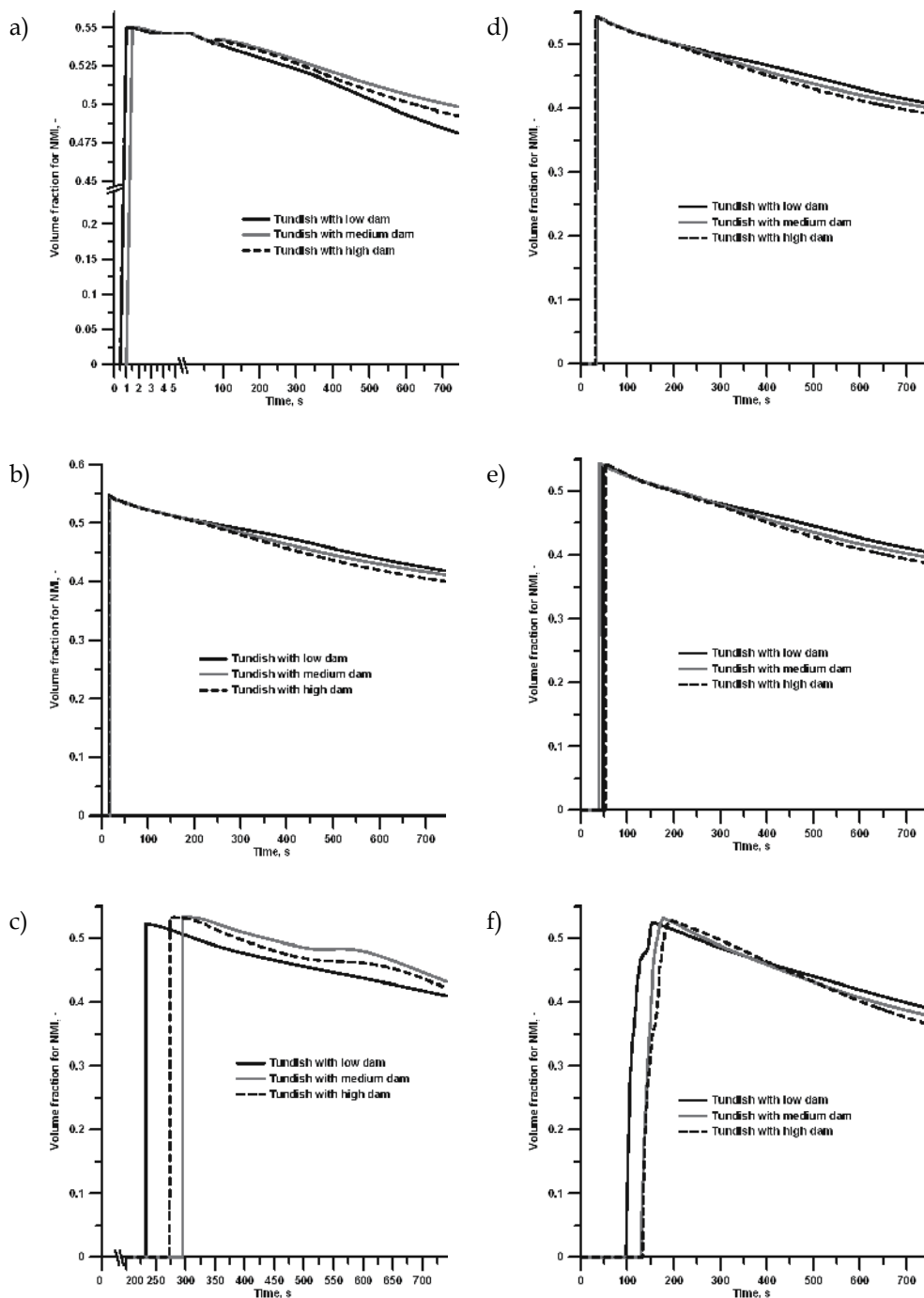


Fig. 11. NMI growth curve for 1  $\mu\text{m}$  diameter inclusions: a) point 1, b) point 2, c) point 3, d) point 4, e) point 5, f) tundish outlet

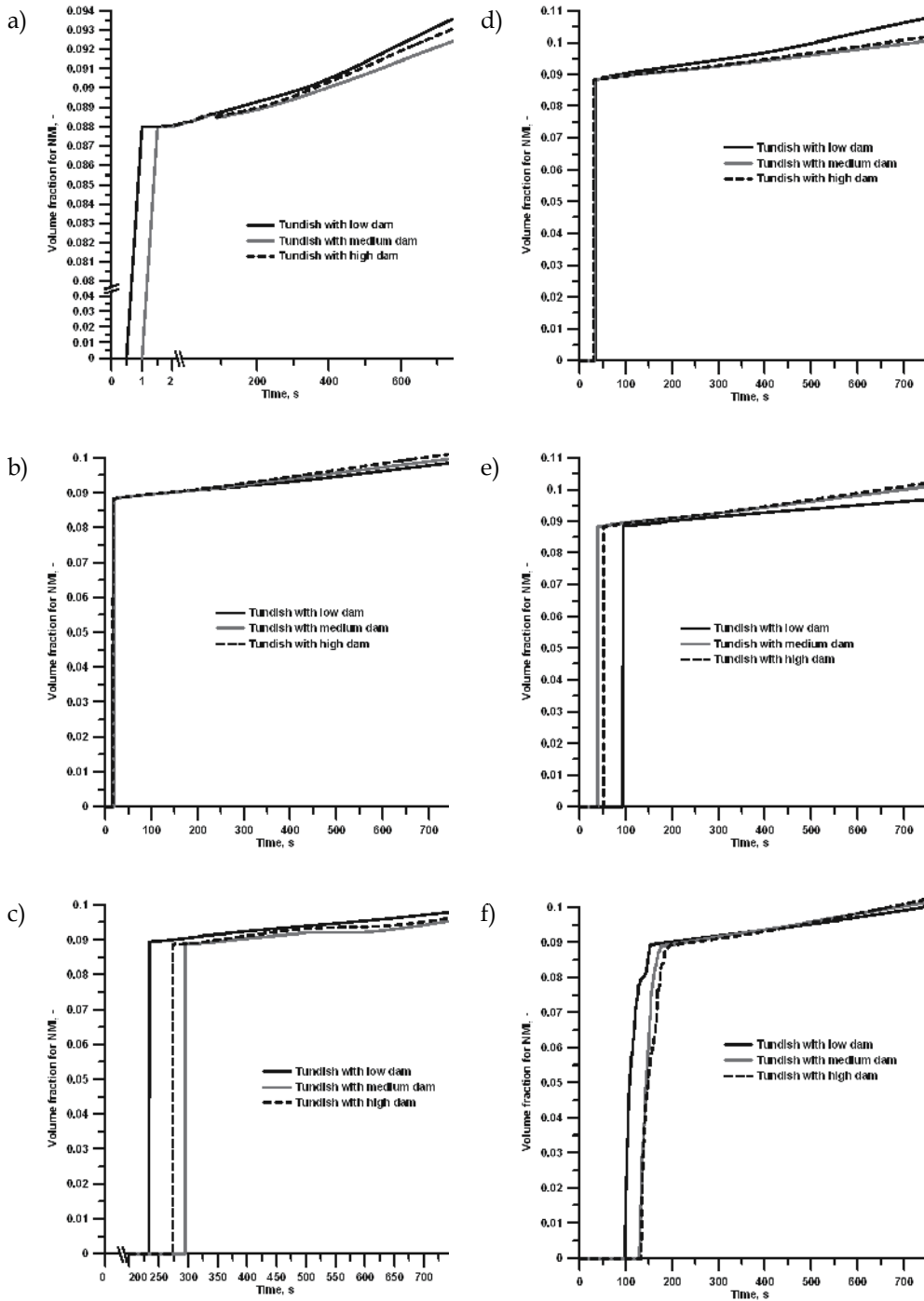


Fig. 12. NMI growth curve for 2,5  $\mu\text{m}$  diameter inclusions: a) point 1, b) point 2, c) point 3, d) point 4, e) point 5, f) tundish outlet

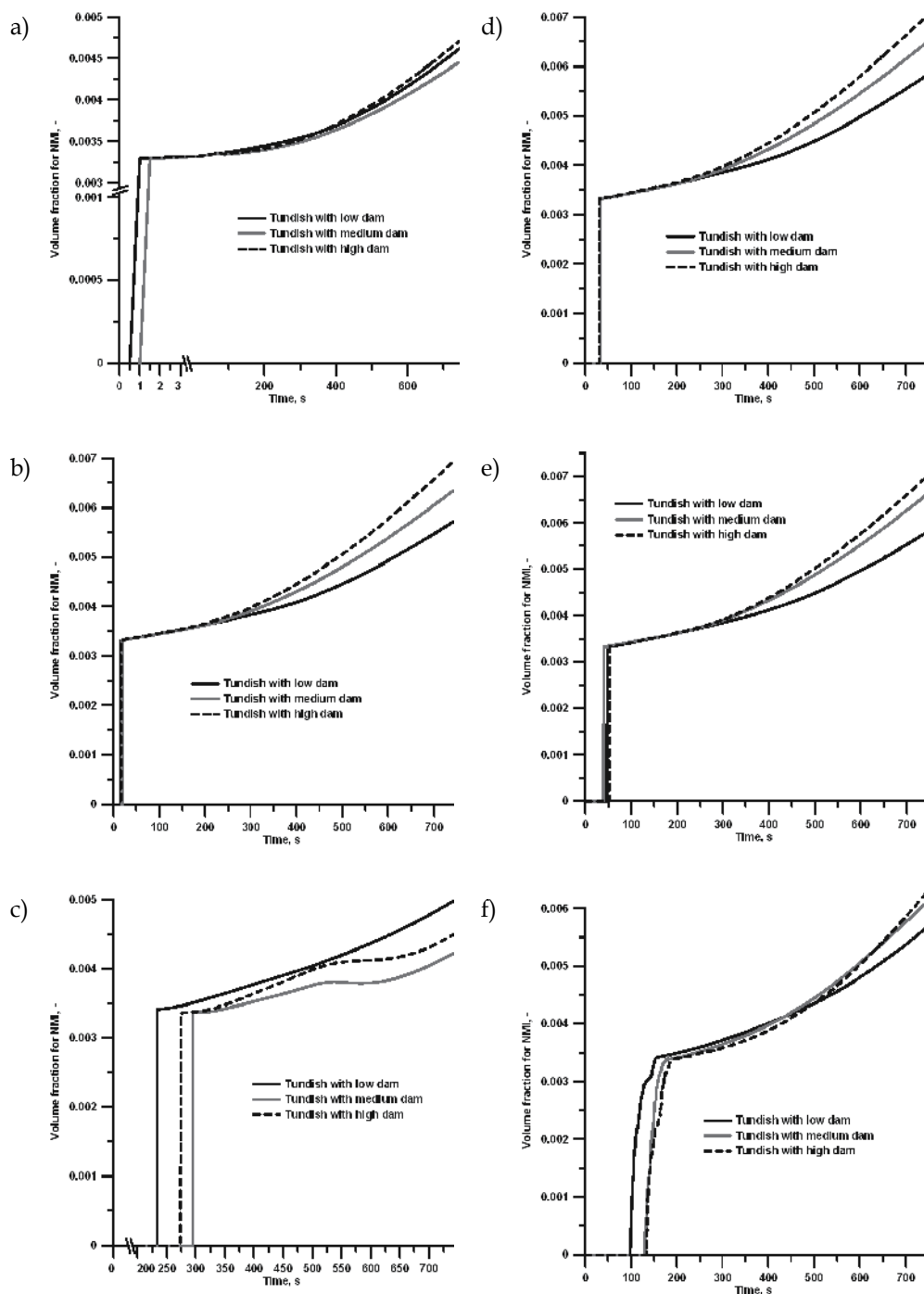


Fig. 13. NMI growth curve for 3,6  $\mu\text{m}$  diameter inclusions: a) point 1, b) point 2, c) point 3, d) point 4, e) point 5, f) tundish outlet

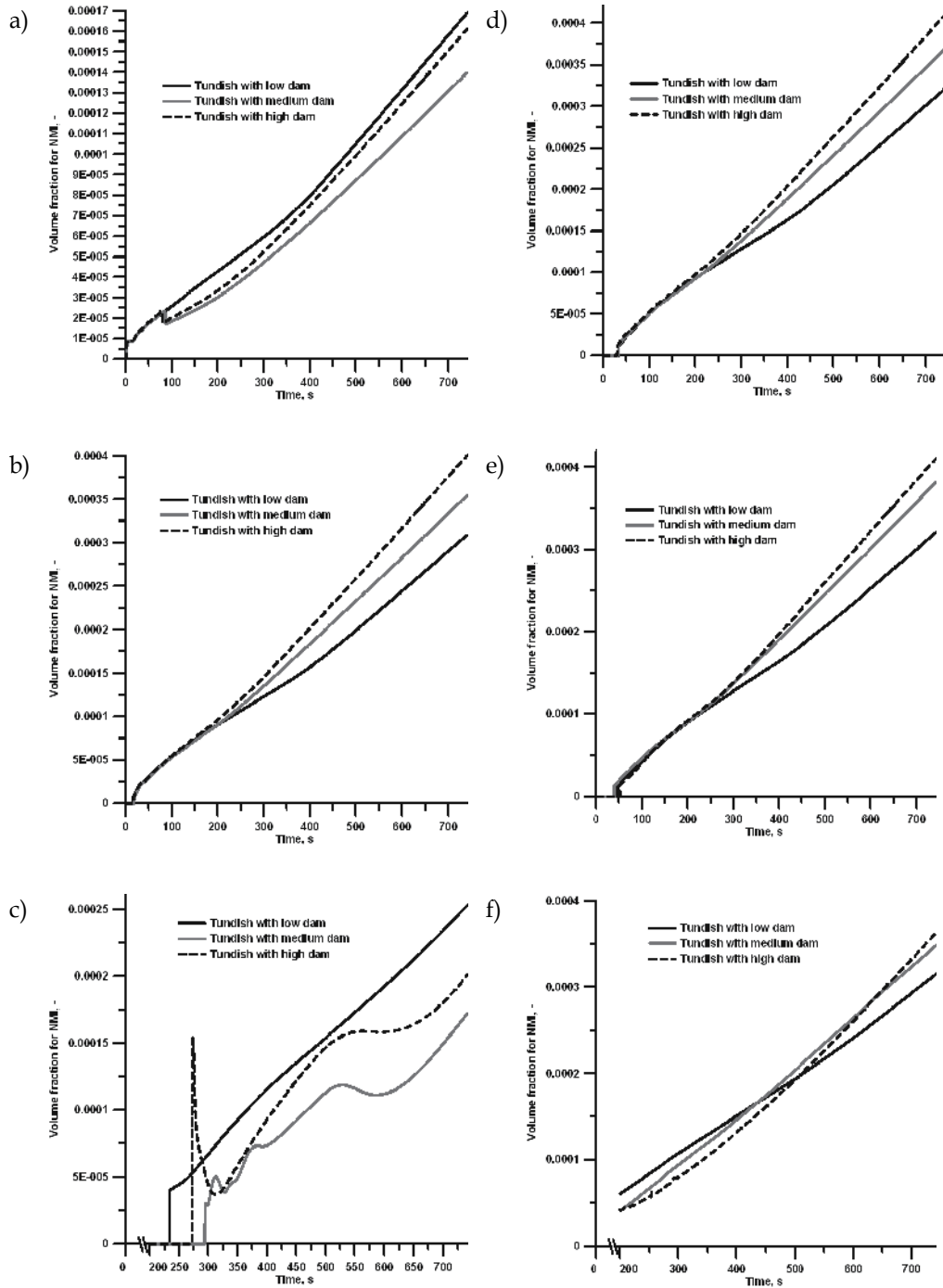


Fig. 14. NMI growth curve for 5,2 μm diameter inclusions: a) point 1, b) point 2, c) point 3, d) point 4, e) point 5, f) tundish outlet



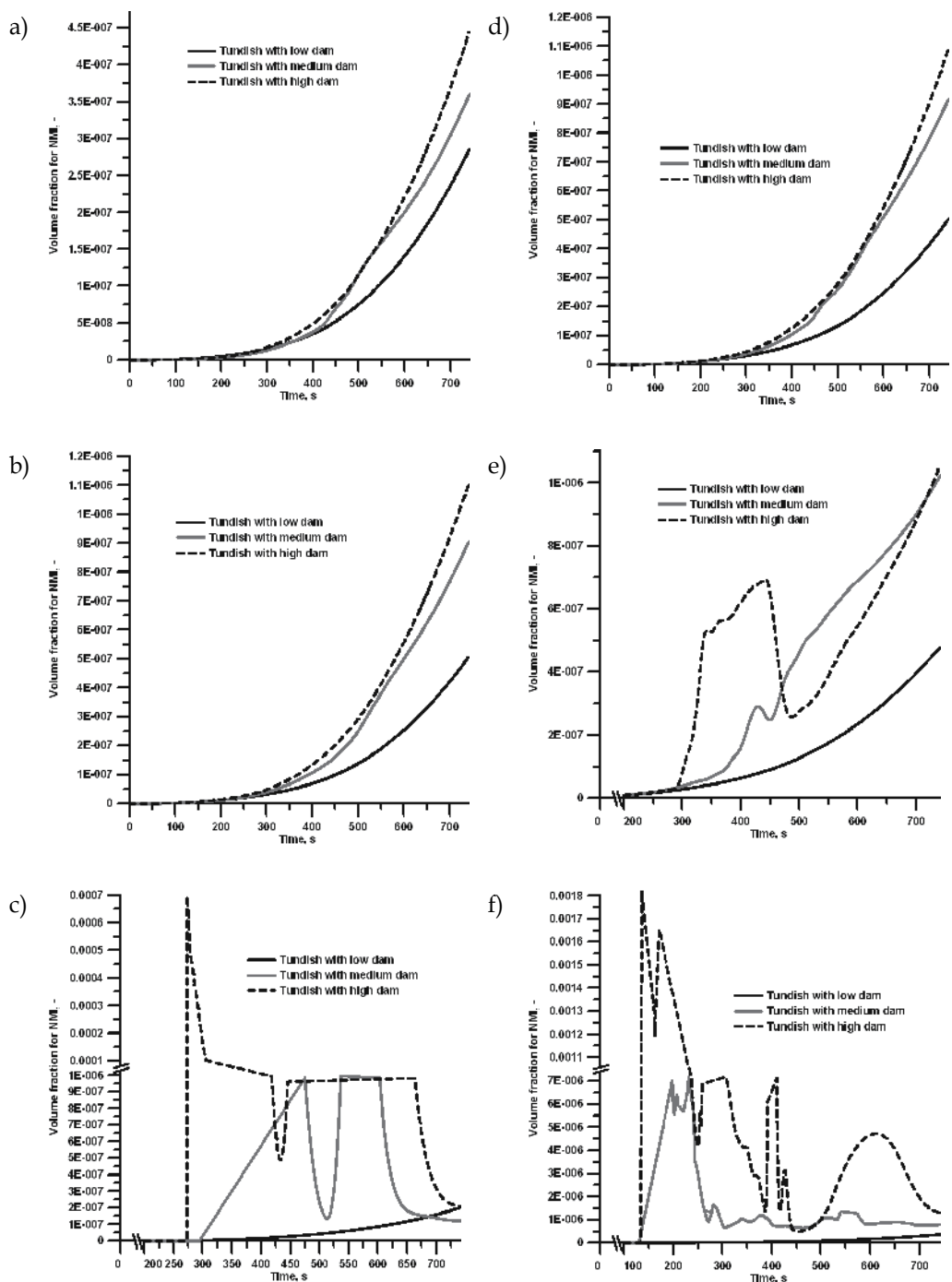


Fig. 15. NMI growth curve for 7,6 μm diameter inclusions: a) point 1, b) point 2, c) point 3, d) point 4, e) point 5, f) tundish outlet

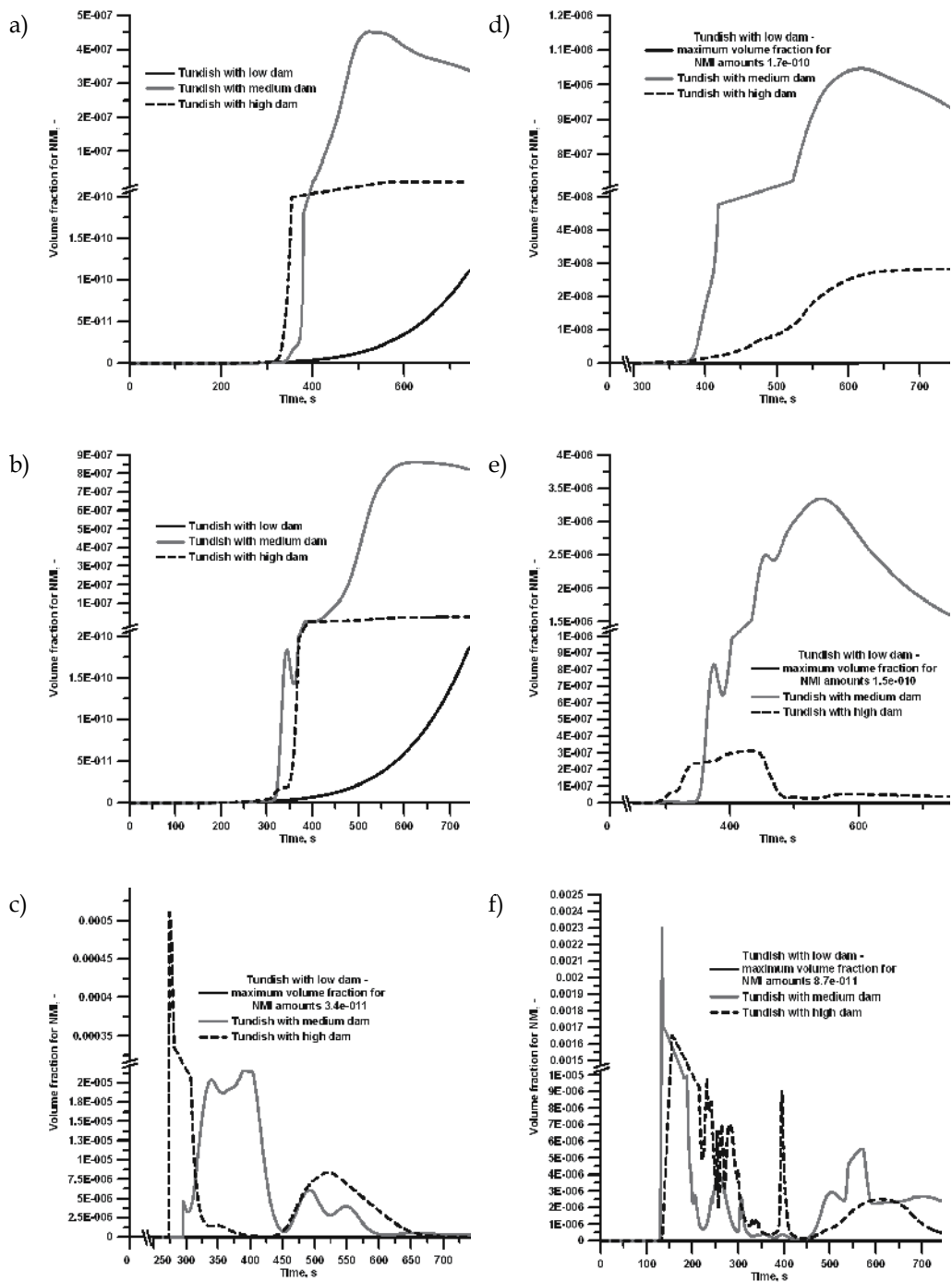


Fig. 16. NMI growth curve for 11 μm diameter inclusions: a) point 1, b) point 2, c) point 3, d) point 4, e) point 5, f) tundish outlet

#### 4. Conclusion

On the basis of the performed computations and industrial experiments it has been established that:

- The numerical steel flow model correctly reflects the hydrodynamic conditions of steel flow in the tundish,
- The numerical NMI growth model, in spite of the lack of satisfactory agreement with the industrial experiment results, can be used for the preliminary analysis of the influence of flow control devices on the NMI growth process,
- Increasing the dam height does not disturb the thermal stability of the tundish
- Raising the dam causes an increase in the plug flow share and a decrease in the stagnant flow share in the steel flow pattern,
- By changing the dam height, the extent of the transient zone between steel grades of different chemical composition being cast is reduced.
- The proposed upgrade of the dam will intensify the process of NMI growth in the tundish.

#### 5. Acknowledgment

This scientific work has been financed from the resources allocated for Science in the years 2009-2011 as Research Project No. N508390437.

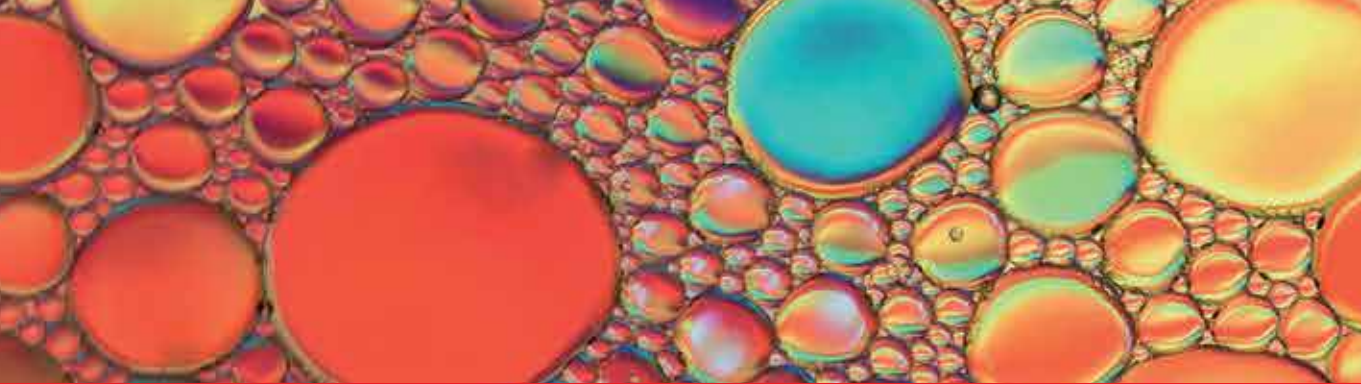
This publication has been made with the financial support by the Foundation for Polish Science

#### 6. References

- Basu, S.; Choudhary, S. K. & Girase N. U. (2004). Nozzle clogging behaviour of Ti-bearing Al-killed ultra low carbon steel. *ISIJ International*, Vol.44, No.10, pp. 1653-1660, online ISSN 1347-5460
- Bessho, N.; Yamasaki, H.; Fujii, T.; Nozaki, T. & Hiwasa, S. (1992). Removal of inclusion from molten steel in continuous casting tundish. *ISIJ International*, Vol.32, No.1, pp. 157-163, online ISSN 1347-5460
- Clark, M.; Wagner, T. & Troussset, A. *Modeling for tundish applications*, 01.2008, Available from [http://www.foseco-steel.com/steel/downloads/technical\\_papers/08.pdf](http://www.foseco-steel.com/steel/downloads/technical_papers/08.pdf)
- Cwudziński, A. (2008). *Control of steel flow in the slab tundish*, PhD Thesis, Czestochowa University of Technology. (in polish)
- Cwudziński, A. (2010). Numerical simulation of liquid steel flow and behaviour of non-metallic inclusions in one-strand slab tundish with subflux turbulence controller and gas permeable barrier. *Ironmaking & Steelmaking*, Vol.37, No.3, pp. 169-180, online ISSN 1743-2812
- Gupta, N. & Chandra S. (2004). Temperature prediction model for controlling casting superheat temperature. *ISIJ International*, Vol.44, No.9, pp. 1517-1526, online ISSN 1347-5460
- Herrera-Trejo, M.; Castro, M. R.; DMendez, J. N.; Solis, H. T.; Tena, J. M. & Guzman, E. (1998). Evolution of inclusion nature during the EAF-LF-CC process. *Scandinavian Journal of Metallurgy*, Vol.27, pp. 233-239, ISSN 0371-0459

- Hou, Q.; Yue, Q.; Wang, H.; Zou, Z. & Yu, A. (2008). Modelling of inclusion motion and flow patterns in swirling flow tundishes with symmetrical and asymmetrical structures. *ISIJ International*, Vol.48, No.6, pp. 787-792, online ISSN 1347-5460
- Ilegbusi, O.; Iguchi, M. & Wahnsiedler, W. (2000). *Mathematical and Physical Modeling of Materials Processing Operations*, Chapman & Hall/CRC, ISBN 9781584880172
- Kuklev, A. V.; Tinyakov, V. V.; Aizin, Y. M.; Gushchin V. N.; Ul'yanin V. A.; Ordin, V. G.; Lamukhin, A. M. & Zagorul'ko V. P. (2004). Optimization of the hydrodynamic characteristics of tundishes in order to remove exogeneous nonmetallic inclusions. *Metallurgist*, Vol.48, No.3-4, pp. 153-157, online ISSN 1573-8892
- Lachmund, H. & Xie, Y. (2003). High purity steels: a challenge to improved steelmaking processes. *Ironmaking & Steelmaking*, Vol.30, No.2, pp. 125-129, online ISSN 1743-2812
- Lopez-Ramirez, S.; Barreto, J. de J.; Palafox-Ramos, J.; Morales, R. D. & Zacharias D. (2001). Modeling study of the influence of turbulence inhibitors on the molten steel flow, tracer dispersion and inclusion trajectories in tundishes. *Metallurgical and Materials Transactions B*, Vol.32, August, pp. 615-627, ISSN 1073-5615
- Matsuura, H.; Wang, C.; Wen, G. & Sridhar S. (2007). The transient stages of inclusion evolution during Al and/or Ti additions to molten iron. *ISIJ International*, Vol.47, No.9, pp. 1265-1274, online ISSN 1347-5460
- Mazumdar, D. & Guthrie, R. I. L. (1999). The Physical and Mathematical Modelling of Continuous Casting Tundish Systems. *ISIJ International*, Vol.39, No.6, pp. 524-547, online ISSN 1347-5460
- Nuspl, M.; Wegscheider, W.; Dekkers, R.; Angeli, J.; Posch, W. & Mayr, M. (2004). Qualitative and quantitative determination of micro-inclusions by automated SEM/EDX analysis. *Analytical and Bioanalytical Chemistry*, Vol.379, No.4, pp. 640-645, online ISSN 1618-2650
- Rocabois, P.; Lehmann, J.; Gatellier, C. & Teres, J. P. (2003). Non-metallic inclusions entrapment by slags: laboratory investigation. *Ironmaking & Steelmaking*, Vol.30, No.2, pp. 95-100, ONLINE ISSN 1743-2812
- Sahai, Y. & Emi, T. (1996). Melt Flow Characterization in Continuous Casting Tundishes. *ISIJ International*, Vol.36, No.6, pp. 667-672, online ISSN 1347-5460
- Solorio-Diaz, G.; Morales, R. D.; Palafox-Ramos, J. & Ramos-Banmderas, A. (2005). Modeling the effects of a swirling flow on temperature stratification of liquid steel and flotation of inclusions in a tundish. *ISIJ International*, Vol.45, No.8, pp. 1129-1137, online ISSN 1347-5460
- Tanaka, H.; Nishihara, R.; Miura, R.; Tsujino, R.; Kimura, T.; Nishi, T. & Imoto T. (1994). Technology for Cleaning of molten steel in tundish. *ISIJ International*, Vol.34, No.11, pp. 868-875, online ISSN 1347-5460
- Van Ende, M-A.; Guo, M.; Dekkers, R.; Burty, M.; Van Dyck, J.; Jones P. T.; Blanpain, B. & Wollants, P. (2009). Formation and evolution of Al-Ti oxide inclusions during secondary steel refining. *ISIJ International*, Vol.49, No.8, pp. 1133-1140, online ISSN 1347-5460
- Xie, D.; Garlick C. & Tran, T. (2005). The wear of tundish stopper refractories by inclusion slags. *ISIJ International*, Vol.45, No.2, pp. 175-182, online ISSN 1347-5460





*Edited by Igor V. Minin and Oleg V. Minin*

This book is planned to publish with an objective to provide a state-of-art reference book in the area of computational fluid dynamics for CFD engineers, scientists, applied physicists and post-graduate students. Also the aim of the book is the continuous and timely dissemination of new and innovative CFD research and developments. This reference book is a collection of 14 chapters characterized in 4 parts: modern principles of CFD, CFD in physics, industrial and in castle. This book provides a comprehensive overview of the computational experiment technology, numerical simulation of the hydrodynamics and heat transfer processes in a two dimensional gas, application of lattice Boltzmann method in heat transfer and fluid flow, etc. Several interesting applications area are also discusses in the book like underwater vehicle propeller, the flow behavior in gas-cooled nuclear reactors, simulation odour dispersion around windbreaks and so on.

Photo by Eureka\_89 / iStock

**IntechOpen**

